Theoretical investigations of charge and spin transport through superconducting tunnel junctions



DISSERTATION

ZUR ERLANGUNG DES DOKTORGRADES DER NATURWISSENSCHAFTEN
(Dr. rer. nat.)

DER FAKULTÄT FÜR PHYSIK

DER UNIVERSITÄT REGENSBURG

vorgelegt von

Andreas Costa
aus Viechtach

im Jahr 2020

Das Promotionsgesuch wurde eingereicht am:	22.10.2020
Das Promotionskolloquium fand statt am:	09.03.2021
Die Arbeit wurde angeleitet von:	Prof. Dr. Jaroslav Fabian

Prüfungsausschuss:

Vorsitzender:	Prof. Dr. Dieter Weiss
1. Gutachter:	Prof. Dr. Jaroslav Fabian
2. Gutachterin:	Prof. Dr. Milena Grifoni
Weiterer Prüfer:	Prof. Dr. Vladimir Braun

Abstract

Superconducting tunnel junctions exhibit not only extraordinary physical phenomena, but simultaneously provide unique possibilities to generate and control spin-polarized supercurrents as the essential ingredients for numerous modern technologies, especially for recent quantum-computing concepts. Bringing superconductivity together with its nominally antagonistic ferromagnetic phase gives rise to particularly rich physics that might soon facilitate additional functionalities in spintronics applications. Prominent examples cover magnetic Josephson junctions, in which the competing superconducting and ferromagnetic properties can add intrinsic π-phase shifts to the junctions' characteristic sinusoidal current-phase relations and thereby even reverse the directions of the Josephson currents. Implementing a reliable control knob between these π- and the junctions' initial 0-states might mark the first great step towards the realization of quantum bits in prospective computers. The interplay between superconductivity and ferromagnetism gets most intriguing in tunnel regions that furthermore host (interfacial) spin-orbit couplings. The resulting competition between the ferromagnetic exchange and the spin-orbit interactions has unambiguous signatures in spectroscopy and electrical transport – mostly due to long-range superconducting proximity effects that induce triplet superconducting correlations even in strongly spin-polarized ferromagnets –, and is moreover expected to support topological superconductivity and emergent Majorana states.

In this dissertation, we will perform systematic and comprehensive microscopic model calculations for various superconducting magnetic tunnel geometries, allowing us to theoretically study the ramifications of combining superconductivity with magnetic exchange and spin-orbit couplings in real devices. The work's main directions cover conductance simulations of ferromagnet/superconductor multilayer junctions, bound state and Josephson current analyses of different classes of magnetic Josephson contacts, and finally a profound discussion of transverse Hall supercurrent phenomena. Paying special attention on unraveling clear fingerprints of the investigated effects and practical feasibility, our results might boost subsequent experimental efforts and contribute to gain more insight into the surprising physics of superconducting magnetic tunnel configurations.

Zusammenfassung der Arbeit

Supraleitende Tunnelkontakte zeichnen sich nicht nur durch außergewöhnliche physikalische Eigenschaften aus, sondern ermöglichen zugleich auf einzigartige Weise, spin-polarisierte Suprastöme und somit die grundlegenden Bausteine modernster Technologien, wie sie beispielsweise aktuelle Quantencomputer-Konzepte erfordern, effektiv zu erzeugen und zu steuern. Beeindruckende physikalische Effekte, die Spinelektronik-Anwendungen bald durch zusätzliche Funktionsvielfalt bereichern könnten, treten durch die Kombination von Supraleitfähigkeit mit ihrer eigentlich stark gegensätzlichen ferromagnetischen Ordnung zu Tage. Zu den bekanntesten Beispielen hierfür zählen magnetische Josephson-Kontakte, in denen die gegensätzlich wirkenden supraleitenden und ferromagnetischen Eigenschaften die charakteristischen Strom-Phase-Relationen der Kontakte um eine intrinsische Phasenverschiebung von π ergänzen und somit schließlich die Richtungen der fließenden Josephson-Ströme invertieren. Eine verlässliche Umschaltmöglichkeit zwischen jenen π- und den anfänglichen 0-Zuständen der Kontakte zu etablieren, könnte den ersten großen Schritt hin zu Quantenbits in zukünftigen Computern markieren. Das Zusammenbringen von Supraleitung und Ferromagnetismus vermag besonders in jenen Bereichen von Tunnelkontakten zu faszinieren, in welchen darüber hinaus Spin-Bahn-Kopplungseffekte (an den Grenzflächen) auftreten. Das daraus resultierende Zusammenspiel zwischen der ferromagnetischen Austausch- und den Spin-Bahn-Wechselwirkungen führt nicht nur zu eindeutigen Modifikationen von Spektroskopie- und elektrischen Transporteigenschaften – vor allem durch langreichweitige supraleitende Proximity-Effekte beeinflusst, die sogar supraleitende Triplett-Korrelationen in stark spin-polarisierten Ferromagneten hervorrufen –, sondern vermutlich auch zu topologischer Supraleitung und damit einhergehenden Majorana-Zuständen.

Im Rahmen der vorliegenden Dissertation werden wir für verschiedenste supraleitende magnetische Tunnelanordnungen systematische und umfassende mikroskopische Modellrechungen durchführen, um letztendlich theoretisch die Auswirkungen von kombinierter Supraleitfähigkeit, magnetischer Austauschwechselwirkung und Spin-Bahn-Kopplungseffekten in realistischen Systemen zu untersuchen. Die Arbeit befasst sich vornehmlich mit der Simulation von Leitfähigkeiten mehrschichtiger Ferromagnet/Supraleiter-Kontakte, mit der Analyse von gebundenen Zuständen und Josephson-Strömen in unterschiedlichen magnetischen Josephson-Kontakten, und schlussendlich mit einer tiefgreifenden Diskussion von transversalen Hall-Suprastömen. Wir werden den beschriebenen Effekten eindeutige Erkennungsmerkmale zuordnen und stets die experimentelle Realisierbarkeit unserer Modellstudien im Auge behalten, so dass unsere Ergebnisse insgesamt zukünftige experimentelle Anstrengungen bereichern und zu einem tieferen Verständnis der erstaunlichen physikalischen Charakteristika von supraleitenden magnetischen Tunnelsystemen beitragen können.

Contents

Front matter

A short note to the reader . . . . . **xi**

Acronyms . . . . . **xiii**

Physical constants . . . . . **xvii**

Part I. Motivation and theoretical basics

1 Introduction and Overview **3**

2 Theoretical basics **11**
2.1 Superconductivity 11
2.1.1 Phenomenology and superconducting materials 12
2.1.2 Macroscopic picture – Ginzburg-Landau theory 20
2.1.3 Microscopic picture – BCS theory 25
2.2 Ferromagnetism – Stoner band model 32
2.3 Spin-orbit coupling in solids 37

Part II. Conductance features of superconducting junctions – from the BTK to the OTBK model

3 Tunneling conductance features of ballistic F/F-S junctions **43**
3.1 Theoretical description 45
3.1.1 Bogoljubov-de Gennes scattering states 45
3.1.2 Differential tunneling conductance – BTK model 51
3.2 Discussion of results for F/S junctions 54
3.2.1 Semiclassical approach of de Jong and Beenakker 54
3.2.2 Numerical results 57
3.3 Discussion of results for F/F-S junctions 61
3.3.1 Chandrasekhar-Clogston limit 61
3.3.2 Numerical results 62
3.4 Short summary 64

4 Subharmonic conductance gap structure in ballistic Josephson junctions 67
4.1 Physical origin of the subharmonic conductance gap structure 71
4.2 Ballistic S/F/S Josephson junctions 75
4.2.1 Theoretical description – OTBK model 75
4.2.2 Discussion of results 81
4.2.2.1 Self-consistent electron distribution functions 81
4.2.2.2 Tunneling current and subharmonic conductance oscillations 83
4.2.2.3 Excess current 86
4.3 Ballistic Al/Ni/Ga Josephson junctions – theory *vs.* experiment 88
4.3.1 Theoretical description – OTBK model *vs.* KWANT simulations 89
4.3.2 Discussion of results and comparison with experiment 92
4.3.2.1 Ferromagnetic exchange effects and limits of OTBK modeling 92
4.3.2.2 Signatures of interfacial triplet pairing 97
4.4 Short summary 99

PART III. DC Josephson effect in magnetic junctions

5 AC and DC Josephson effects – a compact overview 103

6 DC Josephson effect in ballistic S/F/S-like junctions 111
6.1 Microscopic origin of Josephson currents – Andreev bound states 115
6.2 Ballistic S/F/S Josephson junctions with interfacial spin-orbit coupling 120
6.2.1 Theoretical description 120
6.2.1.1 Bogoljubov-de Gennes scattering states 122
6.2.1.2 Josephson current – Furusaki-Tsukada approach 124
6.2.2 Discussion of results 127
6.2.2.1 Geometrical control of 0-π transitions 127
6.2.2.2 Electrical control of 0-π transitions 130
6.2.2.3 Magnetic control of 0-π transitions 133
6.3 Ballistic S/F/I/F/S Josephson spin-valve junctions 137
6.3.1 Theoretical description 140
6.3.1.1 Bogoljubov-de Gennes scattering states 141
6.3.1.2 Josephson current 143
6.3.1.3 Normal-conducting junction regime 144
6.3.2 Discussion of results 144
6.3.2.1 General features 145
6.3.2.2 Magnetic control of 0-π transitions 150
6.3.2.3 Spin-triplet Cooper pair Josephson currents 152
6.4 Short summary 154

7 Bound states and DC Josephson current in ballistic S/F-I/S junctions 155
7.1 Theoretical description 158
7.1.1 Bogoljubov-de Gennes scattering states 159
7.1.2 Josephson current – bound state approach 162
7.2 Discussion of results for singlet pairing 166
7.2.1 Bound state spectrum 166
7.2.2 Josephson current 171
7.2.3 Ground-state phase transition – a qualitative picture 174
7.2.4 Connection between bound states and 0-π transitions 175
7.2.5 Impact of Rashba spin-orbit coupling inside the superconductors 177
7.3 Discussion of results for triplet pairing 179
7.3.1 Bound state spectrum 179
7.3.2 Josephson current 183
7.4 Short summary 185

PART IV. Anomalous Hall and spin Hall effects in superconducting junctions

8 Tunneling anomalous Hall and spin Hall effects in ballistic F/S junctions 189
8.1 Theoretical description 193
8.2 Skew specular and Andreev reflection picture 194
8.3 Tunneling anomalous Hall effect conductances 198
8.3.1 Generalized BTK conductance formula 198
8.3.2 Discussion of results 199
8.3.2.1 Magnetization angle dependence 199
8.3.2.2 Bias voltage dependence 203
8.4 Transverse supercurrent responses 204
8.4.1 Generalized Furusaki-Tsukada supercurrent formula 205
8.4.2 Discussion of results 205
8.5 Tunneling spin Hall effect conductances 206
8.5.1 Generalized BTK spin conductance formula 207
8.5.2 Discussion of results 207
8.6 Short summary 208

9 Anomalous Josephson Hall and spin Hall effects in ballistic S/F-I/S junctions 211
9.1 Theoretical description 212
9.2 Extended skew Andreev reflection picture 214
9.3 Anomalous Josephson Hall effect currents 216
9.3.1 Generalized Furusaki-Tsukada supercurrent formula 217
9.3.2 Discussion of results 217
9.4 Microscopic bound state picture 220
9.4.1 Bound state-based supercurrent formula 221
9.4.2 Discussion of results 221
9.5 Anomalous Josephson spin Hall effect currents 225
9.5.1 Generalized Furusaki-Tsukada spin supercurrent formula 227
9.5.2 Discussion of results 228
9.6 Spin-charge-current cross ratios 231
9.7 Short summary 233

PART V. Conclusions and Outlook

10 Conclusions and Outlook **237**

APPENDIX

A Step-by-step OTBK modeling of Al/Ni/Ga Josephson junctions **245**

B Matsubara Green's function of S/F/S Josephson junctions **251**

C BTK-like conductance formula for N/buffer region/N junctions **259**

D Bound state wave functions for S/F-I/S Josephson junctions **263**

E Transverse BTK conductance and Furusaki-Tsukada supercurrent formulas for F/S junctions **273**

F Transverse Furusaki-Tsukada and bound state supercurrent formulas for S/F-I/S Josephson junctions **283**

BACK MATTER

References . . . . . **xxi**

Curriculum Vitae . . . . . **xlvii**

List of Publications . . . . . **xlix**

Acknowledgments . . . . . **li**

Front matter

A short note to the reader

Investigating transport through superconducting junctions offers basically an infinitely extendible area of research. Thanks to the great progress in microfabrication techniques, particularly during the last decades, even intricate junction configurations can be experimentally realized with an astonishingly high quality nowadays and the systems' transport properties can be reliably measured. But such experimental advance always comes along with new challenges for theory. Already metal/superconductor multilayer systems can be tailored in so many different ways that theorists continuously need to work on adapting and extending earlier formulated descriptions to capture all possible set-ups and make (at best) precise predictions what one could expect in following experiments.

From that point of view, this thesis has been turned into a self-contained handbook that reviews and extends several state-of-the-art approaches to theoretically quantify current flows through different kinds of metal (ferromagnet)/superconductor junctions. The generalizations to cover more complicated cases and study novel transport phenomena are done step by step, illustrating all important details in a pedagogical way. Apart from that, the thesis simultaneously offers an introduction into the general textbook physics associated with superconductivity and ferromagnetism right at its beginning. The decision to dive thus deeply into the physics of superconducting tunnel junctions was mostly made in order to support future students or colleagues, who have not yet worked on related projects and need to immerse themselves into this field of research.

The author apologizes to the reader in case he or she is more interested in the presentation and discussion of the obtained results than in the underlying formalisms. All chapters got thoroughly divided into subsections, distinguishing between the more general methodical parts on the one and the comprehensive analyses of the outcomes on the other hand. The experienced reader could therefore scan the methodology more superficially and mostly focus on the presented physics.

Acronyms

The subsequent list summarizes all acronyms that appear throughout this thesis (in alphabetical order). To avoid confusion while reading, we use only the most common ones in the main text. All other acronyms were primarily introduced to shorten the presented figures' captions, where their meaning becomes additionally clear from the context.

A

AC	alternating current
AJHE	anomalous Josephson Hall effect
AR	Andreev reflection

B

BCS	Bardeen-Cooper-Schrieffer
BTK	Blonder-Tinkham-Klapwijk

C

CODATA	Committee on Data for Science and Technology

D

DC	direct current
DOS	density of states

F

F	ferromagnet
FBCP	finite-bias conductance peak
F-I	ferromagnetic insulator
FFLO	Fulde-Ferrell-Larkin-Ovchinnikov
F-S	ferromagnetic superconductor
F/F-S	ferromagnet/ferromagnetic superconductor
F/N	ferromagnet/normal metal
F/S	ferromagnet/superconductor
F/buffer region/F	ferromagnet/buffer region/ferromagnet

	F/I/F	ferromagnet/insulator/ferromagnet
	F/N/F	ferromagnet/normal metal/ferromagnet
G		
	GMR	giant magnetoresistance
I		
	I	insulator
J		
	JTMR	Josephson tunneling magnetoresistance
K		
	KPM	KWANT's kernel polynomial method
	KWANT	Python package for quantum transport simulations
L		
	LHC	Large Hadron Collider
M		
	MAAR	magnetoanisotropic Andreev reflection
	MAJC	magnetoanisotropic Josephson current
	MIT	Massachusetts Institute of Technology
	MRAM	magnetic random access memory
	MRI	magnetic resonance imaging
N		
	N	normal metal
	NIST	National Institute of Standards and Technology
	NMR	nuclear magnetic resonance
	N/F-S	normal metal/ferromagnetic superconductor
	N/N	normal metal/normal metal
	N/S	normal metal/superconductor
	N/buffer region/N	normal metal/buffer region/normal metal
	N/F/N	normal metal/ferromagnet/normal metal
	N/N/N	normal metal/normal metal/normal metal
	N/F/I/F/N	normal metal/ferromagnet/insulator/ferromagnet/normal metal

O

OTBK	Octavio-Tinkham-Blonder-Klapwijk

S

S	superconductor
SMC	semiconductor
SOC	spin-orbit coupling
SQUID	superconducting quantum interference device
SR	specular reflection
STM	scanning tunneling microscopy
STS	scanning tunneling spectroscopy
S/F/S	superconductor/ferromagnet/superconductor
S/F-I/S	superconductor/ferromagnetic insulator/superconductor
S/I/S	superconductor/insulator/superconductor
S/metal/S	superconductor/metal/superconductor
S/N/S	superconductor/normal metal/superconductor
S/F/I/F/S	superconductor/ferromagnet/insulator/ferromagnet/superconductor

T

T	transmission as an electron(like) or hole(like quasiparticle)
TAHE	tunneling anomalous Hall effect
TAMR	tunneling anisotropic magnetoresistance
TE	transmission as an electron(like quasiparticle)
TH	transmission as a hole(like quasiparticle)
TMR	tunneling magnetoresistance
TSHE	tunneling spin Hall effect

Y

YSR	Yu-Shiba-Rusinov

Physical constants

In this thesis, we use the following notation for fundamental physical constants. The constants' values (third column) were taken from the National Institute of Standards and Technology (NIST) online database [1], in accordance with the latest 2018 Committee on Data for Science and Technology (CODATA) recommendation.

Description	Symbol	Value
Bohr magneton	μ_B	$9.274\,010\,0783 \times 10^{-24}\,\mathrm{J\,T^{-1}}$
Boltzmann's constant	k_B	$1.380\,649 \times 10^{-23}\,\mathrm{J\,K^{-1}}$
Elementary charge	e	$1.602\,176\,634 \times 10^{-19}\,\mathrm{A\,s}$
Free-electron mass	m_e	$9.109\,383\,7015 \times 10^{-31}\,\mathrm{kg}$
Planck's constant	h	$6.626\,070\,15 \times 10^{-34}\,\mathrm{J\,s}$
Reduced Planck's constant	$\hbar = h/(2\pi)$	$1.054\,571\,817 \times 10^{-34}\,\mathrm{J\,s}$
Speed of light (vacuum)	c	$299\,792\,458\,\mathrm{m\,s^{-1}}$
Vacuum permeability	μ_0	$1.256\,637\,062\,12 \times 10^{-6}\,\mathrm{N\,A^{-2}}$

Part *I*

Motivation and theoretical basics

Chapter 1

Introduction and Overview

Modern information technologies' needs to process rapidly growing amounts of data in real time bring along great challenges for industrial research to continuously develop more powerful and, especially during these days in which protecting the environment becomes more important than ever before, less energy-consuming devices. Recent smartphones document the technical advance achieved within the past decades in the perhaps most impressive manner, as a direct comparison with one of the early available portable personal computers illustrates (see Fig. 1.1). Being light and compact "mini-computers" that even fit into tiny pockets of a jacket, smartphones have soon evolved into indispensable tools in our fast-moving world, helping us to stay connected with others at any place and occasion.

The key building blocks in the electrical circuits of present-day personal computers and smartphones are semiconductor transistors, yet mostly based on silicon. Each of them controls the electrical current through individual elements of one circuit and can therefore activate single functionalities of the device, depending on whether current flows through the related part of the circuit or not. Thanks to tremendous activities in academic and industrial research, the microfabrication processes of transistors have been considerably improved and the number of transistors that can be integrated into each electrical circuit has dramatically increased, roughly according to Moore's law [2] predicting the doubling of the number of transistors per chip (circuit) about every two years. More transistors per circuit enable not only designing applications that offer additional, so far unprecedented, features, but simultaneously noticeably decrease the devices' size and manufacturing costs. The 22 nm 3-D tri-gate silicon transistor generation [3], launched by Intel in 2011, certainly set a new milestone. In comparison with Intel's first 4004 transistors [3], entering the market back in 1971, the 22 nm tri-gates run more than 4 000 times as fast, use about 5 000 times less energy, while their manufacturing price has concurrently dropped by a factor of roughly 50 000. Recent Intel quad core computer processors can host more than 1.48 billions tri-gate transistors [3] – an unimaginably huge number.

However, the miniaturization of transistors will not continue forever and Moore's law could face serious (quantum-mechanical) limitations [4]. Engineers might soon reach a point at which the size of transistors can no longer be remarkably reduced without performance losses and novel, fundamentally different, concepts are required. One of the most auspicious perspectives aims at not only exploiting electric charge, as it is the case in transistors up to now, but likewise the flowing electrons' intrinsic angular momentum degree of freedom, called spin, to store additional information and enhance devices' functionalities. Combining spin and conventional electronics might provide the basis for highly efficient applications, and founds a rapidly extending research field [5–8], which was termed *spin electronics* or *spintronics* for short. In fact, all of us are probably already using the first commercially available spintronics application every single day. The read heads of state-of-the-art computer hard disks employ tunneling magnetoresistance (TMR) [9] and giant magnetoresistance (GMR) [10, 11] effects – i.e., the fact that the electrical resistance of spin-valve junctions consisting of two either parallel or antiparallel magnetized and by a thin spacer separated domains abruptly changes when switching the magnetizations' relative orientations – to write and read information. The storage capacity of GMR-based hard disks has



Fig. 1.1: Comparison between an early "Osborne Executive *portable* computer" from 1982 (left) and a modern "Apple iPhone" from 2007 (bottom right corner). The smartphone is 100 times lighter and 500 times smaller in size than the personal computer (and even 10 times cheaper), while its clock frequency, roughly determining how many single tasks an electrical device can perform within one second, exceeds the personal computer's by more than a factor of 100. Taken from Ref. [17].

dramatically increased from 16.8 GB in 1997 to more than 1 TB = 1 000 GB ten years later [12], and more recent magnetic random access memory (MRAM) technologies [13–16] utilizing TMRs might become even more powerful.[1]

Pioneering studies of spin-polarized electrical transport, which can be seen as the actual roots of spintronics, date back to times far before TMR and GMR phenomena were investigated. Already initial experiments [18–22] revealed that connecting two normal-conducting electrodes by means of thin ferromagnetic insulators or ferromagnetic semiconductors polarizes an at first spin-unpolarized current. Shortly afterwards, Meservey and Tedrow initiated similar transport measurements on superconducting ferromagnet/insulator/superconductor junctions [23–25] and demonstrated that tunneling currents can remain spin-polarized even outside the ferromagnet. Mapping such contacts' unique conductance characteristics to theory provides still one of the most reliable ways to quantify ferromagnets' spin polarization. Nevertheless, the experimental observations of the TMR and GMR in ferromagnetic spin valves has drawn researchers' attention mostly to purely metallic [5, 7, 8] and later additionally to semiconductor-based spintronics concepts [26–28]. Semiconductors are particularly appealing since they often inherently possess rather strong spin-orbit couplings (SOCs) that serve as another key ingredient for controlling and manipulating electron spins. In that spirit, Datta and Das [29] proposed to build a *spin* field-effect transistor, linking its ferromagnetic source and drain by an effectively one-dimensional semiconducting channel whose SOC can be tuned adding a top gate. The magnetic source injects then spins into the semiconductor that can finally all enter the drain if their spin orientations are not altered while traveling through the semiconductor (assuming that the magnetizations of source and drain point along the same directions), yielding maximal current flow and indicating the transistor's *ON*-state. Increasing the top-gate voltage locally enhances the SOC strength inside the semiconductor and the spins start to (notably) precess around the perpendicular spin-orbit fields. More spin precession randomizes the electrons' spin orientations and remarkably suppresses the amount of electrons with a spin parallel to the drain's magnetization that

[1] For more information, visit `https://www.mram-info.com/tags/companies/freescale`.

accumulate in the drain. As a result, the measured current becomes heavily damped and the transistor gets switched *OFF*. Many groups around the world are nowadays working on closely related semiconductor spintronics concepts [26–28], highlighting the great potential this field might offer for commercial purposes one day.

Practical realizations of spintronics applications naturally need to meet three essential requirements: (1) effective injection of spins into the system, (2) optimal (usually short) spin-relaxation rates so that polarized spins can carry the information far enough through the system, and (3) reliable detection of "arriving" spins. Aronov predicted already in 1976 [30] that the flow of spin-polarized currents from the ferromagnetic into the normal-metal electrode of ferromagnet/normal metal (F/N) junctions generates a nonequilibrium spin distribution in the normal metal and may therefore be used to efficiently inject spins into initially nonmagnetic materials [31]. Experimentally verified by Johnson and Silsbee a couple of years later [32, 33], this electrical current-based approach has become the preferred method to inject spins into metals. However, nonequilibrium accumulation of spins can also be created using purely optical techniques [34–38], such as optical orientation or optical pumping.[2] Of particular interest for optical spin injection are again semiconductors, in which the in-built SOC splits the electronic band structure into its rather intricate fine structure and optical selection rules allow for various optical transitions between states belonging to different angular momenta. Irradiating the sample with circularly polarized light favors then either electron transitions into spin-up or spin-down levels – depending on the light's helicity – and gives eventually rise to a net spin polarization.

After spins were injected into a certain material, it is of great importance that they can be efficiently manipulated, e.g., by means of tuning applied electric fields, and travel sufficiently far through the sample. In a real solid-state environment, SOC phenomena and momentum relaxation through impurity scattering will always dramatically limit the maximal lifetimes of spins before they finally relax (dephase) [39–41] and the encoded information gets lost. Typical spin lifetimes can nowadays cover the whole range between pico- and microseconds, although nanosecond lifetimes are still most common [5].

Reading out the spin-encoded information finally requires reliable spin detection methods. Recent spin detectors often exploit the Silsbee-Johnson spin-charge coupling [32, 42] in F/N contacts – basically the inverse of the aforementioned electrical spin injection process. Nonequilibrium spin populations within the normal metal cause an electron current flow inside the proximitized ferromagnet that can be electrically detected. Other possibilities to detect nonequilibrium spins include the reversal of the optical spin orientation techniques [34–38] – spin-polarized electrons in semiconductors recombine with holes and emit circularly polarized light with characteristic helicity –, spin (transfer)-torque phenomena [43, 44] – essentially referring to the transfer of spin-polarized current-carrying electrons' angular momentum to ferromagnetic layers, eventually switching the ferromagnet's magnetization even in the absence of external magnetic fields –, or utilizing the unique TMR and GMR spin-valve effects.

Considering all those diverse prerequisites that one has to fulfill to engineer efficient and powerful mass-market spintronics applications, superconducting systems have recently attracted enormous interest. Electrons in a superconductor naturally condense into the superconducting condensate that carries the supercurrent and moreover alters the material's band structure in a remarkable manner [47, 48]. As one consequence, unpaired quasiparticle excitations in superconductors are only allowed at sufficiently large energies (to overcome the gap) and are not pure electron or hole excitations, but rather consist of weighted superpositions of both. At energies close to the superconducting gap's edge, excitations contain equal electronlike and holelike parts, and behave therefore to some extent like chargeless particles. Since their group velocities simultaneously notably diminish, these quasiparticles are only subject

[2] Optical orientation and optical pumping basically describe the same physics. Some authors [5] prefer to use the first term in connection with spin polarization of minority and the second for majority charge carriers (i.e., electrons or holes in doped semiconductors).

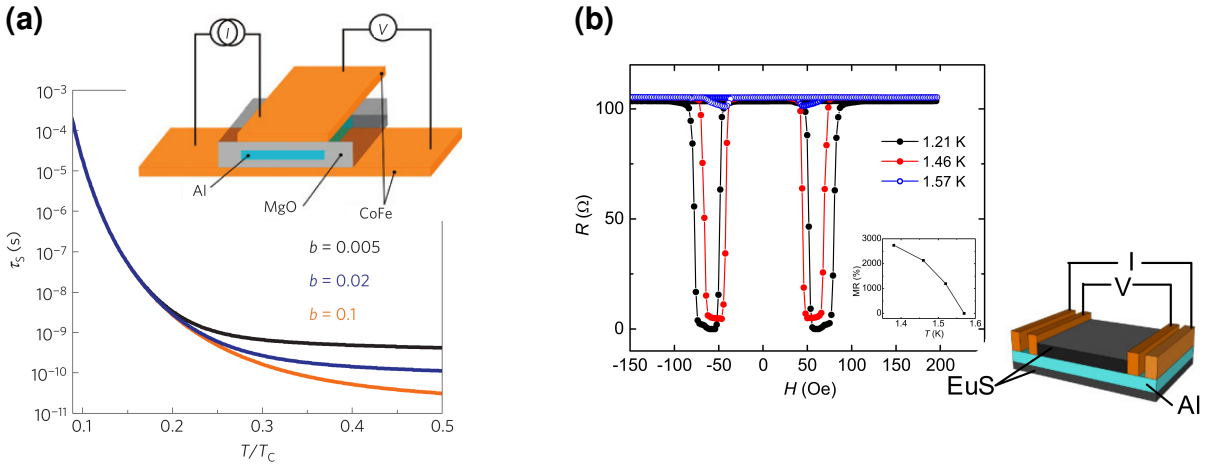


Fig. 1.2: Selection of some outstanding research highlights in the field of superconducting spintronics. **(a)** Theoretical extraction of huge spin lifetimes τ_s (for various SOC strengths b) from experimentally observed TMR oscillations in superconducting aluminum using MgO tunnel spin injectors (see illustration). Adapted from Ref. [45]. **(b)** Measured electrical resistance R of a superconducting EuS/Al/EuS spin-valve geometry (see illustration) as a function of the applied external magnetic field H and at different temperatures. The inset visualizes the calculated TMR ratio as a function of temperature T. The TMR starts to diverge at low temperatures, indicating that flipping the spin-valve magnetizations to their antiparallel alignments fully turns off superconductivity. Adapted from Ref. [46].

to extremely weak SOC scatterings and are expected to support large spin lifetimes when getting spin polarized (see Ref. [49] for a more comprehensive presentation of the theoretical background). Initial experimental studies by Yang *et al.* [45] could indeed generate nonequilibrium quasiparticle spin populations in superconducting aluminum and extract spin lifetimes that are about one million times larger than their normal-state counterparts [see Fig. 1.2(a)], certainly marking a milestone in the newly emerging field of *superconducting spintronics* [49–51].

Following works soon recognized the even greater potential superconductivity might offer when being combined with ferromagnetic regions in nanoscale tunnel junctions. Ginzburg unraveled already in the 1950s [52] – at a time when the physics of superconducting materials was still far from being well understood – that ferromagnetism and superconductivity are two strongly antagonistic phenomena and unprecedented coherence effects might occur at their interface. Ferromagnets' exchange interaction tends to align all electron spins parallel, forming a net macroscopic magnetic moment, and thereby breaks up superconducting Cooper pairs, whose electrons' spins are usually antiparallel to each other. Cooper pairs can nevertheless still survive in proximitized and only weakly polarized ferromagnetic regions through gaining spin-dependent kinetic energies that compensate the different exchange couplings the pairs' spin-up and spin-down electrons are exposed to. As a result, Cooper pairs acquire finite center-of-mass momenta and induce uniquely oscillating unpolarized singlet and spin-polarized (short-range) triplet superconducting pairing potentials inside the ferromagnet – the famous *Fulde-Ferrell-Larkin-Ovchinnikov (FFLO) phase* [53, 54]. Such pairing-potential oscillations lead, for example, to the striking current-reversing 0-π transitions in magnetic Josephson junctions [55, 56] and found a solid basis for several proposed quantum-computing concepts [57–64], encoding quantum bits in the distinct 0- and π-state regimes.

Several practically feasible possibilities to convert singlet and short-range triplet superconducting correlations into long-range triplet pairings, which can even penetrate strongly polarized ferromagnets over length scales in the micron range without having their spins relaxed, are investigated right now. Apart from complex magnetic arrays that "mix" Cooper pair electrons' spins in the desired manner [50, 65–73],

SOC phenomena are believed to play another fundamental role [74–79]. The interest in generating spin-polarized triplet supercurrents has dramatically increased after Keizer and coworkers [74] had measured sizable Josephson current flows through half-metallic CrO_2 links. Since the latter completely suppress the transport of singlet Cooper pairs, the experimental observations must undoubtedly be attributed to the successful generation of triplet currents and can be seen as their very first experimental demonstration. Many other groups around the world intensified their search for triplet supercurrents in various junction configurations, eventually ending in numerous outstanding works (see, e.g., Refs. [73] and [74], and many others).

Thanks to the overwhelming research activities into that direction, set-ups to generate long-range spin-polarized triplet supercurrents are already well within reach nowadays, providing the key input to tailor superconductor-based spintronics applications. Nevertheless, efficient manipulations of these currents inside real solid-state environments and their reliable detection to read out encoded information still require more thorough experimental and theoretical investigations before superconducting spintronics can really enter commercial devices. Besides the charge triplet supercurrents, their accompanying spin supercurrents (due to the Cooper pairs' nonzero spin polarization) might become particularly relevant. The experimental confirmation of such spin-triplet supercurrents is an extremely challenging task and much more intricate than the study of spin currents in normal-state systems. Theoreticians suggested that spin-triplet supercurrents can likewise manifest themselves in spin-transfer torques [80, 81] and characteristic magnetization dynamics [82–84]. Experimental probes are nonetheless highly nontrivial due to the complicated connection between spin supercurrents and the induced spin-transfer torques, and more sophisticated ways – ideally the normal-state Silsbee-Johnson's superconducting spin-charge coupling analog – need to be established. The same applies to more profound detection techniques for triplet supercurrents. One promising approach focuses on superconducting spin-valve junctions, coupling two massive ferromagnetic electrodes by means of an ultrathin superconducting spacer. Flipping the ferromagnets' magnetization directions from their initial configuration, in which they were oriented parallel to each other, to their antiparallel alignments alters then not only the spin valve's electrical resistance, but can simultaneously remarkably increase the junction's overall critical temperature and, in the extreme case, even completely switch off superconductivity [85, 86]. The latter becomes experimentally visible in terms of an extremely huge (nearly infinitely large) magnetoresistance, as observed by Li *et al.* [46] in Moodera's group at the Massachusetts Institute of Technology (MIT) [see Fig. 1.2(b)]. As a next step, integrating (strongly spin-polarized) spin valves into Josephson junctions [87, 88] could profoundly help to gain a deeper understanding and propose novel mechanisms that enable not only a customized control of (charge and spin) triplet supercurrents, but motivate at the same time more elaborate detection methods.

Structure of the thesis

This thesis complements the ongoing research activities and addresses some open questions in the field of charge and spin transport through superconducting tunnel junctions. In large parts of the work, we focus on the ramifications SOC phenomena might have for spin-polarized transport and present several distinct, experimentally feasible, possibilities to tune the (triplet) supercurrent responses arising in magnetic superconducting junction configurations. Furthermore, we unravel unique experimental fingerprints that can be exploited to unambiguously verify the presence of triplet supercurrents and give direct access to quantifying the strength of the involved SOCs, which reflects another important task for engineering systems that might potentially even host Majorana states.

The thesis got structured in the following way. Chapter 2 starts with a brief review of the basics regarding the superconducting and ferromagnetic phases, and gives a short introduction into SOC effects from a solid-state physics perspective. In Chaps. 3 and 4, we are concerned with biased ferromagnet/super-

conductor (F/S) and superconductor/ferromagnet/superconductor (S/F/S) Josephson junctions, studying these systems' most fundamental and striking tunneling conductance anomalies. After shortly reminding ourselves about Josephson effects in general (see Chap. 5), Chap. 6 is dedicated to a comprehensive analysis of SOC effects in simple S/F/S and more complex superconductor/ferromagnet/insulator/ferromagnet/superconductor (S/F/I/F/S) Josephson spin-valve junctions. To gain more physical insight, we consider a simplified superconductor/ferromagnetic insulator/superconductor (S/F-I/S) Josephson junction in Chap. 7 and relate earlier deduced transport features to such geometries' spectral bound state characteristics. Finally, we discuss the emergence of transverse charge and spin Hall currents in spin-active F/S and S/F-I/S junctions, and elaborate on an extensive microscopic physical picture capturing the proposed phenomena, in Chaps. 8 and 9, respectively. At the end of the thesis, Chap. 10 summarizes our main findings and sketches some promising perspectives for future research. Each chapter contains a profound and more specific motivation at its beginning that puts our work into a broader context and recapitulates the state-of-the-art knowledge in the corresponding area. The thesis comprises a detailed Appendix to sum up the most essential technical details of our calculations and guide subsequent studies.

Highlights of the thesis

Figure 1.3 summarizes some of the most rewarding findings presented within this thesis and might additionally navigate the reader through its different parts. In Chap. 3, we explore the tunneling conductance features of biased ferromagnet/insulating barrier/ferromagnetic superconductor junctions [see Fig. 1.3(a)]. Increasing the exchange splitting inside the superconductor splits each of the initially present conductance peaks at the gap edges (i.e., at bias voltages $eV = \pm|\Delta_S(0)|$) – which are usually ascribed to the striking Andreev reflection process occurring at metal/superconductor interfaces – into two distinct peaks as a direct evidence of the quasiparticle bands' spin splitting. Together with a pronounced conductance asymmetry with respect to reversals of the bias voltage's sign [emphasized by blue arrows in Fig. 1.3(a)], which stems from partially allowed transmissions into one of the aforementioned spin-split bands, such conductance peak splittings could allow for reliably quantifying ferromagnetic superconductors' Zeeman splittings.

Chapter 4 focuses on analyzing the (quasiparticle) conductance characteristics of biased S/F/S Josephson contacts [see Fig. 1.3(b)]. Electrons (holes) that approach one of the metal/superconductor interfaces can always undergo Andreev reflections and thus essentially traverse the metallic link (infinitely) many times. Such multiple Andreev reflections lead to unique subharmonic conductance oscillations, which remain clearly visible even at large values of spin polarization inside the metallic link, and nonzero excess currents. We discuss both of them and answer the question to which extent the obtained conductance-voltage relations are altered in more realistic (and already experimentally characterized) Al/Ni/Ga contacts.

Our studies in Chap. 6 reveal that interfacial SOCs, invariably arising at tunnel junctions' interfaces owing to the broken space-inversion symmetry, dramatically modify the Josephson current flows through S/F/S junctions [see Fig. 1.3(c)]. Apart from opening another experimentally promising way to manipulate current-reversing 0-π transitions via tuning the SOC strengths by means of an external gate, we identify marked magnetoanisotropies in the critical Josephson current (when rotating the ferromagnet's magnetization vector). These anisotropies are typically giant when compared to their earlier studied normal-state counterparts and get additionally enhanced close to 0-π transitions, providing vice versa another knob to control the latter through suitably aligning the ferromagnet's magnetization direction.

In Chap. 7, we thoroughly investigate the bound states that typically form around the nonsuperconducting link of S/F-I/S Josephson junctions [see Fig. 1.3(d)]. Besides the well-established Andreev bound states, magnetic ferromagnetic-insulator barriers let additional Yu-Shiba-Rusinov (YSR) states with unique

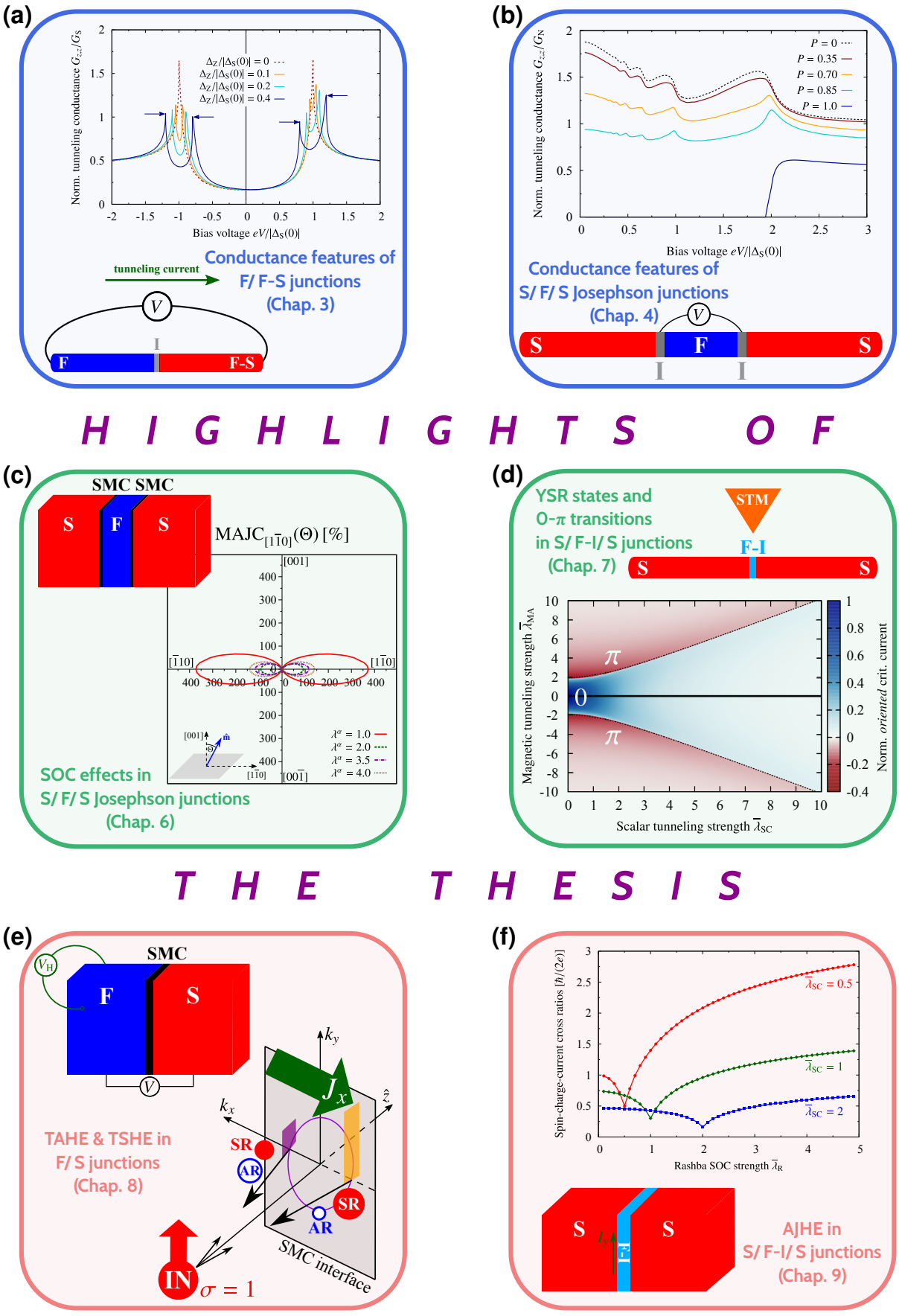


Fig. 1.3: Selection of research highlights presented within this thesis. More details can be found in the text and in the indicated chapters.

spectral and spin properties arise. We connect zero-energy crossings, accompanied by spin flips, of the latter to the emerging Josephson current reversals and thereby unravel the physical origin of 0-π transitions on the microscopic level.

Chapters 8 and 9 summarize our efforts to integrate anomalous Hall physics into superconducting F/S and S/F-I/S Josephson junctions, respectively [see Figs. 1.3(e) and 1.3(f)]. We justify that spin- and momentum-dependent skew reflections (transmissions) at (through) the junction interfaces cause transverse charge imbalances and therefore measurable Hall current flows. It is again the peculiar Andreev reflection process in superconducting systems that makes the effects sizable when compared to usual normal-conducting contacts. We compute not only the charge Hall (super)currents themselves, but additionally also their spin Hall counterparts that originate from the formation of spin-polarized triplet Cooper pairs, and extract the universal spin-charge-current cross ratios that might be exploited in subsequent experimental works to access specific junctions' interfacial SOC parameters. Finally, we extend our bound state analyses given in Chap. 7 and demonstrate that the discussed Hall physics is again closely related to the spectral characteristics of the forming bound states. To be more specific, we argue that SOC-controlled bound state asymmetries (with respect to the transverse wave vector) found the Hall currents' microscopic basis.

Chapter 2

Theoretical basics

Before investigating the unique transport characteristics of several junction configurations that all combine the nominally opposing superconducting and ferromagnetic phases in one and the same device, we have a brief look at the individual components and establish a common theoretical basis. For that purpose, this chapter is divided into three sections. Section 2.1 introduces the physics of superconductivity, starting from such materials' phenomenological properties, giving a compact overview about different material classes that have turned out to become superconducting, and finally summarizing the theoretical milestones on the way towards a comprehensive understanding of these fascinating materials. Regarding ferromagnetism, it is crucial for this thesis to be familiar with the *Stoner band model*, which is presented in Sec. 2.2. Interfacial spin-orbit fields are expected to offer a great tunability of our systems' transport properties. We complete this chapter therefore with a short section on the basics associated with spin-orbit interactions (see Sec. 2.3).

Depending on the reader's familiarity with the aforementioned subjects, the present chapter may be safely skipped at first and used for looking up unclear terms later on.

2.1 Superconductivity

The year 1911 has been profoundly exciting for physicists worldwide. It was not only the year in which Rutherford's discovery of the atomic nucleus [89] revolutionized our common imagination of how atoms – the tiniest units of all chemical elements forming the matter around us – look like in their deepest interior. At the same time, another important, and just as unexpected as mysterious, quantum state of certain solids was experimentally observed in a small laboratory in the Netherlands: the *superconducting state* [90–92]. Since then, superconductivity has evolved from an effect that was solely noticed by a small community of researchers in its early days into a well-recognized phenomenon with a wide range of applications not only in physics laboratories. Examples cover Josephson junction-based [93] *superconducting quantum interference devices (SQUIDs)* [94] that provide essential tools for detecting and reliably quantifying even extremely small magnetic fields down to 5×10^{-18} T with astonishingly high precision [95], or the generation of ultrahigh magnetic fields by superconducting coils. The latter found their way into our everyday life due to their indispensable usage in recent medical diagnostic techniques, such as magnetic resonance imaging (MRI) and nuclear magnetic resonance (NMR) machines [96], and their essential role in state-of-the-art research. An example for the scientific usage of superconducting coils is the Large Hadron Collider (LHC) particle accelerator [97], in which strong electromagnetic fields accelerate particles to energies that were completely unimaginable in the past (13 TeV collision energy [98] definitely marks a new record). To focus the particle beams on circular paths and enhance the probability for collisions, magnetic fields up to 8.3 T are required [97]. Those fields are generated driving huge electrical currents through the superconducting coils. If the coils would be normal conducting, such

currents would be subject to thus giant dissipation losses that a stable operation of the accelerator would be barely possible.

The following sections are intended to give a compact, but nonetheless comprehensive, introduction into the physics of superconductors. Inspired by the historical reviews in Refs. [99] and [100], Sec. 2.1.1 briefly recapitulates the main steps on the exciting way towards the discovery of superconductivity, before drawing a bow to superconductors' phenomenology. The section closes with a compact overview of various superconducting materials that have been discovered up to now. In order to cover the topic from a more theoretical point of view, we finally summarize two theoretical approaches dealing with superconductivity – the *macroscopic Ginzburg-Landau* on the one and the *microscopic Bardeen-Cooper-Schrieffer (BCS) theory* on the other hand – in Secs. 2.1.2 and 2.1.3, respectively. The BCS approach motivates the Bogoljubov-de Gennes description for spatially inhomogeneous superconducting systems, which will be our common starting point for (nearly) all analyses throughout this thesis.

2.1.1 Phenomenology and superconducting materials

Historical overview

Door meten tot weten. —
Through measurement to knowledge.

(Heike Kamerlingh Onnes)

Towards the end of the 19th century, well-known physicists all over the world put tremendous efforts into developing novel cooling mechanisms, which could eventually become effective enough to investigate physical systems' properties at *extremely low temperatures* (meaning in the single Kelvin range at that time). Although the experimental possibilities have been improved a lot as time went by, nobody clearly deduced yet how metals' electrical resistivity might behave as temperature continues to approach absolute zero. So far, there have just been speculations of recognized scientists, which all contradicted each other [99, 100]. While one group around Matthiessen believed in a small finite resistance, governed by impurities and defects in the probes, Lord Kelvin was convinced that the motion of the current-carrying electrons "freezes out" as temperature approaches absolute zero and the electrical conductivity completely vanishes at ultralow temperatures (implying infinitely large electrical resistivity). To make things even more complicated, there has been another community, including Dewar and Onnes, suggesting that metals' resistivity is mostly governed by the excitation of phonons. As less phonons can be excited at lower temperatures, the two researchers expected a continuous decrease of the resistivity with decreasing temperature down to the low-temperature regime, finally approaching zero resistivity exactly at zero temperature.

Dewar and Onnes were also among the ones most intensively struggling to liquefy hydrogen [99, 100], which could set a milestone for providing the efficient cooling mechanisms to experimentally resolve the puzzling question about metals' transport properties at low temperatures. While Dewar and Onnes have still been working on this highly complicated undertaking, Ramsay succeeded to isolate pure helium on earth [101]. Onnes immediately recognized the potential helium might offer and started to rebuild the set-up in his lab at Leiden University to rather liquefy helium instead of hydrogen. In 1911, he was then indeed the first realizing the desired low temperatures down to the 1 K-regime. Such temperatures undoubtedly indicated a new record at that time – a record for which Onnes will have been awarded the Physics Nobel Prize just two years later [102]. Shortly after Onnes's cryostat had been completed to be operated under stable conditions, a sample of mercury was the first probe to be investigated. Onnes decided to study mercury as it was one of just a few materials being available with a very high quality;

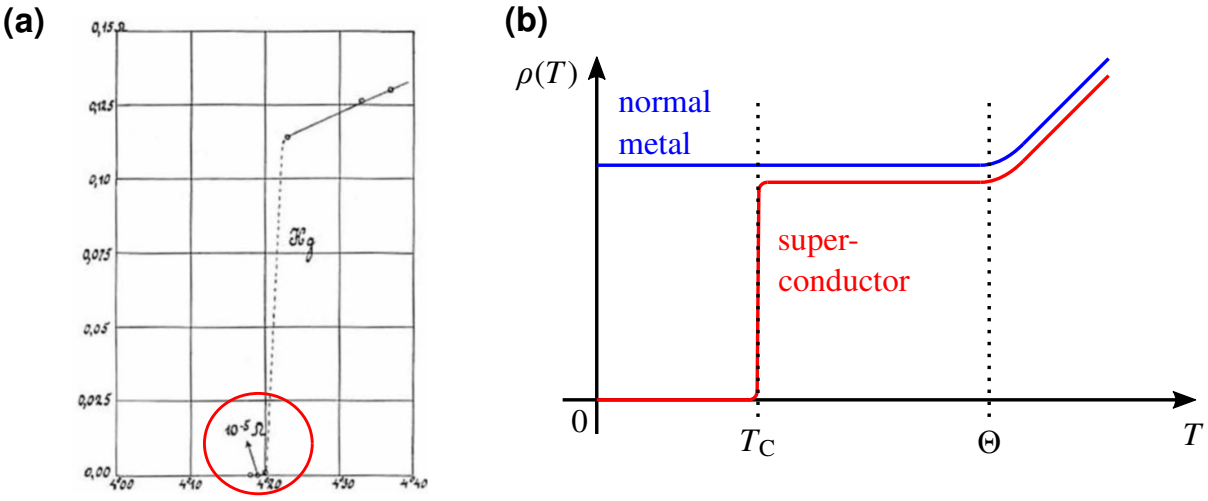


Fig. 2.1: (a) Original plot of the electrical resistance (in Ω) *vs.* temperature (in K) of a mercury sample from Onnes's lab book; adapted from Ref. [100]. The data was taken during a more advanced measurement in October 1911, after earlier attempts had revealed a puzzling behavior of the resistance at low temperatures. The transition between the superconducting and the normal phase (sudden resistance increase with increasing temperature) at a critical temperature of about 4.12 K is clearly visible (highlighted by the red circle). **(b)** Qualitative illustration of the nowadays expected electrical resistivity of a normal metal (blue curve) and a superconductor (red curve) as a function of temperature; Θ is the Debye temperature and T_C the superconductor's critical temperature. The origin of the curves is explained in the text. Note the convincing coincidence of the superconductor's curve with Onnes's early measurement.

too many defects or impurities could have had an unexpected influence on the outcomes. Already the first measurement that was carried out in April 1911 led to striking results. The probe's electrical resistivity seemed to drop immediately to a nearly immeasurably small value as the set-up's temperature was decreased below a certain temperature. When repeating the same measurement one month later, Onnes decided to use improved devices allowing for a greater accuracy. One of the greatest challenges he had to face was the issue of measuring *zero* electrical resistivity. Wheatstone bridge analyses, which are usually used to determine finite electrical resistivities, are not capable of doing that. Nevertheless, Onnes realized that the flow of electrical currents in loop geometries induces magnetic fields. The induced fields decay in a characteristic way on a well-defined time scale (after the current flow was turned off), from which one is able to extract the material's electrical resistivity. The concrete formulas applied for that are summarized, e.g., in Ref. [103]. The subsequent measurement could eventually confirm the previously taken data with a much greater accuracy. The mercury probe again showed a constantly decreasing finite electrical resistivity down to temperatures of about 4.12 K and a sudden jump to (nearly) zero resistivity as the temperature got just slightly decreased further. The original data from this measurement, taken down in Onnes's lab book, is depicted in Fig. 2.1(a). From the mentioned decay rate of the induced magnetic fields, Onnes estimated the probe's resistance at 3 K to be *less than 10^{-7} of the resistance of crystalline mercury extrapolated to 0 °C* [100]. Following his philosophy of life – *through measurement to knowledge* [99] – Onnes had discovered a material that perfectly conducts electricity without any disturbing dissipation effects (like heating) at sufficiently low temperatures. Due to this magical property, Onnes termed mercury to be a *superconductor* [90–92].

Further attempts on other probes in Onnes's lab revealed that superconductivity is not just a feature exclusively reserved for mercury samples; also lead and tin behave similarly, just the required temperature range turned out to be slightly different. Besides the great discovery of superconductivity, which has soon started to completely revolutionize our technical world, a look into Onnes's lab books reveals another

remarkable finding. While cooling down the helium cryostat, he was also the first scientist experimentally observing helium undergoing the transition from the normal into its superfluid phase. However, impressed by the superconducting characteristics of mercury, Onnes did not pay enough attention to look deeper into helium's superfluid phase.

Phenomenology of superconductors

As mentioned in the preceding paragraph, the initially most intriguing fingerprint of superconductors was their suddenly vanishing electrical resistivity at low enough temperatures. We will understand the physics behind and the consequences of that behavior in the following. Electrical currents in a normal metal are usually carried by electrons. After applying a bias voltage across the metal, the initially quite randomly moving electrons are accelerated in the arising electric field and start to propagate all along the same direction with characteristic drift velocities. The resulting spatial charge transfer along the conductor raises a nonzero electrical current, which uniquely increases with the electrons' drift velocities. Infinite drift velocities would, in principle, facilitate infinite current flows and thus perfect electrical conductivities (or equivalently, vanishing electrical resistivities). In real conductors, however, the electrons cannot reach arbitrarily large drift velocities since they are continuously scattered, e.g., at impurities, lattice defects, and phonons, dissipating some of their kinetic energy to the lattice and causing heating effects. These scatterings therefore limit the electron drift velocities and the maximal (dissipative) current flows, defining the upper (lower) boundary of metallic conductors' electrical conductivities (resistivities). According to Matthiessen's rule [104], all the different appearing scattering processes' individual resistivities add up and hence determine the material's *total* resistivity. Particularly at temperatures above the material-specific Debye temperature Θ, the continuous generation (and annihilation) of phonons causes strong electron-phonon scattering, which linearly suppresses the conductivity (indicating a linear increase in the resistivity) as temperature increases. With temperature decreasing below Θ, phonons play no longer an essential role and the metal's conductivity is mostly determined by its purity. Since real solids cannot be grown completely without any defects or impurities, there will always inevitably remain a small amount of electron-impurity scattering that causes dissipation and sets an upper limit to the maximally reachable conductivity. Therefore, one always expects a finite minimal electrical resistivity in normal metals that persists even at zero temperature. The characteristic variation of a normal metal's resistivity $\rho(T)$ as a function of temperature T is qualitatively illustrated by the blue curve in Fig. 2.1(b). On the other hand, the previous arguments hold for a superconductor just as long as the material stays in its normal-conducting state at temperatures above the transition temperature. This transition temperature is known as the *critical temperature* T_C nowadays and turned out to be a characteristic measure for the regarded superconducting material (e.g., $T_\mathrm{C} \approx 4.12\,\mathrm{K}$ in mercury). All the interesting physics associated with superconductivity appears below T_C, at which the material suddenly undergoes a phase transition from the normal to the superconducting state and its total electrical resistivity simultaneously sharply drops to zero; see the red curve in Fig. 2.1(b). Tracing this observation back to our scattering-based interpretation of electrical resistivity, we deduce that scattering must be completely absent in the superconducting state, i.e., superconductors indeed behave like *perfect conductors* below T_C and thus support fully dissipationless electrical transport. Nonetheless, it shall be noted that the microscopic physics in superconductors must be much more intricate since the supercurrent flows do, for example, not require any external bias voltage at all.

As some time went by, detailed investigations of various superconducting candidates could prove that perfect conductivity is not the only striking property of this material class. Indeed, more than 20 years after Onnes had discovered superconductivity, Meissner and Ochsenfeld [105] looked into the effects an applied magnetic field may have on the superconducting state. To exclude an impact stemming

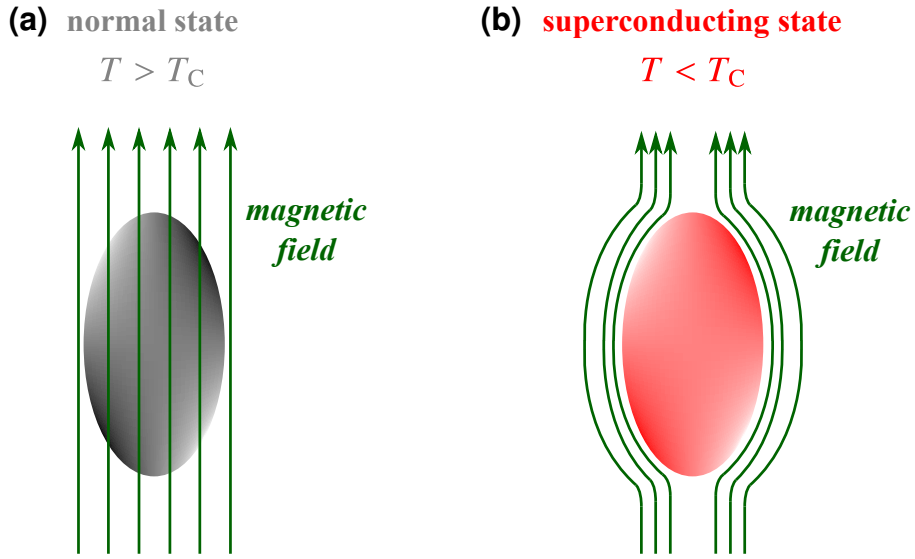


Fig. 2.2: Schematical illustration of the Meissner-Ochsenfeld effect. While the applied (external) magnetic field can fully penetrate the material in its normal state above T_C [see panel **(a)**], the magnetic field is completely expelled from the material's interior in the superconducting state below T_C [see panel **(b)**].

from induction effects, Meissner and Ochsenfeld started with a superconductor in its normal state (at temperatures above T_C) and brought the set-up into the external magnetic field $\mathbf{H}$. The field could fully penetrate the probe, just as one would also expect for a normal metal. Afterwards, the whole setting got cooled down to a temperature below T_C so that the superconductor finally entered its superconducting state. As soon as the probe got superconducting, the magnetic flux got immediately completely expelled from its interior. From what has been known so far, this observation was completely against expectation. Nevertheless, repeating the experiment with several other superconducting samples reproduced the very same characteristics. The only theoretical explanation for this so-called *Meissner-Ochsenfeld effect* relies on the fact that superconductors brought into an external magnetic field must generate an interior magnetization $\mathbf{M}$, which exactly compensates the applied external field so that the total magnetic field inside the material, $\mathbf{B} \propto \mathbf{H} + \mathbf{M}$, vanishes [see Fig. 2.2]. To sustain that "built-in magnetization", Onnes speculated about screening (super)currents that need to flow close to superconductors' surfaces. The Meissner-Ochsenfeld effect illuminated the second peculiarity of superconducting compounds for the first time: below T_C, superconductors turn into *perfect diamagnets* (owing to the magnetization $\mathbf{M} = -\mathbf{H}$, the susceptibility is $\chi_m = -1$, which is a typical property of perfect diamagnets).

A few years earlier, quite shortly after the initial discovery of superconductivity, already Onnes found strong indications that superconductivity and ferromagnetism are two actually opposing states of matter, and applying appropriately large magnetic fields to a superconductor may therefore fully destroy its superconducting property (Onnes did not yet know about the Meissner-Ochsenfeld effect; he always looked for perfect conductivity as superconductors' unique fingerprint). During his lifetime, this has remained the greatest drawback of superconductors since the breakdown of superconductivity in large(r) magnetic fields would define a hard limit for the maximally possible dissipationless currents one can drive through superconductors – a problem which soon made most of the superconducting elements uninteresting for many of the proposed technical applications. From the knowledge we have nowadays, this finding is actually not surprising. While ferromagnets' exchange interactions tend to align *all electron spins parallel* to each other in order to generate a sizable magnetization (see the *Stoner band model*, which we discuss in Sec. 2.2), the famous BCS theory for superconductivity predicts that superconducting *electrons with opposite spins* form pairs, the *Cooper pairs*. As a consequence, ferromagnetic coupling

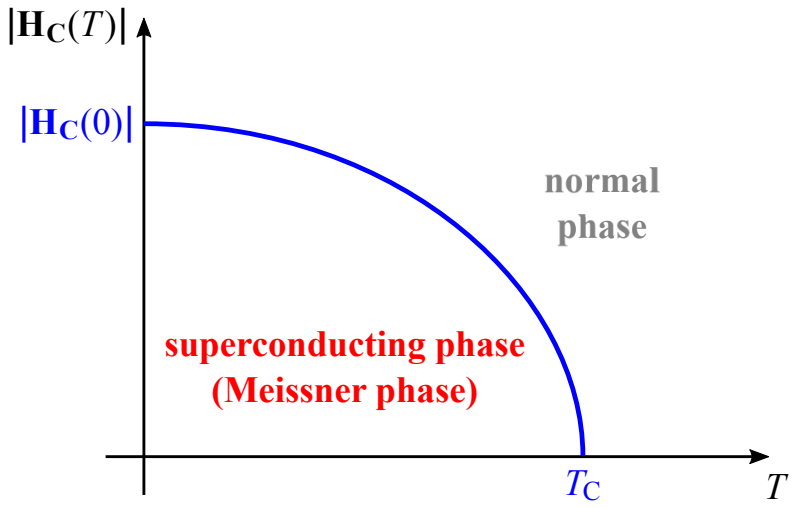


Fig. 2.3: Characteristic phase diagram [i.e., the critical magnetic field $|\mathbf{H_C}(T)|$ *vs.* temperature T] of type-I superconductors, separating the superconducting phase (*Meissner phase*) from the normal phase; T_C denotes the critical temperature.

usually breaks up Cooper pairs into single electrons orienting all their spins parallel [106], and thereby heavily suppresses (and finally even completely destroys) the superconducting phase.

In analogy to the critical temperature, the minimal magnetic field at which superconductivity breaks down has been termed the *critical magnetic field*. Empirical studies with the aim to deduce a connection between a material's critical magnetic field and its critical temperature followed and finally brought up the relation

$$|\mathbf{H_C}(T)| = |\mathbf{H_C}(0)| \left[1 - \left(\frac{T}{T_C}\right)^2\right], \tag{2.1}$$

where $|\mathbf{H_C}(T)|$ denotes the magnitude of the critical magnetic field at temperature T and $|\mathbf{H_C}(0)|$ its corresponding value at absolute zero. Plotting the relation in Eq. (2.1) in a $|\mathbf{H_C}(T)|$-T diagram yields the characteristic phase diagram of superconductors, distinguishing the superconducting state (also called *Meissner phase*) as long as the temperature stays below T_C and the external magnetic fields does not exceed $|\mathbf{H_C}(T)|$ from the normal phase at $T > T_C$ and/or $|\mathbf{H}| > |\mathbf{H_C}(T)|$ (see Fig. 2.3). The latter corresponds to the situation in which the superconducting state breaks down and the external magnetic field starts to completely penetrate the superconductor, which behaves then just like a normal conductor. While most of the elemental superconducting compounds obey such a "simple" phase diagram, it turned out that there is also another class of materials which behave in a more complicated manner. To distinguish both classes, the first have been termed *type-I* and the second *type-II* superconductors. The most important characteristic of type-II superconductors is the existence of two critical magnetic fields, $|\mathbf{H_{C_1}}(T)|$ and $|\mathbf{H_{C_2}}(T)|$, instead of just a single one. In sharp contrast to type-I superconductors, which directly switch from the Meissner phase to the normal phase (full flux penetration) as the magnetic field gets tuned above $|\mathbf{H_C}|$, type-II materials possess an additional "mixed phase" for field strengths $|\mathbf{H_{C_1}}| < |\mathbf{H}| < |\mathbf{H_{C_2}}|$, in which magnetic flux can *partially* enter the superconductor *without immediately destroying the superconducting properties* and forms a *vortexlike flux pattern* in the superconductor's interior. Each of these flux lines (vortices) carries a magnetic flux quantized in units of the magnetic flux quantum $\Phi_0 = h/(2e)$; the vortices' density inside the superconductor typically increases with increasing magnetic field [103]. Since most of the superconducting elements used for technical applications belong to the type-II class, understanding the formation of such vortices and identifying ways to conveniently manipulate them is one of the most fundamental subjects in ongoing research [107].

London equations

From an experimental point of view, Meissner and Ochsenfeld could confirm Onnes's initial speculations regarding the incompatibility of superconducting and ferromagnetic states of matter. However, a theoretical explanation of the Meissner-Ochsenfeld effect had still been missing at those days and remained a mystery until 1935, when the London brothers Fritz and Heinz came up with a way [108] that purely phenomenologically translated the experimental facts into mathematical formulas. As already predicted by Onnes, the shielding of external magnetic fields inside superconductors needs to be maintained by screening (super)currents. Contrary to Onnes's intuition, the London brothers realized that such screening currents are not fully restricted to superconductors' surfaces – a flow of finite currents in a surface layer with effectively zero thickness would imply an infinite electron density there, which would be completely unphysical. To account for their claim, Fritz and Heinz London postulated the existence of a fundamental characteristic length scale in superconductors, which has been termed the *London penetration length* λ_{L}. In a real superconductor, the screening currents are thus not pure surface currents, but rather extend – even though the currents' amplitudes exponentially decay – to a certain depth (determined by λ_{L}) into the superconducting material. As a consequence, electrons in a superconductor are *frictionlessly* accelerated by the electric field $\mathbf{E}$ that emerges close to the material's surface due to the aforementioned screening currents. Combining Newton's second law with the Lorentz force acting on those electrons, we can formally write down the electric field's action as

$$m_{\mathrm{e}} \frac{\partial \mathbf{v}}{\partial t} = -e\mathbf{E}, \tag{2.2}$$

where m_{e} represents the free-electron mass, $\mathbf{v}$ the electrons' velocity (vector), and e the *positive* elementary charge, accordingly. The density of the flowing supercurrent *inside* the superconductor is then obtained from the standard expression

$$\mathbf{j} = -en\mathbf{v}, \tag{2.3}$$

which is commonly also used to describe normal dissipative currents; n denotes the electron density.

Combining Eqs. (2.2) and (2.3) yields a relation between the supercurrent's time dependence and the $\mathbf{E}$-field, i.e.,

$$\frac{\partial \mathbf{j}}{\partial t} = \frac{ne^2}{m_{\mathrm{e}}}\mathbf{E}, \tag{2.4}$$

which is known as the *1st London equation*. To bring Eq. (2.4) into a more familiar form, we take the curl on both sides and use Faraday's induction law [109], $\boldsymbol{\nabla} \times \mathbf{E} = -\,\partial \mathbf{B}/\partial t$, where $\mathbf{B}$ now refers to the total magnetic field *inside* the superconductor (accounting for both the *external field* $\mathbf{H}$ and the *induced interior magnetization* $\mathbf{M}$), to end up with

$$\frac{\partial}{\partial t}\left[(\boldsymbol{\nabla} \times \mathbf{j}) + \frac{ne^2}{m_{\mathrm{e}}}\mathbf{B}\right] = \mathbf{0}. \tag{2.5}$$

The London brothers recognized that the most general and simultaneously physically reasonable solution of Eq. (2.5) requires

$$\boldsymbol{\nabla} \times \mathbf{j} = -\frac{ne^2}{m_{\mathrm{e}}}\mathbf{B}, \tag{2.6}$$

which resembles the *2nd London equation*. Introducing the usually in electrodynamical studies used vector potential $\mathbf{A}$ via $\boldsymbol{\nabla} \times \mathbf{A} = \mathbf{B}$ allows us to extract a simple relation for the supercurrent density,

$$\mathbf{j} = -\frac{ne^2}{m_{\mathrm{e}}}\mathbf{A}. \tag{2.7}$$

Equation (2.7) is quite striking owing to its formal structure. In normal conductors, electrical current is typically carried by electrons accelerated in an electric field; the connection between the two quantities is established by *Ohm's law* $\mathbf{j_N} = \sigma\mathbf{E}$,[1] where σ represents the electrical conductivity of the material. Bringing Eq. (2.7) into a mathematically comparable form, i.e., $\mathbf{j} = -\Lambda\mathbf{A}$, now reveals a peculiar analogy to Ohm's law. While the **E**-field generates the current flow in normal conductors, it is the vector potential **A** that drives the supercurrent through superconductors; $\Lambda = (ne^2)/m_e$ can be treated as some kind of a response function, similarly to σ in Ohm's law.

Finally, we can employ the 2nd London equation [see Eq. (2.6)] to explain the Meissner-Ochsenfeld effect. Substituting Ampere's law [109], $\mu_0\mathbf{j} = \boldsymbol{\nabla} \times \mathbf{B}$ (μ_0 is the vacuum permeability),[2] into Eq. (2.6) leads us to a simple differential equation for the **B**-field *inside a superconductor*,

$$\boldsymbol{\nabla}^2\mathbf{B} = \frac{1}{\lambda_L^2}\mathbf{B}. \tag{2.8}$$

To shorten the notation, we identified the previously mentioned *London penetration length* $\lambda_L = m_e/(\mu_0 ne^2)$. Typical values of λ_L lie between 40 nm and 50 nm in metallic superconductors like aluminum, tin, or lead [103]. From Eq. (2.8), we conclude that the only mathematically allowed solution requires that the **B**-field in the superconductor's interior must exponentially decay on the characteristic length scale determined by λ_L and eventually vanishes far inside the material. Although the last observation exactly coincides with the experimental observations, the London brothers were the first realizing that the magnetic flux is *not completely expelled from the whole superconductor*. Instead, since the shielding currents are not just localized at the material's surface, but can expand in an exponentially damped manner into its interior, also the total magnetic field inside the superconductor decays exponentially with increasing distance from its interface and eventually fully disappears in the superconductor's center, as Meissner and Ochsenfeld detected. The ingenious achievement of the London brothers has been the fact to develop all the presented mathematical framework just from empirical facts without any further input.

Superconducting materials – a compact overview

Although Onnes initially discovered superconductivity in a mercury probe, he soon came across several other materials also possessing this astonishing property. Among them were lead and tin. Together with mercury, those three materials covered the critical temperature range between roughly 4 K and 7 K. Nevertheless, already the enormous efforts Onnes himself had to put into the construction of reliable cryostat set-ups and the huge amounts of helium, which were required for continuous cooling of the probes, showed that such superconductors can only be of limited interest for practical applications. Maintaining optimal conditions for stable superconductivity would soon become too cost-intensive to profitably run technical devices over longer times. To make superconductivity more practical, the search for novel materials, which become superconducting at (much) larger temperatures and would therefore not need expensive cooling mechanisms to be operated, gained tremendous interest. Groups all over the world started to follow various attempts to design superconductors with larger critical temperatures, and even made an ungracious competition out of that. At the end of our generic introduction into superconductivity, we shortly want to recapitulate the most important milestones on the way towards discovering and/or synthesizing new superconducting materials. If not explicitly stated, we always follow Ref. [103], which is also recommended for further reading on the historical achievements in the search for novel superconducting material classes. Such a selection of particular materials is of course

[1] The index **N** in $\mathbf{j_N}$ indicates that we here regard the density of normal currents.

[2] The displacement current (i.e., the contribution proportional to $\partial\mathbf{E}/\partial t$), which would actually additionally appear in Ampere's law [109], can be neglected as the **E**-field is supposed to vary only slightly with time.

Tab. 2.1: Compact (incomplete) summary of certain superconductors and their respective critical temperatures T_C. The materials are ordered according to the year in which they were discovered to become superconducting. Further information on the materials can be found in the indicated reference(s).

Year of discovery	Material	crit. temperature T_C	Reference(s)
1911	Hg	4.1 K	[92]
1930	Nb	9.2 K	[110]
1986	$La_{2-x}(Ba, Sr)_xCuO$	$\approx$ 30 K	[111]
		$\approx$ 40 K @ pressure	[111]
1990	O-deficient $Ba_2YCu_3O_x$	$\approx$ 90 K	[112]
1993	$HgBa_2Ca_2Cu_3O_8$	$>$ 150 K @ pressure	[113]
2001	MgB_2	$\approx$ 39 K	[114–116]
2015	H_2S	$\approx$ 203 K @ pressure	[117, 118]
2018	twisted bilayer graphene	1.7 K	[119, 120]
2020	carbonaceous sulfur hydrides (CH_8S)	$\approx$ 288 K @ pressure	[121]

impacted by the author's subjective preferences and should not be regarded as complete. Detecting superconductivity in niobium in 1930 with a T_C of about 9 K [110] could already more than double the critical temperature when compared to the first mercury probes. However, it soon turned out that just focusing on elemental superconductors will most likely not help to reach the aim of significantly enlarged critical temperatures. That was the time when different groups recognized that synthesizing highly complicated compounds could rather be successful. The following syntheses went into different directions, covering, for instance, diverse organic and fullerene structures. Indeed, some of those materials maintained superconductivity at temperatures notably larger than ever before, and even further tunable within certain limits by applying pressure to the probes. Still hunting after materials that may even get superconducting at room temperature [122] and make cooling completely obsolete, researchers eventually put lots of hope into the family of oxide superconductors. Prominent examples are doped perovskite-oxide crystals like $SrTiO_{3-\delta}$, which just showed doping-dependent critical temperatures in the range of about 0.1 – 0.3 K [123] and thus initially appeared not to be appropriate candidates for high-temperature superconductivity. It took another 22 years until researchers at the IBM labs in Zurich successfully synthesized the copper-oxide perovskite $La_{2-x}(Ba, Sr)_xCuO$ in 1986, finding critical temperatures ranging from roughly 30 K up to $T_C \approx 40$ K at 13 kbar pressure [111]. Replacing some of the lanthanum and barium ions by smaller ones like yttrium and strontium, respectively, soon improved the critical temperature of the compound to about 90 K [112]. The search for cuprate superconductors has continued until $T_C > 150$ K at high pressure was detected in a $HgBa_2Ca_2Cu_3O_8$ sample (1993) [113] –

by far, the largest critical temperature ever found in this class of cuprate superconductors. Although a large variety of such high-T_C superconductors has eventually been experimentally identified over the decades, these materials still bear great challenges for theory. Most of them – for instance, all the copper-based materials – are strong type-II superconductors and can therefore not be described by established theories like the BCS theory in a satisfactory way. The highest T_C recorded in a material that still obeys BCS physics has been around 39 K in a MgB_2 crystal [114–116]; this material is still a very promising candidate for applications in which either high currents need to be sustained or in which Josephson physics plays a significant role.

After the high-T_C cuprates had been discovered, new records of critical temperatures seemed far out of reach. The more stunning the reactions of the physics community have been in August 2015 when a new paper, reporting on the observance of superconductivity in hydrogen sulfide (H_2S) with $T_C \approx 203$ K at high pressure, got published in *Nature* [117].[3] Particularly striking has been the fact that H_2S does not only set a new record for the highest ever detected T_C – significantly larger than those of cuprates –, but additionally indicates to be the first high-T_C superconductor still behaving like "conventional" superconductors, i.e., describable by an effective BCS model [118].

Just three years later, even bilayer graphene in which the two single layers are twisted with respect to each other by a well-defined angle – the so-called *magic-angle (bilayer) graphene* – turned out to become superconducting [119, 120]. Although its T_C seemed to be very low (around 1.7 K), the superconducting coupling in bilayer graphene is believed to be as strong as in cuprates. The much smaller T_C simply comes from the fact that the charge carrier density in the samples was extremely small. Despite the intensive research activities of the past decades, nature might still hide yet unforeseen surprises for us that could indeed pave the way towards efficient room-temperature superconductivity [122] one day. For the sake of compactness, we summarize all the relevant superconducting materials mentioned in this section, with their respective critical temperatures and useful references for further reading, in Tab. 2.1.

2.1.2 Macroscopic picture – Ginzburg-Landau theory

Although the two fundamental properties of superconductors – *perfect electrical conductivity and perfect diamagnetism* – are probably the most recognized qualities of these fascinating materials, the superconducting state bears much more unexpected physics. In particular, a comprehensive analysis demonstrated that superconductors obey rather complicated thermodynamic relations, which make the superconducting state even more attractive for experimental and theoretical studies. Analyzing the full thermodynamics of superconductors goes far beyond the scope of the introduction we want to provide within this thesis. For further reading, we recommend, for instance, Refs. [103] and [124]; we just mention two important findings. On the one hand, the entropy in the superconducting state turns out to be lower than in the normal state. Given the findings of the BCS theory [47, 48], superconductivity is maintained by the formation of electron pairs (Cooper pairs). The entropy decrease can thus be interpreted assigning a higher order to the superconducting than to the normal phase. On the other hand, type-I superconductors reveal a discontinuous jump in their heat capacity as the temperature gets tuned through T_C, indicating that superconductors undergo a *continuous (2nd order) phase transition* from the (more) "disordered" (normal) into the ordered (superconducting) phase. Based on the latter finding and his earlier formulated theory on continuous phase transitions [125], Landau began to work on a *macroscopic (phenomenologically founded) theory* for superconductivity, which was extended to include (external) magnetic fields (necessary to explain the Meissner-Ochsenfeld effect) some years later by

[3] A very recent follow-up work published in October 2020 predicted even larger critical temperatures of about 288 K in modified carbonaceous sulfur hydrides (CH_8S) [121].

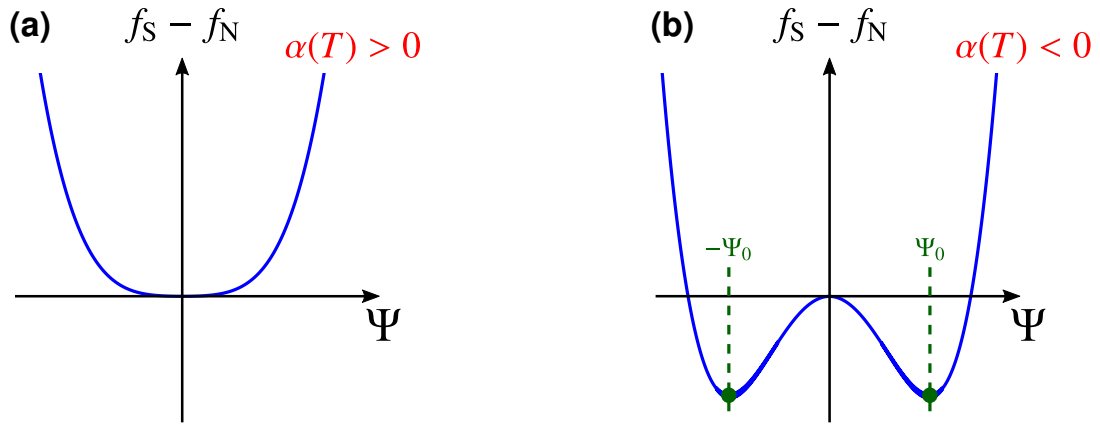


Fig. 2.4: Schematical illustration of the Ginzburg-Landau free-energy density difference between the superconducting and the normal phase, $f_S - f_N$, as a function of the order parameter Ψ, assuming **(a)** $\alpha(T) > 0$ and **(b)** $\alpha(T) < 0$, respectively. A stable superconducting phase can only be established for two particular values of the order parameter, $-\Psi_0$ and Ψ_0, presuming $\alpha(T) < 0$.

Ginzburg. Their *Ginzburg-Landau theory* [126] has become one of the most important approaches for superconductivity. We briefly recall the main steps in its reasoning, following Refs. [124] and [126] if not otherwise indicated, in this section.

Characteristic for continuous phase transitions is the existence of an *order parameter* Ψ, which abruptly changes from zero in the "disordered" to a finite value in the ordered phase. Specifically in our situation, this means that the superconducting phase transition at T_C can be fully described introducing the, in general, complex order parameter $\Psi = |\Psi| e^{i\phi}$ ($|\Psi|$ is the order parameter's amplitude and ϕ its phase) that becomes nonzero solely in the superconducting state, i.e., when T decreases below T_C. Close to the transition point, where $|\Psi|$ increases *slowly* in the superconducting phase, we can then reliably expand system-characteristic quantities by means of power series in $|\Psi|^2$, respecting all the symmetries present in the system. This is also the deeper reason why the Ginzburg-Landau approach models the superconducting state most accurately at temperatures close to the transition. Expanding the *free-energy density* of superconductors close to T_C in $|\Psi|^2$ results in

$$f_S(T) \approx f_N(T) + \alpha(T)\,|\Psi|^2 + \frac{\beta}{2}\,|\Psi|^4, \tag{2.9}$$

where $f_S(T)$ refers to the free-energy density in the superconducting and $f_N(T)$ to the one in the normal phase; $\alpha(T)$ and β are two not yet determined coefficients, for which Ginzburg and Landau assumed that the first varies with temperature T, while the second does not. Inspecting Eq. (2.9) immediately suggests $\beta > 0$. Otherwise, it would be possible to realize a favorable minimal-energy state for $|\Psi|^2 \to \infty$, which is in contradiction to our basic assumption that $|\Psi|$ increases *slowly* at the transition point. To figure out the physically justified values for the remaining parameter $\alpha(T)$, we plot the difference between the superconducting and the normal free-energy density,

$$f_S(T) - f_N(T) \approx \alpha(T)\,|\Psi|^2 + \frac{\beta}{2}\,|\Psi|^4, \tag{2.10}$$

once for $\alpha(T) > 0$ and once for $\alpha(T) < 0$ in Fig. 2.4, and identify the positions of the function's minima. The latter mark those regimes in which the free energy of the superconducting phase falls below the related one of the normal phase, indicating that superconductivity becomes the energetically favorable state. In the first scenario (positive α), the preferred state corresponding to a minimum in the free energy would apparently always be realized for $|\Psi|^2 = 0$ [see Fig. 2.4(a)]. But a globally vanishing order parameter refers to nothing else than simply the normal phase of our superconductor,

which we are currently not interested in at all. Hence, we shall rather concentrate on the second case, presuming negative α. Figure 2.4(b) suggests that then two specific values of Ψ, symmetrically aligned around zero, exist (let us call them $-\Psi_0$ and Ψ_0), for which the superconducting state indeed becomes the system's energetically favored state. Mathematically solving for the minima of Eq. (2.10) yields a compact expression for Ψ_0,

$$\pm\,\Psi_0 = \pm\sqrt{-\frac{\alpha(T)}{\beta}}. \tag{2.11}$$

Taking into account that $\alpha(T) < 0$ in the superconducting state, Eq. (2.11) is well defined and we can substitute the explicit expression for Ψ_0 into Eq. (2.10) to estimate the energy the system gains by undergoing the phase transition into the superconducting phase as

$$f_\mathrm{S}(T) - f_\mathrm{N}(T) = -\frac{\alpha^2(T)}{2\beta}. \tag{2.12}$$

Anticipating the results of the later formulated BCS theory, this energy gain refers to the *condensation energy (density)* of the Cooper pairing process. The only remaining question which we have not answered so far is the precise temperature dependence of the α-parameter. Following his earlier theory on continuous phase transitions [125], Landau suggested $\alpha(T) = \alpha'(T - T_\mathrm{C})$ with some (unimportant) *positive* constant α'. It is easy to check that this choice fulfills all requirements on α we put forward during our analysis, i.e., $\alpha(T_\mathrm{C}) = 0$ and $\alpha(T < T_\mathrm{C}) < 0$.

Although the approach presented up to now already reveals a lot of the superconducting phase transition's physics, it would be desirable to generalize the concepts in order to include the action of magnetic fields, especially as we want to employ the theory to explain the Meissner-Ochsenfeld effect later on. Ginzburg included the impact of **B**-fields into Landau's approach modifying the *free-energy density difference* in Eq. (2.10) to

$$f_\mathrm{S}(T) - f_\mathrm{N}(T) \approx \alpha(T)\,|\Psi|^2 + \frac{\beta}{2}\,|\Psi|^4 + \frac{1}{2m^*}\left|\left(-\mathrm{i}\hbar\boldsymbol{\nabla} + 2e\mathbf{A}\right)\Psi\right|^2 + \frac{\mathbf{B}^2}{2\mu_0}. \tag{2.13}$$

Compared to Landau's situation without magnetic fields, two additional terms appear. They account for the electrons' kinetic energy in the presence of a magnetic field (the momentum operator includes the vector potential **A** via minimal coupling) and the magnetic field energy itself (μ_0 still represents the vacuum permeability), respectively. Assuming an effective electron charge of $-2e$ ($e > 0$ as before) is basically necessary to properly account for the Cooper pairing mechanism. More generally, one might also substitute an effective charge of q^* without determining its actual value. In a similar manner, the appearing mass has to differ from the usual free-electron mass. To avoid too much confusion with not well-justified substitutions, we here indeed simply suppose an effective mass m^* without further specifications. Analogously to the analysis of the ($\mathbf{B} = \mathbf{0}$)-case before, the minima of Eq. (2.13) indicate the transition into the superconducting phase (which becomes then again energetically favorable). As we now not only need to regard the order parameter Ψ, but simultaneously also the vector potential **A** effectively representing the **B**-field, Eq. (2.13) needs to be minimized with respect to Ψ *and* **A**. After some tedious calculations, we extract two fundamental equations describing the superconducting phase transition, namely

$$0 = \frac{1}{2m^*}\left(-\mathrm{i}\hbar\boldsymbol{\nabla} + 2e\mathbf{A}\right)^2\Psi + \alpha(T)\,\Psi + \beta\,|\Psi|^2\Psi \tag{2.14}$$

and

$$\mathbf{j} = -\frac{e\hbar}{\mathrm{i}m^*}\left(\Psi^*\boldsymbol{\nabla}\Psi - \Psi\boldsymbol{\nabla}\Psi^*\right) - \frac{(2e)^2}{m^*}|\Psi|^2\mathbf{A}. \tag{2.15}$$

These equations were (historically) termed *Ginzburg-Landau equations*. The 1st Ginzburg-Landau equation [see Eq. (2.14)] is an *effective* Schroedinger-like equation for the superconducting phase's order parameter. Note that in sharp contrast to the Schroedinger equation for free electrons, the 1st Ginzburg-Landau equation is *nonlinear* in Ψ. The 2nd Ginzburg-Landau equation in Eq. (2.15) generalizes the quantum-mechanical normal-state current density formula to the calculation of the supercurrent density $\mathbf{j}$.

Particularly the latter one is quite rewarding due to various aspects. We learned at the beginning of this section that the phase transition into the superconducting state is governed by the complex order parameter $\Psi = |\Psi|e^{i\phi}$. Substituting this explicit form of Ψ into the 2nd Ginzburg-Landau equation in Eq. (2.15) leads to a more compact expression for the supercurrent density,

$$\mathbf{j} = -\frac{2e\hbar}{m^*}|\Psi|^2\boldsymbol{\nabla}\phi - \frac{(2e)^2}{m^*}|\Psi|^2\mathbf{A}. \tag{2.16}$$

Interpreting $|\Psi|^2$ as the density of superconducting electrons (resembling the Cooper pair density in the BCS picture) and $-2e$ as one Cooper pair's effective charge, the current formula is quite similar to what has been well established in simple quantum-mechanical problems. Nevertheless, the surprising observation now is that a gradient in the order parameter's phase factor, e.g., spatial variations of the superconducting phase in a junction composed of different materials, is sufficient to spontaneously drive a supercurrent through the system. This is an unambiguous precursor of the (DC) Josephson effect [93, 127], which will be a fundamental topic later in this work (see, e.g., Chap. 5). Although 12 years went by between the formulation of the Ginzburg-Landau theory and Josephson's work, it seems to be quite remarkable from our perspective nowadays that all the theoretical prerequisites for the discovery of the Josephson effect were already provided by Ginzburg's and Landau's analyses.

Furthermore, Eq. (2.16) contains the explanation for the Meissner-Ochsenfeld effect. Taking the curl of Eq. (2.16) and substituting Ampere's law [109], $\mu_0\mathbf{j} = \boldsymbol{\nabla}\times\mathbf{B}$, yields the differential equation

$$\boldsymbol{\nabla}^2\mathbf{B} = \frac{1}{\lambda_{\mathrm{GL}}^2}\mathbf{B}, \tag{2.17}$$

from which the spatial variation of the $\mathbf{B}$-field inside a superconductor can again be extracted. Interestingly, Eq. (2.17) is formally fully equivalent to the differential equation for $\mathbf{B}$ which was heuristically established by the London brothers many years earlier; see Eq. (2.8). The only difference is that the prefactor is determined by $\lambda_{\mathrm{GL}} = \sqrt{m^*/(4e^2\mu_0|\Psi|^2)}$, the *Ginzburg-Landau penetration length*. This will of course not dramatically change the mathematical solution of Eq. (2.17). The only allowed solution is still the one representing $\mathbf{B}$-fields that are screened by currents close to the surface and will exponentially decay in the superconductor's interior on a characteristic length scale. The latter is now λ_{GL} instead of Londons' λ_{L}. The fact that the early approach of the London brothers, simply founded on phenomenology without any additional input, traces the Meissner-Ochsenfeld effect back to the same theoretical fundamentals as the much more complex Ginzburg-Landau formulation again emphasizes the brilliant work performed by the London brothers in the early days of superconductivity.

Both theories (London and Ginzburg-Landau) would merge into each other if the two penetration lengths would be equal, i.e., if $\lambda_{\mathrm{L}} = \lambda_{\mathrm{GL}}$. Comparing the explicit relations, the most intuitive choice to ensure that would be to simply substitute the effective electron mass $m^* \approx 2m_{\mathrm{e}}$ and $|\Psi|^2 \approx n/2$. Both expressions mean nothing else than the (energetically favorable) formation of Cooper pairs, finally entering into the BCS description as its key ingredient, and thus appear to be a reasonable choice in elemental (BCS-like) superconductors. However, one shall be aware that owing to the complicated band structures of real materials, this is really just a rough guess. Due to complicated screening effects, m^* and $|\Psi|^2$ can deviate a lot from that in realistic materials, while keeping the ratio $m^*/(|\Psi|^2)$ fixed to obey $\lambda_{\mathrm{L}} = \lambda_{\mathrm{GL}}$.

Another important consequence of the Ginzburg-Landau approach can be extracted when regarding the absence of (magnetic) fields, i.e., $\mathbf{A} = \mathbf{0}$. In that particular case, the 1st Ginzburg-Landau equation [see Eq. (2.14)] can be recast as

$$0 = \xi_{\mathrm{GL}}^2 \boldsymbol{\nabla} \cdot \left[\boldsymbol{\nabla} \left(\frac{\Psi}{\Psi_0} \right) \right] + \frac{\Psi}{\Psi_0} - \frac{\Psi}{\Psi_0} \left| \frac{\Psi}{\Psi_0} \right|^2 , \tag{2.18}$$

where $\Psi_0 = \sqrt{-\alpha(T)/\beta}$ refers to the minimal-energy order parameter found at the beginning of this section and ξ_{GL} abbreviates $\xi_{\mathrm{GL}} = \hbar/\sqrt{2m^*\alpha(T)}$. The striking observation (following from dimensional analysis) is that the Ginzburg-Landau approach apparently contains a second characteristic length scale, ξ_{GL}, besides the penetration length λ_{GL}. This length scale – *the Ginzburg-Landau coherence length* – attracted greater interest in connection with the later published BCS theory, which is based on the assumption that the superconducting phase is described by one *coherent* quantum-mechanical ground-state wave function that can propagate in space. The coherence length defines then the typical length scale over which the wave function can spread without losing its coherence (which would destroy the superconducting phase). Therefore, the coherence length plays an important role in realistic devices, in which superconducting constituents are typically gated by normal electrodes. Due to *proximity effects* [128], superconducting order can be induced even in normal contacts over typical distances governed by the coherence length. We will come back to that issue in the next section.

In its early days, the Ginzburg-Landau theory was not too much appreciated in the western world because it is completely based on phenomenology and was believed to be not general enough to cover the variety of superconducting materials. This changed rapidly in 1959 when Gor'kov proved, based on a Green's function formulation [129], that close to the transition point, at which the Ginzburg-Landau theory is by definition best applicable, it can be immediately rederived from the comprehensive microscopic BCS theory as an important limiting case. From this analogy, it became also possible to relate the Ginzburg-Landau coherence length close to T_{C}, $\xi_{\mathrm{GL}}(T_{\mathrm{C}})$, to the coherence length appearing in the BCS theory, $\xi_{\mathrm{BCS}} = (\hbar v_{\mathrm{F}})/(\pi|\Delta_{\mathrm{S}}|)$. The latter quantity, also known as *Pippard's law*, who already proposed its existence some years before BCS to cure deviations between the London equations and experimental observations [130, 131], contains the Fermi velocity v_{F} and the superconducting energy gap $|\Delta_{\mathrm{S}}|$. The last quantity defines another characteristic material-specific measure of superconductors as we will see in Sec. 2.1.3. For *clean superconductors*, one finds

$$\xi_{\mathrm{GL}}(T) = 0.74 \frac{\xi_{\mathrm{BCS}}}{\sqrt{1 - T/T_{\mathrm{C}}}}, \tag{2.19}$$

whereas in *dirty superconductors*

$$\xi_{\mathrm{GL}}(T) = 0.855 \frac{\sqrt{\xi_{\mathrm{BCS}} \ell}}{\sqrt{1 - T/T_{\mathrm{C}}}}; \tag{2.20}$$

ℓ is the mean free path. Typical BCS coherence lengths in aluminum are of the order of 1600 nm [132].

Finally, the two characteristic lengths we encountered in the Ginzburg-Landau approach – the penetration and coherence lengths – can be used to formally distinguish between type-I and type-II superconductors. For that purpose, one typically defines the temperature-independent *Ginzburg-Landau parameter*

$$\kappa := \frac{\lambda_{\mathrm{GL}}(T)\big|_{\Psi=\Psi_0}}{\xi_{\mathrm{GL}}(T)} = \frac{m^*}{\hbar e} \sqrt{\frac{\beta}{2\mu_0}}. \tag{2.21}$$

For isotropic materials (see, for example, Ref. [103] for the derivation), one finds that the superconductor belongs to the type-I group as long as $\kappa < 1/\sqrt{2}$ and to the type-II class if $\kappa > 1/\sqrt{2}$, accordingly. This

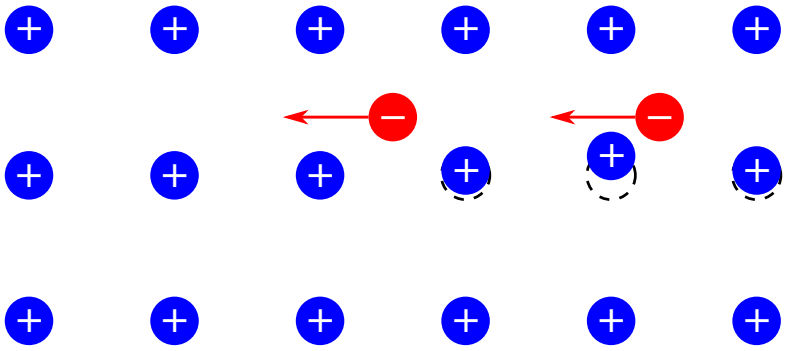


Fig. 2.5: Schematical (strongly simplified) illustration of the physical origin of the phonon-mediated attractive electron-electron interaction in the superconducting phase, which eventually leads to Cooper pairing. The crystal lattice is formed by positively charged ions (blue), while electrons (red) can move freely along the direction indicated by red arrows. Attracting the positively charged ions (Coulomb interaction), the left electron causes lattice distortions (phonons) – exemplarily shown by deflecting three ions from their initial positions – so that the density of positive charge locally fluctuates and the resulting Coulomb interaction attracts then the second (right) electron. The electrons' attraction finally forms one Cooper pair. The two electrons are supposed to be far away to neglect their respective Coulomb repulsion.

eventually leads to the important conclusion that the Ginzburg-Landau approach, though being fully macroscopic and phenomenological, can indeed properly describe the superconducting phase transition not only in type-I, but also in many type-II superconductors. As mentioned before, high-T_C superconductors behave nonetheless exceptional in many aspects and still bear lots of mysteries to existing theories like the Ginzburg-Landau approach.

2.1.3 Microscopic picture – BCS theory

Seven years after the Ginzburg-Landau theory had been formulated, the recognized physicist John Bardeen – he had been awarded the Physics Nobel Prize for his contribution to the development of semiconducting transistors just some months ago [133] – published another theoretical paper on the physical origin of superconductivity, together with his colleagues Leon Cooper and John Robert Schrieffer. At that time (1957), their approach has been the first one describing superconductivity on the *microscopic* level [47, 48]. Their work, soon termed BCS theory according to the first letters of the three scientists' surnames, evolved into the most fundamental theory for conventional superconductors (again, high-T_C superconductors are more complicated to understand, going even beyond the comprehensive BCS theory). Therefore, no introduction into the theory of superconductivity would be complete without summarizing at least the main points of the BCS theory.

The BCS theory is founded on the primary assumption that electrons in the superconducting phase form bound pairs and condense into a bosonlike ground state, which is known as the *superconducting condensate*. Reasoning for this presumption was already given in an earlier work of Cooper [134], who had predicted the possible formation of electron pairs in a degenerate Fermi gas just one year before the BCS paper got published. In his honor, those electron pairs were termed *Cooper pairs* later on.

Before diving into the formalities, we shortly want to recapitulate the physics behind the electrons' pairing mechanism. Let us consider the simple picture shown in Fig. 2.5, assuming for a moment that the superconducting material solely consists of positively charged ions, forming the lattice, and negatively charged electrons. As electrons can move freely through the solid, one of them may attract the positively charged ions via the Coulomb interaction. Consequently, some of the positively charged

ions are deflected from their initial positions and the whole lattice starts to vibrate. The ions' mass is much greater than the one of electrons so that the induced lattice vibrations typically extend over long time scales (*low-frequency vibrations*). On the other hand, these lattice vibrations simultaneously lead to local fluctuations of the positive charge density, which themselves will definitely impact other electrons' motion. To be specific, we can imagine the case in which another electron locally feels a strong positive charge density on its way through the crystal lattice and gets attracted – once again, owing to the Coulomb interaction. As the lattice vibrations (and thus the basis for the attraction of the second electron) were actually caused by the first electron, the whole process may effectively be treated as if an attractive interaction between the two electrons would have been there. The attraction has been mediated by lattice vibrations, usually attributed to the continuous generation and destruction of quasiparticles that we call *phonons*. Of course, our picture strongly oversimplifies the reality. So far, we completely neglected the repulsive Coulomb interaction between the electrons, claiming that the solid consists of just two electrons that are spatially thus well separated that they can only see the phonon-mediated attraction, but do not repulse each other. In a real material, electrons form a dense electron gas and a reliable consideration additionally needs to take care about the Coulomb repulsion. Nevertheless, Cooper's work together with the subsequently following BCS theory convinced that there are indeed certain materials in which the attractive interaction is able to overcome the repulsive one under appropriate conditions (e.g., sufficiently low temperatures) so that the electrons can indeed attract each other and form (Cooper) pairs. It turned out that this pairing is exactly the microscopic origin of the superconducting phase.

Some general properties of Cooper pairs

After agreeing to the fact that all the fascinating physics associated with the superconducting phase must be raised by those peculiar Cooper pairs, let us briefly recover some of their fundamental properties. We follow the arguments provided in Refs. [103] and [134]. At the end of this part, we will be in the position to confirm that the attractive phonon-mediated interaction between electrons can really sustain the pairing mechanism predicted by Cooper [134].

In its simplest picture, the electrons inside the superconducting material are supposed to form a Fermi sea. At the moment, let us neglect all types of interactions. Then, the Fermi sea's Hamiltonian in second quantization reads

$$\hat{\mathcal{H}}_{\mathrm{FS}} = \sum_{\mathbf{k}} \sum_{\sigma \in \{\uparrow;\downarrow\}} \varepsilon_{\mathbf{k}} \hat{a}^{\dagger}_{\mathbf{k},\sigma} \hat{a}_{\mathbf{k},\sigma}, \tag{2.22}$$

where the operator $\hat{a}^{\dagger}_{\mathbf{k},\sigma}$ creates one electron with wave vector $\mathbf{k}$ and spin σ ($\sigma = \uparrow$ for spin up and $\sigma = \downarrow$ for spin down), and $\hat{a}_{\mathbf{k},\sigma}$ represents the corresponding annihilation operator; the single-electron energies are denoted by $\varepsilon_{\mathbf{k}}$. As electrons are fermionic particles and Pauli's exclusion principle holds for them, each available momentum-spin state inside the Fermi sea, labeled by the ket $|\mathbf{k}, \sigma\rangle$, can be maximally filled with one single electron. At zero temperature, all those states below the characteristic Fermi energy ε_{F} must be occupied. Now, we want to add two *additional, noninteracting, electrons* to the Fermi sea, which will turn out to form a (Cooper) pair in the end. The only still possible configuration is the one in which the additional electrons are put into free states at energies above the Fermi energy. Therefore, the total amount of energy needed to bring the electrons into the system exceeds $2\varepsilon_{\mathrm{F}}$. Assuming that the two electrons are classified through wave vectors $\mathbf{k}$ and $\mathbf{k}'$, and their positions by $\mathbf{r}$ and $\mathbf{r}'$, respectively, their wave function's spatial part may be written as a product of two independent plane-wave states,

$$\Psi(\mathbf{r}, \mathbf{r}'; \mathbf{k}, \mathbf{k}') = \langle \mathbf{r}|\mathbf{k}\rangle \, \langle \mathbf{r}'|\mathbf{k}'\rangle = \frac{1}{\mathcal{V}} \mathrm{e}^{\mathrm{i}(\mathbf{k}\cdot\mathbf{r})} \mathrm{e}^{\mathrm{i}(\mathbf{k}'\cdot\mathbf{r}')}; \tag{2.23}$$

the system's volume $\mathcal{V}$ is introduced for normalization reasons. The total kinetic energy of the two electrons, $\mathcal{T} = (\hbar^2\mathbf{k}^2)/(2m_{\mathrm{e}}) + (\hbar^2\mathbf{k}'^2)/(2m_{\mathrm{e}})$, can be brought into a more common form defining the

relative momenta $\mathbf{K} := \mathbf{k} + \mathbf{k}'$ and $\mathbf{K}' := (\mathbf{k} - \mathbf{k}')/2$. The final expression reads then as

$$\mathcal{T} = \frac{\hbar^2}{m_\mathrm{e}} \left[\frac{\mathbf{K}^2}{4} + \mathbf{K}'^2 \right]. \tag{2.24}$$

Apparently, the most favorable (lowest-energy) state is realized for $\mathbf{K} = \mathbf{0}$, i.e., the two electrons occupy free states with antiparallel wave vectors $\mathbf{k}$ and $\mathbf{k}' = -\mathbf{k}$.

As we have anticipated previously, two electrons can only form a Cooper pair if an effective attractive interaction between them comes up. Therefore, we indeed need to regard the more complicated case in which the two additional electrons close to ε_F effectively (via the described phonon-mediated process) attract each other. Without worrying about details, the presence of any interaction immediately modifies the two-particle state in Eq. (2.23). In momentum space, the wave function of the *interacting* electrons, denoted by $|1,2\rangle$, can be expanded in the plane-wave basis formed by $|\mathbf{k},\mathbf{k}'\rangle = |\mathbf{k},-\mathbf{k}\rangle$ as

$$|1,2\rangle = \sum_{\mathbf{k}} c_{\mathbf{k}} \, |\mathbf{k},-\mathbf{k}\rangle. \tag{2.25}$$

To ascertain a reasonable choice for the unknown coefficients $c_\mathbf{k}$, Cooper substituted the ansatz in Eq. (2.25) into the Schroedinger equation for the interacting system and solved the resulting eigenvalue problem. Particularly in the important limit of zero temperature, Cooper obtained that the total energy of the two interacting electrons is given by

$$\varepsilon_{1,2} = 2\varepsilon_\mathrm{F} - 2\hbar\omega_\mathrm{D} \mathrm{e}^{-1/[\mathcal{U} g(\varepsilon_\mathrm{F})]}. \tag{2.26}$$

Equation (2.26) clearly resembles the impact of the phonon-mediated attractive electron-electron interaction via its effective strength $-\mathcal{U}$ (entering the full Hamiltonian of the interacting system) and the appearance of the Debye frequency of phonons ω_D; $g(\varepsilon_\mathrm{F})$ abbreviates the density of states (DOS) at the Fermi level. At Cooper's time, the consequences of Eq. (2.26) were astonishing. He was the first giving mathematical reasoning that (sufficiently strong) attractive interactions between two electrons can entail an instability of the Fermi sea and a novel state, characterized by paired electrons (despite the repulsive electron-electron Coulomb interaction, which seemed to be unbreachable for some time), can form. This novel state is the energetically favorable one (and thus indeed realized) since Eq. (2.26) suggests that the pairing significantly reduces the system's total energy. While we deduced that the energy necessary to bring the two electrons into the *noninteracting* system must be greater than $2\varepsilon_\mathrm{F}$, we finally see that the required amount of energy in the favored *paired* configuration (i.e., in the presence of the attractive electron-electron interaction) is really significantly lower [the exact value strongly depends on the interaction strength $-\mathcal{U}$ though; see Eq. (2.26)].

To complete our study of Cooper pairs, let us come back to their specific wave functions. As mentioned above, each valid wave function for a fermionic two-electron system must comply with Pauli's principle, i.e., it needs to be antisymmetric with respect to exchanging particles. The spatial part of the wave function given in Eq. (2.23) is symmetric. The only allowed configuration is therefore the one in which the total wave function's spin part becomes antisymmetric, completing Cooper pairs' fundamental properties: *Cooper pairs are composed of two electrons with antiparallel wave vectors and opposite spins*.[4]

[4] Strictly speaking, this is valid for (most of) the elemental superconductors that obey the conventional BCS theory. Due to the forming spin-singlet state, these superconductors are referred to as s-wave superconductors. Other pairing mechanisms, including p-wave, d-wave, ..., which could also allow for spin-triplet Cooper pairs (the spatial part of the wave functions becomes then different and indeed antisymmetric) have been proposed, e.g., recently for UTe_2 [135]; to which extent materials *intrinsically* really possess such pairing mechanisms (so-called *unconventional superconductivity*) is still part of intensive ongoing research.

Formal description of the BCS theory

Eventually, we are fully equipped to follow all the mathematical and conceptual steps of the BCS theory [47, 48]. As Cooper's arguments proved, interacting electrons tend to form bound pairs as long as the pairing reduces the system's total energy. All these pairs condense then into one coherent macroscopic ground state – in the case of superconductors, the superconducting condensate. The BCS theory formalizes the condensate's wave function as

$$|\Psi_{\mathrm{BCS}}\rangle = \prod_{\mathbf{k}} \left(u_{\mathbf{k}} + v_{\mathbf{k}} \hat{a}^{\dagger}_{\mathbf{k},\uparrow} \hat{a}^{\dagger}_{-\mathbf{k},\downarrow} \right) |\Psi_0\rangle, \tag{2.27}$$

where $|\Psi_0\rangle$ refers to the vacuum state without electrons. Apparently, Eq. (2.27) incorporates two contributions. Each single bound-pair state can either be occupied by a Cooper pair (two electrons with antiparallel wave vectors and opposite spins) or not occupied at all. The first situation appears with probability $|v_{\mathbf{k}}|^2$, the second one with probability $|u_{\mathbf{k}}|^2$, accordingly. The amplitudes $u_{\mathbf{k}}$ and $v_{\mathbf{k}}$ carry the information about the wave function's phase coherence and are hence known as *BCS coherence factors*. To ensure proper normalization of $|\Psi_{\mathrm{BCS}}\rangle$, they need to fulfill the condition

$$|u_{\mathbf{k}}|^2 + |v_{\mathbf{k}}|^2 = 1, \tag{2.28}$$

which is also consistent with interpreting them as occupation probabilities of the single bound-pair states.

In the spirit of the effective electron-electron interaction, entailing the instability of the Fermi sea and the Cooper pairing (compare to the previous arguments), the BCS Hamiltonian is assumed to possess the form

$$\hat{\mathcal{H}}_{\mathrm{BCS}} = \sum_{\mathbf{k}} \sum_{\sigma \in \{\uparrow;\downarrow\}} \varepsilon_{\mathbf{k}} \hat{a}^{\dagger}_{\mathbf{k},\sigma} \hat{a}_{\mathbf{k},\sigma} - \mathcal{U} \sum_{\mathbf{k}} \sum_{\mathbf{k}'} \hat{a}^{\dagger}_{\mathbf{k},\uparrow} \hat{a}^{\dagger}_{-\mathbf{k},\downarrow} \hat{a}_{-\mathbf{k}',\downarrow} \hat{a}_{\mathbf{k}',\uparrow}. \tag{2.29}$$

As above, the first summand in Eq. (2.29) measures the kinetic energy of the free electrons, while the second summand describes the attractive electron-electron interaction with amplitude $-\mathcal{U}$, finally entailing the formation of Cooper pairs. For convenience, the single-particle energies $\varepsilon_{\mathbf{k}}$ are measured with respect to the Fermi level, i.e., $\varepsilon_{\mathbf{k}} = (\hbar^2 \mathbf{k}^2)/(2m_{\mathrm{e}}) - \varepsilon_{\mathrm{F}}$.

Within mean-field approximation [103, 136], the products of two creation and annihilation operators in Eq. (2.29) may be rewritten in terms of their corresponding expectation values $\langle \ldots \rangle$ to obtain the effective BCS Hamiltonian

$$\begin{aligned} \hat{\mathcal{H}}^{\mathrm{eff.}}_{\mathrm{BCS}} = \sum_{\mathbf{k}} \sum_{\sigma \in \{\uparrow;\downarrow\}} \varepsilon_{\mathbf{k}}\, \hat{a}^{\dagger}_{\mathbf{k},\sigma} \hat{a}_{\mathbf{k},\sigma} - \mathcal{U} \sum_{\mathbf{k}} \left\langle \hat{a}^{\dagger}_{\mathbf{k},\uparrow} \hat{a}^{\dagger}_{-\mathbf{k},\downarrow} \right\rangle \sum_{\mathbf{k}'} \hat{a}_{-\mathbf{k}',\downarrow} \hat{a}_{\mathbf{k}',\uparrow} \\ - \mathcal{U} \sum_{\mathbf{k}} \hat{a}^{\dagger}_{\mathbf{k},\uparrow} \hat{a}^{\dagger}_{-\mathbf{k},\downarrow} \sum_{\mathbf{k}'} \left\langle \hat{a}_{-\mathbf{k}',\downarrow} \hat{a}_{\mathbf{k}',\uparrow} \right\rangle . \end{aligned} \tag{2.30}$$

Due to the coherent character of the superconducting ground-state wave function, products of two creation or annihilation operators can indeed have nonzero expectation values. Introducing the *superconducting pairing potential* (which is basically the superconducting order parameter in the BCS framework)

$$\hat{\Delta}_{\mathrm{S}} := \mathcal{U} \sum_{\mathbf{k}} \left\langle \hat{a}_{-\mathbf{k},\downarrow} \hat{a}_{\mathbf{k},\uparrow} \right\rangle \tag{2.31}$$

brings the effective BCS Hamiltonian [see Eq. (2.30)] into its more compact matrix form

$$\hat{\mathcal{H}}^{\mathrm{eff.}}_{\mathrm{BCS}} = \sum_{\mathbf{k}} \begin{bmatrix} \hat{a}^{\dagger}_{\mathbf{k},\uparrow} & \hat{a}_{-\mathbf{k},\downarrow} \end{bmatrix} \begin{bmatrix} \varepsilon_{\mathbf{k}} & -\hat{\Delta}_{\mathrm{S}} \\ -\hat{\Delta}^{\dagger}_{\mathrm{S}} & -\varepsilon_{\mathbf{k}} \end{bmatrix} \begin{bmatrix} \hat{a}_{\mathbf{k},\uparrow} \\ \hat{a}^{\dagger}_{-\mathbf{k},\downarrow} \end{bmatrix}. \tag{2.32}$$

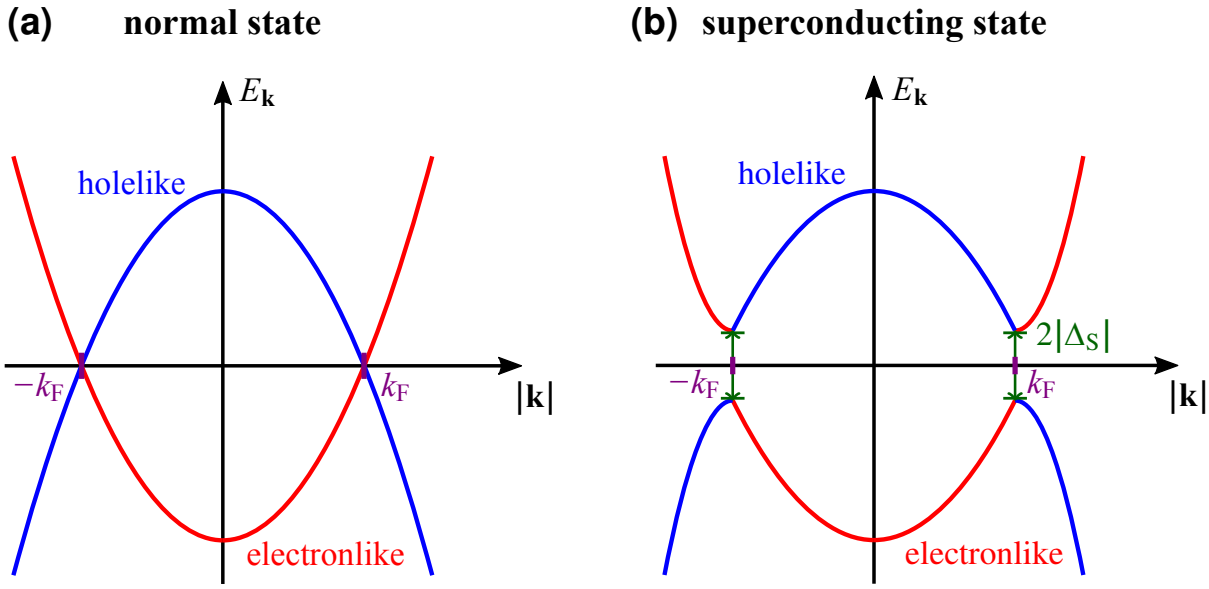


Fig. 2.6: Schematical illustration of the BCS quasiparticle spectra [quasiparticle energies $E_{\mathbf{k}}$ as a function of momentum $|\mathbf{k}|$; see Eq. (2.38)] in the **(a)** normal state and **(b)** superconducting state. The electronlike bands are shown in red and the holelike bands in blue; k_F denotes the Fermi wave vector. The existence of the superconducting energy gap with magnitude $2|\Delta_S|$ is a clear indication of the superconducting condensate's formation.

For conventional (s-wave) superconductors, which we solely consider at the moment, the pairing potential in Eq. (2.31) is simply constant ($\mathbf{k}$-independent), e.g., $\hat{\Delta}_S = |\Delta_S|e^{i\phi_S}$, where $|\Delta_S|$ denotes the pairing potential's absolute magnitude and ϕ_S the superconducting phase (which is related to the phase appearing in the Ginzburg-Landau order parameter and plays a crucial role for Josephson effects as mentioned there).

To diagonalize the effective BCS Hamiltonian in Eq. (2.32), we employ the *Bogoljubov transformation* [137], defining the new fermionic operators

$$\hat{b}_{\mathbf{k},\uparrow} = u^*_{\mathbf{k}}\hat{a}_{\mathbf{k},\uparrow} - v_{\mathbf{k}}\hat{a}^\dagger_{-\mathbf{k},\downarrow} \tag{2.33}$$

and

$$\hat{b}^\dagger_{-\mathbf{k},\downarrow} = v_{\mathbf{k}}\hat{a}_{\mathbf{k},\uparrow} + u_{\mathbf{k}}\hat{a}^\dagger_{-\mathbf{k},\downarrow}. \tag{2.34}$$

It is important to see that the operator $\hat{b}_{\mathbf{k},\uparrow}$, acting on the BCS condensate wave function given in Eq. (2.27), annihilates one spin-up electron with wave vector $\mathbf{k}$ and simultaneously creates a spin-down electron with wave vector $-\mathbf{k}$; the second operator $\hat{b}_{-\mathbf{k},\downarrow}$ effectuates exactly the opposite. Therefore, both operators together break up one Cooper pair and form unpaired particles in the superconductor, so-called *quasiparticles*. This is quite a fundamental observation, as it means that we do no longer need to explicitly deal with Cooper pairs. The BCS theory focuses instead on determining the excitation spectrum of *unpaired* quasiparticles. Due to the condensation of electrons into Cooper pairs, no single quasiparticle states will remain available in a certain energy window around the Fermi level, essentially opening the characteristic *superconducting energy gap* in the quasiparticle spectrum. The superconducting gap has important ramifications on the underlying transport properties and explains superconductors' perfect electrical conductivity. As long as the system's thermal energy k_BT – where k_B stands for Boltzmann's constant and T indicates the temperature – does not exceed the gap's amplitude, no quasiparticles can be excited and scattered at the crystal lattice. As a consequence, all electrical current must be solely carried by the superconducting condensate, which behaves itself like a superfluid [124]

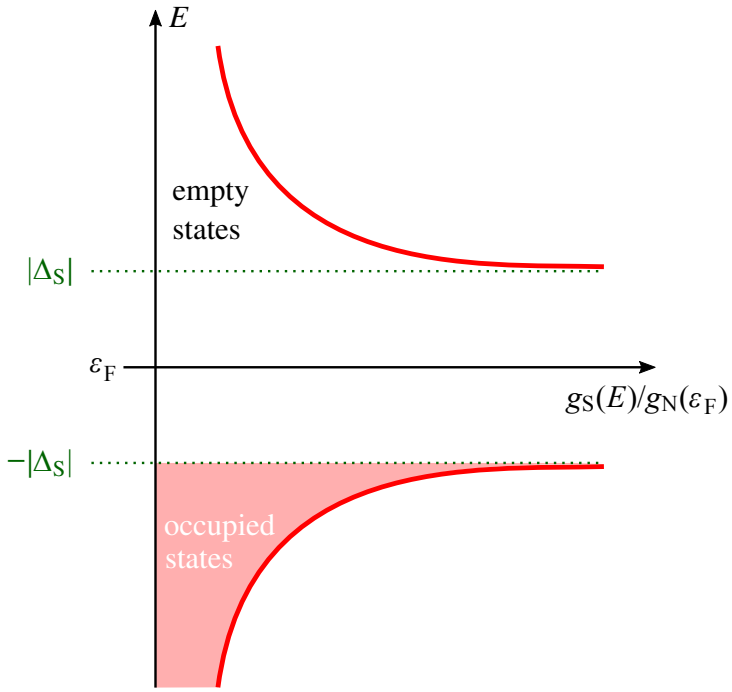


Fig. 2.7: Schematical illustration of the BCS quasiparticle DOS in the superconducting state $g_\mathrm{S}(E)$, normalized to the normal-state DOS $g_\mathrm{N}(\varepsilon_\mathrm{F})$ at the Fermi level. Occupied states are indicated by shading; the superconducting energy gap $2|\Delta_\mathrm{S}|$ is clearly visible.

and is thus not subject to any energy dissipation. The result is a completely dissipationless supercurrent and the superconductor really mimics a perfect conductor.

The off-diagonal components of the effective BCS Hamiltonian in Eq. (2.32) vanish if the BCS coherence factors are, for instance, chosen according to

$$u_\mathbf{k} = \frac{\mathrm{i}}{\sqrt{2}} \mathrm{e}^{\mathrm{i}\phi_\mathrm{S}/2} \sqrt{1 + \frac{\varepsilon_\mathbf{k}}{\sqrt{\varepsilon_\mathbf{k}^2 + |\Delta_\mathrm{S}|^2}}} \tag{2.35}$$

and

$$v_\mathbf{k} = \frac{\mathrm{i}}{\sqrt{2}} \mathrm{e}^{\mathrm{i}\phi_\mathrm{S}/2} \sqrt{1 + \frac{\varepsilon_\mathbf{k}}{\sqrt{\varepsilon_\mathbf{k}^2 + |\Delta_\mathrm{S}|^2}}}; \tag{2.36}$$

this choice apparently fulfills the normalization requirement stated in Eq. (2.28). Eventually, rewriting the diagonalized Hamiltonian in terms of the Bogoljubov operators [defined in Eqs. (2.33) and (2.34)],

$$\hat{\mathcal{H}}_\mathrm{BCS}^\mathrm{eff.} = \sum_\mathbf{k} E_\mathbf{k} \left(\hat{b}_{\mathbf{k},\uparrow}^\dagger \hat{b}_{\mathbf{k},\uparrow} + \hat{b}_{-\mathbf{k},\downarrow}^\dagger \hat{b}_{-\mathbf{k},\downarrow} \right) + \text{constant}, \tag{2.37}$$

yields the quasiparticle excitation energies

$$E_\mathbf{k} = \pm \sqrt{\varepsilon_\mathbf{k}^2 + |\Delta_\mathrm{S}|^2}. \tag{2.38}$$

The positive sign corresponds to the *electronlike* and the negative one to the *holelike* branch of the spectrum. In contrast to semiconductors, electronlike and holelike quasiparticles in the BCS theory are supposed to have equal (effective) masses. The quasiparticle spectrum governed by Eq. (2.38) is schematically plotted once for the normal state ($|\Delta_\mathrm{S}| = 0$) and once for the superconducting state ($|\Delta_\mathrm{S}| \neq 0$)

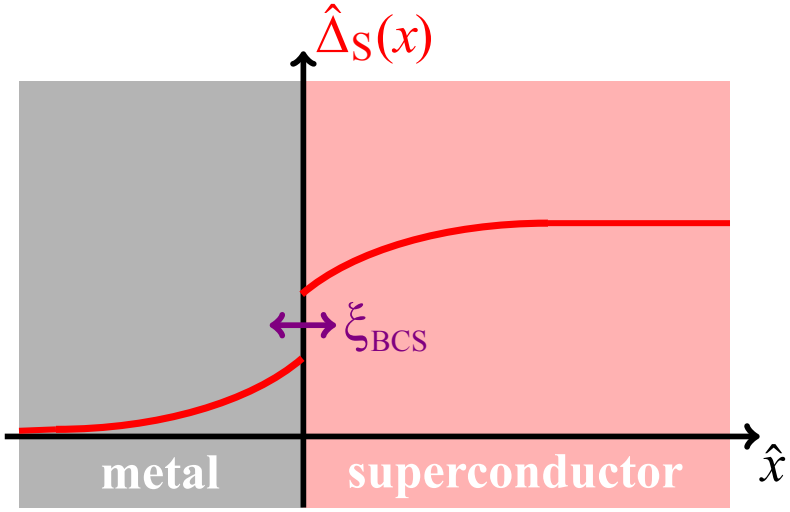


Fig. 2.8: Schematical illustration of the proximity effect close to a metal/superconductor interface (for simplicity, one-dimensional along the $\hat{x}$-direction). Due to the tunneling of unpaired electrons into the superconductor and the leakage of Cooper pairs into the metal, the superconducting pairing potential $\hat{\Delta}_S(x)$ will not immediately drop to zero at the interface, but rather decay over the characteristic BCS coherence length ξ_{BCS}.

in Fig. 2.6. While we recover the well-known parabolic dispersion in the first case, more attention has to be paid to the second scenario. Indeed, the electronlike and holelike branches split close to the Fermi level and an energy gap with magnitude $2|\Delta_S|$ opens. Inside the gap, there are no allowed states to excite (unpaired) quasiparticles so that the only possible configuration there is to really form the superconducting condensate out of the Cooper pairs. The size of the superconducting energy gap – typically in the meV-range – depends on the concrete material and temperature, and is an important quantity in experimental studies as it does not only appear in the quasiparticle spectrum, but also crucially impacts superconductors' quasiparticle DOS

$$\frac{g_S(E)}{g_N(\varepsilon_F)} \approx \frac{E}{\sqrt{E^2 - |\Delta_S|^2}} \Theta(E - |\Delta_S|). \tag{2.39}$$

In Eq. (2.39), we normalized the DOS in the superconducting state $g_S(E)$ at a fixed (quasiparticle) excitation energy E to the normal state's DOS $g_N(\varepsilon_F)$ at the Fermi level; $g_S(E)/g_N(\varepsilon_F)$ is schematically depicted in Fig. 2.7. Measuring the differential conductance of a superconducting tunnel junction composed of aluminum, aluminum oxide, and lead at liquid-helium temperatures, and relating the outcomes to the characteristic DOS in Eq. (2.39), Giaever [138] experimentally extracted valuable information about the superconducting energy gap already shortly after its initial prediction by the BCS theory.

Bogoljubov-de Gennes description

Paving the way towards spintronics applications built out of superconducting materials requires to efficiently combine superconducting regions with other components, e.g., normal-conducting or ferromagnetic electrodes, in one and the same device. Therefore, it becomes indispensable for theorists to have a powerful tool at hand that can be used to reliably describe *spatially-dependent superconducting systems*, as, for instance, metal/superconductor contacts comprising finitely extended metallic and superconducting electrodes. One possibility to formulate a *quasiparticle-based* Hamiltonian for that purpose

is the Bogoljubov-de Gennes Hamiltonian [139]

$$\hat{\mathcal{H}}_{\mathrm{BdG}} = \begin{bmatrix} -\frac{\hbar^2}{2m}\boldsymbol{\nabla}^2 - \varepsilon_{\mathrm{F}} + \hat{\mathcal{U}}(\mathbf{r}) & \hat{\Delta}_{\mathrm{S}}(\mathbf{r}) \\ \hat{\Delta}_{\mathrm{S}}^*(\mathbf{r}) & \frac{\hbar^2}{2m}\boldsymbol{\nabla}^2 + \varepsilon_{\mathrm{F}} - \hat{\mathcal{U}}(\mathbf{r}) \end{bmatrix}. \tag{2.40}$$

A rigorous derivation of this Hamiltonian can be looked up, e.g., in Ref. [140]. Comparing its general form to the (**k**-space) BCS Hamiltonian, [see Eq. (2.32)] is already enough to recognize the close similarity between the BCS approach on the one and the Bogoljubov-de Gennes formulation on the other hand. Simply speaking, one replaces the **k**-space single-particle energies for the electronlike and the holelike quasiparticle branches by their respective real-space Schroedinger Hamiltonians [still measured with respect to the Fermi energy ε_{F}, assuming equal electronlike and holelike quasiparticle masses m, and additionally accounting for possibly present space-dependent potentials $\hat{\mathcal{U}}(\mathbf{r})$]. The superconducting pairing potential (order parameter) $\hat{\Delta}_{\mathrm{S}}(\mathbf{r})$ formally couples the electron and hole blocks, and hence introduces superconductivity into the modeling. Contrary to the situation in a bulk s-wave superconductor, for which we assumed the pairing potential (in **k**-space) to be constant, $\hat{\Delta}_{\mathrm{S}}(\mathbf{r})$ can now strongly modulate in space, depending on the regarded geometry. An important example for that is the contact between a metal and a superconductor, as shown in Fig. 2.8. Due to the close proximity of the two materials, unpaired electrons tunnel from the metal into the superconductor and introduce "disorder" there. Vice versa, Cooper pairs can also leak from the superconducting area into the metal and cause superconducting order in the actually nonsuperconducting component. As a consequence of this *proximity effect*, the superconducting pairing potential will not abruptly drop to zero inside the metal. Instead, $\hat{\Delta}_{\mathrm{S}}(\mathbf{r})$ typically decays over a characteristic length scale with increasing distance from the interface. The exact spatial dependence of $\hat{\Delta}_{\mathrm{S}}(\mathbf{r})$ can be numerically determined for the considered system by means of self-consistent (BCS-based) techniques [141]. In the end, it turns out that the characteristic decay length is again crucially related to the coherent character of the condensate's wave function and is therefore uniquely determined by the BCS coherence length $\xi_{\mathrm{BCS}} = (\hbar v_{\mathrm{F}})/(\pi|\Delta_{\mathrm{S}}|)$, which we already encountered before. Owing to its well-understood mathematical structure and the possibility to extract valuable analytical results, the Bogoljubov-de Gennes Hamiltonian in Eq. (2.40) will be the starting point for nearly all our theoretical investigations presented in the following chapters.

2.2 Ferromagnetism – Stoner band model

This thesis is mostly dedicated to investigating the intriguing interplay of superconductivity and ferromagnetism – two actually opposing states as already Onnes himself noticed – in several junction geometries. To complete our introduction into the physics of the single constituents, we are now concerned with ferromagnetism. The probably most characteristic quality of ferromagnets refers to the fact that all their magnetic moments and electron spins can be spontaneously aligned parallel to each other, even in the absence of external magnetic fields, as long as the temperature does not exceed the material-specific Curie temperature T_{Curie}. This alignment gives rise to a finite net magnetization of the material, reaching saturation when *all* magnetic moments are perfectly aligned along the same direction. Increasing the temperature above T_{Curie}, thermal fluctuations destroy the regular orientation of the spins and the material switches to its normal (nonferromagnetic) state. Following similar considerations as in the case of superconductors, we deduce that the spontaneous phase transition from the "disordered" (nonferromagnetic) into the ordered (ferromagnetic) phase appears if the system can gain energy (reduce its total energy) through aligning the electron spins parallel to each other. While ferromagnetism itself is generally a complex phenomenon, going far beyond the scope of this thesis, Stoner and Wohlfarth succeeded in describing the ferromagnetic properties of transition metals, such as copper, nickel, and iron, by

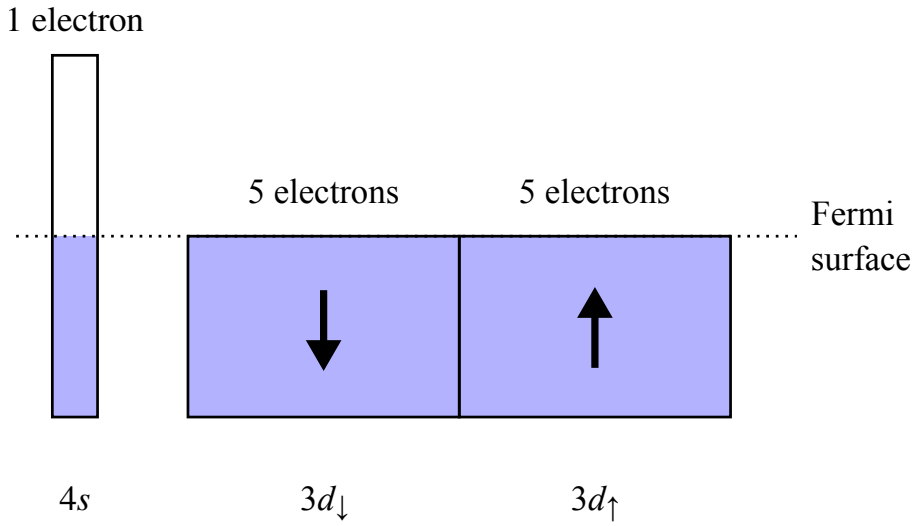


Fig. 2.9: Schematical occupations of the $4s$- and spin-resolved $3d$-subbands, $3d_\uparrow$ and $3d_\downarrow$, in copper. As all (sub)bands contain an equal number of spin-up and spin-down electrons, copper does not become ferromagnetic.

means of a simple model [132]. Understanding this so-called *Stoner band model* is sufficient for our purposes. Although the electronic configurations of copper and nickel are quite similar – copper with the configuration $[\mathrm{Ar}]\,3d^{10}\,4s^1$ has simply one electron (per atom) more than nickel with the configuration $[\mathrm{Ar}]\,3d^8\,4s^2$ –, there must be a fundamental distinction between the two elements since only nickel becomes ferromagnetic. The Stoner band model is able to explain this difference by simply filling the ferromagnets' spin-resolved bands (orbitals) with the available electrons.

Let us start describing the physical situation in the nonferromagnetic copper (for simplicity, we regard copper just at zero temperature). Due to Pauli's exclusion principle, the $4s$-band can be maximally occupied by two electrons with opposite spins and the degenerate $3d$-band at most by ten electrons (five spin-up and five spin-down electrons). Following copper's electronic configuration ($[\mathrm{Ar}]\,3d^{10}\,4s^1$), we deduce that the $3d$-band must indeed be completely filled, whereas the $4s$-band contains only one single valence electron, as schematically depicted in Fig. 2.9. Note that the $4s$-band is usually not split into spin-resolved subbands since this band comprises *on average* equal numbers of spin-up and spin-down electrons. The system's total magnetization M is usually determined by an imbalance between the numbers of spin-up and spin-down electrons, $N_\uparrow$ and $N_\downarrow$. If each single electron contributes one *Bohr magneton* μ_B, we can write M as

$$M = \mu_\mathrm{B}\left(N_\uparrow - N_\downarrow\right). \tag{2.41}$$

Apparently, both the $4s$- and the $3d$-bands in copper are filled with just as many spin-up as spin-down electrons so that the total (effective) magnetization becomes zero and copper is not ferromagnetic.

Nickel with the electronic configuration $[\mathrm{Ar}]\,3d^8\,4s^2$ has one electron less and the spin-resolved $3d$-subbands are thus no longer fully occupied. As the electrons in transition metals are itinerant, they are not strictly located in the $4s$- or $3d$-bands, but can rather be found in all the different bands with certain probabilities. Above the Curie temperature (nonferromagnetic state), each of the two $3d$-subbands contains *on average* 4.73 electrons; the remaining 0.54 electrons are put into the $4s$-band. As before, all bands comprise *on average* the same numbers of spin-up and spin-down electrons, and the net magnetization vanishes (as expected in the nonferromagnetic state). A schematical illustration of the situation can be found in Fig. 2.10(a). If the temperature decreases now below $T_\mathrm{Curie}(\mathrm{Ni}) \approx 631\,\mathrm{K}$ [142], a strong exchange interaction between the electron spins comes into play and the spin-resolved $3d$-subbands

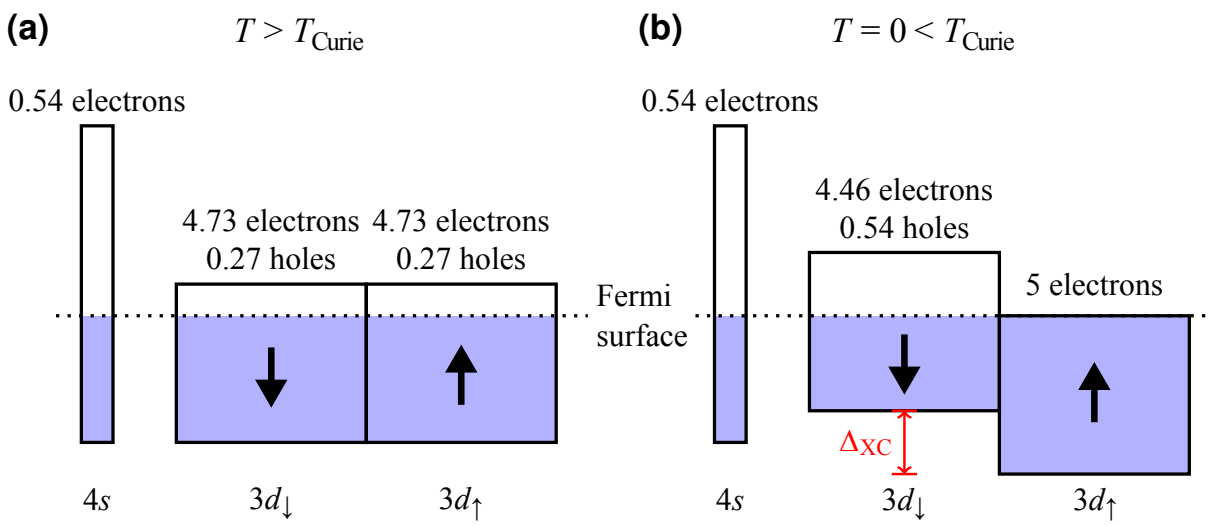


Fig. 2.10: Schematical occupations of the $4s$- and spin-resolved $3d$-subbands, $3d_\uparrow$ and $3d_\downarrow$, in nickel at temperatures **(a)** above T_{Curie} and **(b)** below T_{Curie} (i.e., at $T = 0$). In the second case, the exchange interaction between the electron spins opens the exchange energy gap Δ_{XC} between the $3d_\uparrow$- and the $3d_\downarrow$-subbands. The system reduces its total energy through primarily occupying the lower-energy band, i.e., the $3d_\uparrow$-band. As there are now more electrons in the spin-up than in the spin-down subband, a net magnetization arises and nickel becomes ferromagnetic.

spontaneously split, opening the *exchange energy gap* Δ_{XC}. Compared to the superconducting energy gap ($|\Delta_{\text{S}}| \sim$ meV), ferromagnets' exchange gaps are usually sizable ($\Delta_{\text{XC}} \sim$ eV). Consequently, the system may significantly reduce its total energy through primarily occupying the lower-energy subband, i.e., the $3d_\uparrow$-band in Fig. 2.10(b). At zero temperature, the $3d_\uparrow$-subband becomes eventually completely filled with five electrons, whereas only 4.46 electrons remain *on average* for the $3d_\downarrow$-subband. The occupation of the $4s$-band does not change, but would also not matter as this band still contains *on average* equal numbers of spin-up and spin-down electrons. Due to the imbalance between the $3d_\uparrow$- and the $3d_\downarrow$-subbands – the bands are commonly termed *majority-spin band* (containing the *majority* of electrons) and *minority-spin band* (containing the *minority* of electrons) –, Eq. (2.41) suggests that nickel becomes ferromagnetic (spin polarized) with a net magnetization of $M = 0.54\mu_{\text{B}}$ (per atom).

The key ingredient for ferromagnetism is thus the exchange interaction between electron spins, which causes the spontaneous splitting of subbands and opens Δ_{XC}. Such a band splitting will only occur in real ferromagnets if the system can gain energy through subsequently "redistributing" electrons between the bands. From simple considerations, comparing the involved energy costs for the electron redistribution with the resulting energy gain, Stoner deduced a formal criterion to estimate whether the ferromagnetic state becomes the energetically favorable phase of a system. In the following, we will briefly address his main steps according to Ref. [143]. The DOS for the two regarded spin subbands in the normal state (at $T > T_{\text{Curie}}$) is schematically illustrated in Fig. 2.11. Without any impact of external magnetic fields, all available states below the Fermi energy ε_{F} are occupied and each band contains $N/2$ electrons (with N being the total number of electrons in the system). If the material gets ferromagnetic, Δ_{XC} opens and it becomes favorable to predominantly fill that subband with lower total energy; in our example of nickel, this is the $3d_\uparrow$-subband, as one sees in Fig. 2.10(b). To realize such a configuration, in comparison with the normal state, spin-down electrons in a certain energy interval around ε_{F} (let us call the interval δE) are suddenly brought into free states of the other subband (accompanied by a spin flip). The number of electrons in the spin-down subband after this "redistribution" is roughly given

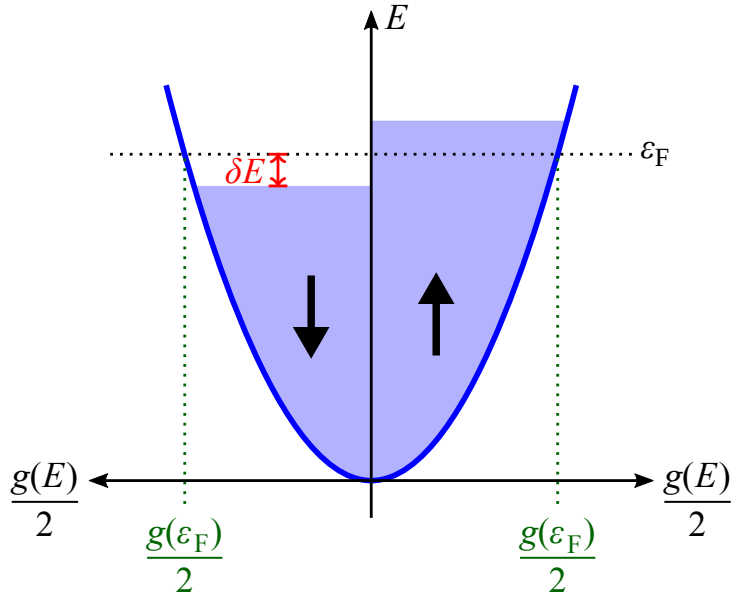


Fig. 2.11: Schematical illustration of the "redistribution" of electrons to switch from the normal to the ferromagnetic state. In the normal state, both spin subbands ↑ and ↓ are initially completely filled with electrons up to the Fermi energy ε_F; the spin bands' DOS $g(\varepsilon_F)$ is indicated by the blue parabola. If the material becomes ferromagnetic, an exchange energy gap opens and the system gains energy through predominantly occupying the majority-spin band (e.g., the spin-up band) with electrons. To derive the Stoner criterion, we suppose the simple case that such an imbalance in occupation can be formed out of the initial normal state "redistributing" spin-down electrons in an energy interval δE around ε_F into the spin-up band (accompanied by a spin flip).

by

$$N_\downarrow \approx \frac{N}{2} - \frac{g(\varepsilon_F)}{2}\delta E \tag{2.42}$$

and that in the spin-up subband by

$$N_\uparrow \approx \frac{N}{2} + \frac{g(\varepsilon_F)}{2}\delta E, \tag{2.43}$$

accordingly; $g(\varepsilon_F)$ is the normal-state DOS at the Fermi level (see also Fig. 2.11).

The kinetic energy required for this process is

$$\Delta\mathcal{T} = \frac{g(\varepsilon_F)}{2}(\delta E)^2, \tag{2.44}$$

while the potential energy is simultaneously reduced by an amount of

$$\Delta\mathcal{U} = -\int_0^M \mathrm{d}M' \, |\mathbf{H}_{\mathbf{XC}}(M')| \,. \tag{2.45}$$

The magnetization $M = |\mathbf{M}|$ got defined in Eq. (2.41) and $|\mathbf{H}_{\mathbf{XC}}(M)|$ refers to the magnetic field caused by the exchange interaction. Weiss approximated the exchange interaction between electron spins considering one spin in the mean field of all others [144] to finally obtain

$$|\mathbf{H}_{\mathbf{XC}}(M)| = \mu_0 \lambda M \tag{2.46}$$

with a temperature-dependent parameter λ; μ_0 is still the vacuum permeability.

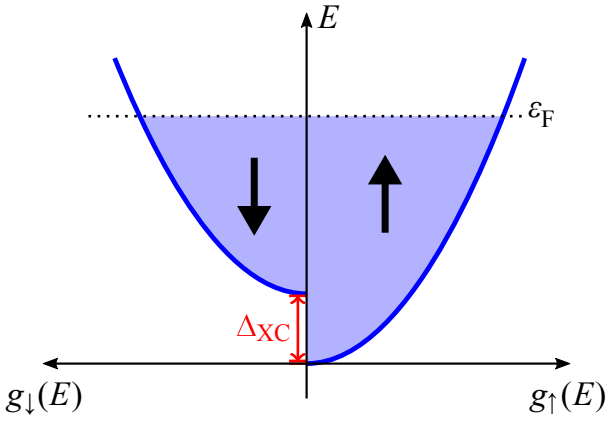


Fig. 2.12: Schematical illustration of the DOS in the ferromagnetic state. Occupied states below the Fermi energy ε_F are indicated by shading; $g_\uparrow$ and $g_\downarrow$ refer to the DOS of the spin-up and spin-down bands, respectively, while Δ_{XC} marks the exchange energy gap.

Inserting Eq. (2.46) into Eq. (2.45), performing the integration, and finally also substituting Eq. (2.44) yields for the system's *total energy change*

$$\Delta E := \Delta\mathcal{T} + \Delta\mathcal{U} = \frac{g(\varepsilon_F)}{2}\,(\delta E)^2\,[1 - Ig(\varepsilon_F)]\,. \tag{2.47}$$

For the magnetization part, Eq. (2.41) was combined with Eqs. (2.42) and (2.43). The *Stoner parameter* $I = \mu_0\lambda\mu_B^2$ provides an effective (material-dependent) measure for the strength of the exchange interaction. The ferromagnetic state becomes favorable if the total energy change gets negative (energy gain), implying $\Delta E < 0$ or equivalently

$$Ig(\varepsilon_F) > 1. \tag{2.48}$$

Equation (2.48) finally provides the claimed way to simply estimate under which conditions the ferromagnetic state of certain materials is the energetically favorable configuration; this criterion is called *Stoner criterion*. Apparently, one important requirement would be to maximize $g(\varepsilon_F)$, demanding a band structure with flat bands close to the Fermi level.

The exchange energy gap Δ_{XC} is also clearly evident in ferromagnets' typical DOS, which is exemplarily shown in Fig. 2.12. As before, the spin-up subband is the energetically favorable one and gets predominantly occupied by electrons (majority-spin subband). Consequently, the DOS close to the Fermi level is also greater in the spin-up than in the spin-down (minority-spin) subband. An alternative measure to quantify the imbalance between up- and down-spins in ferromagnets is the *spin polarization*. There exists a variety of slightly different ways to define the latter quantity; one DOS-based possibility would be

$$P_g = \frac{g_\uparrow(\varepsilon_F) - g_\downarrow(\varepsilon_F)}{g_\uparrow(\varepsilon_F) + g_\downarrow(\varepsilon_F)}, \tag{2.49}$$

which effectively traces the spin imbalance back to the different DOS in the spin-resolved subbands close to the Fermi level, $g_\uparrow(\varepsilon_F)$ and $g_\downarrow(\varepsilon_F)$. Other definitions may, for instance, rather regard directly the electron numbers $N_\uparrow$ and $N_\downarrow$. Anyway, the spin polarization is an unambiguous quantity for the characterization of spintronics devices as it determines, e.g., how efficiently electron spins can be injected from ferromagnets into normal contacts [27]. Particularly puzzling is the limit of maximally spin-polarized materials ($P_g = 1$). Equation (2.49) suggests for those ferromagnets that only majority-spin states can be occupied close to the Fermi level. As a result, *half-metallic* ferromagnets are metallic for majority-spin electrons and perfectly insulating for minority-spin electrons; see Fig. 2.13 for illustration. Such extraordinary properties can lead to diverse unexpected transport features, such as huge magnetoresistance effects [145].

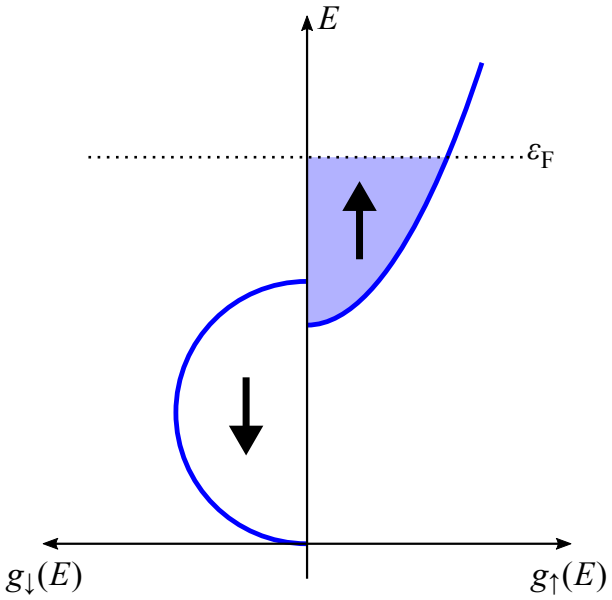


Fig. 2.13: Schematical illustration of the DOS in the *half-metallic* ferromagnetic state. The notation is the same as in Fig. 2.12. At the Fermi level, only majority-spin states are occupied, indicating that the ferromagnet becomes insulating for minority-spin electrons.

2.3 Spin-orbit coupling in solids

Another important ingredient to tailor spintronics devices in the framework of potential technical applications is the *spin-orbit interaction*. Simply speaking, electrons moving through relativistic systems in the presence of electric fields always feel an effective magnetic field in their rest frame. The electron spins can then couple to the effective magnetic field, giving rise to an effective Zeeman interaction (in analogy to the interaction appearing between electron spins with "real" magnetic fields applied to a system), which is termed spin-orbit interaction. Such SOC effects are responsible for various unforeseeable phenomena in solids, such as the sudden splitting of initially degenerate energy bands or g-factors that can strongly deviate from those of free electrons and even become negative in some semiconductors [39, 146]. During our analyses of several superconducting junctions within the next chapters, we will additionally identify SOC as one of the most efficient tools to control the systems' fundamental transport properties like their maximally supported tunneling current flow. The aim of this section is to briefly introduce the basics for the theoretical description of SOC-related effects, mostly based on the detailed presentation in Ref. [27]. This reference is also strongly recommended for additional reading.

A common understanding of SOC is usually developed from the underlying SOC Hamiltonian in its general form,

$$\hat{\mathcal{H}}_{\mathrm{SOC}} = \frac{e\hbar}{4m_{\mathrm{e}}^2c^2}\hat{\boldsymbol{\sigma}} \cdot (\mathbf{E} \times \hat{\mathbf{p}}) \,. \tag{2.50}$$

In the absence of external magnetic fields, $\hat{\mathcal{H}}_{\mathrm{SOC}}$ can, for instance, be extracted as a relativistic correction term appearing in electrons' Pauli equation [147]. Thereby, e denotes the positive elementary charge, m_{e} is the free-electron mass, and c the vacuum speed of light; $\hat{\mathbf{p}} = -\mathrm{i}\hbar\boldsymbol{\nabla}$ refers to the canonical momentum operator and $\hat{\boldsymbol{\sigma}} = \left[\hat{\sigma}_x, \hat{\sigma}_y, \hat{\sigma}_z\right]^\top$ is the vector containing the Pauli spin matrices. The electric field $\mathbf{E}$, entering Eq. (2.50), does not only account for externally supplied electric fields, but also for intrinsic ones. Particularly in solids, the exposure of the electrons to the periodic crystal potential inevitably produces such intrinsic $\mathbf{E}$-fields. On the other hand, this simultaneously suggests that SOC reveals the crystal lattice's symmetry, requiring the SOC Hamiltonian in Eq. (2.50) to obey Bloch's theorem. The

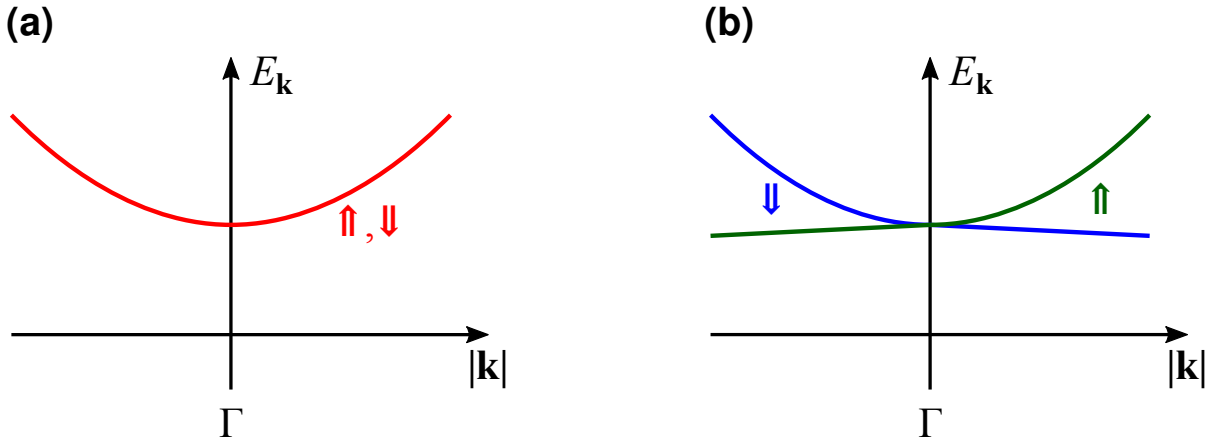


Fig. 2.14: Schematical illustration of the spin-resolved energy bands ($E_{\mathbf{k}}$ *vs.* $|\mathbf{k}|$) in **(a)** *centrosymmetric* and **(b)** *noncentrosymmetric* materials; SOC is present in both cases. As long as space-inversion symmetry is not broken, the SOC Hamiltonian's effective spin-up and spin-down states, indicated by ⇑ and ⇓, have the same eigenenergies [red curve in **(a)**]. Apart from high-symmetry points like the Γ-point, this spin degeneracy is lifted in materials lacking space-inversion symmetry [blue and red curves in **(b)**].

latter finding immediately allows us to construct the eigenstates of the SOC Hamiltonian as Bloch waves. However, as one of its most characteristic properties, SOC couples the different spin bands and hence introduces to a certain extent "spin mixing" into the system. To account for that, we write down the SOC Hamiltonian's eigenstates as Bloch superpositions of the initial spin-up and spin-down states $|\uparrow\rangle$ and $|\downarrow\rangle$ in the absence of SOC (relative to a fixed spin-quantization axis),

$$\Psi_{n,\mathbf{k},\Uparrow}(\mathbf{r}) = \left[a_{n,\mathbf{k}}(\mathbf{r})\,|\uparrow\rangle + b_{n,\mathbf{k}}(\mathbf{r})\,|\downarrow\rangle\right] \mathrm{e}^{\mathrm{i}(\mathbf{k}\cdot\mathbf{r})} \tag{2.51}$$

and

$$\Psi_{n,\mathbf{k},\Downarrow}(\mathbf{r}) = \left[a^*_{n,-\mathbf{k}}(\mathbf{r})\,|\downarrow\rangle - b^*_{n,-\mathbf{k}}(\mathbf{r})\,|\uparrow\rangle\right] \mathrm{e}^{\mathrm{i}(\mathbf{k}\cdot\mathbf{r})}. \tag{2.52}$$

Due to the stated "spin mixing", we call the eigenstates in the presence of SOC *effective spin-up* (⇑) and *effective spin-down* (⇓) states. As usual, $\mathbf{k}$ denotes the wave vector and n a potentially appearing band index. To determine the (spatially-dependent and lattice-periodic) coefficients $a_{n,\mathbf{k}}(\mathbf{r})$ and $b_{n,\mathbf{k}}(\mathbf{r})$, we exploit the fact that SOC is typically weak; thus,

$$|a_{n,\mathbf{k}}(\mathbf{r})| \approx 1 \gg |b_{n,\mathbf{k}}(\mathbf{r})|, \tag{2.53}$$

indeed justifying to term the eigenstates effective spin-up and effective spin-down states.

Applying the time-reversal operator for spin-1/2 particles,

$$\hat{T} = -\mathrm{i}\hat{\sigma}_y\hat{C}, \tag{2.54}$$

where $\hat{C}$ is the operator for complex conjugation, to the SOC Hamiltonian in Eq. (2.50), we conclude that SOC preserves time-reversal symmetry. According to Kramer's postulation [148], the effective spin-up state $\Psi_{n,\mathbf{k},\Uparrow}(\mathbf{r})$ in Eq. (2.51) and its time-reversed state

$$\hat{T}\Psi_{n,\mathbf{k},\Uparrow}(\mathbf{r}) = \left[a^*_{n,\mathbf{k}}(\mathbf{r})\,|\downarrow\rangle - b^*_{n,\mathbf{k}}(\mathbf{r})\,|\uparrow\rangle\right] \mathrm{e}^{-\mathrm{i}(\mathbf{k}\cdot\mathbf{r})} \tag{2.55}$$

must be degenerate and belong to one and the same eigenenergy, say $\varepsilon_{\Uparrow}$. As long as the considered crystal lattice is also symmetric under space inversion, which is generally the case in *centrosymmetric*

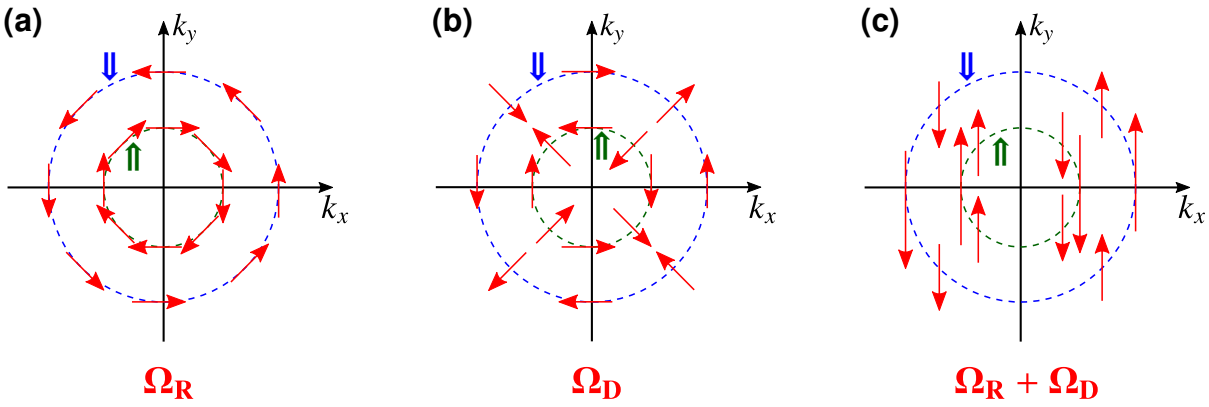


Fig. 2.15: Schematical illustration of the **k**-space orientations of the **(a)** Rashba ($\mathbf{\Omega_R}$) and **(b)** Dresselhaus ($\hat{\mathbf{\Omega}}_\mathbf{D}$) spin-orbit fields ("*spin patterns*") along the two spin-split Fermi surfaces ⇑ (green) and ⇓ (blue). The fields' orientations are indicated by red arrows. **(c)** Simultaneously present Rashba and Dresselhaus spin-orbit fields interfere to the common spin-orbit field $\mathbf{\Omega_R} + \mathbf{\Omega_D}$ with characteristic C_{2v}-symmetry.

materials, additionally replacing the wave vector **k** by **−k** does not change the system's physical properties. But then, the time-reversed effective spin-up state with eigenenergy $\varepsilon_\Uparrow$ [see Eq. (2.55)] simply transforms into the effective spin-down state with eigenenergy $\varepsilon_\Downarrow$ given in Eq. (2.52), thus requiring $\varepsilon_\Uparrow = \varepsilon_\Downarrow$. The latter indicates a central finding of our discussion. The energy bands of centrosymmetric materials are always *twofold spin degenerate*, even when SOC is present; see Fig. 2.14(a) for illustration. The situation turns out to become more interesting in materials that lack space-inversion symmetry. Then, one can no longer replace **k** by **−k** without modifying the physical qualities of the system. Therefore, the effective spin-up and spin-down states in the presence of SOC, given by Eqs. (2.51) and (2.52), then truly represent two independent eigenstates with differing eigenenergies (at least away from high-symmetry points). In other words, SOC breaks the initially twofold spin degeneracy of eigenstates in *noncentrosymmetric materials*, analogously to a "real" Zeeman interaction between electron spins and "real" magnetic fields. The splitting is schematically shown in Fig. 2.14(b). Motivated by that analogy, the SOC Hamiltonian [see Eq. (2.50)] may be rewritten in a more ordinary form as

$$\hat{\mathcal{H}}_{\mathrm{SOC}} = \mathbf{\Omega}(\mathbf{k}) \cdot \hat{\boldsymbol{\sigma}}, \tag{2.56}$$

with the **k**-dependent *spin-orbit field* $\mathbf{\Omega}(\mathbf{k})$ that needs to be an odd function in **k** to preserve the Hamiltonian's time-reversal invariance, i.e., $\mathbf{\Omega}(-\mathbf{k}) = -\mathbf{\Omega}(\mathbf{k})$. Although the way of defining the SOC Hamiltonian in Eq. (2.56) is formally fully equivalent to "real" Zeeman Hamiltonians, the physical analogy is *not* complete. For example, in contrast to the Zeeman interaction, *SOC does preserve time-reversal invariance and does not raise net magnetizations*.

To complete our brief introduction into the physics of SOC, we still need to answer the questions how SOC comes into real systems and the respective spin-orbit fields look like. Overall, one commonly distinguishes between two main SOC mechanisms. The first occurs predominantly in junctions that consist of different electrodes. At the forming interfaces between the constituents, the junctions' space-inversion symmetry is apparently broken and strong electric fields – the key ingredient to SOC, see Eq. (2.50) – arise. According to its discoverers, this mechanism was termed *Bychkov-Rashba SOC* [149, 150] (or just *Rashba SOC* for short). The corresponding Rashba spin-orbit field can be calculated within the Kane model [151], suggesting that – choosing a convenient basis set – one can solve the SOC Hamiltonian in a reduced Hilbert space. Following that procedure, the Rashba spin-orbit field is found to read as

$$\mathbf{\Omega_R} = \alpha(z) \left[k_y, -k_x, 0\right] \tag{2.57}$$

with the material-dependent Rashba SOC parameter $\alpha(z)$. Note that we always work with the principal crystallographic orientations $\hat{x} \parallel [110]$, $\hat{y} \parallel [\bar{1}10]$, and $\hat{z} \parallel [001]$, which is also the most frequently used convention of experimentalists. Concrete values for $\alpha(z)$ can be found, e.g., in Ref. [27].

On the other hand, there exists also a variety of materials in nature that already lack space-inversion symmetry in their bulk. The most prominent representatives of this class are zinc-blende semiconductors like GaAs. The SOC mechanism appearing in such materials is known as *Dresselhaus SOC* [152]; the related spin-orbit field can again be extracted from an extended Kane model [151]. The Dresselhaus spin-orbit field in its original form is of cubic order in $\mathbf{k}$. Nonetheless, the transverse components of $\mathbf{k}$, k_x and k_y, are typically so small that high-order contributions may be neglected and one ends up with the effectively *linearized* (in k_x and k_y) Dresselhaus spin-orbit field

$$\mathbf{\Omega_D}(\mathbf{k}) = \left[-k_y,\, -k_x,\, 0\right] \frac{\mathrm{d}}{\mathrm{d}z}\left(\gamma(z)\frac{\mathrm{d}}{\mathrm{d}z}\right); \tag{2.58}$$

examples for certain materials' Dresselhaus SOC parameters $\gamma(z)$ are again listed in Ref. [27].

Figures 2.15(a) and 2.15(b) depict the $\mathbf{k}$-space orientations of the Rashba and Dresselhaus spin-orbit fields along the two spin-split Fermi surfaces in an illustrative way. Particularly striking seems to be the situation in systems that host both mechanisms simultaneously; see Fig. 2.15(c). The interference of both fields in one system gives rise to an effective spin-orbit field with characteristic C_{2v}-symmetry that will be transferred into the system's transport properties and provides a unique fingerprint for the detection and classification of spin-orbit fields from routine transport measurements, as we will thoroughly discuss for numerous superconducting tunnel junctions throughout this thesis.

Part *II*

Conductance features of superconducting junctions – from the BTK to the OTBK model

Chapter 3

Tunneling conductance features of ballistic F/F-S junctions

The quantum world is full of unexpected and fascinating phenomena. The quantum-mechanical *tunneling effect* [153] is probably one of the most intriguing ones, breaking with all fundamental experiences from our everyday life. Nobody can actually imagine that a classical object, like a football, is thrown against a hard wall, suddenly disappears, and appears again behind the wall just one moment later. Instead, the football simply hits the wall and comes immediately back, as illustrated in Fig. 3.1(a). The region behind the wall is not accessible for classical objects, like our football.

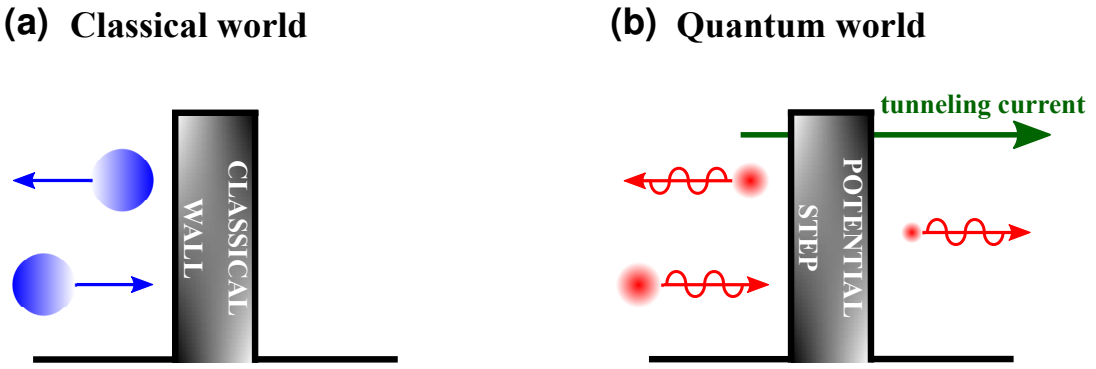


Fig. 3.1: **(a)** "Reflection" of a classical ball (blue) at a hard wall (gray). **(b)** Scattering of an electron (red) at a potential step (gray). The propagation of quantum-mechanical particles is fully characterized by wave functions, which can also extend into the classically forbidden region behind the potential barrier. As a consequence, there is a finite (small) probability that an incident electron tunnels through the step and enters the classically forbidden region, eventually generating a finite tunneling current flow (green). Nevertheless, the probability that electrons undergo reflection processes (like classical objects) is typically still much greater than the tunneling probability (indicated by depicting the tunneling electron much smaller than the incident and reflected ones).

The particularly striking physical features become evident on the quantum scale. Similarly to the classical case, a quantum object, like an electron, incident on a potential step may of course also simply be reflected back. However, all the information available on quantum-mechanical objects is hidden in their respective wave functions that determine the probability for finding the particle at certain positions and time. Schroedinger's equation allows for propagating plane waves as the simplest solution for incoming and scattered particle states. Although the incident wave experiences then an exponential damping inside the scattering region, in which the potential step is present, parts of it can still extend into the region behind the step, even if the height of the potential step exceeds the electron's energy. But measuring a nonzero wave function there simply means that we shall also find our particle (electron) with *nonzero* probability in this region. In other words, the (quantum-mechanical) electron can "choose" between two options: it can either be *reflected* back like a classical object or it may *tunnel* into the classically forbidden area behind the step. Via the wave functions that describe the incoming and scattered particles,

quantum mechanics assigns well-defined probabilities, mostly depending on the incident particle's energy and the concrete potential configuration, to each of these processes. Typically, the tunneling probability is much smaller than the reflection probability so that only a few incoming electrons really tunnel through the potential step [see Fig. 3.1(b) for illustration]. Nevertheless, electrons carry charge and *each* transfer of one electron through the potential step generates a net tunneling current flow in the system. Such tunneling currents have various essential technical applications, e.g., in tunnel diodes [154, 155] or in scanning tunneling microscopy (STM)/scanning tunneling spectroscopy (STS) [156] studies to visualize objects on the scale of single atoms.

The physics of tunnel junctions becomes even more surprising as soon as (at least) one of the regions turns superconducting. For example, one could consider a junction in which the region behind the potential barrier is composed of a superconductor. This might have a substantial impact on the tunneling current, which must then be converted from a normal (dissipative) current into a dissipationless tunneling supercurrent while flowing through the barrier. The latter is of special interest to tailor superconducting spintronics applications [49–51]. Moreover, point contacts between ferromagnetic and superconducting electrodes provide an indispensable and reliable way to experimentally quantify ferromagnets' spin polarization, as reported, e.g., in Refs. [157–163]. From the theoretical perspective, the description of ballistic transport through superconducting junctions by Blonder, Tinkham, and Klapwijk within their Blonder-Tinkham-Klapwijk (BTK) model [164], together with the impressive coincidence between this (strongly) simplified approach and real measurements [158, 162], undoubtedly marked an important milestone on the way towards a universal understanding of superconducting tunneling. Nonetheless, the physical properties of superconducting junctions can *strongly* depend on their concrete composition and the interplay of all of their constituents. Although many different junction geometries, ranging from F/S junctions [165–167] to graphene-based junctions with proximitized ferromagnetic and superconducting regions [168], were investigated, numerous interesting modifications of such geometries have mostly remained untouched so far.

In this chapter, we describe ballistic ferromagnet/ferromagnetic superconductor (F/F-S) junctions within an extended BTK model. The two individual configurations that incorporate ferromagnetism in only one region – F/S junctions [165–167] on the one and normal metal/ferromagnetic superconductor (N/F-S) junctions [168–173] on the other hand – were part of extensive previous studies. The combination of two ferromagnetic components, however, was claimed to cause the most puzzling physical consequences [169] and deserves a fundamental analysis. Ferromagnetic superconductors were mostly excluded in early works as many researchers have believed for quite a long time that bringing ferromagnetism and superconductivity together in one component might be experimentally barely achievable due to their nominally antagonistic properties. Recent studies could show that both can indeed efficiently coexist, e.g., in thin superconducting films [23–25, 174], and generate strongly spin-polarized currents in tunnel junctions [168–173] that make ferromagnetic superconductors appealing candidates for novel junction designs [175].

This chapter aims mostly at introducing the fundamental terminology associated with the BTK model and becoming familiar with the most characteristic transport features of superconducting tunnel junctions. The latter will be important to understand the generalization of the BTK model to Josephson junctions, including two superconducting electrodes, in Chap. 4. The chapter is organized in the following way. After extending the usual quantum-mechanical single-particle tunneling picture to the more general case of superconducting junctions and recapitulating the main points of the BTK model in Sec. 3.1, we are fully equipped to numerically compute the differential tunneling conductance of various realistic junction scenarios. Some of the most relevant results are afterwards discussed in Secs. 3.2 and 3.3, respectively, putting a special emphasis on the influence of ferromagnetic couplings in *both* electrodes on the junctions' transport features. The chapter finally closes with a short summary in Sec. 3.4.

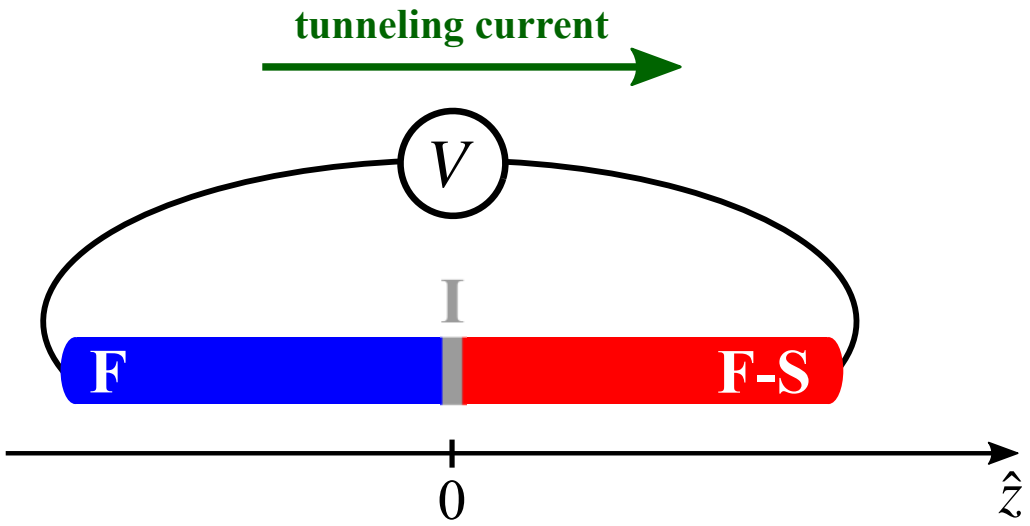


Fig. 3.2: Schematical sketch of the considered *one-dimensional* F/F-S junction grown along the $\hat{z} \parallel [001]$ crystallographic orientation. The two junction electrodes are linked with an ultrathin insulating (I) barrier at $z = 0$. Applying the bias voltage V between the two electrodes induces a tunneling current flow (green) parallel to the $\hat{z}$-direction.

3.1 Theoretical description

We consider an effectively *one-dimensional* biased F/F-S junction grown along the $\hat{z} \parallel [001]$ crystallographic orientation. The junction's two semi-infinite ferromagnet (F) and ferromagnetic-superconductor (F-S) regions are separated by an ultrathin insulating barrier located at $z = 0$ (see Fig. 3.2 for illustration). Such a system might be experimentally realized, for instance, by means of point contact geometries [157, 158] with small interfacial contact cross-section areas and widely extended electrodes along the longitudinal $\hat{z}$-direction.

To model ballistic electrical transport through the system within the BTK model, we first need to fully understand quantum-mechanical scattering of incoming electrons at the interface of the superconducting junction. From the imbalance between incident (*right-moving*) and reflected (*left-moving*) electrons, we can then immediately compute the total tunneling current that is expected to flow.

3.1.1 Bogoljubov-de Gennes scattering states

The starting point for our theoretical discussions is the junction's Bogoljubov-de Gennes Hamiltonian [139] (see Sec. 2.1.3) in the spin-resolved electron-hole Nambu space,

$$\hat{\mathcal{H}}_{\mathrm{BdG}} = \begin{bmatrix} \hat{\mathcal{H}}_{\mathrm{e}} & \hat{\Delta}_{\mathrm{S}}(z) \\ \hat{\Delta}_{\mathrm{S}}^{\dagger}(z) & \hat{\mathcal{H}}_{\mathrm{h}} \end{bmatrix}, \tag{3.1}$$

where

$$\hat{\mathcal{H}}_{\mathrm{e}} = \left[-\frac{\hbar^2}{2} \frac{\mathrm{d}}{\mathrm{d}z} \frac{1}{m(z)} \frac{\mathrm{d}}{\mathrm{d}z} - \mu(z) \right] \hat{\sigma}_0 - \frac{\Delta_{\mathrm{XC}}}{2} \left(\hat{\mathbf{m}} \cdot \hat{\boldsymbol{\sigma}} \right) \Theta(-z) - \frac{\Delta_{\mathrm{Z}}}{2} \left(\hat{\mathbf{n}} \cdot \hat{\boldsymbol{\sigma}} \right) \Theta(z) + V_{\mathrm{I}} d_{\mathrm{I}} \hat{\sigma}_0 \delta(z) \tag{3.2}$$

represents the single-electron Hamiltonian and

$$\hat{\mathcal{H}}_{\mathrm{h}} = -\hat{\sigma}_y \hat{\mathcal{H}}_{\mathrm{e}}^{*} \hat{\sigma}_y \tag{3.3}$$

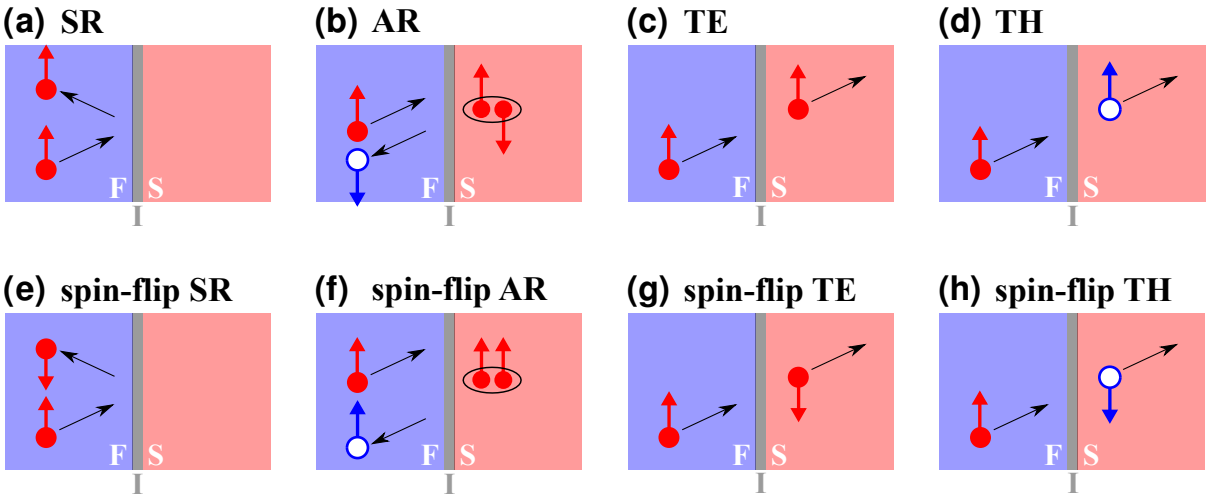


Fig. 3.3: Schematical illustration of the possible scattering processes an incoming spin-up electron from the ferromagnet (F) can undergo at the insulating (I) interface. Electrons are colored red, holes blue, and the electrons' and holes' spins are represented by red and blue arrows; black arrows point along the electrons' and holes' propagation directions. The depicted scattering processes are **(a)** specular reflection (SR), **(b)** Andreev reflection (AR), **(c)** electronlike transmission (TE) into the superconductor (S), **(d)** holelike transmission (TH), **(e)** spin-flip SR, **(f)** spin-flip AR, **(g)** spin-flip TE, and **(h)** spin-flip TH.

its time-reversed holelike counterpart. The two-by-two identity and the ith Pauli spin matrix are denoted by $\hat{\sigma}_0$ and $\hat{\sigma}_i$, respectively, while the vector $\hat{\boldsymbol{\sigma}} = [\hat{\sigma}_x, \hat{\sigma}_y, \hat{\sigma}_z]^\top$ comprises all three Pauli matrices. In general, the effective quasiparticle masses $m(z)$ and Fermi levels $\mu(z)$ differ in the ferromagnet and ferromagnetic superconductor. The latter results from differing charge carrier densities in the materials [167]. Since we are mostly interested in deducing qualitative trends from our model, we assume, for convenience, equal masses and Fermi levels everywhere along the junction, i.e., $m(z) = m$ and $\mu(z) = \mu$. The ferromagnet is described within the Stoner band model (see Sec. 2.2) with the exchange energy gap Δ_{XC}. The unit vector $\hat{\mathbf{m}}$ points along the ferromagnet's magnetization direction. To simplify the following calculations, we solely regard the situation in which the magnetization is aligned parallel to $\hat{z}$ so that $\hat{\mathbf{m}} = [0, 0, 1]^\top$. Similarly, we model the ferromagnetic superconductor in terms of an s-wave superconductor brought into an external magnetic field along $\hat{\mathbf{n}} = [0, 0, 1]^\top$. The magnetic field effectively causes a Zeeman band splitting of magnitude Δ_{Z} inside the superconducting region. Finally, justified by the considerations in earlier studies (see, e.g., Refs. [165–167] and [176]), the ultrathin insulating interface enters our formulation in terms of a deltalike tunneling barrier with height V_{I} and width d_{I}. Since we suppose the junction to be ballistic, we are not concerned with additional (impurity) scattering in the electrodes. The s-wave superconducting pairing potential $\hat{\Delta}_{\mathrm{S}}(z) = |\Delta_{\mathrm{S}}|\hat{\sigma}_0\Theta(z)$ couples the electronlike and holelike blocks of the Bogoljubov-de Gennes Hamiltonian inside the superconductor; $\Theta(\ldots)$ is the Heaviside step function. Thereby, $|\Delta_{\mathrm{S}}|$ refers to the superconducting material's isotropic energy gap, typically of the order of a few meV. It is important to note that writing $\hat{\Delta}_{\mathrm{S}}$ in that steplike form is a rigid approximation. As we discussed in Sec. 2.1.3, proximity effects naturally play a crucial role in real superconducting junctions and $\hat{\Delta}_{\mathrm{S}}$ does therefore not immediately vanish in the ferromagnet, but rather decays on a typical length scale determined by the coherence length. However, the comprehensive analyses in Refs. [177] and [178] showed that, while strongly simplifying the junction's analytical description, working with the idealized steplike $\hat{\Delta}_{\mathrm{S}}$ still yields transport results that are well comparable with experimental measurements. If proximity effects shall be explicitly included, $\hat{\Delta}_{\mathrm{S}}$ would need to be numerically extracted from a self-consistent description, following, for example, the procedure described in Ref. [141].

Once the junction's Bogoljubov-de Gennes Hamiltonian is set up, we can proceed analogously to the description of (nonsuperconducting) scattering problems in fundamental quantum mechanics. There, one solves Schroedinger's equation to extract the scattering states, accounting for the incident electron and all allowed scattering processes in the different regions of the system, and identifies the unknown scattering coefficients applying appropriate boundary conditions at the interface. The crucial difference in our case is that the presence of superconductivity requires to work in electron-hole Nambu space. The Bogoljubov-de Gennes Hamiltonian is then a four-by-four Hamiltonian that allows to include spin-up and spin-down electrons, as well as holes, into just one single Hamiltonian. Consequently, the allowed scattering processes are mathematically modeled by four-component wave functions $\psi(z)$, which we obtain as solutions of the stationary Bogoljubov-de Gennes equation

$$\hat{\mathcal{H}}_{\mathrm{BdG}}\psi(z) = E\psi(z) \tag{3.4}$$

with the electron (quasiparticle) energy E.

Before explicitly constructing the scattering states for our junction, we briefly want to look deeper into the physics associated with scattering at generic F/S interfaces (the superconductor does not necessarily need to be a ferromagnetic superconductor for that). Let us assume, for instance, that a spin-up electron is incident from the ferromagnetic region (spin-down electrons are scattered analogously). That electron propagates through the ferromagnet until it hits the insulating interface and gets scattered. In superconducting junctions, we need to distinguish between *four* scattering processes. Generally speaking, the incoming electron may either be reflected back into the ferromagnet or may enter the superconducting region in terms of an unpaired quasiparticle – in each case, either as an electron(like) or as a hole(like quasiparticle). The four scattering processes are shown in Figs. 3.3(a)–3.3(d). While the incoming spin-up electron undergoing *specular reflection* (sometimes also called *normal reflection*) is again simply reflected as an electron with the same spin, special attention shall be paid to the distinct *Andreev reflection* process [179]. In the latter, the incoming electron [with an energy slightly above the Fermi level, anticipating Eq. (3.6)] becomes retroreflected as a hole with opposite spin [and with an energy slightly below the Fermi level, anticipating Eq. (3.7)]. Effectively, this implies that the incoming electron with spin up and a correlated one with spin down are transferred together into the superconductor (the latter is then missing in the ferromagnet, which we took into account by formally "creating" the Andreev-reflected hole) and form a spin-singlet Cooper pair there. From that point of view, Andreev reflection is *the* crucial scattering process at all types of metal/superconductor interfaces, as it is the microscopic mechanism that converts the incoming normal current into a dissipationless tunneling supercurrent. This demonstrates the strength of the Bogoljubov-de Gennes approach, together with the subsequent BTK modeling, for transport calculations. Via the peculiar Andreev reflection process, even the supercurrent contributions to the tunneling current implicitly enter the model when properly describing scattering of incoming single (quasi)particles, without any need to work out a complicated description that could directly deal with Cooper pairs. Andreev reflection is moreover a phase-coherent process, suggesting that the Andreev-reflected hole carries both the phase information of the initially incident electron and the superconductor's phase. As a consequence, Andreev reflections simultaneously introduce superconducting order into actually nonsuperconducting junction components, like the metal, and are hence closely connected to superconducting proximity effects. A detailed analysis of the coincidence is provided in Ref. [180]. During this thesis, we will come across this puzzling connection several times.

Besides specular and Andreev reflections, the incoming electron could also tunnel through the interface as an unpaired electronlike or holelike quasiparticle with the same spin as the incoming electron. We call these processes *electronlike* and *holelike transmissions*, accordingly. One does often not explicitly distinguish between electronlike and holelike transmissions, and just accumulates both in the term *transmissions*. In the presence of spin-active components, such as semiconducting barriers inducing

strong SOC in the system, each of the four scattering processes can, in principle, additionally be accompanied by a spin flip. Special attention must be paid to the peculiar spin-flip Andreev reflections that essentially facilitate the formation of spin-triplet Cooper pairs in the superconductor. Such *spin-polarized* triplet correlations play, for instance, an intriguing role when generating and controlling sizable charge and spin supercurrents in (strongly) magnetic Josephson junctions, as we will demonstrate in later parts of this thesis. For illustration, all possible spin-flip scattering processes, occurring at the F/S interface, got schematically depicted in Figs. 3.3(e)–3.3(h).

We can eventually formally extract the scattering states, accounting for all the allowed scattering processes in Fig. 3.3, by solving the Bogoljubov-de Gennes equation in Eq. (3.4). Throughout this thesis, we commonly work in the Nambu representation formed by the basis vectors $\psi = \left[\psi^{\uparrow}, \psi^{\downarrow}, (\psi^{\downarrow})^{\dagger}, (-\psi^{\uparrow})^{\dagger}\right]^{\top}$. In addition to the Nambu basis, there are several other conventions used in the literature. Physical observables, like the tunneling current we wish to compute, are of course completely independent of the chosen basis set as long as the formulation is done in a consistent way.

Regarding an incoming electron with spin σ, where $\sigma = 1$ indicates a spin parallel to $\hat{\mathbf{m}}$ (parallel to $\hat{z}$) and $\sigma = -1$ a spin antiparallel to $\hat{\mathbf{m}}$, respectively, the scattering state in the ferromagnet ($z < 0$) is found to be

$$\begin{aligned}\psi^{\sigma}(z<0) = \frac{1}{\sqrt{2}}\begin{bmatrix}\sigma\sqrt{1+\sigma}\\ \sqrt{1-\sigma}\\ 0\\ 0\end{bmatrix} e^{ik^{\sigma}_{z,e}z} + r_e^{\sigma,\sigma}\,\frac{1}{\sqrt{2}}\begin{bmatrix}\sigma\sqrt{1+\sigma}\\ \sqrt{1-\sigma}\\ 0\\ 0\end{bmatrix} e^{-ik^{\sigma}_{z,e}z} + r_e^{\sigma,-\sigma}\,\frac{1}{\sqrt{2}}\begin{bmatrix}-\sigma\sqrt{1-\sigma}\\ \sqrt{1+\sigma}\\ 0\\ 0\end{bmatrix} e^{-ik^{-\sigma}_{z,e}z}\\ + r_h^{\sigma,-\sigma}\,\frac{1}{\sqrt{2}}\begin{bmatrix}0\\ 0\\ \sigma\sqrt{1+\sigma}\\ \sqrt{1-\sigma}\end{bmatrix} e^{ik^{-\sigma}_{z,h}z} + r_h^{\sigma,\sigma}\,\frac{1}{\sqrt{2}}\begin{bmatrix}0\\ 0\\ -\sigma\sqrt{1-\sigma}\\ \sqrt{1+\sigma}\end{bmatrix} e^{ik^{\sigma}_{z,h}z}. \quad (3.5)\end{aligned}$$

For brevity, we will refer to $\sigma = 1$ as spin up and to $\sigma = -1$ as spin down in the following. It is worth to notice that the different parts in the scattering state indeed represent all the reflection processes in Fig. 3.3. The first summand formalizes the incident spin-σ electron, the second and third summands correspond to specular reflections without and with a spin flip, and the fourth and fifth contributions finally to Andreev reflections without and with a spin flip. The related scattering coefficients are denoted by $r_e^{\sigma,\sigma}$, $r_e^{\sigma,-\sigma}$, $r_h^{\sigma,-\sigma}$, and $r_h^{\sigma,\sigma}$; the first σ always determines the incident electron's spin and the second one the spin of the reflected electron (hole). As we explained while discussing the scattering processes, Andreev reflections *without a spin flip* mean that the retroreflected hole must have opposite spin when compared to the incoming particle. Thus, the coefficient $r_h^{\sigma,-\sigma}$ belongs to *spin-conserving* and $r_h^{\sigma,\sigma}$ to *spin-flip Andreev reflections*, contrary to the situation in the specular reflection process. The $\hat{z}$-components of the propagating spin-σ electrons' and holes' wave vectors inside the ferromagnet are given by

$$k^{\sigma}_{z,e} = k^{\sigma}_{z,e}(E) = \sqrt{\frac{2m}{\hbar^2}\left(\mu + E + \sigma\frac{\Delta_{XC}}{2}\right)} \quad (3.6)$$

and

$$k^{\sigma}_{z,h} = k^{\sigma}_{z,h}(E) = \sqrt{\frac{2m}{\hbar^2}\left(\mu - E + \sigma\frac{\Delta_{XC}}{2}\right)}, \quad (3.7)$$

accordingly.

Analogously, the scattering state in the ferromagnetic superconductor ($z > 0$) can be written as

$$\psi^{\sigma}(z>0) = t_{\mathrm{e}}^{\sigma,\uparrow}\begin{bmatrix} u^{\uparrow} \\ 0 \\ v^{\uparrow} \\ 0 \end{bmatrix} \mathrm{e}^{\mathrm{i}q_{z,\mathrm{e}}^{\uparrow}z} + t_{\mathrm{e}}^{\sigma,\downarrow}\begin{bmatrix} 0 \\ u^{\downarrow} \\ 0 \\ v^{\downarrow} \end{bmatrix} \mathrm{e}^{\mathrm{i}q_{z,\mathrm{e}}^{\downarrow}z} + t_{\mathrm{h}}^{\sigma,\uparrow}\begin{bmatrix} v^{\uparrow} \\ 0 \\ u^{\uparrow} \\ 0 \end{bmatrix} \mathrm{e}^{-\mathrm{i}q_{z,\mathrm{h}}^{\uparrow}z} + t_{\mathrm{h}}^{\sigma,\downarrow}\begin{bmatrix} 0 \\ v^{\downarrow} \\ 0 \\ u^{\downarrow} \end{bmatrix} \mathrm{e}^{-\mathrm{i}q_{z,\mathrm{h}}^{\downarrow}z}, \tag{3.8}$$

accounting for transmission of the incident spin-σ electron into the ferromagnetic superconductor as a spin-up ($\uparrow$) or spin-down ($\downarrow$) electronlike (coefficients $t_{\mathrm{e}}^{\sigma,\uparrow}$ and $t_{\mathrm{e}}^{\sigma,\downarrow}$) or holelike (coefficients $t_{\mathrm{h}}^{\sigma,\uparrow}$ and $t_{\mathrm{h}}^{\sigma,\downarrow}$) quasiparticle. Due to the applied Zeeman field in the right electrode, the ferromagnetic superconductor's quasiparticle bands split into a spin-up (essentially a spin parallel to $\hat{\mathbf{n}}$) and a spin-down band (antiparallel to $\hat{\mathbf{n}}$), similarly to the exchange splitting in ferromagnets. Electronlike and holelike excitations within the spin-resolved quasiparticle bands are then characterized by the *spin-resolved coherence factors*

$$u^{\uparrow(\downarrow)} = u^{\uparrow(\downarrow)}(E) = \sqrt{\frac{1}{2}\left\{1 + \sqrt{1 - \frac{|\Delta_{\mathrm{S}}|^2}{[E + (-)\Delta_{\mathrm{Z}}/2]^2}}\right\}}, \tag{3.9}$$

as well as

$$v^{\uparrow(\downarrow)} = v^{\uparrow(\downarrow)}(E) = \sqrt{1 - \left[u^{\uparrow(\downarrow)}(E)\right]^2}; \tag{3.10}$$

the respective spin-resolved $\hat{z}$-projected wave vectors of electronlike quasiparticles are

$$q_{z,\mathrm{e}}^{\uparrow(\downarrow)} = q_{z,\mathrm{e}}^{\uparrow(\downarrow)}(E) = \sqrt{\frac{2m}{\hbar^2}\left\{\mu + \sqrt{\left[E + (-)\frac{\Delta_{\mathrm{Z}}}{2}\right]^2 - |\Delta_{\mathrm{S}}|^2}\right\}} \tag{3.11}$$

and likewise for holelike quasiparticles

$$q_{z,\mathrm{h}}^{\uparrow(\downarrow)} = q_{z,\mathrm{h}}^{\uparrow(\downarrow)}(E) = \sqrt{\frac{2m}{\hbar^2}\left\{\mu - \sqrt{\left[E + (-)\frac{\Delta_{\mathrm{Z}}}{2}\right]^2 - |\Delta_{\mathrm{S}}|^2}\right\}}. \tag{3.12}$$

If the right electrode consists simply of a nonmagnetic superconductor without any external Zeeman field ($\Delta_{\mathrm{Z}} = 0$), the quasiparticle bands' spin splitting is no longer present and the coherence factors in Eqs. (3.9)–(3.10) merge into the usual BCS coherence factors encountered in Sec. 2.1.3. The quasiparticle band structure is then represented by the spin-degenerate case shown in Fig. 2.6(b). Moreover, as a sanity check, one can easily observe that if additionally $|\Delta_{\mathrm{S}}| = 0$, the scattering description in the superconductor reduces to the well-known one for a normal metal.

To assert the unknown reflection and transmission coefficients in the scattering states in Eqs. (3.5) and (3.8), the states are required to fulfill the interfacial ($z = 0$) boundary conditions

$$\psi^{\sigma}(z)\big|_{z=0_-} = \psi^{\sigma}(z)\big|_{z=0_+} \tag{3.13}$$

and

$$\left(\frac{\hbar^2}{2m}\frac{\mathrm{d}}{\mathrm{d}z} + V_{\mathrm{I}}d_{\mathrm{I}}\right)\hat{\eta}\psi^{\sigma}(z)\big|_{z=0_-} = \frac{\hbar^2}{2m}\frac{\mathrm{d}}{\mathrm{d}z}\hat{\eta}\psi^{\sigma}(z)\big|_{z=0_+}, \tag{3.14}$$

with the four-by-four matrix $\hat{\eta} = \mathrm{diag}[\hat{\sigma}_0, -\hat{\sigma}_0]$. Equation (3.13) ensures continuity of the scattering states at the interface, whereas Eq. (3.14) takes the interfacial jumplike behavior of the states' first derivatives, owing to the presence of the deltalike insulating barrier, into account. Applying Eqs. (3.13)–(3.14) to

the states in Eqs. (3.5) and (3.8) yields an eight-dimensional system of equations (for a given spin σ), which can be numerically solved for generic parameter values. In a typical situation, the (quasi)particle excitation energies E and the superconducting energy gap $|\Delta_S|$ (meV-range) are both much smaller than the Fermi energy, i.e., $E \ll \mu$ and $|\Delta_S| \ll \mu$. We can then approximate the wave vectors in the ferromagnet and the ferromagnetic superconductor [see Eqs. (3.6), (3.7), (3.11), and (3.12)] in terms of the Fermi wave vector $k_F = \sqrt{2m\mu}/\hbar$; k_F is the same in both components since we assumed equal Fermi levels. This simplification is particularly helpful if one would aim at finding analytical expressions for the scattering coefficients. Nevertheless, the reflection and transmission coefficients generally still depend on the excitation energies E via the coherence factors [see Eqs. (3.9)–(3.10)].

Once the scattering coefficients are known, we can evaluate the corresponding scattering *probabilities* from the probability currents associated with the incident and scattered waves. If we define for the generic four-component wave function $\psi = \left[\psi_e^{\uparrow}, \psi_e^{\downarrow}, \psi_h^{\uparrow}, \psi_h^{\downarrow}\right]^{\top}$ [$\psi_{e\,(h)}^{\uparrow\,[\downarrow]}$ are the spin-resolved electronlike (holelike) wave function components] the *probability density* for finding either an electron (electronlike quasiparticle) or a hole (holelike quasiparticle) through

$$\rho := \left(\left|\psi_e^{\uparrow}\right|^2 + \left|\psi_e^{\downarrow}\right|^2\right) + \left(\left|\psi_h^{\uparrow}\right|^2 + \left|\psi_h^{\downarrow}\right|^2\right), \tag{3.15}$$

the probability current density, fulfilling the underlying continuity equation (the latter could, for instance, be extracted from the time-dependent Bogoljubov-de Gennes equation similarly to the well-known Schroedinger case), must read

$$j_z^{\rho} = \frac{\hbar}{m}\left\{\mathrm{Im}\left[\left(\psi_e^{\uparrow}\right)^* \frac{\mathrm{d}}{\mathrm{d}z}\psi_e^{\uparrow}\right] + \mathrm{Im}\left[\left(\psi_e^{\downarrow}\right)^* \frac{\mathrm{d}}{\mathrm{d}z}\psi_e^{\downarrow}\right] - \mathrm{Im}\left[\left(\psi_h^{\uparrow}\right)^* \frac{\mathrm{d}}{\mathrm{d}z}\psi_h^{\uparrow}\right] - \mathrm{Im}\left[\left(\psi_h^{\downarrow}\right)^* \frac{\mathrm{d}}{\mathrm{d}z}\psi_h^{\downarrow}\right]\right\}, \tag{3.16}$$

where $\mathrm{Im}(\ldots)$ indicates the imaginary part. Since holes are described as time-reversed electrons within the Bogoljubov-de Gennes approach, they must contribute to the total probability current density with opposite signs when compared to the electrons' contributions. Substituting the scattering states' individual parts, which resemble the different reflection and transmission processes, into Eq. (3.16), we subsequently obtain the probability current densities of all scattered waves. The reflection and transmission probabilities are then given by the ratios of the related scattering probability current densities to the incident one. The final expressions for the scattering probabilities are

$$R_e^{\sigma,\sigma} = R_e^{\sigma,\sigma}(E) = \left|r_e^{\sigma,\sigma}\right|^2, \tag{3.17}$$

$$R_e^{\sigma,-\sigma} = R_e^{\sigma,-\sigma}(E) = \mathrm{Re}\left(\frac{k_{z,e}^{-\sigma}}{k_{z,e}^{\sigma}}\right)\left|r_e^{\sigma,-\sigma}\right|^2, \tag{3.18}$$

$$R_h^{\sigma,-\sigma} = R_h^{\sigma,-\sigma}(E) = \mathrm{Re}\left(\frac{k_{z,h}^{-\sigma}}{k_{z,e}^{\sigma}}\right)\left|r_h^{\sigma,-\sigma}\right|^2, \tag{3.19}$$

$$R_h^{\sigma,\sigma} = R_h^{\sigma,\sigma}(E) = \mathrm{Re}\left(\frac{k_{z,h}^{\sigma}}{k_{z,e}^{\sigma}}\right)\left|r_h^{\sigma,\sigma}\right|^2, \tag{3.20}$$

$$T_e^{\sigma,\uparrow} = T_e^{\sigma,\uparrow}(E) = \mathrm{Re}\left(\frac{q_{z,e}^{\uparrow}}{k_{z,e}^{\sigma}}\right)\left|t_e^{\sigma,\uparrow}\right|^2\left(\left|u^{\uparrow}\right|^2 - \left|v^{\uparrow}\right|^2\right)\Theta\left[E - \left(|\Delta_S| - \frac{\Delta_Z}{2}\right)\right], \tag{3.21}$$

$$T_e^{\sigma,\downarrow} = T_e^{\sigma,\downarrow}(E) = \mathrm{Re}\left(\frac{q_{z,e}^{\downarrow}}{k_{z,e}^{\sigma}}\right)\left|t_e^{\sigma,\downarrow}\right|^2\left(\left|u^{\downarrow}\right|^2 - \left|v^{\downarrow}\right|^2\right)\Theta\left[E - \left(|\Delta_S| + \frac{\Delta_Z}{2}\right)\right], \tag{3.22}$$

$$T_h^{\sigma,\uparrow} = T_h^{\sigma,\uparrow}(E) = \mathrm{Re}\left(\frac{q_{z,h}^{\uparrow}}{k_{z,e}^{\sigma}}\right)\left|t_h^{\sigma,\uparrow}\right|^2\left(\left|u^{\uparrow}\right|^2 - \left|v^{\uparrow}\right|^2\right)\Theta\left[E - \left(|\Delta_S| - \frac{\Delta_Z}{2}\right)\right], \tag{3.23}$$

and

$$T_{\mathrm{h}}^{\sigma,\downarrow} = T_{\mathrm{h}}^{\sigma,\downarrow}(E) = \mathrm{Re}\left(\frac{q_{z,\mathrm{h}}^{\downarrow}}{k_{z,\mathrm{e}}^{\sigma}}\right)\left|t_{\mathrm{h}}^{\sigma,\downarrow}\right|^2\left(\left|u^{\downarrow}\right|^2-\left|v^{\downarrow}\right|^2\right)\Theta\left[E-\left(|\Delta_{\mathrm{S}}|+\frac{\Delta_{\mathrm{Z}}}{2}\right)\right], \tag{3.24}$$

where taking the real part Re(...) of the wave vector ratios ensures that the scattered waves are indeed propagating ones. The Heaviside step function [$\Theta(\ldots)$] in the transmission probabilities got introduced to stress that transmissions into the ferromagnetic superconductor are only allowed if the energy of the incident electron exceeds the superconducting gap; otherwise, there are simply no available quasiparticle states to tunnel into (see Sec. 2.1.3). Owing to the applied Zeeman field and the resulting spin splitting of the quasiparticle bands, the ferromagnetic superconductor can be regarded as an initially nonmagnetic superconductor that opens the *two effective, spin-dependent, superconducting gaps* $\Delta_{\mathrm{S}}^{\uparrow} := |\Delta_{\mathrm{S}}| - \Delta_{\mathrm{Z}}/2$ for spin-up and $\Delta_{\mathrm{S}}^{\downarrow} := |\Delta_{\mathrm{S}}| + \Delta_{\mathrm{Z}}/2$ for spin-down quasiparticles. The existence of two such gaps will have an important impact on the junction's transport characteristics (see Sec. 3.3). Numerically evaluating Eqs. (3.17)–(3.24) completes the comprehensive quantum-mechanical description of scattering at the interface of our considered F/F-S junction and we can proceed to calculate the tunneling current (and the related tunneling conductance) in the next section.

3.1.2 Differential tunneling conductance – BTK model

The BTK model is one of the most powerful analytical approaches to compute tunneling currents in superconducting junctions. One of its greatest advantages is the fact that the Bogoljubov-de Gennes scattering problem discussed in Sec. 3.1 contains all the information that is required to describe transport through the system. It is sufficient to unravel the scattering coefficients (probabilities) belonging to the allowed reflections and transmissions. The supercurrent contributions to the tunneling current are implicitly incorporated in the Andreev reflection process. Consequently, working within the BTK model saves ourselves from developing a complicated formulation that would explicitly capture the Cooper pairs inside the ferromagnetic superconductor. Although the BTK model was restricted to dealing with "simple" normal metal/superconductor (N/S) tunnel junctions in its original version [164], an extension to more complicated systems, as the one we are studying, is straightforward. We will not exactly follow the derivation by BTK in Ref. [164], but rather adapt a slightly different way, which is more transparent and attributes each single current contribution uniquely to its respective scattering process.

Electrical current (in normal conductors) is an effective measure for the net spatial transfer of charge. Throughout the complete thesis, tunneling currents are counted with a *negative sign* if more electrons propagate to the right (along $\hat{z}$) than to the left (along $-\hat{z}$), in order to be consistent with the common convention defining current orientations always *oppositely* to electrons' propagation directions. Therefore, we simply need to figure out the spatial imbalance between right- and left-propagating charge carriers after scattering at the insulating interface. One way would be to compare the ratios of transmitted and reflected carriers. However, since the tunneling current is conserved, we can choose any plane along the junction to calculate the current. It turns out to be most convenient to focus on the ferromagnet, in which only the incident and reflected electrons (holes) carry a net current and no Cooper pairs are present (the Cooper pair contribution implicitly enters our description again via Andreev reflections). In this work, the positive elementary charge is always denoted by e. Although the junction regarded in this chapter is supposed to be (effectively) one-dimensional, we present the current calculation for a generic *three-dimensional* junction since we will need that result later on.

First, we are concerned with the situation of a spin-σ electron (with energy E) incident from the ferromagnetic electrode. This scenario generates a net tunneling current flow, which is given by

$$\left(J_z^\sigma\right)^{\mathrm{LEFT}} = -e \sum_{\mathbf{k}_\parallel} \sum_{k_{z,\mathrm{e}}^\sigma} \left\{ \left[\frac{\hbar k_{z,\mathrm{e}}^\sigma}{m} - \frac{\hbar k_{z,\mathrm{e}}^\sigma}{m} \left| r_\mathrm{e}^{\sigma,\sigma}(E) \right|^2 - \frac{\hbar k_{z,\mathrm{e}}^{-\sigma}}{m} \left| r_\mathrm{e}^{\sigma,-\sigma}(E) \right|^2 \right] f^0(E - eV) \left[1 - f^0(E) \right] \right.$$
$$\left. + \left[-\frac{\hbar k_{z,\mathrm{h}}^{-\sigma}}{m} \left| r_\mathrm{h}^{\sigma,-\sigma}(E) \right|^2 - \frac{\hbar k_{z,\mathrm{h}}^{\sigma}}{m} \left| r_\mathrm{h}^{\sigma,\sigma}(E) \right|^2 \right] \left[1 - f^0(-E - eV) \right] f^0(-E) \right\}. \quad (3.25)$$

We briefly analyze the form of Eq. (3.25). Generally, electrons with charge $-e$ contribute to the electrical current density in a conductor as $j = -env$, where n represents the particle density and v their velocity, respectively. In our case, we can compute the total tunneling current exactly in the same way. The only complication is that we need to include the incident and *all* the scattered particles; each of them gives a net current contribution according to the preceding formula. To give one concrete example, let us look at the first summand in Eq. (3.25). This part refers to the incoming electron with charge $-e$ that propagates *from left to right* with the (*positive*) longitudinal velocity $v_{z,\mathrm{e}}^\sigma = (\hbar k_{z,\mathrm{e}}^\sigma)/m$. At temperature T, the current contribution needs to be multiplied by an appropriate product of Fermi-Dirac distribution functions,[1] ensuring that the incoming state in the ferromagnet is occupied and the superconductor provides free states to tunnel into. Specifically for electrons, this factor has the form $f^0(E - eV)\left[1 - f^0(E)\right]$ [f^0 indicates the generic Fermi-Dirac function]. Note that the shift of the reference energy in one of the electrodes due to the voltage drop V needs to be carefully included into the description. The occupation probability effectively plays the role of the particle density in the generic expression for current densities. To obtain the full current, we finally need to average over all transverse channels in our system, labeled by the wave vector $\mathbf{k}_\parallel = [k_x,\, k_y,\, 0]^\top$ parallel to the F/F-S interface, and over all particle energies E. The latter is done summing over all electron momenta $k_{z,\mathrm{e}}^\sigma$, which themselves depend on E [recall Eq. (3.6)]. Analogously, the remaining parts of Eq. (3.25) count the net current contributions associated with specularly and Andreev-reflected electrons and holes. Since the reflected electrons and holes propagate away from the barrier, their respective velocities enter the current formula with *negative* signs. It is important to note that an incoming electron undergoes specular and Andreev reflections only with certain probabilities, extractable from the reflection coefficients as pointed out in Sec. 3.1. Comparing Eq. (3.25) with the scattering probabilities found in Sec. 3.1 [see Eqs. (3.17)–(3.24)] reveals that the reflection probabilities implicitly enter the current formula via the absolute squares of the reflection coefficients. When setting up the Andreev-reflected hole parts, one must pay special attention to the appearing products of Fermi-Dirac functions. Creating a hole is equivalent to the destruction of an electron. Therefore, the Fermi-Dirac functions for holes need to be chosen such that the corresponding electronic states are unoccupied.

Second, we quantify the current caused by an incoming spin-σ electronlike quasiparticle from the ferromagnetic superconductor (again with energy E), essentially following the same procedure. Instead of dealing with quasiparticles in the ferromagnetic superconductor, it is more common to suppose an incident spin-σ *hole* from the ferromagnet. Both descriptions are fully equivalent for calculating transport properties. The related net tunneling current flow is found to read

$$\left(J_z^\sigma\right)^{\mathrm{RIGHT}} = -e \sum_{\mathbf{k}_\parallel} \sum_{k_{z,\mathrm{h}}^\sigma} \left\{ \left[-\frac{\hbar k_{z,\mathrm{h}}^\sigma}{m} + \frac{\hbar k_{z,\mathrm{h}}^\sigma}{m} \left| \tilde{r}_\mathrm{h}^{\sigma,\sigma}(E) \right|^2 + \frac{\hbar k_{z,\mathrm{h}}^{-\sigma}}{m} \left| \tilde{r}_\mathrm{h}^{\sigma,-\sigma}(E) \right|^2 \right] \left[1 - f^0(E - eV) \right] f^0(E) \right.$$
$$\left. + \left[\frac{\hbar k_{z,\mathrm{e}}^{-\sigma}}{m} \left| \tilde{r}_\mathrm{e}^{\sigma,-\sigma}(E) \right|^2 + \frac{\hbar k_{z,\mathrm{e}}^{\sigma}}{m} \left| \tilde{r}_\mathrm{e}^{\sigma,\sigma}(E) \right|^2 \right] f^0(-E - eV) \left[1 - f^0(-E) \right] \right\}. \quad (3.26)$$

[1] For simplicity, we assume that both junction electrodes are large enough (in fact, they spread even to infinity) so that the populations of incoming particles can be modeled by means of equilibrium Fermi-Dirac functions.

Note that both individual current contributions in Eqs. (3.25) and (3.26) must be expressed within one and the same convention (in our case, *negative currents* flow *to the right*). Otherwise, one could mess up some signs in the end and the total current is no longer balanced. The different parts of Eq. (3.26) have similar physical interpretations as above. The reflection coefficients for an incident hole could, in general, differ from those we obtained for incoming electrons in Sec. 3.1. To stress this difference, we introduced "tilde reflection coefficients" in Eq. (3.26). Particularly in the case of (strongly) antisymmetric junctions, e.g., by having finite-size electrodes, the reflection probabilities for the injection of holes are indeed notably different from the ones for the injection of electrons, and one shall proceed with the given general forms of Eqs. (3.25) and (3.26). However, owing to our junction's particular symmetry, we find that the total specular and Andreev reflection probabilities, averaged across the whole cross-section area, are the same for incoming electrons and holes, i.e.,

$$\sum_{\mathbf{k}_\parallel}\left[k_{z,\mathrm{e}}^{\sigma}\left|r_{\mathrm{e}}^{\sigma,\sigma}(E)\right|^2+k_{z,\mathrm{e}}^{-\sigma}\left|r_{\mathrm{e}}^{\sigma,-\sigma}(E)\right|^2\right]=\sum_{\mathbf{k}_\parallel}\left[k_{z,\mathrm{h}}^{\sigma}\left|\tilde{r}_{\mathrm{h}}^{\sigma,\sigma}(E)\right|^2+k_{z,\mathrm{h}}^{-\sigma}\left|\tilde{r}_{\mathrm{h}}^{\sigma,-\sigma}(E)\right|^2\right] \tag{3.27}$$

and

$$\sum_{\mathbf{k}_\parallel}\left[k_{z,\mathrm{h}}^{-\sigma}\left|r_{\mathrm{h}}^{\sigma,-\sigma}(E)\right|^2+k_{z,\mathrm{h}}^{\sigma}\left|r_{\mathrm{h}}^{\sigma,\sigma}(E)\right|^2\right]=\sum_{\mathbf{k}_\parallel}\left[k_{z,\mathrm{e}}^{-\sigma}\left|\tilde{r}_{\mathrm{e}}^{\sigma,-\sigma}(E)\right|^2+k_{z,\mathrm{e}}^{\sigma}\left|\tilde{r}_{\mathrm{e}}^{\sigma,\sigma}(E)\right|^2\right]. \tag{3.28}$$

This allows us to obtain a rather simple formula for the total tunneling current by combining Eqs. (3.25) and (3.26), rewriting the sums over $\mathbf{k}_\parallel$ and $\sum_{k_{z,\mathrm{e}}^{\sigma}}\{\ldots\}\approx\sum_{k_{z,\mathrm{h}}^{\sigma}}\{\ldots\}$ as integrals within continuum approximation ($\mathcal{A}$ is the interfacial cross-section area), and finally counting the contributions originating from both spin channels,

$$\begin{aligned}J_z=-e\sum_{\sigma=\pm1}\frac{\mathcal{A}}{(2\pi)^3}\int\mathrm{d}^2\mathbf{k}_\parallel\int_{-\infty}^{\infty}\mathrm{d}E\left(\frac{\partial k_{z,\mathrm{e}}^{\sigma}}{\partial E}\right)\Bigg\{\left[\frac{\hbar k_{z,\mathrm{e}}^{\sigma}}{m}-\frac{\hbar k_{z,\mathrm{e}}^{\sigma}}{m}\left|r_{\mathrm{e}}^{\sigma,\sigma}(E)\right|^2-\frac{\hbar k_{z,\mathrm{e}}^{-\sigma}}{m}\left|r_{\mathrm{e}}^{\sigma-\sigma}(E)\right|^2\right]\left[f^0(E-eV)-f^0(E)\right]\\+\left[-\frac{\hbar k_{z,\mathrm{h}}^{-\sigma}}{m}\left|r_{\mathrm{h}}^{\sigma,-\sigma}(E)\right|^2-\frac{\hbar k_{z,\mathrm{h}}^{\sigma}}{m}\left|r_{\mathrm{h}}^{\sigma,\sigma}(E)\right|^2\right]\left[f^0(E+eV)-f^0(E)\right]\Bigg\}.\end{aligned} \tag{3.29}$$

Equation (3.29) is valid at arbitrary temperatures through the general expressions for the Fermi-Dirac functions. However, one should be aware that the intrinsic superconducting energy gap $|\Delta_\mathrm{S}|$ typically decreases with increasing temperature. One could account for that by substituting the gap's BCS-like scaling $|\Delta_\mathrm{S}(T\neq0)|=|\Delta_\mathrm{S}(0)|\tanh(1.74\sqrt{T_\mathrm{C}/T-1})$, where $|\Delta_\mathrm{S}(0)|$ indicates the gap at zero temperature and T_C the superconductor's critical temperature. Within the present study, we restrict our considerations to the simpler case of *zero temperature*.

In experiments, one is basically rather interested in tunnel junctions' conductance, essentially measuring the absolute change of the tunneling current flow with increasing bias voltage. We obtain the *differential tunneling conductance* from $G_{z,z}=-\mathrm{d}J_z/\mathrm{d}V$, adopting the convention that positive conductances indicate negative tunneling currents flowing from left to right. Particularly at zero temperature, we use the approximation $\mathrm{d}f^0(E)/\mathrm{d}E\approx-\delta(E)$ for the first derivatives of Fermi-Dirac functions to arrive at a compact expression for the differential tunneling conductance,

$$\begin{aligned}G_{z,z}\approx\frac{G_0\mathcal{A}}{2(2\pi)^2}\sum_{\sigma=\pm1}\int\mathrm{d}^2\mathbf{k}_\parallel\Bigg\{1-\left[\left|r_{\mathrm{e}}^{\sigma,\sigma}(eV)\right|^2+\frac{k_{z,\mathrm{e}}^{-\sigma}}{k_{z,\mathrm{e}}^{\sigma}}\left|r_{\mathrm{e}}^{\sigma,-\sigma}(eV)\right|^2\right]\\+\left[\frac{k_{z,\mathrm{h}}^{-\sigma}}{k_{z,\mathrm{e}}^{\sigma}}\left|r_{\mathrm{h}}^{\sigma,-\sigma}(-eV)\right|^2+\frac{k_{z,\mathrm{h}}^{\sigma}}{k_{z,\mathrm{e}}^{\sigma}}\left|r_{\mathrm{h}}^{\sigma,\sigma}(-eV)\right|^2\right]\Bigg\},\end{aligned} \tag{3.30}$$

with the conductance quantum $G_0=(2e^2)/h$; $h=2\pi\hbar$ denotes Planck's constant. Equation (3.30) is the generalization of the established BTK conductance formula [164] to ferromagnetic F/F-S junctions. More

commonly, the result gets rewritten in terms of the scattering probabilities determined by Eqs. (3.17)–(3.24) to finally end up with

$$G_{z,z} \approx \frac{G_0 \mathcal{A}}{2(2\pi)^2} \sum_{\sigma=\pm 1} \int \mathrm{d}^2\mathbf{k}_\parallel \left\{ 1 - \left[R_\mathrm{e}^{\sigma,\sigma}(eV) + R_\mathrm{e}^{\sigma,-\sigma}(eV) \right] + \left[R_\mathrm{h}^{\sigma,-\sigma}(-eV) + R_\mathrm{h}^{\sigma,\sigma}(-eV) \right] \right\}. \quad (3.31)$$

As we could have already expected from the fact that holes are modeled as time-reversed electrons (with same effective mass, but opposite charge), the hole-invoking Andreev reflection contributions enter the tunneling conductance with opposite signs compared to the specular reflection parts. As a result, dominant specular reflections decrease the tunneling conductance (which is clear as the incident electrons are then immediately reflected back into the ferromagnet and no tunneling current can be generated at all), whereas pronounced Andreev reflections cause sizable tunneling conductances by transferring correlated electrons through the insulating barrier into the ferromagnetic superconductor. Since the tunneling current is conserved and the junction is considered to be ballistic, its magnitude in the ferromagnetic superconductor is exactly the same as we computed in the ferromagnet. However, the current in the ferromagnetic superconductor flows completely as a tunneling supercurrent, which might have important technical applications due to the suppression of (typically disturbing) dissipative side effects there.

In the following sections, we explore the numerically computed tunneling conductance's features for a variety of realistic parameter regimes. It is worth to notice that the specular and Andreev reflection probabilities entering Eq. (3.31) are *independent* of $\mathbf{k}_\parallel$ for normal incidence on the interface of our (effectively) one-dimensional junction. The integration over $\mathbf{k}_\parallel$ can therefore be analytically performed, simply yielding an effective factor that counts the number of transverse channels. The final expression for the tunneling conductance reads then

$$G_{z,z} \approx \frac{G_\mathrm{S}}{2} \sum_{\sigma=\pm 1} \left\{ 1 - \left[R_\mathrm{e}^{\sigma,\sigma}(eV) + R_\mathrm{e}^{\sigma,-\sigma}(eV) \right] + \left[R_\mathrm{h}^{\sigma,-\sigma}(-eV) + R_\mathrm{h}^{\sigma,\sigma}(-eV) \right] \right\} \Bigg|_{\mathbf{k}_\parallel = \mathbf{0}}, \quad (3.32)$$

where $G_\mathrm{S} = (\mathcal{A} e^2 k_\mathrm{F}^2)/(2\pi h)$ corresponds to the *Sharvin conductance* of a perfectly transparent (three-dimensional) metallic point contact. The only remaining task is to numerically find the reflection (and transmission) probabilities for the given parameter sets, implementing the approach described in Sec. 3.1, by means of a (generalized) LU Decomposition algorithm [181], and to finally substitute the results into Eq. (3.32) to access the junction's tunneling conductance.

3.2 Discussion of results for F/S junctions

Our first analysis focuses on a F/S junction, in which the only ferromagnetic component is the ferromagnet itself and no Zeeman field gets applied to the superconducting region, i.e., we set $\Delta_\mathrm{Z} = 0$ for all calculations in this section. Such junctions are qualitatively and quantitatively well describable within the semiclassical formulation of de Jong and Beenakker [165]. Although this approach is based on rather simple arguments, one can gain valuable physical insight through it. Therefore, we begin this section briefly recapitulating the main aspects of this semiclassical approach. The second part is then dedicated to the discussion of specific numerical calculations, which can be completely understood within the semiclassical picture.

3.2.1 Semiclassical approach of de Jong and Beenakker

To ascertain the impact of the ferromagnet's exchange splitting (or equivalently, its spin polarization's influence) on the (zero-temperature) tunneling conductance, de Jong and Beenakker developed a semi-

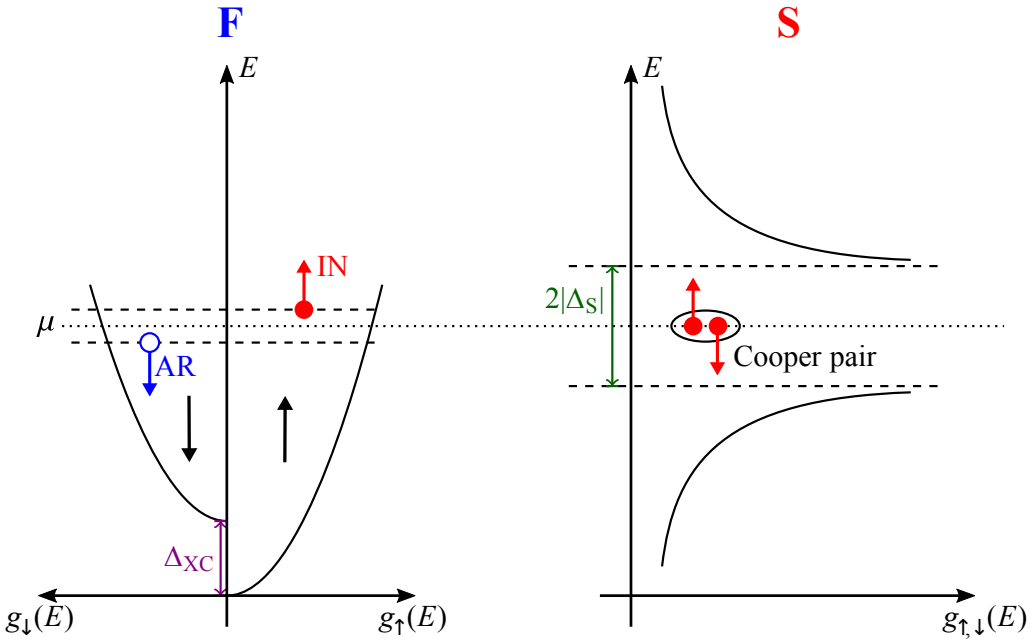


Fig. 3.4: Schematical illustration of the up- and down-spin bands' DOS (as a function of the electron energy E), $g_\uparrow$ and $g_\downarrow$, in the ferromagnet (F; left) and in the superconductor (S; right). The Fermi level is denoted by μ, while $|\Delta_S|$ quantifies the superconductor's isotropic energy gap; electrons are colored red and holes blue. Andreev reflection (AR) of an incident spin-up electron (IN) with an energy slightly above μ formally indicates that the electron gets retroreflected as a hole across the Fermi level, while simultaneously two correlated electrons enter the superconducting region and form a Cooper pair. Due to the finite spin polarization (exchange splitting $\Delta_{XC} \neq 0$) inside the ferromagnet, only a fraction of incoming spin-up electrons finds a spin-down partner to become Andreev reflected. Details are explained in the text.

classical approach [165], which we shortly summarize. To simplify our considerations, we assume that the mean free path of charge carriers in the two junction regions is much greater than the interfacial cross-section area. Moreover, the junction's interface is supposed to be clean, meaning that neither impurity scattering nor a tunneling barrier are present. In the absence of interfacial scattering potentials, specular reflections are suppressed and the incoming electrons must undergo either Andreev reflections or transmissions. If the superconductor is now replaced by a normal metal, Andreev reflection processes become additionally forbidden, and all incident spin-up and spin-down electrons can only be transmitted into the metal. Each tunneling electron contributes then an amount of e^2/h to the F/N junction's total tunneling conductance $G_{z,z}^{\mathrm{F/N}}$. Denoting the number of spin-up and spin-down transmission channels by $N_\uparrow$ and $N_\downarrow$, respectively, we obtain $G_{z,z}^{\mathrm{F/N}}$ in a Landauer-like form simply counting the number of transmitting channels (basically counting the number of transmitted electrons), namely

$$G_{z,z}^{\mathrm{F/N}} = \frac{e^2}{h}\left(N_\uparrow + N_\downarrow\right). \tag{3.33}$$

The situation gets more interesting if the right electrode is indeed superconducting and the unique Andreev reflection processes come fully into play. For convenience, we solely consider electron energies inside the gap (called *subgap energies*) so that transmissions into the superconductor are not possible. As explained previously, Andreev reflection of an incident spin-up electron means that the electron gets retroreflected as a spin-down hole (and vice versa for an electron with spin down), while simultaneously two correlated electrons enter the superconductor and form a spin-singlet Cooper pair. The Andreev reflection process is schematically illustrated in Fig. 3.3(b). Since Andreev reflections

involve both spin-resolved bands of the ferromagnet, it is most natural to trace the underlying physics back to the differing DOS in the corresponding up- and down-spin bands (see Fig. 2.12 for illustration). Figure 3.4 shows a schematic sketch of the the spin-resolved DOS in the ferromagnet on the one and the (still) spin-degenerate quasiparticle DOS inside the superconductor on the other hand. Andreev reflection typically comprises an incoming electron with an energy slightly above the Fermi level [see, e.g., the electron's wave vector in Eq. (3.6)] and a retroreflected hole with opposite spin and an energy slightly below the Fermi level [see, e.g., the hole's wave vector in Eq. (3.7)], and is thus commonly interpreted as retroreflection across the Fermi level (from the electron into the hole band). The incident electron can either be a spin-up or a spin-down electron. Due to the finite exchange splitting (spin polarization) inside the ferromagnetic region, we must be aware that there are naturally more spin-up than spin-down electrons available close to the Fermi level (i.e., $N_\uparrow \geq N_\downarrow$), resulting in a larger Fermi-level DOS in the spin-up band. But since the incoming electron can solely perform Andreev reflection if it simultaneously finds a partner with opposite spin (in order to form a spin-singlet Cooper pair in the superconductor), the imbalance between the up- and down-spin bands suggests that only the fraction $N_\downarrow/N_\uparrow$ of spin-up electrons really finds a spin-down partner to finally undergo Andreev reflections. We do not need to worry about the spin-down electrons as there are enough spin-up partners so that all $N_\downarrow$ spin-down electrons can be Andreev reflected. Accounting for the fact that each Andreev reflection channel carries a conductance quantum of $(2e^2)/h$ (the factor 2 represents the Cooper pairing), the F/S junction's subgap tunneling conductance is given by

$$G_{z,z}^{\mathrm{F/S}} = \frac{2e^2}{h}\left(\frac{N_\downarrow}{N_\uparrow}N_\uparrow + N_\downarrow\right) = \frac{4e^2}{h}N_\downarrow; \tag{3.34}$$

the first summand describes the Andreev reflection channel for incident spin-up and the second summand the one for incoming spin-down electrons. Introducing the particle-number spin polarization

$$P_N = \frac{N_\uparrow - N_\downarrow}{N_\uparrow + N_\downarrow} \tag{3.35}$$

brings Eq. (3.34) into the more compact form

$$G_{z,z}^{\mathrm{F/S}} = \frac{2e^2}{h}\left(N_\uparrow + N_\downarrow\right)\left(1 - P_N\right), \tag{3.36}$$

from which we can already deduce one important consequence. Since the total number of electrons in the system, $N \equiv N_\uparrow + N_\downarrow$, is fixed, the subgap tunneling conductance of F/S junctions decreases linearly with increasing spin polarization P_N in the ferromagnet.

To finish the semiclassical formulation, let us check two particularly relevant limiting cases for consistency. If the ferromagnetic electrode gets replaced by a normal metal ($P_N = 0$), the subgap tunneling conductance reduces to the usual Landauer formula $G_{z,z}^{\mathrm{F/S}}\big|_{P_N=0} = G_0 N$ with the aforementioned conductance quantum $G_0 = (2e^2)/h$ (the factor 2 is again due to the Cooper pairing) and N representing the number of channels in the system. The second limiting case refers to a half-metallic F/S junction. As we explained in Sec. 2.2 (see also Fig. 2.13), only up-spin (majority-spin) states are occupied in half-metallic ferromagnets (around the Fermi level). Therefore, we expect that none of the spin-up electrons can find a spin-down partner to be Andreev reflected and the subgap tunneling conductance of half-metallic junctions must vanish. Indeed, Eq. (3.36) also captures this case in a reasonable way, resulting in $G_{z,z}^{\mathrm{F/S}}\big|_{P_N=1} = 0$. The tunneling conductance's universal scaling behavior with respect to the ferromagnet's spin polarization provides a unique way to extract the latter quantity from point contact transport measurements (see, e.g., Refs. [157] and [158]).

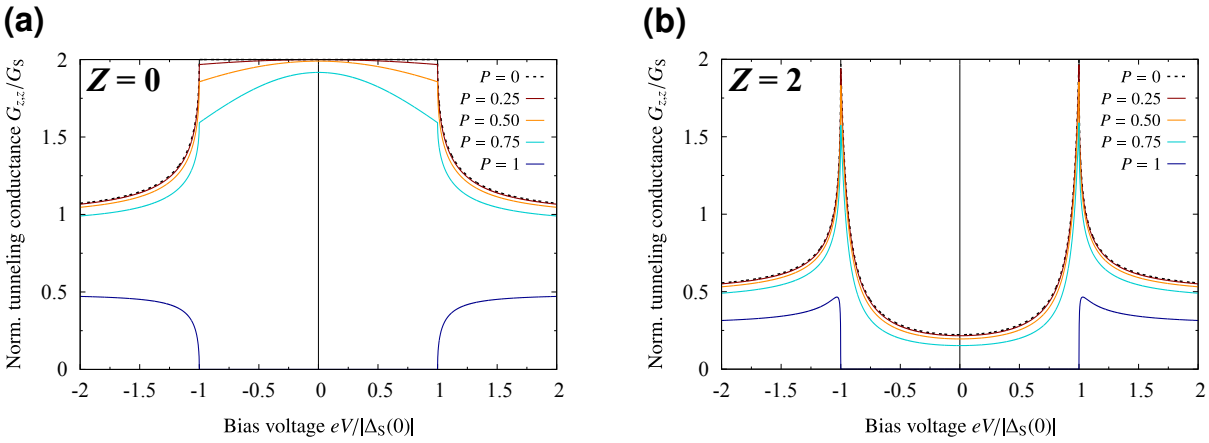


Fig. 3.5: (a) Calculated dependence of F/S junctions' tunneling conductance $G_{z,z}$ (normalized to G_S) on the applied bias voltage V [the associated electron energy eV is given in multiples of the superconductor's gap $|\Delta_S(0)|$] and for various indicated values of spin polarization P in the ferromagnet. The interface is perfectly transparent ($Z = 0$) and the Zeeman splitting inside the superconductor is $\Delta_Z = 0$. **(b)** Same calculation as in **(a)**, but in the additional presence of a moderate tunneling barrier ($Z = 2$).

3.2.2 Numerical results

Being familiar with the predictions of the semiclassical de Jong-Beenakker approach, we are fully equipped to analyze numerical model calculations for various realistic junction scenarios. To shorten the notation, we introduce two common dimensionless junction-classifying parameters. The scattering strength of the insulating barrier, experimentally controllable by its material and the interface quality (roughness), is captured by the BTK-like [164] parameter $Z = (2mV_I d_I)/(\hbar^2 k_F)$, while $P = (\Delta_{XC}/2)/\mu$ measures the ferromagnet's *effective* spin polarization (similarly to P_N above). Figure 3.5 presents the tunneling conductance [evaluated using Eq. (3.32)], normalized to G_S, as a function of the applied bias voltage V and for different spin polarizations P. Tuning the applied bias voltage effectively alters the electron energies $E = eV$, which we need to substitute into Eq. (3.32). In all subsequent discussions, we consider two representative values for the insulating barrier strength, namely $Z = 0$ and $Z = 2$. The first corresponds to a perfectly transparent interface, whereas the second models an experimentally more realistic barrier of height $V_I = 0.75\,\text{eV}$ and width $d_I \approx 0.80\,\text{nm}$ (assuming, for simplicity, $m \approx m_e$ and a typical Fermi wave vector for metals, $k_F \approx 8 \times 10^7\,\text{cm}^{-1}$ [182]). These (quasi)ballistic junctions are routinely accessible within present-day microfabrication techniques [183–185]. To understand the physical origin of the conductance characteristics, incoming electrons' bare reflection and transmission probabilities are shown as functions of the electron energy ($E = eV$ for applied bias voltage V), and for the two specific spin polarizations $P = 0$ and $P = 0.75$, in Figs. 3.6 and 3.7, respectively; the first resembles a N/S junction, while the latter refers roughly to a F/S junction with iron as the ferromagnetic electrode ($P = 0.7$ in iron). Since similar junctions were already studied by several authors (see, e.g., Refs. [165–167] and [176]), we do not give a comprehensive analysis of all present effects, but rather restrict ourselves to a few striking points.

Of particular interest for us is the *subgap regime*, referring to electron energies inside the superconductor's energy gap, $eV \leq |\Delta_S(0)|$. To stress that all calculations are performed at zero temperature and one also needs to use the associated value for $|\Delta_S|$, we explicitly write $|\Delta_S(0)|$ from now on. The simplest junction scenario is the one of a perfectly transparent N/S junction, i.e., $Z = 0$ and $P = 0$ [see the black dashed curve in Fig. 3.5(a) for the tunneling conductance and Fig. 3.6(a) for the related scattering probabilities]. The absence of interfacial scattering potentials in such junctions completely suppresses specular reflections. All incoming electrons that approach the junction interface must undergo

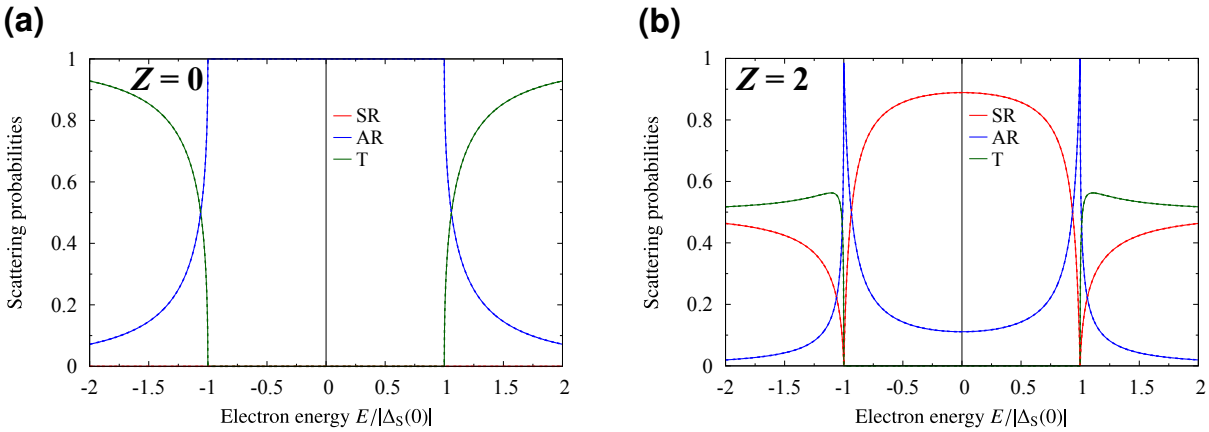


Fig. 3.6: (a) Calculated scattering probabilities of incident electrons at a N/S interface (the spin polarization in the metal is $P = 0$) as functions of the electron energy E [given in multiples of the superconductor's gap $|\Delta_S(0)|$]. The interface is perfectly transparent ($Z = 0$) and the Zeeman splitting inside the superconductor is $\Delta_Z = 0$. The different indicated scattering processes include specular reflection (SR), Andreev reflection (AR), and transmissions (T; effectively counting both electronlike and holelike transmissions). Solid lines correspond to an incoming spin-up, dashed lines to an incoming spin-down electron. As the metallic region is composed of a normal metal without any spin splitting in its band structure, the scattering probabilities are the same in both cases. **(b)** Same calculation as in **(a)**, but in the additional presence of a moderate tunneling barrier ($Z = 2$).

either Andreev reflections or quasiparticle transmissions. Specifically in the subgap region, the latter become additionally forbidden because the superconductor does not host free quasiparticle states to tunnel into, and Andreev reflections eventually remain the only allowed scattering processes. The calculated scattering probabilities in Fig. 3.6(a) clearly resemble these features. Inspecting the general expression for the tunneling conductance given in Eq. (3.32) suggests that perfect Andreev reflection gives rise to a maximal subgap tunneling conductance of $G_{z,z} = 2G_S$ (constant for all subgap energies), coinciding with our numerical calculations [see the black dashed curve in Fig. 3.5(a)] and the semiclassical de Jong-Beenakker approach. The conductance doubling stems from the fact that each Andreev reflection *always* involves two particles (electron and hole), basically modeling the Cooper pairing in the superconductor. The respective normal-conducting F/N junction's tunneling conductance would indeed simply reduce to the ideal point contact conductance G_S. As soon as eV exceeds $|\Delta_S(0)|$, the junction's tunneling conductance is determined by the mutual interplay of both Andreev reflections and transmissions. With increasing eV, however, the Andreev reflection probability gets more and more damped, and the conductance spectrum is mostly governed by single-(quasi)particle transmissions, just as in normal-conducting F/N junctions [see Fig. 3.6(a)]. The related tunneling conductance therefore also decreases with increasing eV [$> |\Delta_S(0)|$] and approaches its normal analog, $G_{z,z} \to G_S$, at $eV \gg |\Delta_S(0)|$ [see the black dashed curve in Fig. 3.5(a)].

Replacing the normal metal by a ferromagnet with finite spin polarization ($P \neq 0$) immediately reduces the subgap tunneling conductance. The reason for this observation is precisely the imbalance between the up- and down-spin electronic bands inside the ferromagnet, which eventually hinders a fraction of spin-up electrons from performing Andreev reflections. Those electrons are instead simply specularly reflected (transmissions are forbidden in the subgap regime), which results in an inevitable decrease of the subgap tunneling conductance [recall Eq. (3.32) and our remarks on the semiclassical de Jong-Beenakker approach]. With increasing P (effectuating a greater spin imbalance), more and more incident electrons can only undergo specular reflections [see, e.g., Fig. 3.7(a)] so that the subgap tunneling conductance becomes continuously suppressed, as shown in Fig. 3.5(a). Eventually, the electrons

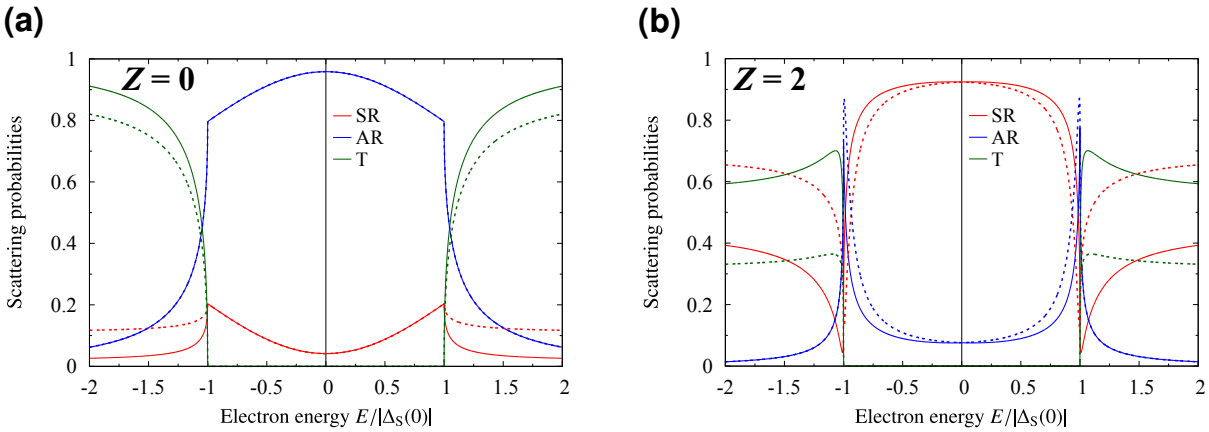


Fig. 3.7: (a) Calculated scattering probabilities of incident electrons at a F/S interface (the ferromagnet's spin polarization is chosen to be $P = 0.75$) as functions of the electron energy E [given in multiples of the superconductor's gap $|\Delta_S(0)|$]. The interface is perfectly transparent ($Z = 0$) and the Zeeman splitting inside the superconductor is $\Delta_Z = 0$. The different indicated scattering processes are labeled in the same way as in Fig. 3.6. Since the metal is now ferromagnetic, the electrons (holes) experience the band structure's effective spin splitting, and the scattering probabilities for incoming spin-up (solid lines) and spin-down (dashed lines) electrons typically differ. **(b)** Same calculation as in **(a)**, but in the additional presence of a moderate tunneling barrier ($Z = 2$).

in a half-metallic F/S junction ($P = 1.0$) occupy only the majority-spin band (close to the Fermi level). All of them will not find a minority-spin partner to undergo Andreev reflections and form Cooper pairs. The (complete) absence of Andreev reflection processes leads to a vanishing subgap tunneling conductance (i.e., all incoming electrons are specularly reflected and *no* tunneling current starts to flow), represented by the blue curve in Fig. 3.5(a). At $eV > |\Delta_S(0)|$, we still recover the transmission-dominated tunneling conductance behavior that resembles the normal-state F/N junctions' at $eV \gg |\Delta_S(0)|$. We want to stress once again that all subgap trends, we extracted from our numerical calculations, are consistent with the predictions of the semiclassical de Jong-Beenakker description.

Already the tunneling conductance spectra of perfectly transparent junctions reveal that the superconductor's energy gap crucially impacts the system's transport features since it separates the (Andreev reflection-dominated) subgap from the quasiparticle tunneling regime. This becomes even more evident when considering a moderate finite interfacial barrier, e.g., $Z = 2$. The presence of interfacial scattering potentials gives typically rise to an enhanced probability for specular reflections so that the subgap tunneling conductance is rather dominated by the *conductance-suppressing* specular reflections (instead of conductance-increasing Andreev reflections); see Figs. 3.6(b) and 3.7(b) for the reflection probabilities' general dependence on the junction parameters. Incoming electrons whose energies match the superconducting gap's amplitude [$eV = |\Delta_S(0)|$] behave nevertheless in an unexpected manner. Owing to superconductors' peculiar DOS [which basically diverges at $eV = |\Delta_S(0)|$; see Fig. 2.7], these electrons are still predominantly Andreev reflected (in sharp contrast to all other electron energies inside the subgap region). The resulting, strongly pronounced, Andreev reflection probability peaks at $eV = |\Delta_S(0)|$ are indeed a universal characteristic of F/S junctions. Even though their amplitudes decrease with increasing P, the peaks themselves remain clearly visible in all considered junction configurations. Given the generic form of the tunneling conductance formula in Eq. (3.32), we deduce that the Andreev reflection peaks must transform into distinct *gap-edge finite-bias conductance peaks (FBCPs)*. The numerical calculations in Fig. 3.5(b) exactly confirm our expectations. The dominant specular reflections heavily suppress the tunneling conductance inside the subgap energies, while simultaneously clearly apparent gap-edge FBCPs form. The peaks' amplitudes decrease with

Tab. 3.1: Normalized gap-edge FBCP amplitudes $G_{z,z}(eV = |\Delta_S(0)|)/G_S$ for different values of spin polarization P in the ferromagnet; the conductance amplitudes are calculated using Eq. (3.42). The same P-values are considered in the numerically evaluated tunneling conductance spectra shown in Fig. 3.5.

P	$G_{z,z}\Big(eV = \lvert\Delta_S(0)\rvert\Big)\Big/G_S$
0	2
0.25	1.97
0.50	1.86
0.75	1.59
1	0

increasing P, reflecting their close connection with the gap-edge Andreev reflection probability peaks that scale in the same way. The half-metallic junction scenario is still characterized by (completely) absent Andreev reflections and zero subgap tunneling conductance. For all regarded spin polarizations inside the ferromagnet, the tunneling conductances at $eV \gg |\Delta_S(0)|$ mimic again the related normal-conducting F/N junction regimes.

Before finishing our short discussion of the F/S junction's tunneling conductance, we shall have a closer look at the addressed gap-edge FBCPs. Approximating the wave vectors in Eqs. (3.6), (3.7), (3.11), and (3.12) by

$$k_{z,e}^{\sigma} \approx k_{z,h}^{\sigma} \approx k_F \sqrt{1+\sigma P} \tag{3.37}$$

inside the ferromagnet and

$$q_{z,e}^{\uparrow(\downarrow)} \approx q_{z,h}^{\uparrow(\downarrow)} \approx k_F \tag{3.38}$$

inside the superconductor (justification for this simplification was given earlier), and substituting $eV = |\Delta_S(0)|$ in the coherence factors in Eqs. (3.9)–(3.10), allows us to extract simple analytical expressions for the *gap-edge reflection coefficients*,

$$\begin{aligned} r_e^{\sigma,\sigma}\Big(eV = |\Delta_S(0)|\Big) = \Big[&\Big(1 - \sqrt{1+\sigma P} + iZ\Big)\Big(1 + \sqrt{1-\sigma P} - iZ\Big) \\ &+ \Big(-1 - \sqrt{1+\sigma P} + iZ\Big)\Big(1 - \sqrt{1-\sigma P} + iZ\Big)\Big]\Big/\Gamma \end{aligned} \tag{3.39}$$

and

$$r_h^{\sigma,-\sigma}\Big(eV = |\Delta_S(0)|\Big) = \Big(4\sqrt{1+\sigma P}\Big)\Big/\Gamma, \tag{3.40}$$

with the common denominator

$$\Gamma = \Big(1 + \sqrt{1+\sigma P} + iZ\Big)\Big(-1 - \sqrt{1-\sigma P} + iZ\Big) + \Big(1 - \sqrt{1+\sigma P} - iZ\Big)\Big(1 - \sqrt{1-\sigma P} + iZ\Big). \tag{3.41}$$

The coefficients belonging to spin-flip reflections, $r_e^{\sigma,-\sigma}$ and $r_h^{\sigma,\sigma}$, are zero since there is no spin-active component (inducing, e.g., SOC) in the junction. Evaluating the corresponding reflection probabilities by

means of Eqs. (3.17)–(3.20) and plugging the results into the conductance formula in Eq. (3.32) yields for the *gap-edge (FBCP) tunneling conductance amplitudes*

$$\frac{G_{z,z}\Big(eV = |\Delta_S(0)|\Big)}{G_S} = \frac{4\sqrt{1-P^2}}{1+\sqrt{1-P^2}}. \tag{3.42}$$

This is a particularly notable result, as it demonstrates that the gap-edge tunneling conductance is neither influenced by the actual strength of the insulating barrier (in fact, the gap-edge conductances for $Z = 0$ have even the same values; $Z \neq 0$ is just required to sharpen the peak structure) nor by the materials' doping level (Fermi wave vector). The ferromagnet's spin polarization P is the only quantity that determines the gap-edge FBCPs' amplitudes. Such a universal scaling of the FBCP magnitudes was predicted by several authors [166, 167] and opens one possibility to experimentally extract ferromagnets' spin polarization from measuring the gap-edge tunneling conductance of superconducting point contacts and fitting the data to a generalized BTK modeling (see, e.g., Refs. [157] and [158]). To give a compact overview, Tab. 3.1 summarizes the gap-edge FBCP amplitudes, as expected from Eq. (3.42), for the spin polarizations used in our numerical calculations. All calculated values agree with the numerical results presented in Fig. 3.5(b).

3.3 Discussion of results for F/F-S junctions

At the end of this chapter, we are finally concerned with a F/F-S junction, in which the superconducting electrode becomes additionally (at least weakly) ferromagnetic. The coexistence of superconductivity and ferromagnetism in one and the same material has remained mysterious for quite some time. As we stated in Chap. 2, both phases are actually strongly antagonistic. Applying even a weak magnetic field to a superconductor typically aligns the electrons' spins along the field and must thus inevitably start to pull apart the Cooper pair electrons. As soon as the field increases above the superconductor's critical field (see Sec. 2.1.1), all Cooper pairs are already completely broken up and the material's superconducting properties disappear. The Chandrasekhar-Clogston limit [186, 187] provides a rough estimate for the maximal strength of magnetic fields that can be applied to a superconductor without significantly suppressing its superconducting features. In this section, we first rederive the Chandrasekhar-Clogston limit in order to figure out a reasonable parameter regime for the Zeeman gaps inside the ferromagnetic superconductor of our junction. Afterwards, we analyze concrete numerical model calculations for the extracted realistic parameter sets.

3.3.1 Chandrasekhar-Clogston limit

To establish a simple relation between the maximally applicable magnetic fields that still allow for the coexistence of superconductivity and ferromagnetism inside a superconducting material, we must regard the involved energy scales. On the one hand, entering the superconducting phase always remains energetically favorable if the system can reduce its total energy density by an amount of

$$\Delta f_S(0) = -\frac{n(0)}{2}|\Delta_S(0)|^2; \tag{3.43}$$

this energy exactly refers to the superconducting condensation energy – the energy gain through forming Cooper pairs –, which we already encountered within the Ginzburg-Landau approach (Sec. 2.1.2) in a slightly different (but equivalent) form [see Eq. (2.12)]. The density of superconducting electrons at zero temperature is given by $n(0)$. On the other hand, aligning all electron spins parallel to a magnetic field

with strength B and thereby switching to a purely magnetic phase reduces the system's total energy by the paramagnetic (polarization) energy density

$$\Delta f_{\mathrm{N}}(0) = -n(0)\mu_{\mathrm{B}}^2 B^2. \tag{3.44}$$

The superconducting and the ferromagnetic phases can coexist as long as the energy gain associated with the purely magnetic state, $\Delta f_{\mathrm{N}}(0)$, does *not* overcome the superconducting condensation energy $\Delta f_{\mathrm{S}}(0)$, i.e., as long as

$$\mu_{\mathrm{B}} B \leq \frac{|\Delta_{\mathrm{S}}(0)|}{\sqrt{2}}. \tag{3.45}$$

Equation (3.45) is known as the *Chandrasekhar-Clogston limit* [186, 187]. Identifying $\mu_{\mathrm{B}} B = \Delta_{\mathrm{Z}}/2$ as the exchange gap effectively induced by the Zeeman field (the latter is also the quantity that enters our modeling in Sec. 3.1), Zeeman splittings of realistic ferromagnetic superconductors *typically* fulfill

$$\Delta_{\mathrm{Z}} \leq \sqrt{2}|\Delta_{\mathrm{S}}(0)| \approx 1.4|\Delta_{\mathrm{S}}(0)|. \tag{3.46}$$

Nevertheless, there are still several materials in which Δ_{Z} can be increased to values far above the Chandrasekhar-Clogston limit. Among the suggestions for such materials are, for instance, the ferromagnetic superconductors $ZrZn_2$ [188], URhGe [189], UGe_2 [190], and UCoGe [191]. Most of the materials are predicted to rather sustain spin-triplet pairing mechanisms, which are much more robust against external magnetic fields than spin-singlet ones [49]. Another (more practical) realization of ferromagnetic superconductors with large Zeeman splittings is the fabrication of ultrathin films (of conventional superconductors), which can be brought into large magnetic fields – up to 5 T for Al films [23–25] and even up to 50 T for Pb films [174] –, while remaining superconducting.

3.3.2 Numerical results

As before, we focus on some of the most peculiar characteristics of F/F-S junctions, considering iron as the ferromagnetic electrode (meaning that we fix $P = 0.7$). For a more extensive study, one could consult Ref. [169]. Figure 3.8 shows the numerically evaluated tunneling conductance as a function of bias voltage V and for several Zeeman gaps Δ_{Z} inside the ferromagnetic superconductor. All values chosen for Δ_{Z} lie well below the Chandrasekhar-Clogston limit [one may compare them to Eq. (3.46)] and correspond to realistic experimental configurations. To be specific, the Chandrasekhar-Clogston limit would even allow for much greater Zeeman splittings than the ones we regard. However, even weak external magnetic fields give rise to (at least partial) Cooper pair breaking and would indirectly modify the value of the superconducting energy gap. A precise formulation would then require to determine $|\Delta_{\mathrm{S}}(0)|$ in the magnetic scenario from self-consistent calculations, which goes far beyond the scope of the mostly phenomenological analyses we want to provide. To ensure that the superconducting gap is not (strongly) affected by the Zeeman field, we restrict our considerations to Δ_{Z}-values well below the upper boundary set by the Chandrasekhar-Clogston limit. Similarly to the preceding section, we differentiate between junctions with a perfectly transparent interface ($Z = 0$) and systems in which a tunneling barrier of moderate strength ($Z = 2$) is present. Already our theoretical modeling done in Sec. 3.1 suggests that a finite Zeeman gap in the ferromagnetic superconductor represents a spin splitting of the initially spin-degenerate quasiparticle bands. From that point of view, we may describe ferromagnetic superconductors as actually nonmagnetic superconductors with the two effective, spin-dependent, superconducting gaps $\Delta_{\mathrm{S}}^{\uparrow} = |\Delta_{\mathrm{S}}(0)| - \Delta_{\mathrm{Z}}/2$ for the spin-up and $\Delta_{\mathrm{S}}^{\downarrow} = |\Delta_{\mathrm{S}}(0)| + \Delta_{\mathrm{Z}}/2$ for the spin-down branch; introducing these gaps formalizes then the Fermi surface's spin splitting and thus, they enter, for example, the coherence factors and wave vectors in the ferromagnetic superconductor [see Eqs. (3.9), (3.10), (3.11), and (3.12)]. The existence of two spin-dependent superconducting gaps should manifest

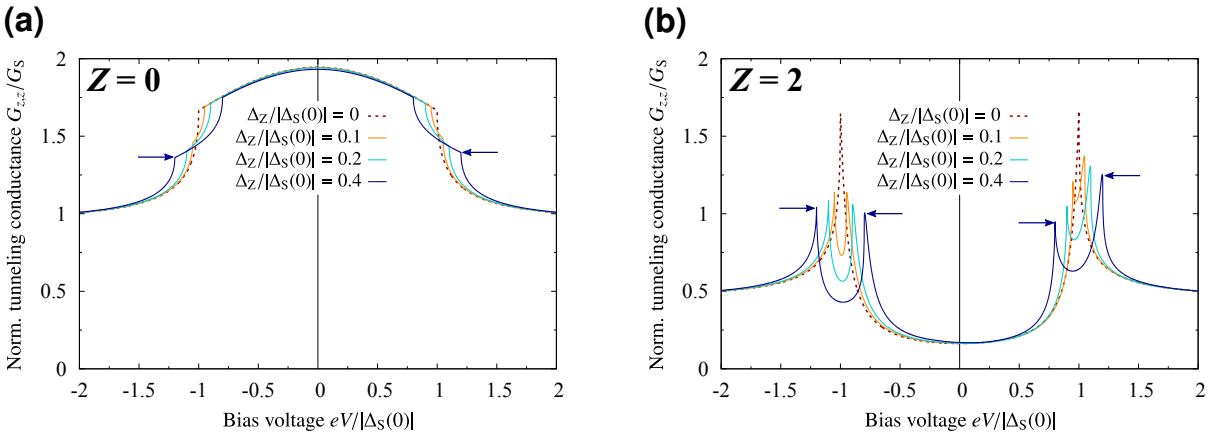


Fig. 3.8: (a) Calculated dependence of F/F-S junctions' tunneling conductance $G_{z,z}$ (normalized to G_S) on the applied bias voltage V [the associated electron energy eV is given in multiples of the superconductor's gap $|\Delta_S(0)|$] and for various indicated values of the induced Zeeman gap Δ_Z in the ferromagnetic superconductor. The interface is perfectly transparent ($Z = 0$) and the ferromagnet's spin polarization is $P = 0.7$ (corresponding to iron). The dark blue arrows indicate the voltage asymmetry of the conductance, exemplarily for $\Delta_Z = 0.4|\Delta_S(0)|$. **(b)** Same calculation as in **(a)**, but in the additional presence of a moderate tunneling barrier ($Z = 2$).

itself not only in the quasiparticle DOS (which now also splits into up- and down-spin branches when compared to Fig. 2.7), but particularly also in extraordinary conductance features.

Motivated by our discussions in Sec. 3.2, we just need to localize FBCPs in the tunneling conductance spectra. The associated electron energies quantify then the amplitude(s) of the system's superconducting gap(s). Analogously to the F/S junction scenario, FBCPs appear again most clearly pronounced for finite interfacial barrier strengths. Inspecting the results presented in Fig. 3.8(b) reveals two important consequences. First, the sharp FBCP that remains located exactly at the gap edge [at electron energy $eV = |\Delta_S(0)|$] as long as there is no Zeeman gap in the superconducting electrode ($\Delta_Z = 0$) splits into two distinct FBCPs with increasing Δ_Z. Extracting the (energetically resolved) positions of these FBCPs, we assert that they indeed appear at $eV = \Delta_S^{\uparrow}$ and $eV = \Delta_S^{\downarrow}$. This is an unambiguous evidence for our key assumption that the ferromagnetic superconductor can be treated as an initially nonmagnetic superconductor in which two spin-dependent energy gaps start to open. Second, larger Δ_Z typically decreases the probability for Andreev reflections (in a similar manner as increasing spin polarization inside the ferromagnet would do; recall our arguments formulated in Sec. 3.2) and therefore damps the maximal amplitudes of the FBCPs. Energies far above the gap edge reflect again the respective normal-conducting junction regimes. The qualitative features for perfectly transparent junctions [see Fig. 3.8(a)] are essentially the same – except that there are no sharp FBCPs, but instead we observe small kinks, which serve as precursors of the FBCPs finally appearing in the presence of finite interfacial scattering potentials –, and not explicitly discussed.

Another surprising property of F/F-S junctions' tunneling conductance spectra relies on the conductances' symmetry with respect to a reversal of the applied bias voltage. We did not pay attention to that when analyzing the F/S junction in Sec. 3.2 since the conductance curves are always perfectly symmetric in those systems. Switching from the "forward-bias" ($V > 0$) to the "backward-bias" ($V < 0$) regime has absolutely no influence on the tunneling conductance. This dramatically changes when both junction electrodes become ferromagnetic. Our calculations presented in Fig. 3.8 reveal a clearly visible voltage asymmetry of F/F-S junctions' tunneling conductance. This asymmetry appears independently of the actual strength of the tunneling barrier (i.e., for both of the regarded Z-scenarios) and becomes more apparent with larger Δ_Z. To understand the physical reason behind that, we have a closer look at incoming

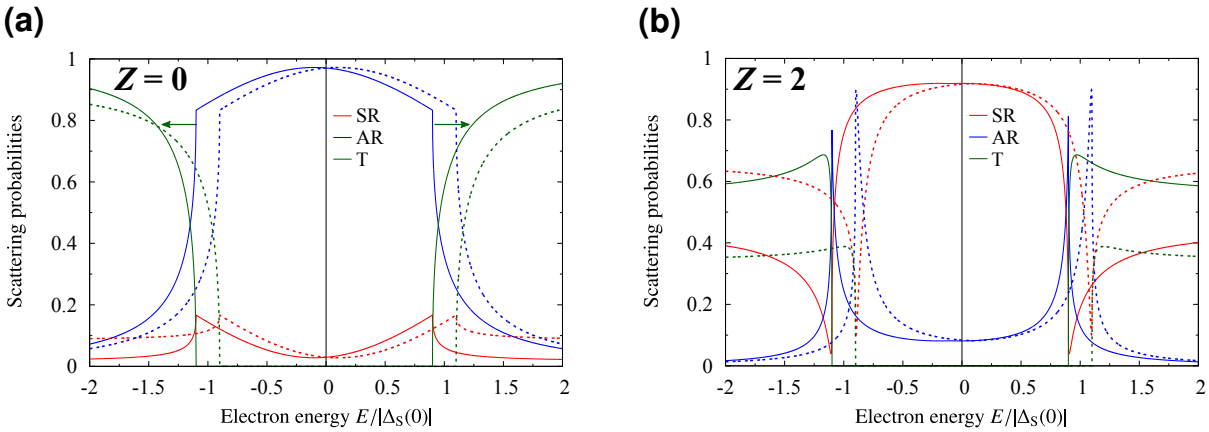


Fig. 3.9: (a) Calculated scattering probabilities of incident electrons at a F/F-S interface (the ferromagnet's spin polarization is chosen to be $P = 0.7$) as functions of the electron energy E [given in multiples of the superconductor's gap $|\Delta_S(0)|$]. The interface is perfectly transparent ($Z = 0$) and the Zeeman splitting inside the superconductor is $\Delta_Z = 0.2|\Delta_S(0)|$. The different indicated scattering processes are labeled in the same way as in Figs. 3.6 and 3.7. Since both electrodes are ferromagnetic, the scattering probabilities for incoming spin-up (solid lines) and spin-down (dashed lines) electrons strongly differ. The green arrows highlight the regime of bias voltages in which the transmission-dominated voltage asymmetry in the scattering probabilities (and finally also in the tunneling conductances; see Fig. 3.8) are most clearly apparent. In fact, the asymmetries are also there for other parameters, but barely recognizable by eyes. **(b)** Same calculation as in **(a)**, but in the additional presence of a moderate tunneling barrier ($Z = 2$).

electrons' bare reflection and transmission processes for one particular Δ_Z [see Fig. 3.9]. The presence of two spin-resolved superconducting gaps alters the scattering probabilities in a highly complicated way. Before (i.e., for F/S junctions), the subgap regime was solely dominated by specular and Andreev reflection processes, while transmissions just came into play at particle energies exceeding the superconducting gap $|\Delta_S(0)|$. Now (i.e., for F/F-S junctions), the system is characterized by the two spin-dependent superconducting gaps $\Delta_S^{\uparrow}$ and $\Delta_S^{\downarrow}$ so that we are effectively concerned with an *intermediate region* at energies $\Delta_S^{\uparrow} \leq E \leq \Delta_S^{\downarrow}$ (and symmetrically also at negative energies). This intermediate regime is not only controlled by the intriguing interplay of specular and Andreev reflections, but additionally by *partial, spin-dependent, transmissions* into one of the superconductor's spin-resolved quasiparticle bands. It is exactly that crucial competition between the still present reflections and the upcoming *asymmetric (with respect to the electron energies' signs) partial quasiparticle transmissions*, which gets transferred into the tunneling conductance. This can be explicitly seen, for instance, in Fig. 3.9(a) (green curves); the interesting voltage regions are highlighted by green arrows there. As we mentioned, the voltage asymmetries in the conductance become more distinct when both the ferromagnet's spin polarization and the ferromagnetic superconductor's Zeeman splitting are raised, making them a sensitive measure to experimentally probe spin-polarized transport through F/F-S point contacts. A detailed physical picture, more thoroughly demonstrating the origin of the conductances' voltage asymmetries and paying additional attention to some other extraordinary transport features of F/F-S junctions, is provided in Ref. [169].

3.4 Short summary

To summarize, we formulated an effective scattering-based technique for theoretically modeling ballistic transport through F/F-S junctions. Despite its high level of simplification and abstraction, the presented approach still provides an astonishingly reliable description, which can even capture state-of-the-art experiments carried out on point contact geometries. More specifically, we understood scattering of incoming

electrons at interfaces of superconducting junctions – particularly the striking Andreev reflection process, which is responsible for many exceptional effects –, and extended established quantum-mechanical concepts for evaluating electrical current flows to our considered system. We eventually obtained a generalized BTK conductance formula, which is by far more universal than its original formulation and applicable to various prototype systems. Both the generic scattering picture and the comprehensive BTK-like conductance equation will appear again several times and significantly simplify our investigations in later parts of this work.

As concrete applications of our analytical results, we numerically evaluated the tunneling conductance for a set of realistic F/S junction regimes. Comparing the numerics to the semiclassical picture of de Jong and Beenakker helped us to understand the peculiar role of ferromagnets' finite spin polarization. The latter typically suppresses Andreev reflections and leads to the formation of pronounced FBCPs with a universal amplitude, which is solely determined by the ferromagnets' spin polarization and can thus be used to extract this quantity from routine conductance measurements.

Even more interesting physics arises in F/F-S junctions, in which the additional Zeeman splitting of the quasiparticle bands in the ferromagnetic superconductor uniquely impacts the transport characteristics. We made plausible that ferromagnetic superconductors can be modeled in the same way as nonmagnetic superconductors introducing two effective, spin-dependent, superconducting gaps. This assumption got justified by our numerical simulations, which indeed confirmed that the initially present FBCPs of F/S junctions split into two peaks with increasing Zeeman splitting. Both peaks are exactly localized at energies corresponding to the effective superconducting gaps. A moreover present voltage asymmetry of F/F-S junctions' tunneling conductance, attributed to partially allowed spin-dependent transmission processes at intermediate particle energies (between the two effective superconducting gaps), completed our analyses. The latter property might become extremely helpful for spin-resolved transport characterizations in future experiments.

Chapter 4

Subharmonic conductance gap structure in ballistic Josephson junctions

The BTK model [164] counts for sure to the most outstanding achievements to establish a common understanding of superconducting tunneling. A citation study back in 2004 [192], covering all articles published within the Physical Review journal family between 1893 and 2003, even lists the related publication by Blonder, Tinkham, and Klapwijk among the "hot" papers, which have been cited more than 200 times (up to 2003). One possible reason might be that the fascinating physics already arising in the rather simple metal/superconductor contacts described by BTK, together with the rapid progress in experimental techniques, soon drove enormous interest to extend further studies to more complex superconducting junctions.

More than two decades before the BTK modeling, a young graduate student named Brian Josephson attracted the attention of physicists worldwide. Josephson predicted [93] that the phase-coherent coupling of two massive superconducting electrodes by means of a thin and actually nonsuperconducting region may cause spontaneous supercurrent flows, even without applying an external bias voltage. On the microscopic level, these currents were found to be the unique result of superconducting *proximity effects* [180], which induce superconducting order in the initially nonsuperconducting link and allow for the tunneling of supercurrent-carrying Cooper pairs. This so-called DC Josephson effect itself offers an extremely rich topic for ongoing research, as many variations of Josephson geometries have remained unstudied up to now and lots of novel physics might still be discovered. In fact, the third (and partly also the fourth) part of this thesis will be devoted to a thorough investigation of DC Josephson effects in several *magnetic* junction configurations.

Besides the actual *zero-bias* Josephson current, follow-up works focused more and more on characterizing the (quasiparticle) tunneling currents that start to flow at finite bias voltages. Initial experiments carried out into that direction [193–195] bore great challenges for theoreticians, as they independently reported on reproducible, and at that time completely unprecedented, current-voltage anomalies (when compared to well-understood normal-state junctions). Probably most puzzling were the detected *nonzero excess current* and the emergent *subharmonic gap structure* in the junctions' differential conductance (resistance). The first refers to the tunneling currents' behavior in the limit of large voltages [i.e., at electron energies remarkably exceeding the superconducting gap, $eV \gg |\Delta_S(0)|$; as before, e is the positive elementary charge, V denotes the applied bias voltage, and $|\Delta_S(0)|$ indicates the zero-temperature superconducting gap] and the second to a series of distinct *subgap* peaks (dips) in the junctions' differential conductance (resistance). For illustration, Fig. 4.1 shows the experimentally taken resistance and tunneling current data of two biased Josephson junctions, clearly resembling both the excess current and the subharmonic gap structure; we will come back to the concrete material compositions later on.

Before, we need to become more familiar with the physical background. In the large-voltage regime, one would essentially expect that Josephson junctions' superconducting properties do no longer play an essential role and the tunneling current behaves then in exactly the same manner as in the junctions'

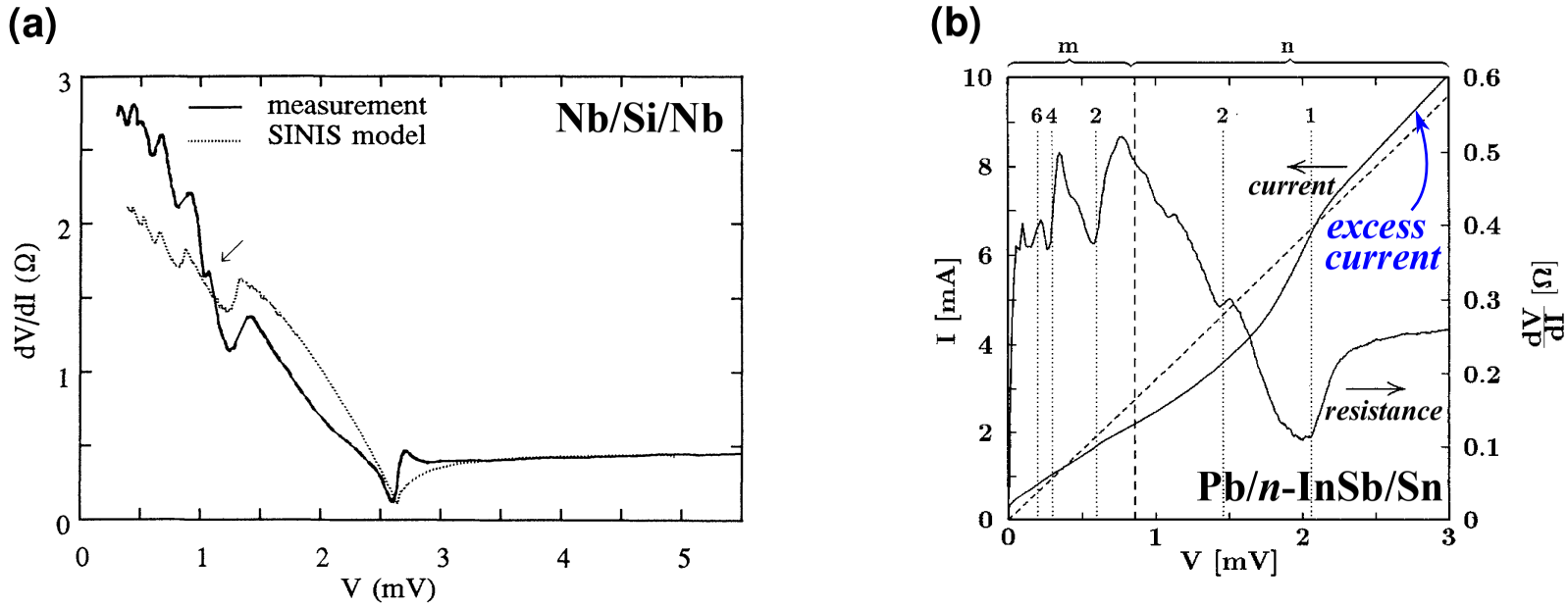


Fig. 4.1: (a) Comparison between Nb/(doped) Si/Nb junctions' *measured* (solid curve) differential resistance $\mathrm{d}V/\mathrm{d}I$ (in Ω) and their *calculated* (within the OTBK model) resistance (dotted curve) as a function of the applied bias voltage V (in mV) and at $T = 1.2\,\mathrm{K}$; adapted from Ref. [196]. The subharmonic resistance gap structure with pronounced resistance minima at voltages $V \approx 2|\Delta_{\mathrm{S,Nb}}(T)|/(ne)$ is clearly visible; for niobium's zero-temperature superconducting gap, one extracts $2|\Delta_{\mathrm{S,Nb}}(0)| \approx 2.6\,\mathrm{meV}$ from the measurement, which is slightly smaller than niobium's bulk gap [197]. **(b)** *Measured* tunneling current I (in mA; values at the left axis) and differential resistance $\mathrm{d}V/\mathrm{d}I$ (in Ω; values at the right axis) of Pb/*n*-doped InSb/Sn junctions as a function of the applied bias voltage V (in mV) and at $T = 1.36\,\mathrm{K}$; adapted from Ref. [198]. The dashed, linearly increasing, line indicates the respective normal-state current-voltage characteristics. The large-voltage tunneling current in the superconducting state slightly exceeds the normal-state current; the difference is termed *excess current*. Due to the large mismatch between the superconductors' (zero-temperature) gaps, $|\Delta_{\mathrm{S,Pb}}(0)| = 1.46\,\mathrm{meV} > 2|\Delta_{\mathrm{S,Sn}}(0)| = 1.2\,\mathrm{meV}$, the subharmonic resistance gap structure splits into three subseries [198, 199] that are characterized by resistance minima at $V \approx [|\Delta_{\mathrm{S,Pb}}(T)| + |\Delta_{\mathrm{S,Sn}}(T)|]/(ne)$ for *odd* n and $V \approx 2|\Delta_{\mathrm{S,Pb}}(T)|/(ne)$ for *even* n as long as $eV > \big||\Delta_{\mathrm{S,Pb}}(T)| - |\Delta_{\mathrm{S,Sn}}(T)|\big|$, as well as resistance minima at $V \approx 2|\Delta_{\mathrm{S,Sn}}(T)|/(me)$ for *even* m and once $eV < \big||\Delta_{\mathrm{S,Pb}}(T)| - |\Delta_{\mathrm{S,Sn}}(T)|\big|$. The values of n and m corresponding to the observed resistance minima are given in the plot; the boundary between the regimes dominated by n and m, $eV = \big||\Delta_{\mathrm{S,Pb}}(T)| - |\Delta_{\mathrm{S,Sn}}(T)|\big| = 0.86\,\mathrm{meV}$, is highlighted by the vertical dashed line.

normal-conducting counterparts. Although the current indeed approaches its linear voltage dependence, which is actually a clear signature that we are concerned with normal-state (metallic) transport, the measured data suggests that the absolute current amplitudes in the superconducting junction typically experience an additional vertical offset, i.e., the current is still slightly larger (smaller) than in the respective fully normal-conducting junction and does not extrapolate to zero at zero bias voltage. The current difference between the superconducting and normal-conducting regimes is usually referred to as *excess current* if the current in the superconducting phase overcomes the normal-state current and *deficient current* if the normal-state current exceeds the current in the superconducting phase.

An alternative and perhaps more common way to quantify the junctions' transport properties relies on their differential conductance (resistance), measuring the absolute change of the tunneling current flow with increasing bias voltage (change of the bias voltage with increasing tunneling current flow). Josephson junctions' anomalous current-voltage relations raise a series of well-distinct conductance maxima (resistance minima) at bias voltages of $V \approx 2|\Delta_S(0)|/(ne)$ – with n being a positive integer and e the positive elementary charge –, i.e., at integer submultiples of twice the superconducting energy gap $|\Delta_S(0)|$, leading to the unique oscillating *subharmonic conductance (resistance) gap structure*. Both the excess current and the subharmonic conductance (resistance) oscillations were rediscovered in several subsequent experiments and for a wide range of possible material compositions (see, e.g., Refs. [200–207]).

In the meantime, various theoretical ideas to explain the subharmonic gap structure's physical origin have been put forward. The initial one by Schrieffer and Wilkins [208] proposed that each conductance maximum at $V \approx 2|\Delta_S(0)|/(ne)$ stems from resonant tunneling of n single electronlike quasiparticles through the nonsuperconducting link. The associated tunneling probability scales usually with $(|T|^2)^n$, where T denotes the transmission-related element of the underlying tunneling matrix. However, already just *one* single electron usually tunnels with an extremely small probability, say, for instance, $|T|^2 \approx 10^{-10}$. But this would mean that n-electron tunneling (with n being notably larger than one) would be thus heavily suppressed that the related conductance maxima should no longer be resolvable, contradicting with most of the aforementioned experiments resolving subgap oscillations up to large order in n (i.e., up to $n = 12$ and beyond). Apart from that, Schrieffer's and Wilkin's description faces a second and even greater deficit. Sequential tunneling of electrons is actually not possible at all as long as their energies remain at values inside the superconducting gap, simply because the electrons cannot find available states in the second superconductor to tunnel into. Strictly speaking, multielectron tunnelings alone can therefore not explain the tunneling current's subgap behavior anyway [209, 210].

A few years later, Werthamer [211] initiated another approach, stating that the subharmonic gap structure originates from the interplay between single-electron tunneling and Josephson effects. Applying a nonzero DC bias voltage to a Josephson junction induces a supercurrent flow that oscillates in time (see Chap. 5 for a detailed summary of this so-called AC Josephson effect) and is accompanied by emission of electromagnetic Josephson radiation. If a single electron tunnels now through the link region, it may absorb one Josephson radiation photon, which increases the electron's tunneling probability (and energy) and gives eventually rise to the observed conductance maxima. This explanation, however, requires physically different absorption processes to explain the subharmonic gap structure's even and odd subseries (i.e., the conductance and resistance anomalies appearing at even and odd n). Since different photon absorptions will not all happen equally likely, either the even or the odd subseries of the subharmonic gap structure shall then become more pronounced. Nevertheless, the experimentally available data did not resemble significant differences between the even and odd subseries, revealing that also Werthamer's argumentation is not sufficient to reliably capture the junctions' rewarding physics.

It should have taken more than another decade until Artemenko, Volkov, and Zaitsev [212–214] came up with a thorough theoretical analysis of the emergent excess currents. Even though their description is predominantly based on an advanced Green's function formulation, which probably not many researchers

could easily follow at that time, this work boosted new hopes to finally understand all the peculiar physics behind the excess currents and the subharmonic conductance gap structure. Just some months later, Blonder, Tinkham, and Klapwijk established their famous BTK model [164] and could thereby relate the current-voltage characteristics of (single) metal/superconductor contacts to the striking Andreev reflection process [179]. Afterwards, unraveling a comprehensive microscopic picture for Josephson junctions, accounting not only for their nonzero excess current, but simultaneously also for their intriguing subharmonic gap structure's source, seemed to be within reach. Indeed, again Klapwijk, Blonder, and Tinkham dove deeper into this subject and generalized their BTK model to simple Josephson junctions [215], i.e., junctions that are composed of two superconducting banks connected by a small nonsuperconducting constriction. It turned out that both the excess current and the subharmonic gap structure are a unique result of *multiple Andreev reflections* between the two constriction/superconductor interfaces. In contrast to the *sequential multielectron tunnelings* through the constriction, Schrieffer and Wilkins [208] initially proposed to cause the junctions' striking features, multiple Andreev reflections of electrons (holes) at the junction interfaces can really lead to clearly visible transport anomalies in the *subgap region* (recall that sequential multielectron tunnelings are actually even forbidden at such energies). Comparing their numerical modeling with real measurements [215], Klapwijk, Blonder, and Tinkham recognized that their approach can qualitatively reproduce the observed trends, but is not yet sufficient to satisfactorily reproduce quantitative aspects. The major drawback of their approach was soon identified. In principle, electrons (holes) can traverse the junctions' link region infinitely many times, possibly undergoing Andreev reflections whenever approaching one of the two interfaces. The inevitable result must be a complicated *nonequilibrium* distribution of charge carriers (electrons and holes) inside the link region, which needs to be computed in a self-consistent manner to access reliable data for the tunneling current flow. Together with Octavio, the previous authors complemented their description by this self-consistent calculation of electron distributions [216, 217], eventually yielding a much better coincidence with earlier conducted experiments [218]. Their approach, commonly known as Octavio-Tinkham-Blonder-Klapwijk (OTBK) model nowadays, evolved into an important tool to theoretically classify tunneling current-voltage relations of a whole bunch of Josephson geometries. Sometimes, the OTBK modeling is considered as a simple generalization of the BTK theory, not appreciating the valuable step of including the self-consistent description that has been lacking in the latter (and is also not required for single metal/superconductor contacts owing to the absence of multiple reflections there).

Since the initial publication of the OTBK model, tremendous efforts have been invested into fabricating Josephson junctions in which the link region consists of degenerately doped semiconductors (see, e.g., Refs. [196], [198], and [199]), offering a great tunability of the superconductor-link coupling strengths and facilitating rather large supercurrent flows. Despite the fact that some more complicated effects like heating, which go far beyond the actual OTBK description, can always cause quantitative deviations between experiment and theory, even those junctions' subharmonic gap structure is well describable within this approach. To give some examples, Fig. 4.1(a) compares the experimentally recorded subharmonic gap structure of Nb/(doped) Si/Nb junctions [196] with the respective one predicted by the OTBK model. Moreover, Fig. 4.1(b) presents the gap structure of more complex Pb/*n*-doped InSb/Sn junctions [198], consisting of two *different* superconducting electrodes (lead and tin); recall that we always assumed two similar superconductors so far. Anyhow, also the latter's subharmonic gap structure can be deduced from the OTBK modeling (the theoretical calculations are not shown here; see Ref. [198] for details), recognizing that the large mismatch between the two distinguished superconductors' gaps (the gap of lead is nearly two times larger than the one of tin) results in nontrivial modifications of the subharmonic gap structure, i.e., the conductance maxima (resistance minima) series split into well-distinct sets of subseries.

This chapter is intended to provide a comprehensive analysis of biased Josephson junctions' most peculiar (quasiparticle) transport features. For that purpose, we split the chapter into four sections. In Sec. 4.1, we recover the strongly simplified semiconductorlike tunneling picture firstly formulated by Arnold [209, 210]. Despite its simplifying assumptions, this approach helps us to argue that multiple Andreev reflection processes at Josephson junctions' interfaces can indeed give rise to the experimentally observed characteristic subharmonic gap structure in the systems' differential conductance (resistance), just as Klapwijk, Blonder, and Tinkham initially claimed [215]. Section 4.2 is then dedicated to developing the theoretical framework for an idealized system. To be more concrete, we consider a ballistic S/F/S Josephson junction, in which the two superconducting electrodes are connected by an ultrathin ferromagnetic film. We recapitulate the main general steps of the OTBK description and eventually generalize the modeling to ferromagnetic S/F/S contacts; recall that the initial OTBK approach [216–218] was restricted to junctions with *non*magnetic links. Numerically evaluating the tunneling current flow and the associated conductance for several realistic junction parameters, we unambiguously identify and further characterize the arising excess current and subharmonic conductance gap structure.

Even richer physics occurs in Al/Ni/Ga Josephson junctions. Previous experimental studies [219, 220] concluded that Ni/Ga bilayers (and likewise Ni/Bi) are profoundly rewarding. Proximity effects can turn the intrinsically just ferromagnetic nickel layer superconducting, and make Ni/Ga and Ni/Bi bilayers to two of just a few experimentally feasible systems in which the nominally antagonistic ferromagnetic and superconducting phases can efficiently coexist. As a follow-up work, the group of Jagadeesh Moodera at MIT experimentally investigated the conductance features of biased Al/Ni/Ga junctions and unraveled unprecedented variations of the subharmonic gap structure when compared to the simpler systems that were at first modeled within the OTBK theory. To gain more physical insight, Sec. 4.3 extends the OTBK modeling to these particular junctions and compares the numerically extracted conductance to the experimentally recorded data. Although this modeling suffices to understand the general features of some samples, we soon discover that the OTBK approach faces serious problems when the left and right superconducting electrodes are not much larger than the intermediate link region, as the emergent interplay between the (now not only ferromagnetic, but additionally also superconducting) link and the electrodes is then no longer properly described. As a more powerful method, we implement the junctions in the Python quantum transport code KWANT [221] and extract the (spatially integrated) tunneling DOS, which is essentially probed by the conductance measurements. KWANT does eventually not only capture the consequences of the finite-size electrodes in a reasonable way, but furthermore illuminates the physics behind the puzzling conductance features. The chapter ends with a brief summary in Sec. 4.4.

The experimental conductance data, presented in Sec. 4.3 and always additionally highlighted by "Experiment" inside the plots, was measured on different Al/Ni/Ga samples in Jagadeesh Moodera's research group at MIT and was approved by Jagadeesh Moodera for the comparison with our theoretical modeling. All analytical and numerical calculations within this chapter (i.e., also the theoretical simulations in Sec. 4.3 that we contrast with the experimental data and mark with "OTBK theory" or "KWANT" inside the plots) were performed by Andreas Costa.

4.1 Physical origin of the subharmonic conductance gap structure

To understand the physical origin of Josephson junctions' unique subharmonic conductance (resistance) gap structure, we briefly revisit the qualitative *semiconductorlike picture* formulated by Arnold [209, 210]. The first successful idea to decompose quasiparticle excitations inside a superconductor into electronlike and holelike parts, similarly to the commonly established description of semiconductors, goes actually back to the initial BTK model for metal/superconductor contacts. The distinction between

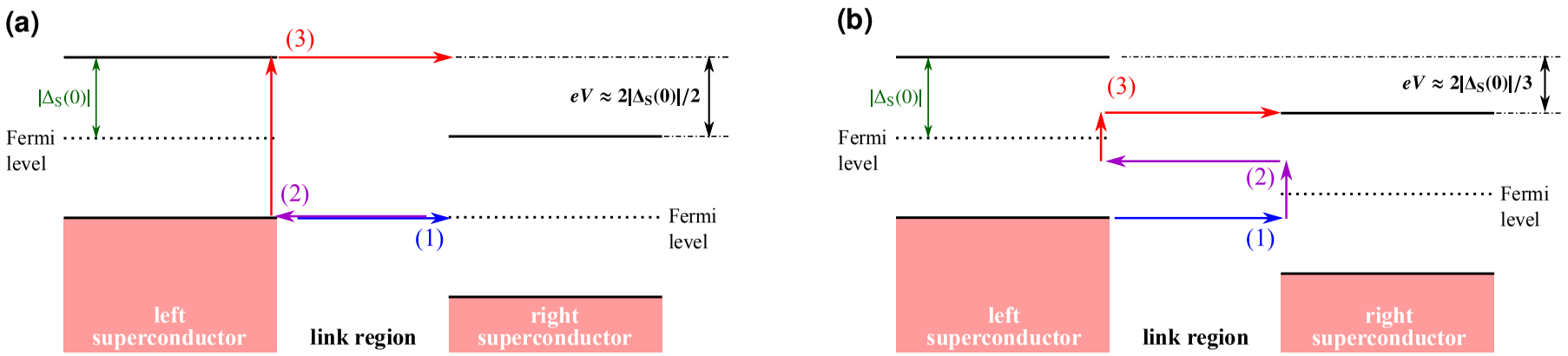


Fig. 4.2: (a) Schematical energy diagram illustrating the semiconductorlike tunneling of electronlike quasiparticles from Josephson junctions' left superconducting electrode into the second one; the link region between the superconductors could consist of an insulator or a metal. The superconductors' energy gap is denoted by $|\Delta_S(0)|$, while the applied bias voltage $V \approx 2|\Delta_S(0)|/(2e)$ entails an effective shift between the electrodes' Fermi levels. Light red shading emphasizes occupied (quasiparticle) states, while the states at energies above the gap are unoccupied. After two Andreev reflections at the link/superconductor interfaces [highlighted by steps (1) and (2); the arrows indicate the electron's (hole's) propagation directions], an electron, stemming from an occupied state in the left superconductor, tunnels into a free (quasiparticle) state in the right superconductor [see step (3)]. **(b)** Same as in **(a)**, but at voltage $V \approx 2|\Delta_S(0)|/(3e)$. A detailed relation between the illustrated multiple Andreev reflections and the experimentally observed conductance (resistance) anomalies is established in the text.

electronlike and holelike quasiparticles offered an easily accessible way to characterize the peculiar Andreev reflection process arising at the contacts' interface. Nevertheless, one should always be aware that the analogy between superconductors' electronlike (holelike) quasiparticles and electrons (holes) in semiconductors is not complete. For instance, while holelike quasiparticles in the Bogoljubov-de Gennes methodology reflect time-reversed electronlike quasiparticles with opposite charge and *same* effective mass, one of the most peculiar features of semiconductors is their complicated conduction and valence band structure that effectuates (strongly) *differing* effective masses for electrons and holes. This and several more deficits were actually the major reasons why many physicists had been skeptical about extending the semiconductor picture to superconductivity (see, e.g., the comments in Ref. [195]) until the BTK modeling demonstrated the great strengths coming along with such a simple description. Afterwards, Klapwijk, Blonder, and Tinkham additionally recognized the striking role of multiple Andreev reflections in Josephson junctions, and suggested to generalize their BTK semiconductor model to capture also these multiple reflections [215]. Their initial work was completed in two publications by Arnold [209, 210], from which we will recover some valuable physical characteristics in the following.

For simplicity, we consider a Josephson junction that consists of two *similar* semi-infinite superconducting electrodes connected by a thin insulating or metallic link. Both superconductors are characterized by the same zero-temperature superconducting energy gap $|\Delta_S(0)|$ that separates occupied from unoccupied quasiparticle states, while their equilibrium Fermi levels lie exactly in the gap center (at zero temperature). Moreover, we assume that the quasiparticle states in each of the superconductors are occupied according to the Fermi-Dirac distribution function. To probe the junction's current-voltage characteristics, we need to apply the finite bias voltage V between the two superconducting electrodes. The resulting voltage drop above the link region shifts the superconductors' individual Fermi levels with respect to each other so that both eventually differ by an amount of eV (e denotes the positive elementary charge), as Fig. 4.2 illustrates in a schematic manner. We distinguish between two representative values of eV, i.e., $eV \approx 2|\Delta_S(0)|/2$ [see Fig. 4.2(a)] and $eV \approx 2|\Delta_S(0)|/3$ [see Fig. 4.2(b)]. These values are basically motivated by the junction's subharmonic gap structure, for which we predicted the conductance maxima (resistance minima) to appear at $eV \approx 2|\Delta_S(0)|/n$. The studied bias voltages must therefore reflect the physics that gives eventually rise to the conductance maxima (resistance minima) of order $n = 2$ and $n = 3$.

Let us start analyzing the first scenario, belonging to $eV \approx 2|\Delta_S(0)|/2$. In that case, an electronlike quasiparticle, originating from one of the left superconductor's occupied high-DOS states close to the gap edge (recall Fig. 2.7), may tunnel into the link region and travel towards the right superconductor. Approaching the right interface, the electron can neither directly tunnel into the second superconducting electrode (since there are no quasiparticle states at energies inside the superconducting gap) nor perform specular reflection (as no scattering potential is assumed to be present at the interface). Instead, the electron must be Andreev reflected across the right superconductor's Fermi level, essentially penetrating the superconductor and immediately pairing into a Cooper pair together with another correlated electron. The simultaneously retroreflected hole propagates to the left and must again undergo an Andreev reflection process at the left interface – this time, across the left superconductor's Fermi level. Thereby, the hole gets transferred into the left superconductor and pairs into a *hole* Cooper pair, which essentially destroys one *electron* Cooper pair. From that viewpoint, multiple Andreev reflections effectively cycle electron Cooper pairs from one superconductor into the second one (from left to right in our case) and generate a net supercurrent flow through Josephson junctions. At zero bias, this current mirrors the respective DC Josephson current. Multiple Andreev reflections are therefore not only responsible for Josephson junctions' peculiar current-voltage anomalies, but additionally provide the microscopic physical explanation of the Josephson effect, as we will thoroughly discuss in Chap. 6. The Andreev-reflected, right-moving, electron finally gained enough energy that it can tunnel into the right superconductor and

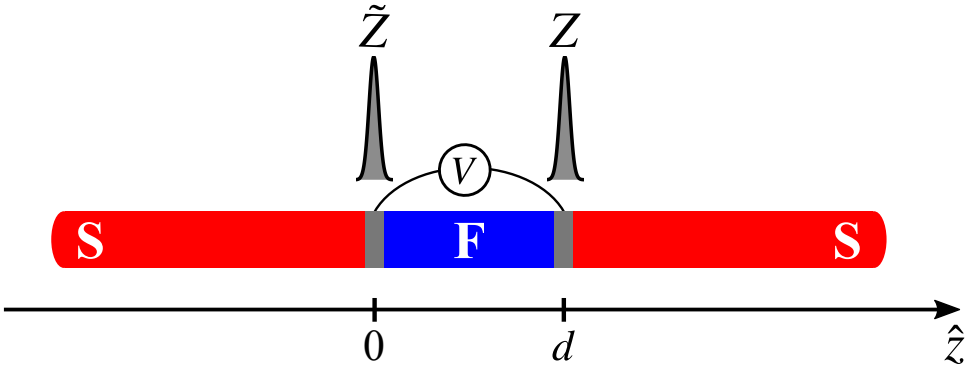


Fig. 4.3: Schematical sketch of the considered *one-dimensional* S/F/S Josephson junction grown along the $\hat{z} \parallel [001]$ crystallographic orientation. Scattering at the two interfaces between the superconducting electrodes (S) and the ferromagnetic link (F) is caused by the presence of two ultrathin tunneling barriers (dark gray) at $z = 0$ and $z = d$, whose barrier strengths are quantified by the two BTK-like parameters $\tilde{Z}$ and Z (see text for the parameters' definitions). Owing to these barriers, the bias voltage V applied between the two superconducting regions drops mostly above the metallic link.

fill an initially unoccupied quasiparticle state there. The experimentally measured tunneling current detects this normal quasiparticle current and the Cooper pair tunneling supercurrent at the same time. This is another remarkable difference to the BTK modeling, in which all supercurrent is solely generated by Andreev reflections and can hence be separated from the remaining (normal) current contributions. In the Josephson junction scenario, however, both quasiparticle and Cooper pair currents stem likewise from the multiple Andreev reflection processes, and cannot be individually resolved [210].

In principle, the described multiple Andreev reflection processes occur in a similar way at all bias voltages $2|\Delta_S(0)|/2 \leq eV < 2|\Delta_S(0)|$. Nevertheless, only at $eV \approx 2|\Delta_S(0)|/2$ (which is the case we addressed), the hole that arises from the first Andreev reflection at the right interface enters one of the left superconductor's high-DOS states around the gap edge as an "intermediate state"; see Fig. 4.2(a). The indicated multiple Andreev reflection processes become consequently most likely at just this particular bias voltage, giving rise to a clearly pronounced additional tunneling current contribution that becomes evident in terms of the anomalous conductance maximum (resistance minimum) in the subharmonic gap structure.

Further lowering the bias involves initially mostly multiple Andreev reflections via low-DOS states, which are not yet enough to facilitate another conductance maximum (the tunneling current starts to decrease notably). The situation turns out to become more interesting once we reach the second considered voltage, i.e., $eV \approx 2|\Delta_S(0)|/3$. After traversing the link region three times, mediated by two subsequent interfacial Andreev reflections, the initially incident electronlike quasiparticle can tunnel into an available quasiparticle state in the second superconductor. Inspecting the energy diagram in Fig. 4.2(b) suggests that the electron's final state (in the right superconductor) refers now to a high-DOS state. The results are again a strongly enhanced (quasiparticle) tunneling probability and tunneling current, which manifest themselves in another conductance maximum (resistance minimum) at $eV \approx 2|\Delta_S(0)|/3$.

Analogously, one can justify all remaining conductance maxima (resistance minima) at $eV \approx 2|\Delta_S(0)|/n$, offering a rather intuitive physical explanation for the intricate subharmonic conductance (resistance) gap structure. Nonetheless, the semiconductor picture relies on several simplifying assumptions (as stated above) and may not cover all effects that play important roles in experiments. To provide a more comprehensive analysis, we will explicitly calculate the tunneling current and its respective differential conductance for an idealized S/F/S junction in the next section, and compare the numerical results against our expectations based on the semiconductor picture.

4.2 Ballistic S/F/S Josephson junctions

As a simple example to gain deeper insight into the OTBK modeling, we consider a ballistic effectively *one-dimensional* S/F/S Josephson junction along the $\hat{z} \parallel [001]$ crystallographic direction. The two semi-infinite superconducting electrodes (S) at $z < 0$ and $z > d$ are coupled by an atomically thin ferromagnetic link region (F) of thickness d. Experimental realizations of such a system might again focus on S/F/S point contact geometries with small interfacial cross-section areas. To simplify our calculations further, we assume that the electrons' mean free path inside the metallic link is larger than the link thickness so that scattering occurs only at the two F/S interfaces and not inside the metallic constriction. Similarly to the BTK model discussed in Chap. 3, the interfacial scattering is then included in terms of ultrathin (deltalike) tunneling barriers that are located at $z = 0$ and $z = d$, respectively. The system is illustrated in Fig. 4.3.

4.2.1 Theoretical description – OTBK model

To unravel the junction's tunneling current-voltage characteristics, and thereby also its unique subharmonic conductance gap structure, we adapt the initial OTBK model to the *magnetic* case we are now concerned with. If not otherwise stated, we follow the main steps presented in Refs. [216] and [217]. Since the total tunneling current flow through the junction is conserved, we can extract its amplitude anywhere in the system. However, as we outlined in connection with the BTK model in Chap. 3, it is most convenient to compute the current inside the ferromagnet, in which all electrical current is solely carried by single electrons (holes) and no Cooper pairs need to be accounted for. To establish a nonzero tunneling current, more charge carriers need to tunnel into the right superconductor than into the left one (or vice versa). Therefore, the overall tunneling current is again determined by the imbalance between right-tunneling and left-tunneling carriers (recall the similarity to the BTK description).

Inside the ferromagnet (i.e., at $0 \leq z \leq d$), we denote the ($\hat{z}$-dependent) distribution function belonging to *right-moving* spin-σ electrons (as usual, $\sigma = 1$ for spin-up and $\sigma = -1$ for spin-down electrons) with an energy E (relative to the chemical potential) by $f_{\rightarrow}^{\sigma}(E; z)$, and the one referring to *left-moving* electrons by $f_{\leftarrow}^{\sigma}(E; z)$. Both distribution functions must essentially cover all contributions coming from incident electrons that approach one of the interfaces and get reflected back into the metal. Because of the peculiar Andreev reflection process, we again need to deal with electrons and holes at the same time – but the latter can simply be included into the electron distribution functions in terms of "missing" electrons. This is actually also the reason that we are only concerned with electron distribution functions in the following (and do not consider additional hole distribution functions). The (conserved) tunneling current at the left interface ($z = 0$) is then given by

$$J_z = -\frac{e}{h} \sum_{\sigma=\pm 1} \sum_{\mathbf{k}_\parallel} \int_{-\infty}^{\infty} \mathrm{d}E \, \left[f_{\rightarrow}^{\sigma}(E; z = 0) - f_{\leftarrow}^{\sigma}(E; z = 0) \right], \tag{4.1}$$

where e stands for the positive elementary charge, the sum over σ counts both spin channels' current contributions, and the integration over the electron energies E ensures that we capture all occupied electron states involved in tunneling. We keep our description general and present the current calculation for the *three-dimensional* junction scenario, explaining the averaging over all transverse channels (indicated by their respective transverse wave vectors $\mathbf{k}_\parallel = [k_x, k_y, 0]^\top$). In our simplified one-dimensional case, however, the left- and right-moving distribution functions will not explicitly depend on $\mathbf{k}_\parallel$, and the summation over $\mathbf{k}_\parallel$ will just yield a constant prefactor one might accumulate in the current normalization.

To evaluate Eq. (4.1), we initially need to find analytical expressions for the left- and right-moving electron distributions. Due to the presence of two deltalike tunneling barriers at the F/S interfaces, the

applied bias voltage V drops mostly above the ferromagnetic region. Moreover, as we assume that scattering occurs only at the interfaces and not inside the metallic link, which could lead to some intricate effects like backscattering inside the ferromagnet, the spatial dependence of the distribution functions becomes trivial. More specifically, the voltage drop simply results in an acceleration of electrons while traveling through the link region, i.e., all right-moving electrons leaving the left interface ($z = 0$) with energy E arrive at the right interface ($z = d$) with energy $E + eV$. Vice versa, all left-moving electrons starting at the right interface ($z = d$) with energy E approach $z = 0$ with energy $E - eV$. Translating these observations into formulas[1] yields

$$f_{\rightarrow}^{\sigma}(E; z = d) = f_{\rightarrow}^{\sigma}(E - eV; z = 0) \tag{4.2}$$

and likewise

$$f_{\leftarrow}^{\sigma}(E; z = d) = f_{\leftarrow}^{\sigma}(E - eV; z = 0). \tag{4.3}$$

The next step is to relate the distribution functions to the scattering processes appearing at the junction interfaces. Let us focus on the left interface at the moment. The distribution of right-moving electrons there, $f_{\rightarrow}^{\sigma}(E; z = 0)$, must essentially describe all electrons (holes) that initially propagated to the left and are then reflected back, as well as all single electronlike (holelike) quasiparticles that tunneled from the left superconductor into the ferromagnet and move towards the right afterwards. A spin-σ electronlike (holelike) quasiparticle with energy E tunnels with probability $\tilde{T}_{\mathrm{e}}^{\sigma}(E)$ [$\tilde{T}_{\mathrm{h}}^{\sigma}(E)$] into the ferromagnetic link, whereas the probability that an incoming electron from the metallic side gets specularly (Andreev) reflected is $\tilde{R}_{\mathrm{e}}^{\sigma}(E)$ [$\tilde{R}_{\mathrm{h}}^{\sigma}(E)$]. Since we do not consider SOC to be present, all these probabilities always solely cover spin-conserving scatterings. Putting everything together, $f_{\rightarrow}^{\sigma}(E)$ can be brought into the form

$$\begin{aligned} f_{\rightarrow}^{\sigma}(E; z = 0) = \tilde{R}_{\mathrm{e}}^{\sigma}(E) f_{\leftarrow}^{\sigma}(E; z = 0) + \tilde{R}_{\mathrm{h}}^{\sigma}(E) \left[1 - f_{\leftarrow}^{\sigma}(-E; z = 0)\right] \\ + \tilde{T}_{\mathrm{e}}^{\sigma}(E) f^{0}(E) + \tilde{T}_{\mathrm{h}}^{\sigma}(E) \left[1 - f^{0}(-E)\right]. \end{aligned} \tag{4.4}$$

Note that the four different parts indeed correspond to all aforementioned scattering processes that might happen at the left F/S interface, i.e., to specular and Andreev reflections of electrons incident from the metallic region, as well as to quasiparticle transmissions from the left superconductor into the metal. Besides the stated scattering probabilities, each contribution needs to be properly weighted by the underlying distribution functions of incoming and scattered particles. This is rather simple for transmissions. Since both superconductors represent massive (semi-infinite) electrodes, the distributions of incoming quasiparticles being transmitted into electron and hole states in the link can be approximated by equilibrium Fermi-Dirac functions (abbreviated by f^0). One just needs to be careful and recognize that transmissions are only possible if quasiparticles initially occupied (did not occupy) the respective electronlike (holelike) states at energy E ($-E$). In fact, we encountered precisely the same within the BTK model.

Regarding reflections, the situation turns out to become much more subtle. When discussing the BTK model in Chap. 3, we were actually concerned with F/S-like contacts. In such systems, incoming

[1] Strictly speaking, Eqs. (4.2) and (4.3) hold only for thin ferromagnetic links, as assumed in our junction. Each electron traveling once through the ferromagnet would actually pick up an additional phase of $\delta\phi = (\Delta_{\mathrm{XC}} d)/(\hbar v_{\mathrm{F}})$ [222], where Δ_{XC} denotes the ferromagnet's exchange energy gap and v_{F} its Fermi velocity. The additional phase factor would need to be carefully included into the relation between electron distributions at the left and right interfaces. In our calculations, we assumed, for convenience, thus small d that the accumulated phase remains negligible, e.g., an atomically thin ferromagnetic film sandwiched between two superconductors.

electrons from the metallic side approach the interface and can only undergo one single scattering process, being either reflected back into the metal or being transmitted into the superconducting electrode (see Fig. 3.3 for an illustration of the allowed scattering processes). Since both junction electrodes are massive (and, in fact, semi-infinitely extended), we can likewise approximate the distribution functions modeling the incident electrons and all scattering processes in terms of equilibrium Fermi-Dirac functions. Contrary, the ferromagnetic link of our regarded Josephson junction is atomically thin and sandwiched between two superconductors. Therefore, an electron that moves towards the left to be reflected at the interface could have traversed the link region several times before. Whenever hitting the junction interfaces, this electron had to perform either specular or Andreev reflection to remain inside the metallic link (if the electron would have been transmitted into one superconducting electrode, it would no longer be available for reflections in the metal). Multiple reflections arising at the two interfaces usually cause highly *nonequilibrium* electron distributions inside the metal, which we generally accounted for defining $f^\sigma_\rightarrow(E;z)$ and $f^\sigma_\leftarrow(E;z)$. But this means that all electrons propagating now towards the left and being reflected at the interface were initially also distributed according to $f^\sigma_\leftarrow(E;z=0)$ – at least as long no spin-flip scatterings are allowed. Similarly to the quasiparticle transmissions, we just need to take care that the involved electron (hole) states with related energies are occupied (not occupied) in order to permit reflections. After scattering, the reflected electron (hole) propagates towards the right and contributes again to the right-mover distribution $f^\sigma_\rightarrow(E;z)$, as inspecting Eq. (4.4) immediately suggests. In that way, we couple the initially independent left- and right-moving distribution functions.

Introducing nonequilibrium distribution functions within the link is essentially the most fundamental difference between the OTBK model and its earlier established BTK precursor. Although we did not specify the concrete form of these functions up to now, we will learn later that the distributions of left- and right-moving electrons are intimately connected [which one would probably already guess from Eq. (4.4)], and can only be determined in a self-consistent manner. Precisely this self-consistent coupling ensures that the multiple reflection cycles between the two junction interfaces, continuously converting left- into right-moving electrons (and vice versa), are properly included into the model.

Abbreviating the total quasiparticle transmission probability by $\tilde{T}^\sigma(E) := \tilde{T}^\sigma_\mathrm{e}(E) + \tilde{T}^\sigma_\mathrm{h}(E)$ and using $1 - f^0(-E) = f^0(E)$, we can reduce Eq. (4.4) to

$$f^\sigma_\rightarrow(E;z=0) = \tilde{R}^\sigma_\mathrm{e}(E) f^\sigma_\leftarrow(E;z=0) + \tilde{R}^\sigma_\mathrm{h}(E)\left[1 - f^\sigma_\leftarrow(-E;z=0)\right] + \tilde{T}^\sigma(E) f^0(E). \tag{4.5}$$

The arising reflection and transmission probabilities solely carry the information about scattering at one single F/S interface, basically described by the usual BTK model. We can thus access these probabilities in exactly the same way as presented in Chap. 3. Recall that we currently restrict ourselves to scattering at the left interface and it is hence justified to simply consider the left F/S half-junction, as illustrated in the left part of Fig. 4.4. An incoming electron from the ferromagnet approaches the tunneling barrier at $z = 0$ and must either be reflected back or transmitted into the superconductor. The left half-junction's Bogoljubov-de Gennes Hamiltonian [139] in Nambu representation,

$$\hat{\mathcal{H}}_\mathrm{BdG} = \begin{bmatrix} \hat{\mathcal{H}}_\mathrm{e} & \hat{\Delta}_\mathrm{S}(z) \\ \hat{\Delta}^\dagger_\mathrm{S}(z) & \hat{\mathcal{H}}_\mathrm{h} \end{bmatrix}, \tag{4.6}$$

couples the single-electron Hamiltonian

$$\hat{\mathcal{H}}_\mathrm{e} = \left(-\frac{\hbar^2}{2m}\frac{\mathrm{d}^2}{\mathrm{d}z^2} - \mu\right)\hat{\sigma}_0 - \frac{\Delta_\mathrm{XC}}{2}\hat{\sigma}_z\Theta(-z) + \tilde{V}_\mathrm{I}\tilde{d}_\mathrm{I}\hat{\sigma}_0\delta(z) \tag{4.7}$$

with its holelike counterpart

$$\hat{\mathcal{H}}_\mathrm{h} = -\hat{\sigma}_y\hat{\mathcal{H}}^*_\mathrm{e}\hat{\sigma}_y, \tag{4.8}$$

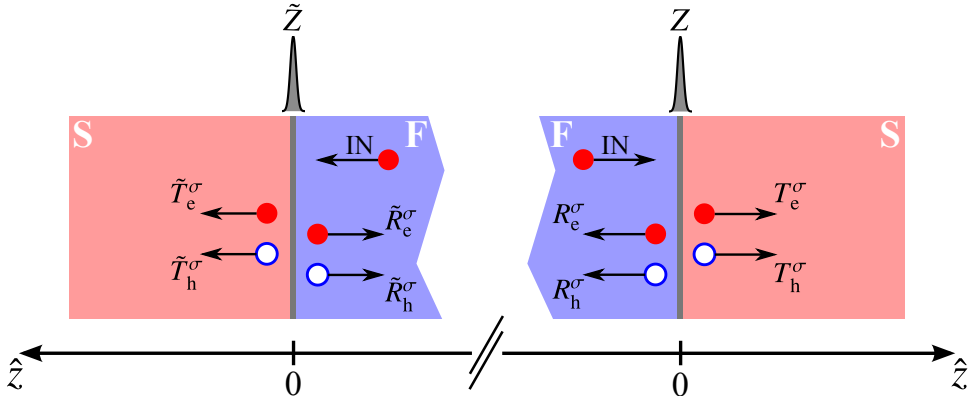


Fig. 4.4: Schematical illustration of the possible scattering processes an incoming electron (IN) from the ferromagnet (light blue) can undergo at the left and right half-junctions' tunneling barriers (gray), parameterized by the barrier measures $\tilde{Z}$ and Z. Electrons are colored red and holes blue; black arrows point along the electrons' and holes' propagation directions. The depicted scattering processes include specular reflections (with probabilities $\tilde{R}_e^\sigma$ and R_e^σ), Andreev reflections (with probabilities $\tilde{R}_h^\sigma$ and R_h^σ), electronlike transmissions (with probabilities $\tilde{T}_e^\sigma$ and T_e^σ), and holelike transmissions (with probabilities $\tilde{T}_h^\sigma$ and T_h^σ). Although these transmissions actually refer to electrons (holes) originating from the ferromagnet and entering the superconductors (light red), electronlike (holelike) quasiparticle tunnelings from the superconductors into the ferromagnet happen with exactly the same probabilities (due to the junctions' symmetry). Since scattering occurs only at the two interfaces and not inside the ferromagnet, we can independently deduce both half-junctions' reflection and transmission probabilities; the coupling between the interfaces, giving rise to intricate multiple reflections, is then included into the electron distribution functions (see text for details). The spatial shift of the right interface (actually located at $z = d$) is not relevant to the individual scattering probabilities and can be neglected.

and the (idealized) s-wave superconducting pairing potential

$$\hat{\Delta}_S(z) = |\Delta_S|\hat{\sigma}_0\Theta(z) \tag{4.9}$$

inside the superconductor. We follow the same notation as in Chap. 3, i.e., m (μ) indicate the equal quasiparticle masses (chemical potentials) in all junction constituents, Δ_{XC} refers to the Stoner ferromagnet's exchange energy gap, $\tilde{V}_I$ ($\tilde{d}_I$) to the barrier's height (width), and $|\Delta_S|$ quantifies the superconductor's energy gap [specifically at zero temperature, we write $|\Delta_S(0)|$]. Note that the magnetization direction in the ferromagnet is aligned perpendicular to the interface (along $\hat{z}$). The most general ansatz for the scattering states in the ferromagnet and superconductor [denoted by $\psi^\sigma(z)$], differentiating between incoming and scattered waves, is then constructed from the stationary Bogoljubov-de Gennes equation $\hat{\mathcal{H}}_{BdG}\psi^\sigma(z) = E\psi^\sigma(z)$. Requiring the states to fulfill appropriate interfacial boundary conditions and solving the resulting set of equations, we eventually identify the reflection and transmission probabilities, in which the tunneling barrier's impact enters via the dimensionless BTK-like parameter $\tilde{Z} = (2m\tilde{V}_I\tilde{d}_I)/(\hbar^2 k_F)$; $k_F = \sqrt{2m\mu}/\hbar$ indicates the Fermi wave vector. In fact, we solved exactly the same problem in Chap. 3 and can simply adopt the results obtained there (setting $\Delta_Z = 0$ and replacing the barrier measure by $\tilde{Z}$). The scattering description in Chap. 3 was limited to one-dimensional junctions, but this does not bother us since we are now also concerned with one-dimensional Josephson junctions. The final tunneling current formula is, nevertheless, more universal and would likewise apply to the three-dimensional case after extending the scattering approach to three dimensions.

Scattering at the right interface can be modeled in an analogous way, giving access to the distribution of left-moving electrons

$$f_{\leftarrow}^\sigma(E; z = d) = R_e^\sigma(E) f_{\rightarrow}^\sigma(E; z = d) + R_h^\sigma(E)\left[1 - f_{\rightarrow}^\sigma(-E; z = d)\right] + T^\sigma(E) f^0(E). \tag{4.10}$$

To provide the most general description, we account for the possibility that the two interfacial tunneling barrier strengths may be different. The reflection and transmission probabilities at the right F/S interface are $R_{\mathrm{e}}^{\sigma}(E)$, $R_{\mathrm{h}}^{\sigma}(E)$, and $T^{\sigma}(E) := T_{\mathrm{e}}^{\sigma}(E) + T_{\mathrm{h}}^{\sigma}(E)$; note the omitted tilde, which distinguishes them from the scattering probabilities at the left interface. We compute these probabilities similarly to those at the left interface, just replacing the barrier height (width) in the Bogoljubov-de Gennes equation's single-particle Hamiltonians by V_{I} (d_{I}) and treating the scattering problem at the right half-junction's interface (see right part of Fig. 4.4) then in the same way as in Chap. 3. The result is essentially the same [setting $\Delta_{\mathrm{Z}} = 0$ and identifying the barrier measure by $Z = (2mV_{\mathrm{I}}d_{\mathrm{I}})/(\hbar^2 k_{\mathrm{F}})$].

For evaluating the tunneling current in Eq. (4.1), we need to unravel both electron distribution functions at the left interface, i.e., at $z = 0$, and at the electron energy E. Exploiting Eqs. (4.2) and (4.3), we can initially rewrite Eq. (4.10) as

$$f_{\leftarrow}^{\sigma}(E-eV;z=0) = R_{\mathrm{e}}^{\sigma}(E)f_{\rightarrow}^{\sigma}(E-eV;z=0)+R_{\mathrm{h}}^{\sigma}(E)\left[1-f_{\rightarrow}^{\sigma}(-E-eV;z=0)\right]+T^{\sigma}(E)f^{0}(E). \quad (4.11)$$

Afterwards, we shift the reference energy by an amount of eV so that $E - eV \longmapsto E$ and simultaneously

$$f_{\leftarrow}^{\sigma}(E;z=0) = R_{\mathrm{e}}^{\sigma}(E+eV)f_{\rightarrow}^{\sigma}(E;z=0) + R_{\mathrm{h}}^{\sigma}(E+eV)\left[1-f_{\rightarrow}^{\sigma}(-E-2eV;z=0)\right] + T^{\sigma}(E+eV)f^{0}(E+eV). \quad (4.12)$$

Substituting Eq. (4.12) into Eq. (4.5) eliminates the distribution of left-moving electrons in the latter, and we finally end up with

$$\begin{aligned} f_{\rightarrow}^{\sigma}(E;z=0) = {} & \tilde{R}_{\mathrm{e}}^{\sigma}(E)\Big\{R_{\mathrm{e}}^{\sigma}(E+eV)f_{\rightarrow}^{\sigma}(E;z=0) + R_{\mathrm{h}}^{\sigma}(E+eV)\left[1-f_{\rightarrow}^{\sigma}(-E-2eV;z=0)\right] \\ & + T^{\sigma}(E+eV)f^{0}(E+eV)\Big\} \\ & + \tilde{R}_{\mathrm{h}}^{\sigma}(E)\Big\{1-R_{\mathrm{e}}^{\sigma}(-E+eV)f_{\rightarrow}^{\sigma}(-E;z=0) - R_{\mathrm{h}}^{\sigma}(-E+eV)\left[1-f_{\rightarrow}^{\sigma}(E-2eV;z=0)\right] \\ & - T^{\sigma}(-E+eV)f^{0}(-E+eV)\Big\} \\ & + \tilde{T}^{\sigma}(E)f^{0}(E). \end{aligned} \quad (4.13)$$

Equation (4.13) relates the unknown distribution of right-moving spin-σ electrons at energy E to its likewise unknown values at energies $(-E-2eV)$, $(-E)$, and $(E-2eV)$, given that all scattering probabilities and the Fermi-Dirac distributions were already specified earlier. In principle, Eq. (4.13) defines an infinite-dimensional system of equations that can only be solved in a self-consistent way to access the distribution function's full energy profile. As we outlined above, this self-consistent description is a consequence of the multiple (Andreev) reflection processes, which play a crucial role and need to be accounted for carefully. Taking electron energies far below the superconducting gap, $E \ll -|\Delta_{\mathrm{S}}(0)|$, and energies well above the gap, $E \gg |\Delta_{\mathrm{S}}(0)|$, $f_{\rightarrow}^{\sigma}(E;z=0)$ is still expected to approach the Fermi-Dirac limit, i.e., $f_{\rightarrow}^{\sigma}(E \ll -|\Delta_{\mathrm{S}}(0)|;z=0) \longrightarrow 1$ and $f_{\rightarrow}^{\sigma}(E \gg |\Delta_{\mathrm{S}}(0)|;z=0) \longrightarrow 0$. Imposing this limiting behavior reduces the infinite system of equations, resulting from Eq. (4.13), to a finite set, which can be numerically solved by means of a Gauss-Seidel iteration algorithm [223] starting from the Fermi-Dirac function as an initial guess. We will comment more on the practical implementation of the required calculations in the next section. After we determined the full energy profile of $f_{\rightarrow}^{\sigma}(E;z=0)$, we plug the results into Eq. (4.12) to consecutively obtain the distribution $f_{\leftarrow}^{\sigma}(E;z=0)$ of left-movers.

Since we investigate an effectively one-dimensional Josephson junction, the scattering probabilities entering the electron distribution functions do not explicitly depend on the transverse wave vector $\mathbf{k}_{\parallel}$

and we can further simplify the tunneling current ansatz in Eq. (4.1) integrating out $\mathbf{k}_\parallel$. Denoting the effective interfacial cross-section area by $\mathcal{A}$, we arrive at

$$J_z \approx -\frac{\mathcal{A}ek_\mathrm{F}^2}{4\pi h}\sum_{\sigma=\pm1}\int_{-\infty}^{\infty}\mathrm{d}E\,\left[f_{\rightarrow}^{\sigma}(E;z=0)-f_{\leftarrow}^{\sigma}(E;z=0)\right]. \tag{4.14}$$

We evaluate Eq. (4.14) substituting the self-consistently computed electron distributions and numerically performing the integration over all involved electron energies E exploiting an adaptive Gauss-Kronrod routine [224]. The need for such adaptive integration algorithms will become clear when discussing some examples for self-consistently computed electron distributions within the following section. Once we calculated the tunneling current J_z, the differential tunneling conductance is given by $G_{z,z} = -\mathrm{d}J_z/\mathrm{d}V$ (see Chap. 3).

The self-consistent coupling of the distributions belonging to left- and right-moving electrons [recall our reasoning to Eq. (4.4)] essentially prevents us from deriving closed analytical expressions for the tunneling current and conductance. Inspecting Eq. (4.13) for another time demonstrates, however, that this coupling disappears if (multiple) Andreev reflection processes are no longer allowed, i.e., if we regard the junction's normal-conducting regime. In the respective normal metal/ferromagnet/normal metal (N/F/N) junction, the Andreev reflection probabilities vanish, $\tilde{R}_\mathrm{h}^{\sigma}(E) = R_\mathrm{h}^{\sigma}(E) = 0$, and Eq. (4.13) can be inverted to identify

$$\left[f_{\rightarrow}^{\sigma}(E;z=0)\right]_{\text{normal state}} = \frac{\tilde{R}_\mathrm{e}^{\sigma}(E)T^{\sigma}(E)f^0(E+eV)+\tilde{T}^{\sigma}(E)f^0(E)}{1-\tilde{R}_\mathrm{e}^{\sigma}(E)R_\mathrm{e}^{\sigma}(E)}. \tag{4.15}$$

Going back to Eq. (4.12), we can furthermore deduce

$$\left[f_{\leftarrow}^{\sigma}(E;z=0)\right]_{\text{normal state}} = \frac{R_\mathrm{e}^{\sigma}(E)\tilde{T}^{\sigma}(E)f^0(E)+T^{\sigma}(E)f^0(E+eV)}{1-\tilde{R}_\mathrm{e}^{\sigma}(E)R_\mathrm{e}^{\sigma}(E)}. \tag{4.16}$$

Left- and right-moving electrons inside normal-state junctions' metallic link are therefore distributed according to (compositions of) equilibrium Fermi-Dirac functions, indicating for another time that the complicated nonequilibrium electron distributions in the superconducting regime are indeed a distinct consequence of the striking multiple Andreev reflections.

Assuming, for simplicity, identical tunneling barriers (meaning that $\tilde{Z} = Z$), the scattering probabilities at both junction interfaces become equal [$\tilde{R}_\mathrm{e}^{\sigma}(E) = R_\mathrm{e}^{\sigma}(E)$ and $\tilde{T}^{\sigma}(E) = T^{\sigma}(E)$]. After approximating the appearing difference of Fermi-Dirac functions by $f^0(E) - f^0(E+eV) \approx eV\delta(E)$, and putting everything together into the tunneling current formula [see Eq. (4.14)], we get

$$\left[J_z(V)\right]_{\text{normal state}} \approx -\frac{\mathcal{A}e^2k_\mathrm{F}^2}{4\pi h}\sum_{\sigma=\pm1}\frac{\left[T_\mathrm{e}^{\sigma}(E=0)\right]^2}{1-\left[R_\mathrm{e}^{\sigma}(E=0)\right]^2}V. \tag{4.17}$$

It may be useful later on to simplify Eq. (4.17) further. Within the outlined Bogoljubov-de Gennes scattering approach, the probabilities for incident *zero-energy* spin-σ electrons to undergo transmissions and specular reflections read as

$$T_\mathrm{e}^{\sigma}(E=0) = \frac{4\sqrt{1+\sigma P}}{(1+\sigma P)+\left(1+Z^2\right)+2\sqrt{1+\sigma P}} = 1-R_\mathrm{e}^{\sigma}(E=0), \tag{4.18}$$

where $P = (\Delta_\mathrm{XC}/2)/\mu$ measures the *effective* spin polarization in the ferromagnetic link. If the metallic link is additionally *nonmagnetic*, we can set $P = 0$ and reduce the expression for the tunneling current to

$$\left[J_z(V)\right]_\mathrm{N} \approx -\frac{G_\mathrm{S}}{1+2\,(Z/2)^2}V, \tag{4.19}$$

with $G_S = (\mathcal{A}e^2k_F^2)/(2\pi h)$ reflecting *Sharvin's conductance* of a perfectly transparent (three-dimensional) metallic point contact. The conductance of nonmagnetic normal metal/normal metal/normal metal (N/N/N) junctions is hence

$$G_N = -\frac{\mathrm{d}\big[J_z(V)\big]_N}{\mathrm{d}V} \approx \frac{G_S}{1+2\,(Z/2)^2}, \tag{4.20}$$

which simply coincides with Sharvin's idealized point contact conductance in the absence of interfacial tunneling barriers (when $Z = 0$), just as one would expect. This result is overall quite rewarding, not only due to its compact form, but particularly also as Eq. (4.20) proposes a unique *linear* dependence of purely normal-conducting systems' tunneling current on the applied bias voltage.

4.2.2 Discussion of results

We closed the theoretical modeling part deducing explicit analytical equations for normal-conducting N/N/N (and N/F/N) junctions' tunneling current and conductance. The linear current-voltage characteristics undoubtedly counts to the most remarkable normal-state features. Owing to the emergent multiple Andreev reflections, significant deviations from this linear current-voltage relation will arise in the junctions' superconducting counterparts and manifest themselves in extraordinary physical features like the excess current and subharmonic conductance gap structure. To become more familiar with those phenomena, we compare numerically evaluated currents (conductances) for the superconducting junction regime to the corresponding analytical normal-state predictions.

4.2.2.1 Self-consistent electron distribution functions

On our way towards a numerical evaluation of the tunneling current by means of Eq. (4.14), we need to determine the nonequilibrium left- and right-moving electron distribution functions' energy profile inside the metallic link in a self-consistent way. All required formulas can be found in the previous section. We essentially start from Eq. (4.13), which relates the distribution of right-moving spin-σ electrons with energies E, $f_{\rightarrow}^{\sigma}(E;z=0)$, to the same distribution's values at energies $(-E-2eV)$, $(-E)$, and $(E-2eV)$. Also the latter, i.e., $f_{\rightarrow}^{\sigma}(-E-2eV;z=0)$, $f_{\rightarrow}^{\sigma}(-E;z=0)$, and $f_{\rightarrow}^{\sigma}(E-2eV;z=0)$ are actually defined by similar equations obtained when appropriately replacing the energy argument. But then, each of the latest equations' right-hand sides contains again three $f_{\rightarrow}^{\sigma}$-terms at other energies, which have likewise not yet been specified and for which we have to go back with Eq. (4.13) another time. Since the distribution's complete energy dependence is initially unknown, setting up those equations proceeds, in principle, forever. In that way, writing out Eq. (4.13) for all upcoming energies (it turns out that we need to do that for $\pm E \pm neV$, where n is an integer) yields an infinite-dimensional system of equations for $f_{\rightarrow}^{\sigma}(E;z=0)$ that can only be solved self-consistently. To reduce the numerical efforts, it is essential to recognize that, while modeling highly nonequilibrium electron distributions at energies inside or comparable to the superconducting gap, $f_{\rightarrow}^{\sigma}$ must approach the equilibrium Fermi-Dirac limit far away from the gap region, i.e., $f_{\rightarrow}^{\sigma}(E \ll -|\Delta_S(0)|;z=0) \longrightarrow 1$ and $f_{\rightarrow}^{\sigma}(E \gg |\Delta_S(0)|;z=0) \longrightarrow 0$. Imposing these "boundary conditions", we can truncate the infinite-dimensional system of equations at energies well outside the subgap regime and reduce it to a computationally better manageable finite set. However, even when this truncation is used, the system of equations we need to work with remains quite large (especially at small bias voltages), limiting the parameter range for which reliable solutions can be extracted within reasonable computation times. We solve the final set of equations by means of an iterative Gauss-Seidel algorithm [223], which takes an initial guess for $f_{\rightarrow}^{\sigma}(E;z=0)$ – in our case, a rational choice for that could be the usual Fermi-Dirac function already fulfilling our "boundary conditions" –, and plugs the starting distribution into the system of equation's right-hand side to obtain a first result for $f_{\rightarrow}^{\sigma}(E;z=0)$.

Afterwards, this result enters again the equations' right-hand sides to access a refined $f^{\sigma}_{\rightarrow}(E;z=0)$. These iteration steps continue until $f^{\sigma}_{\rightarrow}(E;z=0)$ converged to the desired accuracy and further iterations do no longer notably change the output. Finally, we can resubstitute the outcome for $f^{\sigma}_{\rightarrow}(E;z=0)$ into Eq. (4.12) to unravel the left-mover distribution $f^{\sigma}_{\leftarrow}(E;z=0)$.

Figure 4.5 illustrates the numerically extracted zero-temperature distributions for one representative superconductor/normal metal/superconductor (S/N/S) Josephson junction with a normal-metal link region (spin polarization $P=0$) and as functions of electron energy E. The chosen tunneling barrier parameters $\tilde{Z}=Z=1$ correspond, e.g., to experimentally realistic barriers of heights $\tilde{V}_{\mathrm{I}}=V_{\mathrm{I}}=0.75\,\mathrm{eV}$ and widths $\tilde{d}_{\mathrm{I}}=d_{\mathrm{I}}\approx 0.40\,\mathrm{nm}$ (assuming $m\approx m_{\mathrm{e}}$ and $k_{\mathrm{F}}=\sqrt{2m\mu}/\hbar\approx 8\times 10^{7}\,\mathrm{cm}^{-1}$ as a typical metal Fermi wave vector [182]). We distinguish between the four applied bias voltages $V=2|\Delta_{\mathrm{S}}(0)|/(4e)$, $V=2|\Delta_{\mathrm{S}}(0)|/(3e)$, $V=2|\Delta_{\mathrm{S}}(0)|/(2e)$, and eventually $V=2|\Delta_{\mathrm{S}}(0)|/e$ – each of them is expected to cause a distinct conductance maximum in the junction's subharmonic conductance gap structure (recall the semiconductorlike argumentation in Sec. 4.1). As reference parameters for the superconducting electrodes, we use the zero-temperature gap and critical temperature of niobium [197], i.e., $|\Delta_{\mathrm{S}}(0)|\approx 1.6\,\mathrm{meV}$ and $T_{\mathrm{C}}\approx 9\,\mathrm{K}$.

All regarded voltage scenarios unambiguously reveal that, while approaching the equilibrium Fermi-Dirac configuration at energies $E\ll -|\Delta_{\mathrm{S}}(0)|$ and $E\gg|\Delta_{\mathrm{S}}(0)|$, multiple Andreev reflections at the superconducting junction's interfaces indeed entail highly nonequilibrium electron distributions at electron energies within or comparable to the superconducting gap. Both the left- and right-mover distributions deviate a lot from usual Fermi-Dirac functions there. The total tunneling current flow (up to some prefactors) is then basically obtained subtracting left- from right-moving electron populations, $f^{\sigma}_{\rightarrow}(E;z=0)-f^{\sigma}_{\leftarrow}(E;z=0)$, and integrating out E [recall Eq. (4.14)]. Geometrically, the tunneling current becomes therefore proportional to the area that $f^{\sigma}_{\rightarrow}(E;z=0)-f^{\sigma}_{\leftarrow}(E;z=0)$ encloses with the horizontal coordinate axis in Fig. 4.5; as a guide for eyes, these areas are green shaded. Owing to the strongly nonequilibrium individual distributions, also their differences reveal a rather intricate, *sawtoothlike*, energy dependence. The sharp discontinuities arising close to the sawtooths are quite demanding for numerically evaluating the energy integration (tunneling current), which needs to be done with great accuracy to extract reliable conductance data (differentiate the current with respect to bias voltage). Adaptive integration routines, which sample the integration space most dense close to the integrand's discontinuities, count for sure to the most powerful routines for that. In our case, an adaptive Gauss-Kronrod integration [224] turned out to perform most efficiently.

Before analyzing the junction's peculiar tunneling current and conductance anomalies, we shall note another puzzling feature of the presented electron distributions. Comparing the latter, in particular their difference functions, at the indicated bias voltages, we conclude that the pronounced conductance maxima at $eV\approx 2|\Delta_{\mathrm{S}}(0)|/n$ appear because one of the electron distribution differences' sawtooth peaks gets suddenly displaced from the subgap region [defined by $-2|\Delta_{\mathrm{S}}(0)|\leq E\leq 2|\Delta_{\mathrm{S}}(0)|$ since we are concerned with two superconductors, each with gap $|\Delta_{\mathrm{S}}(0)|$] and the remaining sawtooth peaks are considerably sharpened. This sharpening occurs exactly when the bias voltage crosses $V=2|\Delta_{\mathrm{S}}(0)|/(ne)$ and immediately increases the enclosed area, and thereby the tunneling current, by a notable amount – more than likewise increasing the bias at other voltages, $V\neq 2|\Delta_{\mathrm{S}}(0)|/(ne)$, would do. The differential tunneling conductance measures essentially the relative change of the tunneling current amplitudes with increasing bias, i.e., the (positive) slope in the current-voltage relation. Consequently, the large relative increase of the tunneling current at voltages close to $V=2|\Delta_{\mathrm{S}}(0)|/(ne)$ due to the distribution differences' sharpening sawtooth pattern must cause local conductance maxima, which precisely coincide with those founding Josephson junctions' unique subharmonic conductance gap structure (recall our introductory motivation and the semiconductorlike model in Sec. 4.1).

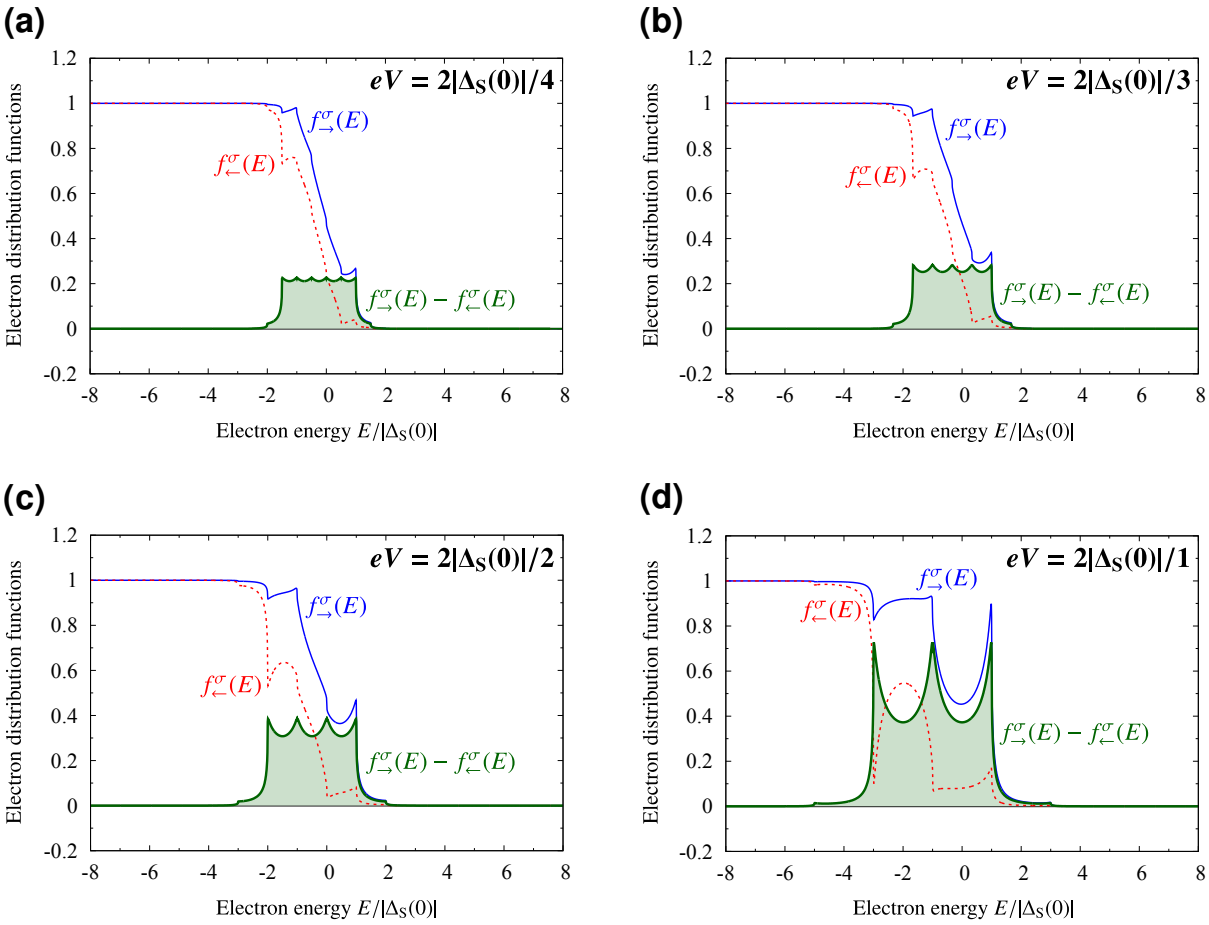


Fig. 4.5: Self-consistently calculated zero-temperature energy profiles of left-moving, $f^{\sigma}_{\leftarrow}(E;z=0)$, and right-moving, $f^{\sigma}_{\rightarrow}(E;z=0)$, spin-$\sigma$ electron distributions at the left interface of S/N/S Josephson junctions (the spin polarization in the metallic link is $P=0$) and for the symmetric tunneling barrier strengths $\tilde{Z}=Z=1$. The green-shaded area, enclosed by the horizontal coordinate axis and the electron distributions' *difference*, effectively measures the flowing tunneling current [recall Eq. (4.14)]. The considered bias voltages are **(a)** $eV=2|\Delta_S(0)|/4$, **(b)** $eV=2|\Delta_S(0)|/3$, **(c)** $eV=2|\Delta_S(0)|/2$, and **(d)** $eV=2|\Delta_S(0)|/1$. Since the metallic link is not spin polarized, the distribution functions for spin-up ($\sigma=1$) and spin-down ($\sigma=-1$) electrons are the same.

4.2.2.2 Tunneling current and subharmonic conductance oscillations

After the self-consistent determination of the energy profiles of left- and right-moving electrons' distributions, we can substitute them into Eq. (4.14) and numerically perform the energy integration (by means of an adaptive Gauss-Kronrod algorithm [224] as mentioned earlier) to unravel the tunneling current flow as a function of applied bias voltage. Figure 4.6(a) summarizes the results obtained for S/N/S Josephson junctions with normal-metal links (spin polarization $P=0$) and for different symmetric tunneling barrier strengths $\tilde{Z}=Z$. The values for Z are given in the plot and mimic realistic scenarios, as we outlined previously when discussing the evaluated electron distributions. For simplicity, all calculations were again performed at zero temperature, although our modeling would be general enough to capture finite-temperature effects.

Gradually increasing the barrier strengths from $Z=0$ (perfectly transparent interfaces) to $Z=4$ (strong interfacial barriers) inevitably suppresses the overall tunneling current. On the microscopic level, strong tunneling barriers remarkably damp the probability that electrons approaching the interfaces undergo

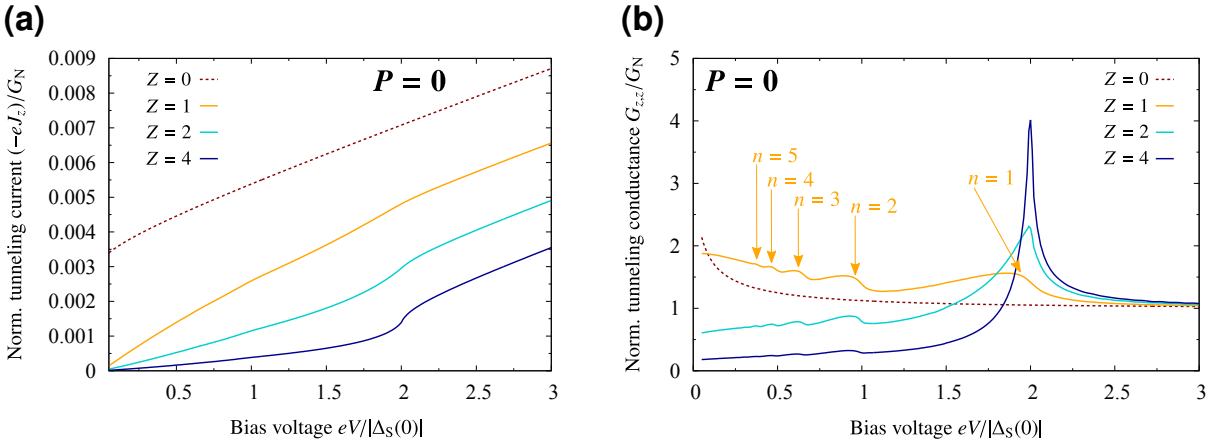


Fig. 4.6: **(a)** Calculated dependence of S/N/S Josephson junctions' (the spin polarization in the metallic link is $P = 0$) zero-temperature tunneling current J_z [normalized as indicated in the plot; G_N is given in Eq. (4.20)] on the applied bias voltage V [the associated electron energy eV is given in multiples of the superconductors' gap $|\Delta_S(0)|$] and for various indicated symmetric tunneling barriers $\tilde{Z} = Z$. **(b)** Calculated tunneling conductance $G_{z,z}$ (normalized to G_N) as a function of eV and for the same junctions considered in **(a)**. For the $(Z = 1)$-case, we additionally highlighted the conductance maxima, arising at $eV \approx 2|\Delta_S(0)|/n$, up to $n = 5$. Higher-order maxima are still there, but are barely resolvable on the used scale.

the multiple Andreev reflections that effectively trigger electron transmissions into the superconductors and sizable tunneling currents. Instead, more and more electrons being now mostly specularly reflected cannot leave the metallic link and contribute no longer to the measured tunneling current. Inspecting the tunneling current-voltage relations in more details, we clearly observe the aforementioned anomalies when compared to normal-state junctions' linear current-voltage characteristics. Particularly striking are the slight kinks that arise at voltages corresponding to $V \approx 2|\Delta_S(0)|/(ne)$ – precisely at those voltages at which the immediate sharpening of the electron distribution differences' discontinuities enhances the tunneling current faster than at slightly smaller or larger voltages –, and become more pronounced at stronger barrier strengths.

For a better resolution of these anomalous features, Fig. 4.6(b) shows the junctions' tunneling conductance,[2] obtained when differentiating the respective tunneling current-voltage relation (with respect to bias voltage). The conductance is conveniently normalized to its N/N/N counterpart G_N [see Eq. (4.20)]. Considering finite tunneling barrier strengths, we indeed recover the junctions' characteristic subharmonic conductance gap structure, characterized by conductance maxima at voltages $V \approx 2|\Delta_S(0)|/(ne)$ as predicted within Arnold's semiconductorlike picture [209, 210] and observed in several experimental works (see, e.g., Refs. [193–195] and [200–207]). In accordance with these experiments, the conductance maxima appear always at voltages slightly smaller than the proposed ones. A possible reason for that might be the lack of specular reflections in Arnold's model, which cannot be neglected once the tunneling barriers' strengths are finite. Surprisingly, the conductance of perfectly transparent Josephson junctions ($Z = 0$) behaves in a different way and decreases simply monotonically with increasing bias voltage, without reflecting the actually unique oscillatory subharmonic gap structure. This is quite a remarkable finding as it suggests that, while the subharmonic conductance gap structure is basically a consequence of the peculiar multiple Andreev reflections at the junction interfaces, additional specular reflections (only happening at nonzero barrier strengths) are required to magnify the structure. This

[2] As a crosscheck, one might compare the $(Z = 1)$-conductance curve in Fig. 4.6(b) to the inverted $(Z = 0.55)$-resistance curve presented in Fig. 2(b) of Ref. [217]; our Z-parameter is twice as large as the related one in Ref. [217]. Our result coincides well with that in Ref. [217].

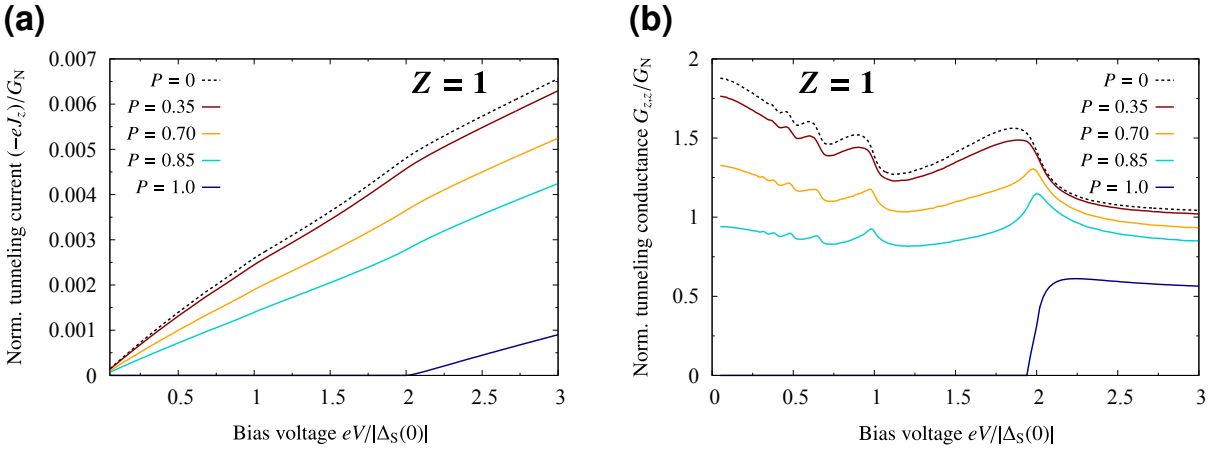


Fig. 4.7: (a) Calculated dependence of S/F/S Josephson junctions' zero-temperature tunneling current J_z [normalized as indicated in the plot; G_N is given in Eq. (4.20)] on the applied bias voltage V [the associated electron energy eV is given in multiples of the superconductors' gap $|\Delta_S(0)|$] and for various indicated spin polarizations P in the metallic link. The symmetric tunneling barriers are $\tilde{Z} = Z = 1$. **(b)** Calculated tunneling conductance $G_{z,z}$ (normalized to G_N) as a function of eV and for the same junctions considered in **(a)**.

becomes most clearly evident at strong barriers, i.e., at $Z = 4$, which turn especially the first-order conductance maximum at $eV \approx 2|\Delta_S(0)|$ into a sharp peak. If specular reflections are completely forbidden – as it is the case in the $(Z = 0)$-scenario –, the still allowed multiple Andreev reflections alone are not yet sufficient to reproduce the oscillating subharmonic conductance pattern (at zero temperature).[3]

To go beyond earlier studies, we extend our model to S/F/S junctions, including atomically thin ferromagnetic links whose spin polarization is measured by the effective parameter $P = (\Delta_{XC}/2)/\mu$ (Δ_{XC} abbreviates the exchange energy gap). These junctions' tunneling current- and tunneling conductance-voltage dependencies are illustrated in Figs. 4.7(a) and Figs. 4.7(b), respectively, keeping the tunneling barrier strengths at the realistic value of $\tilde{Z} = Z = 1$ and successively raising the spin polarization from $P = 0$ (normal-metal link) to $P = 1.0$ (half-metallic link); $P = 0.7$ corresponds to an iron link. Shortly speaking, even strong exchange couplings inside the link region (meaning that $0 \ll P < 1$) do not significantly alter the junctions' transport properties, particularly their subharmonic conductance gap structure, aside from a slight sharpening of some conductance maxima (turning more into sharp peaks) and the expected conductance suppression when increasing P. To some extent, the impact of larger exchange splittings in the link might be compared to the previously analyzed influence of strong interfacial barriers. This is essentially clear since an increase of the exchange coupling entails a pronounced imbalance between majority- and minority-spin bands. Andreev reflections usually involve both spin subbands at the same time and get hence heavily damped at strong spin imbalances (exchange splittings). The inevitable results of less (multiple) Andreev reflection processes are notably lowered tunneling currents and conductances, as we also observed when increasing the barrier strengths. The distinct behavior of half-metallic junctions' ($P = 1.0$) tunneling conductance can likewise be traced back to the peculiar Andreev reflections. As we explained in Chap. 3, Andreev reflections become then completely prohibited since all states around the Fermi level are solely occupied by majority-spin electrons that cannot find minority partners to be Andreev reflected. As the subgap tunneling current [at $0 \leq eV \leq 2|\Delta_S(0)|$ because the junction involves two superconductors] is essentially mainly governed by Andreev reflection, the

[3] If no interfacial tunneling barriers are present, also the self-consistently evaluated electron distributions simply approach (slightly shifted) Fermi-Dirac functions. Therefore, their difference transforms into a rectangular shape and the peculiar sawtoothlike pattern, we identified as one precursor of subharmonic conductance oscillations, disappears.

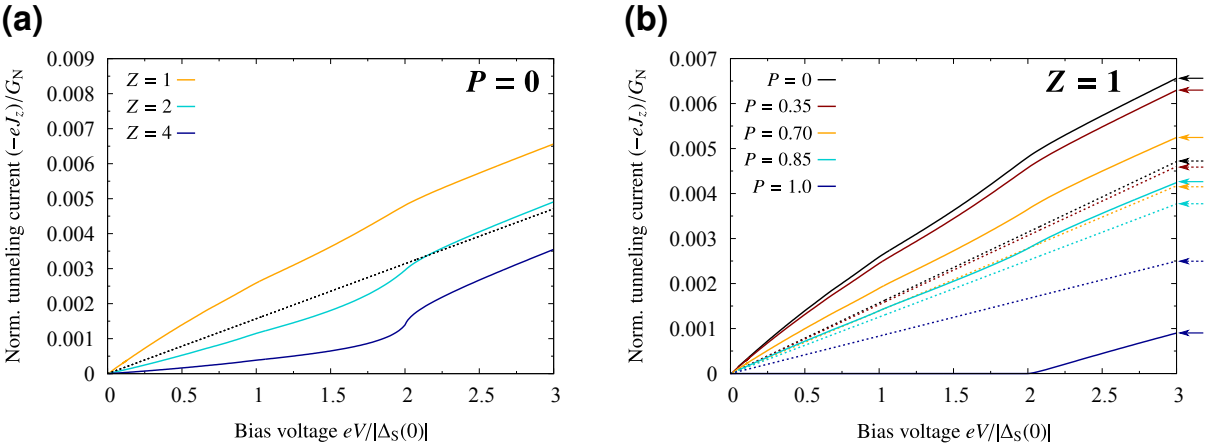


Fig. 4.8: **(a)** Calculated dependence of S/N/S Josephson junctions' (the spin polarization in the metallic link is $P = 0$) zero-temperature tunneling current J_z [normalized as indicated in the plot; G_N is given in Eq. (4.20)] on the applied bias voltage V [the associated electron energy eV is given in multiples of the superconductors' gap $|\Delta_S(0)|$] and for various indicated symmetric tunneling barriers $\tilde{Z} = Z$. The dashed, linearly increasing, curve refers to the junctions' N/N/N counterparts; since the barrier parameters are accumulated in the normalization [recall Eq. (4.20)], the *normalized* N/N/N tunneling current does not depend on Z. **(b)** Calculated dependence of S/F/S Josephson junctions' zero-temperature tunneling current J_z on the applied bias voltage V and for various indicated spin polarizations P in the metallic link. The symmetric tunneling barriers are $\tilde{Z} = Z = 1$. The dashed, linearly increasing, curves refer to the junctions' N/F/N counterparts; as a guide for eyes, superconducting and normal-state current curves that belong together are emphasized by equally colored arrows at the right margin.

latter's absence leads to vanishing subgap tunneling current and conductance. Nevertheless, quasiparticles can directly tunnel from one into free states of the second superconductor once $eV \gtrsim 2|\Delta_S(0)|$, and the tunneling current (conductance) starts to rise outside the subgap regime.

4.2.2.3 Excess current

The second notable quality of biased Josephson junctions' tunneling current refers to its behavior at large voltages, i.e., at $V \gg 2|\Delta_S(0)|/e$. In this regime, one actually expects that the systems' superconducting properties have no longer a substantial impact on transport and the tunneling current should merge into its normal-state junctions' counterpart. We show a comparison between the superconducting and their respective normal-conducting junctions' tunneling current-voltage relations in Fig. 4.8 – once for an S/N/S junction (spin polarization $P = 0$) considering different tunneling barrier strengths and once for S/F/S junctions assuming various spin polarizations and constant barrier strengths $\tilde{Z} = Z = 1$. The normal-state currents are generically obtained combining Eq. (4.18) with Eq. (4.17).

The superconducting junctions' large-voltage tunneling currents approach indeed the same *linear* voltage dependence as their respective normal-state counterparts and increase even with the same slopes, determining the related conductances and justifying that the large-voltage tunneling conductances presented in Figs. 4.6 and 4.7 become really equal to the normal-state conductances. Nevertheless, the tunneling current *amplitudes* in the superconducting state remain always slightly larger or smaller than the normal-state currents, which turned out to be another manifestation of multiple Andreev reflections [212–214]. The *difference* between the tunneling current amplitudes in the superconducting and its related

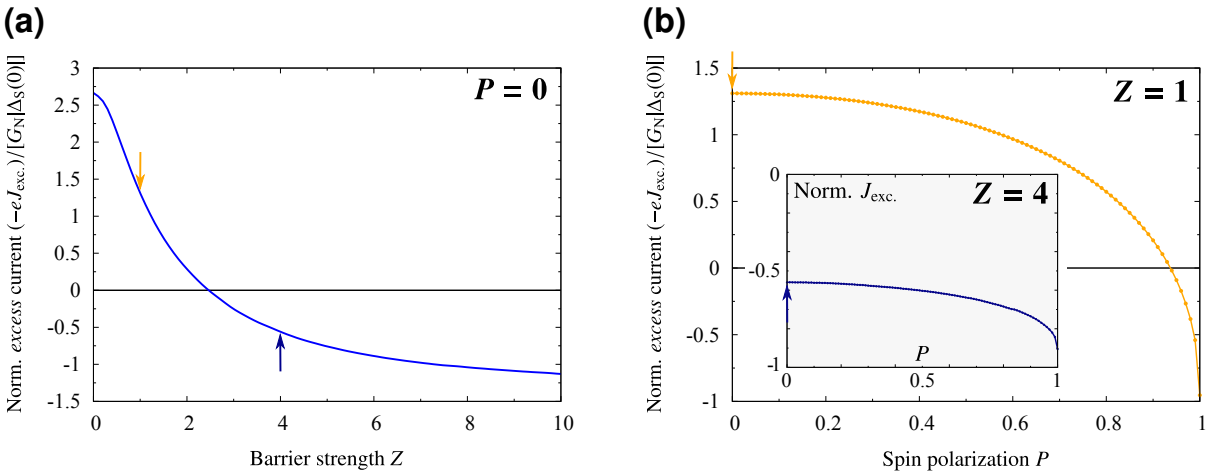


Fig. 4.9: (a) Calculated dependence of S/N/S Josephson junctions' (the spin polarization in the metallic link is $P = 0$) zero-temperature excess current $J_{\text{exc.}}$ [normalized as indicated in the plot; G_{N} is given in Eq. (4.20)] on the strength $\tilde{Z} = Z$ of the symmetric tunneling barriers. **(b)** Calculated dependence of S/F/S Josephson junctions' zero-temperature excess current $J_{\text{exc.}}$ on the metallic link's spin polarization P and for moderate symmetric tunneling barriers ($\tilde{Z} = Z = 1$). The inset shows the same calculation assuming strong tunneling barriers ($\tilde{Z} = Z = 4$). The orange (dark blue) arrows in **(a)** and **(b)** essentially highlight the same parameter regimes.

normal-state junction regime is quantified by

$$J_{\text{exc.}} = J_z(eV \gg 2|\Delta_{\text{S}}(0)|) - \left[J_z(V)\right]_{\text{normal state}}; \tag{4.21}$$

the individual parts are defined in Eqs. (4.14) and (4.17). As long as the superconducting junctions' tunneling current exceeds the normal-state current, $J_{\text{exc.}}$ remains positive and is commonly referred to as *excess current*. Contrary, negative $J_{\text{exc.}}$ is often termed *deficient current*.

The dependence of S/F/S junctions' excess (deficient) current on the tunneling barrier strengths and the metallic link's spin polarization is investigated in Fig. 4.9. Strong interfacial barriers usually suppress multiple Andreev reflections, which are themselves responsible for sizable tunneling currents in the superconducting regime, and transform therefore the initial excess current into a deficient current. As a consistency check, it shall be noted that the results depicted in Fig. 4.9(a) agree perfectly with those obtained in Ref. [217], recognizing that our Z-parameter is twice as large as the one in the aforementioned article. The universal $J_{\text{exc.}}$-Z scaling provides a valuable experimental tool to classify real junctions' tunneling barriers (growth quality) through measuring the tunneling current, fitting the results to the universal (material-independent) curve shown in Fig. 4.9(a), and reading off the related value of Z. Anyhow, Fig. 4.9(b) reveals that magnetic links give rise to a more intricate behavior and one should pay special attention when interpreting experimental data. The excess (deficient) current varies then not only with Z, but additionally with the link's spin polarization, which may also turn excess into deficient currents once the spin polarization becomes sufficiently large and the barriers are rather weak. The physical background is essentially again the aforementioned strong spin imbalance in the link that significantly suppresses multiple Andreev reflections and thereby the tunneling current. In the same way, strong barriers always result in deficient currents for all possible spin polarizations in the ferromagnet.

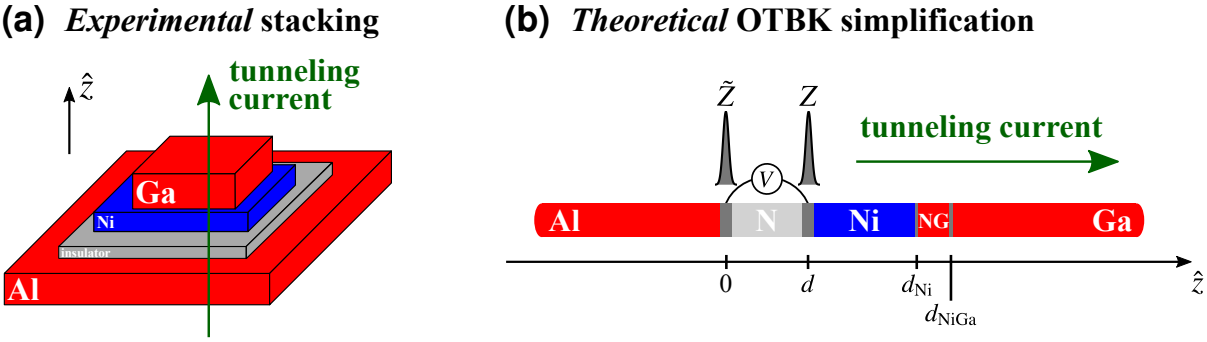


Fig. 4.10: **(a)** Schematical sketch of the *experimentally* investigated Al/insulator/Ni/Ga junctions. Applying a finite bias voltage across the junction and measuring the tunneling current (highlighted by the green arrow) gives direct access to the tunneling conductance. **(b)** *Theoretical* OTBK modeling of the respective simplified *one-dimensional* junction. The insulating layer is modeled in terms of a thin normal-conducting layer (N) that gets separated from the neighboring regions by two ultrathin tunneling barriers (dark gray) at $z = 0$ and $z = d$. The barrier strengths are quantified by the two BTK-like parameters $\tilde{Z}$ and Z. Due to the barriers, the bias voltage V drops mostly above the N region and we can use the same methodology as in Sec. 4.2 to deduce the tunneling current (green). Experimental observations suggest that a thin NiGa alloy forms between the nickel and gallium regions, which we account for by adding such an alloy (indicated by NG) at $d_{Ni} \leq z \leq d_{NiGa}$.

4.3 Ballistic Al/Ni/Ga Josephson junctions – theory *vs.* experiment

Even more interesting physics is bound to arise in junctions that are based on Ni/Ga or Ni/Bi bilayers. Already early transport measurements on such configurations [219, 220] brought along valuable insight into their unprecedented properties. The efficient coexistence of the nominally antagonistic ferromagnetic and superconducting phases in one single system, essentially mediated by strong proximity effects turning the intrinsically ferromagnetic nickel layer additionally superconducting, certainly counts to the most rewarding features of these bilayers. A deeper analysis of various samples' transport data [219, 220] suggested furthermore that the intriguing interplay between ferromagnetism and superconductivity can be controlled altering the ratio of the nickel and gallium parts' thicknesses, and completely unexpected physical phenomena may eventually occur.

As a follow-up work, the group of Jagadeesh Moodera at MIT fabricated high-quality Ni/Ga bilayers stacked on top of aluminum electrodes [see Fig. 4.10(a)] and investigated the tunneling current-voltage characteristics of the resulting Al/Ni/Ga Josephson junctions. All samples with cross-section areas of about 150 µm × 150 µm were prepared by means of *in-situ shadow-masking techniques*, evaporating the different compounds on well-cleaned glass slides held at roughly 80 K. Thin insulating Al_2O_3 tunneling barriers, created by exposing aluminum to controlled oxygen plasma, separate the Ni/Ga bilayers from the bottom aluminum electrodes. The nickel region is *weakly* ferromagnetic. Its spin polarization was classified via Meservey-Tedrow spectroscopy [23–25] and found to increase with an increase of the nickel layer's thickness. For instance, samples with 4 nm thick nickel revealed indications that the spin polarization must be less than one percent and becomes therefore hardly measurable. Depending on the other junction parameters, nickel's ferromagnetic exchange might only cause minor modifications in the recorded transport data. To see a stronger impact, most of the samples' tunneling barriers included a combination of Al_2O_3 and another thin layer of the *ferromagnetic* insulator EuS, whose spin polarization is much greater [21, 225] than that in nickel alone and might raise clear spin-polarized tunneling features.

Apart from the already intrinsically superconducting aluminum and gallium components, proximity effects turn also nickel additionally superconducting. The superconducting energy gaps and critical temperatures

of all the different components vary usually a lot with the distinct layers' thicknesses and had to be deduced from (some of) the experimental samples. For junctions built on 4 nm aluminum, the latter's critical temperature was estimated to be $T_{C,Al} = 2.5\,K$, whereas the one of the Ni/Ga bilayers typically drops with increasing nickel thickness and reaches $T_{C,Ni} = T_{C,Ga} = 4.2\,K$ for about 2 nm thin nickel; note that we use the same critical temperatures everywhere along the Ni/Ga bilayers. The bilayers' superconducting energy gaps were quantified in a sample containing a 2.4 nm nickel layer, while aluminum's gap remains roughly the same as its bulk value. All mentioned parameters enter our subsequent theoretical modeling and are summarized in a compact way in Tab. 4.1.

Tab. 4.1: Parameters estimated from some experimental samples and used for our calculations.

Al electrode	zero-temperature superconducting gap	$\lvert\Delta_{S,Al}(0)\rvert = 0.18\,meV$
	critical temperature	$T_{C,Al} = 2.5\,K$
Ni layer	zero-temperature superconducting gap	$\lvert\Delta_{S,Ni}(0)\rvert = 0.277\,meV$
	critical temperature	$T_{C,Ni} = 4.2\,K$
NiGa alloy	zero-temperature superconducting gap	$\lvert\Delta_{S,NiGa}(0)\rvert = 0.251\,meV$
	critical temperature	$T_{C,NiGa} = 4.2\,K$
Ga electrode	zero-temperature superconducting gap	$\lvert\Delta_{S,Ga}(0)\rvert = 1.358\,meV$
	critical temperature	$T_{C,Ga} = 4.2\,K$

4.3.1 Theoretical description – OTBK model *vs.* KWANT simulations

To compute Al/Ni/Ga Josephson junctions' tunneling current (conductance)-voltage characteristics and compare them against the experimentally taken data, we apply two different methods. The first approach essentially follows the OTBK modeling we introduced for simple model junctions in Sec. 4.2. We idealize the present system such that we can apply most of the earlier derived formulas and only the Bogoljubov-de Gennes scattering description (to access the interfacial scattering probabilities) needs to be adapted. To become concrete, we limit ourselves to an effectively *one-dimensional* Al/N/Ni/NiGa/Ga junction grown along $\hat{z}$; see Fig. 4.10(b). Although reducing the system to one dimension tremendously simplifies the analytical treatment, the obtained results' general trends are still well comparable to the experiment. To make use of Eq. (4.14), measuring the tunneling current flow inside a *nonsuperconducting* link of thickness d, we insert a thin normal-conducting region (N) between the junction's aluminum and nickel layers. Together with two strong ultrathin (deltalike) tunneling barriers at $z = 0$ and $z = d$, the normal-state link basically models the insulating barrier of the experimental samples and ensures that most of the applied bias voltage V drops above the nonsuperconducting part – one of the key assumptions when deducing Eq. (4.14). Moreover, experimental observations indicated that the Ni/Ga bilayers form a thin NiGa alloy at their interface, for which we shall also account in our model.

We evaluate the overall tunneling current flow through the junction in the same manner as outlined in Sec. 4.2. After numerically determining the self-consistent distributions belonging to left- and right-moving electrons inside the normal-conducting buffer layer, we can substitute the outcomes

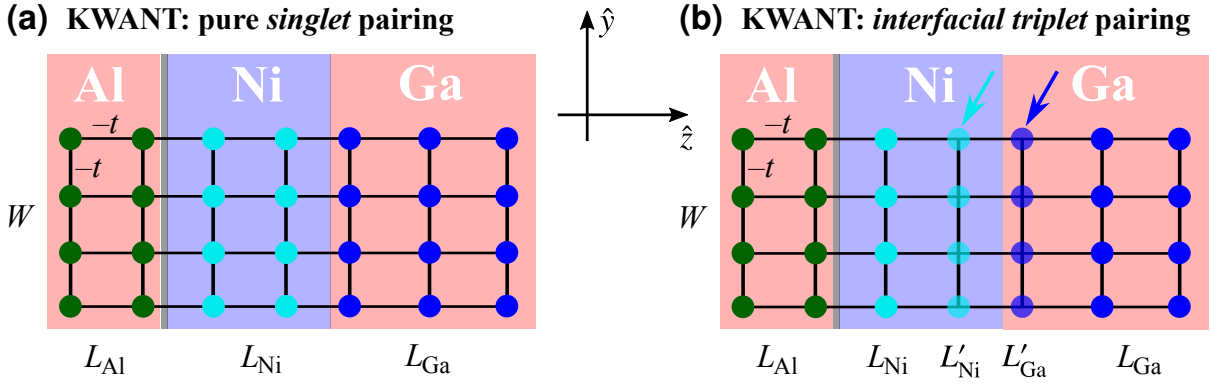


Fig. 4.11: (a) Schematical illustration of Al/Ni/Ga junctions' *tight-binding modeling* within the KWANT transport code, starting from a square lattice with constant spacing $a = 1$ [a.u.]. The numbers of *horizontal* lattice sites inside the junctions' different regions are denoted by L_{Al}, L_{Ni}, and L_{Ga}, respectively, and the one along the transverse direction by W. Colored dots represent the *on-site energies*, determined by the underlying Bogoljubov-de Gennes Hamiltonian stated in Eq. (4.22), while t measures the strength of the *nearest-neighbor hoppings*. All superconducting pairing potentials capture only pure *singlet* pairings. **(b)** Same as in **(a)**, but assuming that the superconducting pairing potentials in the nickel and gallium layers combine singlet and *interfacial triplet* pairings [within the lattice sites $(L'_{\mathrm{Ni}}; L'_{\mathrm{Ga}})$]; the latter are emphasized by colored arrows.

into Eq. (4.14), which will yield the current. The most crucial ingredients to extract the electron distributions are the interfacial reflection and transmission probabilities. In our case, we need to specify these probabilities at the N/Al and N/. . . /Ga interfaces within the common Bogoljubov-de Gennes scattering picture. Since the basic strategy is fully equivalent to that illustrated in Chap. 3 and partly also in Sec. 4.2, the detailed calculations are not shown here and can instead be looked up in Appendix A. Once we identified all scattering probabilities, we can go back with Eqs. (4.12), (4.13), and (4.14) to compute the electron distributions and simultaneously the tunneling current.

The second, and probably more powerful, method relies on the Python package KWANT [221], which can efficiently model electrical transport through many *realistic* physical systems going far beyond our analytical possibilities. To implement the experimentally studied Al/Ni/Ga junctions in KWANT's *tight-binding language*, we need to discretize their continuous Bogoljubov-de Gennes Hamiltonian on a tight-binding lattice, basically following the recipe given in Ref. [226]. For simplicity, we consider a two-dimensional *square lattice* with lattice spacing $a = 1$ [a.u.], in which each lattice site with the real-space coordinates $(z, y) = (ai, aj)$ is uniquely identified by its integer lattice "coordinates" (i, j); see Fig. 4.11(a) for a graphical representation of the tight-binding lattice. The numbers of lattice sites along the *horizontal* $\hat{z}$-direction inside the aluminum, nickel, and gallium junction regions are denoted by L_{Al}, L_{Ni}, and L_{Ga}, respectively, whereas we assume W lattice sites along the *transverse* $\hat{y}$-direction throughout the whole system. Contrary to our analytical OTBK modeling, we do *not* include the thin oxide tunneling barriers and the nickel-gallium alloy into our KWANT description since we are predominantly interested in deducing universal trends, which are not dramatically affected by these two components. The *on-site energies* at lattice site (i, j) are then determined by the discretized [226] Nambu-space Bogoljubov-de Gennes Hamiltonian [139]

$$\hat{\mathcal{H}}_{\mathrm{BdG}}(i,j) = \Big[(4t - \mu)\,\hat{\tau}_0$$

$$+ \left|\Delta^{\mathrm{singlet}}_{\mathrm{S,Al}}\right| \hat{\tau}_2\,\Theta(i)\,\Theta(L_{\mathrm{Al}} - i)$$

$$
\begin{aligned}
&+ \Delta_{\mathrm{XC,Ni}}\,\hat{\tau}_1\,\Theta(i - L_{\mathrm{Al}} - 1)\,\Theta(L_{\mathrm{Al}} + L_{\mathrm{Ni}} + L'_{\mathrm{Ni}} - i) \\
&\qquad + \left|\Delta^{\mathrm{singlet}}_{\mathrm{S,Ni}}\right|\hat{\tau}_2\,\Theta(i - L_{\mathrm{Al}} - 1)\,\Theta(L_{\mathrm{Al}} + L_{\mathrm{Ni}} + L'_{\mathrm{Ni}} - i) \\
&\qquad + \left|\Delta^{\mathrm{triplet}}_{\mathrm{S,Ni}}\right|\hat{\tau}_3\,\Theta(i - L_{\mathrm{Al}} - L_{\mathrm{Ni}} - 1)\,\Theta(L_{\mathrm{Al}} + L_{\mathrm{Ni}} + L'_{\mathrm{Ni}} - i) \\
&+ \left|\Delta^{\mathrm{singlet}}_{\mathrm{S,Ga}}\right|\hat{\tau}_2\,\Theta(i - L_{\mathrm{Al}} - L_{\mathrm{Ni}} - L'_{\mathrm{Ni}} - 1)\,\Theta(L_{\mathrm{Al}} + L_{\mathrm{Ni}} + L'_{\mathrm{Ni}} + L'_{\mathrm{Ga}} + L_{\mathrm{Ga}} - i) \\
&\qquad + \left|\Delta^{\mathrm{triplet}}_{\mathrm{S,Ga}}\right|\hat{\tau}_3\,\Theta(i - L_{\mathrm{Al}} - L_{\mathrm{Ni}} - L'_{\mathrm{Ni}} - 1)\,\Theta\left(L_{\mathrm{Al}} + L_{\mathrm{Ni}} + L'_{\mathrm{Ni}} + L'_{\mathrm{Ga}} - i\right)\Bigg] \\
&\times \Theta(j)\,\Theta(W - 1 - j)
\end{aligned}
\tag{4.22}
$$

and the *nearest-neighbor hoppings* ($\langle i, j\rangle$ indicates nearest-neighbor lattice sites) by

$$
\hat{\mathcal{H}}_{\mathrm{hop}}(\langle i, j\rangle) = -t\,\hat{\tau}_0, \tag{4.23}
$$

where

$$
\hat{\tau}_0 = \begin{bmatrix} 1 & 0 & 0 & 0 \\ 0 & 1 & 0 & 0 \\ 0 & 0 & -1 & 0 \\ 0 & 0 & 0 & -1 \end{bmatrix},\ \hat{\tau}_1 = \begin{bmatrix} 1 & 0 & 0 & 0 \\ 0 & -1 & 0 & 0 \\ 0 & 0 & 1 & 0 \\ 0 & 0 & 0 & -1 \end{bmatrix},\ \hat{\tau}_2 = \begin{bmatrix} 0 & 0 & 1 & 0 \\ 0 & 0 & 0 & 1 \\ 1 & 0 & 0 & 0 \\ 0 & 1 & 0 & 0 \end{bmatrix},\ \text{and } \hat{\tau}_3 = \begin{bmatrix} 0 & 0 & 0 & 1 \\ 0 & 0 & 1 & 0 \\ 0 & 1 & 0 & 0 \\ 1 & 0 & 0 & 0 \end{bmatrix}. \tag{4.24}
$$

Thereby, the hopping parameter can be written as $t = \hbar^2/(2ma^2)$, noting that it is most convenient to use such units that $a = t = 1$ [a.u.], at least as long as one is rather interested in qualitative than quantitative analyses.

Besides the discrete single-particle energies $\varepsilon(i, j) = (4t - \mu)\hat{\tau}_0$, measured with respect to the chemical potential μ (which is taken to be the same everywhere), and nickel's ferromagnetic exchange gap $\Delta_{\mathrm{XC,Ni}}$ (the magnetization vector points again along $\hat{z}$), we need to account for the junction regions' different superconducting pairing potentials. Within the OTBK approach, all superconducting pairing potentials are approximated by their steplike *singlet* (*s*-wave) form (see Appendix A). However, analyzing our numerical simulations and comparing them against the experimental results in the next section will demonstrate that pure singlet pairings alone are not yet sufficient to reproduce all observed features. Instead, some of the samples reveal clear indications of additionally present *triplet pairings close to the Ni/Ga interface*. To cover both singlet and triplet superconducting correlations, the Bogoljubov-de Gennes Hamiltonian contains not only singlet superconducting pairing potentials, coupling spin-up and spin-down electrons to form *spin-singlet* Cooper pairs, but also triplet pairing potentials that facilitate *spin-triplet* Cooper pairs consisting of two spin-up (or spin-down) electrons. The corresponding *singlet* superconducting gaps are abbreviated by $\left|\Delta^{\mathrm{singlet}}_{\mathrm{S,Al}}\right|$, $\left|\Delta^{\mathrm{singlet}}_{\mathrm{S,Ni}}\right|$, and $\left|\Delta^{\mathrm{singlet}}_{\mathrm{S,Ga}}\right|$, while the *interfacial triplet* gaps are $\left|\Delta^{\mathrm{triplet}}_{\mathrm{S,Ni}}\right|$ and $\left|\Delta^{\mathrm{triplet}}_{\mathrm{S,Ga}}\right|$. To assure that triplet correlations arise indeed solely in the vicinity of the Ni/Ga interface, their pairing potential terms are *nonzero only* in $L'_{\mathrm{Ni}} = L_{\mathrm{Ni}}/5$ and $L'_{\mathrm{Ga}} = L_{\mathrm{Ga}}/5$ of nickel's and gallium's lattice sites around the interface, as illustrated in Fig. 4.11(b). Limiting the triplet correlations to this particular range is actually not motivated by the experiment, which could not satisfactorily classify the physics at the Ni/Ga interface so far, but rather an adequate *ad hoc* assumption to recover the most general trends visible in the recorded conductance data. To proceed, we implement the tight-binding on-site Bogoljubov-de Gennes and hopping Hamiltonians [see Eqs. (4.22) and (4.23)] in KWANT and use KWANT's kernel polynomial method (KPM) to extract the junction's (spatially integrated) *zero-temperature tunneling DOS*, which is essentially probed by the conductance measurements and must therefore reveal closely related physical features.

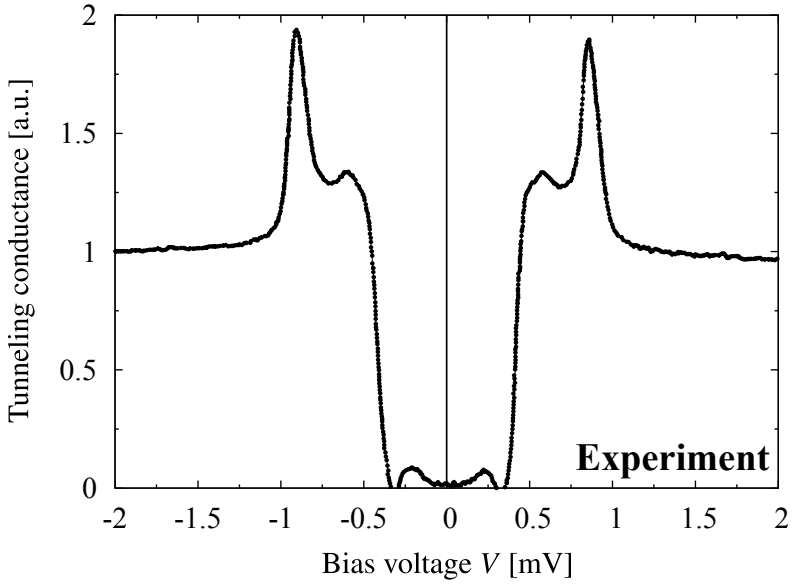


Fig. 4.12: *Measured* tunneling conductance-voltage characteristics of one specific Al (4 nm)/Al_2O_3 (0.4 nm)/Ni (3 nm)/Ga (60 nm) junction at 0.58 K; the experimental data is a courtesy of Jagadeesh Moodera (MIT).

4.3.2 Discussion of results and comparison with experiment

Regarding the experimental studies carried out in Jagadeesh Moodera's research group at MIT, Fig. 4.12 summarizes one of the first tunneling conductance-voltage measurements' results that were obtained for a Al (4 nm)/Al_2O_3 (0.4 nm)/Ni (3 nm)/Ga (60 nm) Josephson junction held at 0.58 K. The observed conductance features deviate a lot from those predicted for simple S/F/S junctions (recall Sec. 4.2). Probably most puzzling is the disappearance of the subharmonic conductance gap structure we identified as one of the most distinct fingerprints of Josephson junctions' conductance-voltage characteristics. Instead of the discrete set of conductance maxima at all integer submultiples of the doubled superconducting energy gap, only three well-defined *local* conductance maxima ("peaks") become now evident (restricting ourselves to positive bias voltages). To unravel which of the Al/Ni/Ga junctions' ingredients might cause such strong modifications in their conductance spectra, we come back to our theoretical model and compare some representative numerical calculations with the experimental data.

4.3.2.1 Ferromagnetic exchange effects and limits of OTBK modeling

The perhaps greatest strength of the OTBK approach is that we can reliably control all single junction parameters and deduce their individual impact on the system's conductance properties. This is not necessarily always the case with the fully numerical tight-binding simulations in KWANT. As a consequence, it seems more common to initially focus on the OTBK model and use KWANT for refining our predictions afterwards.

Figures 4.13(A)–(C) illustrate the normalized tunneling conductance of *symmetric* Ga/N/Ni/NiGa/Ga Josephson junctions at 0.5 K, extracted from the OTBK model outlined above and in Appendix A. Note the fundamental difference to the experimentally investigated samples, as we are now concerned with junctions involving two *similar* massive gallium electrodes. The thickness of the intermediate nickel layer gets gradually increased from $d_{\mathrm{Ni}} = 0.5$ nm to $d_{\mathrm{Ni}} = 2.0$ nm, and finally to $d_{\mathrm{Ni}} = 5.0$ nm, while we suppose the nickel spin polarization $P_{\mathrm{Ni}} = (\Delta_{\mathrm{XC,Ni}}/2)/\mu = 1\,\%$; recall that Meservey-Tedrow spectroscopy

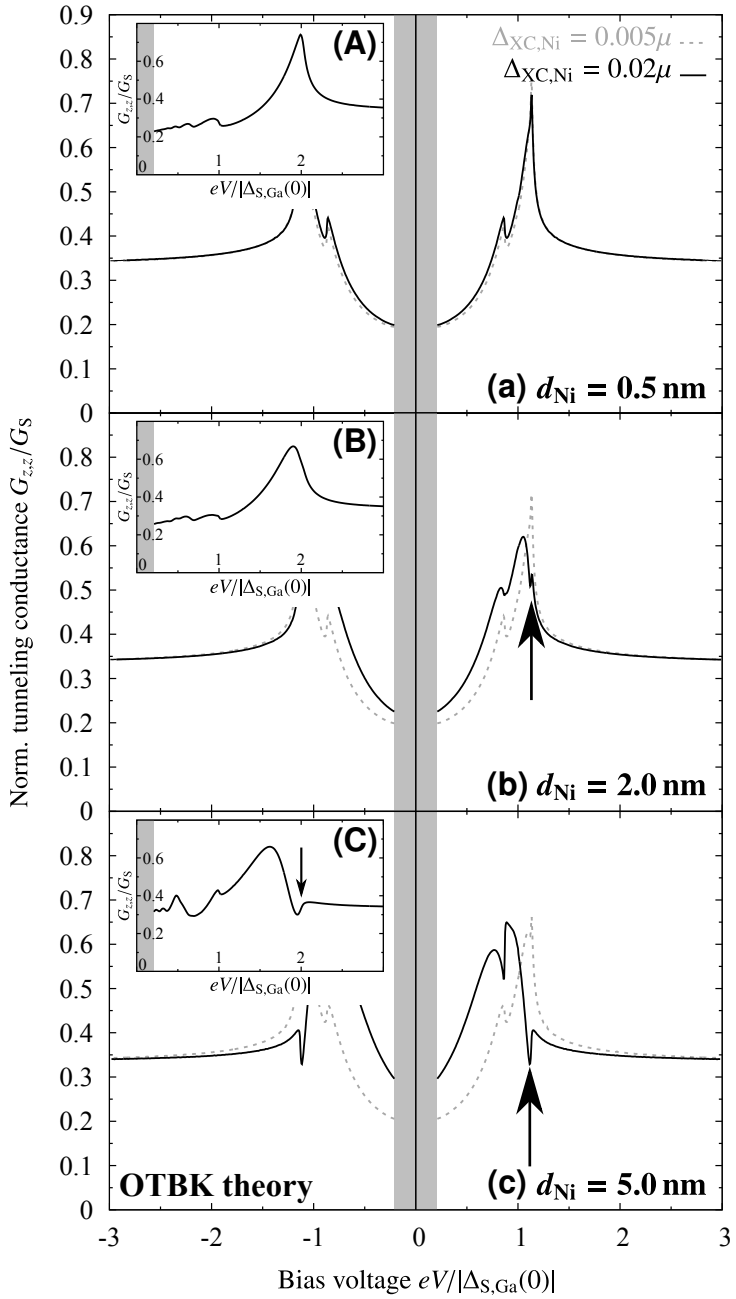


Fig. 4.13: (a)–(c) *Calculated* dependence of Al/N/Ni/NiGa/Ga Josephson junctions' tunneling conductance $G_{z,z}$ [normalized to Sharvin's conductance $G_S = (\mathcal{A}e^2k_F^2)/(2\pi h)$] on the applied bias voltage V [the associated electron energy eV is given in multiples of gallium's zero-temperature gap $|\Delta_{S,Ga}(0)|$] for two indicated nickel exchange splittings $\Delta_{XC,Ni}$ (given in multiples of the chemical potential μ) and nickel thicknesses **(a)** $d_{Ni} = 0.5$ nm, **(b)** $d_{Ni} = 2.0$ nm, and **(c)** $d_{Ni} = 5.0$ nm at 0.5 K. The tunneling barrier strengths are $\tilde{Z} = Z = 2$ and the NiGa alloy is 0.6 nm thick. **(A)–(C)** Same as in **(a)–(c)**, but for *symmetric* Ga/N/Ni/NiGa/Ga junctions. Black arrows highlight *anomalous conductance variations*, i.e., increasing nickel thicknesses turn conductance maxima into minima. At small voltages, the tunneling current becomes tiny and calculating its values accurately would be numerically demanding; we shaded this region and do not present data there.

on the experimental samples concluded that nickel's spin polarization lies below one percent. The tunneling barriers separating the normal-state region (N) from the neighboring gallium and nickel layers are quantified by $\tilde{Z} = (2m\tilde{V}_\mathrm{I}\tilde{d}_\mathrm{I})/(\hbar^2 k_\mathrm{F}) = 2 = (2mV_\mathrm{I}d_\mathrm{I})/(\hbar^2 k_\mathrm{F}) = Z$, corresponding, e.g., to $\tilde{d}_\mathrm{I} = d_\mathrm{I} \approx 0.80\,\mathrm{nm}$ thick barriers with a height of $\tilde{V}_\mathrm{I} = V_\mathrm{I} = 0.75\,\mathrm{eV}$ (assuming $m \approx m_\mathrm{e}$ and $k_\mathrm{F} = \sqrt{2m\mu}/\hbar \approx 8 \times 10^7\,\mathrm{cm}^{-1}$ as a typical metal Fermi wave vector [182]). All remaining parameters used for our calculations are listed in Tab. 4.1.

As long as the nickel region remains thin enough, we indeed recover Josephson junctions' unique subharmonic conductance gap structure, supporting pronounced conductance maxima at all bias voltages that fulfill $V \approx 2|\Delta_{\mathrm{S,Ga}}(0)|/(ne)$ with positive integers n. The physical origin of the subharmonic gap structure is precisely the same we explained within the semiconductorlike picture in Sec. 4.1. Multiple Andreev reflections at the N/Ga and N/Ni interfaces eventually open additional channels through which single electrons tunnel from one gallium electrode into the second one and generate tunneling currents. Only at certain voltages, i.e., at $V \approx 2|\Delta_{\mathrm{S,Ga}}(0)|/(ne)$, these tunnelings involve high-DOS states and become likely enough to maintain *sizable* tunneling currents, visible in terms of local maxima in the conductance-voltage relation. Nevertheless, we need to account for another peculiarity of the Andreev reflections. Each electron (hole) approaching the N/Ni interface and being Andreev reflected picks up the phase $\delta\phi = (\Delta_{\mathrm{XC,Ni}}d_\mathrm{Ni})/(\hbar v_{\mathrm{F,Ni}})$ [222], where $v_{\mathrm{F,Ni}}$ represents nickel's Fermi velocity. Since Andreev reflections are strongly phase sensitive, additional phases of incident electrons (holes) can notably change the probabilities to really undergo Andreev reflections. In the most extreme scenario, it might even be possible that Andreev reflections become completely forbidden at $V \approx 2|\Delta_{\mathrm{S,Ga}}(0)|/(ne)$ and happen then primarily at voltages far below or above these values. But this means that the conductance-enhancing electron tunnelings at $V \approx 2|\Delta_{\mathrm{S,Ga}}(0)|/(ne)$ are no longer possible and the conductance maxima may be converted into conductance minima, simultaneously raising new maxima at other voltages. The full effect is predominantly controllable by means of $\delta\phi$ and thus by altering either $\Delta_{\mathrm{XC,Ni}}$ or d_Ni. In our calculations, we observe such clear modifications when increasing d_Ni from $d_\mathrm{Ni} = 2.0\,\mathrm{nm}$ to $d_\mathrm{Ni} = 5.0$ (for constant $\Delta_{\mathrm{XC,Ni}}$). The initially arising conductance maximum at $eV \approx 2|\Delta_{\mathrm{S,Ga}}(0)|$ really turns into a conductance minimum, just because the additionally accumulated phase heavily suppresses multiple Andreev reflections there.

To come back to the experimentally studied case, we replace the left gallium electrode by aluminum and repeat the same calculations again, distinguishing between the two nickel spin polarizations $P_\mathrm{Ni} = (\Delta_{\mathrm{XC,Ni}}/2)/\mu = 0.25\,\%$ and $P_\mathrm{Ni} = 1\,\%$; see Figs. 4.13(a)–(c). It is extremely important to recognize that gallium's superconducting gap is more than seven times as large as the one of aluminum. Already Rowell and Feldman [201] deduced that such a dramatic imbalance between *dissimilar* electrodes' superconducting gaps strongly alters the subharmonic gap structure and splits the series of conductance maxima into well-distinct subseries. In our case, we can expect local conductance peaks at $eV \approx 2|\Delta_{\mathrm{S,Al}}(0)|/(2n)$ with integer n, $eV \approx |\Delta_{\mathrm{S,Ga}}(0)|$, and $eV \approx |\Delta_{\mathrm{S,Al}}(0)| + |\Delta_{\mathrm{S,Ga}}(0)|$, at least as long as the ferromagnetic exchange in nickel remains negligibly small. The latter two peaks can be clearly identified in Fig. 4.13(a). The peak subseries originating from aluminum, however, cannot be properly resolved since the tunneling current becomes extremely tiny at small bias voltages and calculating its values with the required accuracy would be rather demanding. For that reason, we shaded this area in the plots and do not present numerical data there. The interfacial NiGa alloy has no visible influence on the outcomes as it is assumed to be ultrathin and its superconducting gap is again much smaller than that of the neighboring gallium electrode. Increasing the thickness of nickel or its spin polarization (exchange splitting) acts similarly as before. The additional phases the Andreev-reflected electrons (holes) pick up start to play a major role and significantly change the positions of the conductance peaks. Large enough phases (at large enough nickel thicknesses or spin polarizations) flatten the conductance peaks and can even split them further, as one asserts when inspecting Figs. 4.13(b) and 4.13(c).

Comparing our OTBK calculations in Figs. 4.13(a)–(c) to the experimental results (see Fig. 4.12), we can basically confirm that the spin polarization extracted from Meservey-Tedrow spectroscopy (less than one percent) is a reasonable value. The nickel thickness of the investigated sample, $d_{\mathrm{Ni}} = 3\,\mathrm{nm}$, lies quite close to the theoretical case presented in Fig. 4.13(b), where we considered $d_{\mathrm{Ni}} = 2\,\mathrm{nm}$. Regarding the qualitative conductance-voltage dependence, the experimental data matches then quite well to the theoretical curve indicating $P_{\mathrm{Ni}} = 1\,\%$ except that the additional peak splitting at $eV \approx |\Delta_{\mathrm{S,Ga}}(0)|$ could not be experimentally observed, suggesting that nickel's spin polarization in the sample must be slightly less than one percent as proposed from the Meservey-Tedrow analysis. Nevertheless, we cannot quantitatively fit our model to the experimental data since the junction parameters (like the superconducting gaps) given in Tab. 4.1 were only determined for some samples and are not precisely known for all of them. The experimental output in Fig. 4.12 indeed reveals (slightly) different superconducting gaps than those we substituted into our calculations. The reduction to one-dimensional junctions is another issue our theory might face. Earlier studies [199] demonstrated that the tunneling current flow through real three-dimensional samples is not homogeneous (e.g., due to inhomogeneities in the oxide barriers) and rather carried by different transverse channels. Each channel could be subject to distinct interfacial scattering (barrier) parameters, additionally shifting the conductance peaks and explaining deviations between theory and experiment. Anyhow, extending our model to three dimensions and accounting for different transverse momentum-dependent barrier parameters is feasible, but goes far beyond the scope of our work. For us, it is sufficient to understand that Al/Ni/Ga junctions' peculiar tunneling conductance-voltage characteristics are predominantly governed by the interplay between the strongly differing superconducting gaps of the aluminum and gallium electrodes on the one, and nickel's ferromagnetic exchange on the other hand.

Most surprisingly, the voltages at which conductance maxima arise are not visibly influenced by nickel's superconducting gap, although we claimed above that proximity effects turn nickel superconducting and an unprecedented competition with its intrinsic ferromagnetism might occur. The main reason for that illustrates another great limitation of the OTBK modeling. Since this approach regards the aluminum and gallium regions as massive, infinitely extended, electrodes (recall that we assumed quasiparticles inside the superconducting electrodes to be distributed according to equilibrium Fermi-Dirac distributions, which is only justified in that case), the superconducting gap of the much thinner nickel region, simultaneously being several times tinier than gallium's gap, cannot have any substantial impact on the junction's conductance peak positions and becomes not resolvable in our calculations (see Fig. 4.13). Even enhancing nickel's superconducting gap *within a reasonable range* would not lead to significant changes of the conductance data. At the same time, we assert several precursors of nickel's ferromagnetic exchange splitting, which causes the additional conductance peak splittings observed when increasing the nickel layer thickness. Despite the nickel layer's negligible thickness (compared to gallium), its ferromagnetic exchange still matters since the induced exchange gap [e.g., $\Delta_{\mathrm{XC,Ni}} = 0.02\mu$; typically, $\mu \approx 10^3|\Delta_{\mathrm{S,Ni}}(0)|$] exceeds the superconducting gap by more than one order of magnitude. The experimental results depicted in Fig. 4.12 were recorded for a sample in which the 60 nm thick gallium region indeed remarkably overcomes the nickel layer's thickness of just 3 nm and can hence be treated to some extent like a semi-infinite gallium electrode. This clarifies the good agreement between the OTBK modeling's predictions and the experimental outcomes there. Note that, in contrast to our modeling within the OTBK approach, aluminum is also rather thin (4 nm), but this does not bother us owing to aluminum's tiny superconducting gap (when compared to gallium). Nevertheless, as soon as the gallium electrode becomes much thinner and the nickel layer gains more importance, the OTBK modeling may face serious trouble and we can no longer compare the theoretical calculations with the experimental output.

The large deficits of the OTBK description become immediately clear when having a closer look at the conductance data of Al (4 nm)/Al_2O_3 (0.4 nm)/EuS (1.4 nm)/Ni (0.8 nm)/Ga (20 nm) junctions measured

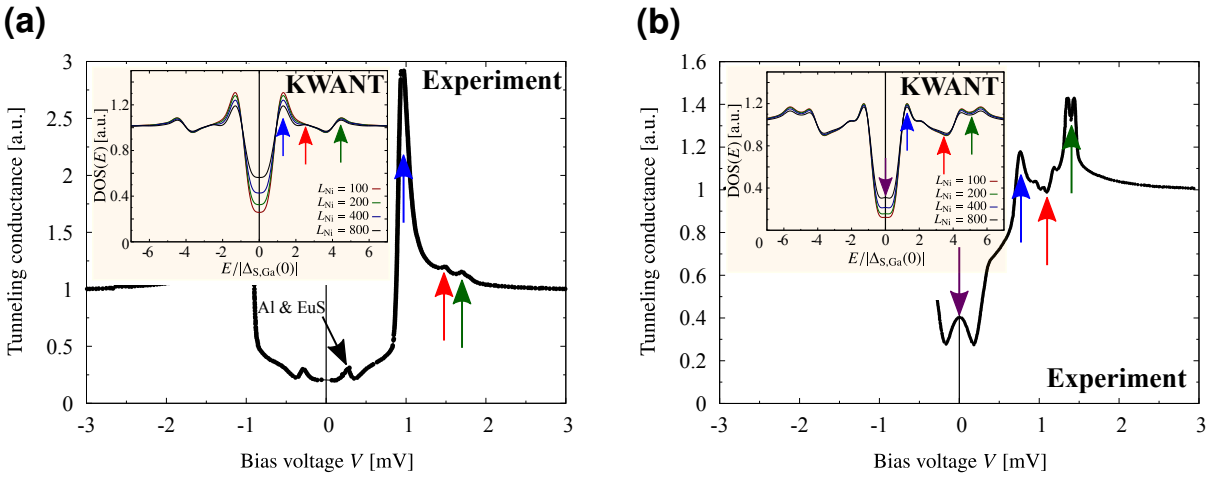


Fig. 4.14: (a) *Measured* tunneling conductance-voltage characteristics of one specific Al (4 nm)/Al_2O_3 (0.4 nm)/EuS (1.4 nm)/Ni (0.8 nm)/Ga (20 nm) junction at 1.07 K. Inset: *Calculated* zero-temperature tunneling DOS as a function of particle energy E and for different indicated thicknesses L_{Ni} of *weakly* ferromagnetic nickel; $L_{Al}/L_{Ga} = 200/1000 = (4\,nm)/(20\,nm)$ is kept constant. Colored arrows highlight experimentally observed and theoretically reproducible conductance maxima. The conductance peak detected at $V \approx 0.36$ mV in the experiment stems from Al and the EuS barrier; the latter is not captured by our theoretical simulations. **(b)** *Measured* tunneling conductance-voltage characteristics of one specific Al (4 nm)/Al_2O_3 (0.4 nm)/Ni (1.6 nm)/Ga (30 nm) junction at 1.2 K. Inset: *Calculated* zero-temperature tunneling DOS assuming *strong* triplet pairing close to the Ni/Ga interface and for different indicated thicknesses L_{Ni} of *weakly* ferromagnetic nickel; $L_{Al}/L_{Ga} = 200/2000 = (4\,nm)/(40\,nm)$ is kept constant. Colored arrows highlight experimentally observed and theoretically reproducible conductance maxima. The experimental data is a courtesy of Jagadeesh Moodera (MIT).

at 1.07 K; see Fig. 4.14(a). The junction's gallium electrode is now much thinner than before and can no longer be treated as a semi-infinite region. Instead, we expect that we shall really see the unique interplay of *all* superconducting energy gaps (including, i.e., also nickel's gap) and ferromagnetic exchange phenomena, which strongly modifies the tunneling conductance-voltage characteristics when compared to samples with much thicker gallium electrodes. The conductance peak close to zero bias, essentially coming from aluminum's superconducting gap, remains mostly unaffected though the additionally present ferromagnetic-insulator EuS barrier might slightly shift its position. The other conductance peaks at larger bias (limiting ourselves to positive voltages only), however, are subject to much more dramatic changes (compare Fig. 4.12 to Fig. 4.14), including a shift to larger voltages, interchanging intensities (the initially suppressed peak turns into the dominant one), and even the formation of additional "*conductance shoulders*" (weakly pronounced local conductance maxima).

More realistic simulations of finite-size Al/Ni/Ga junctions can be performed within KWANT, which allows us to easily vary the gallium electrode's thickness by limiting the number of included lattice sites and captures all kinds of finite-size effects. Along the transverse direction, we consider $W = 500$ lattice sites. Although changes of W do not significantly impact the outcomes, it is reasonable to use rather large numbers to minimize unphysical numerical fluctuations in the generated data. To demonstrate that already *weakly* ferromagnetic nickel raises most of the puzzling physics, we choose an extremely small spin polarization of less than 0.1 % (recall that we deduced values of about one percent from Meservey-Tedrow spectroscopy). As outlined earlier, we compute the (spatially integrated) tunneling DOS, which gets probed by the conductance measurements and resembles the same features. From the microscopic viewpoint, the tunneling conductance's behavior is mostly governed by multiple Andreev reflections (recall the semiconductorlike picture in Sec. 4.1), which lead to the formation of *Andreev bound states* [179,

227] and locally enhance the tunneling DOS. Electrons can then tunnel from one electrode into the second one via these states and drive a notable tunneling current. Therefore, the tunneling DOS and the measured tunneling conductance are intimately related, although one needs to be aware that the tunneling DOS is evaluated at zero temperature and might not properly describe all temperature effects. Particularly in magnetic junctions, as it is the case with our nickel layer, the Andreev states can additionally split into spin-resolved branches and open additional tunneling current channels, resulting in a conductance peak splitting as we will see in the following paragraph.

At the moment, we solely include *singlet* superconducting gaps into the calculation and substitute the values deduced from some samples (see Tab. 4.1). The numerical results are shown in the inset of Fig. 4.14(a). Our calculations cannot reproduce the conductance peak close to zero bias voltage since this peak stems from aluminum and the oxide/EuS barrier, and the latter is not part of our implementation at all. Nevertheless, we indeed identify a clearly magnified DOS peak at $E \approx |\Delta_{\mathrm{S,Ga}}(0)|$, which gets transferred into the conductance data in terms of the dominant conductance peak, as well as another damped DOS peak at $E \approx 4|\Delta_{\mathrm{S,Ga}}(0)|$, corresponding to one of the experimentally deflected "conductance shoulders". Note that the peak positions predicted by our calculations can deviate a lot from the experiment because we use a strongly simplified toy model and do not know all parameters of the experimental samples. We are thus most interested in understanding the *qualitative behavior* and do not want to fit the experimental conductance. Both peaks appear likewise for all regarded nickel thicknesses and originate hence mostly from aluminum and gallium. More interestingly, the experimentally taken conductance curve resembles another "conductance shoulder" in between. Our calculations suggest that this "shoulder" originates from nickel's ferromagnetic exchange, which splits the dominant DOS peak into one flattened peak and the additional "shoulder" as soon as nickel's thickness becomes large enough (owing to the extremely small spin polarization of less than 0.1 %; at larger spin polarization, thinner nickel layers would suffice to cause the same effect). We checked that the additional "DOS shoulder" would immediately disappear when nickel is *nonmagnetic*, i.e., when setting its spin polarization to zero. Consequently, the splitting of conductance peaks into "conductance shoulders" serves as a clear indication of ferromagnetism in nickel. As a crosscheck, we also assured that significantly increasing the gallium electrode's thickness damps the "conductance shoulders" and basically recovers the previous situation described by the OTBK model.

4.3.2.2 Signatures of interfacial triplet pairing

Although simply reducing the thickness of the gallium electrode already leads to highly nontrivial variations of the conductance spectra, an even more intriguing competition between superconductivity and ferromagnetism inside the nickel layer starts to occur when further increasing the nickel-gallium thickness ratio, i.e., when nickel gains even more impact to determine the junction characteristics. The superconducting and ferromagnetic phases are actually antagonistic and cannot efficiently coexist in one system – at least for singlet superconducting pairing, which favors spin-singlet Cooper pairs composed of two electrons with *opposite* spins, whereas ferromagnetism tends to align all electron spins *parallel*. *Triplet* Cooper pairs, however, are much more robust against ferromagnetic exchange and might thus play a major role in Ni/Ga (Ni/Bi) bilayers, probably causing more unprecedented modifications in the tunneling conductance.

The measured tunneling conductance of Al (4 nm)/Al_2O_3 (0.4 nm)/Ni (1.6 nm)/Ga (30 nm) junctions held at 1.2 K,[4] presented in Fig. 4.14(b), indeed reveals a much more intricate conductance-voltage relation. The previously identified, well-defined, conductance peaks split into different peak subseries. Since

[4]This junction's nickel-gallium thickness ratio of roughly 0.053 is somewhat larger than that of the previously studied Al (4 nm)/Al_2O_3 (0.4 nm)/EuS (1.4 nm)/Ni (0.8 nm)/Ga (20 nm) junction (about 0.04). However, it must be noted that also the ferromagnetic EuS barrier got removed, which might have some additional impact.

the ferromagnetic EuS barrier was removed, all arising peak splittings are really triggered by nickel. Particularly rewarding is now the aluminum peak close to zero bias which is likewise divided into one not clearly resolvable peak at slightly larger bias and a second one nearly at zero voltage. The latter merges together with its negative bias counterpart and raises a pronounced *zero-bias conductance peak* – microscopically, this peak might be an indication of the emergent *zero-energy* Andreev bound states. All peak splittings and even first precursors of zero-bias anomalies are qualitatively reproducible within our KWANT DOS simulations when putting nonzero *triplet* superconducting gaps in the vicinity of the Ni/Ga interface (i.e., in 1/5 of nickel's and gallium's lattice sites around the interface); see the inset of Fig. 4.14(b) for the numerical results. To see clear effects, the triplet gaps' amplitudes are nearly *four* times as large as their singlet values. Nickel's spin polarization remains tiny (less than 0.1 %) to verify that even weak ferromagnetic exchange and strong interfacial triplet pairings are enough to recover the experimentally recorded features. Larger spin polarizations and weaker triplet pairings might, nevertheless, cause very similar effects. Moreover, we shall note that we rely on a simple toy model, which only accounts for nonzero triplet gaps, but does not specify the triplet pairing potentials' *orbital* symmetries. This is completely sufficient to deduce reliable qualitative trends, which we aim at. The exaggerated triplet gaps and rather large nickel thicknesses (required as nickel's spin polarization is tiny) are responsible for the more significant peak splittings in the theoretical calculations when compared to the experiment.

The reality might of course be much more subtle. For instance, it seems also possible that the proximitized nickel layer induces ferromagnetic exchange in the gallium electrode (at least close to the interface), which could magnify the resulting phenomena and even trigger more peak splittings. We convinced ourselves that ferromagnetic proximity effects *alone* indeed raise the observed zero-bias conductance peak, but do not suffice to replicate all the arising peak splittings. From that, we might conclude that the experimental measurement detects both – interfacial triplet pairings *and* ferromagnetic proximity effects – at the same time. Similarly, we checked that triplet superconducting pairings in the *bulk* nickel and gallium regions (i.e., *not* only in the vicinity of the interface) are likewise not able to explain the experimental outcomes. In that case, and contrary to the experimental observations, the zero-bias conductance peak would transform into a dip.

To provide another unambiguous experimental confirmation that we are really concerned with interface effects, the measurement was repeated reversing the order of the nickel and gallium layers; all other material parameters, i.e., also their thicknesses, were not modified. Since the junction's qualitative conductance spectrum did not change at all, the peculiar physics must arise right at the Ni/Ga interface and is therefore independent of the regions' order. Furthermore, we already claimed above that singlet superconductivity and ferromagnetism are strongly antagonistic. Applying a sufficiently large external magnetic field to the sample must dramatically suppress its superconducting properties, especially all superconducting gaps that determine the conductance peaks' positions. Anyhow, measurements carried out on Al (4 nm)/Al_2O_3 (0.4 nm)/EuS (1.2 nm)/Ni (1.6 nm)/Ga (30 nm)/Al_2O_3 (12 nm) junctions at 1 K revealed that even a notable increase of the external magnetic field's strength does not impact the conductance peaks. The only reasonable explanation is that most of the emergent physics is not controlled by singlet, but rather by triplet gaps that are much less sensitive to the external magnetic field. Although the experimental data could not yet satisfactorily unravel the specific physics arising at Ni/Ga bilayer's interfaces, all our previous arguments basically indicate that the observed conductance anomalies serve as strong signatures of interfacial triplet pairings. Since these bilayers can be grown with high quality and the strength of their triplet pairings can apparently be controlled by the nickel-gallium thickness ratio, such systems might become extremely auspicious candidates to tailor spin-triplet Cooper pairs. Further experimental works to thoroughly characterize the triplet pairings' properties, inspired and supported by our theoretical simulations, are of course indispensable and partly already on their way.

4.4 Short summary

In summary, we extended the initially for ballistic metal/superconductor contacts established BTK description to understand biased S/F/S Josephson junctions' complex transport characteristics. These systems' ultrathin *magnetic* link regions are actually responsible for most of the puzzling physics that arises. Generally speaking, electrons (holes), whose energies lie well inside the superconductors' energy gaps, must always be reflected back into the metal whenever approaching one of the F/S interfaces. The electrons (holes) simply cannot leave the metal because they are not able to find available quasiparticle states in the superconductors to tunnel into. Starting from an idealized *semiconductorlike tunneling picture*, we demonstrated that the resulting multiple reflections at the interfaces – special attention must again be paid to the distinct *(multiple) Andreev reflections* – repeat several times until the reflected electrons (holes) gained enough energy to be transmitted into free quasiparticle states and drive a sizable tunneling current. Such multiple Andreev reflections happen most likely at all bias voltages equal integer submultiples of the doubled superconducting energy gap and explain thus not only biased Josephson currents' *nonzero excess current*, but simultaneously also their extraordinary *subharmonic conductance gap structure*, raising local conductance maxima precisely at the same voltages.

Working out a reliable theoretical description of multiple (Andreev) reflections is a slightly challenging task, as those typically result in *highly nonequilibrium charge carrier distributions* inside the metallic region. Nevertheless, these distributions count to the most fundamental ingredients we need to extract to evaluate the tunneling current flow and thereby also the junctions' tunneling conductance. One of the most powerful analytical approaches to capture multiple reflections is the OTBK model, essentially generalizing the BTK theory to Josephson junctions and allowing for self-consistently determined electron distributions inside the metal. We adapted the OTBK formalism to the case of *magnetic* S/F/S junctions and recapitulated all main points in the derivation step by step. After we had briefly analyzed some generic features of the self-consistently calculated distribution functions for realistic junction configurations, we proceeded to compute the associated tunneling current flows and tunneling conductances. Our results confirmed not only the excess current's and subharmonic conductance gap structure's proposed qualitative trends, but provided also further quantitative characterizations going beyond earlier works. Particularly relevant to experimental studies might be the universal scaling behavior of the excess (deficient) current, from which one can judge the samples' interface qualities.

The coexistence of the nominally antagonistic ferromagnetic and superconducting phases in Ni/Ga and Ni/Bi bilayers opens novel possibilities for experimental studies, e.g., for investigating the tunneling conductance of Al/Ni/Ga Josephson junctions. To interpret the unprecedented experimental outcomes obtained in Jagadeesh Moodera's research group at MIT, we employed two different theoretical frameworks and compared them against the experimental data. While an extended OTBK formulation sufficed to deduce some general properties of samples in which the gallium electrode is much thicker than all other junction layers, implementing the junctions in KWANT's tight-binding description was even able to cover the emergent finite-size phenomena. We showed that the interplay of superconductivity in all layers and nickel's ferromagnetic exchange can lead to highly nontrivial modifications of the tunneling conductance spectra, mostly controlled by the nickel-gallium thickness ratio. Appropriately tuning the latter lets even more puzzling conductance modulations arise, which we identified as strong signatures of triplet superconducting pairings present close to the Ni/Ga interface. The concrete physical origin of these triplet pairings in the experimental set-up remained unclear. One could speculate that the broken space-inversion symmetry at the interface of three-dimensional junctions gives rise to dominant interfacial SOC that flips some of the Cooper pair electrons' spins and converts hence spin-singlet into spin-triplet pairs. But this can still not answer the question why the Ni/Ga interface is somewhat special and the triplet pairings occur mostly there and not at the Al/Ni interface. To answer this question and

establish Ni/Ga (Ni/Bi) bilayers as auspicious triplet superconductors, following experimental works need to look more into interface-related effects. One possibility could be to focus on the actual Josephson current flow. If the triplet pairings are indeed facilitated by interfacial SOC, the measured (triplet) currents will reveal many of the surprising features we elaborate on in Chap. 6. Detecting some of them and fitting the measured current to the model presented in Chap. 6 would not only yield a clear evidence for interfacial SOC, but would also help to quantify its strength and draw researchers' attention towards Ni/Ga (Ni/Bi) bilayers.

Part *III*

DC Josephson effect in magnetic junctions

Chapter 5

AC and DC Josephson effects – a compact overview

The year 1962 shall have turned out to become another formative one for the superconducting transport community. At that time, 22-year-old Brian Josephson worked as a research assistant at the renowned University of Cambridge in the UK [228]. It was the rapid progress in improving experimental techniques that entailed not only more and more phenomenological insight into the fascinating physics of superconducting systems, but simultaneously also challenged theoreticians to come up with reasonable and consistent interpretations of the recorded data.

Already back in the 1930s, Holm and Meissner (the Meissner who is mostly known from his contributions to the discovery of the Meissner-Ochsenfeld effect; see Sec. 2.1.1) measured the electrical resistance at contacts between superconducting and normal-conducting electrodes [128], finding strong indications that supercurrents can even extend (over small distances) into initially nonsuperconducting components. This early work provided the first experimental evidence that the leakage of Cooper pairs from a superconductor into a metal (given that both components are brought in proximity to ensure good electrical contact) can indeed induce superconducting order into the latter via superconducting proximity effects. During the following years, more advanced methods to fabricate superconductor/metal boundaries have been developed and Meissner's son could eventually investigate the low-temperature current-voltage characteristics of two proximitized tin/cobalt wires [229]. The set-up is schematically depicted in Fig. 5.1. At sufficiently low temperatures, the massive tin wires become superconducting, while their thin normal-conducting cobalt coatings contact the individual wires and effectively act like thin separating tunneling barriers. Observing a fully dissipationless supercurrent flow (meaning finite electrical current without any voltage drop) through the system led to the same striking conclusion as before: Cooper pairs must tunnel from one superconducting tin wire into the second one. Thereby, the correlations between the Cooper pair-forming electrons must again persist even in the nonsuperconducting cobalt.

Particularly the latter experiment inspired Josephson to look deeper into contacts coupling two superconductors by means of nonsuperconducting regions and to generalize the established quantum-mechanical single-particle tunneling picture to paired (superconducting) electrons. In his honor, these contacts are referred to as *Josephson contacts* nowadays. Some important examples cover the weak coupling of superconductors either by point contact geometries or thin tunneling barriers, as well as the connection of two superconducting areas by nonsuperconducting (micro)bridges [illustrated in Figs. 5.2(a)–5.2(c)]. It was not a surprise that the leakage of Cooper pairs (and thus implicitly also the supercurrent flow) must be crucially connected to the order parameters of the superconducting condensates. Nevertheless, Josephson was the first theoretician who remembered that Ginzburg and Landau suggested that the order parameters are not only quantified by their respective amplitudes, but additionally by a well-defined superconducting phase (see Sec. 2.1.2). Already the Ginzburg-Landau theory predicted that spatial variations of the superconducting phase, realized, e.g., by means of two superconducting electrodes that differ in phase, act as driving forces for electrical currents [see Eq. (2.16)], even if no external bias voltage is applied to the system. Bringing everything on one common mathematical ground, Josephson concluded that

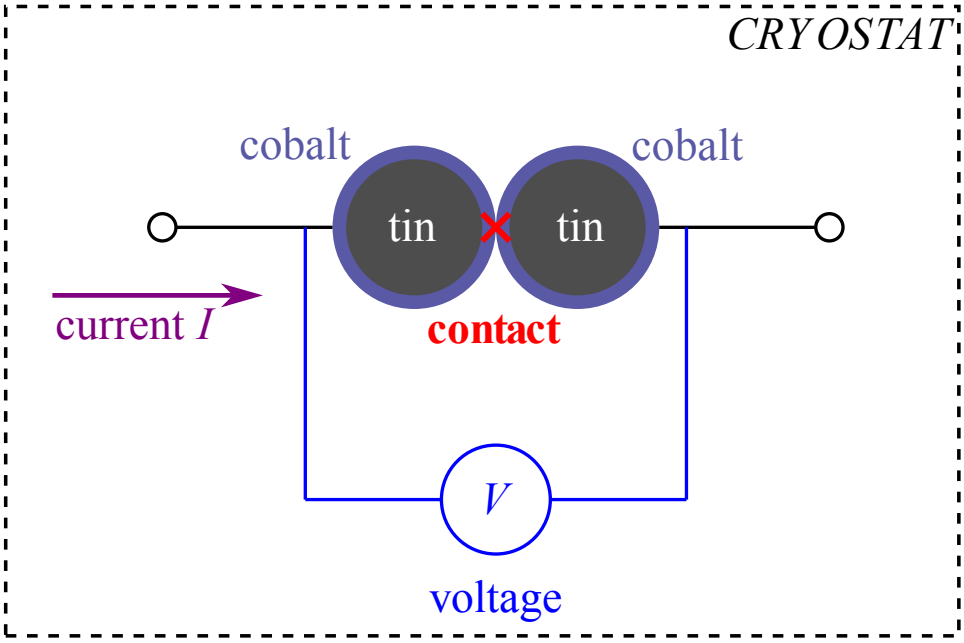


Fig. 5.1: Meissner's set-up to measure the current (I)-voltage (V) characteristics of two proximitized superconductor (tin)/metal (cobalt) wires at low temperatures. The flow of dissipationless supercurrents is a clear evidence for the tunneling of Cooper pairs through the contact, microscopically maintained by superconducting proximity effects.

Cooper pairs can indeed tunnel through barriers (like single electrons can), with a tunneling probability that characteristically modulates with the difference ϕ_S between the two superconductors' individual phases [93]. The publication of Josephson's results [93] stimulated an intense debate among well-known scientists around the world. The most famous physicist involved in the controversial discussions was John Bardeen, who received the Nobel Prize for his transistor proposals just a few years ago [133] and got recognized by the superconducting community for his contributions to the BCS theory [47, 48] (see Sec. 2.1.3). For the latter, he will have been decorated with a second Nobel Prize [230–232] later. Bardeen was strongly convinced that superconducting pairing cannot spread into normal-conducting or insulating tunneling barriers, and the flow of supercurrents through Josephson contacts shall therefore not become evident in experiments. Another argumentation of Pippard [228] relied on the fact that the tunneling probabilities of single particles through a quantum-mechanical barrier themselves are typically already extremely small. The probability for *simultaneous* tunneling of two correlated (Cooper pair) electrons must then scale proportionally to the square of these tiny single-particle tunneling probabilities, getting effectively zero and no supercurrent flow can be present. From a theoretical point of view, Gor'kov's Green's function approach [129] shed new light on resolving this puzzling issue, as it explicitly accounted for spatially varying superconducting order parameters (modeling proximity effects) and verified the possibility of really expecting finite Cooper pair tunneling (super)currents in upcoming experiments. Josephson always believed in his reasoning and did not resign – and he should be right. In the year after he published his theoretical results, Anderson and Rowell [233, 234] succeeded to experimentally detect a tunneling supercurrent that depends on ϕ_S precisely in the predicted characteristic way. After this unique experimental confirmation – in memory of Josephson's achievements [93, 127], the effect was termed *Josephson effect* –, Bardeen withdrew his refusal and Josephson was eventually awarded the Physics Nobel Prize in 1973 [235]. We just summarized the main milestones on the long way from Josephson's initial speculations to an overall acceptance of his predictions. A more comprehensive presentation, which also served as an inspiration for the previous paragraphs, can be found in Ref. [228].

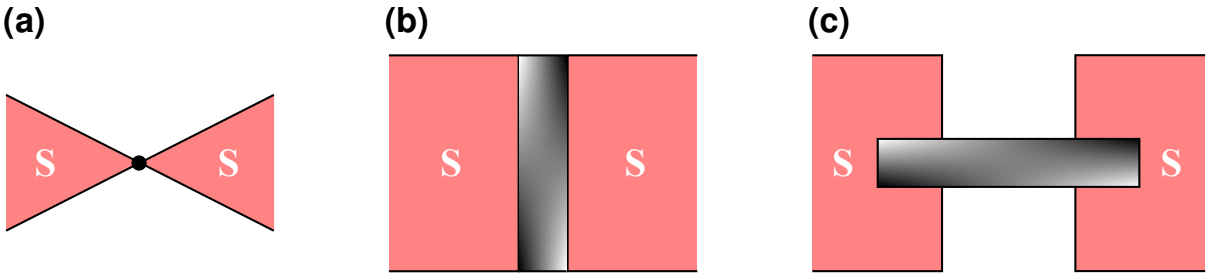


Fig. 5.2: Typical Josephson contacts: **(a)** superconducting constriction (point contact), **(b)** superconducting tunnel junction, and **(c)** microbridge-connected superconductors; S (red) indicates superconducting materials, while the black regions refer to nonsuperconducting tunneling barriers or microbridges.

In the following, we will rederive some of the fundamental formulas that Josephson obtained. We consider a *one-dimensional* superconducting tunnel junction, consisting of two superconducting regions that are phase-coherently coupled by a thin insulating barrier as sketched in Fig. 5.2(b). Both superconductors are exactly identical except that they may differ in the phase factors entering their respective superconducting condensate wave functions. A simple mathematical approach to deal with such junctions, based on elementary quantum mechanics, was developed by Feynman [236]. We recapitulate only the most essential points of Feynman's description.

As long as the two superconductors of the junction are *not coupled*, the superconducting electrons in both of them simply condense into individual coherent quantum states, which we call (at time t) $\psi_1(t)$ in the left and $\psi_2(t)$ in the right superconductor, accordingly. Both states need to fulfill the (time-dependent) condensate Schroedinger equations

$$\mathrm{i}\hbar\frac{\mathrm{d}\psi_i(t)}{\mathrm{d}t} = E_i\psi_i(t), \tag{5.1}$$

from which the associated energies of the superconducting condensates, E_i ($i = 1, 2$), can be determined.

Let us now assume that the two superconductors get weakly coupled by the thin insulating barrier, enabling the exchange of Cooper pairs between them and thus generating a net supercurrent flow. Generally speaking, the total wave function capturing all the superconducting electrons in the coupled system, $\Psi(t)$, can be written as a superposition of the two separate superconducting condensate wave functions,

$$\Psi(t) = \sum_{i=1}^{2} c_i(t)\psi_i(t), \tag{5.2}$$

with the time-dependent (and, in general, complex) coefficients $c_i(t)$. Substituting the ansatz for $\Psi(t)$ into the Schroedinger equation for the full (coupled) system,

$$\mathrm{i}\hbar\frac{\mathrm{d}\Psi(t)}{\mathrm{d}t} = \hat{\mathcal{H}}\Psi(t), \tag{5.3}$$

yields

$$\mathrm{i}\hbar\sum_{i=1}^{2}\left[\frac{\mathrm{d}c_i(t)}{\mathrm{d}t}\psi_i(t) + c_i(t)\frac{\mathrm{d}\psi_i(t)}{\mathrm{d}t}\right] = \sum_{i=1}^{2}\hat{\mathcal{H}}\left[c_i(t)\psi_i(t)\right]. \tag{5.4}$$

At this point, it must be noted that we introduced the Hamiltonian $\hat{\mathcal{H}}$ that describes the full system and hence also implicitly contains the information about Cooper pair exchange between the superconductors due to their coupling. Since the explicit form of $\hat{\mathcal{H}}$ is usually not known, it is more common to rewrite Eq. (5.4) such that only $\hat{\mathcal{H}}$'s matrix elements (which refer to expectation values of physical observables and could be extracted from experiments) need to be specified. In order to do this, we multiply Eq. (5.4)

by the complex conjugated condensate states of the uncoupled superconductors, $\psi_j^*(t)$ ($j = 1, 2$), from the left, and integrate over the system's total volume $\mathcal{V}$ to finally obtain

$$\mathrm{i}\hbar \int_{\mathcal{V}} \mathrm{d}\mathcal{V} \sum_{i=1}^{2} \psi_j^*(t) \frac{\mathrm{d}c_i(t)}{\mathrm{d}t} \psi_i(t) + \mathrm{i}\hbar \int_{\mathcal{V}} \mathrm{d}\mathcal{V} \sum_{i=1}^{2} \psi_j^*(t) c_i(t) \frac{\mathrm{d}\psi_i(t)}{\mathrm{d}t} = \int_{\mathcal{V}} \mathrm{d}\mathcal{V} \sum_{i=1}^{2} \psi_j^*(t) \hat{\mathcal{H}} \left[c_i(t) \psi_i(t) \right]. \tag{5.5}$$

Using Eq. (5.1) and the fact that the single-condensate states $\psi_i(t)$ form a complete orthonormal basis,

$$\int_{\mathcal{V}} \mathrm{d}\mathcal{V}\, \psi_j^*(t) \psi_i(t) = \delta_{i,j}, \tag{5.6}$$

where $\delta_{i,j}$ is the Kronecker delta, Eq. (5.5) reduces to

$$\mathrm{i}\hbar \frac{\mathrm{d}c_j(t)}{\mathrm{d}t} = \sum_{i=1}^{2} \left[\mathcal{H}_{j,i} - E_i \delta_{i,j} \right] c_i(t). \tag{5.7}$$

Thereby,

$$\mathcal{H}_{j,i} = \int_{\mathcal{V}} \mathrm{d}\mathcal{V}\, \psi_j^*(t) \hat{\mathcal{H}} \psi_i(t) \tag{5.8}$$

are the aforementioned matrix elements of $\hat{\mathcal{H}}$; their individual components are labeled by i and j.

In the simplest case, the *diagonal* matrix elements just resemble the ground-state energies of the two superconducting condensates, E_1 and E_2. However, an additional bias voltage $V(t)$ that is applied across the junction acts as an effective potential term in our quantum-mechanical description and eventually shifts the reference energy scale. If we define zero potential exactly in the center between the two superconducting regions, the condensates experience energy shifts of $[qV(t)]/2$ and $[-qV(t)]/2$, respectively, so that the individual condensate energies read then

$$\mathcal{H}_{1,1} = E_1 + \frac{qV(t)}{2} \tag{5.9}$$

in the left and

$$\mathcal{H}_{2,2} = E_2 - \frac{qV(t)}{2} \tag{5.10}$$

in the right superconductor. Since superconducting electrons always occur in Cooper pairs, q stands for an effective charge of $q = -2e$ (e is still the positive elementary charge).

The superconductors' coupling, which is responsible for the exchange of Cooper pairs, enters the *off-diagonal* matrix elements of $\hat{\mathcal{H}}$. For convenience, we suppose that the couplings between both superconductors are equal, formally represented by

$$\mathcal{H}_{1,2} = \mathcal{H}_{2,1} = -K, \tag{5.11}$$

with the coupling constant K.

Combining Eqs. (5.9), (5.10), and (5.11) with Eq. (5.7) yields two coupled equations, determining the still unknown coefficients $c_1(t)$ and $c_2(t)$,

$$\begin{cases} \mathrm{i}\hbar \dfrac{\mathrm{d}c_1(t)}{\mathrm{d}t} &= -eV(t)c_1(t) - Kc_2(t), \\ \mathrm{i}\hbar \dfrac{\mathrm{d}c_2(t)}{\mathrm{d}t} &= eV(t)c_2(t) - Kc_1(t); \end{cases} \tag{5.12}$$

Eq. (5.12) can be solved by means of the general ansatz

$$\begin{cases} c_1(t) &= \sqrt{n_1(t)}\, \mathrm{e}^{\mathrm{i}\phi_{\mathrm{S}_1}(t)}, \\ c_2(t) &= \sqrt{n_2(t)}\, \mathrm{e}^{\mathrm{i}\phi_{\mathrm{S}_2}(t)}, \end{cases} \tag{5.13}$$

where $n_{1\,(2)}(t)$ correspond to the densities of superconducting electrons in the two superconductors and $\phi_{\mathrm{S}_{1\,(2)}}(t)$ are the related superconducting phases. After substituting Eq. (5.13) into Eq. (5.12) and comparing the resulting equations' real and imaginary parts, we end up with

$$\frac{\mathrm{d}\phi_{\mathrm{S}_1}(t)}{\mathrm{d}t} = \frac{K}{\hbar}\sqrt{\frac{n_2(t)}{n_1(t)}}\cos\left[\phi_{\mathrm{S}}(t)\right] + \frac{eV(t)}{\hbar}, \tag{5.14}$$

$$\frac{\mathrm{d}\phi_{\mathrm{S}_2}(t)}{\mathrm{d}t} = \frac{K}{\hbar}\sqrt{\frac{n_1(t)}{n_2(t)}}\cos\left[\phi_{\mathrm{S}}(t)\right] - \frac{eV(t)}{\hbar}, \tag{5.15}$$

$$\frac{\mathrm{d}n_1(t)}{\mathrm{d}t} = \frac{2}{\hbar}K\sqrt{n_1(t)n_2(t)}\sin\left[\phi_{\mathrm{S}}(t)\right], \tag{5.16}$$

and lastly

$$\frac{\mathrm{d}n_2(t)}{\mathrm{d}t} = -\frac{2}{\hbar}K\sqrt{n_1(t)n_2(t)}\sin\left[\phi_{\mathrm{S}}(t)\right]; \tag{5.17}$$

$\phi_{\mathrm{S}}(t) := \phi_{\mathrm{S}_1}(t) - \phi_{\mathrm{S}_2}(t)$ measures the *phase difference* between the superconductors. From Eqs. (5.14)–(5.17), we can now extract how the superconductors' phases and their Cooper pair densities evolve with time.

Of particular interest is the change of the Cooper pair density in one of the superconductors. Since Cooper pairs can only be transferred from one into the other electrode [but *cannot* be destroyed; therefore, $\mathrm{d}[n_1(t) + n_2(t)]/\mathrm{d}t = 0$], changes of the Cooper pair density in one superconductor [say, e.g., according to $\mathrm{d}n_2(t)/\mathrm{d}t$ in the right superconductor; see Eq. (5.17) for the corresponding formula] immediately generate the associated current flow

$$I_{\mathrm{J}}(t) = -2e\frac{\mathrm{d}n_2(t)}{\mathrm{d}t} = I_0(t)\sin\left[\phi_{\mathrm{S}}(t)\right]. \tag{5.18}$$

As usual, this tunneling (super)current – known as the *Josephson current* I_{J} – is obtained multiplying the charge per Cooper pair ($q = -2e$) by the density of Cooper pairs being transferred through the insulating barrier. Equation (5.18), called the *first Josephson relation*, clearly reveals that the phase-coherent coupling, mathematically accounted for in Feynman's approach adding the coupling constant K by hand, indeed drives the tunneling supercurrent, just as predicted by Ginzburg and Landau many years before Josephson [see Sec. 2.1.2; especially Eq. (2.16)]. If both superconductors would not be coupled at all ($K = 0$), there would be neither any transfer of Cooper pairs through the barrier nor a spontaneous supercurrent flow. The critical current $I_0(t) = [4eK\sqrt{n_1(t)n_2(t)}]/\hbar$ is an important measure to classify the experimental quality of Josephson contacts since it determines the maximal supercurrent one can

drive through the system without having any distracting dissipation effects. Therefore, one typically aims at Josephson contacts maintaining large critical currents. The coupling between the superconductors is often thus weak that the critical current's explicit time dependence can be neglected; i.e., $n_1(t)$ and $n_2(t)$ vary just slightly with time as only a small fraction of Cooper pairs indeed tunnels through the barrier. In that case, we simply have $I_0(t) \approx I_0(0) = [4eK\sqrt{n_1(0)n_2(0)}]/\hbar$.

The time evolution of ϕ_S is obtained subtracting Eq. (5.15) from Eq. (5.14),

$$\frac{\mathrm{d}\left[\phi_S(t)\right]}{\mathrm{d}t} = \frac{\mathrm{d}\phi_{S_1}(t)}{\mathrm{d}t} - \frac{\mathrm{d}\phi_{S_2}(t)}{\mathrm{d}t} = \frac{2eV(t)}{\hbar}. \tag{5.19}$$

For simplicity, we again made use of the fact that the coupling between the superconductors is weak, i.e., that $n_1(t) \approx n_2(t)$ at arbitrary t (recall that both superconductors are identical apart from their phases and the amount of tunneling Cooper pairs is small compared to the huge number of Cooper pairs in the initial condensates). Integrating Eq. (5.19) over time finally yields the *second Josephson relation*

$$\phi_S(t) = \phi_S(0) + \frac{2e}{\hbar}\int_0^t \mathrm{d}t'\, V(t'). \tag{5.20}$$

Note that a finite bias voltage $V(t) \neq 0$ generally produces time modulations of the superconducting phase difference $\phi_S(t)$, which are immediately transferred into the Josephson current via the current-phase dependence governed by the first Josephson relation. The first and the second Josephson relations *together* uniquely describe the physics of Josephson contacts.

To complete this introductory chapter on Josephson effects, we have a closer look at two specific cases. First, let us regard the *zero-bias* Josephson contact, for which $V(t) = 0$ at all times t. Evaluating the second Josephson relation in Eq. (5.20) suggests that the superconducting phase difference remains then constant over time, $\phi_S(t) = \phi_S(0)$, and drives the stationary DC Josephson current [obtained plugging $\phi_S(0)$ into the first Josephson relation in Eq. (5.18)]

$$I_J(t) \approx I_J(0) = I_0(0)\sin\left[\phi_S(0)\right]; \tag{5.21}$$

to simplify the expression, we again assumed weak coupling and neglected the critical current's explicit time dependence. The sinusoidal current-phase relation (at arbitrary time) is one of the most astonishing characteristics initially predicted by Josephson's work [93, 127]. In experiments, the superconducting phase difference gets often modulated by coupling the Josephson contact to a superconducting loop and tuning the magnetic flux through the enclosed area [237].

Both the direct current (DC) Josephson effect and the magnetic phase tunability found their probably most important application in DC SQUIDs. A typical SQUID set-up, as the one depicted in Fig. 5.3, consists of a double Josephson contact aligned in a looplike structure. A current injected into the loop from one side, e.g., from the left in Fig. 5.3(a), splits into two current-carrying paths. Each individual current contribution passes one Josephson contact, before both "interfere" again and the final current gets collected at the other side of the loop (in our example, on the right). The loop itself encloses an area which is penetrated by the magnetic flux Φ, essentially controlling the phases of the Josephson contacts and the maximal supercurrents that can flow through them [according to the typical current-phase relation of Josephson contacts given in Eq. (5.21)]. Tuning the flux via external magnetic fields hence varies not only the maximal (super)currents transferred through each of the two Josephson contacts, but in the end also the maximal current extracted from the SQUID. Assuming that the device is composed of two similar Josephson contacts with the same critical current I_0, one finds that the maximal current passing the SQUID is given by

$$I_{\max} = 2I_0\left|\cos\left(\pi\frac{\Phi}{\Phi_0}\right)\right|; \tag{5.22}$$

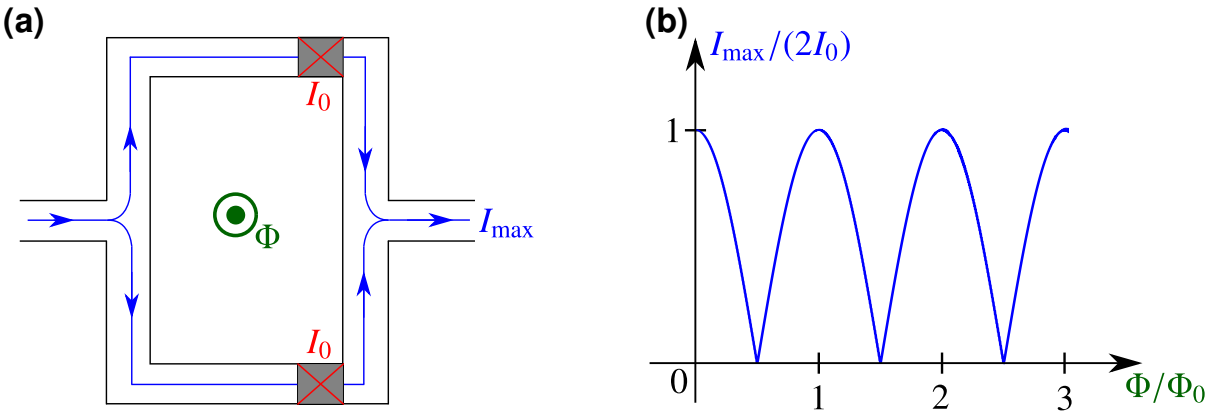


Fig. 5.3: (a) Schematical illustration of a DC SQUID geometry. Current is fed into the loop from the left, splits up into two current-carrying branches, and gets finally extracted at the right after the two paths "interfered" again. Both current branches incorporate a Josephson contact (red) with critical current I_0. The whole loop encloses the total magnetic flux Φ to tune the Josephson contacts' phase differences. **(b)** The maximally extractable current from the DC SQUID, $I_{\max}$, scales characteristically with the number of enclosed magnetic flux quanta Φ/Φ_0; the formal dependence is determined by Eq. (5.22).

$\Phi_0 = h/(2e)$ abbreviates the magnetic flux quantum. The derivation of Eq. (5.22) relies on properly accounting for the phase differences of both Josephson contacts and using the current-phase relation in Eq. (5.21). Details can be looked up, e.g., in Ref. [103]. The passing current's characteristic dependence on the magnetic flux [see Fig. 5.3(b) for an illustration of $I_{\max}$ as a function of the number of magnetic flux quanta] provides one experimental way to quantify (externally applied) magnetic fields from routine current measurements. In fact, DC SQUIDs operate much more sensitively than other techniques and can reliably detect magnetic fields as tiny as 5×10^{-18} T [95] with a precision no other state-of-the-art method can compete with.

Second, let us consider a Josephson contact in the presence of the DC bias voltage $V(t) = V_0$ with the time-independent amplitude V_0. From the second Josephson relation [recall Eq. (5.20)], we deduce that the superconducting phase difference increases now linearly with time according to

$$\phi_{\mathrm{S}}(t) = \phi_{\mathrm{S}}(0) + \frac{2eV_0}{\hbar}t. \tag{5.23}$$

Connecting the explicitly time-dependent phase difference with the first Josephson relation, stated in Eq. (5.18), results in the current-phase dependence

$$I_{\mathrm{J}}(t) = I_0 \sin\left[\phi_{\mathrm{S}}(0) + \omega_{\mathrm{J}}t\right]. \tag{5.24}$$

The Josephson current oscillates therefore with the Josephson frequency $\omega_{\mathrm{J}} = (2eV_0)/\hbar$ in time [equivalently, one could define the Josephson frequency also via $f_{\mathrm{J}} = \omega_{\mathrm{J}}/(2\pi)$]. Typical values for voltages of about $V_0 = 1\,\mu\mathrm{V}$ are around $f_{\mathrm{J}} = 0.5\,\mathrm{GHz}$, and thus experimentally detectable. This so-called alternating current (AC) Josephson effect gives rise to another particularly important consequence. We know from electrodynamics that accelerated charge radiates. In our case, the Cooper pair electrons are essentially accelerated by the nonzero bias voltage and each pair would thus gain an energy amount of $2eV_0$ while tunneling through the barrier. However, since energy conservation implies that the Cooper pairs' energy actually needs to be conserved, the Josephson contact immediately emits the additional energy in terms of photons with frequency ω_{J}; the thereby emitted electromagnetic radiation is known as *Josephson radiation*. More relevant to experimentalists is the opposite case. If microwave radiation is incident on the Josephson contact, the contact starts to absorb radiation quanta at the Josephson frequency ω_{J} and

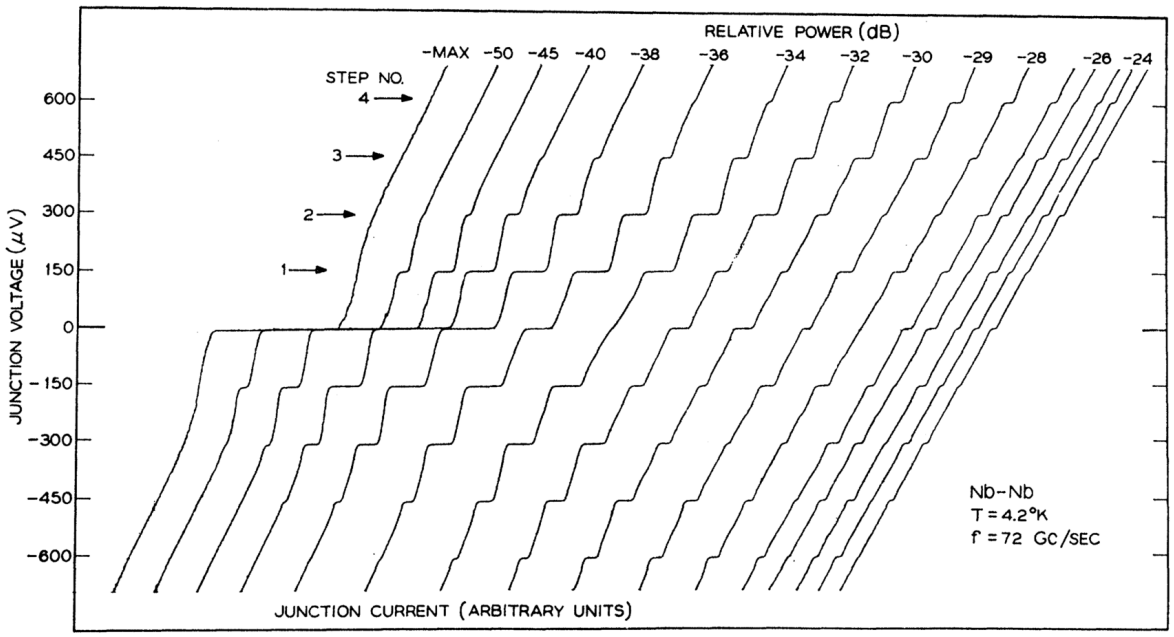


Fig. 5.4: Measured current-voltage characteristics (by Grimes and Shapiro) of a niobium Josephson point contact, taken from Ref. [238]. The data got recorded at a temperature of 4.2 K under the incidence of 72 GHz frequency microwave radiation and for different microwave power levels (for clarity, the different curves got horizontally shifted). The current plateaus at zero bias indicate twice the critical current of the Josephson contact; the other plateaus at finite bias correspond to *Shapiro steps*.

well-distinct steps appear in the recorded current-voltage relation. If n radiation quanta get absorbed, the steps form at voltages satisfying

$$V_n = n\frac{\hbar}{2e}\omega_{\mathrm{J}}. \tag{5.25}$$

Shapiro [239] observed the first experimental indications of such a steplike current-voltage dependence in an aluminum/tin contact already shortly after the Josephson effect itself had been understood. Just a couple of years later, he and Grimes [238] succeeded to characterize this behavior much more profoundly in niobium point contact Josephson geometries. Figure 5.4 replicates their data originally taken in the second (niobium point contact) experiment, clearly showing the expected step pattern. The experimental demonstration of these so-called *Shapiro steps* undoubtedly marked another milestone towards a common acceptance of Josephson's epoch-making work.

Both Josephson effects (DC and AC) have been intensively studied in diverse contact configurations over the past decades. The weak coupling of superconductors can be implemented in nearly uncountably many ways and with all kinds of materials; the only requirements are basically that the contact region's width does not significantly exceed the superconducting coherence length (so that superconducting order gets not destroyed there) and its critical current stays much below that of the two individual superconductors. For example, the insulating barrier considered in our example could be replaced by a thin layer (could be a few nanometers thick) of a normal metal or a ferromagnet. Particularly the latter gives once again rise to the intriguing interplay of superconductivity and ferromagnetism, and might influence the Josephson effect in a completely unexpected manner. In most of the subsequent chapters of this thesis, we will exactly focus on such Josephson contacts and elaborate on some of their most impressive physical features. Due to the vast number of publications dealing with Josephson physics, we decided to mention important references for further reading always in connection with our following studies.

Chapter 6

DC Josephson effect in ballistic S/F/S-like junctions

While the origin of the DC Josephson effect in junctions coupling two superconducting electrodes by means of an ultrathin insulating barrier can be traced back to the tunneling of Cooper pairs from one superconductor into the second one, as we thoroughly illustrated when elaborating on Feynman's picture in Chap. 5, the physical situation becomes more subtle if the barrier is replaced by a metallic interlayer. In the latter case, the superconducting regions of the junction are separated by a layer composed of a normal metal or a ferromagnet, typically a few nanometers thick [240, 241]. One of the particularly striking points is to understand how the superconductors' Cooper pairs can be transferred through such metallic buffer layers and generate net Josephson current flows. The physical mechanisms standing behind these supercurrents must certainly be much more intricate than the rather intuitive Cooper pair tunneling through superconductor/insulator/superconductor (S/I/S) contacts' insulating barriers.

Nonetheless, since the metallic region is well proximitized by the superconductors, recalling our previous discussions concerning proximity effects might help us to resolve the underlying physics. As we briefly mentioned in Sec. 3.1, superconducting proximity effects are closely related to the peculiar, characteristically at metal/superconductor interfaces appearing, Andreev reflection process [179]. To gain a deeper insight into the mechanisms that maintain Josephson current flows through S/N/S (or S/F/S) junctions, it is basically enough to restrict ourselves to a few central consequences of the intriguing connection between proximity effects and Andreev reflections. A more profound analysis of all coincidences can be found in Ref. [180]. Note that it does not make any difference for our *qualitative* arguments whether the interlayer consists of a normal metal or a ferromagnet. We will solely term that layer "metal" in the following.

Let us initially consider the situation in which a spin-up electron inside the metallic region moves to the right, as sketched in Fig. 6.1(a); the description for incoming spin-down electrons is analog and therefore not individually presented. Approaching the (right) metal/superconductor interface, that electron must either be reflected back into the metal or transmitted (as a quasiparticle) into the neighboring superconductor. Assuming that the electron's excitation energy lies inside the superconductor's energy gap, transmissions are forbidden, and only specular and Andreev reflections become possible. If the interface is additionally highly transparent, the electron will most likely perform Andreev reflection and enter the superconducting region, eventually pairing into a spin-singlet Cooper pair together with another correlated electron. The simultaneously retroreflected spin-down hole propagates towards the second (left) metal/superconductor interface, at which it must again be scattered. Under the same circumstances we supposed at the right interface, the Andreev-reflected hole will also predominantly undergo another Andreev reflection process. For an incident hole, Andreev reflection indicates that the spin-down hole is now transferred into the left superconductor and pairs into a *hole* Cooper pair; formally, an electron with spin up gets retroreflected into the metal, moves towards the right interface, and the described cycle starts over. Generating a *hole* Cooper pair inside the left superconducting electrode is equivalent to destroying

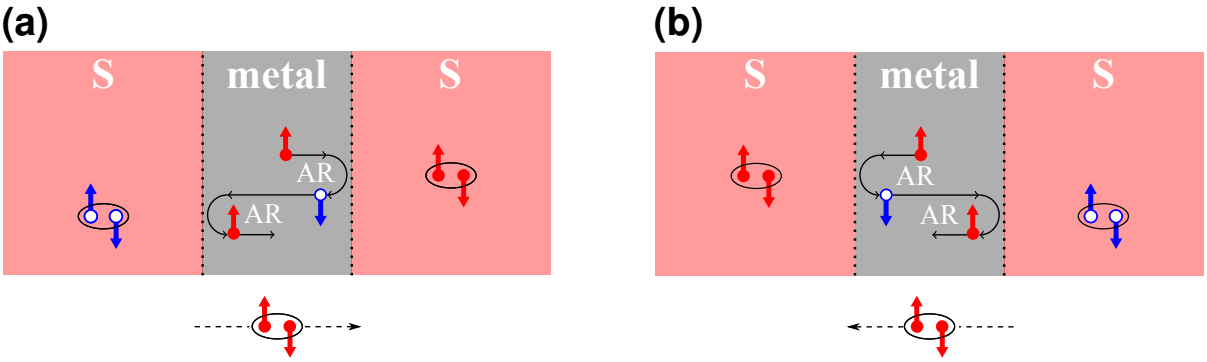


Fig. 6.1: Schematical illustration of the Josephson current flow generation in S/metal/S junctions. Electrons are colored red, holes blue, and electrons' and holes' spins are represented by red and blue arrows; black arrows point along the electrons' and holes' propagation directions. **(a)** Double Andreev reflections (AR) of initially right-propagating spin-up electrons (in the metal) effectively transfer electron Cooper pairs from the left into the right superconductor, generating a nonzero Josephson current flow. **(b)** If the spin-up electrons (in the metal) initially move towards the left, electron Cooper pairs get transferred from the right into the left superconductor and the Josephson current flow is reversed.

one *electron* Cooper pair. As a result, double Andreev reflections transfer electron Cooper pairs from the left into the right superconductor and create a nonzero Josephson (super)current flow.

For a complete picture, we shall not forget to look at the "reversed" process, meaning that the incident spin-up electron initially moves towards the left metal/superconductor interface [see Fig. 6.1(b)]. Following the same considerations as above, double Andreev reflections are then expected to cycle electron Cooper pairs from the right into the left superconductor, exactly opposite to the earlier analyzed case. Effectively, the total (net) Josephson current flow through the junction would vanish. Nevertheless, we did not pay special attention to the superconducting phase difference ϕ_S, which we already encountered in Feynman's fundamental formulation (see Chap. 5), so far. Incoming electrons perform the Andreev reflection cycles, triggering the Cooper pair transfers, only with certain probabilities, mostly depending on the electron's excitation energy, the degree of interfacial transparency, *and* ϕ_S. To be more specific, the processes presented in Figs. 6.1(a) and 6.1(b) are only equally probable if $\phi_S = 0 \pmod{\pi}$. Just for those phase differences, the total Josephson current becomes indeed zero. For all other values of ϕ_S, one of the processes gets more (and the second less) probable so that finally a finite total Josephson current with *positive* sign (whenever Cooper pairs are mostly transferred *from right to left*) or *negative* sign (whenever Cooper pairs are mostly transferred *from left to right*) remains.

We pointed out in Secs. 2.1 and 3.1 that the leakage of Cooper pairs into nonsuperconducting components (into the metal in our case) induces superconducting order there. The fact that the Cooper pair leakage is microscopically enabled by Andreev reflections is another unambiguous evidence for the close correlation between proximity effects on the one and the peculiar Andreev reflection process on the other hand (see Ref. [180]). It is indeed the *phase-coherent* Andreev reflection that brings superconducting order into the actually nonsuperconducting metal, maintains the exchange of Cooper pairs between the superconductors, and essentially causes in that way the expected supercurrent flow. All qualitative statements made up to now hold, in principle, for all superconductor/metal/superconductor (S/metal/S) Josephson junctions. However, since the interplay of the nominally antagonistic superconducting and ferromagnetic phases in one single junction can bring spectacular effects, particularly S/F/S junctions attract enormous attention nowadays [49, 50, 87]. The emergence of current-reversing 0-π transitions [55, 69, 242–245] probably counts to the most striking physical phenomena in such systems. To unravel the physical origin of these transitions, we need to further explore the (via the multiple Andreev reflections and the accompanying Cooper pair leakage) proximity-induced superconducting correlations in the metallic layer.

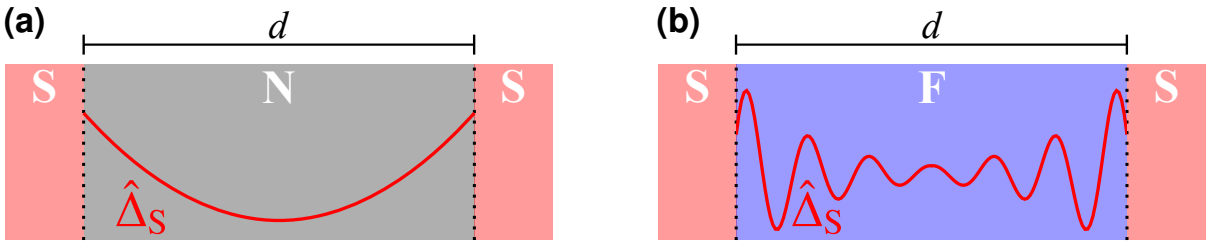


Fig. 6.2: Schematical illustration of the spatial variation of the proximity-induced superconducting pairing potential $\hat{\Delta}_S$ in the metallic region of **(a)** S/N/S and **(b)** S/F/S Josephson junctions; the thickness of the metallic regions is d. While the induced pairing potential simply decays exponentially inside a normal metal (away from the two interfaces), the exchange interaction in the ferromagnet superimposes a complicated oscillatory behavior. Depending on the oscillations' period and the ferromagnetic interlayer's thickness, the Josephson current-phase relation may gain an intrinsic π-phase shift, causing a transition from the usual 0- to the π-state. A more detailed explanation is provided in the text.

As we are concerned with two metal/superconductor interfaces, Cooper pairs leak through *both* and generate a sizable superconducting pairing potential close to the interfaces, eventually decaying exponentially on the scale of the characteristic metal coherence length $\xi_N \approx 100\,\text{nm}$ [74] inside the metal [see Fig. 6.2(a)]. The coherence length defines the length scale, on which the penetrating Cooper pairs lose their coherence due to scattering and the induced superconducting order in the metal gets destroyed. This is also the deeper reason why increasing the thickness of the metallic interlayer generically significantly suppresses Josephson currents so that the most promising candidates for applications are junctions with thin interlayers sustaining maximal current flows. The situation gets more intriguing if the metal is additionally ferromagnetic. In contrast to normal metals, the exchange interaction in Stoner ferromagnets splits the spin subbands and gives rise to a spin imbalance (and hence a finite spin polarization). The finite exchange energy gap Δ_{XC} separates the lower-energy majority-spin subband, which gets predominantly occupied, and the higher-energy minority-spin subband; see our discussions in Sec. 2.2. The Cooper pairs being transferred through the ferromagnet are exposed to precisely that imbalance. As a consequence, the Cooper pairs' majority-spin electrons (typically, the spin-up electrons) immediately lower their potential energy when entering the ferromagnetic part, whereas simultaneously the potential energy of the minority-spin electrons (spin-down electrons) increases. Since the Cooper pairs' total energy needs to be conserved, the electrons' respective kinetic energies must compensate the action of the spin-dependent potential and the pairs eventually acquire nonzero center-of-mass momenta. Demler *et al.* [243] demonstrated that the result is a complicated oscillatory behavior of the induced superconducting pairing potential inside the ferromagnet with an oscillation period of $p \propto 1/\Delta_{XC}$, schematically illustrated in Fig. 6.2(b). These oscillations are superimposed on the distinct exponential decay of the pairing potential, which is still present. Nevertheless, the coherence length in ferromagnets, ξ_F, scales inversely with their exchange gap [246] and is thus much smaller in ferromagnetic materials with a strong exchange interaction (typically, $\xi_F \approx 1\,\text{nm}$ [74]) than in normal metals, providing another manifestation of the antagonistic character of the superconducting and ferromagnetic phases. The exchange interaction in ferromagnets tends to break up (spin-singlet) Cooper pairs and align the electron spins parallel to each other, which unambiguously destroys the induced superconducting correlations much faster than in nonferromagnetic interlayers.

Coming back to the oscillatory pairing potential in the ferromagnet, we can immediately understand the source of 0-π transitions. If the ferromagnetic layer's thickness is tuned such that it becomes comparable to half of the oscillation period, the induced pairing potentials at the two F/S interfaces differ in sign. Correspondingly, the additional intrinsic π-phase shift $\Delta\phi_S = \pi$ enters the usual Josephson current-phase relation $I_J \propto \sin(\phi_S + \Delta\phi_S)$. Since $\sin(\phi_S + \pi) = -\sin(\phi_S)$, the π-state Josephson current gains

a relative negative sign (when compared to the usual 0-state), effectively indicating the reversal of the current's direction. The underlying physical mechanism of 0-π transitions relies hence crucially on the oscillatory pairing potential inside ferromagnetic junction links, explaining the absence of such transitions if the interlayer is formed by a normal metal. Although the existence of π-states had been theoretically predicted back in 1977 [55], it has taken nearly forty years until their first experimental demonstration in Nb/CuNi/Nb trilayers succeeded [56]. Following experimental studies on various junction compositions [62, 87, 247, 248] eventually boosted new hopes for finding ways to reliably control 0-π transitions and thereby the direction of the supercurrent in real devices. Such controls could not only play an indispensable role for manipulating theoretically proposed superconducting π-qubits [61], but also for bringing versatile spintronics functionalities into superconducting quantum-computing circuits [57–60, 62–64] and Josephson junction technology [62, 177, 249].

One of the most essential ingredients to tailor practical spintronics applications is an efficient manipulation of current flows by means of electric and/or magnetic fields. From that point of view, tunnel junctions are particularly promising candidates since their contact interfaces invariably introduce SOC into the constituent regions. Besides the Rashba spin-orbit field [149, 150], which is always present due to the junctions' (interfacial) space-inversion asymmetry, simultaneously an additional spin-orbit field of the Dresselhaus type [152] often emerges. The latter is caused by broken bulk-inversion symmetry, as it is typically the case with tunneling barriers composed of III-V zinc-blende semiconductors such as GaAs or AlP. The interference of Rashba and Dresselhaus spin-orbit fields results in a C_{2v}-symmetric field [27, 250] that reflects the symmetry of the corresponding contact interface and manifests itself, in connection with ferromagnetic components, in pronounced magnetoanisotropic transport features. Examples cover the *tunneling anisotropic magnetoresistance (TAMR)* in normal-state F/N junctions [250, 251], as well as giant *magnetoanisotropic Andreev reflection (MAAR)* effects [176, 182] in superconducting F/S junctions. Besides, many more peculiar phenomena are bound to occur when SOC couples with ferromagnetism and superconductivity. This topic is mainly driven by the research of Majorana states that are expected to form in superconducting proximity regions if SOC is present [76, 252–259]. Furthermore, F/S contacts offer unique ways to generate spin-polarized supercurrents owing to the formation of Cooper pairs with spin-triplet pairing mechanisms [74–79]. The formation of triplet pairs is predominantly facilitated by SOC and leads to long-range superconducting proximity effects in Josephson junctions' ferromagnetic regions [77–79], even in the half-metallic limit [74–76].

Motivated by the rich physics proposed to appear in F/S heterostructures in the presence of SOC, this chapter is dedicated to a comprehensive analysis of the DC Josephson effect in ballistic S/F/S junctions comprising interfacial Rashba and Dresselhaus SOCs. The chapter is structured as follows. Section 6.1 looks into the system within a simple limiting case in order to become once again more familiar with the microscopic origin of Josephson currents in magnetic junctions. In Sec. 6.2, we are then concerned with generic S/F/S junctions including interfacial Rashba and Dresselhaus SOCs. After elaborating on a powerful formal approach, which not only allows us to efficiently compute the Josephson current flow through our system, but can also be straightforwardly generalized to a variety of similar junctions, we analyze numerical results for several realistic junction configurations. We put special emphasis on discussing different electric and magnetic possibilities to control our system's transport features, specifically its 0-π transitions, and on the Josephson current's pronounced magnetoanisotropies that originate from the striking interplay of ferromagnetism and SOC. To demonstrate the strength of the established theoretical framework, we extend our study to more complicated S/F/I/F/S Josephson spin-valve junctions in Sec. 6.3. The magnetization directions of the two subsequent ferromagnetic layers can be switched from the parallel to the antiparallel configuration, giving rise to the Josephson (super)current analog to the (normal-state) TMR effect and opening another experimentally feasible way to manipulate 0-π transitions. We briefly summarize the chapter in Sec. 6.4.

*Section 6.2 is based on the article "Magnetoanisotropic Josephson effect due to interfacial spin-orbit fields in superconductor/ferromagnet/superconductor junctions" by Andreas Costa, Petra Högl, and Jaroslav Fabian, which got published in Phys. Rev. B **95**, 024514 (2017). Andreas Costa was responsible for the analytical modeling of the system, its numerical implementation, and obtained all presented numerical results from the developed methodology. Petra Högl and Jaroslav Fabian contributed to the project with stimulating discussions and feedback.*

6.1 Microscopic origin of Josephson currents – Andreev bound states

Within our introductory motivation to this chapter, we learned about the multiple Andreev reflection cycles that effectively transfer Cooper pairs through metallic interlayers of Josephson junctions and are thus the driving force for supercurrents. On the microscopic level, Andreev [179, 227] showed already back in the 1960s that such multiple Andreev reflections trigger the formation of discrete bound states localized inside the metallic link. Electrons that initially formed Cooper pairs in one of the two superconducting electrodes can then tunnel through the metal via these single-particle states and pair again in the second superconductor, essentially cycling Cooper pairs through the link region and generating the net Josephson current. Several experimental attempts were necessary to verify the existence of such *Andreev bound states*, until Morpurgo and coworkers [260] could observe distinct precursors to substantiate Andreev's claim. Knowing the junction-specific spectrum of Andreev bound states brings along direct access to the Josephson current since all electrical current inside the metal is carried by the (unpaired) tunneling electrons, which can only occupy the available bound states. As the total current must be conserved (and we deal with fully ballistic systems), the amplitudes of the tunneling current computed inside the interlayer and the Josephson currents flowing in the superconductors are equal. In fact, Kulik [261] was the first theoretically extracting the Andreev bound state energies of idealized S/N/S junctions and relating his results to the expected Josephson current flow. Shortly afterwards, a similar work of Ishii [262], as well as a related study by Bardeen and Johnson [263], got published. In this section, we extend Kulik's approach to the particularly interesting S/F/S Josephson junctions. Although we need to assume strong simplifications within that method, we can deduce fully analytical results and provide valuable insight into physical connections. The approach that we adopt in Sec. 6.2 will be much more powerful, but also by far less descriptive.

We consider a ballistic effectively *one-dimensional* S/F/S Josephson junction along the $\hat{z}||[001]$ crystallographic direction, in which the two semi-infinite superconducting electrodes (S) are located at $z < -d/2$ and $z > d/2$. The thickness of the ferromagnetic link (F) is accordingly d, as depicted in Fig. 6.3. For simplicity, we assume that the two superconductors are identical, i.e., they are characterized by the same isotropic energy gap $|\Delta_\mathrm{S}|$ and differ only in their corresponding phases, which we call ϕ_{S_1} in the left and ϕ_{S_2} in the right superconductor. Due to the phase-coherent coupling of the superconducting regions by means of the metallic layer, their phases need to be carefully included into our theoretical model and cannot be set to zero as in Chap. 3, where we solely dealt with one single superconducting electrode. It is precisely the difference of these phases that drives the Josephson current, just as we understood in Chap. 5.

To model our junction, we start from its Bogoljubov-de Gennes Hamiltonian [139]

$$\hat{\mathcal{H}}_\mathrm{BdG} = \begin{bmatrix} \hat{\mathcal{H}}_\mathrm{e} & \hat{\Delta}_\mathrm{S}(z) \\ \hat{\Delta}_\mathrm{S}^\dagger(z) & \hat{\mathcal{H}}_\mathrm{h} \end{bmatrix}, \tag{6.1}$$

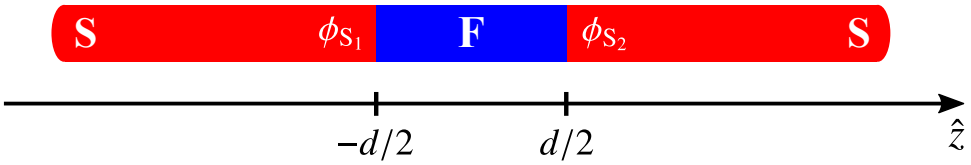


Fig. 6.3: Schematical sketch of the considered *one-dimensional* S/F/S Josephson junction grown along the $\hat{z} \parallel [001]$ crystallographic orientation. The superconductors' (S) phases are ϕ_{S_1} and ϕ_{S_2}, while d indicates the thickness of the ferromagnetic link (F).

where the single-electron Hamiltonian reads

$$\hat{\mathcal{H}}_{\mathrm{e}} = -\frac{\hbar^2}{2m}\frac{\mathrm{d}^2}{\mathrm{d}z^2} - \mu - \sigma\frac{\Delta_{\mathrm{XC}}}{2}\Theta\left(\frac{d}{2} - z\right)\Theta\left(\frac{d}{2} + z\right) \tag{6.2}$$

and its hole counterpart

$$\hat{\mathcal{H}}_{\mathrm{h}} = \frac{\hbar^2}{2m}\frac{\mathrm{d}^2}{\mathrm{d}z^2} + \mu - \sigma\frac{\Delta_{\mathrm{XC}}}{2}\Theta\left(\frac{d}{2} - z\right)\Theta\left(\frac{d}{2} + z\right). \tag{6.3}$$

As we stated in the preceding paragraph, both superconductors are supposed to be identical so that the quasiparticle masses m and the Fermi levels μ are the same in both. To simplify the calculations further, we additionally assume the same effective masses and Fermi levels also inside the ferromagnetic interlayer. The Stoner ferromagnet's exchange energy gap is still Δ_{XC}. Note that, contrary to our description in Chap. 3, we now work just in the electron-hole basis (instead of the additionally *spin-resolved* Nambu formulation). This is possible since we are not concerned with spin-active (SOC-inducing) components at the moment and the underlying Bogoljubov-de Gennes Hamiltonian can be decoupled into its up-spin ($\sigma = 1$) and down-spin ($\sigma = -1$) blocks. The s-wave superconducting pairing potential is approximated by the steplike function

$$\hat{\Delta}_{\mathrm{S}}(z) = |\Delta_{\mathrm{S}}|\left[\mathrm{e}^{\mathrm{i}\phi_{S_1}}\Theta\left(-\frac{d}{2} - z\right) + \mathrm{e}^{\mathrm{i}\phi_{S_2}}\Theta\left(-\frac{d}{2} + z\right)\right]. \tag{6.4}$$

After setting up the junction's Bogoljubov-de Gennes Hamiltonian [see Eq. (6.1)], we can come back to the multiple Andreev reflections that drive the Cooper pairs through the ferromagnetic part of the junction. We gave a detailed qualitative explanation of the related processes and their ramifications within the introduction to this chapter. To remind ourselves, Fig. 6.4(a) exemplifies again the situation corresponding to an initially right-moving electron in the ferromagnet, followed by double Andreev reflections and the transfer of an electron Cooper pair from the left into the right superconductor; Fig. 6.4(b) depicts the "reversed" process, cycling Cooper pairs along the opposite direction. Solving our system's stationary Bogoljubov-de Gennes equation

$$\hat{\mathcal{H}}_{\mathrm{BdG}}\psi^{\sigma}(z) = E\psi^{\sigma}(z) \tag{6.5}$$

for the (spin-dependent) scattering states $\psi^{\sigma}(z)$, we can translate the qualitative picture into a formal (quasiparticle) scattering description. It turns out to be useful later to split the scattering states into two parts,

$$\psi_{+}^{\sigma}(z) = \begin{cases} a_{+}^{\sigma}\mathrm{e}^{\mathrm{i}q_{z,\mathrm{h}}(z+d/2)}\begin{bmatrix} v\mathrm{e}^{\mathrm{i}\phi_{S_1}} \\ u \end{bmatrix} & \text{for } z < -d/2, \\ b_{+}^{\sigma}\mathrm{e}^{\mathrm{i}k_{z,\mathrm{e}}^{\sigma}z}\begin{bmatrix} 1 \\ 0 \end{bmatrix} + c_{+}^{-\sigma}\mathrm{e}^{\mathrm{i}k_{z,\mathrm{h}}^{-\sigma}z}\begin{bmatrix} 0 \\ 1 \end{bmatrix} & \text{for } -d/2 < z < d/2, \\ d_{+}^{\sigma}\mathrm{e}^{\mathrm{i}q_{z,\mathrm{e}}(z-d/2)}\begin{bmatrix} u\mathrm{e}^{\mathrm{i}\phi_{S_2}} \\ v \end{bmatrix} & \text{for } z > d/2, \end{cases} \tag{6.6}$$

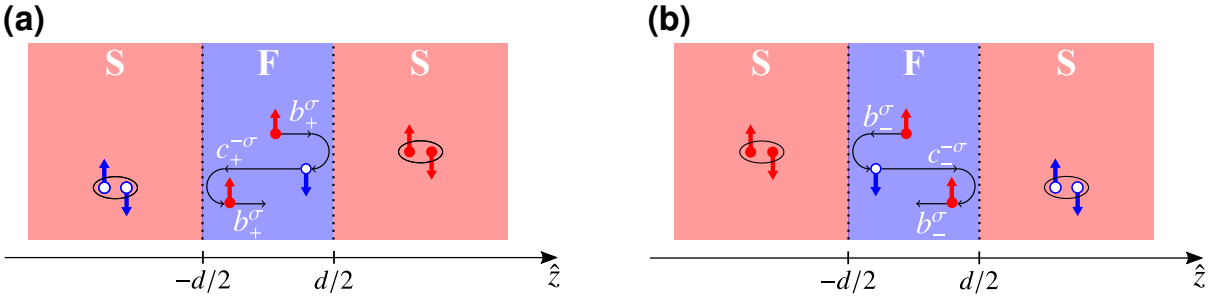


Fig. 6.4: Schematical illustration of the multiple Andreev reflections generating the Josephson current flow through S/F/S junctions (similarly to Fig. 6.1). To clarify the different terms entering the formal scattering states in Eqs. (6.6)–(6.7), we highlighted the incoming **(a)** right-propagating electron (coefficient b_+^σ) and **(b)** left-propagating electron (coefficient b_-^σ). The Andreev-reflected holes move towards the **(a)** left (coefficient $c_+^{-\sigma}$) and **(b)** right (coefficient $c_-^{-\sigma}$); for the depicted scenarios, $\sigma = 1$ (spin up). The remaining coefficients in Eqs. (6.6)–(6.7) simply account for possible quasiparticle transmissions into the superconductors and are not important for our qualitative understanding (and therefore not included into the illustration).

and

$$\psi_-^\sigma(z) = \begin{cases} a_-^\sigma \mathrm{e}^{-\mathrm{i}q_{z,\mathrm{e}}(z+d/2)} \begin{bmatrix} u\mathrm{e}^{\mathrm{i}\phi_{\mathrm{S}_1}} \\ v \end{bmatrix} & \text{for } z < -d/2, \\ b_-^\sigma \mathrm{e}^{-\mathrm{i}k_{z,\mathrm{e}}^\sigma z} \begin{bmatrix} 1 \\ 0 \end{bmatrix} + c_-^{-\sigma} \mathrm{e}^{-\mathrm{i}k_{z,\mathrm{h}}^{-\sigma} z} \begin{bmatrix} 0 \\ 1 \end{bmatrix} & \text{for } -d/2 < z < d/2, \\ d_-^\sigma \mathrm{e}^{-\mathrm{i}q_{z,\mathrm{h}}(z-d/2)} \begin{bmatrix} v\mathrm{e}^{\mathrm{i}\phi_{\mathrm{S}_2}} \\ u \end{bmatrix} & \text{for } z > d/2, \end{cases} \tag{6.7}$$

respectively. The first part, Eq. (6.6), contains all terms referring to electrons (holes) propagating towards the right (left), while the second part, Eq. (6.7), resembles left-moving (right-moving) electrons (holes). The Bogoljubov-de Gennes equation's full solution, given by the superposition $\psi^\sigma(z) = \psi_+^\sigma(z) + \psi_-^\sigma(z)$, formalizes then all scattering processes illustrated in Fig. 6.4. To give one concrete example, the incident right-propagating electron is modeled by the summand with the scattering coefficient b_+^σ and the subsequently Andreev-reflected hole enters with the coefficient $c_+^{-\sigma}$ (accounting for the opposite spin of the hole after the Andreev reflection process). All other processes can be identified in precisely the same way. Analogously to our considerations in earlier chapters of this thesis,

$$u = u(E) = \sqrt{\frac{1}{2}\left(1 + \sqrt{1 - \frac{|\Delta_{\mathrm{S}}|^2}{E^2}}\right)} \qquad \text{and} \qquad v = v(E) = \sqrt{1 - [u(E)]^2} \tag{6.8}$$

represent the BCS coherence factors, while we approximate the electronlike and holelike wave vectors by means of the Fermi wave vector $k_{\mathrm{F}} = \sqrt{2m\mu}/\hbar$ to obtain

$$k_{z,\mathrm{e}}^\sigma \approx k_{z,\mathrm{h}}^\sigma \approx k_{\mathrm{F}}\sqrt{1 + \sigma P} \tag{6.9}$$

and

$$q_{z,\mathrm{e}} \approx q_{z,\mathrm{h}} \approx k_{\mathrm{F}}; \tag{6.10}$$

$P = (\Delta_{\mathrm{XC}}/2)/\mu$ measures the ferromagnet's *effective* spin polarization.

One might note that we did not explicitly incorporate specular reflection terms into our scattering states. We assume perfectly transparent metal/superconductor interfaces, i.e., the single-particle Hamiltonians [see Eqs. (6.2) and (6.3)] do *not* contain any interfacial scattering potentials. Following our considerations in Sec. 3.2, specular reflection is hence expected to be completely forbidden (and can simply be neglected) as long as the metallic interlayer consists of a normal metal. This remains, however, no longer necessarily true if the interlayer becomes ferromagnetic. Strong exchange interactions in ferromagnets typically suppress the probability for Andreev reflections and give rise to additional specular reflections [264] that would then not be captured by our scattering states. Nevertheless, more extensive theoretical studies by Cayssol *et al.* [265] proved that assuming perfect Andreev reflection and completely neglecting all kinds of specular reflections still yields accurate results, even for S/F/S junctions' Josephson current, as long as the ferromagnetic region's effective spin polarization $P = (\Delta_{\mathrm{XC}}/2)/\mu$ does *not* exceed values of $P \approx 0.95$. Therefore, restricting the scattering states to simply deal with Andreev reflections is a well-justified approach for a wide class of S/F/S Josephson junctions. Only the (nearly) half-metallic limiting case ($P \gtrsim 0.95$) would require a more complicated treatment, but we are currently not interested in that case anyway.

Imposing that the scattering states given by Eqs. (6.6)–(6.7) need to be continuous at both interfaces leads to a set of four linear equations, namely

$$v\,\mathrm{e}^{\mathrm{i}\phi_{\mathrm{S}_1}}\,\mathrm{e}^{\mathrm{i}k_{z,\mathrm{e}}^{\sigma}d/2}\left(1+\frac{q_{z,\mathrm{h}}}{k_{z,\mathrm{e}}^{\sigma}}\right)a_{+}^{\sigma} = d_{+}^{\sigma}\,u\,\mathrm{e}^{\mathrm{i}\phi_{\mathrm{S}_2}}\,\mathrm{e}^{-\mathrm{i}k_{z,\mathrm{e}}^{\sigma}d/2}\left(1+\frac{q_{z,\mathrm{e}}}{k_{z,\mathrm{e}}^{\sigma}}\right), \tag{6.11}$$

$$u\,\mathrm{e}^{\mathrm{i}k_{z,\mathrm{h}}^{-\sigma}d/2}\left(1+\frac{q_{z,\mathrm{h}}}{k_{z,\mathrm{h}}^{-\sigma}}\right)a_{+}^{\sigma} = d_{+}^{\sigma}\,v\,\mathrm{e}^{-\mathrm{i}k_{z,\mathrm{h}}^{-\sigma}d/2}\left(1+\frac{q_{z,\mathrm{e}}}{k_{z,\mathrm{h}}^{-\sigma}}\right), \tag{6.12}$$

$$u\,\mathrm{e}^{\mathrm{i}\phi_{\mathrm{S}_1}}\,\mathrm{e}^{-\mathrm{i}k_{z,\mathrm{e}}^{\sigma}d/2}\left(1+\frac{q_{z,\mathrm{e}}}{k_{z,\mathrm{e}}^{\sigma}}\right)a_{-}^{\sigma} = d_{-}^{\sigma}\,v\,\mathrm{e}^{\mathrm{i}\phi_{\mathrm{S}_2}}\,\mathrm{e}^{\mathrm{i}k_{z,\mathrm{e}}^{\sigma}d/2}\left(1+\frac{q_{z,\mathrm{h}}}{k_{z,\mathrm{e}}^{\sigma}}\right), \tag{6.13}$$

and

$$v\,\mathrm{e}^{-\mathrm{i}k_{z,\mathrm{h}}^{-\sigma}d/2}\left(1+\frac{q_{z,\mathrm{e}}}{k_{z,\mathrm{h}}^{-\sigma}}\right)a_{-}^{\sigma} = d_{-}^{\sigma}\,u\,\mathrm{e}^{\mathrm{i}k_{z,\mathrm{h}}^{-\sigma}d/2}\left(1+\frac{q_{z,\mathrm{h}}}{k_{z,\mathrm{h}}^{-\sigma}}\right). \tag{6.14}$$

To eliminate the unknown (colored) scattering coefficients, we divide Eq. (6.11) by Eq. (6.12) and accordingly Eq. (6.13) by Eq. (6.14). After substituting the explicit form of the BCS coherence factors [see Eq. (6.8)], the remaining two equations that ensure continuity of the scattering states can be combined into

$$\mathrm{e}^{-2\mathrm{i}\alpha(E)}\,\mathrm{e}^{\pm\mathrm{i}\phi_{\mathrm{S}}}\,\mathrm{e}^{\mathrm{i}\left(k_{z,\mathrm{e}}^{\sigma}-k_{z,\mathrm{h}}^{-\sigma}\right)d} = 1, \tag{6.15}$$

where the superconducting phase difference is now represented by $\phi_{\mathrm{S}} := \phi_{\mathrm{S}_2} - \phi_{\mathrm{S}_1}$ and $\alpha(E) := \arccos(E/|\Delta_{\mathrm{S}}|)$ contains the Andreev bound state energies E we are looking for (assuming $E > 0$). Making moreover use of the wave vectors given by Eqs. (6.9)–(6.10) and solving Eq. (6.15) for the Andreev bound state energies eventually yields in the *short-junction limit*, in which the junction's contacts are small compared to the BCS coherence length $\xi_{\mathrm{BCS}} = (\hbar v_{\mathrm{F}})/(\pi|\Delta_{\mathrm{S}}|)$,

$$E^{\sigma} = E^{\sigma}(\phi_{\mathrm{S}}) = |\Delta_{\mathrm{S}}|\cos\left[\frac{\phi_{\mathrm{S}}}{2} + \sigma\frac{m v_{\mathrm{F}} d}{2\hbar}\left(\sqrt{1+P} - \sqrt{1-P}\right)\right]; \tag{6.16}$$

$v_{\mathrm{F}} = (\hbar k_{\mathrm{F}})/m$ indicates the Fermi velocity. Owing to the superconductors' fundamental electron-hole symmetry, each bound state with energy $E^{\sigma} > 0$ comes along with another state at energy $-E^{\sigma}$.

Based on our junction's Andreev bound state spectrum [see Eq. (6.16)], we can evaluate the related Josephson current flow. Since the total electrical current is conserved, we can compute it along any vertical plane in our system. It is most common to concentrate on the metallic layer, in which the current

is solely carried by single electrons that tunnel through the metal via the available Andreev bound states. Within that approach, the Andreev bound state spectrum comprises all physical information about the Josephson current and there is no need to work out a complicated description explicitly dealing with Cooper pairs. For instance, one incident spin-σ electron in the E^σ-Andreev bound state carries the electrical current [233]

$$I(E^\sigma) = -\frac{e}{\hbar}\frac{\partial E^\sigma(\phi_\mathrm{S})}{\partial \phi_\mathrm{S}} \tanh\left(\frac{E^\sigma}{2k_\mathrm{B}T}\right), \tag{6.17}$$

where e indicates again the positive elementary charge. The *thermal occupation factor* $\tanh[E^\sigma/(2k_\mathrm{B}T)]$, where k_B still denotes Boltzmann's constant, assures that the E^σ-state gets indeed occupied by an electron (and at a given temperature T). The total Josephson current flow I_J is then simply obtained accounting for both spin-subband contributions,

$$I_\mathrm{J} = \sum_{\sigma=\pm1} I(E^\sigma). \tag{6.18}$$

Substituting the bound state energies we found for our considered junction [see Eq. (6.16)], the *zero-temperature* Josephson current finally reads

$$I_\mathrm{J} = \sum_{\sigma=\pm1} \frac{e|\Delta_\mathrm{S}|}{2\hbar} \sin\left(\frac{\phi_\mathrm{S}}{2} + \Delta\phi_\mathrm{S}\right), \tag{6.19}$$

with the (spin-dependent) intrinsic phase shift

$$\Delta\phi_\mathrm{S} = \sigma\frac{m v_\mathrm{F} d}{2\hbar}\left(\sqrt{1+P} - \sqrt{1-P}\right). \tag{6.20}$$

Equations (6.19) and (6.20) are the central results of this section and provide valuable physical insight; they are furthermore consistent with Cayssol's earlier work [265]. Let us initially suppose an S/N/S Josephson junction (with spin polarization $P = 0$). Inspecting the generic form of Eq. (6.20) suggests that the intrinsic phase shift vanishes in that case, i.e., $\Delta\phi_\mathrm{S} = 0$. Going back to the Josephson current in Eq. (6.19), we deduce that both spin channels contribute the same amount of current [as we expect since the normal metal is *not* spin polarized, also manifested in spin-degenerate Andreev bound states; see Eq. (6.16)] and the Josephson current-phase relation approaches its sinusoidal form $I_\mathrm{J} \propto \sin(\phi_\mathrm{S}/2)$. The modified periodicity stems from the perfectly transparent interfaces and zero temperature. In the presence of interfacial scattering potentials (tunneling barriers), we would really recover $I_\mathrm{J} \propto \sin(\phi_\mathrm{S})$, as predicted by Josephson for S/I/S tunnel junctions (see Chap. 5). Owing to the vanishing (zero) intrinsic phase shift, we refer to the common ground state of S/N/S Josephson junctions as the *0-state*. The situation gets more striking in an S/F/S junction (with spin polarization $P \neq 0$). The Andreev bound state spectrum splits into its individual spin-resolved parts [see Eq. (6.16)] and a *nonzero* intrinsic phase shift, $\Delta\phi_\mathrm{S} \neq 0$, enters the Josephson current-phase relation. Following Eq. (6.20), $\Delta\phi_\mathrm{S}$ is governed by the intriguing interplay of the exchange interaction (spin polarization P) and the ferromagnet's thickness d. This is indeed the formal confirmation of our previous claims. The exchange interaction gives rise to the complicated oscillatory behavior of the proximity-induced superconducting pairing potential inside the ferromagnet, which acts together with this layer's thickness. If both ingredients are tuned in a suitable way, the intrinsic phase shift may equal $\Delta\phi_\mathrm{S} = \pi$ and, according to $I_\mathrm{J} \propto (\phi_\mathrm{S}/2+\pi) = -\sin(\phi_\mathrm{S}/2)$, the Josephson current reverses its direction. Due to the intrinsic π-shift, such a state, unique to magnetic Josephson junctions, is usually called *π-state*.

Although Kulik's bound state method to extract Josephson current flows from the junction's underlying Andreev bound state spectrum allows a deep understanding of the physical background, gaining access to the bound state energies in real junctions can be rather cumbersome, particularly in the presence of interfacial SOC. Therefore, a reliable description of SOC phenomena in Josephson junctions often requires more powerful techniques, for which we will take care in the next section.

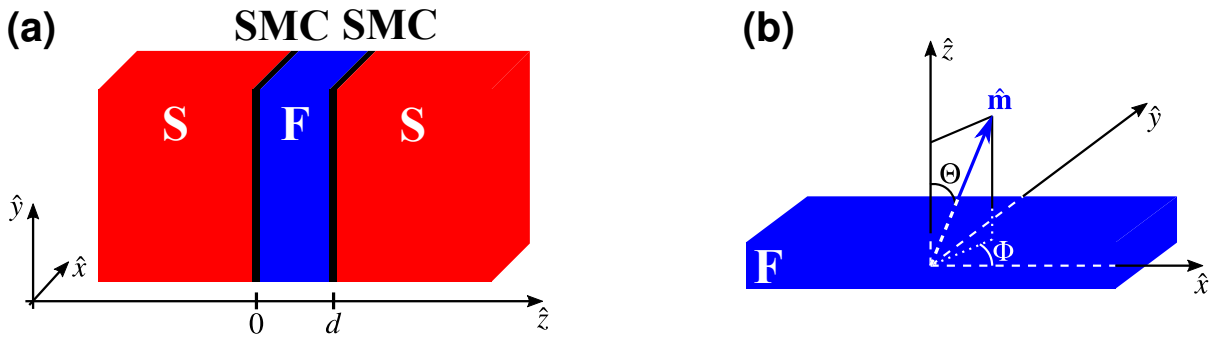


Fig. 6.5: (a) Schematical sketch of the considered *three-dimensional* S/F/S Josephson junction, using the C_{2v} principal crystallographic orientations $\hat{x} \parallel [110]$, $\hat{y} \parallel [\bar{1}10]$, and $\hat{z} \parallel [001]$. The ultrathin semiconducting tunneling barriers (SMC), separating the superconducting (S) and ferromagnetic (F) regions, cause interfacial potential and SOC scatterings. **(b)** The direction of the magnetization (unit) vector $\hat{\mathbf{m}}$ inside the ferromagnet (F) is determined by its azimuthal angle Φ and its polar angle Θ.

6.2 Ballistic S/F/S Josephson junctions with interfacial spin-orbit coupling

As a more realistic system, we consider a ballistic *three-dimensional* S/F/S Josephson junction, consisting of two semi-infinite superconducting regions (S; located at $z < 0$ and $z > d$) that are weakly coupled by a ferromagnet (F) with thickness d. At the flat interfaces between the junction's superconducting and ferromagnetic parts, ultrathin semiconducting tunneling barriers, such as GaAs or AlP, introduce potential and SOC scatterings. The junction is schematically sketched in Fig. 6.5(a).

6.2.1 Theoretical description

To compute the Josephson current flow through our system, we generalize the Furusaki-Tsukada approach [266], which finally relates the current to the Andreev reflection coefficients appearing in the junction's Bogoljubov-de Gennes scattering states. The latter, abbreviated by $\Psi(\mathbf{r})$, are again obtained solving the stationary Bogoljubov-de Gennes equation

$$\hat{\mathcal{H}}_{\mathrm{BdG}}\Psi(\mathbf{r}) = E\Psi(\mathbf{r}). \tag{6.21}$$

The junction's Bogoljubov-de Gennes Hamiltonian [139] in Nambu basis (necessary as SOC is present),

$$\hat{\mathcal{H}}_{\mathrm{BdG}} = \begin{bmatrix} \hat{\mathcal{H}}_{\mathrm{e}} & \hat{\Delta}_{\mathrm{S}}(z) \\ \hat{\Delta}_{\mathrm{S}}^{\dagger}(z) & \hat{\mathcal{H}}_{\mathrm{h}} \end{bmatrix}, \tag{6.22}$$

contains the single-electron Hamiltonian

$$\hat{\mathcal{H}}_{\mathrm{e}} = \left(-\frac{\hbar^2}{2m}\boldsymbol{\nabla}^2 - \mu\right)\hat{\sigma}_0 - \frac{\Delta_{\mathrm{XC}}}{2}\left(\hat{\mathbf{m}}\cdot\hat{\boldsymbol{\sigma}}\right)\Theta(z)\Theta(d-z) + \hat{\mathcal{H}}_{\mathrm{L}}^{\mathrm{SMC}} + \hat{\mathcal{H}}_{\mathrm{R}}^{\mathrm{SMC}}, \tag{6.23}$$

as well as its hole counterpart $\hat{\mathcal{H}}_{\mathrm{h}} = -\hat{\sigma}_y\hat{\mathcal{H}}_{\mathrm{e}}^{*}\hat{\sigma}_y$. For simplicity, and without loss of generality, we assume equal quasiparticle masses m and chemical potentials μ in the superconductors and in the ferromagnet. The effects of mass and chemical potential mismatch (the latter is typically a consequence of different charge carrier densities in the materials and therefore present in all real junctions [167]) are discussed in our article [267]. To summarize, mass and chemical potential mismatch have only minor quantitative and no qualitative impact on the presented features. Note that we now really term μ chemical potential (and

no longer Fermi level as in previous chapters) since we regard the junction at finite temperature. The ferromagnet is still described by the Stoner band model with the exchange energy gap Δ_{XC} and the magnetization direction $\hat{\mathbf{m}} = [\sin(\Theta)\cos(\Phi), \sin(\Theta)\sin(\Phi), \cos(\Theta)]^\top$ – see Fig. 6.5(b) for the definition of the azimuthal angle Φ and the polar angle Θ; $\hat{\sigma}_0$ is still the two-by-two identity matrix, $\hat{\sigma}_i$ the ith Pauli spin matrix, and $\hat{\boldsymbol{\sigma}} = [\hat{\sigma}_x, \hat{\sigma}_y, \hat{\sigma}_z]^\top$ the vector of Pauli spin matrices. The potential and SOC scatterings at the left semiconducting barrier are modeled by

$$\hat{\mathcal{H}}_{\mathrm{L}}^{\mathrm{SMC}} = (V_{\mathrm{L}} d_{\mathrm{L}} \hat{\sigma}_0 + \mathbf{\Omega_L} \cdot \hat{\boldsymbol{\sigma}})\, \delta(z) \tag{6.24}$$

and those at the right barrier by

$$\hat{\mathcal{H}}_{\mathrm{R}}^{\mathrm{SMC}} = (V_{\mathrm{R}} d_{\mathrm{R}} \hat{\sigma}_0 + \mathbf{\Omega_R} \cdot \hat{\boldsymbol{\sigma}})\, \delta(z-d); \tag{6.25}$$

$V_{\mathrm{L\,(R)}}$ and $d_{\mathrm{L\,(R)}}$ are the heights and widths of the deltalike potential barriers, respectively, while the interfacial spin-orbit fields $\mathbf{\Omega_L} = [(\alpha_{\mathrm{L}} - \beta_{\mathrm{L}})k_y, -(\alpha_{\mathrm{L}} + \beta_{\mathrm{L}})k_x, 0]$ and $\mathbf{\Omega_R} = -[(\alpha_{\mathrm{R}} - \beta_{\mathrm{R}})k_y, -(\alpha_{\mathrm{R}} + \beta_{\mathrm{R}})k_x, 0]$ account for both Rashba and (linearized) Dresselhaus terms, parameterized by $\alpha_{\mathrm{L\,(R)}}$ and $\beta_{\mathrm{L\,(R)}}$. Throughout this thesis, we use the C_{2v} crystallographic orientations $\hat{x} \parallel [110]$, $\hat{y} \parallel [\bar{1}10]$, and $\hat{z} \parallel [001]$. The overall negative sign in $\mathbf{\Omega_R}$ accounts for the opposite relative orientation of the spin-orbit fields at the right (metal/superconductor) interface when compared to the left (superconductor/metal) interface. Our formulation is fully consistent with the general spin-orbit fields given in Sec. 2.3 [see Eqs. (2.57) and (2.58)], setting the (z-dependent) Rashba parameters as

$$\alpha_{\mathrm{L}}(z) = \alpha_{\mathrm{L}} \delta(z) \tag{6.26}$$

and

$$\alpha_{\mathrm{R}}(z) = -\alpha_{\mathrm{R}} \delta(z-d), \tag{6.27}$$

and linearizing the Dresselhaus SOC according to

$$\frac{\mathrm{d}}{\mathrm{d}z}\left[\gamma_{\mathrm{L}}(z)\frac{\mathrm{d}}{\mathrm{d}z}\right] \longrightarrow \beta_{\mathrm{L}} \delta(z) \tag{6.28}$$

and

$$\frac{\mathrm{d}}{\mathrm{d}z}\left[-\gamma_{\mathrm{R}}(z)\frac{\mathrm{d}}{\mathrm{d}z}\right] \longrightarrow -\beta_{\mathrm{R}} \delta(z-d). \tag{6.29}$$

We neglect higher-order terms in the spin-orbit fields since earlier studies [250] showed that the dominant contributions to transport quantities, like electrical currents, typically stem from states with small transverse wave vector amplitudes $|\mathbf{k}_\parallel| = (k_x^2 + k_y^2)^{1/2}$. Accounting for SOC terms linear in k_x and k_y is fully sufficient to properly capture all these states. This approach strongly simplifies our model since including higher-order SOC terms would require to extract the additionally appearing SOC parameters from first-principles calculations, which could become intricate for the complicated band structures of heterojunctions. At the same time, our formulation still covers all expected qualitative trends and is hence well justified. Finally, the s-wave superconducting pairing potential is approximated by

$$\hat{\Delta}_{\mathrm{S}}(z) = |\Delta_{\mathrm{S}}| \hat{\sigma}_0 \Big[\Theta(-z) + \mathrm{e}^{\mathrm{i}\phi_{\mathrm{S}}} \Theta(z-d)\Big], \tag{6.30}$$

where $|\Delta_{\mathrm{S}}|$ indicates the isotropic energy gap in the two (similar) superconductors. Since the Josephson current is driven by the phase difference across the junction, it is common to set the left superconductor's phase to zero and the right one's phase to ϕ_{S}. The latter determines then simultaneously the total phase difference across the junction.

6.2.1.1 Bogoljubov-de Gennes scattering states

At first, we solve the Bogoljubov-de Gennes equation, Eq. (6.21), separately in the three regions of the Josephson junction to obtain the corresponding scattering states. In general, we need to distinguish between *four* possible scenarios of incident quasiparticles from the left superconductor: (1) an incoming spin-up electronlike quasiparticle, (2) an incoming spin-down electronlike quasiparticle, (3) an incoming spin-up holelike quasiparticle, and (4) an incoming spin-down holelike quasiparticle. Processes (3) and (4) are necessary to include the possibility of incoming electronlike quasiparticles from the right superconductor. To compute the total current flow in the end, we need to determine the imbalance between the electronlike quasiparticles moving to the right and those moving to the left, and thus cannot simply ignore electronlike quasiparticles incident from the right. It is again worth to mention that we do not need to deal with Cooper pairs. All ingredients required to compute the Josephson current are incorporated in the quasiparticle picture via the striking Andreev reflection process.

Since the transverse wave vector $\mathbf{k}_\parallel = [k_x,\, k_y,\, 0]^\top$ (parallel to the semiconductor interfaces) is conserved, substituting the ansatz

$$\Psi(\mathbf{r}) = \psi(z)\, \mathrm{e}^{\mathrm{i}(\mathbf{k}_\parallel \cdot \mathbf{r}_\parallel)}, \tag{6.31}$$

where $\mathbf{r}_\parallel = [x,\, y,\, 0]^\top$ contains the transverse spatial coordinates, into the Bogoljubov-de Gennes equation [see Eq. (6.21)] reduces our description to an effectively one-dimensional scattering problem along $\hat{z}$. The most general solution for the $\hat{z}$-projected scattering states $\psi(z)$ reads then

$$\begin{aligned}\psi^{(i)}(z<0) = \psi^{(i)}_{\text{incoming}}(z<0) &+ \mathcal{A}^{(i)} \begin{bmatrix} u \\ 0 \\ v \\ 0 \end{bmatrix} \mathrm{e}^{-\mathrm{i}q_{z,\mathrm{e}}z} + \mathcal{B}^{(i)} \begin{bmatrix} 0 \\ u \\ 0 \\ v \end{bmatrix} \mathrm{e}^{-\mathrm{i}q_{z,\mathrm{e}}z} \\ &+ C^{(i)} \begin{bmatrix} v \\ 0 \\ u \\ 0 \end{bmatrix} \mathrm{e}^{\mathrm{i}q_{z,\mathrm{h}}z} + \mathcal{D}^{(i)} \begin{bmatrix} 0 \\ v \\ 0 \\ u \end{bmatrix} \mathrm{e}^{\mathrm{i}q_{z,\mathrm{h}}z}\end{aligned} \tag{6.32}$$

in the left superconductor ($z < 0$),

$$\begin{aligned}\psi^{(i)}(0<z<d) = &\mathcal{E}^{(i)}\chi_{\mathrm{e}}^{\uparrow}\mathrm{e}^{\mathrm{i}k_{z,\mathrm{e}}^{\uparrow}z} + \mathcal{F}^{(i)}\chi_{\mathrm{e}}^{\downarrow}\mathrm{e}^{\mathrm{i}k_{z,\mathrm{e}}^{\downarrow}z} + \mathcal{G}^{(i)}\chi_{\mathrm{h}}^{\uparrow}\mathrm{e}^{-\mathrm{i}k_{z,\mathrm{h}}^{\uparrow}z} + \mathcal{H}^{(i)}\chi_{\mathrm{h}}^{\downarrow}\mathrm{e}^{-\mathrm{i}k_{z,\mathrm{h}}^{\downarrow}z} \\ &+ \mathcal{I}^{(i)}\chi_{\mathrm{e}}^{\uparrow}\mathrm{e}^{-\mathrm{i}k_{z,\mathrm{e}}^{\uparrow}z} + \mathcal{J}^{(i)}\chi_{\mathrm{e}}^{\downarrow}\mathrm{e}^{-\mathrm{i}k_{z,\mathrm{e}}^{\downarrow}z} + \mathcal{K}^{(i)}\chi_{\mathrm{h}}^{\uparrow}\mathrm{e}^{\mathrm{i}k_{z,\mathrm{h}}^{\uparrow}z} + \mathcal{L}^{(i)}\chi_{\mathrm{h}}^{\downarrow}\mathrm{e}^{\mathrm{i}k_{z,\mathrm{h}}^{\downarrow}z}\end{aligned} \tag{6.33}$$

in the ferromagnet ($0 < z < d$), and

$$\begin{aligned}\psi^{(i)}(z>d) = &\mathcal{M}^{(i)} \begin{bmatrix} u\mathrm{e}^{\mathrm{i}\phi_{\mathrm{S}}} \\ 0 \\ v \\ 0 \end{bmatrix} \mathrm{e}^{\mathrm{i}q_{z,\mathrm{e}}z} + \mathcal{N}^{(i)} \begin{bmatrix} 0 \\ u\mathrm{e}^{\mathrm{i}\phi_{\mathrm{S}}} \\ 0 \\ v \end{bmatrix} \mathrm{e}^{\mathrm{i}q_{z,\mathrm{e}}z} \\ &+ \mathcal{O}^{(i)} \begin{bmatrix} v\mathrm{e}^{\mathrm{i}\phi_{\mathrm{S}}} \\ 0 \\ u \\ 0 \end{bmatrix} \mathrm{e}^{-\mathrm{i}q_{z,\mathrm{h}}z} + \mathcal{P}^{(i)} \begin{bmatrix} 0 \\ v\mathrm{e}^{\mathrm{i}\phi_{\mathrm{S}}} \\ 0 \\ u \end{bmatrix} \mathrm{e}^{-\mathrm{i}q_{z,\mathrm{h}}z}\end{aligned} \tag{6.34}$$

in the right superconductor ($z > d$). The superscript i, with $i \in \{1; 2; 3; 4\}$, refers to the four possible quasiparticle injection scenarios ordered in the same way as stated above; the related scattering states

differ in the incoming waves and the respective scattering coefficients. The incoming waves are given by

$$\psi^{(1)}_{\text{incoming}}(z<0) = [u,\,0,\,v,\,0]^{\top}\,\mathrm{e}^{\mathrm{i}q_{z,\mathrm{e}}z}, \tag{6.35}$$

$$\psi^{(2)}_{\text{incoming}}(z<0) = [0,\,u,\,0,\,v]^{\top}\,\mathrm{e}^{\mathrm{i}q_{z,\mathrm{e}}z}, \tag{6.36}$$

$$\psi^{(3)}_{\text{incoming}}(z<0) = [v,\,0,\,u,\,0]^{\top}\,\mathrm{e}^{-\mathrm{i}q_{z,\mathrm{h}}z}, \tag{6.37}$$

and

$$\psi^{(4)}_{\text{incoming}}(z<0) = [0,\,v,\,0,\,u]^{\top}\,\mathrm{e}^{-\mathrm{i}q_{z,\mathrm{h}}z}. \tag{6.38}$$

The physical meaning of the scattering coefficients can be unraveled if we consider, for instance, an incoming spin-up electronlike quasiparticle [process (1)]. That quasiparticle can either be reflected back as an electronlike quasiparticle, which we call specular reflection, or undergo Andreev reflection, getting reflected as a holelike quasiparticle. The spin-resolved reflection coefficients (owing to the SOC, each process can additionally be accompanied by a spin flip) are denoted by $\mathcal{A}^{(1)}$ and $\mathcal{B}^{(1)}$, as well as by $\mathcal{C}^{(1)}$ and $\mathcal{D}^{(1)}$. Analogously, $\mathcal{M}^{(1)}$, $\mathcal{N}^{(1)}$, $\mathcal{O}^{(1)}$, and $\mathcal{P}^{(1)}$ indicate electronlike and holelike transmissions into the right superconducting electrode. For the three remaining injection processes, the coefficients (which are of course different as we explicitly emphasized by the differing superscripts) can be interpreted in a similar manner.

The $\hat{z}$-components of the electronlike and holelike quasiparticles' wave vectors inside the superconductors can be written as

$$q_{z,\mathrm{e}} = q_{z,\mathrm{e}}(E) = \sqrt{\frac{2m}{\hbar^2}\left(\mu + \sqrt{E^2 - |\Delta_{\mathrm{S}}|^2}\right) - \mathbf{k}_{\parallel}^2} \tag{6.39}$$

and

$$q_{z,\mathrm{h}} = q_{z,\mathrm{h}}(E) = \sqrt{\frac{2m}{\hbar^2}\left(\mu - \sqrt{E^2 - |\Delta_{\mathrm{S}}|^2}\right) - \mathbf{k}_{\parallel}^2}, \tag{6.40}$$

while those for electrons and holes in the ferromagnet with a spin parallel ($\uparrow$; meaning spin up) or antiparallel ($\downarrow$; meaning spin down) to the magnetization direction $\hat{\mathbf{m}}$ are

$$k^{\uparrow(\downarrow)}_{z,\mathrm{e}} = k^{\uparrow(\downarrow)}_{z,\mathrm{e}}(E) = \sqrt{\frac{2m}{\hbar^2}\left[\mu + E + (-)\frac{\Delta_{\mathrm{XC}}}{2}\right] - \mathbf{k}_{\parallel}^2} \tag{6.41}$$

and

$$k^{\uparrow(\downarrow)}_{z,\mathrm{h}} = k^{\uparrow(\downarrow)}_{z,\mathrm{h}}(E) = \sqrt{\frac{2m}{\hbar^2}\left[\mu - E + (-)\frac{\Delta_{\mathrm{XC}}}{2}\right] - \mathbf{k}_{\parallel}^2}; \tag{6.42}$$

the BCS coherence factors $u = u(E)$ and $v = v(E)$ are the same as specified in Eq. (6.8). The spinors for electrons and holes inside the ferromagnet have the form

$$\chi^{\uparrow(\downarrow)}_{\mathrm{e}} = \left[\chi^{\uparrow(\downarrow)},\,0\right]^{\top} \qquad \text{and} \qquad \chi^{\uparrow(\downarrow)}_{\mathrm{h}} = \left[0,\,\chi^{\downarrow(\uparrow)}\right]^{\top}, \tag{6.43}$$

both containing

$$\chi^{\uparrow(\downarrow)} = \frac{1}{\sqrt{2}}\begin{bmatrix}(-)\sqrt{1+(-)\cos(\Theta)}\,\mathrm{e}^{-\mathrm{i}\Phi} \\ \sqrt{1-(+)\cos(\Theta)}\end{bmatrix}. \tag{6.44}$$

The still unknown coefficients in the scattering states in Eqs. (6.32)–(6.34) are finally determined by applying the interfacial ($z = 0$) boundary conditions

$$\psi^{(i)}(z)\big|_{z=0_-} = \psi^{(i)}(z)\big|_{z=0_+}, \tag{6.45}$$

$$\psi^{(i)}(z)\big|_{z=d_-} = \psi^{(i)}(z)\big|_{z=d_+}, \tag{6.46}$$

$$\left(-\frac{\hbar^2}{2m}\frac{\mathrm{d}}{\mathrm{d}z} + V_{\mathrm{L}} d_{\mathrm{L}}\right)\hat{\eta}\psi^{(i)}(z)\big|_{z=0_+} + \begin{bmatrix} \mathbf{\Omega_L}\cdot\hat{\boldsymbol{\sigma}} & \hat{0} \\ \hat{0} & -(\mathbf{\Omega_L}\cdot\hat{\boldsymbol{\sigma}}) \end{bmatrix}\psi^{(i)}(z)\big|_{z=0_+} = -\frac{\hbar^2}{2m}\frac{\mathrm{d}}{\mathrm{d}z}\hat{\eta}\psi^{(i)}(z)\big|_{z=0_-}, \tag{6.47}$$

and

$$\left(\frac{\hbar^2}{2m}\frac{\mathrm{d}}{\mathrm{d}z} + V_{\mathrm{R}} d_{\mathrm{R}}\right)\hat{\eta}\psi^{(i)}(z)\big|_{z=d_-} + \begin{bmatrix} \mathbf{\Omega_R}\cdot\hat{\boldsymbol{\sigma}} & \hat{0} \\ \hat{0} & -(\mathbf{\Omega_R}\cdot\hat{\boldsymbol{\sigma}}) \end{bmatrix}\psi^{(i)}(z)\big|_{z=d_-} = \frac{\hbar^2}{2m}\frac{\mathrm{d}}{\mathrm{d}z}\hat{\eta}\psi^{(i)}(z)\big|_{z=d_+}, \tag{6.48}$$

with

$$\hat{\eta} = \begin{bmatrix} \hat{\sigma}_0 & \hat{0} \\ \hat{0} & -\hat{\sigma}_0 \end{bmatrix}, \tag{6.49}$$

to the states ($\hat{0}$ is the two-by-two zero matrix) and numerically solving the resulting linear systems of equations by means of a (generalized) LU Decomposition algorithm [181]. Due to the complexity of the problem, deducing analytical expressions would not provide much insight. Once all scattering coefficients are uniquely identified, we can continue and compute the Josephson current flowing through our S/F/S model junction.

6.2.1.2 Josephson current – Furusaki-Tsukada approach

Furusaki and Tsukada [266] developed a Green's function-based approach that initially related the Andreev reflection coefficients in S/N/S junctions' Bogoljubov-de Gennes scattering states to the respective Josephson current flow. In the following, we will adapt this description to our present case that essentially deals with S/F/S junctions and interfacial SOC.

Without loss of generality (the current is conserved), we conveniently choose one vertical plane inside the asymptotic region of the left superconductor ($z < 0$) to evaluate the Josephson current. We denote the generic ($\hat{z}$-projected) four-component wave function, fulfilling the junction's Bogoljubov-de Gennes equation at a fixed time t, by $\psi(z;t) = \left[\psi_{\mathrm{e}}^{\uparrow}(z;t),\, \psi_{\mathrm{e}}^{\downarrow}(z;t),\, \psi_{\mathrm{h}}^{\uparrow}(z;t),\, \psi_{\mathrm{h}}^{\downarrow}(z;t)\right]^{\top}$; recall that we used precisely the same notation earlier in Chap. 3. The transverse wave vector $\mathbf{k}_{\parallel}$, which plays a crucial role when modeling the interfacial SOC in our three-dimensional configuration, is treated as a constant for the moment. The *continuity equation* for the electrical current is then found to be

$$\frac{\partial}{\partial t}q(z;t) + \frac{\partial}{\partial z}j_z^q(z;t) + s(z;t) = 0, \tag{6.50}$$

where

$$q(z;t) = -e\left\{\left[\left|\psi_{\mathrm{e}}^{\uparrow}(z;t)\right|^2 + \left|\psi_{\mathrm{e}}^{\downarrow}(z;t)\right|^2\right] - \left[\left|\psi_{\mathrm{h}}^{\uparrow}(z;t)\right|^2 + \left|\psi_{\mathrm{h}}^{\downarrow}(z;t)\right|^2\right]\right\} \tag{6.51}$$

represents the *electrical charge density* and

$$j_z^q(z;t) = -\frac{e\hbar}{m}\left\{\mathrm{Im}\left[\left(\psi_{\mathrm{e}}^{\uparrow}(z;t)\right)^* \frac{\mathrm{d}}{\mathrm{d}z}\psi_{\mathrm{e}}^{\uparrow}(z;t)\right] + \mathrm{Im}\left[\left(\psi_{\mathrm{e}}^{\downarrow}(z;t)\right)^* \frac{\mathrm{d}}{\mathrm{d}z}\psi_{\mathrm{e}}^{\downarrow}(z;t)\right]\right.$$
$$\left. + \mathrm{Im}\left[\left(\psi_{\mathrm{h}}^{\uparrow}(z;t)\right)^* \frac{\mathrm{d}}{\mathrm{d}z}\psi_{\mathrm{h}}^{\uparrow}(z;t)\right] + \mathrm{Im}\left[\left(\psi_{\mathrm{h}}^{\downarrow}(z;t)\right)^* \frac{\mathrm{d}}{\mathrm{d}z}\psi_{\mathrm{h}}^{\downarrow}(z;t)\right]\right\} \tag{6.52}$$

the corresponding *electrical current density*. As usual, e refers to the positive elementary charge and $\mathrm{Im}\{\ldots\}$ to the imaginary part. Due to the fact that holelike quasiparticles enter the Bogoljubov-de Gennes modeling as time-reversed electronlike quasiparticles, holelike contributions appear in the electrical charge density in Eq. (6.51) with opposite signs when compared to electronlike terms. In strong contrast to nonsuperconducting systems, the electrical current continuity equation in superconductors contains the additional *source term*

$$s(z;t) = \frac{4e}{\hbar}|\Delta_{\mathrm{S}}|\mathrm{Im}\left[\left(\psi_{\mathrm{e}}^{\uparrow}(z;t)\right)^{*}\psi_{\mathrm{h}}^{\uparrow}(z;t) + \left(\psi_{\mathrm{e}}^{\downarrow}(z;t)\right)^{*}\psi_{\mathrm{h}}^{\downarrow}(z;t)\right], \tag{6.53}$$

which especially accounts for supercurrents not included in $j_z^q(z;t)$. If superconductivity would be absent (i.e., $|\Delta_{\mathrm{S}}| = 0$), this source-term immediately vanishes (as expected since there will be no supercurrent in that case).

We focus on the *DC Josephson effect*. Since our system's Bogoljubov-de Gennes equation, Eq. (6.21), is fully *time-independent*, also the charge and current densities, as well as the source term, do not explicitly depend on time in our case. This observation allows us to rewrite the current continuity equation in Eq. (6.50) in its *stationary* form

$$\frac{\partial}{\partial z}\left[j_z^q(z) + \int_0^z \mathrm{d}z'\, s(z')\right] = 0. \tag{6.54}$$

Equation (6.54) suggests that the conserved electrical current, which is simply the bare Josephson (super)current we want to compute, is given by $\left[j_z^q(z) + \int_0^z \mathrm{d}z'\, s(z')\right]$. The only remaining task for us is to find explicit, *thermally averaged*, expressions for these two individual supercurrent contributions.

By means of *Matsubara Green's functions* [140, 268], the thermally averaged current contribution associated with $j_z^q(z)$ can be extracted from

$$\left\langle j_z^q(z)\right\rangle_{\mathrm{thermal}} = \frac{e\hbar}{4\mathrm{i}m}k_{\mathrm{B}}T\lim_{z'\to z}\left(\frac{\partial}{\partial z'} - \frac{\partial}{\partial z}\right)\sum_{\mathbf{k}_{\parallel}}\sum_{\omega_n}\mathrm{Tr}\left\{\check{\mathcal{G}}(z,z';\mathrm{i}\omega_n)\right\}, \tag{6.55}$$

where $\mathrm{Tr}\{\check{\mathcal{G}}(z,z';\mathrm{i}\omega_n)\}$ indicates the trace taken over the four-by-four Nambu representation of the imaginary-time Matsubara Green's function $\check{\mathcal{G}}(z,z';\mathrm{i}\omega_n)$ with the discrete set of fermionic Matsubara frequencies

$$\omega_n = (2n+1)\pi k_{\mathrm{B}}T \tag{6.56}$$

for integer n. As before, k_{B} denotes Boltzmann's constant and T the temperature. Note that Eq. (6.55) is no longer restricted to one particular $\mathbf{k}_{\parallel}$ as in our initial considerations. Instead, summing over all $\mathbf{k}_{\parallel}$ includes the current contributions from *all* transverse channels of our three-dimensional junction. We provide a detailed derivation of Eq. (6.55) in Appendix B. Despite its formal complexity (our system's Matusbara Green's function is unknown and still needs to be determined), the presented approach brings along several advantages when compared to Kulik's Andreev bound state method (see Sec. 6.1). First, Eq. (6.55) is very general and can, in principle, be applied to any ballistic Josephson junction, given that one has access to the system's Matsubara Green's function. Second, summing over all Matsubara frequencies ω_n includes simultaneously supercurrent contributions originating from the quasiparticle continuum; those parts are not captured by the Andreev bound states which are always located just inside the superconducting gap. Although the continuum contribution is negligible in symmetric Josephson junctions, as the one we are studying, the situation can strongly differ in more complicated geometries [269]. Therefore, we consider the Furusaki-Tsukada approach as the more general description for ballistic Josephson junctions.

To evaluate Eq. (6.55) further, and to eventually find the Josephson current, we need to construct the Matsubara Green's function $\check{\mathcal{G}}(z,z';\mathrm{i}\omega_n)$ in the left superconductor of our junction. Since this requires a

few rather technical steps, we draw the reader's attention to Appendix B for the detailed calculations. After substituting the analytical expression for $\check{\mathcal{G}}(z,z';\mathrm{i}\omega_n)$ into Eq. (6.55), we end up with

$$\left\langle j_z^q(z)\right\rangle_{\text{thermal}} = \frac{ek_\mathrm{B}T}{4\hbar}\,|\Delta_\mathrm{S}(T)| \sum_{\mathbf{k}_\parallel}\sum_{\omega_n} \frac{1}{\sqrt{\omega_n^2+|\Delta_\mathrm{S}(T)|^2}}\left[q_{z,\mathrm{e}}(\mathrm{i}\omega_n)+q_{z,\mathrm{h}}(\mathrm{i}\omega_n)\right] \times\left[\frac{\mathcal{C}^{(1)}(\mathrm{i}\omega_n)+\mathcal{D}^{(2)}(\mathrm{i}\omega_n)}{q_{z,\mathrm{e}}(\mathrm{i}\omega_n)} - \frac{\mathcal{A}^{(3)}(\mathrm{i}\omega_n)+\mathcal{B}^{(4)}(\mathrm{i}\omega_n)}{q_{z,\mathrm{h}}(\mathrm{i}\omega_n)}\right] \mathrm{e}^{-\mathrm{i}\left[q_{z,\mathrm{e}}(\mathrm{i}\omega_n)-q_{z,\mathrm{h}}(\mathrm{i}\omega_n)\right]z}. \quad (6.57)$$

The electronlike and holelike wave vectors inside the superconductor, $q_{z,\mathrm{e}}(\mathrm{i}\omega_n)$ and $q_{z,\mathrm{h}}(\mathrm{i}\omega_n)$, are obtained from those in Eqs. (6.39)–(6.40) through analytically continuing the excitation energies $E \longmapsto \mathrm{i}\omega_n$. The Andreev reflection coefficients $\mathcal{C}^{(1)}(\mathrm{i}\omega_n)$, $\mathcal{D}^{(2)}(\mathrm{i}\omega_n)$, $\mathcal{A}^{(3)}(\mathrm{i}\omega_n)$, and $\mathcal{B}^{(4)}(\mathrm{i}\omega_n)$ are related to the ones introduced in the scattering states [see especially Eq. (6.32)] via the same analytic continuation $E \longmapsto \mathrm{i}\omega_n$. Since we regard our junction at a finite temperature T, we need to properly account for the temperature dependence of the superconducting gap, $|\Delta_\mathrm{S}(T\neq 0)| = |\Delta_\mathrm{S}(0)|\tanh(1.74\sqrt{T_\mathrm{C}/T-1})$, where T_C resembles the superconducting electrodes' critical temperature and $|\Delta_\mathrm{S}(0)|$ their energy gap at zero temperature.

For accessing the total Josephson current, we are still lacking an analytical formula for the source term's contribution. Making use of Eqs. (6.50) and (6.57), we deduce its integrated *thermal average*

$$\int_0^z \mathrm{d}z'\left\langle s(z')\right\rangle_{\text{thermal}} = \frac{ek_\mathrm{B}T}{4\hbar}\,|\Delta_\mathrm{S}(T)| \sum_{\mathbf{k}_\parallel}\sum_{\omega_n} \frac{1}{\sqrt{\omega_n^2+|\Delta_\mathrm{S}(T)|^2}}\left[q_{z,\mathrm{e}}(\mathrm{i}\omega_n)+q_{z,\mathrm{h}}(\mathrm{i}\omega_n)\right] \times\left[\frac{\mathcal{C}^{(1)}(\mathrm{i}\omega_n)+\mathcal{D}^{(2)}(\mathrm{i}\omega_n)}{q_{z,\mathrm{e}}(\mathrm{i}\omega_n)} - \frac{\mathcal{A}^{(3)}(\mathrm{i}\omega_n)+\mathcal{B}^{(4)}(\mathrm{i}\omega_n)}{q_{z,\mathrm{h}}(\mathrm{i}\omega_n)}\right] \left\{1-\mathrm{e}^{-\mathrm{i}\left[q_{z,\mathrm{e}}(\mathrm{i}\omega_n)-q_{z,\mathrm{h}}(\mathrm{i}\omega_n)\right]z}\right\}. \quad (6.58)$$

Putting both contributions, Eqs. (6.57) and (6.58), together, the *thermally averaged* Josephson current flow I_J through the considered junction eventually reads as

$$\begin{aligned} I_\mathrm{J} &= \left\langle j_z^q(z)\right\rangle_{\text{thermal}} + \int_0^z \mathrm{d}z'\left\langle s(z')\right\rangle_{\text{thermal}} \\ &= \frac{ek_\mathrm{B}T}{4\hbar}\,|\Delta_\mathrm{S}(T)| \sum_{\mathbf{k}_\parallel}\sum_{\omega_n} \frac{1}{\sqrt{\omega_n^2+|\Delta_\mathrm{S}(T)|^2}}\left[q_{z,\mathrm{e}}(\mathrm{i}\omega_n)+q_{z,\mathrm{h}}(\mathrm{i}\omega_n)\right] \\ &\qquad\times\left[\frac{\mathcal{C}^{(1)}(\mathrm{i}\omega_n)+\mathcal{D}^{(2)}(\mathrm{i}\omega_n)}{q_{z,\mathrm{e}}(\mathrm{i}\omega_n)} - \frac{\mathcal{A}^{(3)}(\mathrm{i}\omega_n)+\mathcal{B}^{(4)}(\mathrm{i}\omega_n)}{q_{z,\mathrm{h}}(\mathrm{i}\omega_n)}\right]. \end{aligned} \quad (6.59)$$

Inspecting Eq. (6.59) emphasizes the great role Andreev reflections play for the generation of supercurrents. All information that is necessary to quantify the Josephson current is fully included into the Andreev reflection coefficients.[1] Although only the coefficients belonging to *spin-conserving* Andreev reflections explicitly enter Eq. (6.59), those implicitly contain also the impact of *spin-flip* Andreev reflections via the scattering states' interfacial matching. Therefore, the presented approach is well applicable even if (interfacial) SOC is present. We note for another time that the Andreev reflection coefficients belonging to incident electronlike and holelike quasiparticles appear with opposite

[1] In fact, one would obtain additional current contributions that originate from specular reflection processes. Evaluating the trace of the Matsubara Green's function yields specular reflection terms whose prefactors scale with $\left|u(\mathrm{i}\omega_n)\right|^2+\left|v(\mathrm{i}\omega_n)\right|^2=1$, whereas the Andreev reflection terms' prefactors are proportional to $u(\mathrm{i}\omega_n)v(\mathrm{i}\omega_n)\propto -|\Delta_\mathrm{S}(T)|/[(2n+1)\pi k_\mathrm{B}T] = -1/[(2n+1)\pi\times 0.06]\gg 1$ (assuming a temperature of $T=0.1T_\mathrm{C}$ which we will also consider for our numerical calculations later on). The Josephson current is therefore indeed dominated by Andreev reflections, while the specular reflection currents become negligibly small and do not need to be included into the Furusaki-Tsukada formula.

signs in the Josephson current formula. This is the direct consequence of the time-reversed character holes possess in the Bogoljubov-de Gennes picture. As long as SOC is absent, the Andreev reflection coefficients for incoming spin-up and spin-down electrons (holes) are equal, i.e., $\mathcal{C}^{(1)}(\mathrm{i}\omega_n) = \mathcal{D}^{(2)}(\mathrm{i}\omega_n)$ and $\mathcal{A}^{(3)}(\mathrm{i}\omega_n) = \mathcal{B}^{(4)}(\mathrm{i}\omega_n)$, and Eq. (6.59) reduces to the earlier result of Furusaki and Tsukada [266].

The powerful Furusaki-Tsukada approach allows us to investigate Josephson currents through a variety of realistic S/F/S junctions. For that purpose, we determine the Andreev reflection coefficients within the aforementioned Bogoljubov-de Gennes scattering description and substitute the results into Eq. (6.59) to get I_J. The sum over the transverse channels, labeled by $\mathbf{k}_\parallel$, is conveniently approximated by the integral

$$\sum_{\mathbf{k}_\parallel} \ldots \longrightarrow \frac{\mathcal{A}}{4\pi^2} \int \mathrm{d}^2\mathbf{k}_\parallel \ldots, \tag{6.60}$$

which can be numerically efficiently evaluated by means of a Gaussian quadrature algorithm [181]; $\mathcal{A}$ denotes the interfacial cross-section area.

6.2.2 Discussion of results

After completing the modeling of our system, we can discuss concrete calculations of the Josephson current flowing through representative S/F/S junctions, paying special attention to demonstrating various ways that might provide the reliable control of 0-π transitions necessary for practical applications. We use realistic values for the zero-temperature superconducting gap, $|\Delta_\mathrm{S}(0)| \approx 2.5\,\mathrm{meV}$, and the superconducting material's critical temperature, $T_\mathrm{C} \approx 16\,\mathrm{K}$. These values are, for example, comparable to those in the s-wave superconducting V_3Ga alloy [197]. For the chemical potential, we take a typical value of $\mu = 10^3|\Delta_\mathrm{S}(0)|$. All presented simulations are performed at a low temperature of $T = 0.1T_\mathrm{C}$.

To shorten the notation, we define several dimensionless junction parameters. The strength of the potential barrier at the left semiconducting interface is captured by the BTK-like [164] parameter $Z_\mathrm{L} = (2mV_\mathrm{L}d_\mathrm{L})/(\hbar^2 k_\mathrm{F})$, where k_F still abbreviates the Fermi wave vector. Similarly, $Z_\mathrm{R} = (2mV_\mathrm{R}d_\mathrm{R})/(\hbar^2 k_\mathrm{F})$ determines the right semiconducting barrier's strength. For convenience, we suppose that both semiconducting tunneling barriers are identical, i.e., $Z_\mathrm{L} = Z_\mathrm{R} = Z$, where Z could be either $Z = 0$ in the ideal case of perfectly transparent interfaces or $Z = 1$. The latter corresponds to the more realistic experimental configuration of ultrathin GaAs barriers [251] with height $V_\mathrm{L} = V_\mathrm{R} = 0.75\,\mathrm{eV}$ and width $d_\mathrm{L} = d_\mathrm{R} \approx 0.40\,\mathrm{nm}$ (assuming $m \approx m_\mathrm{e}$ and $k_\mathrm{F} = \sqrt{2m\mu}/\hbar \approx 8 \times 10^7\,\mathrm{cm}^{-1}$, which is a typical value for metals [182]). The ferromagnet's *effective* spin polarization is again quantified by $P = (\Delta_\mathrm{XC}/2)/\mu$, whereas $\lambda^\alpha_{\mathrm{L\,(R)}} = [2m\alpha_{\mathrm{L\,(R)}}]/\hbar^2$ and $\lambda^\beta_{\mathrm{L\,(R)}} = [2m\beta_{\mathrm{L\,(R)}}]/\hbar^2$ parameterize the Rashba and Dresselhaus SOC strengths at the two semiconducting interfaces. As mentioned within our model, the specific SOC parameters usually depend strongly on the complicated band structure of the junction and would need to be extracted from first-principles calculations [250]. Therefore, we treat the SOC measures $\lambda^\alpha_{\mathrm{L\,(R)}}$ and $\lambda^\beta_{\mathrm{L\,(R)}}$ rather as tunable phenomenological model parameters. This kind of modeling, strongly simplifying the analytical description, still replicates all physical properties of S/F/S Josephson junctions and might become relevant to extract the SOC parameters of real devices from fitting our model to future experimental data. A compact summary of all introduced junction parameters can be found in Tab. 6.1.

6.2.2.1 Geometrical control of 0-π transitions

Following our earlier explanations, 0-π transitions in S/F/S Josephson junctions originate from the *oscillating* proximity-induced superconducting pairing potential inside the ferromagnetic region [re-

Tab. 6.1: Dimensionless system parameters, classifying the considered S/F/S junction.

$P = \dfrac{\Delta_{\mathrm{XC}}/2}{\mu}$	effective spin polarization in the ferromagnet
$Z_{\mathrm{L}} = \dfrac{2mV_{\mathrm{L}}d_{\mathrm{L}}}{\hbar^2 k_{\mathrm{F}}}$	potential barrier strength at the left semiconducting interface
$Z_{\mathrm{R}} = \dfrac{2mV_{\mathrm{R}}d_{\mathrm{R}}}{\hbar^2 k_{\mathrm{F}}}$	potential barrier strength at the right semiconducting interface
$\lambda_{\mathrm{L}}^{\alpha} = \dfrac{2m\alpha_{\mathrm{L}}}{\hbar^2}$	Rashba SOC strength at the left semiconducting interface
$\lambda_{\mathrm{R}}^{\alpha} = \dfrac{2m\alpha_{\mathrm{R}}}{\hbar^2}$	Rashba SOC strength at the right semiconducting interface
$\lambda_{\mathrm{L}}^{\beta} = \dfrac{2m\beta_{\mathrm{L}}}{\hbar^2}$	Dresselhaus SOC strength at the left semiconducting interface
$\lambda_{\mathrm{R}}^{\beta} = \dfrac{2m\beta_{\mathrm{R}}}{\hbar^2}$	Dresselhaus SOC strength at the right semiconducting interface

call Fig. 6.2(b)]. If the pairing potential's oscillation period $p \propto 1/\Delta_{\mathrm{XC}}$ [243] and the ferromagnet's thickness d match in such a way that the pairing potentials at the junction interfaces differ in sign, the accumulated intrinsic π-phase shift in the Josephson current-phase relations switches the junctions from their initial 0- to their π-states and reverses the direction of the current flows. The most natural ways to control 0-π transitions are therefore either changing the ferromagnetic link's exchange splitting (spin polarization) Δ_{XC} (P) or its thickness d. To mutually compare all our numerical results, we keep the spin polarization $P = 0.7$ fixed and rather vary d. This value of P refers to iron as a representative ferromagnetic material. If not otherwise stated, the ferromagnet's magnetization direction is aligned perpendicular to the semiconducting interfaces (along $\hat{z}$).

Figure 6.6 illustrates the Josephson current's dependence on the dimensionless effective thickness of the ferromagnetic layer $k_{\mathrm{F}}d$ and for the two mentioned specific strengths of symmetric potential barriers. Since $k_{\mathrm{F}} = \sqrt{2m\mu}/\hbar \approx 8 \times 10^7\,\mathrm{cm}^{-1}$ is characteristic for the regarded iron interlayer [182], specifying $k_{\mathrm{F}}d$ uniquely determines this layer's thickness ($k_{\mathrm{F}}d = 8$ indicates, for instance, an iron layer with thickness $d \approx 1\,\mathrm{nm}$). At the moment, neither Rashba nor Dresselhaus SOC are present ($\lambda_{\mathrm{L}}^{\alpha} = \lambda_{\mathrm{R}}^{\alpha} = \lambda_{\mathrm{L}}^{\beta} = \lambda_{\mathrm{R}}^{\beta} = 0$). For a numerical evaluation of the Josephson current by means of Eq. (6.59), the superconducting phase difference across the junctions is set to a constant value, i.e., to $\phi_{\mathrm{S}} = 0.3\pi$. Alternatively, one may also directly compute the respective critical currents, which is numerically a bit more demanding and does basically not yield different qualitative results.

Even in junctions with perfectly transparent interfaces ($Z_{\mathrm{L}} = Z_{\mathrm{R}} = 0$; see the blue curve in Fig. 6.6), the clearly apparent oscillations of the Josephson current with increasing $k_{\mathrm{F}}d$ unambiguously reflect the underlying proximity-induced pairing potential's oscillatory variations. For certain values of $k_{\mathrm{F}}d$, the current direction (sign) can indeed reverse, marking the junctions' unique 0-π transition regimes. Moreover, the previously discussed superimposed exponential damping of the induced pairing potential (on length scales of the coherence length) suppresses the Cooper pair transfer through the ferromagnetic inter-

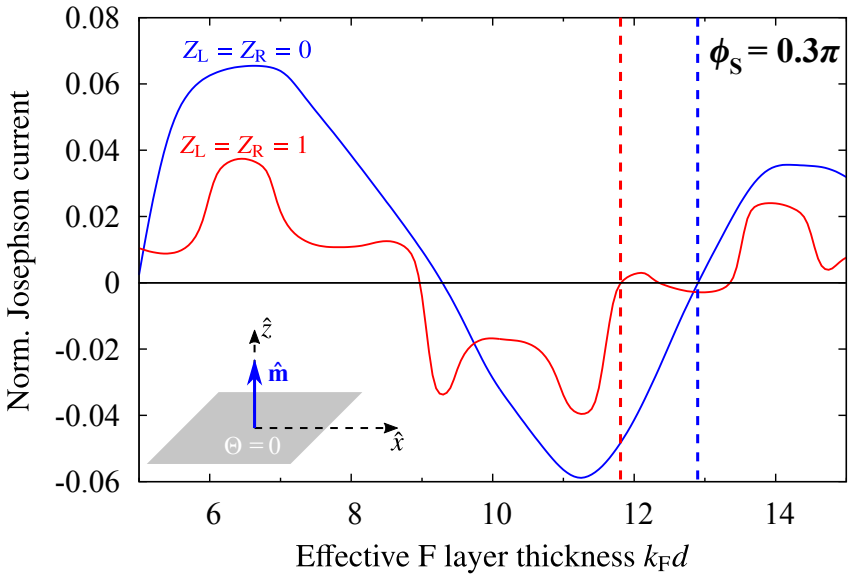


Fig. 6.6: Calculated dependence of S/F/S junctions' Josephson current [normalized according to $(I_J e R_N)/[|\Delta_S(0)|\pi]$, where $R_N = (2\pi^2\hbar)/(\mathcal{A}e^2k_F^2)$ refers to the resistance of a perfectly transparent (three-dimensional) N/N/N tunnel junction] on the effective thickness of the ferromagnetic layer $k_F d$, once for perfectly transparent interfaces ($Z_L = Z_R = 0$) and once for weak interfacial semiconducting barriers ($Z_L = Z_R = 1$); the superconducting phase difference $\phi_S = 0.3\pi$ is fixed. The ferromagnet's spin polarization $P = 0.7$ corresponds to iron, its magnetization orientation points along $\hat{z}$ (see illustration), and neither Rashba nor Dresselhaus SOC are present ($\lambda_L^\alpha = \lambda_R^\alpha = \lambda_L^\beta = \lambda_R^\beta = 0$). The dashed lines indicate the vicinity of one representative π-0 transition, for which we present the Josephson current-phase relations in Fig. 6.7.

layer and simultaneously decreases the overall Josephson current amplitudes as $k_F d$ gets enhanced. This feature becomes also visible in terms of the presented I_J-$k_F d$ relation's exponentially damped envelope.

The overall behavior gets more striking if weak interfacial barriers ($Z_L = Z_R = 1$; see the red curve in Fig. 6.6) are considered. Although the initially present current oscillations, coming from the induced pairing potential and causing the 0-π transitions, as well as the Josephson current's general damping trend with an increase of $k_F d$, are still there, additional and more intricate oscillations get superimposed on the I_J-$k_F d$ relation. More detailed studies [270] confirmed that finite interfacial scattering potentials can indeed generate strongly pronounced quasiparticle tunneling resonances that effectively lead to such a complicated I_J-$k_F d$ dependence. Owing to the fact that the scattering potentials' strengths are mostly determined by the semiconducting material and the junctions' geometrical configurations, these novel oscillations were termed *geometrical oscillations*. Regarding the positions of the 0-π transition points, our simulations predict that stronger potential scattering at the semiconducting interfaces shifts the transition points between 0- and π-states to lower $k_F d$ (since interfacial scatterings additionally decrease the pairing potential's oscillation period).

For a more thorough characterization of the 0-π transitions, we focus on one representative transition between the π- and the 0-state regime (highlighted by the blue and red dashed lines for perfectly transparent semiconducting interfaces and for weak interfacial barriers in Fig. 6.6) and evaluate the Josephson current-phase relations for several $k_F d$-values in the vicinity of this transition; all other junction parameters are kept the same as before. The obtained results are shown in Figs. 6.7(a) and 6.7(b). We start again with analyzing the case of perfectly transparent interfaces [see Fig. 6.7(a)]. Increasing the ferromagnet's effective thickness $k_F d$ from $k_F d \approx 12.6$ to $k_F d \approx 13.3$ triggers a transition from the *pure* π-state [$I_J \propto -\sin(\phi_S)$] to the *pure* 0-state [$I_J \propto \sin(\phi_S)$] regime. The slight deviations from perfectly

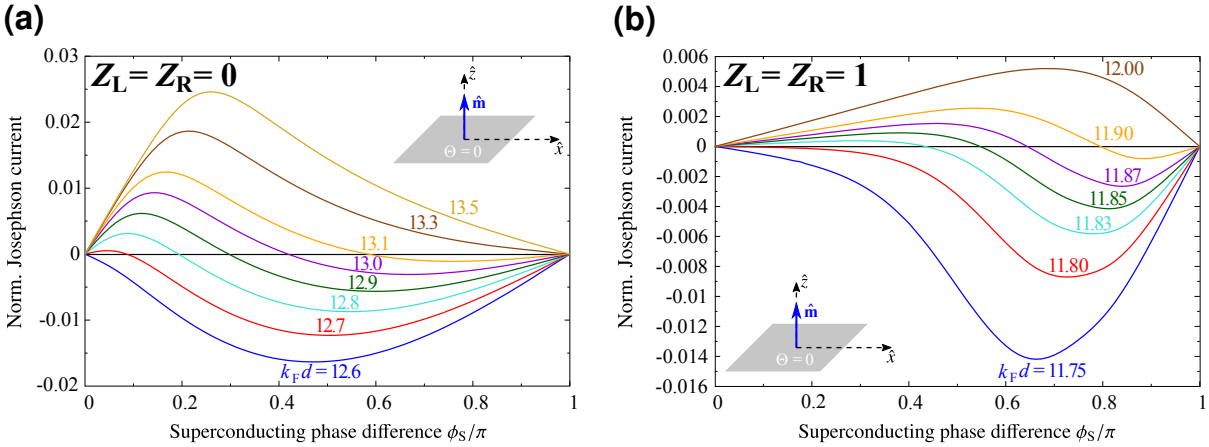


Fig. 6.7: **(a)** Calculated Josephson current-phase relations for S/F/S junctions (Josephson current is normalized in the same way as in Fig. 6.6) with perfectly transparent interfaces ($Z_L = Z_R = 0$) and for various indicated effective thicknesses of the ferromagnetic layer $k_F d$ in the vicinity of one π-0 transition. The ferromagnet's spin polarization $P = 0.7$ corresponds to iron, its magnetization orientation points along $\hat{z}$ (see illustration), and neither Rashba nor Dresselhaus SOC are present ($\lambda_L^\alpha = \lambda_R^\alpha = \lambda_L^\beta = \lambda_R^\beta = 0$). **(b)** Same calculation as in **(a)**, but in the additional presence of weak interfacial barriers ($Z_L = Z_R = 1$).

sinusoidal Josephson current-phase relations stem from the finite ferromagnetic layer thickness and the nonzero temperature assumed in our calculations. In the intermediate $k_F d$-region, $k_F d \approx 12.7 \ldots 13.1$, both π- and 0-states coexist. The presence of higher-harmonic terms leads to highly nonsinusoidal current-phase relations there. Weak interfacial semiconducting barriers shift the 0-π transition points to lower $k_F d$ [see Fig. 6.7(b)]. To facilitate the same π-0 transition we regarded before, one now needs to enhance $k_F d$ just from $k_F d \approx 11.75$ to $k_F d \approx 12.0$. Furthermore, the intermediate region, in which 0- and π-states coexist, is nearly four times narrower ($k_F d \approx 11.8 \ldots 11.9$) than in junctions with perfectly transparent interfaces, probably making "dirty" junctions more auspicious candidates for tailoring 0-π transitions [244, 271].

We finally recovered two ways that allow for an experimental control of 0-π transitions: altering the ferromagnet's thickness or reducing the junctions' interfacial transparency. Since both of them are crucially related to changing the junction geometry (e.g., depositing thicker metallic links or different semiconducting materials at the interfaces), we accumulate those ways in the term *geometrical control* of 0-π transitions. Similar characteristics were predicted by Radović and coworkers [272]. Since the transitions are essentially effectuated by the interplay of the ferromagnetic region's exchange interaction, which itself causes the oscillating proximity-induced superconducting order parameter, and its thickness, tuning the ferromagnet's exchange splitting (spin polarization) while keeping its thickness constant would likewise give rise to 0-π transitions [272–274].

6.2.2.2 Electrical control of 0-π transitions

All ways to control 0-π transitions we introduced up to now have one great disadvantage in common. They all require the fabrication of many similar S/F/S Josephson junctions, which differ in the thickness of the ferromagnetic layer (in the ferromagnet's exchange splitting) or in their interfacial transparency. Depending on the extensively analyzed interplay of their ingredients, some of these junctions will then be 0-junctions (the 0-state is the junctions' ground state) and the others π-junctions (with the π-state as their ground state). For technical applications, especially for realizing two-level systems as the essential basis for quantum computing [57–64], it would be much more convenient to deal

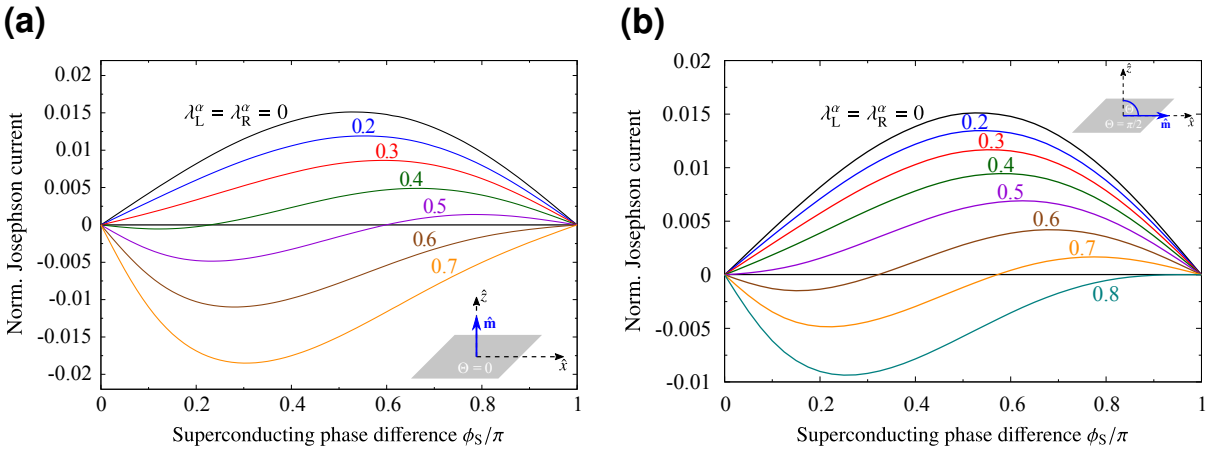


Fig. 6.8: (a) Calculated Josephson current-phase relations for S/F/S junctions (the Josephson current is normalized in the same way as in Fig. 6.6) with weak interfacial barriers ($Z_L = Z_R = 1$) and for various indicated (moderate) Rashba SOC strengths; Dresselhaus SOC is absent ($\lambda_L^\beta = \lambda_R^\beta = 0$). The ferromagnet's spin polarization $P = 0.7$ and its effective thickness of $k_F d = 8.2$ correspond to a roughly 1 nm thick iron layer with a magnetization pointing along $\hat{z}$ (see illustration). **(b)** Same calculation as in **(a)**, but assuming that the ferromagnet's magnetization is aligned along $\hat{x}$ (see illustration).

with only one single junction that can be switched from its 0- to its π-state by means of an external source. The interfacial SOC in our model junctions offers one promising way to accomplish that. For simplifying our analyses, we assume that the Rashba SOC is the dominant SOC mechanism inside the semiconducting barriers, while the Dresselhaus part can be neglected ($\lambda_L^\beta = \lambda_R^\beta = 0$). Finite Dresselhaus SOC would, nonetheless, only cause minor quantitative (but no qualitative) changes. The strengths of the interfacial Rashba SOC are mostly determined by the interface materials and can additionally be (slightly) tuned by electrical gating [250, 251, 275–277].

To study the impact of interfacial Rashba SOC on the Josephson current flowing through a representative S/F/S junction, Figs. 6.8(a) and 6.8(b) illustrate the junction's current-phase relations for various strengths of *symmetric* Rashba SOC $\lambda_L^\alpha = \lambda_R^\alpha$ and two different magnetization orientations in the ferromagnet. *Antisymmetric* Rashba SOC at the semiconducting interfaces ($\lambda_L^\alpha = -\lambda_R^\alpha$) is unrealistic in real junctions and not considered here. The ferromagnetic material's spin polarization $P = 0.7$ and its effective thickness $k_F d = 8.2$ mimic a (roughly) 1 nm thick iron interlayer. Reducing the junction's interfacial transparency (by increasing the barrier parameters) would not significantly alter the qualitative outcomes. Therefore, we restrict our considerations to the realistic weak barrier strengths of $Z_L = Z_R = 1$.

First, we focus on the situation in which the ferromagnet's magnetization is oriented perpendicular to the semiconducting interfaces (along $\hat{z}$); see Fig. 6.8(a). In the absence of interfacial Rashba SOC ($\lambda_L^\alpha = \lambda_R^\alpha = 0$), the junction realizes its stable 0-state and the Josephson current approaches the sinusoidal current-phase dependence (with the aforementioned slight deviations due to the barriers, the finite thickness of the ferromagnetic layer, and nonzero temperature). Already *moderately* increasing the Rashba SOC strengths initially decreases the Josephson current's amplitudes, reverses its direction (sign) triggering a transition into the junction's π-state, and eventually amplifies the π-state current again. Characteristic for the intermediate region ($\lambda_L^\alpha = \lambda_R^\alpha \approx 0.40 \ldots 0.55$), separating pure 0- from pure π-states, are the nonsinusoidal current-phase variations we encountered earlier. For an experimental realization of these features, it is important to stress that the modulations of the Rashba SOC strengths, necessary to switch the junction regime from 0 to π, are thus moderate [changing $\lambda_{L\,(R)}^\alpha$ by 0.1 corresponds to a bare change of $\alpha_{L\,(R)}$ by 0.4 eV Å^2] that they can be controlled fully electrically (by gating) for appropriate barrier widths, without any need to modify the geometrical composition of the junction. Such an *electri-*

cal control might offer novel experimental possibilities to implement π-junctions. The physical origin of the SOC-induced 0-π transitions is basically the same as pointed out previously (geometrical control). Interfacial SOC acts like an additional, spin- and transverse momentum-dependent, barrier. As a result, enhancing the SOC strength simultaneously reduces the interfacial transparency and leads to 0-π transitions, just as increasing the potential barrier strength does in diffusive junctions [244, 271]. Notably, already moderate Rashba SOC of about $\lambda_{\mathrm{L}}^{\alpha} = \lambda_{\mathrm{R}}^{\alpha} = 0.7$ is sufficient that the junction's critical current exceeds the one in the absence of SOC, which is a clear evidence for SOC-controlled long-range spin-triplet superconducting proximity effects inside the ferromagnet. Interfacial spin-flip scatterings open another current channel for spin-triplet Cooper pairs, which acts together with the spin-singlet pairs and enlarges the total Josephson current. Further increasing the Rashba SOC parameters [not explicitly shown in Fig. 6.8(a)] amplifies the Josephson current even more, reaching its maximum for $\lambda_{\mathrm{L}}^{\alpha} = \lambda_{\mathrm{R}}^{\alpha} \approx 2.0$. The maximal critical current is about one order of magnitude larger than in the case without any SOC. In fact, such strongly pronounced triplet supercurrents are most relevant to Josephson junctions with half-metallic links. Although spin-singlet Cooper pairs can actually not leak into the latter (as there are only majority-spin states available, while singlet pairs involve both majority- *and* minority-spin electrons) and the junctions' Josephson current should (nearly) completely vanish, Keizer *et al.* [74] reported on a sizable supercurrent component in the half-metallic CrO_2 of diffusive NbTiN/CrO_2/NbTiN junctions over long (compared to the coherence length) length scales of more than 1 μm. This supercurrent must be attributed to *long-range* spin-triplet Cooper pairs, which are generated via interfacial spin flips [74, 75]. Within our model, these spin flips are enabled by the interfacial SOC, explaining the significant enhancement of the current with increasing SOC strength. Nevertheless, we mentioned above that SOC also introduces more interfacial scattering. This scattering starts to dominate the current at $\lambda_{\mathrm{L}}^{\alpha} = \lambda_{\mathrm{R}}^{\alpha} \gtrsim 4.0$ and eventually reverses the critical current's increasing trend.

In the second scenario that we consider, the ferromagnet's magnetization gets aligned parallel to the junction's semiconducting interfaces (along $\hat{x}$); see Fig. 6.8(b). While the concrete orientation of the magnetization has no influence on the Josephson current as long as SOC is fully absent, the interplay of *nonzero* SOC and magnetism typically causes marked current magnetoanisotropies. These phenomena deserve a more thorough investigation, which we will provide subsequently (magnetic control). Despite the present current magnetoanisotropies [the Josephson current for magnetization along $\hat{x}$ really differs from the one for magnetization along $\hat{z}$, as one sees comparing Fig. 6.8(b) to Fig. 6.8(a)], the main qualitative physical features are not modified. Slightly increasing the Rashba SOC measures once again switches the junction from the 0- to the π-state regime. Compared to the previously discussed case (magnetization along $\hat{z}$), 0-π transitions require now slightly larger Rashba SOC and also the coexistence region of 0- and π-states ($\lambda_{\mathrm{L}}^{\alpha} = \lambda_{\mathrm{R}}^{\alpha} \approx 0.55 \ldots 0.75$) is somewhat larger. The current's nonmonotonic dependence on the Rashba parameters, reflecting the initial decrease during the 0-π transition, followed by an increase owing to the generation of triplet Cooper pairs and the final decrease due to the stronger interfacial scattering, becomes again evident. Nevertheless, the in-plane magnetization (magnetization along $\hat{x}$) critical current is always remarkably smaller than the related one for perpendicular magnetization (magnetization along $\hat{z}$), demonstrating that in-plane magnetizations act against the formation of triplet Cooper pairs and suppress the triplet contribution to the current. The maximal critical current in the presence of SOC [again appearing for $\lambda_{\mathrm{L}}^{\alpha} = \lambda_{\mathrm{R}}^{\alpha} \approx 2.0$; not explicitly shown in Fig. 6.8(b)], composed of both singlet and triplet parts, still clearly exceeds the junction's critical current without SOC. This finding, valid for our *ballistic vertical* system, is well distinct from earlier studies of *diffusive lateral* junctions [78], in which in-plane magnetization allows for a finite long-range spin-triplet supercurrent only in the *simultaneous* presence of Rashba *and* Dresselhaus SOC.

6.2.2.3 Magnetic control of 0-π transitions

While the remarkable enhancement of the Josephson current due to the spin-triplet Cooper pair generation is a first precursor of SOC, magnetoanisotropic transport properties are a clear fingerprint. Such magnetoanisotropies were initially observed in the tunneling conductance spectra of normal-conducting Fe/GaAs/Au junctions [251] and could be theoretically understood within a tunneling picture that is similar to ours (but nonsuperconducting) [250]. Fitting the experimental data to the model could not only qualitatively replicate the anisotropic behavior of this so-called TAMR, but additionally allowed to extract effective SOC parameters for the GaAs barrier. Much larger anisotropies were recently predicted for the tunneling conductance of ferromagnet/semiconductor/superconductor junctions [176, 182], mainly caused by the great sensitivity of Andreev reflections to the magnetization orientation in the presence of SOC inside the semiconductor. The related phenomenon got therefore termed MAAR. Pronounced magnetic anisotropies are moreover expected to occur in the critical (Josephson) current of lateral superconductor/nanowire/superconductor Josephson junctions with an applied Zeeman field [273, 274, 278], as well as in *diffusive* vertical S/F/S junctions [279]. Mostly inspired by the latter, we demonstrate the existence of giant magnetoanisotropies in our *ballistic* model system and conclude that the critical current's huge magnetosensitivity brings along another way for switching between 0- and π-junctions.

Two configurations need to be distinguished when investigating transport anisotropies in vertical junctions: *out-of-plane*, in which the ferromagnetic region's magnetization orientation $\hat{\mathbf{m}}$ is rotated along its polar angle Θ in a plane perpendicular to the magnetic layer and *in-plane* with changes of $\hat{\mathbf{m}}$'s azimuthal angle Φ in a plane parallel to the magnetic layer. To quantify the anisotropies in these two cases, we define the *out-of-plane magnetoanisotropic Josephson current (MAJC)* as

$$\mathrm{MAJC}_{[1\bar{1}0]}(\Theta) = \left.\frac{\left|I^{\mathrm{crit.}}(0,\Phi)\right| - \left|I^{\mathrm{crit.}}(\Theta,\Phi)\right|}{\left|I^{\mathrm{crit.}}(\Theta,\Phi)\right|}\right|_{\Phi=-90^\circ} \tag{6.61}$$

and the *in-plane MAJC* as

$$\mathrm{MAJC}_{[110]}(\Phi) = \left.\frac{\left|I^{\mathrm{crit.}}(\Theta,0)\right| - \left|I^{\mathrm{crit.}}(\Theta,\Phi)\right|}{\left|I^{\mathrm{crit.}}(\Theta,\Phi)\right|}\right|_{\Theta=90^\circ}, \tag{6.62}$$

with $I^{\mathrm{crit.}} = \pm \max_{\phi_S}\left[|I_J(\phi_S)|\right]$ indicating the junctions' *oriented* critical current, which is basically given by the critical current counted positively for 0- and negatively for π-state junction regimes. In general, the out-of-plane MAJC depends on Φ, but we choose $\Phi = -90^\circ$ as its reference. While the out-of-plane MAJC remains finite even if only Rashba *or* Dresselhaus SOC is present, the in-plane MAJC immediately vanishes if one of the two SOC mechanisms is not there. A comprehensive analysis of the physical origin of the normal-state TAMR analog is given in Ref. [250]. To summarize the main points, the presence of either Rashba *or* Dresselhaus SOC at the interface between a ferromagnet and a nonferromagnetic component is sufficient to induce a magnetoanisotropic energy shift between the ferromagnet's up- and down-spin subbands, which scales according to [280]

$$\Delta E \propto \boldsymbol{\Omega}_{\mathbf{R}\,(\mathbf{D})} \cdot \hat{\mathbf{m}}; \tag{6.63}$$

$\boldsymbol{\Omega}_{\mathbf{R}\,(\mathbf{D})}$ denotes the Rashba (Dresselhaus) spin-orbit field, given by Eqs. (2.57) and (2.58). This magnetoanisotropic band splitting is apparently nonzero as long as the magnetization gets rotated in the out-of-plane configuration, leading to the out-of-plane magnetoanisotropic transport features. In-plane magnetization rotations, however, do not give rise to an anisotropic band splitting. The reason for that is the invariance of $\boldsymbol{\Omega}_{\mathbf{R}}$ and $\boldsymbol{\Omega}_{\mathbf{D}}$ under in-plane rotations. In-plane magnetoanisotropies originate

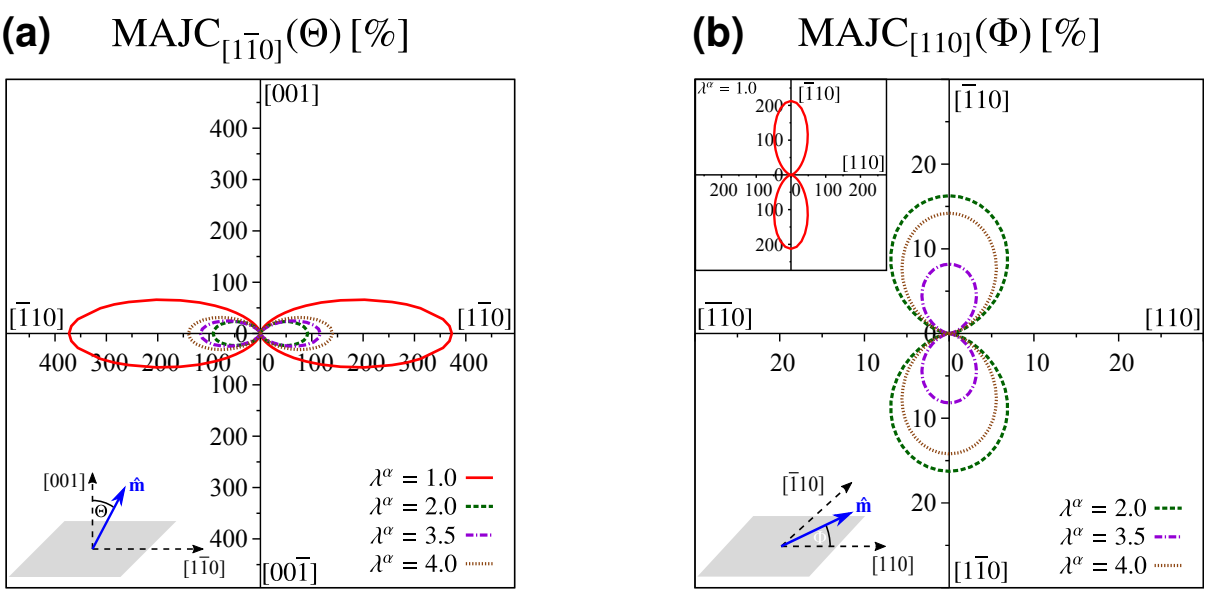


Fig. 6.9: (a) Calculated angular dependence of the *out-of-plane MAJC*, MAJC$_{[1\bar{1}0]}(\Theta)$, with respect to the [1$\bar{1}$0] crystallographic reference axis (see illustration), for S/F/S junctions with weak interfacial barriers ($Z_L = Z_R = 1$) and for various indicated Rashba SOC strengths $\lambda_L^\alpha = \lambda_R^\alpha = \lambda^\alpha$; weak Dresselhaus SOC $\lambda_L^\beta = \lambda_R^\beta = 0.2$ is additionally present. The ferromagnet is again composed of a roughly 1 nm thick iron layer. **(b)** Calculated angular dependence of the *in-plane MAJC*, MAJC$_{[110]}(\Phi)$, with respect to the [110] crystallographic reference axis (see illustration), for the same junction parameters as in **(a)**. The in-plane MAJC for $\lambda^\alpha = 1.0$ is shown in the inset.

instead from the *interference of Rashba and Dresselhaus spin-orbit fields*, which leads to a characteristic C_{2v}-symmetric field. Therefore, in-plane magnetoanisotropies are commonly used as a sensitive probe of interfacial symmetries, while out-of-plane anisotropy measurements offer a robust probe for the general presence of interfacial SOC.

Figures 6.9(a) and 6.9(b) present the out-of-plane and in-plane MAJCs' computed angular dependencies for the same representative S/F/S Josephson junction that we focused on when outlining the electrical control of 0-π transitions (i.e., $Z_L = Z_R = 1$, $P = 0.7$, and $k_F d = 8.2$). To observe both finite out-of-plane and in-plane MAJCs, we now assume nonzero Rashba and Dresselhaus SOC strengths. We again treat the SOC parameters phenomenologically and suppose that Rashba SOC is still the dominant mechanism. The related parameters get varied from $\lambda_L^\alpha = \lambda_R^\alpha = 1.0$ to $\lambda_L^\alpha = \lambda_R^\alpha = 4.0$, whereas the Dresselhaus measures are fixed at weak values of $\lambda_L^\beta = \lambda_R^\beta = 0.2$; stronger Dresselhaus SOC would not dramatically alter the discussed outcomes. As expected from our qualitative statements, the intricate interplay of ferromagnetism and interfacial SOC gives rise to marked out-of-plane and in-plane magnetoanisotropies in the critical current. The spin-orbit fields' characteristic C_{2v}-symmetry gets one-to-one transferred into the MAJCs' angular dependence, clearly indicating that the effects precisely stem from this interplay. The overall amplitudes of the out-of-plane and in-plane MAJCs are quite sensitive to (and scale nonmonotonically with) changes of the Rashba SOC strengths. Most notably, the maximal calculated MAJC ratios are all *giant* when compared to TAMR values in similar nonsuperconducting junctions. For example, the in-plane TAMR in normal-state Fe/GaAs/Au junctions is typically less than 1 % [251], while the out-of-plane (superconducting) MAJC can reach 373 % for $\lambda_L^\alpha = \lambda_R^\alpha = 1.0$. Even larger values would be possible for different junction parameters, e.g., for other interlayer thicknesses [267]. Rotating the magnetization direction influences the Josephson current in an extreme way in the vicinity of 0-π transitions, where only a slight change of the magnetization orientation might be enough to

suddenly reverse the current as we shall see in the next paragraph. As a result, especially giant MAJC amplitudes invariably occur close to 0-π transition points. This is exactly the case for $\lambda_{\mathrm{L}}^{\alpha} = \lambda_{\mathrm{R}}^{\alpha} = 1.0$, initiating $\mathrm{MAJC}_{[1\bar{1}0]}(\Theta = \pi/2) \approx 373\,\%$ in the out-of-plane and $\mathrm{MAJC}_{[110]}(\Phi = \pi/2) \approx 213\,\%$ in the in-plane scenario [see the red curves in Figs. 6.9(a) and 6.9(b)]. At greater Rashba SOC strengths, the junction already switched to a pure π-state and the MAJC ratios are heavily damped, but still sizable compared to normal-conducting TAMRs. This observation provides another way to experimentally detect 0-π transitions from MAJC measurements, without the need to change other system parameters.

Coming back to our actual motivation and the discussions within the previous paragraph, we can exploit the Josephson current's marked magnetoanisotropies to demonstrate another way for controlling 0-π transitions. The oriented critical current's dependence on the polar magnetization angle Θ and the effective ferromagnet thickness $k_{\mathrm{F}}d$ is presented in Fig. 6.10(a). For simplicity, the azimuthal magnetization angle is fixed to $\Phi = 0$. The ferromagnetic material's spin polarization is still $P = 0.7$, the potential barriers are again $Z_{\mathrm{L}} = Z_{\mathrm{R}} = 1$, and for the Rashba SOC parameters, we take $\lambda_{\mathrm{L}}^{\alpha} = \lambda_{\mathrm{R}}^{\alpha} = 0.8$. Since we are predominantly interested in the out-of-plane anisotropies, we can furthermore set the Dresselhaus SOC to zero ($\lambda_{\mathrm{L}}^{\beta} = \lambda_{\mathrm{R}}^{\beta} = 0$). As long as the magnetization is aligned perpendicular to the semiconducting interface ($\Theta = 0$), the junction always stays in its pure π-state, indicated by the corresponding negative oriented critical current. In a narrow window close to $k_{\mathrm{F}}d = 14$, however, simply rotating the magnetization towards the interface suddenly reverses the Josephson current direction (positive oriented critical current) and signifies π-0 transitions. In that spirit, the pronounced magnetoanisotropies in our model junction offer a *magnetic control* of 0-π transitions. To unravel the impact of the Rashba SOC strengths (which regulate the magnetoanisotropies and simultaneously also the magnetically controlled 0-π transitions), Fig. 6.10(b) plots the critical current *amplitudes* as a function of the magnetization polar angle Θ and for various Rashba SOC parameters. The effective ferromagnet thickness $k_{\mathrm{F}}d = 14.0$ refers to the range in which the 0-π transitions reliably appear; all remaining parameters are the same as before. The results shown in Fig. 6.10(a) correspond to the $\lambda_{\mathrm{L}}^{\alpha} = \lambda_{\mathrm{R}}^{\alpha} = 0.8$ (red) curve in Fig. 6.10(b). Transitions between π- and 0-states occur now as dips in the $|I^{\mathrm{crit.}}|$-Θ relations. Our simulations suggest that the magnetization rotation-induced transitions are extremely sensitive to the Rashba SOC, which might make an experimental implementation of this kind of control nontrivial. For instance, increasing the Rashba parameters just from $\lambda_{\mathrm{L}}^{\alpha} = \lambda_{\mathrm{R}}^{\alpha} = 0.8$ to $\lambda_{\mathrm{L}}^{\alpha} = \lambda_{\mathrm{R}}^{\alpha} = 1.0$ shifts the first π-0 transition from $\Theta \approx 0.11\pi$ to $\Theta \approx 0.40\pi$. For slightly weaker ($\lambda_{\mathrm{L}}^{\alpha} = \lambda_{\mathrm{R}}^{\alpha} = 0.7$) or stronger ($\lambda_{\mathrm{L}}^{\alpha} = \lambda_{\mathrm{R}}^{\alpha} = 1.1$) Rashba SOC, transitions are already no longer possible and the junction remains in a pure 0- in the first and in a pure π-state in the second situation. Similar phenomena were predicted for lateral superconductor/nanowire/superconductor junctions with Zeeman splitting and uniform Rashba coupling [273, 274, 278], and eventually complete our systematic study of various possibilities that might bring the desired experimental control of 0-π transitions.

At the end of this part, let us shortly comment on the experimental realizability of our theoretical predictions. To observe MAJC effects, a junction geometry comparable to previous TAMR studies [251] might be used. The magnetization direction inside the ferromagnetic link gets typically rotated by an external magnetic field. In order to implement this in our considered S/F/S structure, special attention must be paid to the following aspects. On the one hand, the thicknesses of the massive superconducting electrodes have to be in such a range that the applied magnetic field can still penetrate the ferromagnet and align the magnetization there. On the other hand, one needs to ensure that the magnetic field does not (significantly) suppress the superconducting electrodes' properties. One alternative perspective could be the usage of dysprosium magnets [281], in which the magnetization can be aligned by an external magnetic field and remains in that orientation even when the field gets removed. The dysprosium layer inside the Josephson junction could thus be premagnetized by applying an appropriate magnetic field that suitably rotates its magnetization. After turning off the field, the magnetic layer is still magnetized along the chosen direction and the related MAJC amplitude can be measured, without disturbing the

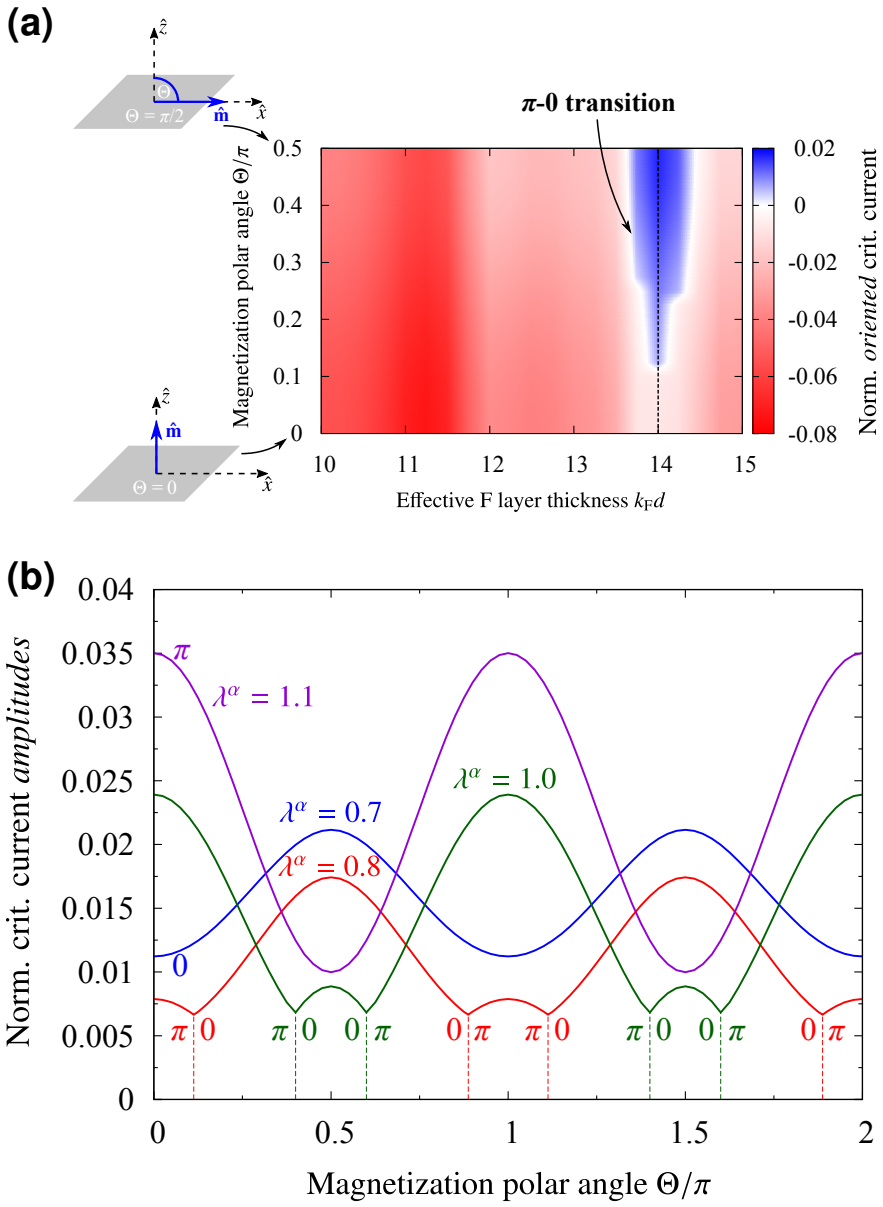


Fig. 6.10: (a) Calculated (normalized as in Fig. 6.6) *oriented* critical current (amplitude of the critical current with positive sign in the 0- and negative sign in the π-state) as a function of the magnetization polar angle Θ and effective thickness of the ferromagnetic layer $k_F d$ for S/F/S junctions with weak interfacial barriers ($Z_L = Z_R = 1$); the magnetization azimuthal angle is fixed to $\Phi = 0$. The ferromagnet's spin polarization $P = 0.7$ still corresponds to iron, the Rashba SOC parameters are $\lambda_L^\alpha = \lambda_R^\alpha = 0.8$, and Dresselhaus SOC is again absent ($\lambda_L^\beta = \lambda_R^\beta = 0$). The oriented critical current's sign change around $k_F d = 14.0$ (white regions) marks transitions from π- to 0-junction regimes. **(b)** Calculated dependence of the critical current *amplitudes* $|I^{\text{crit.}}|$ (normalized as in Fig. 6.6) on the magnetization polar angle Θ for one *specific* S/F/S junction, classified through the parameters $Z_L = Z_R = 1$, $P = 0.7$, $k_F d = 14.0$, $\lambda_L^\beta = \lambda_R^\beta = 0$, and for various indicated Rashba SOC strengths $\lambda_L^\alpha = \lambda_R^\alpha = \lambda^\alpha$. Dips indicate transitions between 0- and π-states; the related junction states (0 or π) are additionally emphasized in the plot.

superconducting features. Moreover, junctions with superconducting NbN contacts attracted lots of attention quite recently [185]. Owing to their large critical fields ($H_C > 16\,T$), Josephson junctions with NbN electrodes might also be of special interest to investigate the predicted MAJC. The magnetic fields necessary to tilt the magnetization in ferromagnets are much smaller than NbN's critical field (typically, 0.1 T up to a few tesla are large enough for aligning ferromagnets' magnetization) and do therefore not compete with superconductivity.

6.3 Ballistic S/F/I/F/S Josephson spin-valve junctions

Since its initial discovery by Jullière in 1975 [9], the TMR effect has evolved into a widely investigated phenomenon and has become indispensable in modern information technology. Jullière observed that the electrical resistance of magnetic tunnel junctions, composed of two ferromagnetic electrodes (iron and cobalt) separated by a thin semiconducting barrier (germanium), depends in a remarkable manner on the relative magnetization orientations in the two ferromagnetic regions. In particular, an antiparallel alignment of the magnetization orientations gives rise to a larger electrical resistance (smaller tunneling current flow) than a parallel magnetization configuration. As the tunneling currents basically originate from tunneling of electrons through the ferromagnet/semiconductor/ferromagnet spin valve, Jullière's results suggest that antiparallel magnetized ferromagnetic bilayers generically suppress sequential electron tunneling. To stress the unique connections between electron tunneling on the one and the junction resistances' strong magnetization sensitivity on the other hand, the effect was finally termed TMR. To understand the physical origin of the TMR, Jullière formulated a simple qualitative picture that we illustrate in Fig. 6.11. Assuming, for simplicity, that tunneling conserves spin (spin-flip tunneling is not present in the absence of SOC), we can split the total tunneling current into its two spin-resolved contributions stemming from the up- and down-spin channels, respectively. Spin-up (spin-down) electrons in the left ferromagnetic electrode are only allowed to tunnel into unoccupied spin-up (spin-down) states in the right ferromagnet. Let us initially consider the parallel magnetization configuration in which majority-spin electrons have the same spin (say, spin up) in both electrodes. A schematical sketch of the junction can be found in Fig. 6.11(a), while Fig. 6.11(A) simultaneously illustrates the tunneling in the DOS picture. Tunneling currents are mostly determined by the tunneling of electrons with energies close to the Fermi level ε_F. Applying a (small) bias voltage to the junction (necessary to measure electrical transport), however, slightly shifts the spin subbands (and likewise the Fermi level) in the right ferromagnet. As a result, spin-down electrons can now tunnel into high-DOS states and sustain a sizable tunneling current. Note that, although spin-up electrons are then restricted to tunneling into low-DOS states, there are still much more occupied spin-up than spin-down electronic states in the left electrode so that the up channel likewise maintains a finite tunneling current (smaller than the down channel though).

Flipping the right ferromagnet's magnetization to realize the antiparallel configuration severely modifies the tunneling picture [see Figs. 6.11(b) and 6.11(B)]. While the band structure in the left part remains unaffected, the right ferromagnet's majority and minority bands are exchanged. Spin-up electrons can now only tunnel from majority-spin into minority-spin states. Since there are less unoccupied states in the right than occupied ones in the left electrode, only a certain fraction of spin-up electrons can tunnel, generating a rather low tunneling current contribution. The down-spin channel carries also just a small amount of current since there are much less spin-down electrons originating from the left ferromagnet involved in the tunneling processes (and would even need to tunnel into low-DOS states in the right ferromagnet). This qualitative picture demonstrates that the overall tunneling current flow becomes larger in the parallel (than in the antiparallel) magnetization scenario, explaining the parallel magnetized configuration's smaller electrical resistance. The TMR effect is hence a distinct consequence of spin-

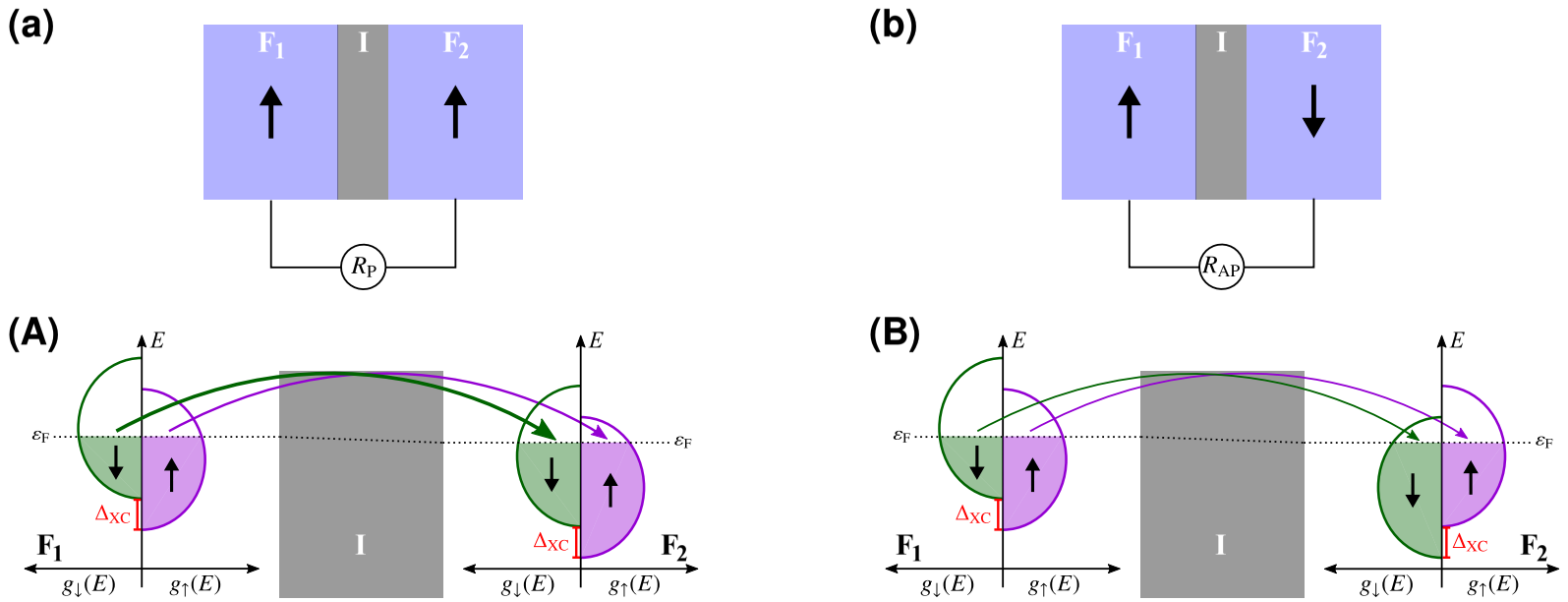


Fig. 6.11: Simplified illustration of Jullière's tunneling picture, explaining TMR effects; adapted from Ref. [27]. **(a)** Schematical sketch of a magnetic tunnel junction, consisting of two ferromagnets (labeled with F_1 and F_2) separated by an insulator (I) (could also be a semiconductor), for *parallel* magnetizations (black arrows). The junction's electrical resistance is denoted by R_P. **(b)** Same junction as in **(a)**, but for *antiparallel* magnetizations; the electrical resistance is now R_{AP}. **(A)** Spin-up, $g_\uparrow(E)$, and spin-down, $g_\downarrow(E)$, electronic DOS (as a function of the electron energy E) in the left and right ferromagnet for *parallel* aligned magnetizations; Δ_{XC} indicates the ferromagnets' exchange energy gap (for simplicity, Δ_{XC} is taken to be the same in both electrodes). Assuming that tunneling from the left into the right ferromagnetic electrode preserves spin, spin-up (spin-down) electrons close to the Fermi level ε_F can only tunnel into unoccupied spin-up (spin-down) states, highlighted by the violet (spin up) and green (spin down) arrows. The magnitudes of the resulting tunneling current contributions are indicated by the arrows' thicknesses. **(B)** Same illustration as in **(A)**, but for *antiparallel* magnetizations. Comparing **(B)** to **(A)** suggests that the overall tunneling current (sum of up- and down-spin current channels) is larger for parallel magnetizations, resulting in a smaller electrical resistance.

polarized tunneling through ferromagnetic spin-valve geometries, caused by the electrodes' intrinsic spin imbalance (exchange splitting).

One commonly accepted possibility to quantify the TMR (other ways are also used in the literature) reads as

$$\mathrm{TMR} = \frac{R_{\mathrm{AP}} - R_{\mathrm{P}}}{R_{\mathrm{P}}} = \frac{G_{\mathrm{P}} - G_{\mathrm{AP}}}{G_{\mathrm{AP}}}, \tag{6.64}$$

where R_{P} (G_{P}) and R_{AP} (G_{AP}) refer to the junction's resistance (conductance) in the parallel and antiparallel magnetization configurations [see Figs. 6.11(a) and 6.11(b) for illustration]. While the initially by Jullière obtained TMR in Fe/Ge/Co junctions of about TMR $\approx 14\,\%$ required liquid-helium temperatures and could never be reproduced, Maekawa and Gävfert [282] later unraveled strong indications of reproducible TMR effects at room temperature. Eventually, it took about 20 years until progresses in fabricating ferromagnet/insulator/ferromagnet (F/I/F) spin-valve junctions revealed pronounced room-temperature TMRs of TMR $\approx 18\,\%$ in high-quality systems [283, 284]. Such clearly measurable magnetoresistance signals, together with the great advantage that expensive cooling mechanisms were no longer required, made the room-temperature TMR an essential ingredient in present-day information devices and considerably extended earlier techniques that were solely based on the GMR – a similar phenomenon meanwhile discovered in ferromagnet/normal metal/ferromagnet (F/N/F) junctions [10, 11]. TMR effects find their probably most auspicious application in the construction of storage devices that combine nonvolatile magnetic storage methods with short access times to efficiently write and read data on future hard drives [6]. First realizations of such MRAM devices [13–16] are already available.[2] Following experimental and theoretical works came to the conclusion that magnetic junctions' maximally reachable TMR ratios crucially depend on the material compositions and could still be optimized a lot. For instance, purely semiconductor-based junctions, relying on ferromagnetic semiconductors as magnetic junction electrodes, exhibit huge TMRs of more than 250 % [285–287].

Similarly to the significant enhancement of MAAR effects in superconducting junctions [176, 182] when compared to their normal-conducting TAMR analogs [250, 251], the coexistence of superconductivity and TMR effects in one single system might also amplify the latter even more and unexpected physics might arise. To exploit most of the theoretical framework presented in Sec. 6.2, we focus on S/F/I/F/S Josephson spin-valve junctions, in which the magnetizations of the two subsequent ferromagnetic layers, separated by a thin insulating barrier, can be aligned either in the parallel or antiparallel configurations. Combining the TMR spin valve with two semi-infinite superconducting electrodes is expected to host an interesting interplay between (superconducting) Josephson and (actually nonsuperconducting) TMR effects, inducing triplet pairing mechanisms [288, 289], tuning the Josephson coupling in magnitude and phase [87, 290, 291], and finally resembling characteristic Josephson current modulations one could exploit to efficiently control the current. Connecting the ferromagnetic parts by means of a thin insulator ensures a larger normal-state resistance [247, 292] and a better current control than it would be the case for F/N/F-based structures [293]. While the first experimental implementations of the considered Josephson-TMR geometry relied on niobium (as superconducting) and nickel (as ferromagnetic) electrodes [294], a recent work [88] successfully integrated TMR physics also into Nb/Fe/Al/Al_2O_3/Fe/Nb Josephson junctions (Al/Al_2O_3 serves as insulating barrier). Despite the experimental progress, theoretical studies covering S/F/I/F/S (or slightly modified) junctions [222, 295–297] were mostly restricted to a quasiclassical treatment to deduce general trends. A systematic parameter study, as performed for superconductor/ferromagnetic semiconductor/semiconductor/ferromagnetic semiconductor/superconductor Josephson junctions [298, 299], has been missing up to now. We therefore generalize the methodology introduced in Sec. 6.2 to S/F/I/F/S junctions. Our subsequent comprehensive analysis of the Josephson current in the parallel and antiparallel magnetization configurations demonstrates the

[2] For more information, visit `https://www.mram-info.com/tags/companies/freescale`.

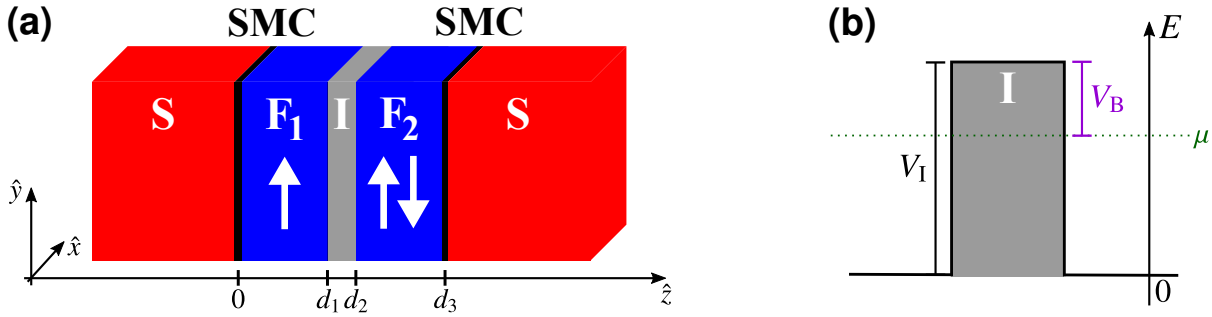


Fig. 6.12: (a) Schematical sketch of the considered *three-dimensional* S/F/I/F/S Josephson spin-valve junction, using the C_{2v} principal crystallographic orientations $\hat{x} \parallel [110]$, $\hat{y} \parallel [\bar{1}10]$, and $\hat{z} \parallel [001]$. Ultrathin semiconducting tunneling barriers (SMC) between the superconductors (S) and the ferromagnetic regions (F) induce interfacial potential and SOC scatterings. The magnetization in the left ferromagnet (labeled with F_1) is fixed along $\hat{y}$, while the one in the right ferromagnet (labeled with F_2) can also point along $\hat{y}$, corresponding to the parallel magnetization configuration, or along $-\hat{y}$, realizing the antiparallel magnetization configuration; the magnetization orientations are indicated by white arrows. Assuming that the thicknesses of F_1, the insulator (I), and F_2 are given by d_{F_1}, d_I, and d_{F_2}, respectively, the spatial $\hat{z}$-coordinates d_1, d_2, and d_3 fulfill $d_1 = d_{F_1}$, $d_2 = d_{F_1} + d_I$, as well as $d_3 = d_{F_1} + d_I + d_{F_2}$. **(b)** The insulating barrier's (I) height (bandgap) V_B is measured with respect to the chemical potential μ within the Bogoljubov-de Gennes approach. The related Hamiltonians therefore contain the potential term $V_I = V_B + \mu$.

existence of a strongly pronounced superconducting "TMR analog", which we term *Josephson tunneling magnetoresistance (JTMR)*.[3] We extend Jullière's TMR tunneling picture to the tunneling of Cooper pairs through the Josephson junctions' spin valve and relate the numerically evaluated currents to the qualitative physical mechanisms, paying again special attention to the magnetization orientations' impact on 0-π transitions. The obtained results, fully agreeing with the initially proposed qualitative trends [295], could provide a valuable guide for tailoring future experimental set-ups to maximize the mutual interplay between Josephson and TMR effects.

6.3.1 Theoretical description

We consider a ballistic *three-dimensional* S/F/I/F/S Josephson junction, whose two semi-infinite superconducting regions (S; spanning $z < 0$ and $z > d_3$) are coupled by means of a ferromagnetic F/I/F spin valve. The two ferromagnets (F) are located at $0 < z < d_1$ as well as $d_2 < z < d_3$, and are separated by the intermediate insulating barrier (I; $d_1 < z < d_2$). As before, the flat interfaces between the superconducting and ferromagnetic components still consist of ultrathin semiconductors, causing potential and SOC scatterings. Figure 6.12(a) shows a schematical sketch of the junction. Since we aim at investigating the interplay of Josephson and TMR effects in the regarded system, we need to differentiate between the parallel and antiparallel F/I/F magnetization configurations. Suppose, for simplicity, that the magnetization in the left ferromagnet (let us call this ferromagnet F_1) is fixed along the $\hat{y}$ reference direction ($\hat{y}$ defines then also the spin-quantization axis), while the right ferromagnet's (F_2's) magnetization orientation can be aligned either along $\hat{y}$ or $-\hat{y}$ to realize the overall parallel or antiparallel magnetization configurations.

[3] To stress the physical analogies between the normal-state TMR, we refer to the superconducting effect as JTMR. Nevertheless, one should be aware that Josephson current flows are dissipationless and the JTMR does not measure an electrical resistance, but rather quantifies the suppression of Cooper pair tunnelings through the spin valve when switching the ferromagnets' relative magnetization orientations. Instead of JTMR, one could alternatively term the phenomenon *Josephson spin-valve effect* (to avoid "resistance" in connection with supercurrents).

To model the junction by means of the Bogoljubov-de Gennes equation in Eq. (6.21), we need to adapt the single-electron Hamiltonian, entering the Bogoljubov-de Gennes Hamiltonian [see Eq. (6.22)], according to

$$\hat{\mathcal{H}}_{\mathrm{e}} = \left(-\frac{\hbar^2}{2m}\boldsymbol{\nabla}^2 - \mu\right)\hat{\sigma}_0 - \frac{\Delta_{\mathrm{XC}}}{2}\left(\hat{\mathbf{m}}_{\mathbf{1}}\cdot\hat{\boldsymbol{\sigma}}\right)\Theta(z)\Theta(d_1 - z) + V_{\mathrm{I}}\hat{\sigma}_0\Theta(z-d_1)\Theta(d_2-z) - \frac{\Delta_{\mathrm{XC}}}{2}\left(\hat{\mathbf{m}}_{\mathbf{2}}\cdot\hat{\boldsymbol{\sigma}}\right)\Theta(z-d_2)\Theta(d_3-z) + \hat{\mathcal{H}}_{\mathrm{L}}^{\mathrm{SMC}} + \hat{\mathcal{H}}_{\mathrm{R}}^{\mathrm{SMC}}. \quad (6.65)$$

Note that we are now concerned with two magnetization terms that refer to F_1 and F_2, accordingly. To simplify our considerations, we assume that both ferromagnets are characterized by the same exchange energy gap Δ_{XC} and differ only in their magnetization orientations as stated above. More specifically, F_1's magnetization is aligned along $\hat{\mathbf{m}}_{\mathbf{1}} = [0,\,1,\,0]^\top$, while that of F_2 points along the unit vector $\hat{\mathbf{m}}_{\mathbf{2}} = [\cos(\Phi),\,\sin(\Phi),\,0]^\top$ with $\Phi = \pi/2$ for the parallel and $\Phi = 3\pi/2$ for the antiparallel magnetization configurations [see Fig. 6.5(b) for the definition of the azimuthal magnetization angle Φ]. We account for the insulating barrier adding the scattering potential V_{I}, which is nonzero only inside the insulator. It is important to recall that the Bogoljubov-de Gennes description measures *all* energies with respect to the chemical potential μ. Therefore, we need to substitute $V_{\mathrm{I}} = V_{\mathrm{B}} + \mu$, where V_{B} refers to the insulating barrier's actual barrier height (bandgap) that is typically given in experimental works [see Fig. 6.12(b)]. Scattering at the semiconducting tunneling barriers is captured by

$$\hat{\mathcal{H}}_{\mathrm{L}}^{\mathrm{SMC}} = \left(V_{\mathrm{L}}d_{\mathrm{L}}\hat{\sigma}_0 + \boldsymbol{\Omega}_{\mathbf{L}}\cdot\hat{\boldsymbol{\sigma}}\right)\delta(z) \quad (6.66)$$

and

$$\hat{\mathcal{H}}_{\mathrm{R}}^{\mathrm{SMC}} = \left(V_{\mathrm{R}}d_{\mathrm{R}}\hat{\sigma}_0 + \boldsymbol{\Omega}_{\mathbf{R}}\cdot\hat{\boldsymbol{\sigma}}\right)\delta(z-d_3); \quad (6.67)$$

the semiconducting barriers' heights (widths) are again denoted by $V_{\mathrm{L\,(R)}}$ [$d_{\mathrm{L\,(R)}}$] and also the interfacial spin-orbit fields $\boldsymbol{\Omega}_{\mathbf{L}}$ and $\boldsymbol{\Omega}_{\mathbf{R}}$, we declared in Sec. 6.2, do not need to be modified. The single-hole Hamiltonian is then obtained from $\hat{\mathcal{H}}_{\mathrm{h}} = -\hat{\sigma}_y\hat{\mathcal{H}}_{\mathrm{e}}^{*}\hat{\sigma}_y$, while we approximate the s-wave superconducting pairing potential by

$$\hat{\Delta}_{\mathrm{S}}(z) = |\Delta_{\mathrm{S}}|\hat{\sigma}_0\left[\Theta(-z) + \mathrm{e}^{\mathrm{i}\phi_{\mathrm{S}}}\Theta(z-d_3)\right], \quad (6.68)$$

where $|\Delta_{\mathrm{S}}|$ measures the superconductors' isotropic energy gap (assumed to be the same in both superconducting electrodes) and ϕ_{S} indicates the phase difference across the junction.

6.3.1.1 Bogoljubov-de Gennes scattering states

After setting up the junction's Bogoljubov-de Gennes Hamiltonian, we are fully equipped to proceed in the same way as in Sec. 6.2 to extract the Bogoljubov-de Gennes scattering states, still fulfilling $\Psi(\mathbf{r}) = \psi(z)\,\mathrm{e}^{\mathrm{i}(\mathbf{k}_\parallel\cdot\mathbf{r}_\parallel)}$. The $\hat{z}$-projection $\psi(z)$ has the final form

$$\psi^{(i)}(z<0) = \psi^{(i)}_{\text{incoming}}(z<0) + \mathcal{A}^{(i)}\begin{bmatrix}u\\0\\v\\0\end{bmatrix}\mathrm{e}^{-\mathrm{i}q_{z,\mathrm{e}}z} + \mathcal{B}^{(i)}\begin{bmatrix}0\\u\\0\\v\end{bmatrix}\mathrm{e}^{-\mathrm{i}q_{z,\mathrm{e}}z} + \mathcal{C}^{(i)}\begin{bmatrix}v\\0\\u\\0\end{bmatrix}\mathrm{e}^{\mathrm{i}q_{z,\mathrm{h}}z} + \mathcal{D}^{(i)}\begin{bmatrix}0\\v\\0\\u\end{bmatrix}\mathrm{e}^{\mathrm{i}q_{z,\mathrm{h}}z} \quad (6.69)$$

in the left superconductor ($z < 0$),

$$\psi^{(i)}(0<z<d_1)=\left[\varepsilon_1^{(i)}\mathrm{e}^{\mathrm{i}k_{z,\mathrm{e}}^{\uparrow}z}+\varepsilon_2^{(i)}\mathrm{e}^{-\mathrm{i}k_{z,\mathrm{e}}^{\uparrow}z}\right]\frac{1}{\sqrt{2}}\begin{bmatrix}-\mathrm{i}\\1\\0\\0\end{bmatrix}+\left[\varepsilon_3^{(i)}\mathrm{e}^{\mathrm{i}k_{z,\mathrm{e}}^{\downarrow}z}+\varepsilon_4^{(i)}\mathrm{e}^{-\mathrm{i}k_{z,\mathrm{e}}^{\downarrow}z}\right]\frac{1}{\sqrt{2}}\begin{bmatrix}\mathrm{i}\\1\\0\\0\end{bmatrix}$$
$$+\left[\eta_1^{(i)}\mathrm{e}^{-\mathrm{i}k_{z,\mathrm{h}}^{\uparrow}z}+\eta_2^{(i)}\mathrm{e}^{\mathrm{i}k_{z,\mathrm{h}}^{\uparrow}z}\right]\frac{1}{\sqrt{2}}\begin{bmatrix}0\\0\\\mathrm{i}\\1\end{bmatrix}+\left[\eta_3^{(i)}\mathrm{e}^{-\mathrm{i}k_{z,\mathrm{h}}^{\downarrow}z}+\eta_4^{(i)}\mathrm{e}^{\mathrm{i}k_{z,\mathrm{h}}^{\downarrow}z}\right]\frac{1}{\sqrt{2}}\begin{bmatrix}0\\0\\-\mathrm{i}\\1\end{bmatrix}\tag{6.70}$$

in F_1 $(0<z<d_1)$,

$$\psi^{(i)}(d_1<z<d_2)=\left[\tilde{\varepsilon}_1^{(i)}\mathrm{e}^{-\kappa_{z,\mathrm{e}}z}+\tilde{\varepsilon}_2^{(i)}\mathrm{e}^{\kappa_{z,\mathrm{e}}z}\right]\begin{bmatrix}1\\0\\0\\0\end{bmatrix}+\left[\tilde{\varepsilon}_3^{(i)}\mathrm{e}^{-\kappa_{z,\mathrm{e}}z}+\tilde{\varepsilon}_4^{(i)}\mathrm{e}^{\kappa_{z,\mathrm{e}}z}\right]\begin{bmatrix}0\\1\\0\\0\end{bmatrix}$$
$$+\left[\tilde{\eta}_1^{(i)}\mathrm{e}^{\kappa_{z,\mathrm{h}}z}+\tilde{\eta}_2^{(i)}\mathrm{e}^{-\kappa_{z,\mathrm{h}}z}\right]\begin{bmatrix}0\\0\\0\\1\end{bmatrix}+\left[\tilde{\eta}_3^{(i)}\mathrm{e}^{\kappa_{z,\mathrm{h}}z}+\tilde{\eta}_4^{(i)}\mathrm{e}^{-\kappa_{z,\mathrm{h}}z}\right]\begin{bmatrix}0\\0\\1\\0\end{bmatrix}\tag{6.71}$$

in the insulator $(d_1<z<d_2)$,

$$\psi^{(i)}(d_2<z<d_3)=\left[\overline{\varepsilon}_1^{(i)}\mathrm{e}^{\mathrm{i}k_{z,\mathrm{e}}^{\uparrow}z}+\overline{\varepsilon}_2^{(i)}\mathrm{e}^{-\mathrm{i}k_{z,\mathrm{e}}^{\uparrow}z}\right]\chi_{\mathrm{e}}^{\uparrow}+\left[\overline{\varepsilon}_3^{(i)}\mathrm{e}^{\mathrm{i}k_{z,\mathrm{e}}^{\downarrow}z}+\overline{\varepsilon}_4^{(i)}\mathrm{e}^{-\mathrm{i}k_{z,\mathrm{e}}^{\downarrow}z}\right]\chi_{\mathrm{e}}^{\downarrow}$$
$$+\left[\overline{\eta}_1^{(i)}\mathrm{e}^{-\mathrm{i}k_{z,\mathrm{h}}^{\uparrow}z}+\overline{\eta}_2^{(i)}\mathrm{e}^{\mathrm{i}k_{z,\mathrm{h}}^{\uparrow}z}\right]\chi_{\mathrm{h}}^{\uparrow}+\left[\overline{\eta}_3^{(i)}\mathrm{e}^{-\mathrm{i}k_{z,\mathrm{h}}^{\downarrow}z}+\overline{\eta}_4^{(i)}\mathrm{e}^{\mathrm{i}k_{z,\mathrm{h}}^{\downarrow}z}\right]\chi_{\mathrm{h}}^{\downarrow}\tag{6.72}$$

in F_2 $(d_2<z<d_3)$ – the spinors are given by Eqs. (6.43) and (6.44) setting $\Theta=\pi/2$ –, and

$$\psi^{(i)}(z>d_3)=\mathcal{E}^{(i)}\begin{bmatrix}u\mathrm{e}^{\mathrm{i}\phi_{\mathrm{S}}}\\0\\v\\0\end{bmatrix}\mathrm{e}^{\mathrm{i}q_{z,\mathrm{e}}z}+\mathcal{F}^{(i)}\begin{bmatrix}0\\u\mathrm{e}^{\mathrm{i}\phi_{\mathrm{S}}}\\0\\v\end{bmatrix}\mathrm{e}^{\mathrm{i}q_{z,\mathrm{e}}z}+\mathcal{G}^{(i)}\begin{bmatrix}v\mathrm{e}^{\mathrm{i}\phi_{\mathrm{S}}}\\0\\u\\0\end{bmatrix}\mathrm{e}^{-\mathrm{i}q_{z,\mathrm{h}}z}+\mathcal{H}^{(i)}\begin{bmatrix}0\\v\mathrm{e}^{\mathrm{i}\phi_{\mathrm{S}}}\\0\\u\end{bmatrix}\mathrm{e}^{-\mathrm{i}q_{z,\mathrm{h}}z}\tag{6.73}$$

in the right superconductor $(z>d_3)$. The $\hat{z}$-components of the electrons' and holes' wave vectors inside the insulator read

$$\kappa_{z,\mathrm{e}}=\kappa_{z,\mathrm{e}}(E)=\sqrt{\frac{2m}{\hbar^2}\left(V_{\mathrm{I}}-E-\mu\right)+\mathbf{k}_{\parallel}^2}\quad\text{and}\quad\kappa_{z,\mathrm{h}}=\kappa_{z,\mathrm{h}}(E)=\sqrt{\frac{2m}{\hbar^2}\left(V_{\mathrm{I}}+E-\mu\right)+\mathbf{k}_{\parallel}^2},\tag{6.74}$$

while those in the superconducting and ferromagnetic junction constituents, as well as the BCS coherence factors, are the same as given previously [see Eqs. (6.39)–(6.40), (6.41)–(6.42), and (6.8)]. The superscript i distinguishes between the four different quasiparticle injection processes we explained in Sec. 6.2 and the associated incoming waves got defined in Eqs. (6.35)–(6.38).

Applying the interfacial ($z=0$, $z=d_1$, $z=d_2$, and $z=d_3$) boundary conditions

$$\psi^{(i)}(z)\big|_{z=0_-}=\psi^{(i)}(z)\big|_{z=0_+},\qquad\psi^{(i)}(z)\big|_{z=d_{1_-}}=\psi^{(i)}(z)\big|_{z=d_{1_+}},\tag{6.75}$$

$$\psi^{(i)}(z)\big|_{z=d_{2_-}}=\psi^{(i)}(z)\big|_{z=d_{2_+}},\qquad\psi^{(i)}(z)\big|_{z=d_{3_-}}=\psi^{(i)}(z)\big|_{z=d_{3_+}},\tag{6.76}$$

as well as

$$\left(-\frac{\hbar^2}{2m}\frac{\mathrm{d}}{\mathrm{d}z}+V_{\mathrm{L}}d_{\mathrm{L}}\right)\hat{\eta}\psi^{(i)}(z)\big|_{z=0_+}+\begin{bmatrix}\mathbf{\Omega_L}\cdot\hat{\boldsymbol{\sigma}} & \hat{0}\\ \hat{0} & -(\mathbf{\Omega_L}\cdot\hat{\boldsymbol{\sigma}})\end{bmatrix}\psi^{(i)}(z)\big|_{z=0_+}=-\frac{\hbar^2}{2m}\frac{\mathrm{d}}{\mathrm{d}z}\hat{\eta}\psi^{(i)}(z)\big|_{z=0_-}, \tag{6.77}$$

$$\frac{\mathrm{d}}{\mathrm{d}z}\psi^{(i)}(z)\big|_{z=d_{1-}}=\frac{\mathrm{d}}{\mathrm{d}z}\psi^{(i)}(z)\big|_{z=d_{1+}},\qquad \frac{\mathrm{d}}{\mathrm{d}z}\psi^{(i)}(z)\big|_{z=d_{2-}}=\frac{\mathrm{d}}{\mathrm{d}z}\psi^{(i)}(z)\big|_{z=d_{2+}}, \tag{6.78}$$

and

$$\left(\frac{\hbar^2}{2m}\frac{\mathrm{d}}{\mathrm{d}z}+V_{\mathrm{R}}d_{\mathrm{R}}\right)\hat{\eta}\psi^{(i)}(z)\big|_{z=d_{3-}}+\begin{bmatrix}\mathbf{\Omega_R}\cdot\hat{\boldsymbol{\sigma}} & \hat{0}\\ \hat{0} & -(\mathbf{\Omega_R}\cdot\hat{\boldsymbol{\sigma}})\end{bmatrix}\psi^{(i)}(z)\big|_{z=d_{3-}}=\frac{\hbar^2}{2m}\frac{\mathrm{d}}{\mathrm{d}z}\hat{\eta}\psi^{(i)}(z)\big|_{z=d_{3+}} \tag{6.79}$$

to the scattering states [see Eq. (6.49) for the definition of $\hat{\eta}$], and numerically solving the resulting systems of equations by means of a (generalized) LU Decomposition algorithm [181] allows us to determine all unknown scattering coefficients, which are the key ingredient for calculating the Josephson current.

6.3.1.2 Josephson current

Based on the obtained Bogoljubov-de Gennes scattering coefficients and the generic Furusaki-Tsukada expression [see Eq. (6.59)],we evaluate the junction's Josephson current-phase relation $I_{\mathrm{J}}=I_{\mathrm{J}}(\phi_{\mathrm{S}})$ once in the parallel ($\Phi=\pi/2$) and once in the antiparallel ($\Phi=3\pi/2$) magnetization configuration, and finally extract the related *oriented* critical currents

$$I_{\mathrm{P}}^{\mathrm{crit.}}=\pm\max_{\phi_{\mathrm{S}}}\left\{\left[|I_{\mathrm{J}}(\phi_{\mathrm{S}})|\right]\big|_{\Phi=\pi/2}\right\}\qquad\text{and}\qquad I_{\mathrm{AP}}^{\mathrm{crit.}}=\pm\max_{\phi_{\mathrm{S}}}\left\{\left[|I_{\mathrm{J}}(\phi_{\mathrm{S}})|\right]\big|_{\Phi=3\pi/2}\right\}. \tag{6.80}$$

As before, we added by hand a positive (negative) sign to 0 (π)-junctions' critical currents to clearly distinguish between the different junction regimes. Specifying a reasonable JTMR measure is, however, more subtle. While the normal-state tunneling conductance in the parallel magnetization configuration always clearly exceeds that in the antiparallel magnetization scenario (as we explained within Jullière's picture when motivating our study), this is no longer necessarily the case for the Josephson (super)currents. In fact, we will learn that dominant Josephson currents can flow for both parallel and antiparallel magnetizations, mostly depending on the remaining junction parameters. The parameter regimes in the vicinity of 0-π transitions become even more striking. Switching from parallel to antiparallel magnetized interlayers may again induce transitions between the different junction regimes (similarly to our discussions when analyzing Fig. 6.10) and suddenly reverse the Josephson current's sign. An experimentally meaningful JTMR ratio that properly captures the *relative* change of the critical current (in analogy to the normal-state TMR) might be

$$\mathrm{JTMR}=\frac{I_{\mathrm{MAX}}^{\mathrm{crit.}}-I_{\mathrm{MIN}}^{\mathrm{crit.}}}{I_{\mathrm{MIN}}^{\mathrm{crit.}}}, \tag{6.81}$$

where subtracting the smaller critical current $I_{\mathrm{MIN}}^{\mathrm{crit.}}=\min\left[|I_{\mathrm{P}}^{\mathrm{crit.}}|;|I_{\mathrm{AP}}^{\mathrm{crit.}}|\right]$ from the larger current $I_{\mathrm{MAX}}^{\mathrm{crit.}}=\max\left[|I_{\mathrm{P}}^{\mathrm{crit.}}|;|I_{\mathrm{AP}}^{\mathrm{crit.}}|\right]$ ensures that the JTMR ratio measures the *relative* current change and no (meaningless and probably confusing) negative JTMRs appear. Note that writing the JTMR measure in that way generalizes the initial proposals in Ref. [295] to scenarios in which it is a priori unknown whether parallel or antiparallel magnetizations cause larger Josephson current flows.

6.3.1.3 Normal-conducting junction regime

For comparing the JTMR's qualitative and quantitative behavior in the superconducting S/F/I/F/S Josephson junction to its normal-conducting TMR analog, we simultaneously have to determine the differential tunneling conductance of the corresponding normal-state normal metal/ferromagnet/insulator/ferromagnet/normal metal (N/F/I/F/N) junction (after applying the bias voltage V across the junction). The Bogoljubov-de Gennes scattering approach described above formally recovers the normal-state junction regime when considering the limit $u(E) \to 1$, $v(E) \to 0$, and $|\Delta_S| \to 0$. All other ingredients in the modeling do not need to be changed when accessing the normal-conducting system's scattering coefficients. Similarly to the simple junctions discussed in Chap. 3, we can relate the scattering coefficients to the junction's *zero-temperature* tunneling conductance (extrapolated to zero bias) by means of the extended BTK-like formula [300–303]

$$G_{z,z} \approx \frac{G_0 \mathcal{A}}{(2\pi)^2} \int \mathrm{d}^2\mathbf{k}_\parallel \Big[C^{(1)}(eV) + \mathcal{D}^{(1)}(eV) + C^{(2)}(eV) + \mathcal{D}^{(2)}(eV) + \mathcal{E}^{(1)}(eV) + \mathcal{F}^{(1)}(eV) + \mathcal{E}^{(2)}(eV) + \mathcal{F}^{(2)}(eV) \Big]\Big|_{eV=0}; \quad (6.82)$$

for simplicity, we approximated $q_{z,\mathrm{e}} \approx q_{z,\mathrm{h}}$ (since $E \ll \mu$). As before, $G_0 = (2e^2)/h$ denotes the conductance quantum and $\mathcal{A}$ refers to the interfacial cross-section area. Although we use the same notation as in the superconducting case, mind that the scattering coefficients in Eq. (6.82) correspond now to the normal-state junction [setting $u(E) \to 1$, $v(E) \to 0$, and $|\Delta_S| \to 0$]. Equation (6.82) is a general result that can be applied to a variety of normal metal/buffer region/normal metal (N/buffer region/N) junctions with quite arbitrary buffer regions (could also be a *superconducting* multilayer structure instead of the ferromagnetic spin valve we are concerned with). All junction-specific information is accumulated in the scattering description, which can be straightforwardly adapted to other junctions. For the sake of completeness, we present the derivation of Eq. (6.82) in Appendix C. The junction's tunneling conductances in the parallel and antiparallel magnetization configurations are eventually numerically computed from $G_\mathrm{P} = G_{z,z}\big|_{\Phi=\pi/2}$ and $G_\mathrm{AP} = G_{z,z}\big|_{\Phi=3\pi/2}$, allowing us to extract the TMR ratio from $\mathrm{TMR} = (G_\mathrm{P} - G_\mathrm{AP})/G_\mathrm{AP}$. In contrast to the (superconducting) JTMR measure, we do not need to worry about negative TMRs since typically $G_\mathrm{P} > G_\mathrm{AP}$ (see our discussion of Jullière's tunneling picture).

6.3.2 Discussion of results

To gain a deeper insight into the physics associated with JTMR effects, we analyze several model calculations for realistic S/F/I/F/S Josephson junction regimes together with their normal-state TMR counterparts. The superconducting material parameters $|\Delta_S(0)| \approx 2.5\,\mathrm{meV}$ and $T_C \approx 16\,\mathrm{K}$, the chemical potential $\mu = 10^3|\Delta_S(0)|$, as well as the temperature $T = 0.1T_C$ are the same we considered in Sec. 6.2. Scalar and SOC scatterings at the two semiconducting interfaces (separating the superconductors from the neighboring ferromagnets) are still included into the dimensionless variables Z_L, Z_R, $\lambda_\mathrm{L}^\alpha$, $\lambda_\mathrm{R}^\alpha$, λ_L^β, and λ_R^β, whose definition can be looked up in Tab. 6.1. The S/F/I/F/S junctions' ferromagnets consist of the same material (we assumed one Δ_{XC} for both) and may only differ in their relative magnetization orientations. Since one might be interested in comparing the results to the ones obtained for S/F/S junctions in Sec. 6.2, we use the same effective spin polarization of $P = 0.7$, which basically corresponds to iron layers. The additionally present insulating barrier is characterized by its barrier height (bandgap) V_B [recall that eventually $V_\mathrm{I} = V_\mathrm{B} + \mu$ enters the Bogoljubov-de Gennes Hamiltonian; see Fig. 6.12(b)]. The ferromagnets' and insulator's effective thicknesses are determined by the dimensionless parameters $k_\mathrm{F} d_{\mathrm{F}_1}$ (d_{F_1} is the bare thickness of F_1), $k_\mathrm{F} d_{\mathrm{F}_2}$ (d_{F_2} is the bare thickness of F_2), and $k_\mathrm{F} d_\mathrm{I}$ (d_I is the bare thickness of the insulator); as before, $k_\mathrm{F} \approx 8 \times 10^7\,\mathrm{cm}^{-1}$ corresponds to iron's Fermi wave vector [182].

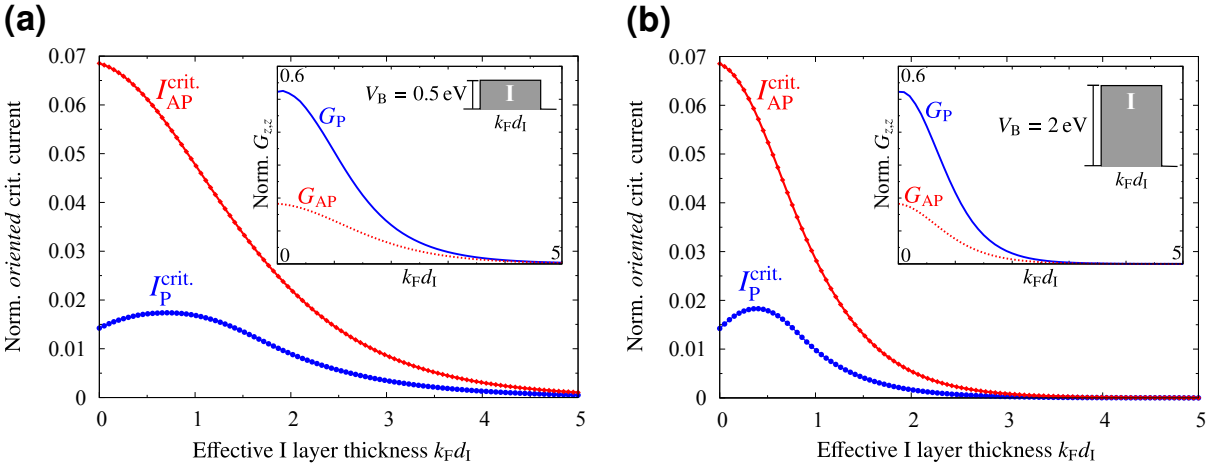


Fig. 6.13: (a) Calculated dependence of S/F/I/F/S junctions' *oriented* critical current on the effective insulator thickness $k_F d_I$ for parallel, $I_P^{crit.}$, and antiparallel, $I_{AP}^{crit.}$, magnetized ferromagnetic regions (normalized as in Fig. 6.6), and for the barrier height $V_B = 0.5\,eV$ (see illustration); since $k_F \approx 8 \times 10^7\,cm^{-1}$, $k_F d_I = 4$ exemplarily models a roughly 0.5 nm thick insulator. The ferromagnets' spin polarization $P = 0.7$ corresponds to iron, while their effective thicknesses are $k_F d_{F_1} = k_F d_{F_2} = 15$ (so that $d_{F_1} = d_{F_2} \approx 1.9\,nm$). The remaining parameters are $Z_L = Z_R = \lambda_L^\alpha = \lambda_R^\alpha = \lambda_L^\beta = \lambda_R^\beta = 0$. The inset shows the respective normal-state N/F/I/F/N junctions' tunneling conductance in the parallel, G_P, and antiparallel, G_{AP}, magnetization configurations [normalized to Sharvin's conductance $G_S = (\mathcal{A}e^2k_F^2)/(2\pi h)$ of a perfectly transparent (three-dimensional) metallic point contact]. **(b)** Same calculation as in **(a)**, but for the (larger) barrier height $V_B = 2\,eV$.

6.3.2.1 General features

We initially focus on extracting some valuable universal trends of JTMR effects. Figure 6.13 compares the oriented critical current's variation with respect to the effective insulator thickness $k_F d_I$ for parallel to that for antiparallel magnetized F/I/F spin valves (the ferromagnets' thicknesses $d_{F_1} = d_{F_2} \approx 1.9\,nm$ are kept constant). Moreover, we increase the insulator's barrier height from a rather small value of $V_B = 0.5\,eV$ [see Fig. 6.13(a)] to $V_B = 2\,eV$ [see Fig. 6.13(b)]. The insets show the related tunneling conductances for the junction entering its purely normal-conducting N/F/I/F/N regime.[4] To avoid unnecessary complications, we set $Z_L = Z_R = \lambda_L^\alpha = \lambda_R^\alpha = \lambda_L^\beta = \lambda_R^\beta = 0$ if not otherwise indicated.

As the most remarkable feature, flipping the ferromagnets' magnetizations from the parallel to the antiparallel alignment impacts the (superconducting) critical currents ($I_P^{crit.}$ and $I_{AP}^{crit.}$) and the (normal-state) tunneling conductances (G_P and G_{AP}) in exactly the *opposite* way. While the favorable tunneling of unpaired electrons through parallel magnetized F/I/F layers indeed leads to the strongly pronounced G_P (when compared to G_{AP}), just as Jullière predicted, it is the critical current in the *anti*parallel magnetization configuration that significantly exceeds the one for the parallel magnetization scenario. Translating the latter finding into a "Jullière-like" tunneling picture for Cooper pairs suggests that parallel magnetizations must strongly suppress the transfer of *spin-singlet* electron pairs through the junction's ferromagnetic region. Note that SOC is absent at the moment so that solely spin-singlet Cooper pairs contribute to the Josephson current. A simplified version of such a Cooper pair tunneling picture is depicted in Figs. 6.14(a) and 6.14(b). Shortly speaking, both the spin-up and the spin-down electron, originally forming the

[4] For simplicity, we perform the normal-state calculations at zero temperature [see Eq. (6.82)] and not at $T = 0.1T_C$ like the superconducting calculations. The results of both are nevertheless still comparable since we convinced ourselves that temperature effects do not play any significant role at $T = 0.1T_C$. In fact, temperature effects are mostly governed by the temperature dependence of the superconducting energy gap, $|\Delta_S(T \neq 0)| = |\Delta_S(0)| \tanh(1.74\sqrt{T_C/T - 1})$, which is nearly unaffected when increasing the temperature from zero to $T = 0.1T_C$.

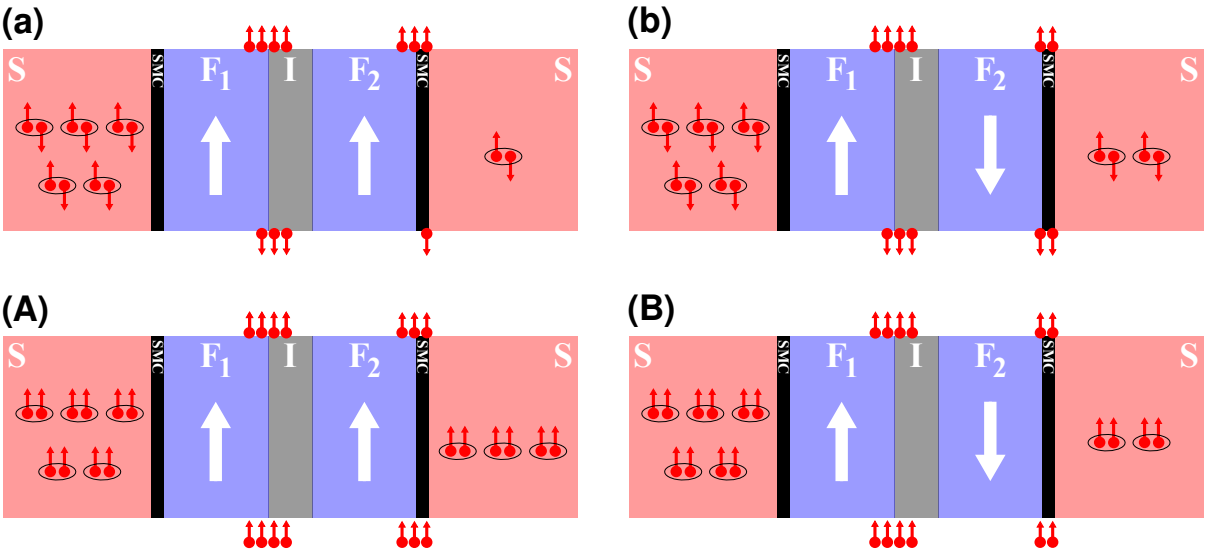


Fig. 6.14: **(a)** Simplified illustration of a "Jullière-like" tunneling picture for *spin-singlet* Cooper pairs through a *parallel* magnetized F/I/F spin-valve sequence. Electrons are colored red, their spins are indicated by red arrows, and the ferromagnets' magnetizations are emphasized by white arrows. All electrons initially forming Cooper pairs in the left superconductor *sequentially* tunnel through the intermediate layers. Each ferromagnet primarily supports the tunneling of electrons, whose spin corresponds to the ferromagnet's majority spin. Only a small fraction of electrons entering the right superconductor finds a partner with opposite spin to form a Cooper pair. Effectively, just a small amount of Cooper pairs is transferred from one into the other superconductor, resulting in a small Josephson current flow. **(b)** Same illustration as in **(a)**, but for *antiparallel* magnetized ferromagnets. Spin-up electrons mostly pass F_1, whereas spin-down electrons are preferentially transmitted through F_2. Finally, (nearly) all electrons pair again with a partner so that more Cooper pairs got transferred into the right superconductor and a larger Josephson current flows. **(A)** [**(B)**] Same illustration as in **(a)** [**(b)**], but for *spin-triplet* Cooper pair tunneling. Large Josephson current flows require now the predominant tunneling of electrons with the *same* spin, i.e., parallel magnetized F/I/F spin valves. The currents can even exceed the associated spin-singlet currents [see **(a)** and **(b)**].

singlet pair in the left superconductor, must *sequentially* tunnel through the F/I/F spin valve and finally pair again inside the right superconductor. The resulting effective transfer of a Cooper pair from one into the other superconductor causes then precisely the calculated Josephson current flow, similarly to our argumentation for S/F/S junctions at the beginning of this chapter. Each ferromagnetic region lets predominantly pass electrons whose spin corresponds to the ferromagnet's majority spin (due to the larger Fermi-level DOS in the majority band). Therefore, if both ferromagnets are magnetized such that their majority-spin bands are the up-spin bands, primarily spin-up (and only sporadically spin-down) electrons are transmitted through the F/I/F region. Most of the spin-up electrons are not able to find spin-down partners for Cooper pairing in the right superconductor so that basically just a small fraction of Cooper pairs from the left superconductor really reaches the right one, which heavily damps the Josephson current.

Contrary, antiparallel magnetizations (the majority spins are now, e.g., spin up in F_1 and spin down in F_2) reduce transmissions via the up- and down-spin tunneling channels in a comparable way (under the assumption that both ferromagnetic layers are equally thick). The excess of spin-up electrons after passing F_1 is compensated by F_2. Consequently, (roughly) as many spin-up as spin-down electrons enter the right superconductor and all electrons pair with partners. The flowing Josephson current clearly exceeds the current in the parallel magnetized junction. Such an extreme current enhancement for antiparallel magnetizations was initially proposed to be a novel phenomenon in the pioneering quasiclassical study

of *diffusive* S/F/I/F/S junctions [295], could be reproduced later by follow-up works on similar [67, 222, 296, 297] and modified superconductor/ferromagnetic semiconductor/semiconductor/ferromagnetic semiconductor/superconductor geometries [298, 299], and got eventually verified for *ballistic* junctions by our simulations. Although all important characteristics can be deduced from our Cooper pair tunneling picture, we must be aware that it strongly simplifies the reality. Due to the complete neglect of superconducting proximity effects inside the F/I/F sequence, which we identified as the *microscopic* origin of Cooper pair transfers and π-state regimes in S/F/S Josephson junctions, our tunneling picture can only yield general trends and cannot, for instance, differentiate between 0- and π-phases.

Let us briefly focus on the role of the insulating barrier. Since the Josephson current is governed by the tunneling of Cooper pairs through the intermediate junction region, and hence also by (usually strongly suppressed) tunneling through the insulator, one expects that increasing either the barrier height V_B or its effective thickness $k_\mathrm{F}d_\mathrm{I}$ should immediate result in a considerable reduction of the current flow. Checking the outcomes in Fig. 6.13(a) against those in Fig. 6.13(b) reveals a more intricate interplay between V_B and $k_\mathrm{F}d_\mathrm{I}$, which gets additionally influenced by the magnetization configuration. While the current in the antiparallel scenario follows our expectations and gets remarkably suppressed with increasing $k_\mathrm{F}d_\mathrm{I}$ (and faster for larger barrier heights), the one in the parallel magnetized geometry even slightly increases for moderately rising $k_\mathrm{F}d_\mathrm{I}$ (more visible for larger barrier heights). Since this slight current increase happens only for parallel and not for antiparallel magnetizations, we attribute it to precisely those proximity effects our simple picture in Fig. 6.14 is not able to capture (see previous paragraph). In fact, we pointed out earlier that Cooper pairs being transferred through ferromagnetic junction interlayers can gain a finite center-of-mass momentum. It is this response of the electrons to ferromagnets' spin imbalance that leads to the highly complicated oscillatory behavior of the proximity-induced superconducting order parameter and is finally responsible for unexpected physical features like 0-π transitions. Generalizing these considerations to S/F/I/F/S junctions suggests that the Cooper pairs' acquired center-of-mass momenta become maximal for parallel and minimal for antiparallel magnetizations. In the latter, the spin imbalances in the two subsequent ferromagnetic regions are exactly reversed to each other so that Cooper pairs accumulate opposite center-of-mass momenta (but with the same amplitudes) in both ferromagnets (still supposing two identical materials with the same spin polarizations and equal thicknesses) [244, 288]. Therefore, Cooper pairs leaking through the antiparallel magnetized F/I/F region do actually not feel any spin imbalance. The corresponding proximity-induced superconducting order parameter's oscillations are washed out so that it eventually simply decays (exponentially) with an increase of the F/I/F sequence's overall thickness (as we discussed for S/N/S junctions earlier), explaining the sudden decay of the critical current with increasing $k_\mathrm{F}d_\mathrm{I}$. In the parallel magnetization configuration, however, the Cooper pairs feel the maximal impact of the ferromagnets' spin imbalances; the center-of-mass momenta acquired in both ferromagnetic parts mutually amplify, *depending on the insulator's thickness which may cause additional "screening" effects*. The resulting, particularly at low $k_\mathrm{F}d_\mathrm{I}$ strongly enhanced, oscillatory modulations of the superconducting order parameter can manifest themselves in the unexpected initial increase of the critical current. Anyhow, $I_\mathrm{P}^\mathrm{crit.}$ ultimately also reveals the expected decreasing trend already for slightly larger $k_\mathrm{F}d_\mathrm{I}$ when the junction's transport properties are again predominantly controlled by the order parameter's superimposed exponential decay, similarly to the parallel magnetization scenario.

After we discussed and understood how switching the ferromagnets' relative magnetizations modifies the Josephson current, we substitute the obtained critical currents into Eq. (6.81) and extract the respective JTMRs. Numerical results for the JTMR ratios are presented in dependence on the effective insulator thickness $k_\mathrm{F}d_\mathrm{I}$ and for various barrier heights V_B in Fig. 6.15(a). For comparison, Fig. 6.15(b) shows the outcomes of similar calculations for the normal-state TMR analog, keeping all other parameters the same. The critical current's great magnetosensitivity, we exemplarily discussed for some representative junction parameters in Fig. 6.13, is a generic feature and effectuates strongly pronounced JTMRs –

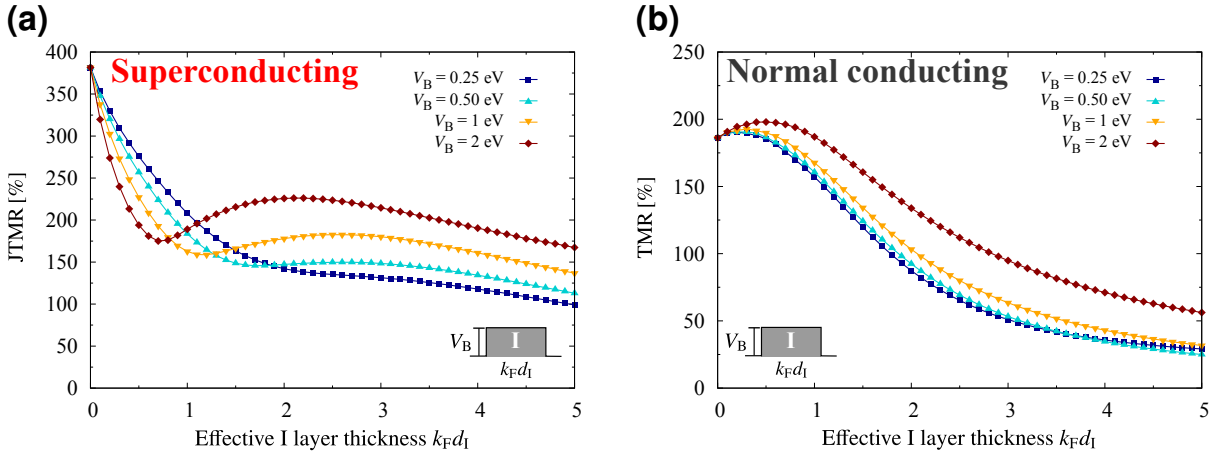


Fig. 6.15: (a) S/F/I/F/S junctions' calculated JTMR as a function of the effective insulator thickness $k_F d_I$ and for various indicated barrier heights V_B. All other parameters are the same as in Fig. 6.13. **(b)** Calculated normal-state TMR counterpart when the junctions considered in **(a)** enter their fully normal-conducting N/F/I/F/N regimes. Recall that we evaluated the normal-state tunneling conductances, and likewise the TMR ratios, at *absolute zero*, explaining the rather large absolute TMR amplitudes when compared to experimental values, which are usually taken at room temperature [283, 284].

clearly detectable in experiments – for all considered values of V_B. Just as one could deflect from the superconducting MAAR phenomena [176, 182], whose amplitudes drastically exceed those of the normal-conducting TAMR counterpart [250, 251], or from S/F/S junctions' huge MAJCs we deduced in Sec. 6.2, also the JTMR remarkably overcomes its normal-state TMR analog for a wide range of parameter combinations. Nevertheless, it shall be noted that the presence of the insulating barrier gives still rise to sizable normal-state TMRs (which increase even further with increasing V_B at $k_F d_I > 0$) when compared to superconductor/ferromagnet/normal metal/ferromagnet/superconductor junctions [293], demonstrating that S/F/I/F/S Josephson spin valves offer the perhaps most versatile platform to investigate the efficient coexistence of Josephson and TMR effects [88]. Apparently, the JTMR values approach their maximum when $k_F d_I \to 0$, i.e., when the ferromagnetic regions are not separated by an insulator at all. One should not pay too much attention to that since controlling the magnetization of two neighboring ferromagnetic layers without an intermediate buffer layer is not only experimentally quite challenging, but also additionally changing the ferromagnets' thicknesses might immediately modify these characteristics. In fact, we will see in the next paragraph that slightly thinner or thicker ferromagnetic layers indeed maintain maximal JTMRs at finite $k_F d_I$, at which the experimental control of the magnetization configuration can be much better implemented. The JTMR amplitudes' highly nonmonotonic variations with respect to $k_F d_I$ (i.e., their initial decrease followed by another increase that eventually merges into the generic decreasing trend at larger $k_F d_I$; most clearly evident for larger barrier heights such as $V_B \gtrsim 0.50\,\mathrm{eV}$) reflect the unexpected monotony of $I_P^{\mathrm{crit.}}$ that we related to the proximity-induced superconducting order parameter.

Experimentally detecting JTMR features requires the integration of the effect into a well-controllable junction. In the above investigated junction, maximal JTMR ratios appear for $k_F d_I \to 0$, which is experimentally barely achievable. To resolve this issue, we may simultaneously alter the thicknesses of the ferromagnets, which themselves crucially impact the critical current (via the proximity-induced superconducting order parameter; see our argumentation in Sec. 6.2). Figures 6.16(a) and 6.16(b) therefore compare the critical current-$k_F d_I$ relations for $d_{F_1} = d_{F_2} \approx 1.9\,\mathrm{nm}$ to those for the doubled ferromagnet thicknesses $d_{F_1} = d_{F_2} \approx 3.8\,\mathrm{nm}$. While the first junction (with thinner ferromagnetic regions) always reflects the 0-state regime, flipping the magnetizations from their parallel to their antiparallel alignment

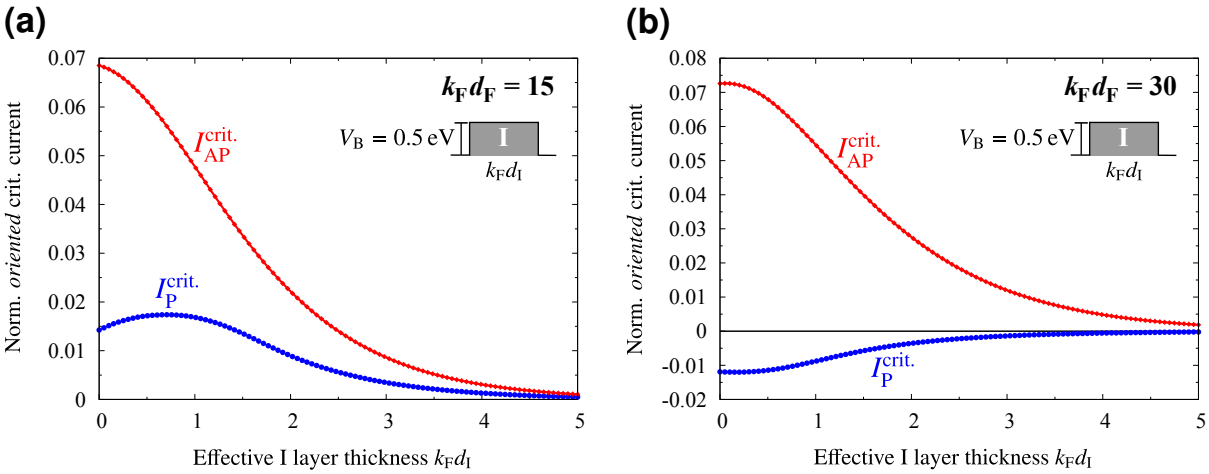


Fig. 6.16: (a) Calculated dependence of S/F/I/F/S junctions' *oriented* critical current on the effective insulator thickness $k_F d_I$ for parallel, $I_P^{crit.}$, and antiparallel, $I_{AP}^{crit.}$, magnetized ferromagnetic regions (normalized as in Fig. 6.6), and for the barrier height $V_B = 0.5$ eV (see illustration). The ferromagnets' (still composed of iron) effective thicknesses $k_F d_{F_1} = k_F d_{F_2} = k_F d_F = 15$ refer to bare thicknesses of about $d_{F_1} = d_{F_2} \approx 1.9$ nm. All other parameters are the same as in Fig. 6.15. **(b)** Same calculation as in **(a)**, but both ferromagnets are twice as thick ($k_F d_{F_1} = k_F d_{F_2} = 30$ mimics $d_{F_1} = d_{F_2} \approx 3.8$ nm).

actually switches the second junction (with thicker ferromagnets) from its initial π- to its 0-state. Moreover, the maximal 0-state critical current becomes more than four times larger than that in the π-regime. All these characteristics can be uniquely traced back to our previous analyses of the proximity-induced superconducting order parameter. Recall that we consider two identical ferromagnetic layers with the same thicknesses. As deduced above, parallel magnetizations then maximize the center-of-mass momenta Cooper pairs pick up inside the F/I/F region and the resulting strong order parameter oscillations can more easily stabilize the π-state regime. This is exactly the case in our junction for $d_{F_1} = d_{F_2} \approx 3.8$ nm. In sharp contrast, if F_2 got magnetized antiparallel to F_1, the center-of-mass momenta Cooper pairs acquire in F_1 are (nearly completely) compensated by F_2 [244, 288]. Basically, the F/I/F spin valve behaves then similarly to a normal-metal region (with the same thickness) and π-states are no longer energetically favorable (recall that the 0-state is the ground state of S/N/S junctions). As a result, antiparallel magnetized S/F/I/F/S junctions must *always* realize the 0-state regime as long as all our presumptions are fulfilled, i.e., both ferromagnets must be equally thick and no (interfacial) SOC is allowed to be present. The large critical currents in the antiparallel magnetization configuration are expected from our Cooper pair tunneling picture in Figs. 6.14(a) and 6.14(b). In particular, the accompanying *huge* relative change of the critical current during the 0-π transition is already a first precursor indicating a further enhancement of the underlying JTMR amplitudes. The calculated JTMRs, depicted in Fig. 6.17(a), indeed coincide with this speculation. Maximal JTMR ratios, approaching JTMR $\approx 800\,\%$, can now be realized for experimentally accessible insulator thicknesses of $k_F d_I \approx 3.5$ ($d_I \approx 0.4$ nm). The JTMR curve may also be compared to analog calculations for junctions in which the ferromagnets' thicknesses are once decreased by a factor of two and once by a factor of four. Both scenarios, however, do by far not support thus huge JTMR ratios like $d_{F_1} = d_{F_2} \approx 3.8$ nm. Figure 6.17(b) demonstrates that the huge JTMRs can furthermore be slightly tuned by means of the insulating barrier's height V_B.

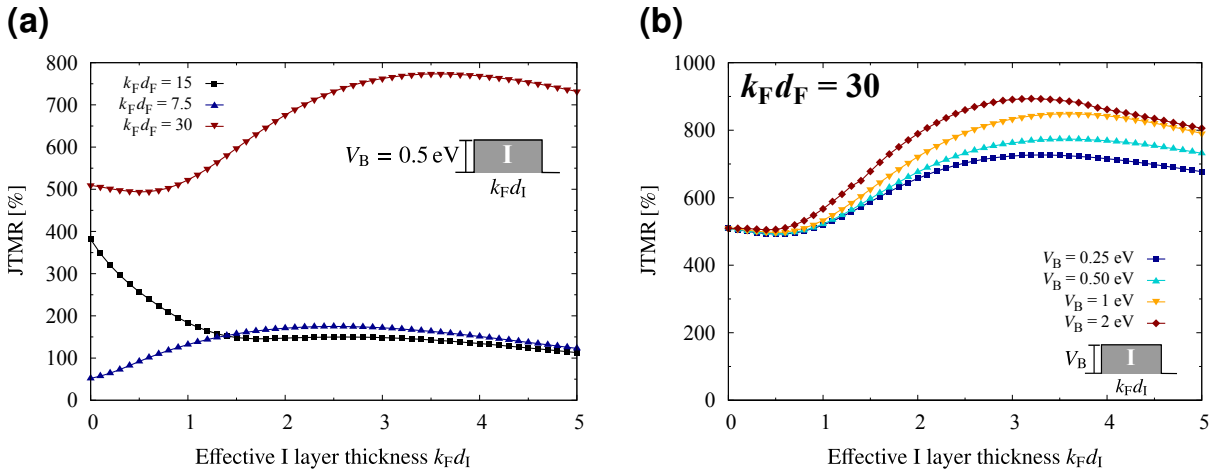


Fig. 6.17: (a) S/F/I/F/S junctions' calculated JTMR as a function of the effective insulator thickness $k_F d_I$ for the barrier height $V_B = 0.5\,\text{eV}$ (see illustration) and various indicated effective thicknesses of the ferromagnetic layers $k_F d_{F_1} = k_F d_{F_2} = k_F d_F$ [$k_F d_F = 15$ was studied above (see Fig. 6.15) and serves as a reference]. All remaining parameters are the same as in Fig. 6.13. **(b)** Same calculation as in **(a)**, but now the effective thicknesses of the ferromagnetic layers $k_F d_{F_1} = k_F d_{F_2} = k_F d_F = 30$ (resembling $d_{F_1} = d_{F_2} \approx 3.8\,\text{nm}$) are kept constant, while the barrier height V_B is varied (specific values are indicated).

6.3.2.2 Magnetic control of 0-π transitions

Our calculations for the S/F/I/F/S junction with the effective ferromagnet thicknesses $k_F d_{F_1} = k_F d_{F_2} = 15$ (or equivalently $d_{F_1} = d_{F_2} \approx 1.9\,\text{nm}$) and $k_F d_{F_1} = k_F d_{F_2} = 30$ (or equivalently $d_{F_1} = d_{F_2} \approx 3.8\,\text{nm}$), we discussed above [see also Fig. 6.16], serve as a motivation to propose another way enabling a stable magnetic control of 0-π transitions. While the parallel magnetization configuration supports both 0- and π-junctions, mostly depending on the ferromagnets' thicknesses (and their spin polarizations), we concluded that antiparallel magnetized ferromagnetic regions (with the same thicknesses) completely compensate the intrinsic π-shift so that only the 0-state regime survives. We related these findings to the unique behavior of the proximity-induced superconducting order parameter inside the F/I/F sequence, tunable by switching the magnetization alignments in the subsequent ferromagnets; see our discussions within the previous paragraph for details. From the experimental viewpoint, one could fabricate a junction with such $k_F d_{F_1} = k_F d_{F_2}$ that parallel magnetizations in the F/I/F spin valve maintain the π-state regime. Flipping the magnetization in F_2 by means of an externally applied magnetic field (while keeping F_1's magnetization untouched) is then sufficient to undergo a transition into the 0-state. In sharp contrast to S/F/S junctions' magnetically controlled 0-π transitions exploiting MAJC effects (see Sec. 6.2), which rely on the interplay of the ferromagnet's magnetization orientation and the interfacial SOC, the transitions in S/F/I/F/S junctions originate from the relative misalignment of the neighboring ferromagnetic areas' magnetizations and do not require any kind of SOC. Although several earlier theoretical works already predicted the appearance of 0-π transitions in ferromagnetic Josephson junctions containing quite intricate arrays of inhomogeneously magnetized regions (see, e.g., Refs. [67],[87], [222], and [304–312]), our JTMR-based realization combines experimental feasibility with an especially effective control of 0-π transitions, and might thus be of special interest for experimental follow-up works.

To provide the necessary input for experiments, we need to convince ourselves that the fundamental phenomena are general enough to be integrated into real junctions. For that purpose, we study the role of the ferromagnets' effective thicknesses in Fig. 6.18(a). The insulating barrier is considered to be $d_I \approx 0.5\,\text{nm}$ thick and its respective barrier height is set to the representative value of $V_B = 0.5\,\text{eV}$, just as we assumed in our previous calculations. Comparing the critical current curve in the parallel

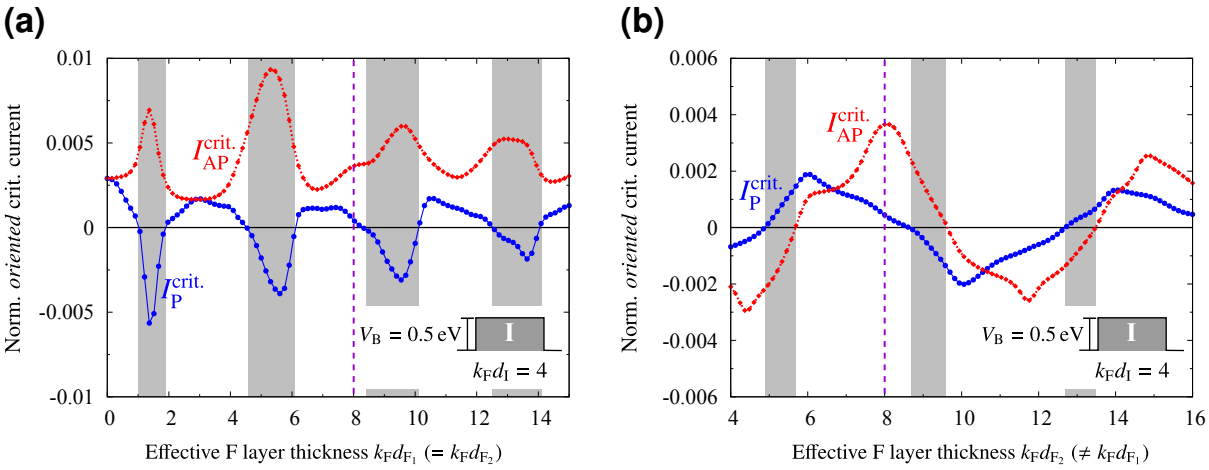


Fig. 6.18: (a) Calculated dependence of S/F/I/F/S junctions' *oriented* critical current on the effective thicknesses of the ferromagnetic layers $k_F d_{F_1} = k_F d_{F_2}$ for parallel, $I_P^{crit.}$, and antiparallel, $I_{AP}^{crit.}$, magnetized ferromagnetic regions (normalized as in Fig. 6.6), the effective insulator thickness $k_F d_I = 4$ (so that $d_I \approx 0.5\,\text{nm}$), and the barrier height $V_B = 0.5\,\text{eV}$ (see illustration). All other parameters are the same as in Fig. 6.13. The ferromagnets' thicknesses for which flipping the magnetization orientations from the parallel to the antiparallel configuration causes 0-π transitions are shaded. **(b)** Same calculation as in **(a)**, but now the left ferromagnet's effective thickness is fixed to $k_F d_{F_1} = 8$ ($d_{F_1} \approx 1\,\text{nm}$), while only that of the right ferromagnet is tuned. The violet dashed lines in **(a)** and **(b)** essentially indicate the same junction.

to the one in the antiparallel magnetization scenario confirms that experiments could focus on several, relatively large, regions of ferromagnet thicknesses that all facilitate the discussed magnetic control of 0-π transitions. We furthermore notice that the related thicknesses lie well within the experimentally accessible regime (e.g., $k_F d_{F_1} = k_F d_{F_2} = 9$, corresponding to $d_{F_1} = d_{F_2} \approx 1.1\,\text{nm}$, could be one reasonable choice) and still maintain sufficiently large Josephson current flows that can be reliably measured.

Before closing this part, we wish to demonstrate that the underlying physical mechanism, clarifying the presence (absence) of π-states in the parallel (antiparallel) magnetization configurations, really relies on the superconducting order parameter oscillations induced in the F/I/F region via proximity effects, as we claimed several times. We explained earlier that sufficiently strong oscillations provoke π-state regimes; see, for instance, our introductory motivation to Chap. 6. Parallel magnetizations mutually enhance, whereas antiparallel magnetizations mutually weaken the order parameter's oscillatory character [244, 288]. Specifically for equally thick ferromagnets, to which we limited our considerations up to now, the order parameter oscillations (nearly completely) disappear in the second magnetization configuration. As a consequence, parallel magnetized F/I/F arrays are likewise compatible with 0- and π-states, while only the 0-state regime remains energetically favorable for antiparallel magnetizations. The characteristic oscillatory variations of the critical current with increasing ferromagnet thicknesses are still a clear fingerprint of the connections between the Josephson current flow and the oscillating proximity order parameter, elucidated already for S/F/S junctions in Sec. 6.2. The simplest way to check the validity of our argumentation would be to concentrate on a junction in which the ferromagnets' thicknesses *differ*. Then, the antiparallel magnetization configurations can no longer remarkably weaken the order parameter oscillations and *both* parallel and antiparallel magnetized F/I/F links must give rise to strongly oscillating critical currents, covering 0- *and* π-regimes. Figure 6.18(b) shows precisely these simulations for one concrete parameter combination, keeping F_1's effective thickness $k_F d_{F_1} = 8$ (meaning $d_{F_1} \approx 1\,\text{nm}$) fixed, while we uniformly vary the effective thickness of F_2 from $k_F d_{F_2} = 4$ to $k_F d_{F_2} = 16$ (from $d_{F_2} \approx 0.5\,\text{nm}$ to $d_{F_2} \approx 2\,\text{nm}$). The insulator's parameters were not modified. The results coincide one-to-one with our speculations, providing the unique evidence that the absence of π-states in antiparallel magnetized

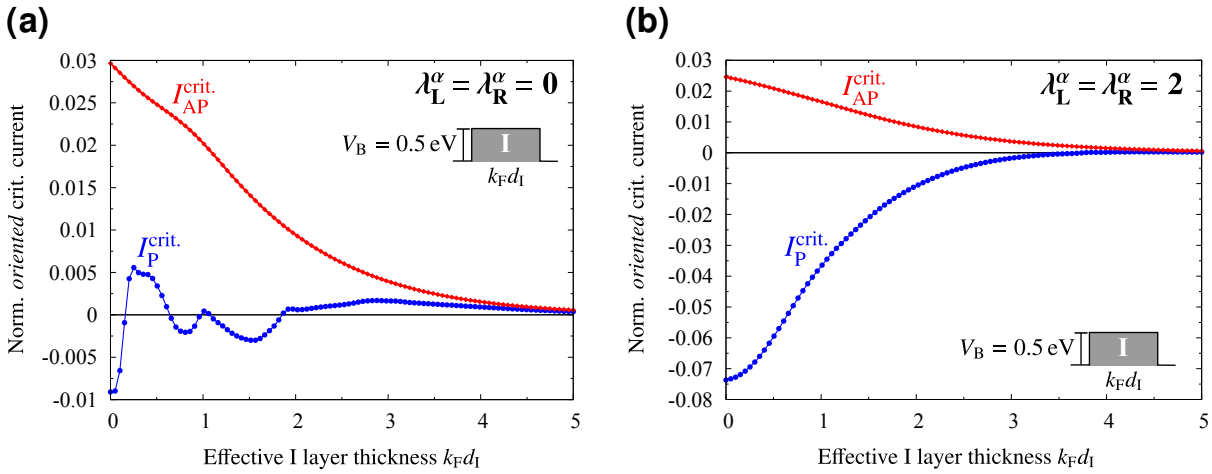


Fig. 6.19: (a) Calculated dependence of S/F/I/F/S junctions' *oriented* critical current on the effective insulator thickness $k_F d_I$ for parallel, $I_P^{crit.}$, and antiparallel, $I_{AP}^{crit.}$, magnetized ferromagnetic regions (normalized as in Fig. 6.6), and for the barrier height $V_B = 0.5\,eV$ (see illustration). The effective ferromagnet thicknesses of $k_F d_{F_1} = k_F d_{F_2} = 15$ correspond again to 1.9 nm thick iron layers. SOC is absent ($\lambda_L^\alpha = \lambda_R^\alpha = \lambda_L^\beta = \lambda_R^\beta = 0$) so that only *spin-singlet* Cooper pairs contribute to the total supercurrent. The strengths of the thin semiconducting barriers, separating the superconductors and ferromagnets, are increased to moderate values of $Z_L = Z_R = 1$ [to strengthen the effect of SOC in **(b)**]; all remaining parameters are the same as chosen in Fig. 6.13. **(b)** Same calculation as in **(a)**, but the additional presence of moderate interfacial (at the semiconducting interfaces) Rashba SOC $\lambda_L^\alpha = \lambda_R^\alpha = 2$ gives rise to a sizable *spin-triplet* Cooper pair supercurrent contribution, which noteworthy dominates the critical current in the parallel magnetization configuration.

S/F/I/F/S junctions with *equally thick ferromagnets* really originates from the strong weakening of the proximity order parameter's oscillations. Junctions in which the ferromagnets' thicknesses differ are therefore only of limited usefulness for implementing the proposed magnetic control of 0-π transitions. Nevertheless, such geometries attract attention for efficiently generating spin-triplet supercurrent components [313].

6.3.2.3 Spin-triplet Cooper pair Josephson currents

All preceding calculations were performed in the absence of SOC so that the Josephson current is solely carried by spin-singlet Cooper pairs. To make our analysis more general and to relate the outcomes to those in Sec. 6.2, we still need to figure out the influence of finite interfacial SOC (i.e., at the ultrathin semiconducting interfaces separating the superconductors and ferromagnets). Since the Josephson current is then composed of spin-singlet *and* spin-triplet Cooper pairs, interpreting the numerically obtained results finally requires us to extend our simplified Cooper pair tunneling picture to triplet pairing.

Figure 6.19(b) contrasts the critical current's effective insulator thickness ($k_F d_I$) dependence in the parallel with that in the antiparallel magnetization configuration, assuming moderate interfacial Rashba SOC with strengths $\lambda_L^\alpha = \lambda_R^\alpha = 2$ to ensure that the overall Josephson current is mostly determined by spin-triplet pairs. Weak barriers at the semiconducting interfaces ($Z_L = Z_R = 1$) additionally enhance the probability for spin-flip scatterings and generate even more sizable spin-triplet Josephson currents; Dresselhaus SOC is not taken into account ($\lambda_L^\beta = \lambda_R^\beta = 0$). The effective thicknesses of the ferromagnets are exemplarily chosen to be $k_F d_{F_1} = k_F d_{F_2} = 15$ (suggesting $d_{F_1} = d_{F_2} \approx 1.9\,nm$). For comparison, we present similar calculations for vanishing Rashba SOC in Fig. 6.19(a). The latter case basically refers to all the junctions we regarded up to now except that the semiconducting barrier strengths are

now nonzero, which may allow for further 0-π transitions not present in the absence of interfacial barriers (recall our discussions related to 0-π transitions caused by reducing interfacial transparencies in Sec. 6.2). Alternating 0- and π-state regimes in the parallel magnetization configuration,[5] as well as the disappearance of π-states and the critical current's significant enhancement if the ferromagnets' magnetizations are switched to their antiparallel alignment, count to such systems' most conspicuous properties.

Turning on finite Rashba SOC at the semiconducting interfaces strongly changes most of the characteristics. While antiparallel magnetizations still support only 0-junctions (owing to the strong compensation of the order parameter oscillations, which is not influenced by interfacial SOC), parallel magnetized F/I/F layers then necessarily entail the π-state regime and do no longer allow for alternating 0- and π-states, as it was possible in the absence of SOC. In fact, sufficiently strong SOC in S/F/I/F/S junctions favors the π-state regime for the same reasons we extracted for S/F/S junctions in Sec. 6.2 and exploited for proposing the electric 0-π transition control. Shortly speaking, interfacial SOC reduces the junction transparency and can impact the oscillations of the proximity-induced order parameter such that the current-phase relation continuously accumulates the π-phase shift. This happens predominantly in the parallel magnetized case. Antiparallel magnetizations damp the order parameter's oscillatory behavior so heavily that SOC has no longer a significant impact and cannot add intrinsic π-shifts to the current-phase relation, explaining the overall absence of π-states in the antiparallel magnetization scenario. Moreover, the trends in the critical current amplitudes start to reverse. While pure spin-singlet currents are maximized for antiparallel magnetizations, it is the parallel configuration that leads to maximal spin-triplet currents. This is the deeper reason why we had to carefully distinguish between the maximal and minimal currents when formulating a reasonable JTMR measure [see Eq. (6.81)]. Otherwise, finite SOC could suddenly change the JTMR's sign and lead to confusion. Coming back to our aforementioned Cooper pair tunneling picture, we can extract the qualitative reasoning for the large triplet currents in the parallel magnetized junction. Tunneling of spin-triplet Cooper pairs through the F/I/F sequence is sketched in Figs. 6.14(A) and 6.14(B); the spin-singlet case was discussed previously [see Figs. 6.14(a) and 6.14(b)]. The fundamental ingredient is to notice that triplet pairs are formed by electrons with the *same* spin. Therefore, a large fraction of the electrons can *sequentially* tunnel through the intermediate region and form again triplet pairs in the right superconductor if both ferromagnetic parts are magnetized parallel (so that their majority spin corresponds to the Cooper pair electrons' spin). Large triplet Josephson currents in the parallel configuration result and even exceed the enhanced singlet Josephson currents in the antiparallel scenario [compare, e.g., Fig. 6.14(A) to Fig. 6.14(b)], just as we observe in Fig. 6.19. Recall that the SOC parameters got increased to $\lambda_{\mathrm{L}}^{\alpha} = \lambda_{\mathrm{R}}^{\alpha} = 2$ to assure that the Josephson current is mostly governed by the tunneling of triplet pairs. Otherwise, the features would be less clearly apparent. The authors of the pioneering quasiclassical work on diffusive S/F/I/F/S junctions [295] already spotted that spin-singlet and spin-triplet Cooper pair currents must behave in a different manner, but did not further comment on the details. Our comprehensive study eventually clarified this puzzling issue and sketched the great potential Josephson spin-valve junctions might possess as detectors for spin-triplet supercurrents. Nevertheless, especially the effects associated with SOC might still be much richer than we outlined and might deserve a deeper analysis in the future. One could, for instance, keep the magnetization orientation in F_1 fixed and rotate F_2's magnetization, while looking for MAJC-related phenomena (see Sec. 6.2).

[5] Note that the transitions between 0- and π-junction regimes are now triggered by simply altering the thickness of the insulating barrier instead of the ferromagnets' thicknesses. The reason for that are the previously mentioned "screening" effects caused by the barrier. These additionally impact the oscillatory behavior of the proximity-induced superconducting order parameter inside the ferromagnetic regions (in the parallel magnetization scenario) and provide therefore an alternative knob to control 0-π transitions.

6.4 Short summary

To summarize, we worked out a universal theoretical framework capturing DC Josephson current flows through ballistic S/F/S-like junctions. Based on the elementary Bogoljubov-de Gennes scattering description, we already came across in Chaps. 3 and 4, we generalized the Furusaki-Tsukada Josephson current formula such that it also applies to junctions that involve spin-active components. The latter attract considerable attention in research as many recent proposals to realize Majorana physics [252, 253, 314–327] rely on suitably combining superconductivity, ferromagnetism, and SOC in one single device. We put special emphasis on keeping our formulation as general as possible. All junction-specific information is accumulated in the Bogoljubov-de Gennes states, which can be straightforwardly adapted to modified junctions. The central results, like the final expression obtained for the extended Furusaki-Tsukada formula, remain then valid for a broad variety of Josephson junctions. In fact, a closely related approach will also be our starting point when studying *transverse* Hall supercurrents in Chaps. 8 and 9.

Numerically evaluating the Josephson currents through several representative S/F/S junctions and thoroughly analyzing the physics behind the outcomes, we demonstrated that our modeling is extremely powerful and replicates all fundamental characteristics of such systems. The current-reversing 0-π transitions certainly count to the most puzzling features of magnetic Josephson contacts. We put a special focus on unraveling different and simultaneously experimentally feasible mechanisms to effectively tune these transitions. Besides the well-established geometrical control, relying on altering either the ferromagnet's thickness or the interfacial transparency between neighboring junction constituents, we deduced more efficient electrical and magnetic ways to induce 0-π transitions. Both are unique results of the interfacial SOC, which the broken space-inversion symmetry at the thin semiconducting interfaces between the superconducting and ferromagnetic components invariably causes in real junctions. Mostly due to their complexity, earlier theoretical works only rarely covered SOC in (superconducting) tunnel junctions. From that point of view, our novel studies might attract great interest among the Josephson physics community. The proposed magnetic control of 0-π transitions comes along with *giant* out-of-plane and in-plane Josephson current magnetoanisotropies, which furthermore reflect the SOC's distinct symmetry as a clear experimental signature of their physical origin. We quantified these MAJC phenomena introducing critical current-based measures that are extractable from following experiments and might contribute to a further characterization of magnetic Josephson junctions.

S/F/I/F/S junctions integrate (ferromagnetic) F/I/F spin-valve structures into (superconducting) Josephson junctions, and might be auspicious candidates for tailoring unexpected physics. Motivated by the experimental progress in designing such devices and their potential technical relevance, we finally exploited our formalism to explore supercurrent transport through these junctions. We identified a strong sensitivity of the critical Josephson current with respect to the relative alignment of the neighboring ferromagnets' magnetization orientations, which effectively resembles the JTMR effect as the superconducting analog to its normal-state TMR counterpart. Similarly to the MAJC phenomena we encountered in S/F/S junctions, the predicted JTMR ratios can dramatically overcome the normal-conducting TMRs and additionally offer another promising possibility to facilitate 0-π transitions by flipping the magnetization direction in one of the ferromagnets. In contrast to the magnetically induced transitions in S/F/S, it is now the misalignment of the ferromagnetic layers' magnetizations that triggers 0-π transitions, even if interfacial SOC is completely absent. We qualitatively connected the current's strong magnetosensitivity to a simplified "Jullière-like" Cooper pair tunneling picture, suggesting that Josephson currents mostly carried by spin-singlet pairs behave in a significantly different manner than triplet currents and allowing for an unambiguous experimental classification of the dominant pairing mechanism in real junctions, together with a reliable detection of spin-polarized triplet supercurrents. Our detailed parameter study closes gaps in the literature and might help experimentalists to find the most interesting junction regimes.

Chapter 7

Bound states and DC Josephson current in ballistic S/F-I/S junctions

Shortly after Josephson had published his groundbreaking and soon renowned transport studies on S/I/S contacts [93, 127], Andreev [179, 227] and Kulik [261] identified quantized *subgap bound states*, being strongly localized around S/I/S and likewise S/N/S junctions' weak link regions, as the Josephson effects' *microscopic* origin. Electrons that initially formed Cooper pairs in the left superconductor may simultaneously tunnel through the actually nonsuperconducting layer via these *Andreev bound states* and pair again in the right superconductor. The effectively resulting transfer of Cooper pairs from one into the second superconducting electrode precisely drives the Josephson (super)current through the junctions. From the experimental point of view, the spectral characteristics of Andreev bound states and their influence on electrical transport have been mostly studied in Josephson junctions in which the two superconducting regions are coupled by means of a single quantum dot [321, 328–330]. Such systems come along with the great advantage that the underlying Josephson current flow can be efficiently controlled either via the superconductor-quantum dot coupling strengths or the quantum dot's charging energy [331–342], even offering another practical possibility to experimentally realize π-junctions [254, 321, 328–330, 343–354]. In recent years, Su *et al.* [355] successfully implemented superconductor/*double* quantum dot/superconductor Josephson junctions. The coupling of each superconducting electrode to one quantum dot results in the formation of initially independent Andreev bound states that finally hybridize into Andreev *molecular* states. Since adding more and more quantum dots to such a system is expected to host Majorana states [76, 252–259, 316, 356, 357] at its end sites, Su's experimental progress might open novel perspectives for implementing Majorana physics into Josephson junctions in the near future.

Understanding the spectral features of inherently *magnetic* Josephson junctions, however, becomes much more intricate. Magnetism typically tends to break up Cooper pairs in the superconductors and might thus lead to the creation of actually unexpected single-particle bound states inside the superconducting energy gap. Moreover, magnetic Josephson junctions' bound state spectra must certainly reflect the systems' ability to switch between 0- and π-state regimes in some ways. After the pioneering theoretical paper by Abrikosov and Gor'kov [358] had firstly described the impact of a small amount of paramagnetic impurities on *bulk* superconductors' thermodynamic and transport features, the interest to dive deeper into this topic was rapidly growing. Several researchers [359, 360] claimed that already a small concentration of paramagnetic impurities in a bulk superconductor might induce additional subgap states. First attempts to thoroughly characterize these states, especially their energies' tunability inside the superconducting gap, followed quite soon. The independent publications of Yu [361], Shiba [362], and Rusinov [363] during the 1960s ultimately entailed valuable physical insight how the presence of (single) impurity spins modifies superconductors' excitation band structure. To emphasize the three scientists' essential contributions to this subject, the forming subgap states have been termed *Yu-Shiba-Rusinov (YSR) states*. Since the states' most fundamental characteristics are fully captured by Shiba's paper [362], the states are often simply abbreviated as Shiba states; nevertheless, we always refer to them as YSR states. Shiba considered a localized spin $\hat{\mathbf{S}}$, which could stem, e.g., from a mag-

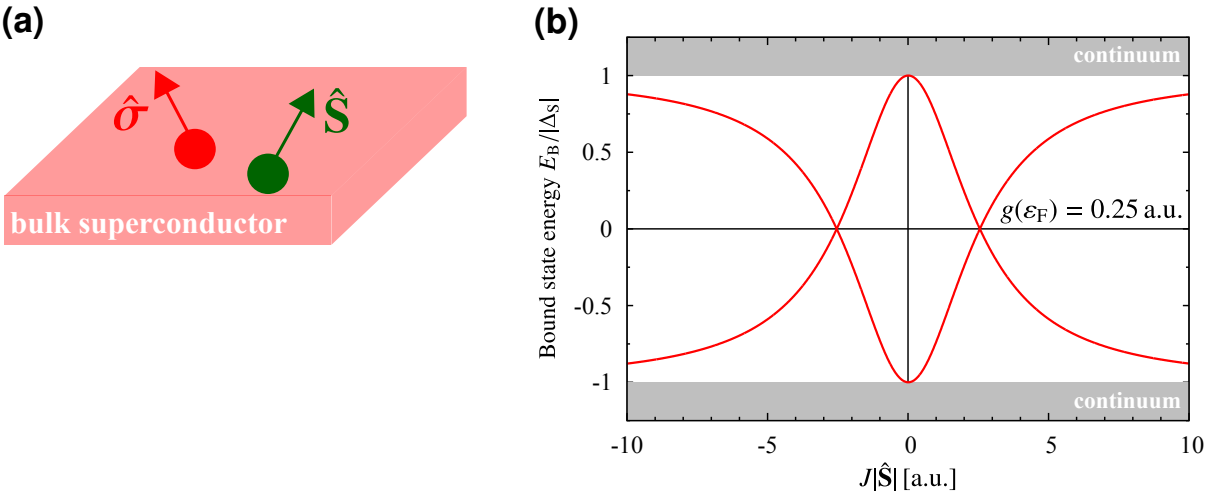


Fig. 7.1: (a) Schematical sketch of the system considered by Shiba [362]. After placing a localized spin ($\hat{\mathbf{S}}$; green) in a bulk superconductor, the resulting interaction between this spin and the conduction band electrons' spins ($\hat{\sigma}$; red; for simplicity, just one electron is shown) triggers the formation of excited YSR states *inside* the superconductor's energy gap. **(b)** Characteristic "band structure" of YSR states (E_B *vs.* $J|\hat{\mathbf{S}}|$, covering both antiferromagnetic and ferromagnetic coupling scenarios; red curve), treating the normal-state DOS $g(\varepsilon_F)$ as a phenomenological parameter [i.e., we set $g(\varepsilon_F) = 0.25$ a.u. for the plot].

netic impurity, inside a bulk *s-wave superconductor*; see Fig. 7.1(a). The *s-d* interaction between the N electron spins in the superconductor's s-like conduction band and the localized d-like spin is governed by the $\mathbf{k}$-space Hamiltonian

$$\hat{\mathcal{H}}_{s\text{-}d} = -\frac{J}{2N}\sum_{\mathbf{k}}\sum_{\mathbf{k}'}\hat{a}^{\dagger}_{\mathbf{k}}\hat{\boldsymbol{\sigma}}\hat{a}_{\mathbf{k}'}\cdot\hat{\mathbf{S}}, \tag{7.1}$$

where $\hat{a}^{\dagger}_{\mathbf{k}}$ ($\hat{a}_{\mathbf{k}}$) creates (annihilates) a conduction band electron with momentum $\mathbf{k}$. The coupling strength between the electron spins (represented by $\hat{\sigma}$) and the localized spin is denoted by J. The $\mathbf{k}$-space summations effectively average over the interactions between *all* individual electrons' spins and the localized (impurity) spin.

For simplicity, Shiba restricted his considerations to the classical limit ($J \to 0$, $|\hat{\mathbf{S}}| \to \infty$, and $J|\hat{\mathbf{S}}|$ = finite), in which the spins' quantum nature gets completely neglected. After combining the interaction Hamiltonian with the effective BCS Hamiltonian in Eq. (2.32), which models the bulk material's superconducting properties, and setting up the system's Green's function, Shiba concluded that the interaction between the electrons' spins and the localized spin indeed results in the formation of "low-lying" excited subgap states with energies

$$E_B = \pm|\Delta_S(T)|\frac{1-\left[\,(J/2)\,|\hat{\mathbf{S}}|\pi g(\varepsilon_F)\right]^2}{1+\left[\,(J/2)\,|\hat{\mathbf{S}}|\pi g(\varepsilon_F)\right]^2}; \tag{7.2}$$

$g(\varepsilon_F)$ measures the normal-state DOS at the Fermi level ε_F. The states' symmetry with respect to the gap center originates from the fundamental electron-hole symmetry in superconductors. Note that the temperature dependence of the excitation energies is solely determined by the (BCS-like) temperature scaling of the superconducting energy gap [$|\Delta_S(T \neq 0)| = |\Delta_S(0)|\tanh(1.74\sqrt{T_C/T-1})$]. Plotting E_B as a function of $J|\hat{\mathbf{S}}|$ yields the characteristic "band structure" of YSR states, depicted in Fig. 7.1(b). Motivated by Shiba's (and also Yu's and Rusinov's) results, YSR states have been intensively investigated in various systems, for instance, in superconducting substrates hosting magnetic adatoms [364–371] or in nanowires that connect N/S junctions [372, 373].

Besides conventional s-wave superconductivity, Shiba and also we exclusively assumed up to now, superconducting materials in which the dominant pairing mechanism is the triplet one attract considerable interest in ongoing research. This subject is mainly driven by several proposals to generate single (zero-energy) Majorana modes at the boundaries of (spinless) p-wave superconductors [374, 375]. Since the superconducting materials that are believed to possess inherent p_x- or $(p_x \pm \mathrm{i}p_y)$-wave pairing are quite complicated (e.g., certain organic compounds [376–378] or chiral Sr_2RuO_4 [379, 380]), common theoretical suggestions to implement Majorana physics and topological superconductivity rather focus on artificially designed systems that mimic p-wave superconductors. The probably most auspicious candidates might be noncentrosymmetric semiconductor-based nanowires with strong (Rashba) SOC. When brought in proximity to an s-wave superconductor and applying an appropriately aligned magnetic field, these wires effectively behave like a p-wave superconductor and might host Majorana states [252, 253, 314–327, 381]. Many groups around the world are hardly working on the final experimental confirmation of these states' existence, predominantly looking for expected zero-bias transport anomalies (see, e.g., Ref. [252–255], [317], and [318]). Particularly rewarding in this context are several recent theoretical works [323, 324, 326] that predict the formation of zero-energy Majorana modes in phase-controlled Josephson junctions invoking an intriguing interplay between strong (Rashba [149, 150] and Dresselhaus [152]) SOCs and in-plane Zeeman fields. First experiments [327, 381], aiming at detecting the proposed transport anomalies as an unambiguous proof for the existence of Majorana bound states, are already on the way.

In this chapter, we profoundly investigate the subgap bound states forming around the ultrathin ferromagnetic-insulator barriers of ballistic S/F-I/S Josephson junctions. To keep our study general, we account for possibly present Rashba SOC inside the superconducting electrodes, which might be realized proximitizing a semiconductor nanowire with a superconductor, similarly to the mentioned Majorana proposals. The superconducting pairing potential itself is considered to be either the pure *singlet* s-wave or the pure *triplet* p_x-wave one. As mentioned above, the latter plays a crucial role in connection with Majorana states and needs therefore a more fundamental study to unravel further (experimental) signatures of such states' appearance. The chapter is divided into four sections. Section 7.1 is dedicated to the generic description of our system. After introducing the theoretical framework from which the junctions' bound state spectra can be extracted, we establish another powerful technique that allows us to compute the related Josephson current flow. The latter simply requires the bound state energies as an input and is therefore a reasonable alternative to the Furusaki-Tsukada formulation (see Chap. 6) once the bound state spectrum is known.

In Sec. 7.2, we discuss analytically and numerically obtained results for S/F-I/S Josephson junctions with singlet (s-wave) pairing symmetry. As long as Rashba SOC inside the superconducting regions stays absent, the bound state energies are fully determined by closed analytical formulas. We demonstrate that these states, composed of Andreev bound states *and* YSR states owing to the magnetic tunneling through ferromagnetic-insulator barriers, possess unique spectral [333, 382] and *spin* characteristics, which are widely tunable by altering either the scalar and magnetic tunneling strengths, or the superconducting phase difference. The striking interplay between both types of states may eventually manifest itself in anomalous conductance peaks [254, 342]. Special attention needs to be paid to *zero-energy* YSR states, which can signal a crossover between trivial and topological superconductivity [383–385], or ground-state phase transitions [386]. Evaluating the Josephson current from the earlier computed bound state spectra, we clearly distinguish the 0- and π-state regimes of S/F-I/S Josephson junctions [382, 387, 388] and elucidate the 0-π transition mechanism on the *microscopic* level. It is the ground-state phase transition close to the zero-energy YSR states that reverses the tunneling direction of Cooper pairs through the YSR channel and simultaneously the orientation (sign) of the Josephson current flow. To show that the proposed 0-π transition mechanism is universal, we numerically identify the 0-π transitions emerging in

the presence of Rashba SOC inside the superconductors. While providing an experimentally feasible tunability of the transition points, the crucial coincidence with the zero-energy YSR states persists even for nonzero Rashba SOC.

Assuming triplet p_x-wave pairing in the superconductors strongly affects the bound states' properties, as we briefly illustrate in Sec. 7.3. In this case, the junctions do no longer support the formation of YSR states since those are unique to s-wave superconductors. Instead, the Andreev bound states simply split into spin-resolved branches. As a remarkable consequence, the YSR states' intriguing zero-energy crossings, to which we connected the appearing 0-π transitions in the s-wave scenario, disappear so that p_x-wave S/F-I/S Josephson junctions usually cannot enter the π-phase. Our analytical and numerical calculations are fully consistent with these expectations and reveal additional indications of robust – against both scalar and magnetic scattering – zero-energy Andreev bound states, which are usually regarded as precursors of Majorana bound states [356, 357]. Following the aforementioned proposals, one might also engineer S/F-I/S Josephson junctions that host the latter by combining strong Rashba SOC with appropriately large magnetic tunneling strengths, even if the superconductors' pairing symmetry is simply the s-wave one. Although the slightly different, recently published, theoretical predictions [323, 324, 326] seem to be more auspicious for that – mostly due to the fact that SOC and magnetism are spatially separated in our system (the first appears only inside the superconductors and the second just at the ferromagnetic-insulator interface) and not suitably oriented so that both cannot act together efficiently enough –, our analysis might still help to extend the proposed relations between superconducting junctions and Majorana physics. We did not further optimize our set-up from the Majorana viewpoint since we laid our studies' focus on unraveling the physical connections between magnetic Josephson junctions' bound state spectra and the puzzling 0-π transitions in their Josephson current, and not on Majorana physics. The chapter eventually closes with a short summary in Sec. 7.4.

Section 7.2 is based on the article "Connection between zero-energy Yu-Shiba-Rusinov states and 0-π transitions in magnetic Josephson junctions" by Andreas Costa, Jaroslav Fabian, and Denis Kochan, which got published in Phys. Rev. B ***98****, 134511 (2018). Andreas Costa performed all presented analytical and numerical calculations. The qualitative picture explaining the coincidence between the YSR states' unique characteristics and the Josephson current-reversing 0-π transitions was jointly developed by Andreas Costa and Denis Kochan. Moreover, Denis Kochan and Jaroslav Fabian supported the project with stimulating discussions and feedback.*

7.1 Theoretical description

The S/F-I/S Josephson contact considered throughout this chapter is composed of two effectively *one-dimensional noncentrosymmetric* superconductors (S; located at $x < 0$ and $x > 0$ using the $\hat{x} \parallel [110]$ crystallographic orientation as reference), which are coupled by an ultrathin ferromagnetic-insulator (F-I) barrier; see Fig. 7.2 for illustration. Noncentrosymmetric superconductors, which can inherently sustain strong (Rashba) SOC owing to their lacking space-inversion symmetry, have attracted lots of attention in recent years [389]. They are of particular interest for our studies since SOC might provide one key ingredient to tailor the junction's bound state spectrum and Josephson current flow. Instead of dealing with complicated (noncentrosymmetric) superconducting materials, future experiments could essentially also focus on two semi-infinite semiconductor nanowires (inducing the SOC), which are proximitized by two s-wave superconductors (at $x < 0$ and $x > 0$) and connected by the thin ferromagnetic-insulator interlayer (e.g., a thin layer of EuS [21] or EuO [225]). As we mentioned above, such nanowire-based Josephson junctions count to the probably most promising proposals for observing Majorana states [252, 253, 314–322] and deserve therefore a comprehensive analysis. To access the junction's spectral proper-

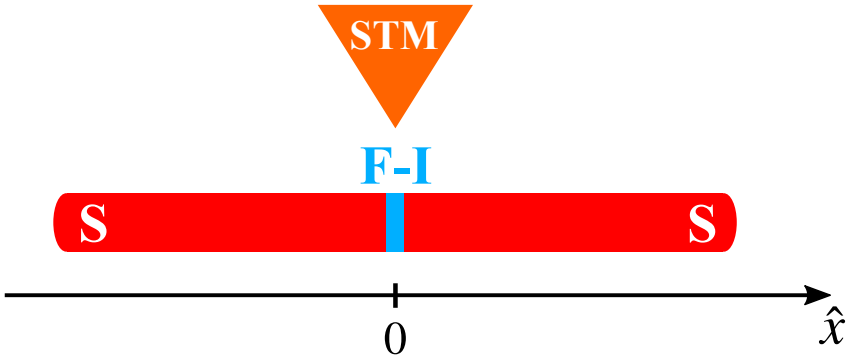


Fig. 7.2: Schematical sketch of the considered *one-dimensional* S/F-I/S Josephson junction grown along the $\hat{x} \parallel [110]$ crystallographic orientation; the ultrathin ferromagnetic-insulator (F-I) barrier between the two superconducting electrodes (S) introduces *scalar and magnetic tunnelings*. The bound states forming around the interface may be experimentally probed by means of STM spectroscopy.

ties, predominantly its characteristic bound state spectrum, we rely again on the previously established Bogoljubov-de Gennes approach.

7.1.1 Bogoljubov-de Gennes scattering states

Within Nambu representation, the S/F-I/S junction's Bogoljubov-de Gennes Hamiltonian [139] reads

$$\hat{\mathcal{H}}_{\mathrm{BdG}} = \begin{bmatrix} \hat{\mathcal{H}}_{\mathrm{e}} & \hat{\Delta}_{\mathrm{S}}(x) \\ \hat{\Delta}_{\mathrm{S}}^{\dagger}(x) & \hat{\mathcal{H}}_{\mathrm{h}} \end{bmatrix}, \tag{7.3}$$

where

$$\hat{\mathcal{H}}_{\mathrm{e}} = \left(-\frac{\hbar^2}{2m}\frac{\mathrm{d}^2}{\mathrm{d}x^2} - \mu \right) \hat{\sigma}_0 - \lambda_{\mathrm{R}} k_x \hat{\sigma}_y + \hat{\mathcal{H}}^{\text{F-I}} \tag{7.4}$$

corresponds to the single-electron Hamiltonian and $\hat{\mathcal{H}}_{\mathrm{h}} = -\hat{\sigma}_y \hat{\mathcal{H}}_{\mathrm{e}}^{*} \hat{\sigma}_y$ to its hole counterpart. For the sake of simplicity, we restrict ourselves to the case of two similar superconductors, i.e., the chemical potential μ and quasiparticle masses m are equal everywhere in the junction, and do therefore not explicitly depend on position. The superconducting electrodes' built-in Rashba SOC enters via its effective strength λ_{R}, while $\hat{\mathcal{H}}^{\text{F-I}} = (\lambda_{\mathrm{SC}}\hat{\sigma}_0 + \lambda_{\mathrm{MA}}\hat{\sigma}_z)\,\delta(x)$ accounts for interfacial scalar and magnetic tunnelings through the ultrathin ferromagnetic insulator with the effective coupling strengths λ_{SC} (scalar) and λ_{MA} (magnetic), respectively; the two-by-two identity and the ith Pauli spin matrix are still denoted by $\hat{\sigma}_0$ and $\hat{\sigma}_i$. Within our strongly simplified description, magnetic tunneling simply means that incoming spin-up and spin-down electrons (spin is quantized with respect to $\hat{\sigma}_z$) are exposed to different scattering potentials. The most natural choice for a Hamiltonian satisfying this requirement is the given one, formally combining a *spin-independent* scalar tunneling Hamiltonian (e.g., $\lambda_{\mathrm{SC}}\hat{\sigma}_0$) with a *spin-dependent* Zeeman Hamiltonian (e.g., $\lambda_{\mathrm{MA}}\hat{\sigma}_z$). It is thus not essential for the discussed physics that the junction interface is really composed of a ferromagnetic insulator. Future experimental studies could instead likewise focus on ultrathin insulating barriers and apply a magnetic field aligned perpendicular to the junction's growth direction (along $\hat{z}$).

Since we want to keep our theoretical modeling as general as possible, the superconducting pairing potential *simultaneously* allows for s-wave and p_x-wave pairing terms, namely

$$\hat{\Delta}_{\mathrm{S}}(x) = \left(|\Delta_{\mathrm{S}}^{s}|\hat{\sigma}_0 - |\Delta_{\mathrm{S}}^{p}|\frac{k_x}{|k_x|}\hat{\sigma}_y \right)\Theta(-x) + \left(|\Delta_{\mathrm{S}}^{s}|\hat{\sigma}_0 - |\Delta_{\mathrm{S}}^{p}|\frac{k_x}{|k_x|}\hat{\sigma}_y \right)\mathrm{e}^{\mathrm{i}\phi_{\mathrm{S}}}\Theta(x). \tag{7.5}$$

As before, we neglect proximity effects, which would require a self-consistent determination of the pairing amplitudes' spatial variations. The s-wave (singlet) pairing's isotropic energy gap is given by $|\Delta_{\mathrm{S}}^{s}|$, whereas $|\Delta_{\mathrm{S}}^{p}|$ refers to the superconducting energy gap associated with p_x-wave (triplet) pairing;[1] ϕ_{S} indicates the phase difference between the two superconducting regions, just as in Chap. 6. Our approach would, in principle, even properly capture a mixture of s-wave and p_x-wave pairings, which has been predicted to induce a topologically nontrivial quantum spin Hall regime with protected Andreev bound states as helical edge modes [391]. We restrict our subsequent considerations, nevertheless, to superconductors in which the pairing possesses either *pure* s-wave or *pure* p_x-wave symmetry.

Solving the stationary Bogoljubov-de Gennes equation

$$\hat{\mathcal{H}}_{\mathrm{BdG}}\psi(x) = E\psi(x), \tag{7.6}$$

we extract the most general wave function ansatz describing bound states with energy E as

$$\begin{aligned}\psi(x<0;E) = a(E)\begin{bmatrix}-\mathrm{i}u^{\Uparrow}(E)\\ u^{\Uparrow}(E)\\ -\mathrm{i}v^{\Uparrow}(E)\\ v^{\Uparrow}(E)\end{bmatrix}\mathrm{e}^{-\mathrm{i}q_{x,\mathrm{e}}^{\Uparrow}(E)x} + b(E)\begin{bmatrix}\mathrm{i}v^{\Uparrow}(E)\\ v^{\Uparrow}(E)\\ \mathrm{i}u^{\Uparrow}(E)\\ u^{\Uparrow}(E)\end{bmatrix}\mathrm{e}^{\mathrm{i}q_{x,\mathrm{h}}^{\Uparrow}(E)x}\\ + c(E)\begin{bmatrix}\mathrm{i}u^{\Downarrow}(E)\\ u^{\Downarrow}(E)\\ -\mathrm{i}\gamma v^{\Downarrow}(E)\\ -\gamma v^{\Downarrow}(E)\end{bmatrix}\mathrm{e}^{-\mathrm{i}q_{x,\mathrm{e}}^{\Downarrow}(E)x} + d(E)\begin{bmatrix}-\mathrm{i}v^{\Downarrow}(E)\\ v^{\Downarrow}(E)\\ \mathrm{i}\gamma u^{\Downarrow}(E)\\ -\gamma u^{\Downarrow}(E)\end{bmatrix}\mathrm{e}^{\mathrm{i}q_{x,\mathrm{h}}^{\Downarrow}(E)x}\end{aligned} \tag{7.7}$$

in the left superconductor ($x < 0$) and

$$\begin{aligned}\psi(x>0;E) = e(E)\begin{bmatrix}\mathrm{i}u^{\Uparrow}(E)\mathrm{e}^{\mathrm{i}\phi_{\mathrm{S}}}\\ u^{\Uparrow}(E)\mathrm{e}^{\mathrm{i}\phi_{\mathrm{S}}}\\ \mathrm{i}v^{\Uparrow}(E)\\ v^{\Uparrow}(E)\end{bmatrix}\mathrm{e}^{\mathrm{i}q_{x,\mathrm{e}}^{\Uparrow}(E)x} + f(E)\begin{bmatrix}-\mathrm{i}v^{\Uparrow}(E)\mathrm{e}^{\mathrm{i}\phi_{\mathrm{S}}}\\ v^{\Uparrow}(E)\mathrm{e}^{\mathrm{i}\phi_{\mathrm{S}}}\\ -\mathrm{i}u^{\Uparrow}(E)\\ u^{\Uparrow}(E)\end{bmatrix}\mathrm{e}^{-\mathrm{i}q_{x,\mathrm{h}}^{\Uparrow}(E)x}\\ + g(E)\begin{bmatrix}-\mathrm{i}u^{\Downarrow}(E)\mathrm{e}^{\mathrm{i}\phi_{\mathrm{S}}}\\ u^{\Downarrow}(E)\mathrm{e}^{\mathrm{i}\phi_{\mathrm{S}}}\\ \mathrm{i}\gamma v^{\Downarrow}(E)\\ -\gamma v^{\Downarrow}(E)\end{bmatrix}\mathrm{e}^{\mathrm{i}q_{x,\mathrm{e}}^{\Downarrow}(E)x} + h(E)\begin{bmatrix}\mathrm{i}v^{\Downarrow}(E)\mathrm{e}^{\mathrm{i}\phi_{\mathrm{S}}}\\ v^{\Downarrow}(E)\mathrm{e}^{\mathrm{i}\phi_{\mathrm{S}}}\\ -\mathrm{i}\gamma u^{\Downarrow}(E)\\ -\gamma u^{\Downarrow}(E)\end{bmatrix}\mathrm{e}^{-\mathrm{i}q_{x,\mathrm{h}}^{\Downarrow}(E)x}\end{aligned} \tag{7.8}$$

in the right superconductor ($x > 0$); $\Uparrow$ and $\Downarrow$ refer to the superconductors' *effective* spin-up and spin-down quasiparticle bands, which split owing to the bulk Rashba SOC and the finite triplet pairing potential.[2] Since we are only looking for bound state solutions corresponding to evanescent waves, the ansatz in Eqs. (7.7)–(7.8) does not need to account for incoming waves. Because of the formal similarities

[1] Note that other authors often write the Bogoljubov-de Gennes Hamiltonian including p_x-wave pairing potentials in *tunneling representation* – one common alternative to the Nambu basis; see, e.g., Refs. [390] and [391]. One can easily rewrite the tunneling Bogoljubov-de Gennes Hamiltonian $\hat{\mathcal{H}}_{\mathrm{BdG}}^{\mathrm{T}}$ in its corresponding Nambu version $\hat{\mathcal{H}}_{\mathrm{BdG}}^{\mathrm{N}}$ according to $\hat{\mathcal{H}}_{\mathrm{BdG}}^{\mathrm{N}} = \hat{\mathcal{U}}^{-1}\hat{\mathcal{H}}_{\mathrm{BdG}}^{\mathrm{T}}\hat{\mathcal{U}}$, making use of the unitary transformation

$$\hat{\mathcal{U}} = \begin{bmatrix}1 & 0 & 0 & 0\\ 0 & 1 & 0 & 0\\ 0 & 0 & 0 & -1\\ 0 & 0 & 1 & 0\end{bmatrix}.$$

[2] Note the close formal analogy between the (Rashba) SOC Hamiltonian and the triplet pairing potential.

with the "true" scattering problem (including incident particles as we accounted for in Chap. 6), the wave function coefficients might still be connected to specular reflections without and with spin flips [coefficients $a(E)$ and $c(E)$], Andreev reflections [coefficients $b(E)$ and $d(E)$], as well as quasiparticle transmissions [coefficients $e(E)$, $f(E)$, $g(E)$, and $h(E)$].

The spin-resolved electronlike quasiparticle wave vectors inside the superconducting regions are given by

$$q_{x,\mathrm{e}}^{\Uparrow}(E) = \sqrt{\frac{2m}{\hbar^2}\left[\mu + \sqrt{E^2 - \left(\Delta_{\mathrm{S}}^{\Uparrow}\right)^2}\right] + \left(\frac{m\lambda_{\mathrm{R}}}{\hbar^2}\right)^2} - \frac{m\lambda_{\mathrm{R}}}{\hbar^2} \tag{7.9}$$

and

$$q_{x,\mathrm{e}}^{\Downarrow}(E) = \sqrt{\frac{2m}{\hbar^2}\left[\mu + \sqrt{E^2 - \left(\Delta_{\mathrm{S}}^{\Downarrow}\right)^2}\right] + \left(\frac{m\lambda_{\mathrm{R}}}{\hbar^2}\right)^2} + \frac{m\lambda_{\mathrm{R}}}{\hbar^2}, \tag{7.10}$$

with the effective superconducting energy gaps

$$\Delta_{\mathrm{S}}^{\Uparrow} := |\Delta_{\mathrm{S}}^{s}| + |\Delta_{\mathrm{S}}^{p}| \qquad \text{and} \qquad \Delta_{\mathrm{S}}^{\Downarrow} := \left||\Delta_{\mathrm{S}}^{s}| - |\Delta_{\mathrm{S}}^{p}|\right|. \tag{7.11}$$

Similarly, we obtain for holelike quasiparticles

$$q_{x,\mathrm{h}}^{\Uparrow}(E) = \sqrt{\frac{2m}{\hbar^2}\left[\mu - \sqrt{E^2 - \left(\Delta_{\mathrm{S}}^{\Uparrow}\right)^2}\right] + \left(\frac{m\lambda_{\mathrm{R}}}{\hbar^2}\right)^2} - \frac{m\lambda_{\mathrm{R}}}{\hbar^2}, \tag{7.12}$$

as well as

$$q_{x,\mathrm{h}}^{\Downarrow}(E) = \sqrt{\frac{2m}{\hbar^2}\left[\mu - \sqrt{E^2 - \left(\Delta_{\mathrm{S}}^{\Downarrow}\right)^2}\right] + \left(\frac{m\lambda_{\mathrm{R}}}{\hbar^2}\right)^2} + \frac{m\lambda_{\mathrm{R}}}{\hbar^2}. \tag{7.13}$$

It is worth to notice that the electronlike and holelike wave vectors contain evanescent (imaginary) parts for energies inside the effective superconducting energy gaps, already serving as a first precursor that the formation of bound subgap states must be possible in our system. The associated BCS-like coherence factors are

$$u^{\Uparrow(\Downarrow)}(E) = \sqrt{\frac{1}{2}\left\{1 + \sqrt{1 - \frac{\left[\Delta_{\mathrm{S}}^{\Uparrow(\Downarrow)}\right]^2}{E^2}}\right\}} \quad \text{and accordingly} \quad v^{\Uparrow(\Downarrow)}(E) = \sqrt{1 - \left[u^{\Uparrow(\Downarrow)}(E)\right]^2}. \tag{7.14}$$

Finally, the wave function ansatz in Eqs. (7.7)–(7.8) contains the additional "phase factor"

$$\gamma = \mathrm{sgn}\left(|\Delta_{\mathrm{S}}^{s}| - |\Delta_{\mathrm{S}}^{p}|\right), \tag{7.15}$$

which becomes particularly important if the pairing potential consists of a mixture of singlet and triplet parts.

To access the unknown wave function coefficients, we apply the interfacial ($x = 0$) boundary conditions

$$\psi(x;E)\big|_{x=0_-} = \psi(x;E)\big|_{x=0_+} \tag{7.16}$$

and

$$\left\{\left(\frac{\hbar^2}{2m}\frac{\mathrm{d}}{\mathrm{d}x} + \lambda_{\mathrm{SC}}\right)\hat{\eta} + \lambda_{\mathrm{MA}}\hat{\omega}\right\}\psi(x;E)\big|_{x=0_-} = \frac{\hbar^2}{2m}\frac{\mathrm{d}}{\mathrm{d}x}\hat{\eta}\psi(x;E)\big|_{x=0_+}, \tag{7.17}$$

with

$$\hat{\eta} = \begin{bmatrix} \hat{\sigma}_0 & \hat{0} \\ \hat{0} & -\hat{\sigma}_0 \end{bmatrix} \qquad \text{and} \qquad \hat{\omega} = \begin{bmatrix} \hat{\sigma}_z & \hat{0} \\ \hat{0} & \hat{\sigma}_z \end{bmatrix}, \tag{7.18}$$

to Eqs. (7.7)–(7.8), essentially yielding a homogeneous system of eight linear equations; $\hat{0}$ is the two-by-two zero matrix. To obtain a nontrivial solution (indicating the formation of a bound state at that particular energy), the determinant of the system's coefficient matrix must vanish. Imposing this condition yields a secular equation, which we solve (analytically in some limiting cases and numerically in general) for energy to assign the bound state energies; the latter will be denoted by E_B in the following in order to clearly separate them from generic energies E. For completeness, let us mention two mathematical intricacies. First, the coherence factors [see Eq. (7.14)] depend on energy in a complicated way. The resulting secular equation is therefore not a simple polynomial of eighth degree and we will not necessarily obtain eight independent bound state solutions one would actually expect for eighth order polynomials. In fact, we will end up with four bound state solutions instead. Second, the wave function ansatz in Eqs. (7.7)–(7.8) refers basically only to *positive-energy* bound states. Nevertheless, owing to superconductors' characteristic electron-hole symmetry, each bound state with energy $E_\mathrm{B} > 0$ will be accompanied by a second one at energy $-E_\mathrm{B}$.

Once all bound state energies E_B are identified, we can proceed unraveling the still unknown bound state wave function coefficients, which will be required for computing the Josephson current within the technique introduced in the next part. These calculations are rather technical and can be found in Appendix D.

7.1.2 Josephson current – bound state approach

Given closed analytical expressions for the bound state wave functions, *including all appearing coefficients*, we can relate the junction's bound state characteristics to the Josephson current flowing through it. The results that we will extract from this approach serve not only as an essential crosscheck for the Furusaki-Tsukada technique (see Chap. 6), but bring along the great advantage to draw unique connections between the bound states' features and the Josephson current.

Since the whole junction is assumed to be ballistic, the total electrical current is conserved and can be calculated anywhere along the system. To avoid further complications, probably emerging when directly dealing with Cooper pairs inside the superconducting electrodes, we evaluate the current inside the ferromagnetic insulator. Electrons that initially formed Cooper pairs in one of the superconductors tunnel through the thin ferromagnetic-insulator barrier via the available bound states and pair again in the second superconductor. The effectively resulting Cooper pair exchange between the superconductors generates a net Josephson current flow as long as more Cooper pairs get transferred into the right than into the left superconductor (or vice versa). All electrical current in the ferromagnetic insulator is hence carried by single electrons occupying the bound states, which we are able to fully characterize within the methodology introduced in the previous section.

To extract the net (balanced) current, we need to properly account for Cooper pair electrons tunneling from the left into the right superconductor via the bound states *and* for Cooper pair electrons simultaneously tunneling along the opposite direction. The most common way exploits the electron-hole symmetry in the Bogoljubov-de Gennes framework, similarly to what we encountered when recapitulating the BTK model in Chap. 3. It is sufficient to consider just right-moving (or equivalently, just left-moving) electrons *and* holes; the hole contribution includes then automatically the current stemming from left-moving (right-moving) electrons. Our bound state wave functions [see Eqs. (7.7)–(7.8)] indeed contain superpositions of electronlike and holelike parts, and thus already capture all relevant information to compute the Josephson current in the correct way. The current contribution of *one single occupied*

bound state with energy E_B, described by the wave function $\psi(x;E_\mathrm{B})$, is obtained applying the electrical current density operator $\hat{j}_x$ to $\psi(x;E_\mathrm{B})$. Recall that we are concerned with a one-dimensional problem along $\hat{x}$ so that there is no need to regard the transverse directions. The ferromagnetic insulator is supposed to be ultrathin and the bound state wave functions must be continuous at the interface [see, e.g., the boundary condition in Eq. (7.16)]. We can therefore either exploit the bound state wave functions inside the left superconducting electrode, $\psi(x<0;E_\mathrm{B})$, in Eq. (7.7), or the related ones inside the right superconductor, $\psi(x>0;E_\mathrm{B})$, in Eq. (7.8), and consider the limit $x\to 0_+$ in the end.

We rely on the bound state wave functions in the right half-junction, $\psi(x>0;E_\mathrm{B})$, which describe the tunneling of electrons (holes) *from the left into the right superconductor* via the bound states with energy E_B. Note once again that the tunneling of holes covers then the current actually stemming from electrons being transferred *from the right into the left superconductor*. The *average* contribution of the *occupied* bound state $\psi(x>0;E_\mathrm{B})$ to the electrical current density $j_x(E_\mathrm{B})$ is then given by the related current density operator's expectation value in this state, i.e., by

$$\begin{aligned} j_x(E_\mathrm{B}) &= \lim_{x\to 0_+}\left\{\left\langle\hat{j}_x\right\rangle\Big|_{\psi(x>0;E_\mathrm{B})}\right\} \\ &= \lim_{x\to 0_+}\left\{\left\langle\psi(x>0;E_\mathrm{B})\middle|\hat{j}_x\middle|\psi(x>0;E_\mathrm{B})\right\rangle\tanh\left(\frac{E_\mathrm{B}}{2k_\mathrm{B}T}\right)\right\}, \end{aligned} \tag{7.19}$$

where

$$\begin{aligned} \hat{j}_x &= -e\begin{bmatrix} \left.\dfrac{\partial\hat{\mathcal{H}}_\mathrm{e}}{\hbar\partial k_x}\right|_{k_x\longmapsto -\mathrm{i}(\mathrm{d}/\mathrm{d}x)} & \hat{0} \\ \hat{0} & -\hat{\sigma}_y\left[\left.\dfrac{\partial\hat{\mathcal{H}}_\mathrm{e}}{\hbar\partial k_x}\right|_{k_x\longmapsto -\mathrm{i}(\mathrm{d}/\mathrm{d}x)}\right]^*\hat{\sigma}_y \end{bmatrix} \\ &= -e\begin{bmatrix} -\dfrac{\mathrm{i}\hbar}{m}\dfrac{\mathrm{d}}{\mathrm{d}x} & \dfrac{\mathrm{i}\lambda_\mathrm{R}}{\hbar} & 0 & 0 \\ -\dfrac{\mathrm{i}\lambda_\mathrm{R}}{\hbar} & -\dfrac{\mathrm{i}\hbar}{m}\dfrac{\mathrm{d}}{\mathrm{d}x} & 0 & 0 \\ 0 & 0 & -\dfrac{\mathrm{i}\hbar}{m}\dfrac{\mathrm{d}}{\mathrm{d}x} & \dfrac{\mathrm{i}\lambda_\mathrm{R}}{\hbar} \\ 0 & 0 & -\dfrac{\mathrm{i}\lambda_\mathrm{R}}{\hbar} & -\dfrac{\mathrm{i}\hbar}{m}\dfrac{\mathrm{d}}{\mathrm{d}x} \end{bmatrix} \end{aligned} \tag{7.20}$$

represents the electrical current density operator. Let us give short reasoning for its general form. Single electrons' quantum-mechanical electrical current density operators $\hat{J}_x=-e\hat{v}_x$ are usually defined via the product of the electrons' charge $-e$ and their respective velocity operators along the considered direction (say, e.g., $\hat{v}_x$ along $\hat{x}$). Since we are now dealing with the Nambu Bogoljubov-de Gennes Hamiltonian, combining electronlike and holelike excitations in just one Hamiltonian, we need to replace the "scalar" current density operator by a "matrix operator". The upper block of the operator acts then on the electronlike and the lower block on the holelike part of the bound state wave functions. Inspecting Eq. (7.20), the diagonal elements indeed correspond to free electrons' (holes') current density operators, identifying $\hat{v}_x=(-\mathrm{i}\hbar)/m(\mathrm{d}/\mathrm{d}x)$ as free electrons' (holes') velocity operators along $\hat{x}$. At first, it might seem counterintuitive that the current density operator's electron and hole blocks become formally identical. We mentioned above that holes essentially cover the remaining current contribution originating from electrons tunneling through the ferromagnetic insulator along the reversed direction,

i.e., from right to left in our example. One might thus expect that the electron and hole parts of the electrical current (density) should differ by a relative sign. In fact, when calculating the Josephson current, we will learn that this information is already captured by the wave functions themselves and therefore not again included into the current density operator. Moreover, owing to the Rashba SOC present in our system, we need to account for additional off-diagonal SOC-related contributions ($\propto \lambda_\mathrm{R}$) to the electron and hole velocity operators.[3] Owing to the close formal analogy between the Rashba SOC Hamiltonian and the p_x-wave superconducting pairing potential, one might probably look for another contribution to the current density operator that scales with the triplet gap ($\propto |\Delta_\mathrm{S}^p|$). A rigorous calculation indicates, however, that these terms scale *inversely* with the chemical potential μ and become negligibly small for realistic junction parameters (e.g., $\mu \approx 10^3 |\Delta_\mathrm{S}|$). To ensure that we finally solely count the current contributions originating from states that are indeed occupied (at a given temperature T), we furthermore included the thermal occupation factor $\tanh[E_\mathrm{B}/(2k_\mathrm{B}T)]$, where k_B stands for Boltzmann's constant, into the current formula in Eq. (7.19), just as in Sec. 6.1 [see Eq. (6.17)].

Evaluating Eq. (7.19) by means of Eq. (7.20) and the explicit from of the bound state wave functions $\psi(x > 0; E_\mathrm{B})$ stated in Eq. (7.8), we arrive at

$$
\begin{aligned}
I_\mathrm{J}(E_\mathrm{B}) &= \sum_{\mathbf{k}_\parallel} j_x(E_\mathrm{B}) \\
&= -e \sum_{\mathbf{k}_\parallel} \Bigg\{ \left[\frac{\hbar q_{x,\mathrm{e}}^{\Uparrow}(E_\mathrm{B})}{m} + \frac{\lambda_\mathrm{R}}{\hbar} \right] \left[\left|u^{\Uparrow}(E_\mathrm{B})\right|^2 + \left|v^{\Uparrow}(E_\mathrm{B})\right|^2 \right] \left|e(E_\mathrm{B})\right|^2 \\
&\qquad - \left[\frac{\hbar q_{x,\mathrm{h}}^{\Uparrow}(E_\mathrm{B})}{m} + \frac{\lambda_\mathrm{R}}{\hbar} \right] \left[\left|u^{\Uparrow}(E_\mathrm{B})\right|^2 + \left|v^{\Uparrow}(E_\mathrm{B})\right|^2 \right] \left|f(E_\mathrm{B})\right|^2 \\
&\qquad + \left[\frac{\hbar q_{x,\mathrm{e}}^{\Downarrow}(E_\mathrm{B})}{m} - \frac{\lambda_\mathrm{R}}{\hbar} \right] \left[\left|u^{\Downarrow}(E_\mathrm{B})\right|^2 + \left|v^{\Downarrow}(E_\mathrm{B})\right|^2 \right] \left|g(E_\mathrm{B})\right|^2 \\
&\qquad - \left[\frac{\hbar q_{x,\mathrm{h}}^{\Downarrow}(E_\mathrm{B})}{m} - \frac{\lambda_\mathrm{R}}{\hbar} \right] \left[\left|u^{\Downarrow}(E_\mathrm{B})\right|^2 + \left|v^{\Downarrow}(E_\mathrm{B})\right|^2 \right] \left|h(E_\mathrm{B})\right|^2 \Bigg\} \tanh\left(\frac{E_\mathrm{B}}{2k_\mathrm{B}T} \right). \qquad (7.21)
\end{aligned}
$$

The sum over the transverse momenta $\mathbf{k}_\parallel$ essentially averages the total electrical current density over all transverse channels in our junction and hence yields the total Josephson current $I_\mathrm{J}(E_\mathrm{B})$ *per* occupied bound state (with energy E_B). Since we consider an effectively *one-dimensional* junction, the averaging simply results in an additional (constant) prefactor, which counts the number of transverse channels and can be accumulated in the current's normalization. Once again, we note the rewarding formal coincidence between our current formula in Eq. (7.21) and its simple quantum-mechanical counterpart for free electrons $J_x = -env_x$ (n usually indicates the electron density); we are now interested in the current (expectation value) itself and therefore dropped the operator hats when compared to our previous explanations. The overall Josephson current (meaning the current flowing along $\hat{x}$) is really given by the electron charge $-e$ multiplied by the electrons' (holes') velocities along $\hat{x}$ and an additional "weighting factor" that ensures occupation of the regarded bound state and replaces the particle density appearing in the usual quantum-mechanical current formula. This "weighting factor" stems from the interfacial wave function matching and contains thus not only the (spin-resolved) coherence factors, but also the absolute squares of the wave function coefficients. The latter are determined in Appendix D.

[3] One can check that neglecting the terms proportional to λ_R would yield an electrical current that is no longer conserved along the junction.

As long as Rashba SOC remains absent, the velocity terms appearing in Eq. (7.21) simply merge into free electrons' (holes') velocities, i.e., $v_{x,\mathrm{e}} = (\hbar q_{x,\mathrm{e}})/m$ [$v_{x,\mathrm{h}} = (-\hbar q_{x,\mathrm{h}})/m$], where $q_{x,\mathrm{e}}$ ($q_{x,\mathrm{h}}$) refers to the electronlike (holelike) wave vectors for $\lambda_\mathrm{R} = 0$ (assuming pure s- or p_x-wave superconducting pairings); see Eqs. (7.9), (7.10), (7.12), and (7.13). Recall that we are actually dealing with electrons *and* holes that tunnel into the right superconductor (move all along $\hat{x}$). Nevertheless, since holes enter our description in terms of time-reversed electrons, their $\hat{x}$-velocities differ from the electrons' velocities by a relative sign. As a consequence, electrons and holes indeed contribute to the overall Josephson current with opposite signs, as we expected from the beginning on and Eq. (7.21) formally confirms [compare the hole contributions, proportional to $|f(E_\mathrm{B})|^2$ and $|h(E_\mathrm{B})|^2$, to the electron contributions, proportional to $|e(E_\mathrm{B})|^2$ and $|g(E_\mathrm{B})|^2$]. The relative sign is accumulated in the bound state wave functions' plane-wave vectors [see Eqs. (7.7)–(7.8)] and does not explicitly appear in the abstract formulation of the electrical current density operator in Eq. (7.20), as we claimed earlier.

Nonzero Rashba SOC finally lifts the initial spin degeneracy of the electronlike and holelike states, giving rise to *spin-dependent* electron and hole velocities, i.e., $v_{x,\mathrm{e}}^{\Uparrow(\Downarrow)} = [\hbar q_{x,\mathrm{e}}^{\Uparrow(\Downarrow)}]/m$ and $v_{x,\mathrm{h}}^{\Uparrow(\Downarrow)} = [-\hbar q_{x,\mathrm{h}}^{\Uparrow(\Downarrow)}]/m$, where the spin-resolved wave vectors are given by Eqs. (7.9), (7.10), (7.12), and (7.13).[4] Besides these spin-resolved free-particle velocities, Rashba SOC causes additional "anomalous" velocity components coupling spin-up and spin-down parts of the bound state wave functions [$\propto \lambda_\mathrm{R}$; recall the off-diagonal parts in Eq. (7.20)]. Notice that the "anomalous" velocities (and likewise the spin-dependent part in the wave vectors) vanish for $\lambda_\mathrm{R} = 0$ so that we essentially recover the simple situation discussed in the previous paragraph then.

In *non*magnetic Josephson junctions, the whole bound state spectrum is solely composed of Andreev bound states and the effectively flowing Josephson current is already fully determined by Eq. (7.21). Magnetic barriers, however, split the junctions' bound state spectra into the (usual) Andreev bound states on the one and the superimposed YSR states on the other hand. To extract a well-balanced current in that more generic scenario, we need to average Eq. (7.21) over both branches of bound states, yielding the total Josephson current

$$\begin{aligned} I_\mathrm{J} = -e \sum_{E_\mathrm{B}} \frac{1}{2} \sum_{\mathbf{k}_\parallel} \Bigg\{ & \left[\frac{\hbar q_{x,\mathrm{e}}^{\Uparrow}(E_\mathrm{B})}{m} + \frac{\lambda_\mathrm{R}}{\hbar} \right] \left[\left|u^{\Uparrow}(E_\mathrm{B})\right|^2 + \left|v^{\Uparrow}(E_\mathrm{B})\right|^2 \right] \left|e(E_\mathrm{B})\right|^2 \\ & - \left[\frac{\hbar q_{x,\mathrm{h}}^{\Uparrow}(E_\mathrm{B})}{m} + \frac{\lambda_\mathrm{R}}{\hbar} \right] \left[\left|u^{\Uparrow}(E_\mathrm{B})\right|^2 + \left|v^{\Uparrow}(E_\mathrm{B})\right|^2 \right] \left|f(E_\mathrm{B})\right|^2 \\ & + \left[\frac{\hbar q_{x,\mathrm{e}}^{\Downarrow}(E_\mathrm{B})}{m} - \frac{\lambda_\mathrm{R}}{\hbar} \right] \left[\left|u^{\Downarrow}(E_\mathrm{B})\right|^2 + \left|v^{\Downarrow}(E_\mathrm{B})\right|^2 \right] \left|g(E_\mathrm{B})\right|^2 \\ & - \left[\frac{\hbar q_{x,\mathrm{h}}^{\Downarrow}(E_\mathrm{B})}{m} - \frac{\lambda_\mathrm{R}}{\hbar} \right] \left[\left|u^{\Downarrow}(E_\mathrm{B})\right|^2 + \left|v^{\Downarrow}(E_\mathrm{B})\right|^2 \right] \left|h(E_\mathrm{B})\right|^2 \Bigg\} \tanh\left(\frac{E_\mathrm{B}}{2k_\mathrm{B}T} \right); \end{aligned} \tag{7.22}$$

note the additional $\sum_{E_\mathrm{B}} 1/2 \ldots$, averaging over Andreev bound states' *and* YSR states' current contributions. Equation (7.22) will be our starting point for (numerically) evaluating Josephson currents through various realistic S/F-I/S junction configurations from their bound state spectra.

[4] Electrons inside a band with $\mathbf{k}$-space excitation energies $E(\mathbf{k})$ are characterized by the velocities $\mathbf{v} = [\partial E(\mathbf{k})]/[\hbar(\partial \mathbf{k})]$. An additional *spin-dependent* [$\sigma = 1$ (-1) for spin up (spin down)] energy shift $E(\mathbf{k}) \longmapsto E(\mathbf{k}) + \sigma \Delta E(\mathbf{k})$, caused, for instance, by SOC, gives thus rise to the appearance of additional *spin-dependent* velocity terms. In our notation, these terms are accumulated in the *spin-resolved* wave vectors.

We want to finish this section with some brief remarks, underlining the universality of the presented approach. First, Eq. (7.22) can be regarded as a generalization of the simple thermodynamic relation [261]

$$I_{\mathrm{J}} = -\frac{2e}{\hbar}\sum_{E_{\mathrm{B}}}\frac{1}{2}\frac{\partial E_{\mathrm{B}}(\phi_{\mathrm{S}})}{\partial\phi_{\mathrm{S}}}\tanh\left(\frac{E_{\mathrm{B}}}{2k_{\mathrm{B}}T}\right), \tag{7.23}$$

typically used in the literature to relate *one-dimensional* Josephson junctions' bound state spectra to the flowing Josephson current. Our *three-dimensional* approach is, nonetheless, much more general and captures, e.g., the additional current contributions due to the bulk Rashba SOC inside the superconducting electrodes in a proper way; this is not necessarily the case when one relies just on Eq. (7.23). Within our approach, it is sufficient to extract the (absolute squares) of the bound state wave functions, following the methodology described in Appendix D, and to substitute the results into Eq. (7.22) to access the overall Josephson current. Particularly for complicated Josephson geometries that require a fully numerical treatment, such a procedure can be routinely implemented, whereas numerically evaluating the derivatives in Eq. (7.23) might generate convergence issues and is by far much less reliable (and efficient) than our technique. Second, and as an important crosscheck for our derivation, taking the limit $\lambda_{\mathrm{R}} \to 0$, Eq. (7.22) replicates the central result of Furusaki [392], who initially employed a similar bound state-based framework to quantify the Josephson current through S/N/S constrictions. The consequences of magnetic barriers – specifically those associated with ferromagnetic insulators –, and the role of SOC, we want to investigate in this chapter, were not included there.

7.2 Discussion of results for singlet pairing

At first, we discuss the bound state spectrum of and Josephson current flow through an S/F-I/S junction in which the pairing mechanism inside the superconductors is the *pure* singlet (s-wave) one. This refers not only to the experimentally most relevant case, but gives simultaneously rise to particularly rich physics originating from the interplay of Andreev bound states and YSR states. The superconducting pairing potential in Eq. (7.5) reduces then to the previously established one describing s-wave superconductivity, i.e., to

$$\hat{\Delta}_{\mathrm{S}}(x) = |\Delta_{\mathrm{S}}^{s}|\hat{\sigma}_0\left[\Theta(-x) + \mathrm{e}^{\mathrm{i}\phi_{\mathrm{S}}}\Theta(x)\right]. \tag{7.24}$$

From now on, we substitute $|\Delta_{\mathrm{S}}^{s}| = |\Delta_{\mathrm{S}}(0)|$, where $|\Delta_{\mathrm{S}}(0)|$ measures the superconductors' isotropic energy gap at zero temperature, for the pairing amplitude. Generalizing our results to finite temperature is straightforward as one just needs to replace $|\Delta_{\mathrm{S}}(0)|$ by its BCS-like temperature-dependent version $|\Delta_{\mathrm{S}}(T \neq 0)| = |\Delta_{\mathrm{S}}(0)|\tanh(1.74\sqrt{T_{\mathrm{C}}/T-1})$. To simplify our analysis further, we initially consider the bulk Rashba SOC inside the superconducting regions to be absent; SOC-related effects will be shortly addressed at the end of this section.

7.2.1 Bound state spectrum

Implementing the technique outlined in Sec. 7.1, we can compute the bound state spectra of generic (one-dimensional) S/F-I/S Josephson junctions. Within our assumptions (i.e., s-wave superconducting coupling and $\lambda_{\mathrm{R}} = 0$), the electron-hole symmetric bound state energies $E_n^{\pm}$, with $n \in \{1;2\}$, are given by

$$\frac{E_{\mathrm{B}}}{|\Delta_{\mathrm{S}}(0)|} \equiv \frac{E_n^{\pm}}{|\Delta_{\mathrm{S}}(0)|} = \pm\left\{\left(\overline{\lambda}_{\mathrm{SC}}^2 - \overline{\lambda}_{\mathrm{MA}}^2\right)^2 + 8\left[2\cos^2\left(\frac{\phi_{\mathrm{S}}}{2}\right) + \frac{\overline{\lambda}_{\mathrm{SC}}^2}{2}\left[\cos^2\left(\frac{\phi_{\mathrm{S}}}{2}\right)+1\right] + \frac{\overline{\lambda}_{\mathrm{MA}}^2}{2}\sin^2\left(\frac{\phi_{\mathrm{S}}}{2}\right)\right.\right.$$
$$\left.\left.+(-1)^n\left|\overline{\lambda}_{\mathrm{MA}}\right|\sqrt{\sin^2(\phi_{\mathrm{S}}) + \overline{\lambda}_{\mathrm{SC}}^2\sin^2\left(\frac{\phi_{\mathrm{S}}}{2}\right) + \overline{\lambda}_{\mathrm{MA}}^2\cos^2\left(\frac{\phi_{\mathrm{S}}}{2}\right)}\right]\right\}^{1/2} \Bigg/ \left[\left(\overline{\lambda}_{\mathrm{SC}}^2 - \overline{\lambda}_{\mathrm{MA}}^2 + 4\right)^2 + 16\overline{\lambda}_{\mathrm{MA}}^2\right]^{1/2}. \tag{7.25}$$

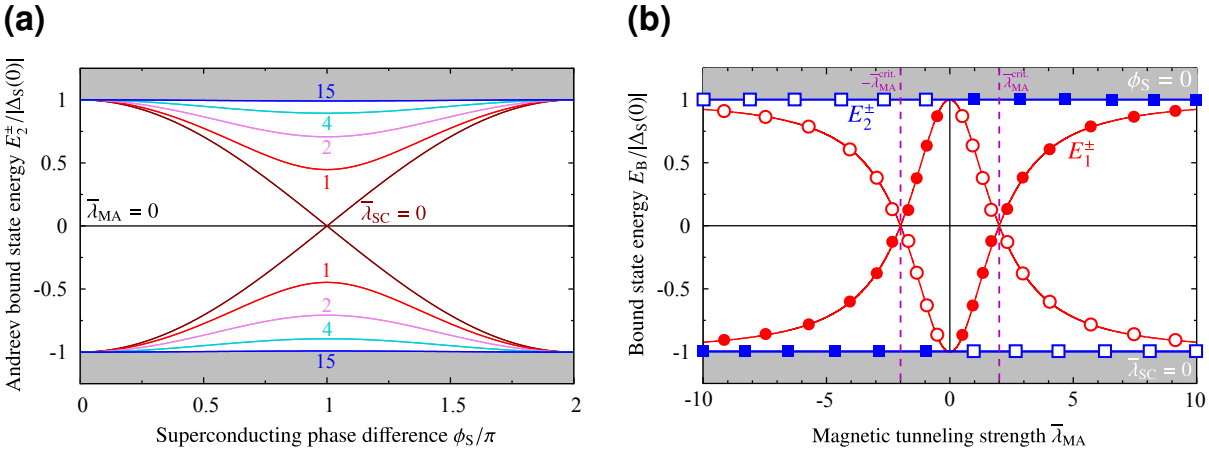


Fig. 7.3: (a) Calculated bound state energies of the Andreev bound states ($E_2^{\pm}$) as functions of the superconducting phase difference ϕ_S, and in the absence of magnetic tunneling ($\overline{\lambda}_{MA} = 0$) and Rashba SOC ($\lambda_R = 0$). Different scalar tunneling strengths $\overline{\lambda}_{SC}$ are color coded; all states are doubly spin degenerate. **(b)** Calculated (spin-resolved) bound state energies of the Andreev bound states ($E_2^{\pm}$; blue) and YSR states ($E_1^{\pm}$; red) as functions of $\overline{\lambda}_{MA}$ and for $\phi_S = 0$, $\overline{\lambda}_{SC} = 0$, as well as $\lambda_R = 0$. Filled (empty) squares indicate spin-up (spin-down) Andreev bound states and filled (empty) circles spin-up (spin-down) YSR states. The violet dashed lines highlight $\pm\overline{\lambda}_{MA}^{crit.} = \pm 2$, at which the YSR states cross zero energy.

Most remarkably, the bound state energies are tunable by altering either the superconducting phase difference ϕ_S or (one of) the two dimensionless parameters $\overline{\lambda}_{SC} = (2m\lambda_{SC})/(\hbar^2 k_F)$ and $\overline{\lambda}_{MA} = (2m\lambda_{MA})/(\hbar^2 k_F)$, resembling the effective scalar and magnetic tunneling strengths; $k_F = \sqrt{2m\mu}/\hbar$ still denotes the Fermi wave vector. To gain more physical insight into the junction's general spectral features, let us briefly examine Eq. (7.25) in some important limiting cases.

Andreev limit. In the absence of magnetic tunneling through the ferromagnetic insulator, our system essentially behaves like an S/I/S Josephson junction, firstly studied by Andreev [179] and Kulik [261]. Taking the limit $\overline{\lambda}_{MA} \to 0$ in Eq. (7.25), we recover the dispersion of S/I/S junctions' (usual) Andreev bound states,

$$E_1^{\pm} = E_2^{\pm} = \pm|\Delta_S(0)| \sqrt{\frac{\overline{\lambda}_{SC}^2 + 4\cos^2(\phi_S/2)}{\overline{\lambda}_{SC}^2 + 4}}, \tag{7.26}$$

which additionally simplifies to

$$E_1^{\pm} = E_2^{\pm} = \pm|\Delta_S(0)| \cos(\phi_S/2) \tag{7.27}$$

for perfectly transparent junctions (considering also $\overline{\lambda}_{SC} \to 0$).

The Andreev bound states' energies are uniquely determined by the interfacial scalar tunneling measure $\overline{\lambda}_{SC}$ and the phase difference ϕ_S between the superconductors. Comparing $\overline{\lambda}_{SC}$ to the BTK-like barrier parameter Z [164], introduced in the previous chapters, suggests that $\overline{\lambda}_{SC} = 1$ essentially models a realistic ferromagnetic-insulator barrier with a height of 0.75 eV and a width of about 0.40 nm.[5] We illustrate the Andreev bound state energies' ϕ_S-dependence for various representative values of $\overline{\lambda}_{SC}$ in Fig. 7.3(a). Since there are no spin-active components in the junction (both magnetic tunnel-

[5] To recover the BTK-like Z-parameter [164], we substitute $\lambda_{SC} \longmapsto V_{F\text{-}I} d_{F\text{-}I}$, where $V_{F\text{-}I}$ indicates the scalar scattering potential (bandgap) and $d_{F\text{-}I}$ the thickness of the ferromagnetic-insulator layer. Requiring $\overline{\lambda}_{SC} = (2m\lambda_{SC})/(\hbar^2 k_F) = 1$ allows then, e.g., for $V_{F\text{-}I} = 0.75\,\text{eV}$ and $d_{F\text{-}I} \approx 0.40\,\text{nm}$ (assuming $m \approx m_e$ and $k_F \approx 8 \times 10^7\,\text{cm}^{-1}$).

ing and Rashba SOC are absent), each state is doubly spin degenerate. The zero-energy crossing of two Andreev bound state branches at $\phi_S = \pi \pmod{2\pi}$ [assuming $\overline{\lambda}_{SC} = 0$; see Eq. (7.27) and the dark red curve in Fig. 7.3(a)] recently attracted considerable attention in connection with Majorana physics. Zero-energy (bound) states forming in superconductors typically involve *equal superpositions of electronlike and holelike parts*, and might therefore be seen as precursors of the formation of *Majorana zero modes* in the system [393]. However, the main obstacle acting against the zero-energy (Andreev) bound states in our junction is the required perfect interfacial junction transparency. Already slightly lowered transparency (meaning slightly increasing the scalar tunneling strength $\overline{\lambda}_{SC}$) expels the Andreev bound state bands from the center and shifts them towards the gap edges, approaching $E_1^{\pm} = E_2^{\pm} = \pm|\Delta_S(0)|$ for $\overline{\lambda}_{SC} \to \infty$. The situation becomes different in topological insulator-based Josephson junctions, in which the existence of topologically protected zero-energy Majorana states – surviving even in the presence of finite tunneling potentials – indeed manifests itself in extraordinary transport properties, such as 4π-periodic Josephson currents [356].

YSR limit. If scalar tunneling through the ferromagnetic insulator is absent ($\overline{\lambda}_{SC} \to 0$) and the superconducting phase difference is tuned to zero ($\phi_S = 0$), the junction effectively reduces to a uniform bulk superconductor with magnetic impurity centers (modeled by the nonzero magnetic tunneling potential in its center). Equation (7.25) comprises then the two independent bound state energy branches

$$E_1^{\pm} = \pm|\Delta_S(0)|\frac{\overline{\lambda}_{MA}^2 - 4}{\overline{\lambda}_{MA}^2 + 4} \tag{7.28}$$

and

$$E_2^{\pm} = \pm|\Delta_S(0)|. \tag{7.29}$$

Returning to full-dimensional $\lambda_{MA} = (\hbar^2 k_F \overline{\lambda}_{MA})/(2m)$ and identifying $g(\mu) = (2m)/(\pi\hbar^2 k_F)$ with the one-dimensional Fermi-level DOS (per unit length), Eq. (7.28) transforms into Shiba's expression [362] for the celebrated YSR states [see Eq. (7.2)]. The two remaining states at $E_2^{\pm} = \pm|\Delta_S(0)|$ coincide with the aforementioned (usual) Andreev bound states at $\phi_S = 0$. For these reasons, we refer to $E_1^{\pm}$ as YSR states and to $E_2^{\pm}$ as Andreev bound states from now on (at least in the generic case when $\overline{\lambda}_{MA} \neq 0$ and the bound state branches become well distinguishable). The bound state spectrum in the so-called YSR limit, shown in Fig. 7.3(b) as a function of $\overline{\lambda}_{MA}$ (and still for $\overline{\lambda}_{SC} = 0$), is characterized by quite an intriguing spin structure.[6] The chosen strengths of $\overline{\lambda}_{MA}$ vary from -10 to 10, covering both antiferromagnetic and ferromagnetic coupling scenarios. To give concrete numbers, $\overline{\lambda}_{MA} = 1$ corresponds to a roughly 0.40 nm thick ferromagnetic insulator with an exchange gap of about 1.5 eV.[7] Although some of the studied values seem to be rather large (especially $\overline{\lambda}_{MA} \to \pm 10$), several experimental works already confirmed that the exchange splitting in ferromagnetic insulators can indeed become sizable [21, 225], making such materials promising candidates for implementing efficient spin-polarized tunneling into junction geometries and justifying our parameter choice. Regarding $\overline{\lambda}_{MA} = 0$, both the Andreev and the YSR parts of the spectrum merge into the same (spin-degenerate) states at $E_1^{\pm} = E_2^{\pm} = \pm|\Delta_S(0)|$, and we simply arrive at the aforementioned Andreev limit. Rising $\overline{\lambda}_{MA}$ splits the bound state bands into

[6] To ascertain the states' spins, one could rely on the bound state wave functions constructed in Appendix D and compute their spin expectation values (with respect to $\hat{\sigma}_z$). However, as long as SOC remains absent, it is much more convenient to decompose the Nambu basis into its spin-resolved blocks (see also Appendix D) and to simply check which of the bound state energies given by Eq. (7.25) essentially come as solutions from the up-spin block and which stem from the down-spin block.

[7] To estimate the ferromagnetic insulator's exchange gap, we substitute $\lambda_{MA} \longmapsto (\Delta_{XC}/2)d_{F\text{-}I}$, where Δ_{XC} abbreviates the ferromagnetic insulator's exchange gap and $d_{F\text{-}I} \approx 0.40\,\text{nm}$ its thickness. Given $m \approx m_e$ and $k_F \approx 8 \times 10^7\,\text{cm}^{-1}$, $\overline{\lambda}_{MA} = (m\Delta_{XC}d_{F\text{-}I})/(\hbar^2 k_F) = 1$ requires $\Delta_{XC} \approx 1.5\,\text{eV}$.

their Andreev and their YSR components with bound state energies governed by Eqs. (7.28) and (7.29), respectively. Setting $\phi_S = 0$, we can unambiguously distinguish between the Andreev bound states, always located exactly at the gap edges, and the YSR states with their unique "band structure" already deduced by Shiba [362]; see, e.g., Fig. 7.1(b). While the Andreev bound states' energies and spins do not change with increasing $\overline{\lambda}_{MA}$ (and as long as $\overline{\lambda}_{MA}$'s sign is not reversed), the YSR bands are initially shifted towards the center of the superconducting energy gap, cross zero energy at the *critical* magnetic tunneling strengths $\pm\overline{\lambda}_{MA}^{crit.} = \pm(2m\lambda_{MA}^{crit.})/(\hbar^2 k_F) = \pm 2$, and are eventually again expelled from the gap center, approaching the gap-edge energies at $\overline{\lambda}_{MA} \to \pm\infty$ [similarly to the Andreev bound states in the limit $\overline{\lambda}_{SC} \to \infty$; see Fig. 7.3(a)]. As the most remarkable feature, the YSR states' zero-energy crossings at $\pm\overline{\lambda}_{MA}^{crit.} = \pm 2$ are accompanied by spin flips, which will turn out to be the crucial ingredient for understanding 0-π transitions in S/F-I/S junctions' Josephson current. For completeness, let us mention that negative-energy states are always classified through opposite spins when compared to their positive-energy counterparts, being a consequence of the bound state wave functions electron-hole symmetry (see Appendix D). Moreover, also flipping $\overline{\lambda}_{MA}$'s sign reverses the states' spins.

Interplay between Andreev bound states and YSR states. After we explored the two special cases – the Andreev limit on the one and the YSR limit on the other hand –, we are now concerned with the combined situation, i.e., with an S/F-I/S junction in which the ferromagnetic-insulator barrier simultaneously introduces scalar *and* magnetic tunnelings. To differentiate between the Andreev bound states and the YSR states, we start our analyses again with the peculiar scenario of zero superconducting phase difference ($\phi_S = 0$), effectively representing one single bulk superconductor that comprises scalar and magnetic tunneling (impurities) in its center. Under these assumptions, Eq. (7.25) reduces to

$$E_1^{\pm} = \pm|\Delta_S(0)| \sqrt{\frac{\left(\overline{\lambda}_{SC}^2 - \overline{\lambda}_{MA}^2 + 4\right)^2}{\left(\overline{\lambda}_{SC}^2 - \overline{\lambda}_{MA}^2 + 4\right)^2 + 16\overline{\lambda}_{MA}^2}} \tag{7.30}$$

for the YSR states, as well as

$$E_2^{\pm} = \pm|\Delta_S(0)| \tag{7.31}$$

for the Andreev bound states. Figures 7.4(a) and 7.4(A) illustrate the positive energies of the Andreev bound states and YSR states for a wide range of scalar and magnetic tunneling strengths; the corresponding negative-energy states (not shown) are obtained from $E_1^- = -E_1^+$ and $E_2^- = -E_2^+$ [see Eqs. (7.30)–(7.31)]. As we could have expected either from our previous arguments or when inspecting Eq. (7.31) – recall that we fixed $\phi_S = 0$) –, the Andreev bound states' energies are just given by $E_2^{\pm} = \pm|\Delta_S(0)|$, and are fully independent of the actually chosen $\overline{\lambda}_{SC}$ and $\overline{\lambda}_{MA}$. The situation turns out to become much more striking for the YSR part of the spectrum. To be more specific, we deduce that one can always find critical magnetic tunneling strengths $\pm\overline{\lambda}_{MA}^{crit.}$ to each given $\overline{\lambda}_{SC}$ so that both the positive- and negative-energy branches of the YSR states cross zero energy and flip their spins, just as outlined for one concrete example when analyzing Fig. 7.3(b). The presence of magnetic tunneling supports zero-energy YSR states for a wide range of junction parameters – in sharp contrast to zero-energy Andreev bound states, which require perfect interfacial transparency and $\phi_S = 0 \pmod{2\pi}$ [see Eq. (7.27) and Fig. 7.3(a)]. Zero-energy YSR states might therefore become particularly relevant to realize Majorana zero modes in magnetic Josephson junction configurations one day.

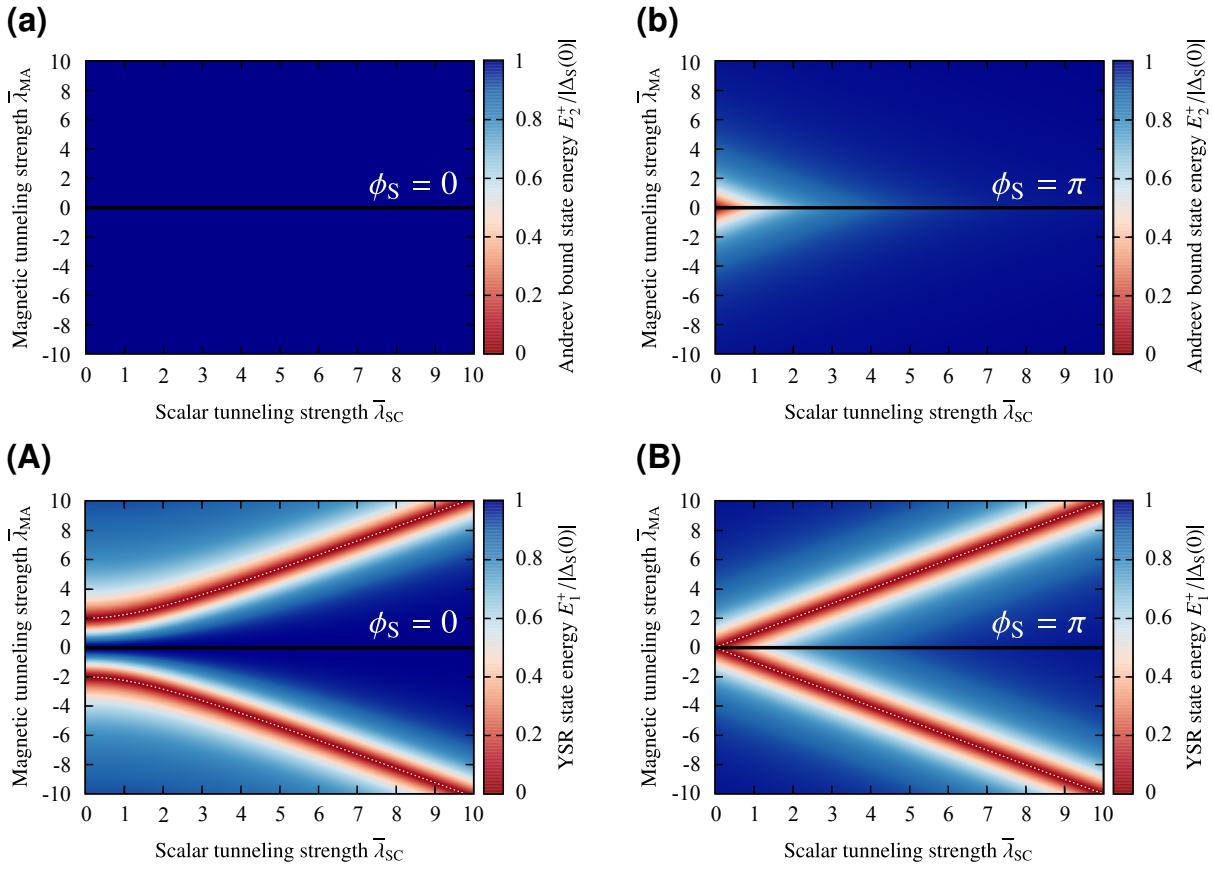


Fig. 7.4: (a) Calculated (positive-energy) bound state energies of the Andreev bound states (E_2^+) as functions of the scalar tunneling strength $\overline{\lambda}_{SC}$ and the magnetic tunneling strength $\overline{\lambda}_{MA}$; the superconducting phase difference is fixed to $\phi_S = 0$ and Rashba SOC is not present ($\lambda_R = 0$). **(b)** Same calculation as in **(a)**, but at $\phi_S = \pi$. **(A)** Calculated (positive-energy) bound state energies of the YSR states (E_1^+) as functions of $\overline{\lambda}_{SC}$ and $\overline{\lambda}_{MA}$, considering $\phi_S = 0$ and $\lambda_R = 0$. The white dotted lines highlight the tunneling parameter regimes that support the formation of zero-energy YSR states [according to Eq. (7.35)]. **(B)** Same calculation as in **(A)**, but at $\phi_S = \pi$.

Another important scenario refers to $\phi_S = \pi$. Equation (7.25) captures then the YSR state energies

$$E_1^{\pm} = \pm|\Delta_S(0)| \sqrt{\frac{\left(\overline{\lambda}_{SC}^2 - \overline{\lambda}_{MA}^2\right)^2 + 4\left(\overline{\lambda}_{SC}^2 + \overline{\lambda}_{MA}^2\right) - 8\overline{\lambda}_{SC}}{\left(\overline{\lambda}_{SC}^2 - \overline{\lambda}_{MA}^2 + 4\right)^2 + 16\overline{\lambda}_{MA}^2}}, \tag{7.32}$$

as well as the Andreev bound state energies

$$E_2^{\pm} = \pm|\Delta_S(0)| \sqrt{\frac{\left(\overline{\lambda}_{SC}^2 - \overline{\lambda}_{MA}^2\right)^2 + 4\left(\overline{\lambda}_{SC}^2 + \overline{\lambda}_{MA}^2\right) + 8\overline{\lambda}_{SC}}{\left(\overline{\lambda}_{SC}^2 - \overline{\lambda}_{MA}^2 + 4\right)^2 + 16\overline{\lambda}_{MA}^2}}. \tag{7.33}$$

It is worth to note that the Andreev bound state and the YSR state branches cross at $\phi_S = \pi$ if scalar tunneling is absent. Their energies at the crossing points,

$$E_{\text{crossing}}^{\pm} = \pm|\Delta_S(0)| \sqrt{\frac{\overline{\lambda}_{MA}^2}{\overline{\lambda}_{MA}^2 + 4}}, \tag{7.34}$$

are extracted from Eqs. (7.32)–(7.33) substituting $\overline{\lambda}_{\mathrm{SC}} = 0$. The Andreev bound states' and YSR states' (positive) energies, presented in Figs. 7.4(b) and 7.4(B) for the same combinations of $\overline{\lambda}_{\mathrm{SC}}$ and $\overline{\lambda}_{\mathrm{MA}}$ as before, but now assuming the superconducting phase difference $\phi_{\mathrm{S}} = \pi$, essentially confirm all main characteristics we already discussed for $\phi_{\mathrm{S}} = 0$. The above mentioned zero-energy Andreev bound states forming in perfectly transparent junctions ($\overline{\lambda}_{\mathrm{SC}} = 0$) and at phase differences of $\phi_{\mathrm{S}} = \pi \pmod{2\pi}$ become now clearly visible. However, weak perturbations in terms of finite scalar and/or magnetic tunneling strengths immediately destroy the zero-energy states and shift the Andreev bound state bands back towards the gap edges. Contrary, the parameter space of zero-energy YSR states is again much richer and entails the existence of zero-energy YSR states for all regarded scalar tunneling strengths, as long as one chooses "suitable" values of $\overline{\lambda}_{\mathrm{MA}}$, i.e., $\pm\overline{\lambda}_{\mathrm{MA}}^{\mathrm{crit.}}$. Analyzing the generic YSR energies, determined by Eq. (7.25), we conclude that zero-energy YSR states appear at all $\overline{\lambda}_{\mathrm{MA}}^{\mathrm{crit.}}$ that fulfill

$$\overline{\lambda}_{\mathrm{MA}}^{\mathrm{crit.}} = \sqrt{\overline{\lambda}_{\mathrm{SC}}^2 + 4\cos^2(\phi_{\mathrm{S}}/2)}, \tag{7.35}$$

assuming $0 \leq \overline{\lambda}_{\mathrm{MA}}^2 - \overline{\lambda}_{\mathrm{SC}}^2 \leq 4$. For the parameters studied in Fig. 7.3(b), i.e., $\overline{\lambda}_{\mathrm{SC}} = 0$ and $\phi_{\mathrm{S}} = 0$, Eq. (7.35) predicts zero-energy crossings (accompanied by spin flips) of the YSR bands at $\pm\overline{\lambda}_{\mathrm{MA}}^{\mathrm{crit.}} = \pm 2$, which coincide one-to-one with the graphically extracted value. Moreover, the zero-energy YSR contour defined by Eq. (7.35) matches perfectly the computed zero-energy YSR states in Figs. 7.4(A) and 7.4(B); see the white dotted curves there which serve as a guide for eyes.

To compute and understand the Josephson current-phase relations, we shall have a brief look at the bound state energies' dependence on the superconducting phase difference ϕ_{S}. For the scalar tunneling strength $\overline{\lambda}_{\mathrm{SC}}$, we consider the two representative values of $\overline{\lambda}_{\mathrm{SC}} = 0$ [see Figs. 7.5(a)–7.5(c)] and $\overline{\lambda}_{\mathrm{SC}} = 2$ [see Figs. 7.5(d)–7.5(f)]. In both cases, the magnetic tunneling parameter is initially increased from $\overline{\lambda}_{\mathrm{MA}} = 1$ to $\overline{\lambda}_{\mathrm{MA}} = 2$, and afterwards to $\overline{\lambda}_{\mathrm{MA}} = 3$. Even at nonzero phase difference, the Andreev bound state branches lie always closer to the gap edges than their YSR counterparts, which provides an important spectroscopic fingerprint to distinguish both states in STM experiments. As long as scalar tunneling remains absent ($\overline{\lambda}_{\mathrm{SC}} = 0$), the Andreev and YSR branches cross at $\phi_{\mathrm{S}} = \pi$. The related "crossing energies" are obtained from Eq. (7.34), yielding $E^{\pm}_{\mathrm{crossing}} \approx \pm 0.45|\Delta_{\mathrm{S}}(0)|$ for $\overline{\lambda}_{\mathrm{MA}} = 1$, $E^{\pm}_{\mathrm{crossing}} \approx \pm 0.71|\Delta_{\mathrm{S}}(0)|$ for $\overline{\lambda}_{\mathrm{MA}} = 2$, and $E^{\pm}_{\mathrm{crossing}} \approx \pm 0.83|\Delta_{\mathrm{S}}(0)|$ for $\overline{\lambda}_{\mathrm{MA}} = 3$, accordingly. The YSR states reveal again their intriguing characteristics, such as their puzzling spin flips when crossing zero energy. The parameter combinations that allow for the formation of zero-energy crossings are still determined by Eq. (7.35). However, instead of keeping $\overline{\lambda}_{\mathrm{SC}}$ and ϕ_{S} constant and looking for $\overline{\lambda}_{\mathrm{MA}}^{\mathrm{crit.}}$, we fix now $\overline{\lambda}_{\mathrm{MA}}$ and look for the respective $\phi_{\mathrm{S}}^{\mathrm{crit.}}$ that maintains zero-energy YSR states (restricting ourselves to $0 \leq \phi_{\mathrm{S}}^{\mathrm{crit.}} \leq \pi$). In particular, we find $\phi_{\mathrm{S}}^{\mathrm{crit.}} = (2\pi)/3$ for the tunneling parameter combination ($\overline{\lambda}_{\mathrm{SC}} = 0; \overline{\lambda}_{\mathrm{MA}} = 1$), $\phi_{\mathrm{S}}^{\mathrm{crit.}} = 0$ for ($\overline{\lambda}_{\mathrm{SC}} = 0; \overline{\lambda}_{\mathrm{MA}} = 2$), and $\phi_{\mathrm{S}}^{\mathrm{crit.}} = \pi$ for ($\overline{\lambda}_{\mathrm{SC}} = 2; \overline{\lambda}_{\mathrm{MA}} = 2$); the other regarded combinations of $\overline{\lambda}_{\mathrm{SC}}$ and $\overline{\lambda}_{\mathrm{MA}}$ do not give rise to zero-energy YSR states (since they do *not* meet the aforementioned requirement $0 \leq \overline{\lambda}_{\mathrm{MA}}^2 - \overline{\lambda}_{\mathrm{SC}}^2 \leq 4$).

7.2.2 Josephson current

After we identified the striking characteristics associated with YSR states in magnetic Josephson junctions, particularly their intriguing spin flips when crossing zero energy, we need to answer the question to which extent these extraordinary properties might simultaneously impact experimentally accessible quantities. The Josephson current flowing through such junctions counts for sure to their most relevant experimental measures. Substituting the general expression for the bound state energies in Eq. (7.25) into Eq. (7.22), we can immediately connect the discussed bound state spectra to the expected Josephson current flow. For convenience, the Josephson current is evaluated at zero temperature, at which we also computed

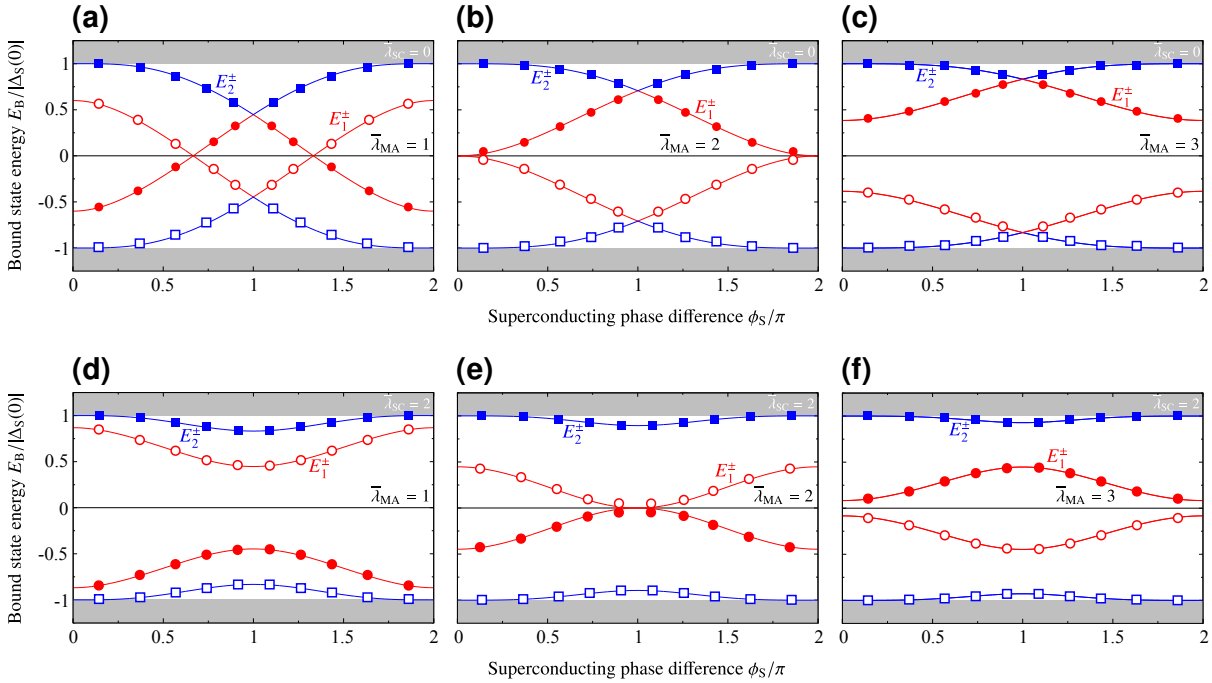


Fig. 7.5: (a) Calculated (spin-resolved) bound state energies of the Andreev bound states ($E_2^\pm$; blue) and YSR states ($E_1^\pm$; red) as functions of the superconducting phase difference ϕ_S, and for the scalar tunneling strength $\overline{\lambda}_{SC} = 0$, as well as the magnetic tunneling strength $\overline{\lambda}_{MA} = 1$; Rashba SOC is absent ($\lambda_R = 0$). Filled (empty) squares indicate spin-up (spin-down) Andreev bound states and filled (empty) circles spin-up (spin-down) YSR states. **(b)** Same calculation as in **(a)**, but for $\overline{\lambda}_{SC} = 0$ and $\overline{\lambda}_{MA} = 2$. **(c)** Same calculation as in **(a)**, but for $\overline{\lambda}_{SC} = 0$ and $\overline{\lambda}_{MA} = 3$. **(d)** Same calculation as in **(a)**, but for $\overline{\lambda}_{SC} = 2$ and $\overline{\lambda}_{MA} = 1$. **(e)** Same calculation as in **(a)**, but for $\overline{\lambda}_{SC} = 2$ and $\overline{\lambda}_{MA} = 2$. **(f)** Same calculation as in **(a)**, but for $\overline{\lambda}_{SC} = 2$ and $\overline{\lambda}_{MA} = 3$.

the bound state energies in the previous part. Finite temperatures would not dramatically modify the Josephson current as long as the temperature stays well below the critical temperature of the superconducting electrodes. Regarding the superconductors' material parameters, we assume $|\Delta_S(0)| \approx 2.5\,\text{meV}$ and $T_C \approx 16\,\text{K}$, just as in Chap. 6.

Instead of analyzing the full Josephson current-phase dependence, we rather focus on the *oriented* critical current $I^{\text{crit.}}$, which is given by the positively counted critical current amplitudes for 0- and the negatively counted critical current amplitudes for π-junctions. Figure 7.6(a) presents the critical current's *amplitudes* $|I^{\text{crit.}}|$ as functions of the magnetic tunneling strength $\overline{\lambda}_{MA}$, essentially covering the same parameter regimes as earlier when we analyzed the bound state properties. The scalar tunneling strength $\overline{\lambda}_{SC}$ gets gradually increased from $\overline{\lambda}_{SC} = 0$ (cold colors) to $\overline{\lambda}_{SC} = 8$ (warm colors). Besides the significant damping of the overall critical current with increasing $\overline{\lambda}_{SC}$, originating from the accompanying reduction of the interfacial junction transparency and the resulting suppression of Cooper pair tunneling through the barrier, the nonmonotonic $|I^{\text{crit.}}|$-$\overline{\lambda}_{MA}$ variations attract special attention. For all regarded values of $\overline{\lambda}_{SC}$, $|I^{\text{crit.}}|$ suddenly drops into sharp dips when $\overline{\lambda}_{MA}$ becomes sufficiently large. We already met such "critical current dips" in S/F/S junctions and attributed them to the appearance of current-reversing 0-π transitions [see, e.g., Fig. 6.10(b) and the related explanations]. In precisely the same manner, dips in S/F-I/S junctions' $|I^{\text{crit.}}|$-$\overline{\lambda}_{MA}$ relations serve as unambiguous precursors of 0-π transitions. Moreover, we deduce from our calculations that stronger scalar tunneling (meaning less interfacial junction transparency) requires also larger magnetic tunneling strengths to really induce 0-π transitions.

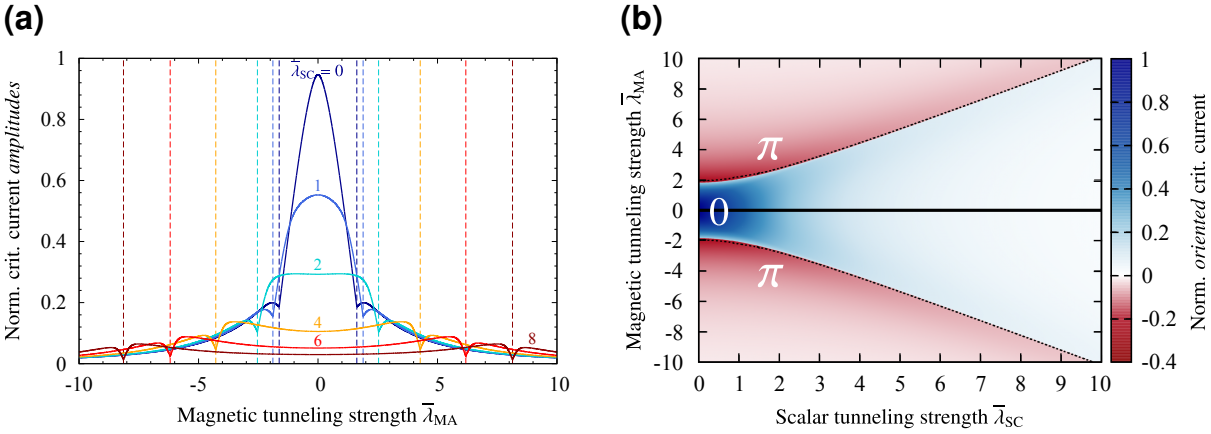


Fig. 7.6: (a) Calculated dependence of the critical (Josephson) current *amplitudes* [normalized according to $(|I^{\text{crit.}}|eR_S)/[|\Delta_S(0)|\pi]$, where R_S refers to Sharvin's resistance of the respective normal-state point contact] on the magnetic tunneling strength $\overline{\lambda}_{MA}$ and for various indicated scalar tunneling strengths $\overline{\lambda}_{SC}$; Rashba SOC is absent ($\lambda_R = 0$). The dips, additionally highlighted by dashed lines, indicate transitions from the 0- to the π-state junction regime. **(b)** Calculated *oriented* critical current [normalized as in **(a)**] as a function of $\overline{\lambda}_{SC}$ and $\overline{\lambda}_{MA}$, and in the absence of Rashba SOC ($\lambda_R = 0$). Blue and red regions represent 0- and π-junction regimes. The transition lines separating the two phases are emphasized by white borderlines and the tunneling parameters supporting zero-energy YSR states [determined by Eq. (7.35) at the critical superconducting phase difference $\phi_S^{\text{crit.}}$] by black dashed lines.

To offer a more general analysis, we calculate the critical current at arbitrary combinations of tunneling strengths, similarly to the bound state energies shown in Fig. 7.4. The color plot in Fig. 7.6(b) illustrates the *oriented* critical current's dependence on $\overline{\lambda}_{SC}$ and $\overline{\lambda}_{MA}$ for quite a rich set of tunneling measures, confirming all our previous statements. For a given $\overline{\lambda}_{SC}$, one can always find a sufficiently large $\overline{\lambda}_{MA}$ to trigger a transition from the 0- to the π-state. Moreover, increasing $\overline{\lambda}_{SC}$ typically shifts the transition points to greater $\overline{\lambda}_{MA}$. Regarding the current amplitudes, the maximal critical current in the 0-state is about twice as large as in the π-state. Most notably, the transition lines separating 0- and π-states coincide (nearly) one-to-one with the contours signifying the formation of zero-energy YSR states [which are determined by Eq. (7.35) substituting the critical superconducting phase difference $\phi_S^{\text{crit.}}$ since we want to compare them with the critical current]. This finding is the most rewarding one of this chapter as it suggests that there is indeed a distinct correlation between YSR states' unique spectral properties and the measurable Josephson current, becoming evident through the latter's striking 0-π transitions. Although the coincidence got already clearly apparent, we definitely need to elaborate more on the theoretical background within the next paragraphs to really develop a common understanding of the connections.

As an important crosscheck, we extracted the presented results for the Josephson current not only from the bound state approach, but also from the Furusaki-Tsukada method (see Sec. 6.2) adapted to the considered S/F-I/S geometry. Both methods essentially yield the same currents and might therefore be equally important when aiming at a universal theoretical description of Josephson physics. Both methods come along with advantages and disadvantages. Particularly for complex junctions, comprising several different interlayers, a numerical implementation of the Furusaki-Tsukada formalism becomes typically much more efficient than initially determining the bound state spectra and connecting them to the current. Nevertheless, whenever one wants to gain a deeper insight into the microscopic physics, just as in our case to establish the relation between the bound states' properties and the Josephson current reversals, the bound state approach might be the more favorable one.

7.2.3 Ground-state phase transition – a qualitative picture

In the preceding part, we claimed that it is the zero-energy crossing of the YSR states, accompanied by their puzzling spin flips, that simultaneously causes the 0-π transitions in S/F-I/S junctions' Josephson current. From that point of view, the states' spin ordering must inevitably reflect important properties of the junctions' ground state [386], which we briefly want to discuss.

Assuming that the deltalike tunneling perturbation terms in the single-particle Hamiltonians and the bulk Rashba SOC inside the superconducting regions are absent, i.e., $\lambda_{\mathrm{SC}} = \lambda_{\mathrm{MA}} = \lambda_{\mathrm{R}} = 0$, and setting the superconducting phase difference to zero ($\phi_{\mathrm{S}} = 0$), our system's Bogoljubov-de Gennes Hamiltonian [see Eq. (7.3)] effectively reduces to the Hamiltonian just describing the BCS ground state and can therefore be easily diagonalized; see Sec. 2.1.3. Let us denote the creation (annihilation) operators for *positive-energy* Bogoljubov-de Gennes eigenmodes with momentum $\mathbf{k}$ and spin σ ($\sigma = \uparrow = 1$ for spin up and $\sigma = \downarrow = -1$ for spin down) by $\hat{\alpha}^{\dagger}_{\mathbf{k},\sigma}$ ($\hat{\alpha}_{\mathbf{k},\sigma}$), and the related operators for *negative-energy* Bogoljubov-de Gennes eigenmodes by $\hat{\beta}^{\dagger}_{\mathbf{k},\sigma}$ ($\hat{\beta}_{\mathbf{k},\sigma}$). The system's BCS-like ground state $|\Psi\rangle$ is then given by a Slater product over the occupied and unoccupied Bogoljubov-de Gennes eigenmodes,

$$|\Psi\rangle = \prod_{\mathbf{k}} \hat{\alpha}_{\mathbf{k},\uparrow}\hat{\alpha}_{-\mathbf{k},\downarrow}\hat{\beta}^{\dagger}_{\mathbf{k},\uparrow}\hat{\beta}^{\dagger}_{-\mathbf{k},\downarrow}|\Psi_0\rangle, \tag{7.36}$$

where $|\Psi_0\rangle$ indicates the Fermi vacuum.

What happens to $|\Psi\rangle$ when we add a small deltalike magnetic perturbation (impurity), parameterized by λ_{MA}, to the Bogoljubov-de Gennes Hamiltonian? It is again most convenient to start with $\lambda_{\mathrm{SC}} = \phi_{\mathrm{S}} = 0$. Already a small positive λ_{MA} is sufficient to shift the spin-up states to slightly higher energies than their spin-down counterparts. This essentially means that the initially spin-degenerate Bogoljubov-de Gennes eigenmodes split and form spatially localized impurity subgap states – the Andreev and YSR states we thoroughly investigated. Anticipating the results of Eq. (7.25) in the limiting case of $\overline{\lambda}_{\mathrm{SC}} \propto \lambda_{\mathrm{SC}} = 0$ and $\phi_{\mathrm{S}} = 0$, the Andreev bound states' positive (negative) energies E_2^+ (E_2^-) and the YSR states' positive (negative) energies E_1^+ (E_1^-) fulfill $0 < E_1^+ < E_2^+ \simeq |\Delta_{\mathrm{S}}(0)|$ and $-|\Delta_{\mathrm{S}}(0)| \simeq E_2^- < E_1^- < 0$. We label the related, spin-resolved, bound state wave functions as $|\psi^{\downarrow}_{\mathrm{YSR}}\rangle$ (corresponding to E_1^+), $|\psi^{\uparrow}_{\mathrm{ABS}}\rangle$ (corresponding to E_2^+), $|\psi^{\downarrow}_{\mathrm{ABS}}\rangle$ (corresponding to E_2^-), and $|\psi^{\uparrow}_{\mathrm{YSR}}\rangle$ (corresponding to E_1^-). Recall that we still consider thus small values of λ_{MA} that the YSR states do not yet cross zero energy or even flip their spins. We could therefore immediately read off the states' spins from Fig. 7.3(b), taking into account that $0 < \overline{\lambda}_{\mathrm{MA}} \propto \lambda_{\mathrm{MA}} < \overline{\lambda}^{\mathrm{crit.}}_{\mathrm{MA}}$. The states $|\psi^{\downarrow}_{\mathrm{YSR}}\rangle$ and $|\psi^{\uparrow}_{\mathrm{YSR}}\rangle$ are typically located more inside the center of the superconducting energy gap than $|\psi^{\uparrow}_{\mathrm{ABS}}\rangle$ and $|\psi^{\downarrow}_{\mathrm{ABS}}\rangle$, and become hence spatially more localized around the impurity (see Appendix D for details).

With a further increase of λ_{MA}, the energy of $|\psi^{\downarrow}_{\mathrm{YSR}}\rangle$ continuously lowers, while that of $|\psi^{\uparrow}_{\mathrm{ABS}}\rangle$ rises. Before reaching the critical $\lambda^{\mathrm{crit.}}_{\mathrm{MA}} \approx \xi_{\mathrm{BCS}}|\Delta_{\mathrm{S}}(0)|$ (ξ_{BCS} is the BCS coherence length; see Sec. 2.1.3), $|\psi^{\downarrow}_{\mathrm{YSR}}\rangle$ remains unoccupied and $|\psi^{\uparrow}_{\mathrm{YSR}}\rangle$ occupied; see Fig. 7.7(a) for illustration. Denoting the creation (annihilation) operators for the subgap states $|\psi^{\sigma}_{\mathrm{ABS}}\rangle$ and $|\psi^{\sigma}_{\mathrm{YSR}}\rangle$ by $\hat{\mathcal{A}}^{\dagger}_{\sigma}$ ($\hat{\mathcal{A}}_{\sigma}$) and $\hat{\mathcal{Y}}^{\dagger}_{\sigma}$ ($\hat{\mathcal{Y}}_{\sigma}$), respectively, the ground state below $\lambda^{\mathrm{crit.}}_{\mathrm{MA}}$, $|\Psi_{<}\rangle$, can be written as a product state involving the occupied subgap bound states and the aforementioned (still present) quasiparticle eigenmodes,

$$|\Psi_{<}\rangle \propto \hat{\mathcal{A}}^{\dagger}_{\uparrow}\hat{\mathcal{Y}}_{\downarrow}\hat{\mathcal{Y}}^{\dagger}_{\uparrow}\hat{\mathcal{A}}^{\dagger}_{\downarrow}\prod_{\mathbf{n}} \hat{\tilde{\alpha}}_{\mathbf{n},\uparrow}\hat{\tilde{\alpha}}_{-\mathbf{n},\downarrow}\hat{\tilde{\beta}}^{\dagger}_{\mathbf{n},\uparrow}\hat{\tilde{\beta}}^{\dagger}_{-\mathbf{n},\downarrow}|\Psi_0\rangle. \tag{7.37}$$

The "tilde operators" have the same meaning as before, essentially creating (annihilating) quasiparticle eigenmodes (now perturbed) with energies above and below the gap. Since momentum is no longer a good quantum number in the perturbed system, we use the general index $\mathbf{n}$ (instead of $\mathbf{k}$) to label the states.

As soon as λ_{MA} overcomes its critical value $\lambda_{\mathrm{MA}}^{\mathrm{crit.}}$, the YSR states cross zero energy and flip their spins. Consequently, the energy of $|\psi_{\mathrm{YSR}}^{\downarrow}\rangle$ becomes smaller than that of $|\psi_{\mathrm{YSR}}^{\uparrow}\rangle$ and the relative occupations of both states essentially interchange; see Fig. 7.7(b) for illustration. The respective ground-state wave function (above $\lambda_{\mathrm{MA}}^{\mathrm{crit.}}$) is then expected to be

$$|\Psi_{>}\rangle \propto \hat{\mathcal{A}}_{\uparrow}\hat{\mathcal{Y}}_{\uparrow}\hat{\mathcal{Y}}_{\downarrow}^{\dagger}\hat{\mathcal{A}}_{\downarrow}^{\dagger}\prod_{\mathbf{n}}\hat{\tilde{\alpha}}_{\mathbf{n},\uparrow}\hat{\tilde{\alpha}}_{-\mathbf{n},\downarrow}\hat{\tilde{\beta}}_{\mathbf{n},\uparrow}^{\dagger}\hat{\tilde{\beta}}_{-\mathbf{n},\downarrow}^{\dagger}|\Psi_0\rangle. \tag{7.38}$$

Inside the gap, the ground state below $\lambda_{\mathrm{MA}}^{\mathrm{crit.}}$, $|\Psi_{<}\rangle$, has apparently a modified spin content when compared to the ground state above $\lambda_{\mathrm{MA}}^{\mathrm{crit.}}$, $|\Psi_{>}\rangle$. Both states indicate therefore well-distinct quantum phases. Our analyses in the next part will demonstrate that $|\Psi_{<}\rangle$ and $|\Psi_{>}\rangle$ effectively describe the two different phases in which Cooper pairs indeed predominantly tunnel from one superconductor into the second one along *opposite* directions (via the available YSR states). Both phases coincide thus with the 0- and π-Josephson junction regimes, explaining the close connection between the zero-energy YSR contours (YSR states' spin flips) and the 0-π transition lines we asserted in Fig. 7.6(b).

Turning on λ_{SC} and ϕ_{S}, the generic bound state energies evolve in a complex way [see Eq. (7.25) for $\overline{\lambda}_{\mathrm{SC}} \propto \lambda_{\mathrm{SC}} \neq 0$ and $\phi_{\mathrm{S}} \neq 0$]. Nevertheless, the YSR states' zero-energy crossings still mark similar changes in the junction's ground-state spin ordering, triggering the transitions between 0- and π-phases.

7.2.4 Connection between bound states and 0-π transitions

After we identified the YSR states' spin flips as the driving force of quantum phase transitions, we are just left with verifying that these manifest themselves in the measurable current reversals at 0-π transition points. From the microscopic viewpoint, Josephson currents originate from Cooper pairs that tunnel through the ferromagnetic-insulator barrier via the available (initially unoccupied) bound states forming there. Since our considered junction hosts Andreev bound states and YSR states at the same time, Cooper pairs can also tunnel either via the Andreev or the YSR channels, as we illustrate in a schematic way in Fig. 7.7; the Andreev channel is colored blue and the YSR channel red there. To figure out the correct transport direction of Cooper pairs, we split each occupied and unoccupied bound state into its electronlike and holelike components, and extract the respective electron-hole density differences [represented by the sketched evanescent tails in Fig. 7.7, where upward (downward) tails indicate electron (hole) excess]. The technical details to really compute such electron-hole differences from the constructed bound state wave functions are outlined in Appendix D. The Andreev bound states always reveal an electronlike excess in the left and a holelike excess in the right superconductor, meaning that the Andreev channel continuously transfers electron Cooper pairs *from the right into the left superconductor*[8] via the individual steps (1)–(3). In step (1), a spin-up electron tunnels to an unoccupied state at energy E_2^{+}. Afterwards, this electron pairs with a spin-down electron residing at energy E_2^{-} and both create a spin-singlet Cooper pair inside the left superconductor [step (2)]. Finally, step (3) uses the remaining electron from the initial Cooper pair to fill the vacant state at energy E_2^{-}. This argumentation persists even when $\overline{\lambda}_{\mathrm{MA}}$ reaches its critical values since the Andreev bound states' spectral characteristics are not remarkably affected by that. The situation becomes more intriguing for the YSR channel. Since the YSR states' spin flips at $\overline{\lambda}_{\mathrm{MA}}^{\mathrm{crit.}}$ entail a quantum phase transition, we need to distinguish $\overline{\lambda}_{\mathrm{MA}} < \overline{\lambda}_{\mathrm{MA}}^{\mathrm{crit.}}$ (essentially the 0-state) from $\overline{\lambda}_{\mathrm{MA}} > \overline{\lambda}_{\mathrm{MA}}^{\mathrm{crit.}}$ (π-state). In the first case, shown in Fig. 7.7(a), the YSR states show electronlike excess on the left side and holelike excess on the right side, just as we encountered for the Andreev bound states. Hence, the same transport mechanism holds

[8] Note that the computed Josephson current for the same set of parameters is *positive*. *Positive* Josephson currents indeed indicate that Cooper pairs are mostly transferred *from right to left* since Cooper pairs possess an effective electrical charge of $-2e$. Our qualitative picture is therefore fully consistent with the earlier presented numerical results.

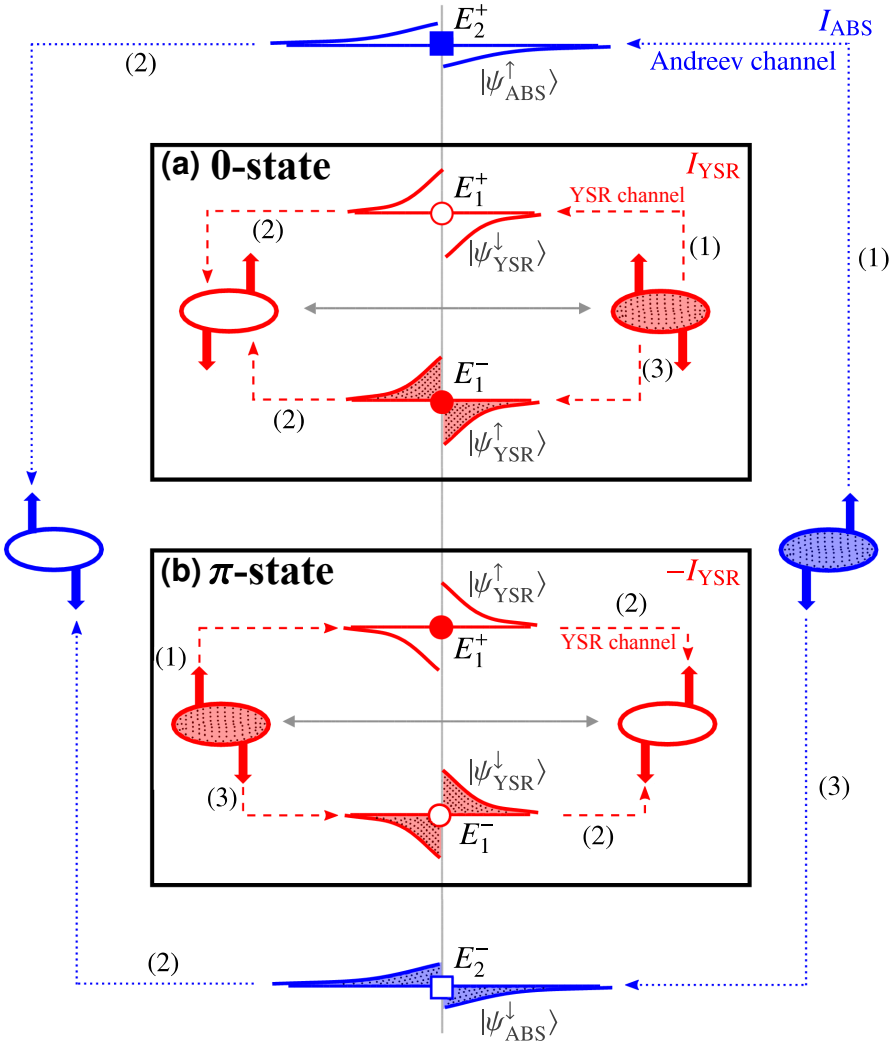


Fig. 7.7: Schematical picture of the 0- and π-junction ground states, and the associated Cooper pair transfers. Filled (empty) squares/circles display spin-up (spin-down) Andreev/YSR states. Andreev states with energies $E_2^{\pm}$ are labeled as $|\psi^{\sigma}_{ABS}\rangle$ and YSR states with energies $E_1^{\pm}$ as $|\psi^{\sigma}_{YSR}\rangle$; $\sigma = \uparrow = 1$ for spin up and $\sigma = \downarrow = -1$ for spin down. Each of the (sketched) evanescent tails indicates the spatial electron-hole density difference for one given state (see Appendix D for details). Occupied states (and Cooper pairs) are shaded. The blue dotted lines describe the Cooper pair transfer via the Andreev channel (carrying the current contribution I_{ABS}) and the red dashed lines via the YSR channel (current contribution I_{YSR}). The individual steps of the Cooper pair transfers, (1)–(3), are explained in the text. The 0-state junction is displayed in panel **(a)** and the π-state junction in panel **(b)**; note that both phases differ qualitatively only in the Cooper pair transfer via the YSR channel, while Cooper pairs being transferred via the Andreev channel are not affected. The peculiar change of the YSR states' spectral characteristics at the 0-π transition point (i.e., their interchanged spin ordering) reverses I_{YSR}, whereas I_{ABS}'s direction remains unchanged.

and also the YSR channel predominantly transfers electron Cooper pairs from the right superconductor into the left one. Both individual contributions – I_{ABS} originating from the Andreev and I_{YSR} from the YSR channel – to the overall Josephson current I_{J} flow along the same direction and add together, eventually yielding $I_{\mathrm{J}} = I_{\mathrm{ABS}} + I_{\mathrm{YSR}}$.

Contrary, the YSR states' electronlike and holelike contents in the π-state are interchanged [see Fig. 7.7(b)], and the YSR channel starts to drive electron Cooper pairs mostly *from left to right*, i.e., *against the direction of the Andreev channel*. The total Josephson current is then determined by $I_{\mathrm{J}} = I_{\mathrm{ABS}} - I_{\mathrm{YSR}}$. The transition probabilities of the "activation step" [step (1)] scale proportionally with $\mathrm{e}^{-E_n^+/|\Delta_{\mathrm{S}}(0)|}$. Since the YSR states' energies lie closer to the gap center than the Andreev bound states' energies, $E_1^+ < E_2^+$, the YSR current contribution is typically the dominant one. A reversal of I_{YSR} reverses therefore simultaneously the total Josephson current and mirrors the transition from the initial 0- to the π-state regime.

Putting all arguments of our discussions together persuades ourselves that the zero-energy YSR states' surprising spectral features and the Josephson current-reversing 0-π transitions are uniquely correlated, just as our calculations presented in Fig. 7.6(b) suggest. Following experiments might thus benefit from both. Since the critical current can be measured with great accuracy, one could exploit this quantity to tune the superconducting phase difference such that the junction gets close to the 0-π transition regime. By means of STM/STS spectroscopy, the bound states forming in the vicinity of the ferromagnetic-insulator interface could then be investigated and unambiguous fingerprints of the YSR states' peculiar properties, particularly their spin flips when crossing zero energy, might be detected.

7.2.5 Impact of Rashba spin-orbit coupling inside the superconductors

Up to now, we did not pay attention to the impact nonzero SOC might have on the Josephson current flow and, more interestingly, on the predicted distinct coincidence between zero-energy YSR states and 0-π transitions. Our modeling (see Sec. 7.1) captures SOC in terms of finite Rashba SOC in both superconducting electrodes (with the same effective strength, parameterized by λ_{R}). Note that such a situation is more complex than the one we initially considered in our article (see Ref. [394]). In the latter, Rashba SOC was only allowed to be present in one superconductor (i.e., in the right one) since we evaluated the Josephson currents from the simple current formula in Eq. (7.23), which does not necessarily properly account for the additional current contributions originating from SOC. The bound state technique presented in Sec. 7.1 and used for all current calculations within this chapter may thus indeed be regarded as an important generalization of earlier established approaches.

Figure 7.8 illustrates the (zero-temperature) oriented critical current's scaling with both tunneling measures $\overline{\lambda}_{\mathrm{SC}}$ and $\overline{\lambda}_{\mathrm{MA}}$, and for two specific Rashba SOC strengths quantified by the dimensionless variable $\overline{\lambda}_{\mathrm{R}} = (m\lambda_{\mathrm{R}})/(\hbar^2 k_{\mathrm{F}})$. Substituting $m \approx m_{\mathrm{e}}$ (free-electron mass) and the typical (metal) Fermi wave vector $k_{\mathrm{F}} \approx 8 \times 10^7\,\mathrm{cm}^{-1}$ [182], we estimate that the two chosen dimensionless SOC parameters $\overline{\lambda}_{\mathrm{R}} = 1$ and $\overline{\lambda}_{\mathrm{R}} = 2$ refer to bare Rashba SOC values of $\lambda_{\mathrm{R}} \approx 6\,\mathrm{eV\,Å}$ and $\lambda_{\mathrm{R}} \approx 12\,\mathrm{eV\,Å}$. Such Rashba SOCs may seem huge when compared to typical materials [27]. Nevertheless, a recent study [395] demonstrated that certain bismuth-based semiconductors, like BiTeI or BiTeBr, indeed exhibit comparably large Rashba parameters of about $\lambda_{\mathrm{R}} = 3.85\,\mathrm{eV\,Å}$ and $\lambda_{\mathrm{R}} = 2.0\,\mathrm{eV\,Å}$, and even larger SOCs might be reachable. The characteristics that we will discuss in the following might therefore become experimentally accessible in Josephson junctions whose electrodes consist of bismuth compounds proximitized by s-wave superconductors. Apart from that, we predominantly selected such large SOC measures to observe the consequences of SOC most clearly; all discussed qualitative effects would likewise appear at much lower $\overline{\lambda}_{\mathrm{R}}$. The analytical expression describing the junction's bound state spectrum [see Eq. (7.25)]

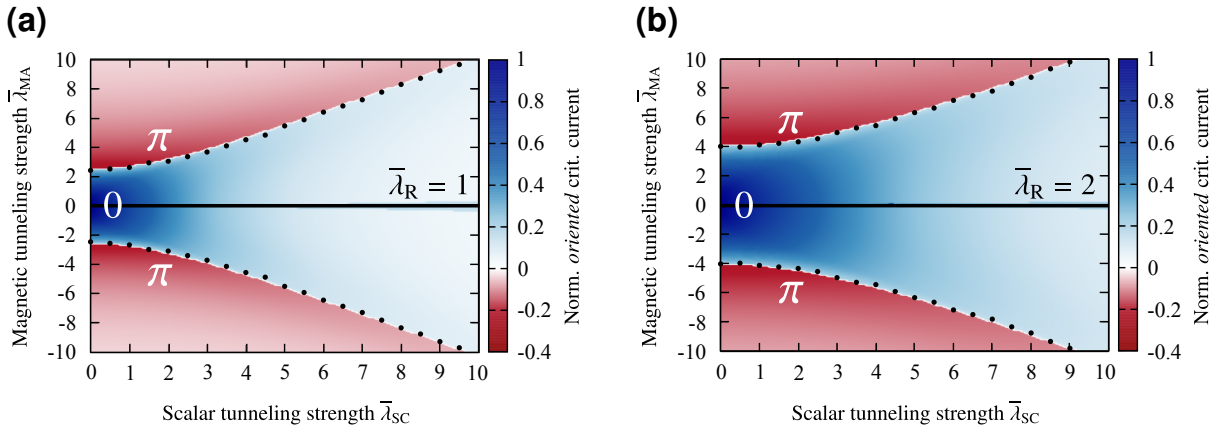


Fig. 7.8: (a) Calculated *oriented* critical current (normalized as in Fig. 7.6) as a function of $\overline{\lambda}_{SC}$ and $\overline{\lambda}_{MA}$, and for the Rashba SOC strength $\overline{\lambda}_R = (m\lambda_R)/(\hbar^2 k_F) = 1$. Blue and red regions represent 0- and π-junction regimes. The transition lines separating the two phases are emphasized by white borderlines; black dots highlight (some) numerically estimated tunneling parameters that support zero-energy YSR states. **(b)** Same calculation as in **(a)**, but for $\overline{\lambda}_R = 2$.

was initially derived in the absence of SOC. The same methods are, nevertheless, still applicable at nonzero Rashba SOC. Since extracting closed analytical expressions in such generic cases would be rather cumbersome, we compute the Andreev bound states' and YSR states' energies fully numerically, and substitute the results into Eq. (7.22) to access the critical (Josephson) currents.

Increasing the Rashba SOC strength (either by electrical gating [250, 251, 275–277] or by making use of different material combinations) provides an efficient way to continuously shift the 0-π transition points to larger magnetic tunneling strengths $\overline{\lambda}_{MA}$, completely independent of the actual scalar tunneling strength $\overline{\lambda}_{SC}$. Let us exemplarily illustrate this observation for $\overline{\lambda}_{SC} = 0$. While the junction undergoes its 0-π transition at $\pm\overline{\lambda}_{MA}^{crit.} \approx \pm 1.82$ as long as SOC is fully absent ($\overline{\lambda}_R = 0$), $\overline{\lambda}_R = 1$ requires already a critical magnetic tunneling strength of $\pm\overline{\lambda}_{MA}^{crit.} \approx \pm 2.55$ and $\overline{\lambda}_R = 2$ even $\pm\overline{\lambda}_{MA}^{crit.} \approx \pm 4.10$. Dramatically weaker Rashba SOC still allows for a similar tunability of the 0-π transitions; $\overline{\lambda}_{MA}^{crit.}$ does then not increase thus rapidly (with $\overline{\lambda}_R$). Moreover, nonzero Rashba SOC noticeably enhances the critical current's *amplitudes* in both the 0- and π-state regimes. This is another indirect evidence that SOC gives rise to the formation of spin-polarized triplet Cooper pairs. The overall Josephson current is then composed of its initial singlet and the additionally generated triplet contribution. The latter becomes particularly dominant at strong SOC (i.e., at the $\overline{\lambda}_R$-values we considered) and explains the sudden increase of the current amplitudes.

As the most central finding of our previous analyses, we related the current-reversing 0-π transitions to zero-energy crossings (and accompanying spin flips) of the YSR states. Dealing with nonzero Rashba SOC inside the superconducting electrodes, the earlier given analytical condition determining which combinations of tunneling measures and superconducting phase differences maintain zero-energy YSR states [recall Eq. (7.35)] is of course no longer valid. Instead, we numerically localize the zero-energy YSR state parameters (at least for some of the zero-energy states) and additionally emphasize them by black dots in Fig. 7.8. Notably, the proposed unique coincidence between the formation of zero-energy YSR states and the 0-π transition regions in the Josephson current persists even at extremely strong Rashba SOC, and is hence a universal fingerprint of S/F-I/S junctions.

7.3 Discussion of results for triplet pairing

As a second important application of our theoretical model, we briefly investigate to which extent *pure* p_x-wave pairing inside the superconducting electrodes modifies the junction's bound state spectrum and the resulting Josephson current flow. In this particular case, the (now k_x-dependent; therefore, this type of pairing is termed p_x-wave pairing) superconducting pairing potential, initially defined in Eq. (7.5), simplifies to

$$\hat{\Delta}_{\mathrm{S}}(x) = -|\Delta_{\mathrm{S}}^{p}|\frac{k_x}{|k_x|}\hat{\sigma}_y\left[\Theta(-x) + \mathrm{e}^{\mathrm{i}\phi_{\mathrm{S}}}\Theta(x)\right]. \tag{7.39}$$

Analogously to the previously studied s-wave scenario, we substitute $|\Delta_{\mathrm{S}}^{p}| = |\Delta_{\mathrm{S}}(0)|$, with $|\Delta_{\mathrm{S}}(0)|$ indicating the superconductors' isotropic energy gap, for the pairing potential's (constant) amplitude and restrict ourselves to the bound state energies (Josephson currents) at zero temperature. To cover temperature effects, one could again replace $|\Delta_{\mathrm{S}}(0)|$ by its BCS-like temperature dependence $|\Delta_{\mathrm{S}}(T \neq 0)| = |\Delta_{\mathrm{S}}(0)|\tanh(1.74\sqrt{T_{\mathrm{C}}/T-1})$.

7.3.1 Bound state spectrum

Following the universal methodology we introduced in Sec. 7.1, we can directly evaluate the energies of the bound states that are expected to form around the ferromagnetic-insulator junction interface. Although the pairing potential itself looks now slightly more complicated than in the (standard) s-wave case we considered in Sec. 7.2 [compare, e.g., Eq. (7.39) to Eq. (7.24)], the p_x-wave bound state energies become actually much simpler. Assuming that Rashba SOC is not present (i.e., $\lambda_{\mathrm{R}} = 0$), the electron-hole symmetric bound state energies $E_n^{\pm}$, with $n \in \{1;2\}$, are determined by

$$\frac{E_{\mathrm{B}}}{|\Delta_{\mathrm{S}}(0)|} \equiv \frac{E_n^{\pm}}{|\Delta_{\mathrm{S}}(0)|} = \pm\sqrt{\frac{4}{4+\left[\overline{\lambda}_{\mathrm{SC}} + (-1)^n\overline{\lambda}_{\mathrm{MA}}\right]^2}}\cos\left(\frac{\phi_{\mathrm{S}}}{2}\right). \tag{7.40}$$

Similarly to the s-wave junction, the bound state energies solely depend on the phase difference ϕ_{S} between the two superconducting regions, and the two dimensionless variables $\overline{\lambda}_{\mathrm{SC}} = (2m\lambda_{\mathrm{SC}})/(\hbar^2 k_{\mathrm{F}})$ and $\overline{\lambda}_{\mathrm{MA}} = (2m\lambda_{\mathrm{MA}}/(\hbar^2 k_{\mathrm{F}})$, still quantifying the strengths of scalar and magnetic tunnelings, respectively. In agreement with earlier studies [390],[9] Eq. (7.40) transforms into

$$E_1^{\pm} = E_2^{\pm} = \pm|\Delta_{\mathrm{S}}(0)|\sqrt{\frac{4}{4+\overline{\lambda}_{\mathrm{SC}}^2}}\cos\left(\frac{\phi_{\mathrm{S}}}{2}\right) \tag{7.41}$$

when considering $\overline{\lambda}_{\mathrm{MA}} = 0$, referring to a junction in which the tunneling barrier is *nonmagnetic* and introduces hence only a scalar scattering potential. The particularly rewarding physics associated with magnetic barriers was not discussed in Ref. [390].

In order to get more familiar with the influence magnetic tunneling has on the junction's bound state characteristics, we illustrate the spin-resolved[10] bound state energies as functions of $\overline{\lambda}_{\mathrm{MA}}$ in Fig. 7.9, covering again antiferromagnetic and ferromagnetic couplings. The scalar tunneling parameter $\overline{\lambda}_{\mathrm{SC}}$ gets consecutively increased from $\overline{\lambda}_{\mathrm{SC}} = 0$, indicating transparent interfaces, to a moderate value of $\overline{\lambda}_{\mathrm{SC}} = 2$, and eventually to a large barrier strength of $\overline{\lambda}_{\mathrm{SC}} = 5$. For simplicity, we assume zero superconducting phase difference ($\phi_{\mathrm{S}} = 0$) for the moment. Remarkably, the states' fundamental characteristics

[9] To compare the bound state energies extracted from our study [see Eq. (7.41)] to those given in Ref. [390], one just needs to replace our scalar tunneling parameter $\overline{\lambda}_{\mathrm{SC}}$ by the (BTK-like) Z-barrier parameter used there.

[10] The states' spins can be identified in the same way as in Sec. 7.2. One can either compute their spin expectation values (with respect to $\hat{\sigma}_z$) or decompose the Nambu Bogoljubov-de Gennes description into its spin-resolved blocks.

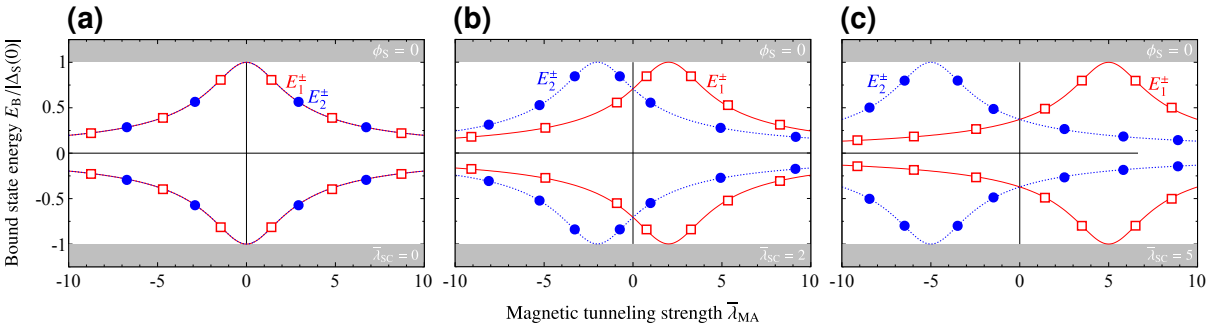


Fig. 7.9: (a) Calculated bound state energies of the spin-up ($E_2^{\pm}$; blue) and spin-down ($E_1^{\pm}$; red) Andreev bound states (assuming p_x-wave superconducting pairing) as functions of the magnetic tunneling strength $\overline{\lambda}_{MA}$ and for the scalar tunneling strength $\overline{\lambda}_{SC} = 0$, the superconducting phase difference $\phi_S = 0$, as well as absent Rashba SOC ($\lambda_R = 0$). Filled circles (empty squares) highlight spin-up (spin-down) states. **(b)** Same calculation as in **(a)**, but for $\overline{\lambda}_{SC} = 2$. **(c)** Same calculation as in **(a)**, but for $\overline{\lambda}_{SC} = 5$.

differ strongly from those we unraveled in the s-wave pairing case. As long as scalar tunneling remains absent ($\overline{\lambda}_{SC} = 0$) and only $\overline{\lambda}_{MA}$ is varied, the bound state bands simply merge into two doubly spin-degenerate branches (appearing symmetrically with respect to the center of the superconducting gap owing to the unique electron-hole symmetry in the junction). Anticipating the results of Eq. (7.40), the associated bound state energies read as

$$E_1^{\pm} = E_2^{\pm} = \pm|\Delta_S(0)| \sqrt{\frac{4}{4+\overline{\lambda}_{MA}^2}} \cos\left(\frac{\phi_S}{2}\right), \tag{7.42}$$

approaching $E_1^{\pm} = E_2^{\pm} = \pm|\Delta_S(0)|$ at $\overline{\lambda}_{MA} = 0$ and shifting more into the center of the superconducting gap at $\overline{\lambda}_{MA} \neq 0$. These states will not cross zero energy at zero superconducting phase difference.

Furthermore, Eq. (7.42) reflects another quite surprising finding. As long as there is only *either* scalar *or* magnetic tunneling present at the ferromagnetic-insulator interface, the expressions for the bound state energies look formally identical [compare Eq. (7.41) to Eq. (7.42)] – invoking only $\overline{\lambda}_{SC}$ in the first and $\overline{\lambda}_{MA}$ in the second scenario. Increasing the tunneling strength simply adds more disorder to the system (in terms of reducing its interfacial transparency) and shifts the energies more towards the superconducting energy gap's center. Although the spin splitting of initially degenerate bound state bands is essentially caused by the spin-dependent magnetic tunneling potential, it actually completely disappears once the scalar tunneling vanishes, i.e., in junctions with perfectly transparent ferromagnetic-insulator interfaces. The observation of spin-split Andreev bound states is therefore an evidence for the intricate interplay between (finite) scalar *and* magnetic tunnelings in one single S/F-I/S junction.

More remarkably, the bound state bands do no longer reflect the spectral features of YSR states. This observation becomes even more stressed with raising $\overline{\lambda}_{SC}$. The interplay of both nonzero $\overline{\lambda}_{SC}$ and $\overline{\lambda}_{MA}$ indeed splits the bound state spectrum into distinct *spin-resolved* branches. The *spin-up branches*, whose energies are given by

$$E_2^{\pm} = \pm|\Delta_S(0)| \sqrt{\frac{4}{4+\left(\overline{\lambda}_{SC}+\overline{\lambda}_{MA}\right)^2}} \cos\left(\frac{\phi_S}{2}\right), \tag{7.43}$$

are apparently obtained from the initial bands (when considering $\overline{\lambda}_{\mathrm{MA}} = 0$) by *horizontally* (meaning along the $\overline{\lambda}_{\mathrm{MA}}$-axis) shifting one of the bands by $-\overline{\lambda}_{\mathrm{MA}}$ and the *spin-down branches*, with energies

$$E_1^{\pm} = \pm|\Delta_{\mathrm{S}}(0)| \sqrt{\frac{4}{4 + \left(\overline{\lambda}_{\mathrm{SC}} - \overline{\lambda}_{\mathrm{MA}}\right)^2}} \cos\left(\frac{\phi_{\mathrm{S}}}{2}\right), \tag{7.44}$$

via a *horizontal* shift by $+\overline{\lambda}_{\mathrm{MA}}$; the band splitting becomes hence most clearly evident at large $\overline{\lambda}_{\mathrm{MA}}$. The generic form of Eqs. (7.43) and (7.44) is quite rewarding as it reveals that the results obtained for the simple nonmagnetic junction [390] can be generalized to the magnetic case simply replacing the scalar tunneling parameter by a *spin-dependent combination of the scalar and magnetic tunneling measures*, i.e., by $\overline{\lambda}_{\mathrm{SC}} + \overline{\lambda}_{\mathrm{MA}}$ for spin up and $\overline{\lambda}_{\mathrm{SC}} - \overline{\lambda}_{\mathrm{MA}}$ for spin down. The bound state energies approach the gap edge now for $\overline{\lambda}_{\mathrm{MA}} = -\overline{\lambda}_{\mathrm{SC}}$ in the spin-up and for $\overline{\lambda}_{\mathrm{MA}} = \overline{\lambda}_{\mathrm{SC}}$ in the spin-down branch, respectively. In sharp contrast to the previously regarded s-wave case, in which the YSR states even flip their spins with increasing $\overline{\lambda}_{\mathrm{MA}}$, finally marking 0-$\pi$ transitions, the states' spins *inside one of the bands* are now no longer affected by altering the magnetic tunneling parameter. As a direct consequence, p_x-wave Josephson junctions must continuously remain in the 0-state regime and even strong magnetic tunnelings are not sufficient to induce transitions into the π-state. Inspecting Eqs. (7.43) and (7.44), we deduce that each spin-up state with energy $E_2^{\pm}$, forming at a magnetic tunneling strength of $\overline{\lambda}_{\mathrm{MA}}$, comes along with its spin-down counterpart ($E_1^{\pm}$) at $-\overline{\lambda}_{\mathrm{MA}}$ (and vice versa). Moreover, one shall also notice that positive *and* negative bound states possess now the *same* spins (while being opposite in the s-wave junction). In fact, already Shiba's considerations [362] (see our introductory remarks to this chapter) predicted that YSR states are unique to systems with singlet (s-wave) superconducting pairing and do not form in p_x-wave junctions. For that reason, we will not use the term *YSR states* in connection with p_x-wave junctions, but call the states *spin-split Andreev bound states* instead.

To complete our analyses, Fig. 7.10 depicts the energies of the spin-split Andreev bound states as functions of the superconducting phase difference ϕ_{S}. Analogously to our calculations performed in the s-wave coupling configuration (see Fig. 7.5), we differentiate between the two representative scalar tunneling strengths $\overline{\lambda}_{\mathrm{SC}} = 0$ and $\overline{\lambda}_{\mathrm{SC}} = 2$, while the magnetic tunneling strength gets again consecutively increased from $\overline{\lambda}_{\mathrm{MA}} = 1$ to $\overline{\lambda}_{\mathrm{MA}} = 2$, and eventually to $\overline{\lambda}_{\mathrm{MA}} = 3$. Our simulations confirm all mentioned previous characteristics. As long as scalar tunneling remains fully absent [$\overline{\lambda}_{\mathrm{SC}} = 0$; see Figs. 7.10(a)–7.10(c)], increasing the magnetic tunneling parameter $\overline{\lambda}_{\mathrm{MA}}$ simply adds more interfacial disorder to the system and shifts the bound state bands more towards the superconducting gap's center. Owing to the peculiar interplay of both tunnelings ($\overline{\lambda}_{\mathrm{SC}}$ and $\overline{\lambda}_{\mathrm{MA}}$) we outlined above, nonzero $\overline{\lambda}_{\mathrm{MA}}$ alone is not yet sufficient to break the states' twofold spin degeneracy. The doubly spin-degenerate states' energies $E_1^{\pm} = E_2^{\pm}$ are determined by Eq. (7.42). The states' periodicity with respect to the superconducting phase difference ϕ_{S} is governed by the $\cos(\phi_{\mathrm{S}}/2)$-term in Eq. (7.42) and does not depend on the actual values of the tunneling parameters. As a consequence, the Andreev bound state spectrum becomes 4π-periodic in ϕ_{S} – being well-distinct from the s-wave case (recall our discussions in Sec. 7.2) in which both the Andreev bound states and the YSR states follow a 2π ϕ_{S}-periodicity –, and (doubly degenerate) zero-energy states form at $\phi_{\mathrm{S}} = \pi \pmod{2\pi}$ for *all* possible combinations of $\overline{\lambda}_{\mathrm{SC}}$ and $\overline{\lambda}_{\mathrm{MA}}$. Such zero-energy bound states, robust against interfacial scattering (in comparison with the s-wave case in which zero-energy Andreev bound states get immediately destroyed when increasing $\overline{\lambda}_{\mathrm{SC}}$; see Fig. 7.3), essentially serve as the key motivation for trying to host zero-energy Majorana modes in spatially confined Josephson junctions [323, 324, 326, 327, 381]. However, to avoid dealing with rather complicated materials that possess inherent p_x-wave superconducting coupling, most of these suggestions focus on semiconductor nanowires with strong SOC, which are proximitized by s-wave superconductors and brought into an appropriately aligned magnetic field. Such set-ups effectively behave like p_x-wave junctions, realizing similar zero-energy Andreev bound states as the ones we discussed.

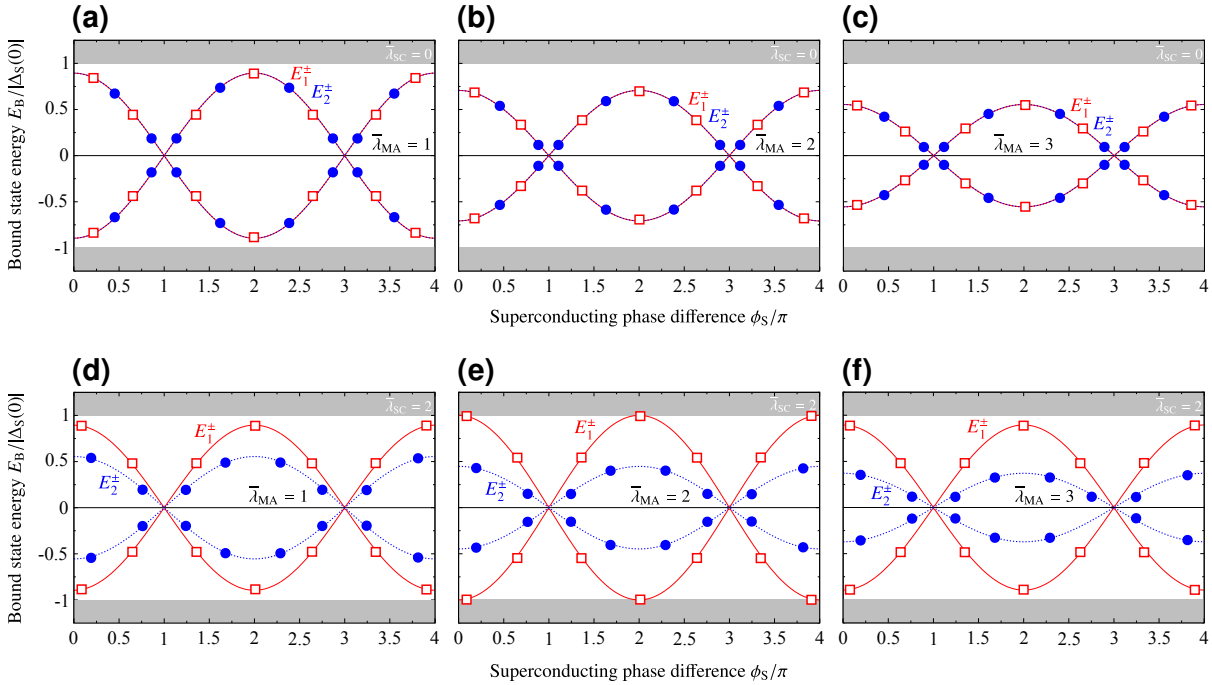


Fig. 7.10: **(a)** Calculated bound state energies of the spin-up ($E_2^{\pm}$; blue) and spin-down ($E_1^{\pm}$; red) Andreev bound states (assuming p_x-wave superconducting pairing) as functions of the superconducting phase difference ϕ_S, and for the scalar tunneling strength $\overline{\lambda}_{SC} = 0$, as well as the magnetic tunneling strength $\overline{\lambda}_{MA} = 1$; Rashba SOC is absent ($\lambda_R = 0$). Filled circles (empty squares) highlight spin-up (spin-down) states. **(b)** Same calculation as in **(a)**, but for $\overline{\lambda}_{SC} = 0$ and $\overline{\lambda}_{MA} = 2$. **(c)** Same calculation as in **(a)**, but for $\overline{\lambda}_{SC} = 0$ and $\overline{\lambda}_{MA} = 3$. **(d)** Same calculation as in **(a)**, but for $\overline{\lambda}_{SC} = 2$ and $\overline{\lambda}_{MA} = 1$. **(e)** Same calculation as in **(a)**, but for $\overline{\lambda}_{SC} = 2$ and $\overline{\lambda}_{MA} = 2$. **(f)** Same calculation as in **(a)**, but for $\overline{\lambda}_{SC} = 2$ and $\overline{\lambda}_{MA} = 3$.

At that point, one might ask the question to which extent our studied S/F-I/S system might become relevant when establishing Majorana modes in superconducting junctions. Indeed, we checked also for our junction that s-wave superconducting coupling inside the superconductors together with large magnetic tunneling ($\overline{\lambda}_{MA} \gg 1$)[11] and strong Rashba SOC ($\overline{\lambda}_R \gg 1$) essentially mimics the characteristics of p_x-wave junctions, and maintains hence likewise the bound state spectra we encountered in Fig. 7.10. Nevertheless, the required (large) values of $\overline{\lambda}_{MA}$ and $\overline{\lambda}_R$, which originate from the spatial separation of the magnetic ferromagnetic-insulator component and the superconductors' Rashba SOC, might act against our system. The recently published Majorana proposals in the literature [323, 324, 326, 327, 381] take advantage of combining magnetism and SOC in the same constituent and are thus more auspicious candidates for realizing zero-energy Majorana modes in real devices. Since our work aims at developing

[11] Recall that the magnetization part of the Hamiltonian considered for our study actually models a magnetic field applied perpendicular to the one-dimensional junction (i.e., along $\hat{z}$). As long as the superconducting pairing potential is the s-wave one, no magnetoanisotropic behavior appears and the bound state spectra are not affected by rotating the magnetic field. This changes fundamentally in p_x-wave junctions. To a certain extent, the formal structure of the p_x-wave pairing potential can be compared to SOC. As we outlined in Chap. 6, the interplay of (ferro)magnetism and SOC in one junction can lead to pronounced magnetoanisotropies. Mathematically, the p_x-wave pairing potential involves the $\hat{\sigma}_y$-Pauli matrix [see, e.g., Eq. (7.39)] and can therefore couple to a magnetic field oriented along $\hat{y}$ (whose Hamiltonian simultaneously invokes the $\hat{\sigma}_y$-Pauli matrix). As a consequence, we expect that the discussed bound state characteristics in the p_x-wave scenario are modified as soon as the magnetic tunneling Hamiltonian involves a nonzero component scaling proportionally with $\hat{\sigma}_y$. In fact, we checked this case (the results are not shown in this thesis) and found that large magnetic tunnelings $\propto \hat{\sigma}_y$ essentially destroy the unique bound state features associated with p_x-wave pairing, and we finally simply recover the bound state spectra of s-wave junctions discussed in Sec. 7.2.

a universal understanding of the bound state physics associated with magnetic Josephson junctions and we are actually not particularly interested in Majorana physics at the moment, we do not pay special attention to probably possible improvements of our geometry into that direction.

Let us come back to our junction's Andreev bound state spectra in the presence of moderate scalar tunneling ($\overline{\lambda}_{\mathrm{SC}} = 2$); see Figs. 7.10(d)–7.10(f). Both scalar and magnetic tunnelings come now fully into play and split the initially degenerate bound state energy bands into spin-up bands with energies $E_2^{\pm}$ [determined by Eq. (7.43)] and the related spin-down bands with energies $E_1^{\pm}$ [determined by Eq. (7.44)]. The spin-up branches lie always closer to the gap center than their spin-down counterparts. Looking up the formulas we obtained for the bound state energies [see Eqs. (7.43) and (7.44)] reminds us that scalar and magnetic tunnelings essentially combine into an effective spin-dependent tunneling potential. Regarding the spin-up branches, both tunneling strengths simply add up, $\overline{\lambda}_{\mathrm{SC}} + \overline{\lambda}_{\mathrm{MA}}$, suggesting that an increase of $\overline{\lambda}_{\mathrm{SC}}$ and/or $\overline{\lambda}_{\mathrm{MA}}$ inevitably results in stronger interfacial scattering and shifts the $E_2^{\pm}$-branches more towards the gap's center. The situation becomes more interesting when considering the spin-down branches, which are described by the effective tunneling potential $\overline{\lambda}_{\mathrm{SC}} - \overline{\lambda}_{\mathrm{MA}}$. If we keep $\overline{\lambda}_{\mathrm{SC}} = 2$ constant, rising $\overline{\lambda}_{\mathrm{MA}}$ initially decreases the effective tunneling potential and the $E_1^{\pm}$ branches move towards the gap *edges*, approaching $E_1^{\pm} = \pm|\Delta_{\mathrm{S}}(0)|\cos(\phi_{\mathrm{S}}/2)$ for $\overline{\lambda}_{\mathrm{MA}} = \overline{\lambda}_{\mathrm{SC}} = 2$. In the latter case, the scalar and magnetic tunnelings mutually compensate (at least for spin down) and we recover the bound state spectrum of perfectly transparent junctions (which one could also compare to the findings in the nonmagnetic case presented in Ref. [390]). A further increase of $\overline{\lambda}_{\mathrm{MA}}$ enhances the overall tunneling potential again and the $E_1^{\pm}$-bands are continuously shifted back towards the central region of the superconducting energy gap. All considered tunneling strengths leave the states' unique 4π phase-periodicity, as well as the promising (still doubly spin-degenerate) zero-energy Andreev bound states forming at $\phi_{\mathrm{S}} = \pi \pmod{2\pi}$, unaffected, and provide another indication that S/F-I/S Josephson junctions might host topologically protected zero-energy Majorana modes.

7.3.2 Josephson current

Similarly to the above studied s-wave case, we are finally able to connect the bound states' spectral characteristics to the Josephson current flowing through the p_x-wave junction. When dealing with the most general situation, i.e., if additionally the Rashba SOC strength becomes nonzero, one shall again proceed with the universal current formula stated in Eq. (7.22) and substitute the related bound state energies for p_x-wave coupling (which differ from the given analytical expressions as soon as the Rashba SOC strength becomes finite). Since we restricted ourselves to p_x-wave junction's bound state energies in the absence of Rashba SOC ($\lambda_{\mathrm{R}} = 0$) and extracted compact analytical formulas for that scenario, it is more common to continue with the simplified Josephson current expression in Eq. (7.23). This approach allows for a fully analytical calculation of the Josephson current and will help us to gain more insight into the physics. Substituting the bound state energies [see Eq. (7.40)] and summing over all branches of states, we obtain the total *zero-temperature* Josephson current as

$$I_{\mathrm{J}} = I_{\mathrm{J}}(\phi_{\mathrm{S}}) = \frac{e}{2\hbar}|\Delta_{\mathrm{S}}(0)|\left[\sqrt{\frac{4}{4+\left(\overline{\lambda}_{\mathrm{SC}}+\overline{\lambda}_{\mathrm{MA}}\right)^2}} + \sqrt{\frac{4}{4+\left(\overline{\lambda}_{\mathrm{SC}}-\overline{\lambda}_{\mathrm{MA}}\right)^2}}\right]\sin\left(\frac{\phi_{\mathrm{S}}}{2}\right). \tag{7.45}$$

It is easy to see that the current is composed of two individual contributions that stem from the bound states' spin-up and spin-down parts, respectively.

To illustrate the impact of the scalar and magnetic tunneling strengths on the Josephson current, we present the Josephson current-phase relations for various tunneling parameters in Fig. 7.11. More

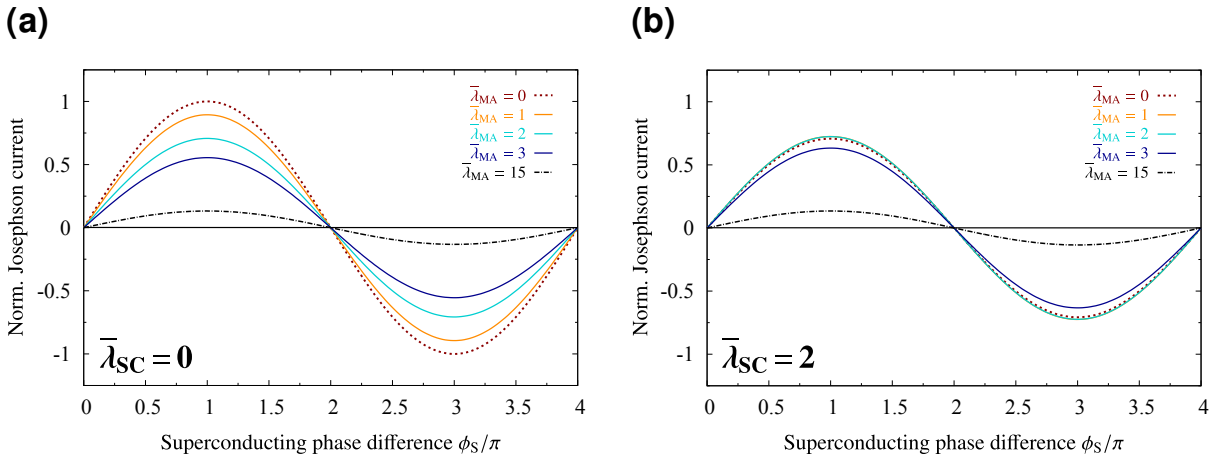


Fig. 7.11: (a) Calculated Josephson current-phase relations (assuming p_x-wave superconducting pairing; the Josephson current is normalized in the same way as in Fig. 7.6) in the absence of scalar tunneling ($\overline{\lambda}_{SC} = 0$) and for various indicated magnetic tunneling strengths $\overline{\lambda}_{MA}$; Rashba SOC is not present ($\lambda_R = 0$). **(b)** Same calculation as in **(a)**, but for $\overline{\lambda}_{SC} = 2$.

precisely, we distinguish again between the two scalar tunneling strengths $\overline{\lambda}_{SC} = 0$ and $\overline{\lambda}_{SC} = 2$, while the magnetic tunneling measure $\overline{\lambda}_{MA}$ gets increased from $\overline{\lambda}_{MA} = 0$ to $\overline{\lambda}_{MA} = 15$ in discrete steps. As a remarkable feature, the bound states' characteristic 4π-periodicity (with respect to the superconducting phase difference ϕ_S), coming along with the formation of the promising zero-energy Andreev bound states, gets transferred one-to-one into the junction's current-phase relations. Many researchers are therefore convinced that detecting 4π-periodic Josephson currents could be a strong indirect signature that the junction might support (zero-energy) Majorana modes under appropriate conditions [357, 396, 397]. Unfortunately, reality turns out to be slightly more complicated. In junctions that are not strictly one-dimensional (as it is the case with most of the experimentally available systems), the Josephson current consists, e.g., of additional 2π-periodic transverse-channel contributions [356, 390, 398, 399]. The effectively measured Josephson current-phase relations comprise then a complex mixture of 2π- and 4π-periodic parts, and it might become extremely difficult to unravel the different components.

In the absence of scalar tunneling [$\overline{\lambda}_{SC} = 0$; see Fig. 7.11(a)], raising $\overline{\lambda}_{MA}$ simply adds more interfacial disorder into the system and monotonically damps the Josephson current's amplitudes (recall our discussions of the bound state characteristics in that case). Once $\overline{\lambda}_{SC}$ becomes finite [see Fig. 7.11(b)], the Josephson current depends on the actually chosen value of $\overline{\lambda}_{MA}$ in a *non*monotonic manner. The reason for that got already explained in connection with the bound states. Both tunnelings effectively combine into $\overline{\lambda}_{SC} + \overline{\lambda}_{MA}$ for spin-up and $\overline{\lambda}_{SC} - \overline{\lambda}_{MA}$ for spin-down states. At finite $\overline{\lambda}_{SC}$, an enhancement of $\overline{\lambda}_{MA}$ continuously increases the scattering potential for the spin-up channel and suppresses likewise the related Josephson current contribution [i.e., the first part of Eq. (7.45)]. Contrary, the spin-down channel's effective scattering potential primarily decreases until $\overline{\lambda}_{MA} = \overline{\lambda}_{SC}$, leading to an initial (slight) increase of the Josephson current [captured by the second part of Eq. (7.45)]. The overall Josephson current is only moderately enhanced as the current originating from the spin-up channel gets simultaneously reduced (nearly by the same amount by which the spin-down channel current increases). As soon as $\overline{\lambda}_{MA}$ overcomes $\overline{\lambda}_{SC}$, the increasing trend starts to reverse. Both the spin-up and spin-down channels' contributions to the Josephson current, and therefore also the total current, are then noticeably suppressed.

When analyzing the junction's bound state characteristics, we claimed that the absence of YSR states with their unique properties, to which we basically attributed the 0-π transitions appearing in the s-wave coupling scenario, must have one unambiguous consequence: p_x-wave junctions remain always in their 0-state and cannot undergo transitions into the π-phase. Our Josephson current calculations,

shown in Fig. 7.11, precisely confirm this expectation. Even extremely strong magnetic tunneling of $\overline{\lambda}_{\mathrm{MA}} = 15$ does not facilitate 0-π transitions. In fact, a more comprehensive study [400], going beyond the scope of our work, concluded that 0-π transitions would require an intricate combination of two helical superconductors with *different* p-wave pairing potentials, e.g., $(p_x + \mathrm{i}p_y)$-wave in the left and $(p_x - \mathrm{i}p_y)$-wave pairing in the right electrode. Such a configuration modifies the junction's bound state spectrum in a highly nontrivial way and may finally let 0-π transitions emerge.

7.4 Short summary

In summary, we developed a general theoretical approach to investigate the spectral and transport characteristics associated with the bound states that form at the ferromagnetic-insulator interfaces of magnetic S/F-I/S Josephson junctions. Starting from such junctions' Bogoljubov-de Gennes scattering description, we initially obtained analytical formulas for the allowed bound state energies, worked out the states' wave functions, and finally related the latter to the expected Josephson current flow. Evaluating the current by means of the underlying bound state wave functions offers not only an important crosscheck for the results obtained within the Green's function-based Furusaki-Tsukada technique (see Chap. 6), but provides also a powerful alternative that allows us to resolve the bound states' individual current contributions and gain deeper insight into the physics. To keep our study more general, we differentiated between junctions in which the pairing mechanism inside the superconducting electrodes is either the s-wave or the p_x-wave one, covering the essential ingredients of most of the intensively discussed proposals to tailor Majorana modes in condensed-matter systems [252, 253, 314–327, 381].

Our comprehensive analyses focused particularly on the experimentally relevant s-wave coupling. Besides the usual Andreev bound states, which are known from earlier works on nonmagnetic Josephson junctions, the magnetic ferromagnetic-insulator barrier gives rise to the formation of additional YSR states with striking features. We identified the energies of both types of bound states for several realistic junction parameters, and demonstrated their large experimental tunability by means of the scalar and magnetic tunneling strengths, or the phase difference between the superconductors. In sharp contrast to the Andreev bound states, the YSR states cross zero energy for a wide range of parameter combinations and flip their spins. Such zero-energy crossings serve as clear fingerprints of ground-state quantum phase transitions. We unraveled that these transitions precisely correspond to S/F-I/S junctions' Josephson current-reversing 0-π transitions and understood the appearing current reversals in terms of a simple qualitative picture, which connects the direction of the current flow to the tunneling of Cooper pairs from one into the second superconductor via the interfacial Andreev bound states and YSR states. The predicted coincidence between the zero-energy YSR states and the 0-π transition points in the Josephson current persists even in the presence of (strong) Rashba SOC in both superconducting electrodes and is thus universal. In fact, though we restricted ourselves to one-dimensional junctions, similar arguments apply to three-dimensional junctions renormalizing the tunneling parameters as we illustrate elsewhere (see Ref. [394]). Our reasoning got furthermore confirmed by Rouco *et al.* [401], who concluded just shortly after our work that the same mechanism holds for *diffusive* S/F/S junctions. We furthermore discuss in our article (see Ref. [394]) that the intriguing interplay of Andreev bound states and YSR states manifests itself in characteristic modulations of the quasiparticle DOS coherence peaks [329, 353] – one possible explanation for the aforementioned transport anomalies in magnetic Josephson junctions [254, 342] and the unexpected spin-flip dynamics in resonant superconducting systems [402].

The bound state characteristics change completely when assuming p_x-wave pairing inside both superconducting electrodes. Instead of being concerned with a puzzling superposition of the (usual) Andreev bound states on the one and the peculiar YSR states on the other hand, the latter disappear

and the (positive-energy) spectrum simply reduces to two spin-split Andreev bound state branches. We classified in which way the scalar and magnetic tunneling strengths act together, altering the allowed bound state energies. In contrast to the s-wave situation, p_x-wave junctions continuously support (degenerate) zero-energy Andreev bound states at phase differences of $\phi_S = \pi \pmod{2\pi}$. These robust zero-energy states recently attracted enormous interest for realizing zero-energy Majorana modes in Josephson junctions [252, 253, 314–327, 381]. Since we attributed the Josephson current-reversing 0-π transitions to s-wave junctions' distinct YSR states and their striking spin structure, we stated that the absence of these states in the p_x-wave scenario immediately implies that the system must always remain in its initial (0-state) ground state and cannot undergo transitions into the π-state regime. Evaluating the Josephson current within our theoretical formulation verified this expectation and underlined the universality of the proposed correlations between the formation of zero-energy YSR states in the junctions' bound state spectra and the emergence of 0-π transitions for another time.

Part *IV*

Anomalous Hall and spin Hall effects in superconducting junctions

Chapter 8

Tunneling anomalous Hall and spin Hall effects in ballistic F/S junctions

At the time when Edwin Hall joined Johns Hopkins University in Baltimore as a graduate student to continue his research [403], he was one of the pioneers studying the impact of magnetic fields on electrical transport through conductors. The main motivation for Hall's work was actually founded by James Maxwell just a couple of years ago. Maxwell formulated step by step a comprehensive set of differential equations [109, 404, 405] – soon termed *Maxwell relations* –, which many scientists considered to offer the universal mathematical description of all the striking phenomena associated with electromagnetism. Despite that some of Maxwell's predictions, and the concrete physical mechanisms standing behind them, still needed further experimental analyses, another essential question on the microscopic level remained completely unanswered. It was not yet clear whether an externally applied magnetic field interacts simply with the conductor or rather with the flowing electrical current itself. To tackle this issue, Hall planned a series of experiments conducted in Baltimore and partly also during several research visits abroad [403].

After optimizing the set-ups and measurement technologies, the first unexpected results were finally obtained in 1879 [406]. Hall observed that placing a current-carrying metallic conductor in a perpendicular magnetic field generates an additional voltage drop transverse to the initially driven current. This voltage is nowadays known as *Hall voltage*, while the whole effect itself is typically referred to as *(ordinary) Hall effect*. From the voltage drop's sign, Hall deduced that electrical current in metals must be carried by moving negative charges. Subsequent experiments [407] revealed nevertheless that there concurrently exist several "more extraordinary" materials, in which a reversal of the Hall voltage's sign suggests that it is more realistic to ascribe current flows to the movement of positive charges. Later on, these positive carriers turned out to correspond to holes that usually drive electrical currents through p-doped semiconductors. Hall contributed therefore unconsciously to the birth of semiconductor physics some decades after his work. For that reason, the Hall effect is sometimes viewed as the "queen of solid-state transport experiments" [408].

Developing a thorough pictorial explanation for the Hall effect provided a great challenge since it should have lasted another eighteen years until the diverse experimental attempts to verify the existence of electrons succeeded [409] – for sure, one of the most outstanding breakthroughs in the history of physics. Afterwards, Hendrik Lorentz extended Maxwell's formulation and proposed that the presence of electromagnetic fields facilitates a characteristic force acting on electrons and holes [410], and thereby really an interaction between the fields on the one and the electrical current on the other hand. Anticipating this so-called *Lorentz force*, the Hall effect was immediately understood in terms of charge accumulation on the conductor's transverse sides. Currents through the conductor are maintained either by propagating electrons or holes, depending on the dominant charge carrier type in the regarded material. If a magnetic field perpendicular to the current flow gets applied, the Lorentz force deflects the moving electrons and holes from their straight to curved paths. All electrons accumulate on one transverse side of the conductor and the holes on the second one. The resulting asymmetric charge density raises a spontaneous transverse

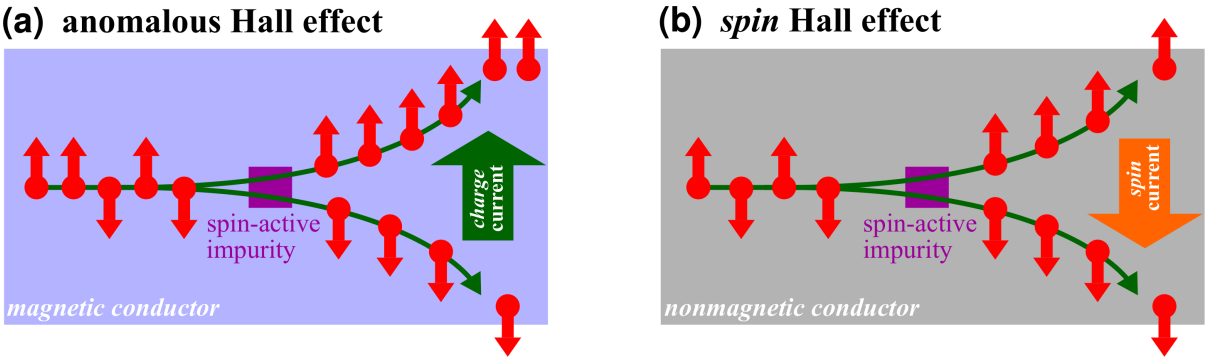


Fig. 8.1: (a) Schematical illustration of the microscopic origin of the *extrinsic anomalous Hall effect* in a magnetic conductor (light blue). Red circles indicate electrons and red arrows their spins. Spin-dependent skew scattering of electrons at SOC-inducing impurities (violet) gives rise to an excess of spin-up electrons at one transverse side of the conductor and an excess of spin-down electrons at the opposite side, and acts thus like a transverse electron "spin filter". The magnetic conductor contains already more majority-spin than minority-spin electrons, e.g., more spin-up than spin-down electrons. Therefore, this skew scattering mechanism generates an electron imbalance, which gets compensated by the spontaneous flow of a transverse anomalous (charge) Hall current (green). **(b)** Similar illustration as in **(a)** for the *extrinsic spin Hall effect* arising in a nonmagnetic conductor (gray). Skew scattering at the impurity acts again like a "spin filter" for electrons. Since the nonmagnetic material comprises equal numbers of spin-up and spin-down electrons, half of all electrons (i.e., the spin-up electrons) are collected on one side and the remaining half (spin-down electrons) on the second side of the conductor. As a result, no transverse charge imbalance (i.e., no charge current) builds up and a pure transverse spin Hall current (orange) starts to flow.

Hall electron or hole current flow (the latter is opposite to the first, being consistent with the Hall voltage's sign reversal in some samples) to compensate the charge imbalance and a nonzero Hall voltage drop if the transverse contact sides are electrically connected. Due to its unprecedented properties, the Hall effect found its way into several present-day laboratory applications, ranging, e.g., from Hall sensors that can quantify magnetic field strengths by measuring the Hall current flow [411] to the reliable characterization of carrier types (electrons or holes) and concentrations in intricate material compositions like $Eu_{1-x}Ca_xB_6$ compounds (with different x-fractions) [412].

Hall was even more surprised when repeating his measurements on *ferromagnetic* conductors [413], in which the dropping Hall voltages significantly exceeded those expected from nonmagnetic probes. Remarkably, the Hall voltages' amplitudes were mostly determined by the ferromagnetic conductors' *intrinsic magnetizations* and persisted even after completely switching off the external magnetic field, essentially indicating that the observed (ferromagnetic) Hall effect can no longer be traced back to Lorentz forces and its physical origin must be entirely different. To stress its anomalous behavior when compared to the (ordinary) Hall effect in nonmagnetic conductors, this "novel" phenomenon was soon named *anomalous Hall effect*. Owing to its puzzling behavior, working out a theoretical framework to fully cover the anomalous Hall effect's underlying physics was even more intricate than it was the case with the ordinary Hall effect, and took nearly one century.

Karplus and Luttinger were the first contributing to the theoretical progress [414, 415], proposing that strong SOC inside ferromagnetic conductors can lead to *anomalous electron velocities* transverse to the initially driven current (electron) flow. The anomalous velocities result again in an electron accumulation on one transverse side of the conductors and cause simultaneously the transverse Hall current flows without requiring external magnetic fields. More than forty years later, a series of papers [416–421] picked up this initial idea and demonstrated that the anomalous electron velocities are actually closely related to

topological concepts, i.e., to the Berry phase [422] of occupied Bloch states. The Berry phase curvature acts like an effective *fictitious* magnetic field in momentum space, eventually introducing the anomalous transverse electron velocities. As unraveled by Karplus and Luttinger, the presence of SOC and broken time-reversal symmetry (due to the exchange interaction in the ferromagnetic conductors) are essential for anomalous Hall effects. This claim is consistent with the subsequent Berry phase-related works [416–421], which clarified that the anomalous transverse velocities, and thereby the anomalous Hall effect itself, would indeed vanish otherwise; detailed reviews interpreting anomalous Hall effects in terms of Berry phase characteristics are provided, for example, in Refs. [423] and [424]. The intimate correlations between the anomalous Hall effect and topology are especially notable in recent days since topological aspects attract rapidly growing interest in modern condensed-matter physics mostly in connection with topological materials.

Apart from the *intrinsic* anomalous velocity contribution, *side-jump* [425, 426] and *skew scatterings* [427, 428] at SOC-inducing impurities or lattice defects give rise to an *extrinsic* anomalous Hall effect. In the following, we will pay special attention to the *skew scattering mechanism* illustrated in Fig. 8.1(a), while the interested reader may consult, e.g., Ref. [408] for a short summary of the side-jump scattering process. The electrical current that flows through a magnetic conductor is carried by propagating spin-up and spin-down electrons. Once these carriers approach one of the SOC-inducing impurities, they must undergo *spin-dependent* skew scatterings, entailing that spin-up electrons are deflected towards one and spin-down electrons towards the second transverse side of the conductor. Skew scattering mimics therefore a transverse "*spin filter*", which separates spin-up and spin-down electrons along the transverse direction and accumulates them on the conductor's *opposite* transverse sides. At that point, it becomes moreover crucial to recall that – owing to their characteristic exchange interaction – magnetic conductors comprise more majority-spin than minority-spin electrons, for instance, more spin-up than spin-down electrons. As a consequence, skew scattering likewise generates an electron imbalance (i.e., more electrons accumulate on that side at which spin-up electrons are collected) and a nonzero anomalous Hall current builds up.

Basically the same skew scattering mechanism explains the *extrinsic spin Hall effect* as a fully spin-based phenomenon that occurs already in *non*magnetic conductors, requiring neither external magnetic fields nor internal magnetizations [see Fig. 8.1(b) for illustration]. Shortly speaking, spin-dependent skew scattering of electrons at SOC-inducing impurities separates again spin-up from spin-down electrons transverse to the actual current flow's direction. Since nonmagnetic samples contain just as many spin-up as spin-down electrons, this electron separation does not cause a net transverse charge imbalance, contrary to ordinary and anomalous Hall effects, and thus no charge Hall currents. The spin filtering leads instead to a pure spin Hall current and converts thereby initially driven charge into spin currents, which might find various groundbreaking applications in spintronics devices and enables, e.g., an electrical control of electron spins [27]. Although being firstly predicted by Dyakonov and Perel back in 1971 [429, 430], the spin Hall effect's experimental confirmation took more than thirty years, mostly because the extrinsic spin Hall effect is usually rather weak and barely measurable. The measurements eventually succeeded in thin films of p-doped GaAs and InGaAs semiconductors [431, 432], in which the SOC-induced band splittings effectuate an additional and more sizable *intrinsic* spin Hall effect contribution [423, 433]. For completeness, we shall also mention that the whole "family" of Hall effects is even much richer and covers additionally also the quantized versions of the discussed phenomena, i.e., the quantum Hall [434], the quantum anomalous Hall [350, 435], and the quantum spin Hall [436, 437] effects, whose discussion goes far beyond the scope of this thesis.

Apart from the intriguing Hall physics already arising in *bulk* conductors, recent theoretical works [438, 439] proposed the existence of extrinsic anomalous Hall and spin Hall effects in F/I/F tunnel junctions, essentially originating from side-jump and skew scatterings of tunneling current electrons at impurity sites located inside the insulating barrier. These studies were soon extended to capture F/N tunnel junctions in

which the ferromagnetic and normal-metal electrodes are separated by an ultrathin semiconducting tunneling barrier [440–442]. The latter hosts interfacial Rashba [149, 150] and Dresselhaus [152] SOCs that likewise facilitate electron skew scatterings (though not caused by SOC-inducing impurities, but instead by the barrier's interfacial SOC), and pronounced anomalous Hall and spin Hall effects – even in the absence of impurities. To stress that these phenomena are linked with skew scatterings of *tunneling* electrons, they were termed *tunneling anomalous Hall effect (TAHE)* and *tunneling spin Hall effect (TSHE)*, respectively. Although realistic barrier materials' typically rather small SOC strengths entail only weak TAHE (TSHE) conductances and make an experimental verification highly nontrivial, first measurements on granular junctions [443] looked extremely promising. Another interesting theoretical suggestion focused more on junctions including ferroelectric barriers [444], whose strong SOCs already maintain sizable Hall conductances that could be much easier detected in laboratories.

In this chapter, we generalize the description of the TAHE to ballistic *superconducting* F/S junctions, in which the normal-metal electrode of the previously studied F/N constrictions is replaced by a superconductor. The crucial ingredient is still the semiconducting tunneling barrier between the ferromagnetic and superconducting parts, introducing interfacial SOC and electron skew scatterings, which are again the TAHE's (TSHE's) basis. The chapter is structured in the following way. Section 8.1 briefly recapitulates the employed theoretical model, which benefits a lot from the approaches described in the previous chapters and does therefore not require to present all details another time. In Sec. 8.2, we formulate a qualitative physical picture demonstrating that skew reflections of tunneling current electrons at the semiconducting barrier indeed found nonzero TAHE conductances inside the ferromagnet. Note that we now need to pay special attention to the ferromagnetic electrode since no Hall voltage can drop above the superconductor. Close to the barrier, we must account for two skew reflection processes: *skew specular* and *skew Andreev reflections*. Our qualitative arguments emphasize that both can act together and significantly enhance the TAHE conductances when compared to normal-state junctions, in which skew Andreev reflections are actually forbidden – an auspicious finding for experimentalists, particularly as our system supports large TAHE conductances without relying on intricate ferroelectric barriers [444]. Quantitatively analyzing various model calculations for realistic junction configurations in Sec. 8.3 confirms not only all characteristics deduced from our qualitative skew reflection mechanism, but additionally illuminates the TAHE conductances' unique magnetization dependence and SOC scaling, making the effect a fundamental tool to identify and characterize interfacial SOC as the key input to tailor junctions that might host Majorana states [76, 252–259].

Besides, it is the skew Andreev reflection process that gives rise to another noteworthy quality. Andreev reflections [179] effectively transfer Cooper pairs into the superconductor. While tunneling through the barrier, also the Cooper pair electrons are subject to skew scatterings, eventually resulting in spontaneous *transverse supercurrent responses* close to the junction interface, which were initially discovered within a phenomenological Ginzburg-Landau treatment [445]. Evaluating these supercurrent responses starting from a generalized Furusaki-Tsukada approach in Sec. 8.4 allows us to further classify their properties and wide tunability with respect to the most common junction parameters. Section 8.5 shortly comments on the TSHE in our system's nonmagnetic N/S junction regime, asserting another surprising feature. While skew specular and skew Andreev reflections add up and lead to giant TAHE conductances, their individual contributions to the TSHE spin conductances mutually cancel and thereby completely suppress the TSHE, contrary to normal-state contacts in which skew Andreev reflections are per se absent and sizable TSHE conductances appear [440]. Section 8.6 provides a compact summary of our analyses.

This chapter is mostly based on the Rapid Communication "Skew Andreev reflection in ferromagnet/superconductor junctions" by Andreas Costa, Alex Matos-Abiague, and Jaroslav Fabian, which got published in Phys. Rev. B ***100****, 060507(R) (2019). Section 8.5 reviews some results published in the Supplemental Material to the follow-up article "Anomalous Josephson Hall effect charge and transverse*

spin currents in superconductor/ferromagnetic-insulator/superconductor junctions" by Andreas Costa and Jaroslav Fabian, which was published in Phys. Rev. B ***101****, 104508 (2020). All presented analytical and numerical calculations were performed by Andreas Costa. Alex Matos-Abiague and Jaroslav Fabian supported the projects with stimulating discussions and feedback.*

8.1 Theoretical description

Throughout this chapter, we consider a *three-dimensional* biased F/S junction, whose semi-infinite ferromagnetic (F) and superconducting (S) electrodes are separated by an ultrathin semiconducting barrier placed at $z = 0$ [see Fig. 8.2(a) for illustration]. The barrier might be composed of a thin layer of zinc-blende materials, like GaAs or InAs, and induces therefore not only potential scattering, but simultaneously also distinct interfacial Rashba and Dresselhaus SOCs.

We model the system again by means of its Nambu-basis Bogoljubov-de Gennes Hamiltonian [139]

$$\hat{\mathcal{H}}_{\mathrm{BdG}} = \begin{bmatrix} \hat{\mathcal{H}}_{\mathrm{e}} & \hat{\Delta}_{\mathrm{S}}(z) \\ \hat{\Delta}_{\mathrm{S}}^{\dagger}(z) & \hat{\mathcal{H}}_{\mathrm{h}} \end{bmatrix}, \tag{8.1}$$

where

$$\hat{\mathcal{H}}_{\mathrm{e}} = \left(-\frac{\hbar^2}{2m}\boldsymbol{\nabla}^2 - \mu\right)\hat{\sigma}_0 - \frac{\Delta_{\mathrm{XC}}}{2}(\hat{\mathbf{m}}\cdot\hat{\boldsymbol{\sigma}})\Theta(-z) + V_{\mathrm{SMC}}d_{\mathrm{SMC}}\hat{\sigma}_0\delta(z) + \hat{\mathcal{H}}^{\mathrm{SOC}} \tag{8.2}$$

represents the single-electron Hamiltonian and $\hat{\mathcal{H}}_{\mathrm{h}} = -\hat{\sigma}_y\hat{\mathcal{H}}_{\mathrm{e}}^{*}\hat{\sigma}_y$ its holelike counterpart. As before, $\hat{\sigma}_0$ and $\hat{\sigma}_i$ indicate the two-by-two identity and the ith Pauli matrix, respectively, while $\hat{\boldsymbol{\sigma}} = [\hat{\sigma}_x, \hat{\sigma}_y, \hat{\sigma}_z]^{\top}$ is the vector containing all three Pauli matrices. The Stoner ferromagnet's exchange energy gap is denoted by Δ_{XC} and its magnetization direction $\hat{\mathbf{m}} = [\cos(\Phi), \sin(\Phi), 0]^{\top}$ determined by the angle Φ measured with respect to the $\hat{x}$-axis [see Fig. 8.2(b)]. The ultrathin semiconducting interlayer is included into our model as a deltalike barrier with height V_{SMC} and width d_{SMC}. Its SOC enters the Hamiltonian

$$\hat{\mathcal{H}}^{\mathrm{SOC}} = \big[\alpha(k_y\hat{\sigma}_x - k_x\hat{\sigma}_y) - \beta(k_y\hat{\sigma}_x + k_x\hat{\sigma}_y)\big]\delta(z), \tag{8.3}$$

where the first part formalizes SOC of the Rashba type and the second part resembles linearized Dresselhaus SOC, both with the effective strengths α and β, accordingly. Recall that we use the C_{2v} crystallographic orientations $\hat{x} \parallel [110]$, $\hat{y} \parallel [\bar{1}10]$, and $\hat{z} \parallel [001]$ as reference directions. Inside the superconducting junction electrode, the idealized s-wave superconducting pairing potential $\hat{\Delta}_{\mathrm{S}}(z) = |\Delta_{\mathrm{S}}|\hat{\sigma}_0\Theta(z)$, with $|\Delta_{\mathrm{S}}|$ measuring the isotropic energy gap of the superconductor, couples the Bogoljubov-de Gennes Hamiltonian's electron and hole blocks. For the sake of simplicity, we further suppose equal quasiparticle masses m and the same chemical potential μ in the ferromagnet and superconductor.

Assuming translational invariance parallel to the semiconducting barrier, the solutions of the stationary Bogoljubov-de Gennes equation

$$\hat{\mathcal{H}}_{\mathrm{BdG}}\Psi^{\sigma}(\mathbf{r}) = E\Psi^{\sigma}(\mathbf{r}) \tag{8.4}$$

factorize into

$$\Psi^{\sigma}(\mathbf{r}) = \psi^{\sigma}(z)\,\mathrm{e}^{\mathrm{i}(\mathbf{k}_{\parallel}\cdot\mathbf{r}_{\parallel})}, \tag{8.5}$$

where $\mathbf{k}_{\parallel} = [k_x, k_y, 0]^{\top}$ ($\mathbf{r}_{\parallel} = [x, y, 0]^{\top}$) denotes the transverse wave (position) vector and $\psi^{\sigma}(z)$ are the Bogoljubov-de Gennes equation's individual solutions for the reduced one-dimensional scattering problem along $\hat{z}$. The latter account for the different scattering processes that are involved at the semiconducting barrier. Incoming spin-σ electrons [$\sigma = +(-)1$ for spin up (spin down), which

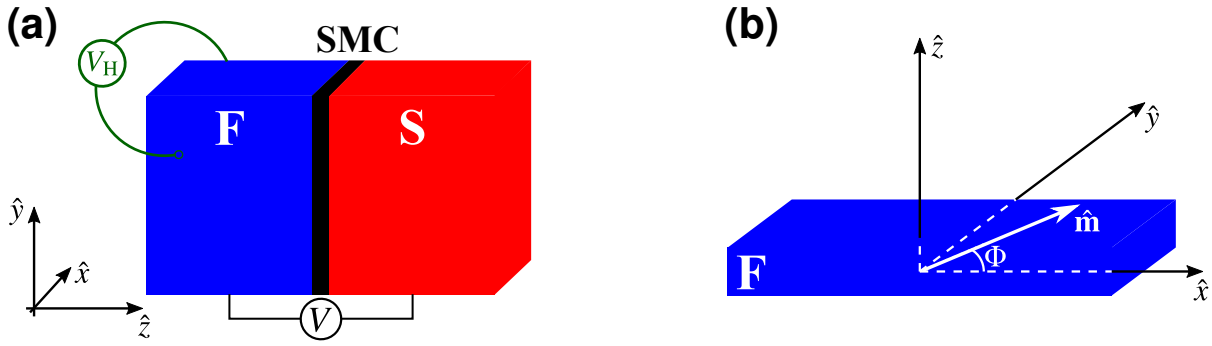


Fig. 8.2: (a) Schematical sketch of the considered *three-dimensional* F/S junction, using the C_{2v} principal crystallographic orientations $\hat{x} \parallel [110]$, $\hat{y} \parallel [\bar{1}10]$, and $\hat{z} \parallel [001]$. The bias voltage applied between the two junction electrodes is denoted by V. The ultrathin semiconducting tunneling barrier (SMC) between the ferromagnetic and superconducting components induces interfacial potential and SOC *skew* scatterings; the latter cause the transverse (anomalous) Hall voltage drop V_H (green). **(b)** The direction of the in-plane magnetization (unit) vector $\hat{\mathbf{m}}$ inside the ferromagnet (F) is determined by the angle Φ.

effectively entails a spin parallel (antiparallel) to $\hat{\mathbf{m}}$] may either undergo specular or Andreev reflections, or may be transmitted as (electronlike or holelike) quasiparticles into the superconductor. The full scattering states $\psi^\sigma(z)$ can then be constructed in the same manner as in Chap. 3, providing access to the scattering coefficients (probabilities) and eventually likewise to the tunneling (transverse TAHE) current flows. The underlying formulas themselves become slightly technical and are therefore provided in Appendix E.

8.2 Skew specular and Andreev reflection picture

Before we proceed with the numerical evaluation of the regarded junction's TAHE conductances for some representative parameter scenarios, we formulate a universal, skew reflection-based, qualitative picture, from which we can already deduce the TAHE's most fundamental features. Due to the presence of interfacial SOC, tunneling current electrons approaching the ultrathin semiconducting barrier are essentially exposed to an effective scattering potential that incorporates besides the usual potential barrier (determined by the barrier's height and width) also the spin- and transverse momentum-dependent contribution of the SOC. To simplify our considerations, we focus on the simple situation in which only Rashba SOC is present ($\alpha > 0$; the Dresselhaus SOC parameter is $\beta = 0$), the ferromagnet's magnetization is aligned along the $\hat{y}$-direction (meaning that $\Phi = \pi/2$), and the transverse wave vector's $\hat{y}$-projection vanishes (i.e., $k_y = 0$). In this particular case, the aforementioned effective scattering potential reads as

$$V_{\text{eff}}^{\sigma} = V_{\text{SMC}} d_{\text{SMC}} - \sigma \alpha k_x, \tag{8.6}$$

where the first part represents the barrier's usual spin-independent scalar scattering potential and the second the spin-dependent SOC part. Although Eq. (8.6) is based on various simplifying assumptions, we wish to stress that the following arguments are universal and apply likewise to the more generic case in which, for instance, also Dresselhaus SOC is present or the magnetization direction gets rotated inside the plane of the ferromagnet.[1]

[1] As the TAHE arises from the intricate interplay between ferromagnetism and SOC, it is essential that the ferromagnet's magnetization and the interfacial spin-orbit fields are aligned in the same plane, i.e., parallel to the tunneling barrier. Out-of-plane magnetizations (perpendicular to the interface) do, however, not completely destroy the TAHE as long as an additional in-plane magnetization component remains.

Assuming that SOC is thus weak that spin-flip scattering becomes negligible, all incident electrons that cannot be transmitted into the superconductor (this is actually always the case as long as the electron energies remain inside the superconductor's gap) can only undergo spin-conserving specular or Andreev reflections, each with certain probabilities that are predominantly determined by $V_{\mathrm{eff}}^{\sigma}$ and hence by the electrons' spins and transverse k_x-momenta. Since SOC is weak, we can decouple the Bogoljubov-de Gennes Hamiltonian in Eq. (8.1) into its *spin-resolved two-by-two blocks*

$$\hat{\mathcal{H}}_{\mathrm{BdG}}^{\sigma} = \begin{bmatrix} \hat{\mathcal{H}}_{\mathrm{e}}^{\sigma} & |\Delta_{\mathrm{S}}|\Theta(z) \\ |\Delta_{\mathrm{S}}|\Theta(z) & \hat{\mathcal{H}}_{\mathrm{h}}^{\sigma} \end{bmatrix}, \tag{8.7}$$

where the Hamiltonians for single spin-σ electronlike and holelike quasiparticles take the forms

$$\hat{\mathcal{H}}_{\mathrm{e}}^{\sigma} = \left(-\frac{\hbar^2}{2m}\boldsymbol{\nabla}^2 - \mu\right) - \sigma\frac{\Delta_{\mathrm{XC}}}{2} + \left(V_{\mathrm{SMC}}d_{\mathrm{SMC}} - \sigma\alpha k_x\right)\delta(z) \tag{8.8}$$

and

$$\hat{\mathcal{H}}_{\mathrm{h}}^{\sigma} = -\left(-\frac{\hbar^2}{2m}\boldsymbol{\nabla}^2 - \mu\right) - \sigma\frac{\Delta_{\mathrm{XC}}}{2} - \left(V_{\mathrm{SMC}}d_{\mathrm{SMC}} - \sigma\alpha k_x\right)\delta(z); \tag{8.9}$$

note that we made use of the aforementioned simplifications. After setting up the corresponding Bogoljubov-de Gennes scattering states in the ferromagnet and superconductor, applying appropriate interfacial boundary conditions, and solving the resulting system of equations for the scattering coefficients, we can extract the spin-conserving specular and Andreev reflection probabilities in terms of rather compact analytical formulas, i.e.,

$$R_{\mathrm{e}}^{\sigma,\sigma} = R_{\mathrm{e}}^{\sigma,\sigma}(E) = \left|r_{\mathrm{e}}^{\sigma,\sigma}\right|^2, \tag{8.10}$$

as well as

$$R_{\mathrm{h}}^{\sigma,-\sigma} = R_{\mathrm{h}}^{\sigma,-\sigma}(E) = \sqrt{\frac{1-\sigma P}{1+\sigma P}}\left|r_{\mathrm{h}}^{\sigma,-\sigma}\right|^2. \tag{8.11}$$

Recall that Andreev reflection without a spin flip refers to reflecting incoming spin-σ electrons as holes with *opposite* spin $-\sigma$. The related scattering coefficients are found to be

$$r_{\mathrm{e}}^{\sigma,\sigma} = r_{\mathrm{e}}^{\sigma,\sigma}(E) = \frac{2}{\Gamma}\frac{k_z^{\sigma}}{k_{\mathrm{F}}}\left[\frac{k_z^{-\sigma}}{k_{\mathrm{F}}}\left(u^2 - v^2\right) + \frac{q_z}{k_{\mathrm{F}}}\left(u^2 + v^2\right) - \mathrm{i}Z_{\mathrm{eff}}^{\sigma}\left(u^2 - v^2\right)\right] - 1 \tag{8.12}$$

and

$$r_{\mathrm{h}}^{\sigma,-\sigma} = r_{\mathrm{h}}^{\sigma,-\sigma}(E) = \frac{4}{\Gamma}\frac{k_z^{\sigma}q_z}{k_{\mathrm{F}}^2}uv, \tag{8.13}$$

with the common denominator

$$\begin{aligned}\Gamma = \Gamma(E) = {} & \frac{k_z^{\sigma}q_z}{k_{\mathrm{F}}^2}\left(u^2 + v^2\right) - \mathrm{i}\frac{k_z^{\sigma}}{k_{\mathrm{F}}}Z_{\mathrm{eff}}^{\sigma}\left(u^2 - v^2\right) + \frac{k_z^{-\sigma}}{k_{\mathrm{F}}}\left[\frac{k_z^{\sigma}}{k_{\mathrm{F}}}\left(u^2 - v^2\right) + \frac{q_z}{k_{\mathrm{F}}}\left(u^2 + v^2\right)\right. \\ & \left. + \mathrm{i}Z_{\mathrm{eff}}^{\sigma}\left(u^2 - v^2\right)\right] + \frac{q_z^2}{k_{\mathrm{F}}^2}\left(u^2 - v^2\right) + \left(Z_{\mathrm{eff}}^{\sigma}\right)^2\left(u^2 - v^2\right).\end{aligned} \tag{8.14}$$

As in earlier parts of this thesis, $P = (\Delta_{\mathrm{XC}}/2)/\mu$ effectively measures the ferromagnet's spin polarization and $k_{\mathrm{F}} = \sqrt{2m\mu}/\hbar$ denotes the Fermi wave vector. Furthermore, we identify

$$Z_{\mathrm{eff}}^{\sigma} = \frac{2mV_{\mathrm{eff}}^{\sigma}}{\hbar^2 k_{\mathrm{F}}} = Z - \frac{2\sigma m\alpha k_x}{\hbar^2 k_{\mathrm{F}}} \tag{8.15}$$

as the dimensionless BTK-like parameter for the effective scattering potential stated in Eq. (8.6), combining the usual spin-independent barrier strength $Z = (2mV_{\mathrm{SMC}}d_{\mathrm{SMC}})/(\hbar^2 k_{\mathrm{F}})$ with the additional (Rashba) SOC-dependent scattering potential. The BCS coherence factors can still be written as

$$u = u(E) = \sqrt{\frac{1}{2}\left(1 + \sqrt{1 - \frac{|\Delta_{\mathrm{S}}|^2}{E^2}}\right)} \qquad \text{and} \qquad v = v(E) = \sqrt{1 - [u(E)]^2}, \tag{8.16}$$

while the $\hat{z}$-projected wave vectors of spin-σ electrons and holes inside the ferromagnet are approximated by

$$k_z^{\sigma} \approx \sqrt{k_{\mathrm{F}}^2\,(1 + \sigma P) - \mathbf{k}_{\parallel}^2} \tag{8.17}$$

and those in the superconductor by

$$q_z \approx \sqrt{k_{\mathrm{F}}^2 - \mathbf{k}_{\parallel}^2}. \tag{8.18}$$

As outlined in Chap. 3, the (quasi)particle excitation energies E and the superconducting gap $|\Delta_{\mathrm{S}}|$ are typically much smaller than the chemical potential μ, justifying to approximate all wave vectors in such a way.

Figure 8.3 illustrates the *zero-bias* specular and Andreev reflection probabilities for incoming spin-up tunneling current electrons [essentially evaluated from Eqs. (8.10) and (8.11) substituting the excitation energy $E = eV = 0$ and $\sigma = 1$] as a function of the effective dimensionless scattering potential $Z_{\mathrm{eff}}^{\sigma=1}$, once for the normal-state and once for the superconducting junction. The ferromagnet's spin polarization is set to a realistic value of $P = 0.7$, usually referring to iron. In the *normal-state scenario*, Andreev reflections are completely forbidden and all incident electrons must either be specularly reflected or transmitted into the right normal-conducting electrode. We focus on the specular reflection probability, which increases with increasing effective scattering potential $V_{\mathrm{eff}}^{\sigma=1}$ (or likewise $Z_{\mathrm{eff}}^{\sigma=1}$) as Fig. 8.3(a) suggests. To elaborate on the skew reflection mechanism arising at the spin-active semiconducting barrier, we assume some representative junction parameters. The usual spin-independent barrier strength $Z = 1$ [see the black dotted line in Fig. 8.3(a)] corresponds, e.g., to a realistic tunneling barrier of height $V_{\mathrm{SMC}} = 0.75\,\mathrm{eV}$ and width $d_{\mathrm{SMC}} \approx 0.40\,\mathrm{nm}$ (substituting $m \approx m_{\mathrm{e}}$ and $k_{\mathrm{F}} = \sqrt{2m\mu}/\hbar \approx 8 \times 10^7\,\mathrm{cm}^{-1}$ as a typical metal Fermi wave vector [182]), whereas we consider the Rashba SOC strength $\overline{\lambda}_{\mathrm{R}} = (2m\alpha)/\hbar^2 = 1$ (indicating $\alpha \approx 4\,\mathrm{eV\,\AA}$). Inspecting Eq. (8.6) for those parameters, we deduce that incident spin-up electrons with *positive* transverse momenta k_x (e.g., $k_x = k_{\mathrm{F}}/2$) experience a lowered effective scattering potential [$Z_{\mathrm{eff}}^{\sigma=1} = 0.5$; see the violet dashed line in Fig. 8.3(a)] and thus undergo specular reflections with a significantly lower probability than those with the corresponding *negative* k_x-counterpart [$k_x = -k_{\mathrm{F}}/2$ entails the raised effective scattering potential $Z_{\mathrm{eff}}^{\sigma=1} = 1.5$, at which specular reflections happen much more likely; see the orange dashed line in Fig. 8.3(a)]. As a result, these spin- and transverse momentum-dependent *skew specular reflections*[2] inside the ferromagnet give rise to an excess of reflected electrons at $x < 0$ [additionally illustrated in a pictorial way in the inset of Fig. 8.3(a)]. The generated spatial electron imbalance must be compensated by the transverse TAHE current J_x along $-\hat{x}$ (recall that the current and electron flow directions are usually *opposite* so that electrons really flow along $\hat{x}$ to compensate the charge imbalance). Strictly speaking, the situation would reverse for incoming spin-down electrons. Nevertheless, since more spin-up (majority-spin) states inside the ferromagnet are occupied, both channels' contributions cannot completely cancel and a finite small TAHE current remains.

If the junction turns *superconducting*, additional Andreev reflections come into play, and a complex interplay between skew specular and skew Andreev reflections might arise. Quasiparticle transmissions

[2] As explained in the motivation to this chapter, *skew scattering* actually refers to momentum- and spin-dependent scattering of spin-polarized charge carriers at *SOC-inducing impurities*. To clearly distinguish between that and the *spin-dependent reflections* at the considered junction's *spin-active tunneling barrier*, which does not require the presence of impurities at all, we introduce the terms *skew (specular and Andreev) reflections.*

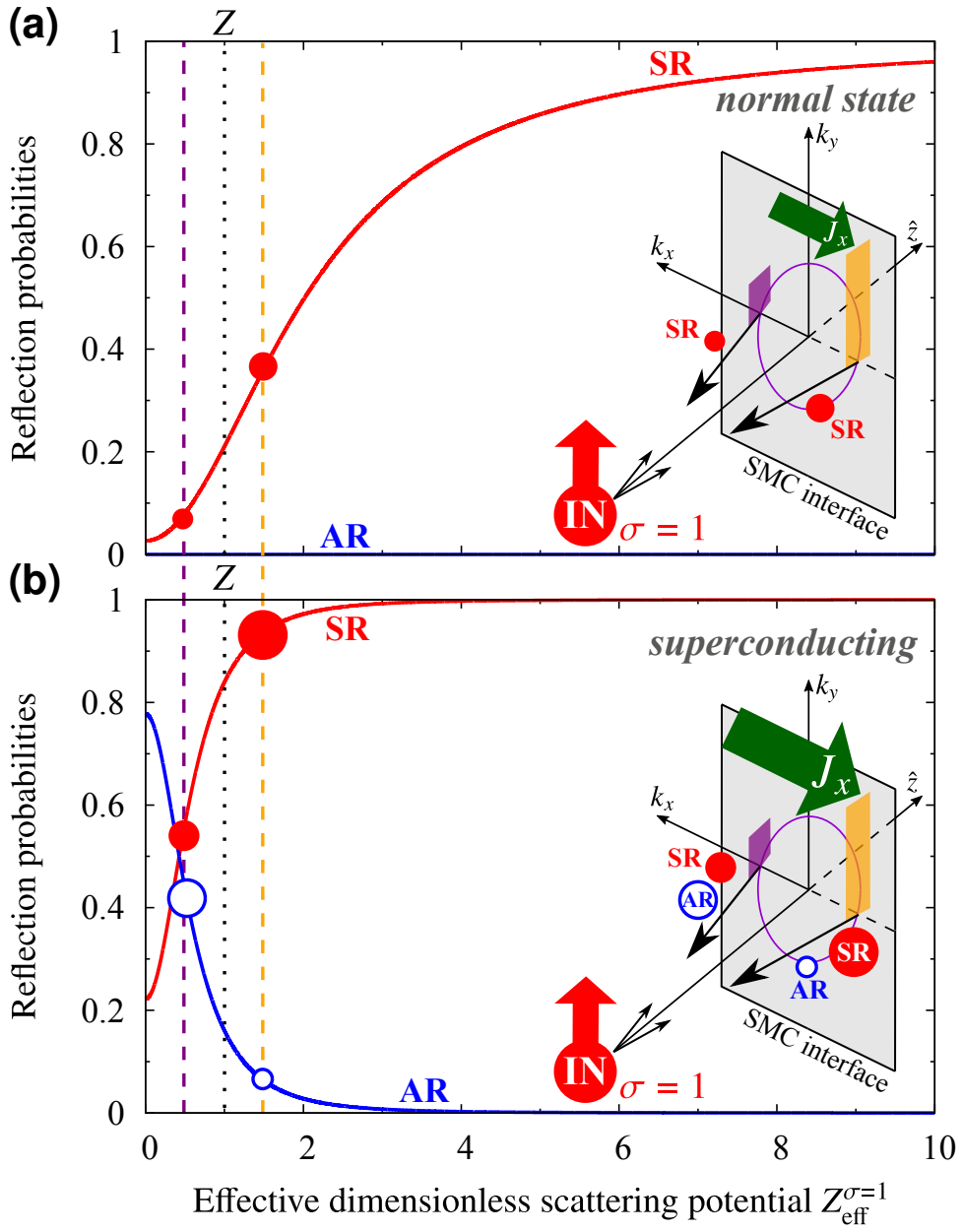


Fig. 8.3: **(a)** Calculated *zero-bias normal-state* reflection probabilities for spin-up electrons (IN) incident on the semiconductor (SMC) interface – covering specular reflections (SR) and Andreev reflections (AR) – and as functions of the effective (dimensionless) BTK-like scattering potential $Z_{\rm eff}^{\sigma=1} = (2mV_{\rm eff}^{\sigma=1})/(\hbar^2 k_{\rm F}) = Z - (2m\alpha k_x)/(\hbar^2 k_{\rm F})$; $Z = (2mV_{\rm SMC}d_{\rm SMC})/(\hbar^2 k_{\rm F})$ (see the black dotted line for an example) is the usual *spin-independent* tunneling barrier strength. Spin-up electrons with $k_x > 0$ are exposed to an effectively *lowered* (violet dashed line) and those with $k_x < 0$ to an effectively *raised* (orange dashed line) scattering potential. Therefore, primarily electrons with negative k_x get specularly reflected. Such spin- and transverse momentum-dependent *skew specular reflections* generate a transverse electron imbalance along the $\hat{x}$-direction (electron densities are proportional to the size of the red filled circles), which must be compensated by a spontaneous transverse electron flow, eventually raising the transverse TAHE current J_x; note that the direction of the current is usually defined *oppositely* to the electron flow direction. The inset illustrates the skew specular reflection process in a pictorial manner; as usual, electrons are colored red, holes blue, and black arrows indicate their propagation directions. **(b)** Same calculation as in **(a)** for the *superconducting* scenario, in which additionally emergent *skew Andreev reflections* play a crucial role. The schematical illustration in the inset demonstrates that the individual TAHE currents originating from skew specular and skew Andreev reflections add up, notably exceeding the related normal-state TAHE currents in panel **(a)**. More detailed explanations are provided in the text.

into the superconductor are simultaneously not allowed since we suppose zero bias voltage so that the incident electrons' excitation energies $E = eV = 0$ lie well below the superconducting gap's amplitude and no quasiparticle states to tunnel into are available. As one asserts when inspecting Fig. 8.3(b), the Andreev reflection probability generally decreases with increasing $V_{\mathrm{eff}}^{\sigma=1}$ ($Z_{\mathrm{eff}}^{\sigma=1}$), meaning that predominantly incoming spin-up electrons with transverse momenta $k_x > 0$ get Andreev reflected. Anyhow, the crucial point is to recall that Andreev reflections involve reflected holes. Consequently, *skew Andreev reflections* produce an excess of holes at $x > 0$ [illustrated in the inset of Fig. 8.3(b)], which is equivalent to an electron excess at $x < 0$, just as it was the case in the skew specular reflection process, and raises likewise a TAHE current along $-\hat{x}$. Skew specular and skew Andreev reflections act therefore together in superconducting junctions and noticeably increase the TAHE current flow when compared to the normal-state regime, making these systems promising candidates for further experimental studies. This finding, though yet based on simplified qualitative arguments, counts to the most central results of this chapter and will be uniquely confirmed by our fully numerical (and more general) calculations in Sec. 8.3.

Finally, we can draw another important conclusion in the limit of large effective scattering potentials, i.e., at $V_{\mathrm{eff}}^{\sigma=1} \gg (\hbar^2 k_{\mathrm{F}})/(2m)$ or equivalently $Z_{\mathrm{eff}}^{\sigma=1} \gg 1$, as the specular reflection probability in the superconducting junction approaches unity there much faster than in the normal state and varies only slightly with $V_{\mathrm{eff}}^{\sigma=1}$ ($Z_{\mathrm{eff}}^{\sigma=1}$). The effective scattering potential is then mostly determined by the usual spin-independent barrier strength Z and the spin-dependent skew reflections, and likewise the TAHE currents, are expected to be strongly damped – in superconducting even more than in normal-conducting junctions.

8.3 Tunneling anomalous Hall effect conductances

The simplified physical picture formulated in Sec. 8.2 demonstrates that measuring notably enhanced TAHE conductances in superconducting F/S junctions – when compared to their normal-state F/N counterparts – serves as a unique experimental fingerprint to detect the peculiar skew Andreev reflections. In this section, we complement the qualitative description by quantitatively calculating the TAHE conductances of realistic junction configurations, and thoroughly discussing their most important and general features.

8.3.1 Generalized BTK conductance formula

To evaluate the TAHE conductances along the *transverse* $\hat{\eta}$-directions ($\hat{\eta} \in \{\hat{x}; \hat{y}\}$) inside the ferromagnet, we generalize the BTK model [164], which was actually our starting point to deduce the longitudinal tunneling current flow of superconducting junctions in Chap. 3. The full derivation is rather technical and summarized in Appendix E. The *zero-temperature* TAHE conductance components *close to the interface* can eventually be computed from

$$G_{\eta,z} \approx -\frac{G_0 \mathcal{A}_\eta}{2(2\pi)^2} \sum_{\sigma=\pm 1} \int \mathrm{d}^2\mathbf{k}_\parallel \, \frac{k_\eta}{k_z^\sigma} \left\{ \left[\left| r_{\mathrm{e}}^{\sigma,\sigma}(eV) \right|^2 + \left| r_{\mathrm{e}}^{\sigma,-\sigma}(eV) \right|^2 \right] + \left[\left| r_{\mathrm{h}}^{\sigma,-\sigma}(-eV) \right|^2 + \left| r_{\mathrm{h}}^{\sigma,\sigma}(-eV) \right|^2 \right] \right\}, \quad (8.19)$$

where $G_0 = (2e^2)/h$ abbreviates the conductance quantum (e is the positive elementary charge), $\mathcal{A}_\eta$ stands for the corresponding Hall contact areas, $k_z^\sigma \approx \sqrt{k_{\mathrm{F}}^2 (1 + \sigma P) - \mathbf{k}_\parallel^2}$ represents the (approximated) $\hat{z}$-component of electrons' and holes' wave vectors inside the ferromagnet with *effective* spin polarization $P = (\Delta_{\mathrm{XC}}/2)/\mu$, and $k_{\mathrm{F}} = \sqrt{2m\mu}/\hbar$ is still the Fermi wave vector. The reflection coefficients $r_{\mathrm{e}}^{\sigma,\sigma}(eV)$ and $r_{\mathrm{e}}^{\sigma,-\sigma}(eV)$ correspond to spin-conserving (spin-flip) specular reflections incoming electrons with excitation energy $E = eV$ undergo (V quantifies the applied bias voltage), whereas

$r_{\mathrm{h}}^{\sigma,-\sigma}(-eV)$ and $r_{\mathrm{h}}^{\sigma,\sigma}(-eV)$ likewise indicate spin-conserving and spin-flip Andreev reflections. Contrary to the simplifications considered in Sec. 8.2, we are now again concerned with the full scattering problem formulated in Sec. 8.1 and account also for spin-flip reflections.

Adapting the description provided in Chap. 3 [recall Eq. (3.30)] to the present notation, the junction's tunneling conductance is given by

$$G_{z,z} \approx \frac{G_0 \mathcal{A}}{2(2\pi)^2} \sum_{\sigma=\pm 1} \int \mathrm{d}^2\mathbf{k}_\parallel \left\{ 1 - \left[\left| r_{\mathrm{e}}^{\sigma,\sigma}(eV) \right|^2 + \frac{k_z^{-\sigma}}{k_z^{\sigma}} \left| r_{\mathrm{e}}^{\sigma,-\sigma}(eV) \right|^2 \right] + \left[\frac{k_z^{-\sigma}}{k_z^{\sigma}} \left| r_{\mathrm{h}}^{\sigma,-\sigma}(-eV) \right|^2 + \left| r_{\mathrm{h}}^{\sigma,\sigma}(-eV) \right|^2 \right] \right\}, \quad (8.20)$$

with $\mathcal{A}$ referring to its interfacial cross-section area. Comparing the tunneling conductance formula against the expression for the TAHE conductances in Eq. (8.19), we immediately spot their fundamental difference. While specular and Andreev reflections contribute with *opposite* signs to the tunneling conductance, both must enter the TAHE conductances with the *same* sign. This observation is well justified having a brief look at the reflected electrons' (holes') transverse velocities. The specularly reflected electron and the Andreev-reflected hole move along *opposite* transverse directions, i.e., their transverse velocities differ in sign. When evaluating currents (conductances), this relative sign gets, nevertheless, compensated by electrons' and holes' opposite charges so that specular and Andreev reflection parts indeed arise with the same sign in the final TAHE conductance formula, basically verifying our previous statement that skew specular and skew Andreev reflections can mutually magnify and lead to sizable TAHE responses in superconducting junctions.

8.3.2 Discussion of results

To further characterize the TAHE conductances, we numerically evaluate Eq. (8.19) for Fe/GaAs/Nb model junctions. The spin polarization in iron is $P = 0.7$ (with the corresponding Fermi wave vector $k_{\mathrm{F}} \approx 8 \times 10^7\,\mathrm{cm}^{-1}$ [182]) and $|\Delta_{\mathrm{S}}| \equiv |\Delta_{\mathrm{S}}(0)| \approx 1.6\,\mathrm{meV}$ refers to the zero-temperature superconducting gap of niobium [197]. The material-specific Dresselhaus SOC strength of the semiconducting GaAs barrier can be approximated [27, 250] by $\beta \approx k_{\mathrm{F}}\gamma \times Z \approx 19.2\,\mathrm{eV\,\AA}^2 \times Z$, substituting $\gamma \approx 24\,\mathrm{eV\,\AA}^3$ for the cubic Dresselhaus SOC parameter of GaAs [27]. As in Sec. 8.2, the GaAs barrier's height and width are captured by the BTK-like barrier measure $Z = (2mV_{\mathrm{SMC}}d_{\mathrm{SMC}})/(\hbar^2 k_{\mathrm{F}})$. For a realistic barrier of height $V_{\mathrm{SMC}} = 0.75\,\mathrm{eV}$ [251], $Z = 1$ represents a roughly $d \approx 0.40\,\mathrm{nm}$ thick GaAs barrier (setting, for simplicity, $m \approx m_{\mathrm{e}}$). We suppose furthermore that the Hall contact areas $\mathcal{A}_\eta$ and the interfacial tunneling cross-section area $\mathcal{A}$ are equal, i.e., $\mathcal{A}_x = \mathcal{A}_{\mathrm{y}} = \mathcal{A}$.

8.3.2.1 Magnetization angle dependence

The TAHE conductances' scaling with respect to the ferromagnet's in-plane magnetization orientation resembles one of their most unique properties we wish to examine. Before discussing the related numerical model calculations, we dive deeper into Eq. (8.19)'s symmetries, which might allow us to extract valuable physical information, for instance, about the conductances' Φ-dependence without applying any numerics.

Keeping the transverse wave vector $\mathbf{k}_\parallel = [k_x, k_y, 0]^\top$ fixed, the junction's two preferential spatial directions are determined by the orientation of the spin-orbit fields $\boldsymbol{\Omega}(\mathbf{k}_\parallel) = [(\alpha - \beta)k_y, -(\alpha + \beta)k_x, 0]$ on the one and the magnetization (unit) vector $\hat{\mathbf{m}} = [\cos(\Phi), \sin(\Phi), 0]^\top$ on the other hand. In the limit

of *weak SOC*, we can therefore expand the reflection coefficient-dependent parts occurring in Eq. (8.19) into a Taylor series containing only powers of $[\hat{\mathbf{m}} \cdot \boldsymbol{\Omega}(\mathbf{k}_\parallel)]$. Most generally, we may start from

$$-\left\{\left[\left|r_{\mathrm{e}}^{\sigma,\sigma}(eV)\right|^2+\left|r_{\mathrm{e}}^{\sigma,-\sigma}(eV)\right|^2\right]+\left[\left|r_{\mathrm{h}}^{\sigma,-\sigma}(-eV)\right|^2+\left|r_{\mathrm{h}}^{\sigma,\sigma}(-eV)\right|^2\right]\right\} \approx \sum_{i=0}^{\infty} \xi^{(i)} \left[\hat{\mathbf{m}} \cdot \boldsymbol{\Omega}(\mathbf{k}_\parallel)\right]^i . \quad (8.21)$$

Since SOC is assumed to be weak, the *constant* expansion coefficients $\xi^{(i)}$ could actually be evaluated even in the absence of SOC, which would dramatically simplify the calculations. However, we do not need to specify their concrete forms at all to proceed.

Putting Eq. (8.21) into Eq. (8.19) and terminating the power series after the *quadratic* order in $[\hat{\mathbf{m}}\cdot\boldsymbol{\Omega}(\mathbf{k}_\parallel)]$ yields for the approximated TAHE conductances (in the presence of weak SOC)

$$G_{\eta,z} \approx G_{\eta,z}^{(0)} + G_{\eta,z}^{(1)} + G_{\eta,z}^{(2)} + \ldots , \quad (8.22)$$

with the single constituents

$$G_{\eta,z}^{(i)} = \frac{G_0 \mathcal{A}_\eta}{2(2\pi)^2} \sum_{\sigma=\pm1} \int \mathrm{d}^2\mathbf{k}_\parallel \, \frac{k_\eta}{k_z^\sigma} \, \xi^{(i)} \left[\hat{\mathbf{m}} \cdot \boldsymbol{\Omega}(\mathbf{k}_\parallel)\right]^i . \quad (8.23)$$

Let us initially focus on $G_{x,z}$. After introducing the polar coordinates $k_x = |\mathbf{k}_\parallel|\cos(\theta)$ and $k_y = |\mathbf{k}_\parallel|\sin(\theta)$, and writing out the two-dimensional $\mathbf{k}_\parallel$-integration, we arrive at

$$G_{x,z}^{(i)} = \frac{G_0 \mathcal{A}_\eta}{2(2\pi)^2} \sum_{\sigma=\pm1} \int_0^{|\mathbf{k}_\parallel|_{\max}^\sigma} \mathrm{d}|\mathbf{k}_\parallel| \int_0^{2\pi} \mathrm{d}\theta \, \frac{|\mathbf{k}_\parallel|\cos(\theta)}{k_z^\sigma} \, \xi^{(i)} \left[\hat{\mathbf{m}} \cdot \boldsymbol{\Omega}(\mathbf{k}_\parallel)\right]^i ; \quad (8.24)$$

the upper limit in the $|\mathbf{k}_\parallel|$-integration needs to be chosen such that we only count contributions associated with propagating incident electrons (holes), i.e., $|\mathbf{k}_\parallel|_{\max}^\sigma = \min[k_\mathrm{F}\sqrt{1+\sigma P}; k_\mathrm{F}]$. Inspecting all arising factors' parities with respect to changing the sign of $\mathbf{k}_\parallel$, we can deduce which of the integrals finally entering Eq. (8.22) lead to nonzero contributions (to lowest order). There are two parts with *odd* $\mathbf{k}_\parallel$-parity: $k_x = |\mathbf{k}_\parallel|\cos(\theta)$ itself and $[\hat{\mathbf{m}} \cdot \boldsymbol{\Omega}(\mathbf{k}_\parallel)]$ [recall that $\boldsymbol{\Omega}(-\mathbf{k}_\parallel) = -\boldsymbol{\Omega}(\mathbf{k}_\parallel)$]. As a result, only those $G_{x,z}^{(i)}$-terms in Eq. (8.22) containing *odd powers* of $[\hat{\mathbf{m}} \cdot \boldsymbol{\Omega}(\mathbf{k}_\parallel)]$ give rise to an overall *even* $\mathbf{k}_\parallel$-integrand that does not vanish after integrating out $\mathbf{k}_\parallel$. In our regarded case, only $G_{x,z}^{(1)}$ raises hence a nonzero TAHE conductance contribution in Eq. (8.22).

Substituting the explicit expression for $\boldsymbol{\Omega}(\mathbf{k}_\parallel)$, we obtain in polar coordinates

$$\begin{aligned} G_{x,z} \approx G_{x,z}^{(1)} \propto \sum_{\sigma=\pm1} \int_0^{|\mathbf{k}_\parallel|_{\max}^\sigma} \mathrm{d}|\mathbf{k}_\parallel| \int_0^{2\pi} \mathrm{d}\theta \Big[& (\alpha-\beta)\cos(\Phi)|\mathbf{k}_\parallel|^2\cos(\theta)\sin(\theta) \\ & - (\alpha+\beta)\sin(\Phi)|\mathbf{k}_\parallel|^2\cos^2(\theta)\Big] \\ \propto -(\alpha+\beta)\sin(\Phi). & \end{aligned} \quad (8.25)$$

In the last step, we used the parity arguments another time. The first summand [$\propto \cos(\theta)\sin(\theta)$] reflects *odd* $\mathbf{k}_\parallel$-parity and does not contribute to $G_{x,z}$ when performing the integrations. The characteristic magnetization angle scaling $G_{x,z}(\Phi) \propto -(\alpha+\beta)\sin(\Phi)$ follows consequently solely from symmetries and provides a unique (experimental) fingerprint that the TAHE originates from the striking interplay of ferromagnetism and SOC[3] – not only in the superconducting, but likewise in the normal-state junction regime [440]. Treating $G_{y,z}$ in an analogous manner suggests moreover $G_{y,z}(\Phi) \propto (\alpha-\beta)\cos(\Phi)$.

[3] Recall that our key assumption was indeed that only those two ingredients – the ferromagnet's exchange coupling and the interfacial SOC – define the junction's preferred spatial directions.

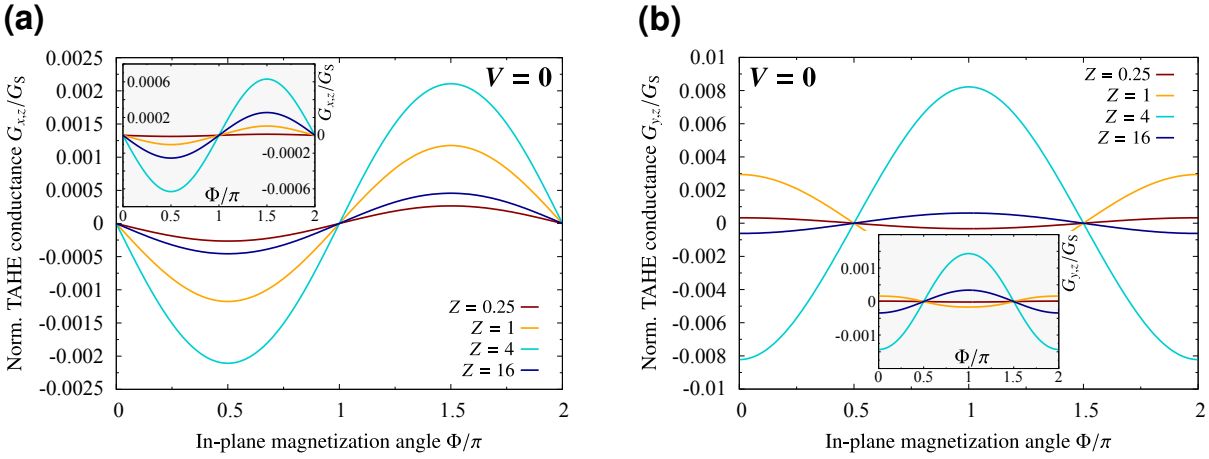


Fig. 8.4: Calculated dependence of the *zero-bias* TAHE conductances **(a)** $G_{x,z}$ and **(b)** $G_{y,z}$ [normalized to Sharvin's conductance $G_S = (\mathcal{A}e^2k_F^2)/(2\pi h)$ of a perfectly transparent (three-dimensional) metallic point contact] on the in-plane magnetization angle Φ and for various indicated tunneling barrier strengths Z. The Rashba and Dresselhaus SOC parameters are $\alpha = 42.3\,\text{eV}\,\text{Å}^2$ and $\beta \approx 19.2\,\text{eV}\,\text{Å}^2 \times Z$. The insets show the corresponding *normal-state* TAHE conductances when the superconducting electrode is replaced by a normal metal.

In-plane rotations of the ferromagnet's magnetization cause therefore distinct *TAHE magnetoanisotropies* that persist even if Dresselhaus SOC would be absent, contrary to the tunneling conductance's (in-plane magnetization) magnetoanisotropies that originate from the interference of Rashba and Dresselhaus SOCs, and disappear in that case [176].[4]

After formulating the general arguments – the simplified skew reflection-based picture in Sec. 8.2 and the TAHE conductances' symmetry-based magnetization angle variations in the preceding paragraphs –, we are fully equipped to come back to the numerical results and understand the outcomes. Figure 8.4 shows the dependence of the normalized *zero-bias* TAHE conductances $G_{x,z}$ and $G_{y,z}$ on the ferromagnet's in-plane magnetization orientation angle Φ and for various barrier strengths Z. The Rashba SOC parameter is set to $\alpha \approx 42.3\,\text{eV}\,\text{Å}^2$, which was basically extracted from theoretically fitting transport data of normal-state Fe/GaAs/Au junctions [250, 251], but seems to be a rather large value for superconducting systems. However, the same physics occurs likewise at much lower Rashba SOCs and the related TAHE conductances might even be additionally enhanced then, as we illustrate extensively in the Supplemental Material to Ref. [446]. For a quantitative comparison, the insets of Fig. 8.4 illustrate the TAHE conductances in the junction's normal-conducting counterpart. In fact, the calculations confirm all our previously stated expectations, i.e., the deduced sinelike (cosinelike) Φ-dependencies of $G_{x,z}$ ($G_{y,z}$), as well as the claim that skew specular and skew Andreev reflections can indeed act together, leading to sizable TAHE conductances. For the regarded parameter combinations, the superconducting junction's $G_{x,z}$ can maximally increase by more than one order of magnitude and $G_{y,z}$ still roughly by a factor of four when compared to the normal-state regime (insets). The full physical behavior is, however, more intricate than one might initially guess from our simple arguments in Sec. 8.2. Inspecting $G_{y,z}$ in Fig. 8.4(b) suggests, for instance, that tuning the usual (spin-independent) barrier's strength (more specifically, increasing Z from $Z = 1$ to $Z = 4$) suffices to reverse the Hall current's direction (and the respective TAHE conductance's sign). Anyhow, even such reversals can be traced back to our

[4] The in-plane magnetoanisotropies arising in the junction's tunneling conductance are not part of our study. These were, in fact, attributed to pronounced magnetoanisotropies in the Andreev reflection process (termed MAAR) and extensively discussed in Ref. [176]. Nevertheless, their physical origin is related to the interference of Rashba and Dresselhaus SOCs, and thus basically comparable to the mechanism that causes in-plane MAJCs in Josephson junctions (see Sec. 6.2).

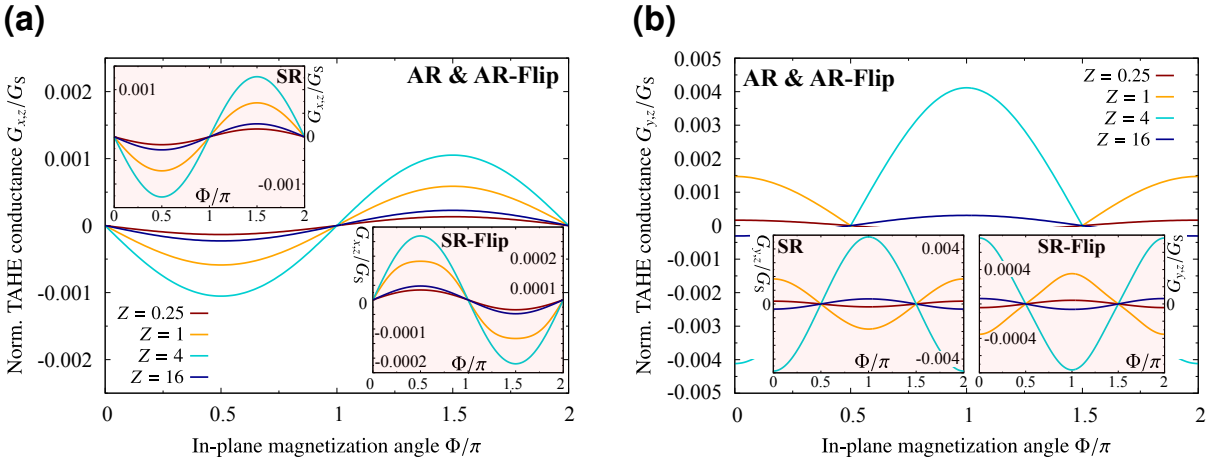


Fig. 8.5: Calculated dependence of the *zero-bias* TAHE conductances **(a)** $G_{x,z}$ and **(b)** $G_{y,z}$ (normalized as in Fig. 8.4) on the in-plane magnetization angle Φ and for the same parameters as in Fig. 8.4. The individual contributions stemming from specular reflections (SR), *spin-flip* specular reflections (SR-Flip), Andreev reflections (AR), and *spin-flip* Andreev reflections (AR-Flip) are resolved.

skew reflection picture. The crucial point is to note that Fig. 8.3 illustrates the skew reflection mechanism only at one particular scenario of barrier and SOC strengths, as well as at fixed k_x (neglecting k_y). To extract the full TAHE current (conductance), we need to average over all possible momenta k_x (and k_y). For sufficiently large $|k_x|$, and appropriately chosen barrier and SOC parameters, incoming electrons with $k_x > 0$ can be exposed to *strong negative* effective scattering potentials V_{eff}^{σ} [also visible in the simple example captured by Eq. (8.6)] and electrons with $k_x < 0$ simultaneously to *moderate positive* V_{eff}^{σ}. The computed specular and Andreev reflection probabilities are symmetric with respect to V_{eff}^{σ}'s sign. Therefore, incident ($k_x > 0$)-electrons are now subject to the raised scattering potential and skew reflections generate an electron excess at $x > 0$ – exactly opposite to the case studied in Fig. 8.3. As a result, also the related TAHE current (conductance) reverses its direction (sign). This behavior cannot be resolved by the presented $G_{x,z}$-calculations since reversing $G_{x,z}$ requires slightly different barrier and/or SOC parameters than those we considered, but is demonstrated in the Supplemental Material to Ref. [446]. Nevertheless, similar arguments hold for $G_{y,z}$ and explain the sudden reversal of $G_{y,z}$ in Fig. 8.4(b) when increasing the barrier strength from $Z = 1$ to $Z = 4$. Note that the barrier and/or SOC parameters required to reverse $G_{x,z}$ and $G_{y,z}$ are typically different (owing to the $\mathbf{k}_{\parallel}$-dependent interference of Rashba and Dresselhaus SOCs).

In the limit of strong tunneling barriers, the skew reflection formulation predicts that all the physics is mostly governed by the usual (spin-independent) barrier and the TAHE gets remarkably suppressed – in the superconducting even much faster than in the normal-conducting junction scenario. Our numerical simulations verify also this proposal, becoming most clearly evident when comparing the relative changes of the (superconducting and normal-state) TAHE amplitudes while increasing the barrier strength Z from $Z = 4$ to $Z = 16$.

In Fig. 8.5, we visualize the individual spin-resolved skew specular and Andreev reflection conductance contributions for the same set of parameters stated above. The spin-flip Andreev reflection parts are thereby not separately presented since their amplitudes are up to two orders of magnitude smaller than those of spin-conserving Andreev reflections. Most interestingly, the TAHE conductances' qualitative and quantitative behavior is indeed nearly completely dominated by the intriguing interplay of *spin-conserving* specular and Andreev reflections. Both their contributions become comparable in magnitude and enter the overall TAHE conductances with the same sign, so that skew specular and skew

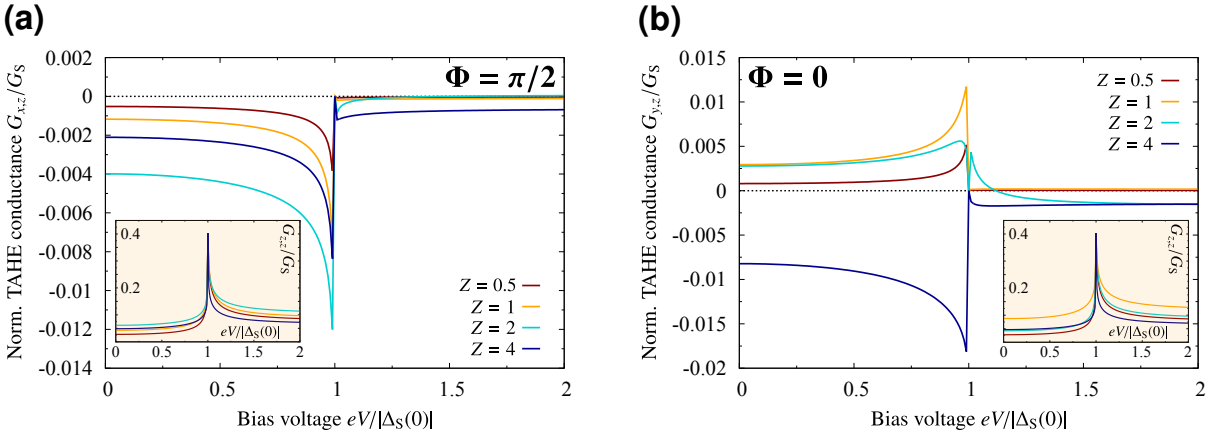


Fig. 8.6: Calculated dependence of the *maximal* TAHE conductances **(a)** $G_{x,z}(\Phi = \pi/2)$ and **(b)** $G_{y,z}(\Phi = 0)$, normalized as in Fig. 8.4, on the applied bias voltage V [the associated electron energy eV is given in multiples of the superconductor's gap $|\Delta_S(0)|$] and for various indicated tunneling barrier strengths Z. The SOC parameters are the same as considered in Fig. 8.4. For comparison, the insets present the corresponding *tunneling conductances* $G_{z,z}$, normalized in the same way as the TAHE conductances.

Andreev reflections indeed add up and result in sizable TAHE signals. Spin-flip specular reflections involve electrons with opposite spin, for which the effective scattering potential picture in Sec. 8.2 reverses and the related TAHE conductance contributions change their sign. Nevertheless, their relative amplitudes are much smaller than those belonging to spin-conserving reflections and do therefore not visibly alter the TAHE conductances' overall qualitative features.

8.3.2.2 Bias voltage dependence

Real measurements might not only detect the Hall conductances that really stem from the TAHE, but simultaneously also parts coming from the "usual" anomalous Hall effect, making an experimental verification of skew Andreev reflections challenging. To separate both parts, one could exploit their unique magnetoanisotropies: the anomalous Hall effect conductances typically vanish when getting measured along the magnetization orientation, whereas the TAHE conductance contributions remain finite [440]. Apart from that, we propose another important distinguishing feature in superconducting junctions, focusing on the TAHE conductances' peculiar bias voltage dependence illustrated in Fig. 8.6. Regarding the ferromagnet's in-plane magnetization orientation, we suppose $\Phi = \pi/2$ for $G_{x,z}$ and $\Phi = 0$ for $G_{y,z}$, each facilitating the *maximal* TAHE conductance amplitudes as outlined when elaborating on the TAHE conductances' symmetries. Particularly relevant is the *subgap regime* $eV \leq |\Delta_S(0)|$ that corresponds to the junction's fully superconducting state. Considering $eV \gg |\Delta_S(0)|$ effectively reduces our description to its normal-conducting counterpart and replicates therefore simply the normal-state TAHE conductances. As pointed out for the zero-bias scenario above, the TAHE conductance amplitudes become much more sizable in the superconducting than in the normal-state junction – mostly due to their mutual amplification by skew specular and skew Andreev reflections. Our present calculations demonstrate that this feature is not only limited to zero voltages, but applies likewise to the whole subgap range. Constantly increasing the bias causes even a further notable enhancement of the TAHE conductances, eventually ending in a unique *TAHE conductance peak* slightly below $eV = |\Delta_S(0)|$. Exactly at the gap edge $eV = |\Delta_S(0)|$, both TAHE conductances surprisingly drop to zero before approaching the dramatically damped normal-state TAHE conductance magnitudes at $eV \gg |\Delta_S(0)|$. To understand these striking voltage variations of the TAHE conductances, we come back to the simplified skew reflection picture formulated in Sec. 8.2 and additionally account for the impact of nonzero bias. Finite bias voltages predominantly impact the

probabilities with which incident electrons undergo specular or Andreev reflections (recall Fig. 8.3). To be more concrete, both reflection probabilities change then much faster with the effective scattering potential $V_{\mathrm{eff}}^{\sigma}$ (or equivalently with $Z_{\mathrm{eff}}^{\sigma}$) than observed at zero bias. As a consequence, incoming electrons with opposite transverse momenta are exposed to much stronger reflection probability *asymmetries*. Skew specular and skew Andreev reflections generate thus remarkably enhanced electron imbalances, and simultaneously more sizable TAHE currents (conductances) when compared to the zero-bias regime. The skew specular and skew Andreev reflection conductance contributions increase, in fact, monotonically with the applied bias voltage until approaching the gap edge [$eV = |\Delta_{\mathrm{S}}(0)|$], at which more intricate physics starts to arise.

When investigating F/S junctions' tunneling conductance in Sec. 3.2, we unraveled universal FBCPs that form at $eV = |\Delta_{\mathrm{S}}(0)|$ and are uniquely connected to Andreev reflection probability peaks [recall in particular Figs. 3.5(b) and 3.6(b), as well as Eq. (3.42)]. We argued that the gap-edge reflection probabilities (and thereby also the FBCP amplitudes) are solely determined by the ferromagnet's spin polarization and do not depend on the interfacial barrier's scattering strength. Analogous conclusions can be drawn in our case, in which the reflection probabilities at $eV = |\Delta_{\mathrm{S}}(0)|$ scale also only with the spin polarization in the ferromagnet and are, most importantly, no longer affected by the effective scattering potential $V_{\mathrm{eff}}^{\sigma}$ ($Z_{\mathrm{eff}}^{\sigma}$). Incident electrons with opposite transverse momenta are therefore equally likely specularly (Andreev) reflected and the skew reflection mechanism, actually responsible to generate TAHEs, breaks down. The inevitable results are the *vanishing gap-edge TAHE conductances*, contrary to the "usual" anomalous Hall effect contributions which remain finite even at the gap edge. This finding – being unique to superconducting junctions and hence not evident in previous normal-state studies [440] – might play an essential role to experimentally differentiate between TAHEs and conventional anomalous Hall effects.

Resolving the individual specular and Andreev reflection TAHE conductance parts (not explicitly shown; see the Supplemental Material to Ref. [446] for details) highlights that, while skew specular and skew Andreev reflections are both equally important at zero bias, it is now predominantly the skew Andreev reflection process that governs the finite-bias TAHE conductance variations. The pronounced TAHE conductance peaks close to the gap edge originate likewise mostly from skew Andreev reflections, as one might guess from our arguments demonstrating that the gap-edge physics is indeed mostly controlled by the peculiar Andreev reflection process (recall Sec. 3.2).

To estimate the size of the TAHE conductance amplitudes with respect to the junction's tunneling conductance, the latter is additionally shown (for the same parameters) in the insets of Fig. 8.6. Comparing the tunneling conductances obtained at the magnetization angle $\Phi = \pi/2$ [see Fig. 8.6(a)] to those at $\Phi = 0$ [see Fig. 8.6(b)] exhibits the clear MAAR magnetoanisotropies, which were extensively studied in Ref. [176]. Regarding the TAHE conductances in the superconducting regime [i.e., at $eV \leq |\Delta_{\mathrm{S}}(0)|$], we assert maximal values reaching more than ten percent of the related tunneling conductance. Such values are indeed sizable when compared to the normal-state scenario [$eV \gg |\Delta_{\mathrm{S}}(0)|$], in which the TAHE *vs.* tunneling conductance ratios remain usually below one percent [440].

8.4 Transverse supercurrent responses

The striking Andreev reflection process is not only essential for the junction's sizable TAHE conductances measured in the ferromagnet, but founds furthermore also the crucial microscopic mechanism that transfers Cooper pair-forming electrons into the superconductor and converts normal dissipative currents into dissipationless supercurrents. These Cooper pair electrons arouse particular interest since they are also subject to the effective spin- and transverse momentum-dependent scattering potential while tunneling through the interfacial semiconducting barrier. Subsequent electron *skew tunnelings* (mind

the analogy to the previously discussed skew reflections) entail that Cooper pairs form predominantly either at $\eta > 0$ or at $\eta < 0$, building up a spontaneous *transverse supercurrent response* (along the $\hat{\eta} \in \{\hat{x}; \hat{y}\}$-directions) in the superconductor [see the inset of Fig. 8.7(a) for a pictorial illustration]. Although a phenomenological Ginzburg-Landau description [445] basically confirmed this claim, a more thorough analysis has been missing so far and can be provided within our approach.

8.4.1 Generalized Furusaki-Tsukada supercurrent formula

We compute the supercurrent responses generalizing the initially for tunneling (Josephson) supercurrents established Furusaki-Tsukada approach [266] to transverse current flows. The main steps are essentially similar to the Josephson current case (see Sec. 6.2) and presented in Appendix E. After some calculations, the *interfacial* supercurrents are given by

$$I_\eta \approx \frac{e k_\mathrm{B} T}{2\hbar} |\Delta_\mathrm{S}(T)| \frac{\mathcal{A}_\eta}{(2\pi)^2} \int \mathrm{d}^2\mathbf{k}_\parallel \sum_{\omega_n} \frac{k_\eta}{\sqrt{k_\mathrm{F}^2 - \mathbf{k}_\parallel^2}} \left[\frac{C^{(1)}(\mathrm{i}\omega_n) + \mathcal{D}^{(2)}(\mathrm{i}\omega_n) + \mathcal{A}^{(3)}(\mathrm{i}\omega_n) + \mathcal{B}^{(4)}(\mathrm{i}\omega_n)}{\sqrt{\omega_n^2 + |\Delta_\mathrm{S}(T)|^2}} \right], \quad (8.26)$$

where e still denotes the positive elementary charge, k_B stands for Boltzmann's constant, and $\omega_n = (2n+1)\pi k_\mathrm{B} T$, with integer n, indicates the fermionic Matsubara frequencies (at temperature T). The *spin-conserving* Andreev reflection coefficients $C^{(1)}(\mathrm{i}\omega_n)$ [$\mathcal{D}^{(2)}(\mathrm{i}\omega_n)$] for spin-up (spin-down) electronlike quasiparticles and $\mathcal{A}^{(3)}(\mathrm{i}\omega_n)$ [$\mathcal{B}^{(4)}(\mathrm{i}\omega_n)$] for spin-up (spin-down) holelike quasiparticles – all approaching the interface from the superconducting region – are extracted solving the generic Bogoljubov-de Gennes scattering problem (recall Sec. 6.2 and see Appendix E for details) and analytically continuing the excitation energies $E \longmapsto \mathrm{i}\omega_n$.

8.4.2 Discussion of results

To compare the expected supercurrent responses to the TAHE conductances in the ferromagnet, we numerically evaluate Eq. (8.26) in the *zero-temperature* limit (meaning $T \to 0_+$) and for the same set of parameters as stated in the TAHE analysis, i.e., also assuming $\mathcal{A}_x = \mathcal{A}_y = \mathcal{A}$. Figure 8.7 exemplarily summarizes the results obtained when computing the supercurrent responses as functions of the in-plane magnetization angle Φ and at *zero bias* (the Furusaki-Tsukada approach does not include the possibility of regarding finite voltages). The intimate physical correlations between the TAHE currents (conductances) inside the ferromagnet and the supercurrent responses on the superconducting side of the junction – mediated by the peculiar (skew) Andreev reflections – suggest that both the TAHE currents and supercurrents must essentially reveal the same properties. Indeed, not only the supercurrents' Φ-dependencies [$I_x(\Phi) \propto \sin(\Phi)$ and $I_y(\Phi) \propto \cos(\Phi)$], but also their orientations reflect one-to-one the characteristics deflected for the TAHE currents inside the ferromagnet.[5] Furthermore, even $G_{y,z}$'s sign change encountered when altering the Z-barrier parameter from $Z = 1$ to $Z = 4$ [recall Fig. 8.4(b)] gets transferred into the corresponding supercurrent response I_y. In spite of all analogies, we spot one important difference between the TAHE conductances and the supercurrent responses, concerning the quantities' magnitudes. The supercurrent responses are caused by two single electrons that tunnel into the superconductor and form a Cooper pair there. Sizable supercurrents can only start to flow if both electrons concurrently (skew) tunnel across the barrier. Simultaneous electron tunnelings, however, happen much less likely in the presence of strong interfacial barriers than single-electron tunnelings. The maximal

[5] The supercurrents' signs are actually exactly opposite than those of the earlier discussed TAHE conductances. Nevertheless, we need to compare the supercurrents to the TAHE *currents*, which differ by another sign from the TAHE conductances. All in all, the orientations of the TAHE currents in the ferromagnet and the supercurrent responses in the superconductor are hence the same, as one expects from their close physical connections.

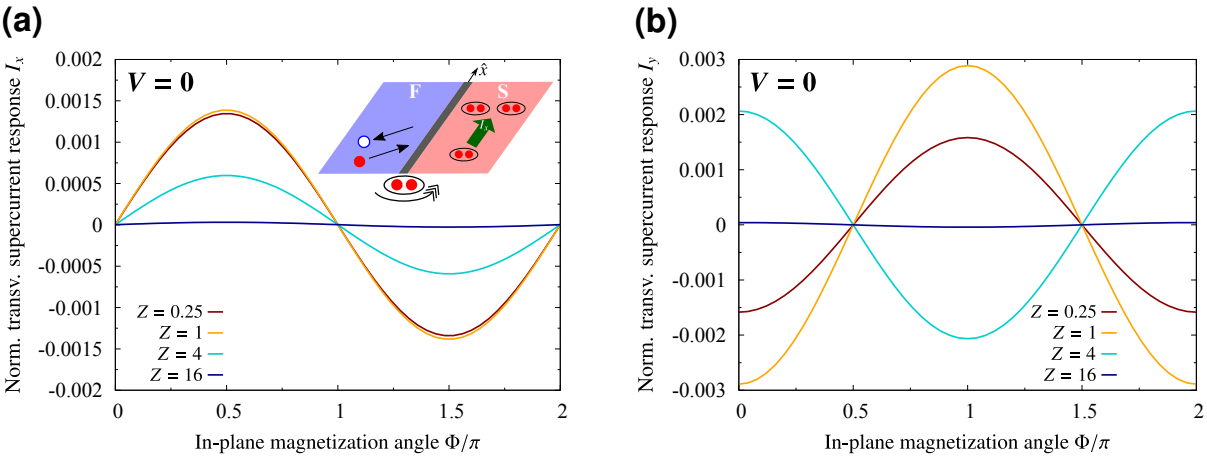


Fig. 8.7: Calculated dependence of the *zero-bias* transverse supercurrent responses **(a)** I_x and **(b)** I_y, normalized according to $[I_{x\,(y)}e]/[G_S|\Delta_S(0)|\pi]$, on the in-plane magnetization angle Φ and for the same parameters as in Fig. 8.4. Panel **(a)**'s inset illustrates the intimate connection between skew Andreev reflections and the supercurrent response; more details can be found in the text.

supercurrent responses in the superconductor occur therefore always at smaller barrier strengths Z than the maximal TAHE conductance amplitudes in the ferromagnet.

From the experimental viewpoint, half-metallic junctions might attract considerable interest. As we explained in Sec. 3.2, spin-conserving Andreev reflections are completely forbidden at interfaces between half-metallic ferromagnets and superconductors since incoming majority-spin electrons are not able to find minority-spin partners. The result is not only a remarkably damped subgap tunneling conductance, but likewise a strong suppression of the TAHE conductances. Owing to the interfacial SOC, spin-flip Andreev reflections become additionally possible so that the conductances are not strictly zero (though being usually much smaller than in junctions including ferromagnets with lower spin polarizations). Nevertheless, already sporadic spin-flip Andreev reflections suffice to generate *sizable and fully spin-polarized (triplet) supercurrent responses* inside the superconductor. We provide a comprehensive analysis of these supercurrents in the Supplemental Material to our Rapid Communication [446]. Such dissipationless spin-polarized currents might find their way into several superconducting spintronics applications and open novel perspectives, e.g., the possibility to experimentally verify superconducting magnetoelectric effects [447, 448].

8.5 Tunneling spin Hall effect conductances

Apart from the TAHE charge currents, also their TSHE spin current counterparts offer an auspicious subject for deeper studies and might likewise play an important role in upcoming spintronics devices. The recent work focusing on (normal-conducting) normal metal/normal metal (N/N) junctions [440] concluded that electron skew tunnelings through the interfacial semiconducting barrier induce spin filtering along the transverse directions and generate thereby indeed sizable TSHE spin currents. The TAHE charge currents simultaneously vanish since the junction is nonmagnetic (recall our introductory motivation to this chapter). From that point of view, integrating TSHE physics into *superconducting* N/S junctions might attract considerable attention of researchers. Similarly to the above investigated TAHE phenomena, TSHEs might raise spontaneous transverse spin supercurrent responses in the superconductor and complement such junctions' unprecedented transport features. Anyhow, once at least one of the systems' electrodes turns superconducting, the again emergent intriguing competition between skew specular

and skew Andreev reflections might lead to a more complicated behavior, which we need to understand within our qualitative skew reflection picture.

8.5.1 Generalized BTK spin conductance formula

To unravel the coincidence between the two different skew reflection processes on the one and TSHEs on the other hand, we extend the BTK-like formula capturing transverse TAHE charge conductances [see Eq. (8.19)] to transverse TSHE spin conductances. Shortly speaking, the *interfacial* TSHE spin currents $J^{\mathrm{s}}_{\eta,\hat{\mathbf{m}}}$ in the normal-conducting electrode – projected onto the spin quantization axis defined by the unit vector $\hat{\mathbf{m}} = [\cos(\Phi), \sin(\Phi), 0]^{\top}$ to keep our description general and also applicable in the magnetic F/S case[6] – are obtained from the corresponding TAHE charge currents J_{η} [see Eq. (E.32) in Appendix E] replacing the electron charge $-e$ by $\hbar/(2e)$ and properly accounting for the incident and reflected electrons' (holes') spins. We are interested in *particle* spin currents, meaning that we only differentiate between up- and down-spins, but not between electrons' and holes' differing charges (contrary to the TAHE charge currents). We use the convention that spin-up electrons and holes propagating along $\hat{\eta}$ (recall that $\hat{\eta} \in \{\hat{x}; \hat{y}\}$) contribute *positively* to the TSHE spin currents, spin-down electrons and holes that move along $\hat{\eta}$ are weighted *negatively*, and vice versa for electrons and holes traveling along $-\hat{\eta}$. An overall positive sign of the TSHE spin currents indicates then that skew reflections accumulate spin-up charge carriers at $\eta > 0$ and their spin-down counterparts at $\eta < 0$, respectively. Translating everything into formulas, the *interfacial* TSHE spin conductances $G^{\mathrm{s}}_{\eta,\hat{\mathbf{m}}} = \mathrm{d}J^{\mathrm{s}}_{\eta,\hat{\mathbf{m}}}/\mathrm{d}V$ are given by

$$G^{\mathrm{s}}_{\eta,\hat{\mathbf{m}}} \approx -\frac{\hbar}{2e}\frac{G_0\mathcal{A}_{\eta}}{2(2\pi)^2}\sum_{\sigma=\pm1}\int \mathrm{d}^2\mathbf{k}_{\parallel}\,\frac{k_{\eta}}{k_z^{\sigma}}\sigma\Big\{\Big[\big|r_{\mathrm{e}}^{\sigma,\sigma}(eV)\big|^2 - \big|r_{\mathrm{e}}^{\sigma,-\sigma}(eV)\big|^2\Big] - \Big[\big|r_{\mathrm{h}}^{\sigma,\sigma}(-eV)\big|^2 - \big|r_{\mathrm{h}}^{\sigma,-\sigma}(-eV)\big|^2\Big]\Big\}. \quad (8.27)$$

In sharp contrast to the TAHE charge conductances, the specular reflection coefficients $r_{\mathrm{e}}^{\sigma,\pm\sigma}$ and the Andreev reflection coefficients $r_{\mathrm{h}}^{\sigma,\pm\sigma}$ enter the TSHE spin conductance expression with *opposite* signs, indicating an even more puzzling interplay between both. While skew specular and skew Andreev reflections mutually enhance superconducting systems' TAHE charge conductances, they remarkably damp the TSHE spin conductance counterparts at the same time.

8.5.2 Discussion of results

To provide a more thorough analysis, Fig. 8.8 illustrates the TSHE spin conductances' bias voltage dependence, numerically evaluated by means of Eq. (8.27) and for the same parameters as before (i.e., also setting $\mathcal{A}_x = \mathcal{A}_y = \mathcal{A}$) except that we consider the spin polarization limit $P \to 0$ referring to nonmagnetic N/S junctions. Most surprisingly, the competing skew specular and skew Andreev reflections not only notably damp the *subgap* TSHE spin conductances, but even completely suppress them. This is a unique consequence of superconducting junction's electron-hole (time-reversal) symmetry, which couples skew specular and skew Andreev reflections, and eventually enables the full cancellation of the two processes' individual TSHE spin conductance contributions. The detailed physical picture behind the zero subgap TSHE spin conductances can again be deduced from the qualitative skew reflection mechanism outlined in Sec. 8.2. We discuss this mechanism in Fig. 8.9 and its caption, and do not repeat the same arguments

[6] To make use of the reflection coefficients we analytically computed for the *magnetic* F/S junction scenario (see Appendix E), we initially start from that system and take the spin polarization limit $P \to 0$ afterwards to mimic the nonmagnetic N/S junction situation.

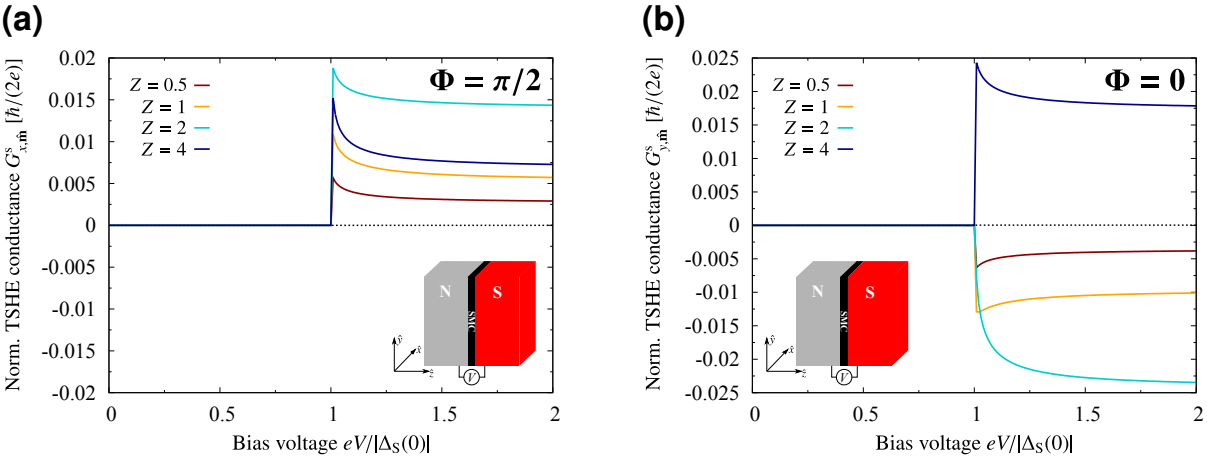


Fig. 8.8: Calculated dependence of the *maximal* TSHE spin conductances **(a)** $G^{s}_{x,\hat{\mathbf{m}}}(\Phi = \pi/2)$ and **(b)** $G^{s}_{y,\hat{\mathbf{m}}}(\Phi = 0)$, normalized to Sharvin's conductance given in the caption to Fig. 8.4, on the applied bias voltage V [the associated electron energy eV is given in multiples of the superconductor's gap $|\Delta_S(0)|$] and for various indicated tunneling barrier strengths Z. The SOC parameters are the same as considered in Fig. 8.4. The insets illustrate the studied junction. Note that TSHEs are usually studied in nonmagnetic junctions and we therefore consider the limit $P \to 0$, turning the ferromagnet into a normal metal.

here. For the same reason, electron skew tunnelings through N/S junctions' spin-active interfaces cannot facilitate transverse spin supercurrent responses in the superconductor. We checked that reformulating the transverse Furusaki-Tsukada charge supercurrent formula [see Eq. (8.26)] to treat also spin supercurrents; the corresponding results are as expected and therefore not explicitly shown.

Generating nonzero TSHE spin conductances in N/S contacts requires to further increase the bias voltage such that eV overcomes the gap edge, i.e., $eV \geq |\Delta_S(0)|$. Besides specular and Andreev reflections, electrons can then furthermore skew tunnel into the initially superconducting electrode. Such skew tunnelings maintain sizable TSHE spin conductances, approaching the earlier studied N/N configuration at $eV \gg |\Delta_S(0)|$ [440]. We assured that our results in this normal-state limit become consistent with those presented in Ref. [440]. Even in magnetic F/S junctions, in which the ferromagnetic exchange coupling breaks the fundamental electron-hole (time-reversal) symmetry, the competition between skew specular and skew Andreev reflections still heavily damps the subgap TSHE spin conductances (not explicitly shown). Moreover, the resulting tiny transverse spin currents are then invariably accompanied by sizable TAHE charge currents (as computed in Sec. 8.3). Both considered superconducting N/S and F/S junction scenarios do thus not offer any practical possibility to switch between pure subgap TAHE charge and TSHE spin current regimes, which undoubtedly limits their applicability in the framework of superconducting spintronics. In Chap. 9, however, we widen our study to Josephson junctions and unravel that these can independently support *pure* transverse charge and spin current regimes, making them the more promising candidates for (experimental) follow-up works.

8.6 Short summary

To summarize, we established a generic and powerful methodology to qualitatively understand and quantitatively capture extrinsic TAHEs and TSHEs in superconducting F/S junctions comprising spin-active semiconducting tunneling barriers. Based on a simplified physical picture, we deduced that skew specular and skew Andreev reflections of tunneling current electrons, approaching the junction interface, cause remarkable transverse electron imbalances in the ferromagnetic region and thus nonzero

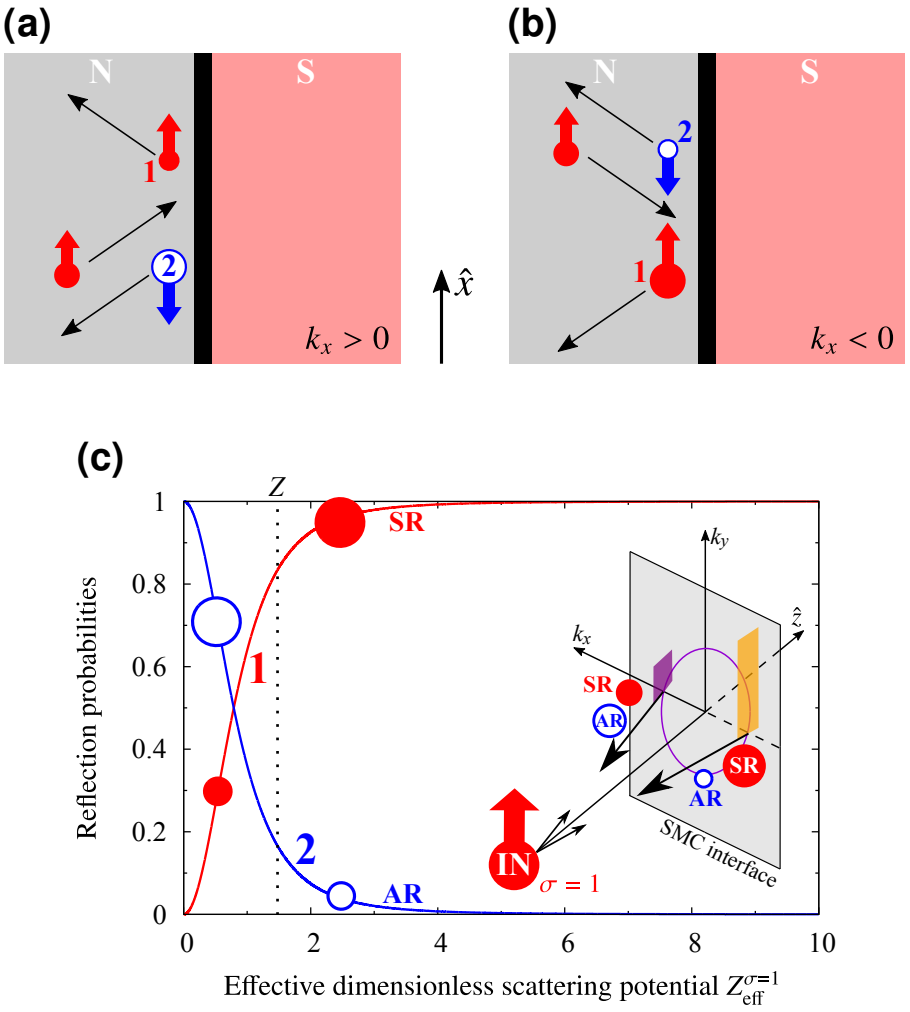


Fig. 8.9: (a) Illustration of a spin-up electron with transverse momentum $k_x > 0$ (assuming $k_y = 0$) that approaches the N/S interface (IN) and undergoes either specular (**1**) or Andreev (**2**) reflection. Electrons are colored red and holes blue, while the colored (black) arrows indicate their spins (propagation directions). Spin-flip reflections do not need to be included since interfacial spin flips convert on average equal numbers of up-spins to down-spins (and vice versa) and do therefore not contribute to N/S junctions' TSHE spin conductances. **(b)** Same illustration as in **(a)**, but for an incident spin-up electron with $k_x < 0$. **(c)** Scattering at the spin-active semiconductor (SMC) interface can be understood in terms of skew specular and skew Andreev reflections at the effective scattering potential $Z_{\rm eff}^{\sigma=1}$ (see Sec. 8.2). Process **(a)** essentially causes a *positive* TSHE spin current (conductance) contribution since spin-up carriers (electrons or holes) accumulate at $x > 0$ and spin-down carriers at $x < 0$, respectively, and vice versa for process **(b)**. The overall skew specular and skew Andreev reflection contributions to the TSHE spin conductance are proportional to the *differences* of the related skew reflection probabilities at $k_x > 0$ and $-k_x$ [as we need to multiply each of them by the oppositely oriented transverse velocities $v_x = (\hbar k_x)/m$ and integrate over all k_x in the end]; we show the calculated zero-energy reflection probabilities (recall Sec. 8.2). Since the specular and Andreev reflection probabilities' k_x-*differences* become equal in nonmagnetic junctions (basically, subtracting the probabilities indicated by the large electrons and holes from those highlighted by the small electrons and holes yields the same), processes **(a)** and **(b)** must generate the *same amounts of TSHE* spin currents, flowing along *opposite* directions, and the total TSHE spin current (conductance) must vanish. Similar arguments hold also for incoming spin-down electrons and all other *subgap* energies (as well as for the skew scatterings along $\hat{y}$), explaining the full suppression of the subgap TSHE. Finite TSHE spin conductances require therefore bias voltages $V > |\Delta_S(0)|/e$ so that additional *skew tunnelings* come into play and the skew reflection parts can no longer cancel.

TAHE charge currents. Both skew reflection processes' current contributions essentially add up, resulting in giant TAHE signals when compared to earlier studied normal-conducting junctions [440] and drawing following experiments' attention towards superconducting systems. From the theoretical viewpoint, we extended the BTK model – introduced to unravel F/S junctions' tunneling conductances in Chap. 3 – to cover transverse TAHE currents. Numerically evaluating the TAHE conductance components for a couple of realistic parameter configurations and comparing the outcomes against the related normal-state results unambiguously confirmed the intriguing interplay between skew specular and skew Andreev reflections. Furthermore, we analyzed the TAHE conductances' peculiar bias voltage dependence and gave physical reasoning for the initially surprising and universal disappearance of all TAHE conductance parts precisely at the superconducting gap edge. This behavior separates the TAHE from in experimental set-ups potentially simultaneously arising "usual" anomalous Hall effects and can be considered as TAHEs' – and likewise skew Andreev reflections' – unique fingerprint.

On the microscopic level, it is again the peculiar Andreev reflection mechanism that transfers electrons across the barrier, forming Cooper pairs in the superconductor and converting normal dissipative tunneling currents into dissipationless supercurrents. Due to the presence of the spin-active interface, also these Cooper pair electrons skew tunnel into the superconductor and more Cooper pairs may be created either along the transverse $\hat{\eta}$- or $(-\hat{\eta})$-directions, raising spontaneous transverse supercurrent responses. Generalizing the Furusaki-Tsukada (Josephson) supercurrent formula encountered in Sec. 6.2, we quantified the supercurrent responses for the same set of parameters assumed when elaborating on the TAHE conductances. Our simulations illustrated the supercurrents' most essential scaling with respect to common junction parameters – significantly enriching their previous analysis by means of a phenomenological Ginzburg-Landau approach [445] – and their intimate connection with the TAHE conductances in the ferromagnet, indicating that both essentially stem (mostly) from the intricate skew Andreev reflections. The discussed unique features associated with TAHE conductances and the related supercurrent responses open feasible experimental possibilities to detect and characterize superconducting tunnel junctions' interfacial SOC.

Besides the transverse TAHE charge currents, their spin current counterparts might provide promising perspectives for spintronics applications. We adapted the derived BTK-like TAHE charge conductance formula to their related TSHE spin conductance parts and calculated the latter for nonmagnetic N/S junctions. Although the interplay of skew specular and skew Andreev reflections notably magnifies the TAHE charge conductances, both reflection processes' TSHE spin conductance parts mutually cancel and completely suppress the *subgap* TSHE – in sharp contrast to normal-state junctions [440], in which sizable TSHE signals were predicted. In spite of all the extraordinary transverse transport phenomena we demonstrated throughout this chapter, the absent TSHE reflects for sure a great drawback of superconducting tunnel junctions when thinking about their usability for spintronics devices. Nevertheless, we will learn in Chap. 9 that Josephson junctions can independently support *pure* charge and spin Hall regimes, and are therefore probably more relevant to technological applications.

Chapter 9

Anomalous Josephson Hall and spin Hall effects in ballistic S/F-I/S junctions

Superconducting junctions offer unique possibilities to generate and control dissipationless charge and spin supercurrents, which themselves provide the key ingredients for efficiently operating spintronics devices. The TAHE, thoroughly discussed in Chap. 8 for a F/S contact, probably counts to the most puzzling of those phenomena. Skew reflections of tunneling current electrons at the ultrathin SOC-inducing barrier, which separates the ferromagnetic and superconducting electrodes, raise not only distinct transverse TAHE currents in the metal, but at the same time also unique transverse (charge) supercurrent responses inside the superconductor. Owing to the peculiar interplay between skew specular and skew Andreev reflections – the latter essentially cause the supercurrent responses –, the TAHE signals become much more sizable in superconducting than in normal-state junctions. Their characteristic scaling and wide tunability with respect to common junction parameters makes TAHE conductance and supercurrent response measurements auspicious experimental tools to classify superconducting contacts' interfacial SOC.

Thinking one step ahead, interfacial SOC in Josephson junctions might likewise attract considerable interest to combine anomalous Hall and Josephson effects in one single system. The resulting, *fully dissipationless*, transverse *charge and spin Hall supercurrents* might not only be efficiently tuned by the SOC parameters similarly to the F/S case, but additionally by means of the superconducting phase difference between the junction electrodes. Such a control might bring new functionalities into spintronics applications. However, already one of the early works into that direction [449] demonstrated that stationary Josephson junctions' fundamental electron-hole (time-reversal) symmetry usually acts against spontaneous (spin) Hall supercurrents, dramatically limiting these junctions' practical use. To overcome this obstacle, it was suggested to either apply a finite-bias voltage to the system [450] – which might cause other unfavorable effects – or to modify the whole junction geometry. Several proposals focused on intricate magnetic multilayer configurations [445, 451–465] that break time-reversal symmetry and whose strong SOCs simultaneously facilitate a mixture of spin-singlet as well as spin-triplet superconducting correlations. Both might eventually lead to pronounced charge Hall supercurrents [445, 457, 462, 466] and their spin current counterparts [453, 454, 456, 459, 461, 463–465, 467].

The aim of this chapter is to extend the analysis of superconducting F/S contacts' TAHEs and TSHEs provided in Chap. 8 to S/F-I/S Josephson junctions. The ultrathin ferromagnetic-insulator barrier turns out to be crucial for the discovered Hall physics since this layer induces strong interfacial SOC that gives again rise to peculiar skew scatterings and detectable Hall responses. We split the chapter into seven sections. In Sec. 9.1, we briefly summarize the main steps of the theoretical model employed for our investigations. Owing to its similarity with the descriptions presented in earlier parts of this thesis, we do not need to outline all details once again. Section 9.2 generalizes the qualitative skew reflection picture we came across in connection with F/S junctions (recall Sec. 8.2) to the tunneling of Cooper pairs and demonstrates that these pairs *skew tunnel* through the spin-active ferromagnetic-insulator interface, eventually generating sizable charge Hall supercurrents to which we refer as *anomalous Josephson Hall effect (AJHE) cur-*

rents.[1] When compared to most of the previously predicted geometries (see, e.g., Refs. [445] and [451–465]), S/F-I/S junctions bring along the great advantage that their physical properties can be much better tailored in future experiments. Numerically evaluating the AJHE currents for several representative junction parameters in Sec. 9.3 reveals the currents' unique magnetization and SOC dependencies we encountered in F/S junctions before, as well as their unprecedented scaling with respect to the superconducting phase difference not explored up to now.

A clear spectroscopic fingerprint of Josephson junctions is the formation of *subgap bound states* that are strongly localized around the nonsuperconducting link region. In fact, we identified two well-distinct types of bound states that play a major role in S/F-I/S junctions: the *Andreev bound states* [179, 227] and the *YSR states* [361–363]. These bound states turned out to be responsible for most of the junctions' puzzling physical qualities like the Josephson current-reversing 0-π transitions (see our comprehensive study in Chap. 7). Nevertheless, the coincidence between the bound states' spectroscopic features on the one and the AJHE on the other hand remained unclear so far. Therefore, we characterize *three-dimensional* S/F-I/S junctions' Andreev bound state and YSR state energies in Sec. 9.4 and elaborate on an alternative approach that allows us to directly relate the underlying bound state wave functions to the AJHE currents. This alternative modeling serves not only as an essential crosscheck for our previous results, but enables us at the same time to resolve the Andreev bound states' and YSR states' individual AJHE current contributions, which was not possible when following our initial theoretical description. The additional bound state calculations suggest moreover that AJHEs *microscopically* originate from SOC-controlled bound state asymmetries – most clearly apparent in the YSR branches.

The ferromagnetic-insulator barrier's strong interfacial SOC raises spin-flip scatterings and converts thereby some spin-unpolarized singlet into spin-polarized triplet Cooper pairs. Based on the established Cooper pair skew tunneling mechanism, which basically acts like a transverse "*Cooper pair spin filter*" separating spin-unpolarized from spin-polarized pairs, we develop a qualitative physical understanding to unravel the resulting transverse anomalous Josephson *spin* Hall effect currents' most general characteristics in Sec. 9.5. We evaluate the spin current amplitudes for various realistic junction parameters and emphasize that rotating the ferromagnetic insulator's in-plane magnetization and tuning the superconducting phase difference found fundamental experimental control knobs for transverse Josephson Hall currents. Finally, we introduce the *magnetization-independent spin-charge-current cross ratios* in Sec. 9.6. These ratios' universal scaling offers another promising tool to experimentally classify the junctions' interfacial SOC. The chapter closes with a short summary in Sec. 9.7.

This chapter is based on the article "Anomalous Josephson Hall effect charge and transverse spin currents in superconductor/ferromagnetic-insulator/superconductor junctions" by Andreas Costa and Jaroslav Fabian, which got published in Phys. Rev. B ***101****, 104508 (2020). All presented analytical and numerical calculations were performed by Andreas Costa. Jaroslav Fabian supported the project with stimulating discussions and feedback.*

9.1 Theoretical description

We consider a ballistic *three-dimensional* S/F-I/S Josephson junction, in which the two semi-infinite superconducting regions (S) are separated by an ultrathin ferromagnetic-insulator barrier (F-I) located at $z = 0$. The barrier might, for example, consist of a thin layer of EuS [21], EuO [225], a GaAs/Fe slab [468], or another thin semiconducting region proximitized by a ferromagnet. The system is illustrated in Fig. 9.1(a).

[1] In an earlier study [462], the term *AJHE* corresponds to the anomalous Hall conductances appearing in the magnetic electrode of magnet/triplet superconductor junctions. Although we adopt the same terminology, it shall be noted that the physics is different in our case.

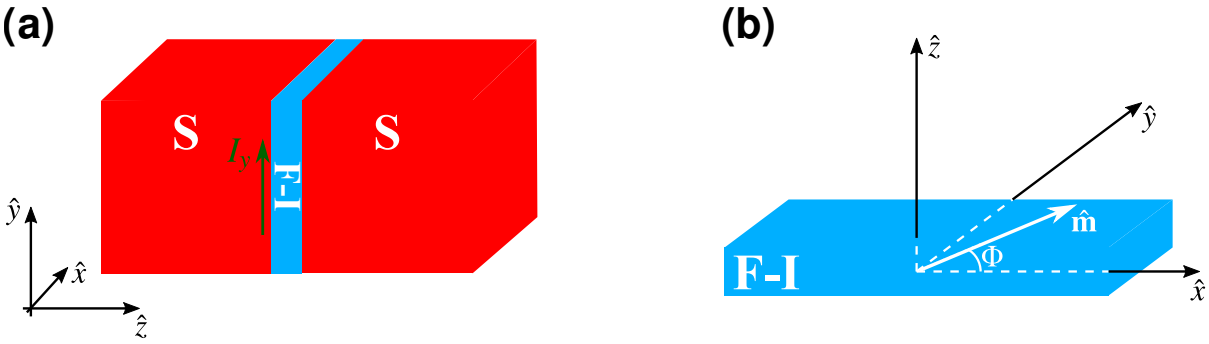


Fig. 9.1: (a) Schematical sketch of the considered *three-dimensional* S/F-I/S Josephson junction, using the C_{2v} principal crystallographic orientations $\hat{x} \parallel [110]$, $\hat{y} \parallel [\bar{1}10]$, and $\hat{z} \parallel [001]$. Skew tunnelings of Cooper pairs through the ferromagnetic-insulator (F-I) barrier generate interfacial AJHE (charge) currents along the transverse $\hat{x}$- and $\hat{y}$-directions; I_y is exemplarily illustrated by the green arrow. **(b)** The direction of the in-plane magnetization (unit) vector $\hat{\mathbf{m}}$ inside the ferromagnetic insulator (F-I) is determined by the angle Φ.

The ferromagnetic insulator introduces scalar and magnetic tunnelings and, owing to the broken space-inversion symmetry, simultaneously interfacial Rashba [149, 150] and – for additionally C_{2v}-symmetrical interfaces – Dresselhaus [152] SOCs.

The system's Bogoljubov-de Gennes Hamiltonian [139] in Nambu representation reads as

$$\hat{\mathcal{H}}_{\mathrm{BdG}} = \begin{bmatrix} \hat{\mathcal{H}}_{\mathrm{e}} & \hat{\Delta}_{\mathrm{S}}(z) \\ \hat{\Delta}_{\mathrm{S}}^{\dagger}(z) & \hat{\mathcal{H}}_{\mathrm{h}} \end{bmatrix}, \tag{9.1}$$

with

$$\hat{\mathcal{H}}_{\mathrm{e}} = \left(-\frac{\hbar^2}{2m} \boldsymbol{\nabla}^2 - \mu \right) \hat{\sigma}_0 + \hat{\mathcal{H}}^{\mathrm{F\text{-}I}} \tag{9.2}$$

representing the single-electron Hamiltonian and $\hat{\mathcal{H}}_{\mathrm{h}} = -\hat{\sigma}_y \hat{\mathcal{H}}_{\mathrm{e}}^{*} \hat{\sigma}_y$ its holelike counterpart ($\hat{\sigma}_0$ and $\hat{\sigma}_i$ indicate the two-by-two identity and the ith Pauli matrix). The ultrathin ferromagnetic-insulator region enters our model in terms of the effective deltalike barrier

$$\hat{\mathcal{H}}^{\mathrm{F\text{-}I}} = \Big[\lambda_{\mathrm{SC}}\, \hat{\sigma}_0 + \lambda_{\mathrm{MA}}\, (\hat{\mathbf{m}} \cdot \hat{\boldsymbol{\sigma}}) + \alpha\, (k_y\, \hat{\sigma}_x - k_x\, \hat{\sigma}_y) - \beta\, (k_y\, \hat{\sigma}_x + k_x\, \hat{\sigma}_y) \Big]\, \delta(z), \tag{9.3}$$

where the first two parts describe scalar and magnetic tunnelings with amplitudes λ_{SC} and λ_{MA}, respectively. The barrier's in-plane magnetization direction $\hat{\mathbf{m}} = [\cos(\Phi), \sin(\Phi), 0]^{\top}$ is determined by the angle Φ with respect to the $\hat{x}$-axis [see Fig. 9.1(b)], while the vector $\hat{\boldsymbol{\sigma}} = [\hat{\sigma}_x, \hat{\sigma}_y, \hat{\sigma}_z]^{\top}$ comprises the Pauli spin matrices. Finally, the remaining contributions in $\hat{\mathcal{H}}^{\mathrm{F\text{-}I}}$ resemble the interfacial Rashba and linearized Dresselhaus SOCs with the effective strengths α in the first and β in the second case. As usual, the SOC Hamiltonian is given within the C_{2v} crystallographic orientations $\hat{x} \parallel [110]$, $\hat{y} \parallel [\bar{1}10]$, and $\hat{z} \parallel [001]$. The s-wave superconducting pairing potential inside the superconductors is approximated by $\hat{\Delta}_{\mathrm{S}}(z) = |\Delta_{\mathrm{S}}| \hat{\sigma}_0 [\Theta(-z) + \mathrm{e}^{\mathrm{i}\phi_{\mathrm{S}}} \Theta(z)]$, where $|\Delta_{\mathrm{S}}|$ refers to the two similar superconductors' isotropic energy gap and ϕ_{S} to their respective phase difference. For further simplification, we additionally suppose equal quasiparticle masses m and the same chemical potential μ in all junction constituents.

Assuming translational invariance parallel to the ferromagnetic-insulator interface, we can factorize the solutions of the stationary Bogoljubov-de Gennes equation

$$\hat{\mathcal{H}}_{\mathrm{BdG}} \Psi(\mathbf{r}) = E \Psi(\mathbf{r}) \tag{9.4}$$

into

$$\Psi(\mathbf{r}) = \psi(z)\, \mathrm{e}^{\mathrm{i}(\mathbf{k}_{\parallel} \cdot \mathbf{r}_{\parallel})}, \tag{9.5}$$

where $\mathbf{k}_\parallel = [k_x, k_y, 0]^\top$ ($\mathbf{r}_\parallel = [x, y, 0]^\top$) is the transverse wave (position) vector and $\psi(z)$ are the Bogoljubov-de Gennes equation's individual solutions for the reduced one-dimensional scattering problem along $\hat{z}$. The latter distinguish between the involved quasiparticle scattering processes at the ferromagnetic-insulator barrier. Quasiparticles incident from one of the superconducting electrodes may either undergo specular or Andreev reflections, or may be transmitted as (electronlike or holelike) quasiparticles into the second superconductor. Understanding the peculiar Andreev reflection process will turn out to be crucial to unravel the physical origin of (transverse) supercurrent flows in the junction since these Andreev reflections are responsible for Cooper pair transfers across the barrier and eventually drive all emergent supercurrents on the microscopic level. Putting the full scattering picture on a mathematical ground is rather technical and basically similar to the concepts presented in Chaps. 6 and 7. The detailed formal description can be looked up in Appendix F. Once the scattering states' Andreev reflection coefficients are known, we get immediate access to the (tunneling) Josephson and the (transverse) AJHE currents.

9.2 Extended skew Andreev reflection picture

As we briefly mentioned in Sec. 9.1, the exchange of Cooper pairs between the junction's superconducting electrodes, eventually generating net supercurrent flows, is mediated by (quasiparticle) Andreev reflections. An unpaired electronlike quasiparticle approaching the ferromagnetic-insulator barrier from one superconductor gets thereby transmitted into the second superconductor and pairs with another correlated electronlike quasiparticle there, effectively transferring a Cooper pair across the barrier. The transmission of two correlated electronlike quasiparticles is formally modeled by having the incoming electronlike quasiparticle Andreev reflected as a holelike quasiparticle with opposite spin. As long as more Cooper pairs enter the right superconductor than the left one (or vice versa), nonzero (tunneling) Josephson currents build up. For brevity, we will refer to electronlike (holelike) quasiparticles as electrons (holes) from now on.

Electrons incident on the ferromagnetic-insulator barrier are exposed to an effective scattering potential that combines the scalar and (spin-dependent) magnetic tunneling terms with an additional spin- and transverse momentum-dependent contribution originating from the interfacial SOC. Assuming, for simplicity, that only Rashba SOC is present ($\alpha > 0$; the Dresselhaus SOC parameter is $\beta = 0$), the ferromagnetic insulator's in-plane magnetization points along the $\hat{x}$-direction (meaning that $\Phi = 0$), and the transverse wave vector's $\hat{x}$-projection vanishes (i.e., $k_x = 0$),[2] the effective scattering potential for incoming spin-σ electrons [$\sigma = +(-)1$ for spin up (spin down), which effectively indicates a spin parallel (antiparallel) to $\hat{x}$] takes the form

$$V_{\text{eff}}^{\sigma} = \lambda_{\text{SC}} + \sigma\lambda_{\text{MA}} + \sigma\alpha k_y. \tag{9.6}$$

To unravel the coincidence between the puzzling Andreev reflections of incoming electrons (holes) at the ferromagnetic-insulator barrier and the emergent AJHEs, we follow analogous arguments as in the TAHE case (recall Sec. 8.2). If SOC is so weak that spin-flip scattering can be neglected, we can again decouple the Bogoljubov-de Gennes Hamiltonian in Eq. (9.1) into its *spin-resolved two-by-two blocks* and find its most general scattering states accounting for spin-conserving reflections and transmissions. The reflection and transmission coefficients are afterwards determined applying appropriate interfacial boundary conditions and solving the resulting systems of equations. Within the

[2] In Sec. 8.2, we understood the generation of TAHE currents along $\hat{x}$ in terms of a similar mechanism. To demonstrate that the arguments used there are universal, we focus now on the $\hat{y}$-direction and show that the AJHE currents along $\hat{y}$ can be explained in an analogous manner.

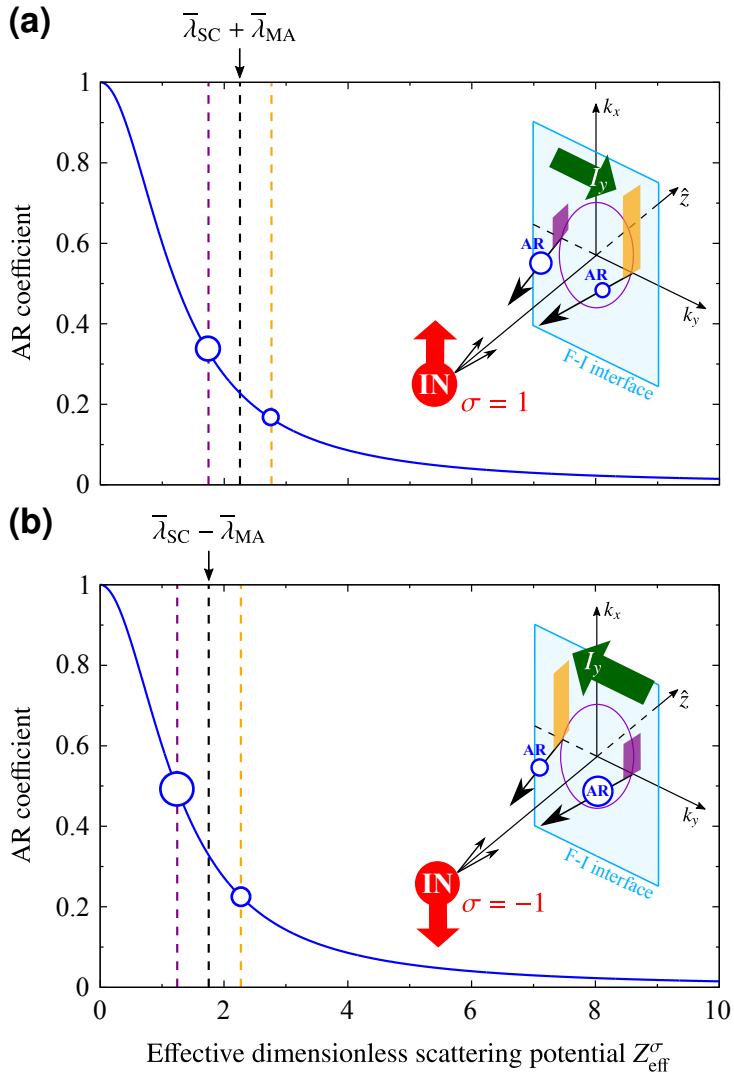


Fig. 9.2: **(a)** Calculated *zero-energy* Andreev reflection (AR) coefficient (determining the Andreev reflection probability) for spin-up electrons (IN) incident on the ferromagnetic-insulator (F-I) interface and as a function of the effective (dimensionless) BTK-like scattering potential $Z^{\sigma}_{\text{eff}} = (2mV^{\sigma}_{\text{eff}})/(\hbar^2 k_{\text{F}}) = \overline{\lambda}_{\text{SC}} + \sigma\overline{\lambda}_{\text{MA}} + \sigma\overline{\lambda}_{\text{R}} k_y/k_{\text{F}}$, where $\overline{\lambda}_{\text{SC}} = (2m\lambda_{\text{SC}})/(\hbar^2 k_{\text{F}})$, $\overline{\lambda}_{\text{MA}} = (2m\lambda_{\text{MA}})/(\hbar^2 k_{\text{F}})$, and $\overline{\lambda}_{\text{R}} = (2m\alpha)/\hbar^2$ represent the dimensionless scalar tunneling, magnetic tunneling, and Rashba SOC strengths, respectively; for the calculation, we set the superconducting phase difference to $\phi_{\text{S}} = \pi/2$. To give an example, the black dashed line indicates the scalar and magnetic tunneling parameters $\overline{\lambda}_{\text{SC}} = 2$ and $\overline{\lambda}_{\text{MA}} = 0.25$, adding up to $\overline{\lambda}_{\text{SC}} + \overline{\lambda}_{\text{MA}} = 2.25$ for spin-up electrons (since $\sigma = 1$). Assuming additionally the Rashba SOC strength $\overline{\lambda}_{\text{R}} = 1$, incoming spin-up electrons with $k_y > 0$ are exposed to a *raised* (orange dashed line) and those with $k_y < 0$ to a *lowered* (violet dashed line) effective scattering potential. Andreev reflection becomes therefore suppressed at positive k_y and favorable at negative k_y, highlighted by the different size of the blue Andreev-reflected holes. These *skew Andreev reflections* eventually generate a hole excess (electron deficit) at $y < 0$, which is compensated by the net transverse AJHE (super)current flow I_y along $\hat{y}$; the direction of the current is again defined *oppositely* to the electron flow direction. The inset illustrates the skew Andreev reflection process in a pictorial manner; as usual, electrons are colored red, holes blue, and black arrows indicate their propagation directions. **(b)** Same calculation as in **(a)**, but for incident spin-down electrons. Skew Andreev reflections cause now the AJHE current I_y along $-\hat{y}$. Since the scalar and magnetic tunneling strengths for spin-down electrons subtract to $\overline{\lambda}_{\text{SC}} - \overline{\lambda}_{\text{MA}} = 1.75$ (as $\sigma = -1$), the skew Andreev reflection coefficients (probabilities) for spin-down electrons are always slightly greater than those for their spin-up counterparts. Skew Andreev reflections of spin-down electrons raise thus a slightly larger AJHE current than skew Andreev reflections of spin-up electrons so that both spin channels' AJHE current contributions – though flowing along opposite directions – do not completely compensate.

given simplifications, we can either obtain closed analytical expressions for the scattering coefficients or extract them fully numerically. As pointed out several times, special attention must be paid to the unique Andreev reflection process. Figure 9.2 shows the numerically evaluated dependence of the *zero-energy* Andreev reflection coefficients, essentially defining the probability to undergo Andreev reflections, on the effective dimensionless scattering potential $Z_{\mathrm{eff}}^{\sigma} = (2mV_{\mathrm{eff}}^{\sigma})/(\hbar^2 k_{\mathrm{F}})$ for incident spin-up ($\sigma = 1$) and spin-down ($\sigma = -1$) electrons. To illustrate the mechanism that causes AJHEs, we suppose some realistic junction parameters. The dimensionless scalar and magnetic tunneling strengths $\overline{\lambda}_{\mathrm{SC}} = (2m\lambda_{\mathrm{SC}})/(\hbar^2 k_{\mathrm{F}}) = 2$ and $\overline{\lambda}_{\mathrm{MA}} = (2m\lambda_{\mathrm{MA}})/(\hbar^2 k_{\mathrm{F}}) = 0.25$ mimic, e.g., a roughly 0.80 nm thick ferromagnetic-insulator barrier with height 0.75 eV and a ferromagnetic exchange splitting of about 200 meV (setting $m \approx m_{\mathrm{e}}$ and $k_{\mathrm{F}} = \sqrt{2m\mu}/\hbar \approx 8{\times}10^7\ \mathrm{cm}^{-1}$ as a typical metal Fermi wave vector [182]). The exchange splitting is comparable to the one of bulk EuS, which lies about 360 meV [469]. The considered Rashba SOC parameter $\overline{\lambda}_{\mathrm{R}} = (2m\alpha)/\hbar^2 = 1$ is kept the same as in Sec. 8.2, resembling $\alpha \approx 4\,\mathrm{eV\,\mathring{A}}^2$.

Substituting those parameters into Eq. (9.6) suggests that incident spin-up electrons with *positive* transverse momenta k_y (e.g., $k_y = k_{\mathrm{F}}/2$) are exposed to a raised effective scattering potential [$Z_{\mathrm{eff}}^{\sigma=1} = 2.75$; see the orange dashed line in Fig. 9.2(a)] and get thus Andreev reflected with a remarkably lower probability than their *negative* k_y-counterparts [$k_y = -k_{\mathrm{F}}/2$ facilitates the lowered effective scattering potential $Z_{\mathrm{eff}}^{\sigma=1} = 1.75$ at which Andreev reflections happen much more likely; see the violet dashed line in Fig. 9.2(a)]. In precisely that way, spin- and transverse-momentum dependent *skew Andreev reflections* generate an excess of Andreev-reflected holes at $y < 0$ [additionally illustrated in a pictorial way in the inset of Fig. 9.2(a)], which is compensated by raising the transverse AJHE *quasiparticle* current I_y along $\hat{y}$ (recall that hole currents flow *oppositely* to electron currents and thus *parallel* to the usual current direction). Although we are solely dealing with quasiparticle currents at the moment, skew Andreev reflections effectively cycle Cooper pairs across the ferromagnetic-insulator interface and invariably trigger supercurrent responses (see particularly our argumentation in Sec. 8.4). Transverse AJHE quasiparticle currents are consequently immediately converted into dissipationless AJHE supercurrents inside the superconducting electrodes – microscopically mediated by Andreev reflection-assisted *skew tunnelings* of Cooper pairs through the barrier.

Flipping the incoming electrons' spin reverses simultaneously the skew Andreev reflection picture, as depicted in Fig. 9.2(b). It is then the positive k_y-range that entails preferential Andreev reflections, eventually leading to an AJHE current flow along $-\hat{y}$. If the barrier would be nonmagnetic, the net AJHE current amplitudes stemming from the spin-up and spin-down channels would indeed become equal and – as they flow along opposite directions – no net AJHE current occurs. Nevertheless, already a *weakly magnetic* barrier suffices that (skew) Andreev reflections happen more likely for incident spin-down than for spin-up electrons. The reason for this distinct behavior is that scalar and magnetic tunnelings add up to $\overline{\lambda}_{\mathrm{SC}} + \overline{\lambda}_{\mathrm{MA}}$ [i.e., $\overline{\lambda}_{\mathrm{SC}} + \overline{\lambda}_{\mathrm{MA}} = 2.25$ in our example; see the black dashed line in Fig. 9.2(a)] for spin-up electrons, while they subtract to $\overline{\lambda}_{\mathrm{SC}} - \overline{\lambda}_{\mathrm{MA}}$ [i.e., $\overline{\lambda}_{\mathrm{SC}} - \overline{\lambda}_{\mathrm{MA}} = 1.75$ in our example; see the black dashed line in Fig. 9.2(b)] for spin-down electrons. Even if SOC is absent, spin-down electrons are hence always subject to a (at least slightly) lowered effective scattering potential than their spin-up counterparts and undergo Andreev reflections with (slightly) greater probabilities. The individual spin channels' AJHE currents in (weakly) magnetic S/F-I/S junctions do therefore not completely cancel and a nonzero AJHE current is expected to build up.

9.3 Anomalous Josephson Hall effect currents

Measuring sizable AJHE current signals provides thus an unambiguous experimental evidence for Cooper pair skew tunnelings through the ferromagnetic-insulator barrier. The aim of this section is to

compute the AJHE currents' amplitudes for several realistic junction scenarios and thereby characterize their most intriguing physical features further.

9.3.1 Generalized Furusaki-Tsukada supercurrent formula

To access the AJHE currents along the *transverse* $\hat{\eta}$-directions ($\hat{\eta} \in \{\hat{x}; \hat{y}\}$), we essentially follow the same strategy as for computing F/S junctions' supercurrent responses in Sec. 8.4 and extend the Furusaki-Tsukada approach [266] to cover transverse currents. More details on the methodology are summarized in Appendix F. The *interfacial* AJHE currents, flowing through the Hall contact areas $\mathcal{A}_\eta$, are finally given by

$$I_\eta \approx \frac{e k_\mathrm{B} T}{2\hbar} |\Delta_\mathrm{S}(T)| \frac{\mathcal{A}_\eta}{(2\pi)^2} \int \mathrm{d}^2\mathbf{k}_\parallel \sum_{\omega_n} \frac{k_\eta}{\sqrt{k_\mathrm{F}^2 - \mathbf{k}_\parallel^2}} \left[\frac{C^{(1)}(\mathrm{i}\omega_n) + \mathcal{D}^{(2)}(\mathrm{i}\omega_n) + \mathcal{A}^{(3)}(\mathrm{i}\omega_n) + \mathcal{B}^{(4)}(\mathrm{i}\omega_n)}{\sqrt{\omega_n^2 + |\Delta_\mathrm{S}(T)|^2}} \right], \tag{9.7}$$

where e denotes the positive elementary charge, k_B Boltzmann's constant, and $\omega_n = (2n+1)\pi k_\mathrm{B} T$, with integer n, indicates the fermionic Matsubara frequencies (at temperature T). All information necessary to evaluate the AJHE current components enters again via the *spin-conserving* Andreev reflection coefficients $C^{(1)}(\mathrm{i}\omega_n)$ $[\mathcal{D}^{(2)}(\mathrm{i}\omega_n)]$ for incoming (from the left) spin-up (spin-down) electronlike quasiparticles, as well as $\mathcal{A}^{(3)}(\mathrm{i}\omega_n)$ $[\mathcal{B}^{(4)}(\mathrm{i}\omega_n)]$ belonging to incident spin-up (spin-down) holelike quasiparticles. We determine these coefficients solving the generic Bogoljubov-de Gennes scattering problem (recall Sec. 6.2 and see Appendix F for details) and analytically continuing the excitation energies $E \longmapsto \mathrm{i}\omega_n$.

9.3.2 Discussion of results

Figure 9.3 visualizes the numerically computed AJHE current components I_x and I_y as functions of the ferromagnetic insulator's in-plane magnetization angle Φ and for different Rashba SOC parameters $\overline{\lambda}_\mathrm{R} = (2m\alpha)/\hbar^2$. For all calculations discussed in this chapter, we assume the rather weak scalar tunneling $\overline{\lambda}_\mathrm{SC} = (2m\lambda_\mathrm{SC})/(\hbar^2 k_\mathrm{F}) = 1$, which mimics a roughly 0.40 nm thick potential barrier of height 0.75 eV [251] (substituting, for simplicity, $m \approx m_\mathrm{e}$ and $k_\mathrm{F} \approx 8 \times 10^7\,\mathrm{cm}^{-1}$ as a typical Fermi wave vector [182]). To demonstrate that already weakly magnetic S/F-I/S junctions support strong AJHEs, we take the extremely small magnetic tunneling parameter $\overline{\lambda}_\mathrm{MA} = (2m\lambda_\mathrm{MA})/(\hbar^2 k_\mathrm{F}) = 0.005$, modeling a 0.40 nm thick ferromagnetic insulator with an exchange splitting of just about 8 meV – nearly two orders of magnitude lower than the splitting of bulk EuS (360 meV [469]). Analogously to earlier parts of this thesis, the superconductors' zero-temperature gap and their critical temperature are set to $|\Delta_\mathrm{S}(0)| \approx 2.5\,\mathrm{meV}$ and $T_\mathrm{C} \approx 16.2\,\mathrm{K}$. We evaluate all AJHE currents at a low temperature of $T = 0.1 T_\mathrm{C}$, basically meaning that we also need to account for the superconducting energy gap's BCS-like temperature dependence $|\Delta_\mathrm{S}(T \neq 0)| = |\Delta_\mathrm{S}(0)| \tanh(1.74\sqrt{T_\mathrm{C}/T - 1})$. The chosen Dresselhaus SOC parameter $\overline{\lambda}_\mathrm{D} = (2m\beta)/\hbar^2 = 0.5$ corresponds to a bare Dresselhaus SOC strength of $\beta \approx 1.9\,\mathrm{eV\,\AA}^2$ (an AlP barrier with the considered height and width would have $\beta \approx 1.7\,\mathrm{eV\,\AA}^2$ [27]), while the Rashba SOC measure is varied between $\overline{\lambda}_\mathrm{R} = 0.5$ and $\overline{\lambda}_\mathrm{R} = 4.0$, referring to bare Rashba SOC strengths between $\alpha \approx 1.9\,\mathrm{eV\,\AA}^2$ and $\alpha \approx 15.2\,\mathrm{eV\,\AA}^2$. A recent study [182] concluded that the Rashba SOC arising at Fe/MgO/V junctions' interfaces can reach values up to $\alpha \approx 4.6\,\mathrm{eV\,\AA}^2$ (for a 1.7 nm thick MgO barrier), which lies well within the considered range. Even remarkably larger Rashba couplings were furthermore predicted to appear at BiTeBr interfaces [395]. For simplicity, the Hall contact areas $\mathcal{A}_\eta$ and the interfacial tunneling cross-section area $\mathcal{A}$ are supposed to be equal, i.e., $\mathcal{A}_x = \mathcal{A}_y = \mathcal{A}$.

Let us initially comment on the AJHE currents' Φ-dependence at zero superconducting phase difference ($\phi_\mathrm{S} = 0$). In fact, I_x (I_y) reveal precisely the same unique sinelike (cosinelike) variations with

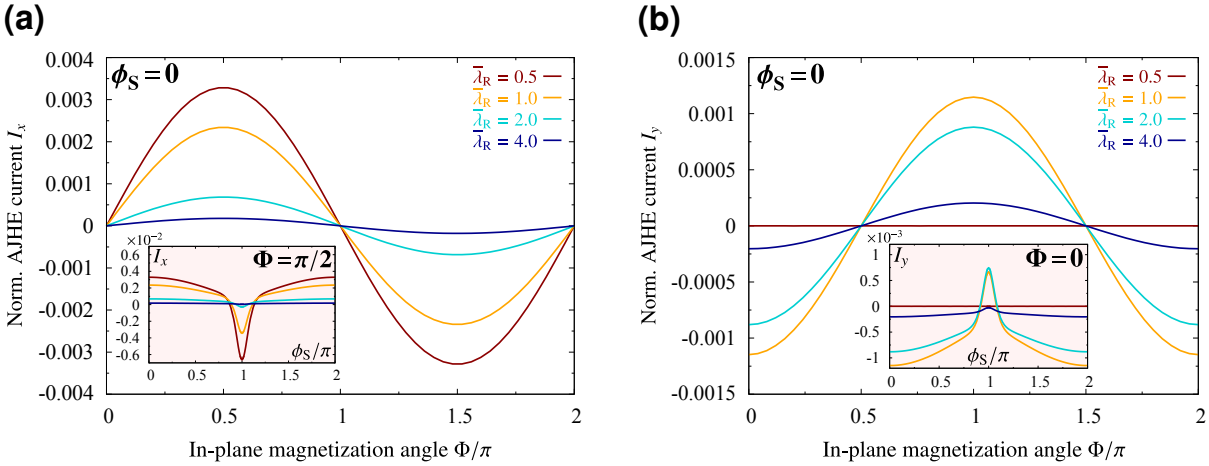


Fig. 9.3: Calculated dependence of the *zero-phase difference* AJHE currents **(a)** I_x and **(b)** I_y [normalized according to $[I_{x\,(y)}eR_S]/[|\Delta_S(0)|\pi]$, where $R_S = (2\pi h)/(\mathcal{A}e^2k_F^2)$ corresponds to Sharvin's resistance of a perfectly transparent (three-dimensional) metallic point contact] on the ferromagnetic insulator's in-plane magnetization angle Φ and for various indicated Rashba SOC strengths $\overline{\lambda}_R$. The scalar and magnetic tunneling strengths, as well as the Dresselhaus SOC parameter, are $\overline{\lambda}_{SC} = 1$, $\overline{\lambda}_{MA} = 0.005$, and $\overline{\lambda}_D = 0.5$. The insets show the *maximal* AJHE currents (i.e., I_x at $\Phi = \pi/2$ and I_y at $\Phi = 0$) as functions of the superconducting phase difference ϕ_S.

respect to the magnetization angle Φ as F/S junctions' TAHE conductances (recall Sec. 8.3), serving as a clear fingerprint of the intricate interplay between magnetic coupling and SOC. Since the physical mechanisms causing TAHEs on the one and AJHEs on the other hand are closely related – the first stem from mutually amplifying skew specular and skew Andreev reflections, while the second are caused by Andreev reflection-assisted Cooper pair skew tunnelings –, the intimate coincidence between the TAHE conductances' and AJHE currents' Φ-modulations could actually be deduced even without performing any numerical simulations. To become more specific, all the symmetry arguments outlined in Sec. 8.3 can be transferred one-to-one to the AJHE current formula in Eq. (9.7), finally suggesting that $I_x \propto -(\alpha+\beta)\sin(\Phi)$ and $I_y \propto (\alpha-\beta)\cos(\Phi)$. Similarly as for the TAHE conductances, nonzero SOC causes therefore pronounced magnetoanisotropies in both AJHE currents, apart from the special case of equal Rashba and Dresselhaus SOC strengths ($\alpha = \beta$) in which I_y vanishes anyway. For the regarded parameters, disappearing I_y requires $\alpha \propto \overline{\lambda}_R = 0.5 = \overline{\lambda}_D \propto \beta$, illustrated by the dark red curve in Fig. 9.3(b). To give a more physical explanation, we may recall the qualitative skew Andreev reflection picture in Sec. 9.2 and inspect the single-particle Hamiltonian's SOC part [see Eq. (9.3)] for another time. Substituting $\alpha = \beta$ there suggests that the k_y-dependent SOC terms disappear. The result is a full suppression of the skew Andreev reflection mechanism, and thereby the AJHE current, along the $\hat{y}$-direction, exactly as observed in our numerical calculations.

Owing to the skew Andreev reflections' great sensitivity to the SOC strengths, slightly changing one of them – e.g., the Rashba SOC parameter – typically significantly alters the upcoming AJHE currents' magnitudes, and offers thus a feasible experimental way to control the currents and the underlying skew Andreev reflections. Suitably tuned parameter regimes even reverse the skew reflection picture and likewise the AJHE currents' directions (signs), as it happens, for example, in I_y when tuning $\overline{\lambda}_R$ through $\overline{\lambda}_R = 0.5$. Similar features occur in F/S junctions' TAHE conductances and get thoroughly explained in Sec. 8.3; note that we changed the barrier's strength instead of the SOC there, which entails comparable current reversals. Strong SOCs act moreover like large (additional) interfacial scattering potentials and start to notably damp the AJHE currents. When compared to anomalous Hall effects in normal-conducting systems, e.g., to the normal-state TAHE [440], the AJHE currents are sizable. Maximal AJHE currents reach

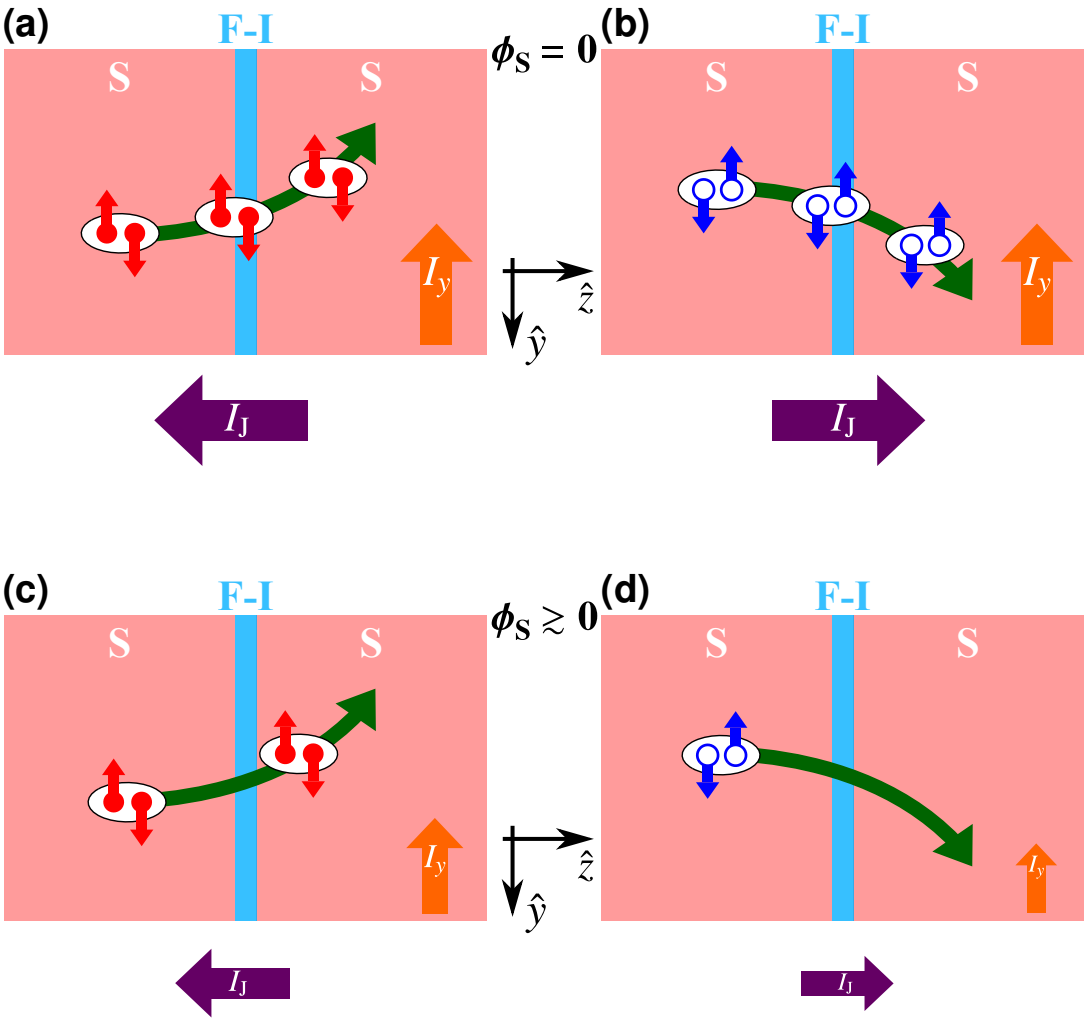


Fig. 9.4: **(a)** Schematical illustration of the *electron* Cooper pair tunneling across the S/F-I/S junction's ferromagnetic-insulator (F-I) barrier, generating the (tunneling) Josephson current I_J and, owing to the skew tunneling mechanism (highlighted by the green arrows), the transverse AJHE current I_y. The superconducting phase difference is $\phi_S = 0$ and the current amplitudes are proportional to the size of the violet and orange arrows. **(b)** Same illustration as in **(a)** for the tunneling of *hole* Cooper pairs from the left into the right superconductor (S), essentially modeling *electron* Cooper pair tunnelings from right to left. At $\phi_S = 0$, the amplitude of I_J is the same as in **(a)**, but the current flows along the *opposite* direction (recall that *hole* currents count with opposite signs). The overall (tunneling) Josephson current vanishes. Contrary, the transverse AJHE current contributions – both again with the same magnitudes – flow along the *same* directions and add up to sizable total AJHE currents. **(c)** [**(d)**] Same illustrations as in **(a)** [**(b)**], but at $\phi_S \gtrsim 0$. Finite phase difference introduces a "bias" so that more *electron* Cooper pairs tunnel from left to right than vice versa, and the overall (tunneling) Josephson current initially starts to increase with increasing ϕ_S. Nevertheless, the individual currents associated with *electron* Cooper pairs tunneling from left to right and from right to left are both (notably) smaller than at $\phi_S = 0$, which simultaneously damps their contributions to the AJHE currents.

values of more than ten percent of the junction's (tunneling) Josephson current,[3] whereas normal-state TAHE conductances are usually less than one percent of the tunneling conductance [440].

Next, we analyze the role of the superconducting phase difference ϕ_S, which turns out to be much more surprising. The insets of Fig. 9.3 illustrate the *maximal* AJHE current amplitudes' (i.e., supposing $\Phi = \pi/2$ when evaluating I_x and $\Phi = 0$ for the I_y-calculations) ϕ_S-dependence, keeping all other junction parameters the same as before. While the junction's (tunneling) Josephson current always follows well-established sinusoidal current-phase relations (not explicitly shown; recall the arguments in Chap. 5), the transverse AJHE currents modulate with ϕ_S in a remarkably different way. The greatest AJHE currents flow at those phase differences at which the (tunneling) Josephson current itself simultaneously vanishes, i.e., at $\phi_S = 0 \pmod{\pi}$. To develop a simple physical understanding of the AJHE currents' striking phase difference variations, we recall once again the qualitative Cooper pair skew tunneling picture introduced in Sec. 8.2. All supercurrent flows through the junction are microscopically generated by the tunneling of Cooper pairs from one into the second superconducting electrode, each happening with certain probabilities. At zero superconducting phase difference ($\phi_S = 0$), tunnelings of Cooper pairs from the left into the right superconductor and vice versa become equally likely. All Cooper pairs leaving one superconductor are therefore fully "compensated" by the same number of other pairs entering this superconductor, and no net (tunneling) Josephson currents flow, as sketched in Figs. 9.4(a) and 9.4(b); note that the tunneling of (electron) Cooper pairs from right to left is depicted in terms of *hole* Cooper pairs that tunnel from left to right. Increasing ϕ_S acts now as an effective "bias". While the probability for *forward tunnelings* of Cooper pairs (meaning *from the left into the right superconductor*) is only barely affected, *backward tunnelings* (meaning *from the right into the left superconductor*) become much less probable. In the end, more (electron) Cooper pairs are transferred into the right superconductor than leave, leading to a finite (tunneling) Josephson current. The imbalance ("bias") between forward and backward tunnelings gets more distinct with further enhancements of ϕ_S and the (tunneling) Josephson current rises. Due to the tunneling probabilities' characteristic ϕ_S-periodicity, the whole situation eventually reverses at a critical $\phi_S^{\text{crit.}} \approx \pi/2$ (in ideal junctions) and the Josephson current decreases again, finally resembling the typical sinusoidal Josephson current-phase relation.

In sharp contrast to forward and backward tunnelings' Josephson current contributions, which need to be subtracted from each other, their AJHE current parts flow along the *same* transverse directions and hence add up. Particularly large AJHE currents appear consequently whenever forward and backward Cooper pair tunnelings become most likely (and equal in magnitudes), i.e., at $\phi_S = 0 \pmod{\pi}$, as clearly visible in our numerical results (see the insets of Fig. 9.3). Increasing ϕ_S suppresses then primarily backward tunnelings (and slightly also forward tunnelings), and thereby the total AJHE currents, as illustrated in Figs. 9.4(c) and 9.4(d).

9.4 Microscopic bound state picture

The formation of interfacial subgap bound states belongs to Josephson junctions' most intriguing spectroscopic features. Particularly striking is the case of magnetic junctions, in which the bound state spectrum splits into distinct Andreev bound states on the one and YSR states on the other hand. Our comprehensive analysis for *one-dimensional* S/F-I/S contacts in Chap. 7 demonstrated that the YSR states possess intricate spectral and spin characteristics, eventually entailing the Josephson current-reversing 0-π transitions. Since all electrical current inside the ferromagnetic-insulator region is carried by electrons that initially formed Cooper pairs inside the superconductors and tunnel through the interface via the available

[3] The Josephson currents are evaluated by means of the "usual" Furusaki-Tsukada formula [266] given in Sec. 6.2 [see, in particular, Eq. (6.59)]. The results are not explicitly shown in this thesis.

bound states, we can compute both the (tunneling) Josephson and the transverse AJHE currents not only within the Furusaki-Tsukada approach, but equivalently also from the bound states' wave functions. In this section, we recalculate the AJHE currents discussed in Sec. 9.3 starting from the junction's bound states. The results provide an essential crosscheck for the Furusaki-Tsukada method and furthermore allow us to draw unique connections between the bound state spectrum and the AJHE.

9.4.1 Bound state-based supercurrent formula

Shortly speaking, we relate the junction's AJHE currents to its bound state wave functions in a similar manner as we accessed the (tunneling) Josephson current in Sec. 7.1. The full calculations are rather cumbersome and are carried out in all details in Appendix F. The final expression to obtain the *interfacial* AJHE current components reads as

$$I_\eta = -e \sum_{E_\mathrm{B}} \frac{|\Delta_\mathrm{S}(T)|}{2E_\mathrm{B}} \frac{\mathcal{A}_\eta}{(2\pi)^2} \int \mathrm{d}^2\mathbf{k}_\parallel \, \frac{\hbar k_\eta}{m} \Big[\big|e(\mathbf{k}_\parallel; E_\mathrm{B})\big|^2 + \big|f(\mathbf{k}_\parallel; E_\mathrm{B})\big|^2 + \big|g(\mathbf{k}_\parallel; E_\mathrm{B})\big|^2 + \big|h(\mathbf{k}_\parallel; E_\mathrm{B})\big|^2 \Big] \tanh\left(\frac{E_\mathrm{B}}{2k_\mathrm{B}T}\right), \quad (9.8)$$

where E_B refers to the emergent Andreev bound states' and YSR states' energies, and $e(\mathbf{k}_\parallel; E_\mathrm{B})$, $f(\mathbf{k}_\parallel; E_\mathrm{B})$, $g(\mathbf{k}_\parallel; E_\mathrm{B})$, as well as $h(\mathbf{k}_\parallel; E_\mathrm{B})$ represent the electronlike and holelike coefficients of the states' wave functions. The bound state energies E_B and their wave functions (see Appendix F for the specific equations) are determined following the same strategy as in Chap. 7, whereas the thermal occupation factor $\tanh[E_\mathrm{B}/(2k_\mathrm{B}T)]$ ensures that only occupied states count to the AJHE currents. Inspecting Eq. (9.8), the AJHE currents are basically obtained regarding all bound states occupied by electrons moving with velocity $v_\eta = (\hbar k_\eta)/m$ along the transverse $\hat{\eta}$-directions (subsequently called propagating electrons) and the respective states in which the counterpropagating electrons (traveling along $-\hat{\eta}$) reside. All these states carry AJHE currents given by the electrons' transverse velocities multiplied by their charge $-e$ and a wave function-dependent electron density "weighting factor". Nonzero AJHE currents require therefore that either the propagating or counterpropagating electrons raise greater amounts of transverse currents (otherwise their contributions, differing in sign, would cancel), basically mimicking the skew tunneling-induced transverse electron (density) imbalances. More concretely, this happens only if each propagating and its related counterpropagating electron tunnel through the ferromagnetic insulator via bound states with (slightly) different energies. The latter give rise to distinct "weighting factors" in Eq. (9.8), and the propagating and counterpropagating electrons' AJHE current parts – though flowing along opposite directions – do then not completely compensate. In other words, finite AJHE currents serve as clear experimental signatures of pronounced *bound state asymmetries* that occur with respect to reversals of electrons' transverse velocities (transverse wave vectors $\mathbf{k}_\parallel$).

9.4.2 Discussion of results

To elaborate more on the bound states' $\mathbf{k}_\parallel$-asymmetries and convince ourselves that they indeed found the AJHE currents' *microscopic* physical origin, we numerically compute the considered S/F-I/S junction's typical bound state spectrum and compare the outcomes against the expected AJHE signals.

We profoundly investigated *one-dimensional* S/F-I/S contacts' Andreev bound states and YSR states in Chap. 7, paying special attention to their modulations with the magnetic tunneling strength and the superconducting phase difference. However, the bound state features become much more subtle in the present *three-dimensional* junction, whose interfacial SOC scales *linearly* with the components of $\mathbf{k}_\parallel =$

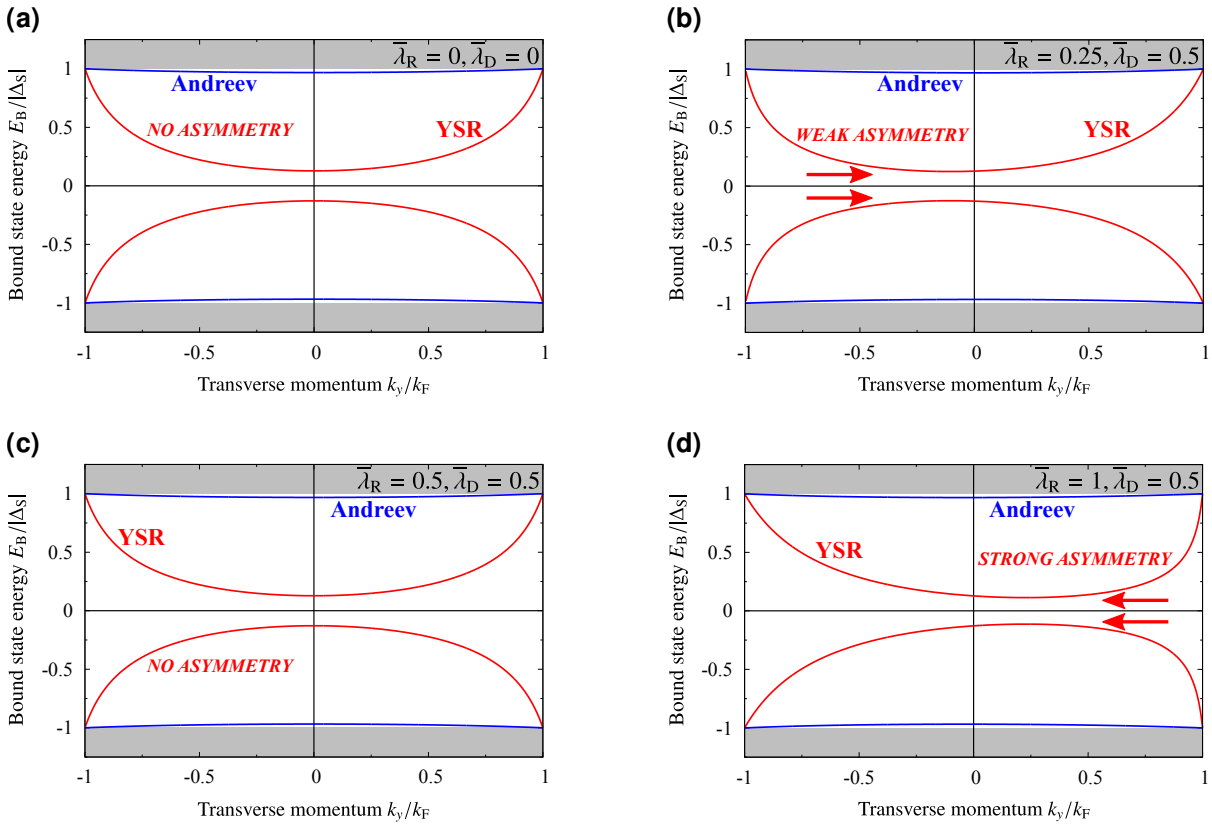


Fig. 9.5: **(a)** Calculated bound state energies of the Andreev bound states (blue) and YSR states (red) as functions of the transverse momentum k_y (normalized to the Fermi wave vector k_F) and for the scalar tunneling strength $\overline{\lambda}_{SC} = 1$, as well as the (exaggerated) magnetic tunneling strength $\overline{\lambda}_{MA} = 2$, assuming $k_x = 0$ and the superconducting phase difference $\phi_S = \pi/2$. The ferromagnetic-insulator barrier's magnetization is aligned along $\hat{x}$ (indicating that $\Phi = 0$), and both Rashba and Dresselhaus SOCs are absent ($\overline{\lambda}_R = \overline{\lambda}_D = 0$). **(b)** Same calculation as in **(a)**, but for the finite SOC strengths $\overline{\lambda}_R = 0.25$ and $\overline{\lambda}_D = 0.5$. The red arrows indicate k_y-regions for which the YSR bound state energies lie slightly closer to the gap center than their corresponding $(-k_y)$-states. **(c)** Same calculation as in **(a)**, but for the finite SOC strengths $\overline{\lambda}_R = 0.5$ and $\overline{\lambda}_D = 0.5$. **(d)** Same calculation as in **(a)**, but for the finite SOC strengths $\overline{\lambda}_R = 1$ and $\overline{\lambda}_D = 0.5$. The red arrows indicate k_y-regions for which the YSR bound state energies lie notably closer to the gap center than their corresponding $(-k_y)$-states.

$[k_x, k_y, 0]^\top$ (i.e., with k_x and k_y) and facilitates nontrivial asymmetries in the bound state energies when reversing $\mathbf{k}_\parallel$'s sign. Figure 9.5 plots the numerically extracted Andreev bound state and YSR state energies as functions of the transverse momentum k_y, keeping, for simplicity, $k_x = 0$ and the superconducting phase difference $\phi_S = \pi/2$ constant. The scalar tunneling parameter $\overline{\lambda}_{SC} = (2m\lambda_{SC})/(\hbar^2 k_F) = 1$ is the same as in all previous calculations, whereas its magnetic tunneling counterpart is set to an exaggeratedly large value of $\overline{\lambda}_{MA} = (2m\lambda_{MA})/(\hbar^2 k_F) = 2$ to observe clear trends. The ferromagnetic insulator's in-plane magnetization is oriented along the $\hat{x}$-direction (indicating $\Phi = 0$).

In the absence of interfacial SOC, both the Andreev bound states' and the YSR states' energies are not affected by reversing k_y's sign; see Fig. 9.5(a). Since no $\mathbf{k}_\parallel$-dependent bound state asymmetries arise, electrons propagating along the transverse $\hat{y}$-direction and their counterpropagating electrons always carry the same AJHE currents along opposite directions, and no net AJHE response builds up, coinciding with our skew tunneling mechanism that likewise breaks down in the absence of SOC. The situation changes when the SOC strengths start to increase. In Fig. 9.5(b), we suppose the finite Rashba and Dresselhaus SOC strengths $\overline{\lambda}_R = (2m\alpha)/\hbar^2 = 0.25$ and $\overline{\lambda}_D = (2m\beta)/\hbar^2 = 0.5$. Focusing on the YSR branch of

the spectrum, we already assert minor indications of a k_y-dependent bound state asymmetry, i.e., the YSR states at small negative k_y-values lie slightly closer to the gap center than the respective positive k_y-states [additionally emphasized by red arrows in Fig. 9.5(b)]. According to our formal arguments in the previous part, this k_y-bound state asymmetry must support a nonzero AJHE current along $\hat{y}$. Similar asymmetries emerge, in fact, for the Andreev bound states, but these are much weaker and barely visible – mostly because the Andreev bound states are always located more around the gap edges anyway and therefore less sensitive to parameter changes, i.e., also to reversals of k_y.

Further enhancing the Rashba SOC parameter (while leaving the Dresselhaus SOC constant) or the magnetic tunneling measure may even lead to more distinct bound state asymmetries as becoming evident, e.g., at $\overline{\lambda}_\mathrm{R} = 1$ in Fig. 9.5(d). It is now moreover the positive k_y-range for which the YSR states are located deeper inside the superconducting gap, suggesting that simultaneously the direction (sign) of the AJHE current gets reversed. Equal Rashba and Dresselhaus SOCs behave in an extraordinary fashion [see Fig. 9.5(c)] since their k_y-dependent SOC parts of the ferromagnetic insulator's Hamiltonian [recall Eq. (9.3)] drop then out and we eventually recover the case without any SOC (under the aforementioned assumptions). Thus, the bound states' k_y-asymmetries disappear and no AJHE current is maintained, just as we calculated in Fig. 9.3(b) (see the dark red curve there) and attributed to the suppression of skew Andreev reflections. All the outlined connections provide clear evidence that AJHEs in S/F-I/S junctions can equivalently be understood either in terms of skew Andreev reflections or within SOC-controlled $\mathbf{k}_\parallel$-asymmetries in the bound states forming around the ferromagnetic-insulator interface. Particularly the latter could be substantially rewarding for us since they allow us to gain novel physical insight that goes beyond the findings of earlier works.

At much lower magnetic tunnelings, however, the bound state asymmetries and thereby the AJHE currents become notably damped. To resolve the bound state asymmetries even at the extremely weak magnetic tunneling parameter $\overline{\lambda}_\mathrm{MA} = 0.005$ considered for all calculations in Sec. 9.3, we rather compute the absolute squares of the states' real-space bound state wave functions belonging to the $(k_\eta > 0)$- and the $(-k_\eta)$-states, i.e., $\left|\Psi(x, y, z; k_x > 0, k_y > 0; E_\mathrm{B})\right|^2$ and $\left|\Psi(x, y, z; -k_x, -k_y; E_\mathrm{B})\right|^2$, and finally evaluate their absolute square *differences*

$$\Delta \text{ W. f. s.} = \left|\Psi(x, y, z; k_x > 0, k_y > 0; E_\mathrm{B})\right|^2 - \left|\Psi(x, y, z; -k_x, -k_y; E_\mathrm{B})\right|^2. \tag{9.9}$$

As long as SOC remains absent, the energies of the bound states occurring at $k_\eta > 0$ and $-k_\eta$, and likewise their wave functions' absolute squares, are equal and Δ W. f. s. = 0. Nonzero Δ W. f. s. are hence direct measures for k_η-dependent bound state asymmetries; more specifically, Δ W. f. s. > 0 indicates that the wave function squares at $k_\eta > 0$ exceed their $(-k_\eta)$-counterparts and vice versa. Rewriting the AJHE current formula in Eq. (9.8) by means of Δ W. f. s. yields (see Appendix F for details)

$$I_\eta \propto -|k_\eta| \sum_{E_\mathrm{B}} \int_{k_x>0} \mathrm{d}k_x \int_{k_y>0} \mathrm{d}k_y \; (\Delta \text{ W. f. s.})\Big|_{z\to 0_+} \tanh\left(\frac{E_\mathrm{B}}{2k_\mathrm{B}T}\right) \tag{9.10}$$

and mathematically confirms our previous claim. Experimentally detectable AJHE signals are microscopically caused by bound state SOC asymmetries and increase with their strength (i.e., with Δ W. f. s.). Figure 9.6(a) presents the numerically determined wave function squares of Andreev bound states and YSR states as functions of the transverse momentum k_y. To simplify our analysis, we set $k_x = 0$. For the tunneling and SOC measures, we substitute the realistic values $\overline{\lambda}_\mathrm{SC} = 1$, $\overline{\lambda}_\mathrm{MA} = 0.005$, $\overline{\lambda}_\mathrm{R} = 1$, and $\overline{\lambda}_\mathrm{D} = 0.5$, whereas the finite superconducting phase difference $\phi_\mathrm{S} = \pi/2$ is used to demonstrate that our predictions are universal and not necessarily restricted to zero phase difference. The expected k_y-asymmetries in the bound state wave function squares are indeed thus tiny that we cannot properly resolve them within this plot. Therefore, we exemplarily take the wave function squares at $k_y = \pm 0.99 k_\mathrm{F}$ and quantify the asymmetry evaluating the respective Δ W. f. s., whose spatial dependence is shown

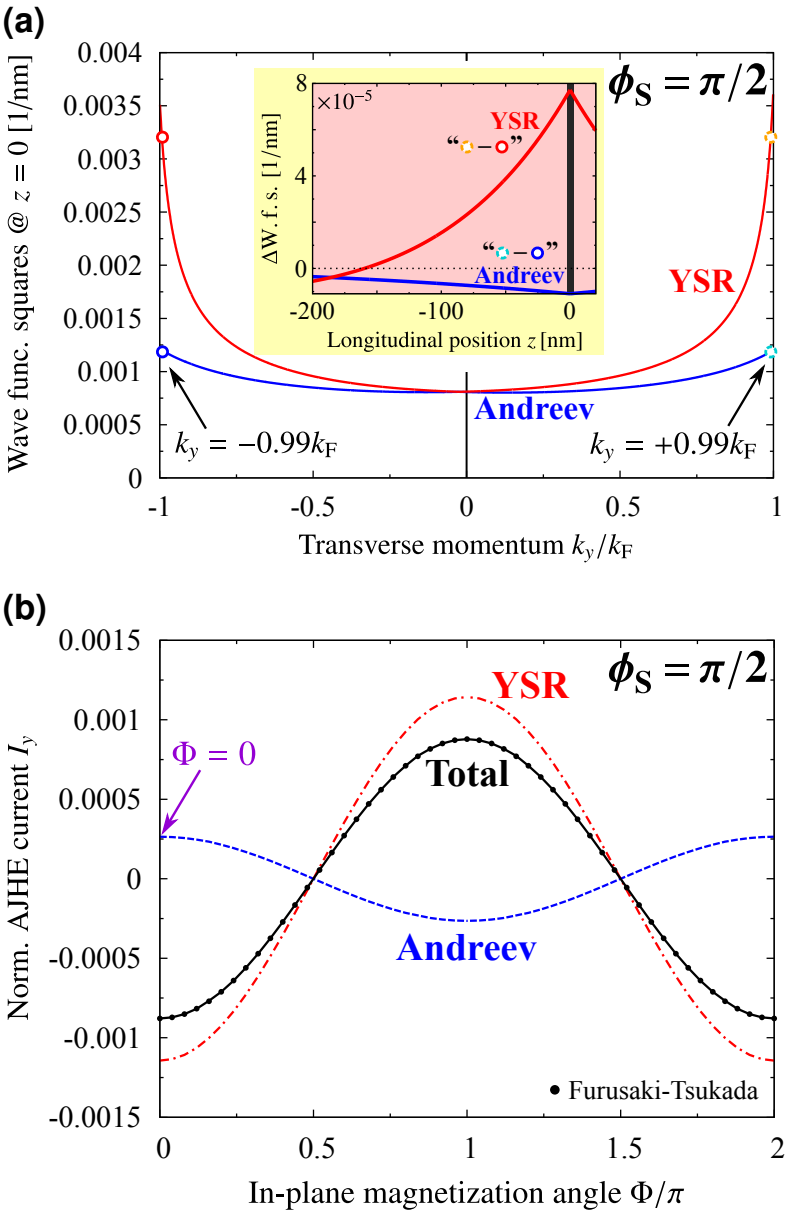


Fig. 9.6: **(a)** Calculated dependence of the *interfacial* ($z = 0$) bound state wave functions' absolute squares on the transverse momentum k_y (normalized to the Fermi wave vector k_F) and for the superconducting phase difference $\phi_S = \pi/2$, setting $k_x = 0$ and $\Phi = 0$. The Rashba SOC strength is $\overline{\lambda}_R = 1$ and all other parameters are the same as in Fig. 9.3. The blue curve corresponds to Andreev bound states and the red curve to YSR states. The inset illustrates the *spatial dependence* of the bound state wave functions' absolute square *differences* Δ W. f. s. – exemplarily in the left superconductor ($z < 0$) and for $|k_y| = 0.99k_F$, as a deeper analysis (see Appendix F) suggests that the dominant AJHE current contributions stem from states with $|\mathbf{k}_\parallel| \to k_F$. The positive YSR tail indicates that the wave function squares at $k_y = 0.99k_F$ exceed those at $k_y = -0.99k_F$ (and vice versa for the Andreev bound states). Though being small (as expected from the rather small AJHE currents), the k_y-asymmetry explained in the text becomes clearly evident. **(b)** Dependence of the AJHE current I_y (normalized as in Fig. 9.3) on the ferromagnetic insulator's in-plane magnetization angle Φ and for the Rashba SOC strength $\overline{\lambda}_R = 1$, *calculated from the bound state spectrum*. All other parameters are the same as in Fig. 9.3 apart from the superconducting phase difference $\phi_S = \pi/2$. The individual contributions of Andreev bound states and YSR states are separately resolved, while the black dots represent the respective AJHE current obtained from the Furusaki-Tsukada approach as a crosscheck.

in Fig. 9.6(a)'s inset and clearly reveals the bound states' k_y-asymmetries. Regarding the choice of k_y, we wish to mention that analogous results for Δ W. f. s. are actually obtained at all $|k_y| \in]0; k_\mathrm{F}]$ (see Fig. F.1 in Appendix F). The largest Δ W. f. s. and greatest AJHE currents arise, nevertheless, at $|k_y| \to k_\mathrm{F}$, motivating to study, for instance, $|k_y| = 0.99 k_\mathrm{F}$.

As we already deduced when exploring the generic bound state features in the previous part, the k_y-asymmetries are again more pronounced for the spectrum's YSR than for its Andreev bound state branches (entailing greater Δ W. f. s.) and their corresponding Δ W. f. s. differ in signs. Translating both observations into AJHE currents, we propose that the YSR states' individual currents must be the dominant ones [recall that the AJHE current amplitudes increase with Δ W. f. s.; see Eq. (9.10)] and flow along opposite directions when compared to the Andreev bound states' current contributions. Calculating the AJHE current I_y directly from the bound state spectrum by means of Eq. (9.8) – see Fig. 9.6(b) and assume $\mathcal{A}_x = \mathcal{A}_y = \mathcal{A}$ – indeed verifies all our previous predictions, and confirms the distinct coincidence between the bound state asymmetries on the one and the AJHE on the other hand. As another crosscheck, the black dots represent the related AJHE current extracted from the Furusaki-Tsukada approach [recall Eq. (9.7)], which perfectly agrees with the current evaluated from the bound states. Although the second method is computationally more demanding and generalizations to different junctions might not be straightforward, it allows us to gain valuable physical insight and draw unprecedented microscopic connections between junctions' spectral properties and their transport features.

Attributing the AJHE responses to SOC-controlled $\mathbf{k}_\parallel$-asymmetries in the emerging bound states, we can eventually also give physical reasoning for the currents' peculiar magnetization angle dependence. The bound state asymmetries are basically caused by the intriguing interplay between the barrier's magnetic exchange coupling and the interfacial SOC. If the barrier would be nonmagnetic, the bound state spectrum simply consists of usual Andreev bound states and its asymmetries (and likewise the AJHE currents) immediately disappear – even in the presence of SOC. Looking up the magnetization and SOC parts of the barrier Hamiltonian [see Eq. (9.3)], we recognize that fully aligning the magnetization along the $\hat{x}$-direction (i.e., $\Phi = 0$) couples the exchange and k_y-dependent SOC terms via the $\hat{\sigma}_x$-Pauli matrix. The result is the bound states' distinct k_y-asymmetry becoming evident in Figs. 9.5 and 9.6(a), while no k_x-asymmetries can be detected (the related calculations are not explicitly depicted). The I_y-AJHE current becomes consequently maximal at $\Phi = 0$ and I_x vanishes. Contrary, magnetizations pointing along $\hat{y}$ (i.e., $\Phi = \pi/2$) involve the SOC Hamiltonian's k_x-parts, giving rise to unique k_x-bound state asymmetries (whose features are essentially similar to the discussed k_y-asymmetries) and maximal I_x, whereas the k_y-asymmetries and I_y are completely suppressed. Intermediate magnetization angles $0 < \Phi < 2\pi$ couple the exchange Hamiltonian to both the SOC's k_x- and k_y-terms, and raise thus simultaneously nonzero I_x and I_y.

9.5 Anomalous Josephson spin Hall effect currents

Besides the AJHE charge supercurrents, their transverse spin current counterparts might provide appealing ingredients for future spintronics applications. When tunneling through the spin-active ferromagnetic-insulator interface, some of the spin-singlet Cooper pairs' electrons flip their spins and generate spin-polarized triplet pairs [467]. Those pairs' *spin wave functions* may be composed of all possible triplet pairings $|\uparrow\uparrow\rangle$, $|\downarrow\downarrow\rangle$, and $(|\uparrow\downarrow\rangle + |\downarrow\uparrow\rangle)/\sqrt{2}$, where $|\uparrow\rangle$ ($|\downarrow\rangle$) denotes a single-electron spin-up (spin-down) state with respect to the $\hat{z}$-spin quantization axis (inside the superconductors). The $(|\uparrow\downarrow\rangle+|\downarrow\uparrow\rangle)/\sqrt{2}$-contribution is usually neglected since it decays rapidly inside real tunneling barriers [467]. The remaining $|\uparrow\uparrow\rangle$- and $|\downarrow\downarrow\rangle$-pairs, however, are subject to the proposed skew tunneling mechanism and may separate along the transverse directions. From that point of view, skew tunneling acts like a transverse "Cooper pair

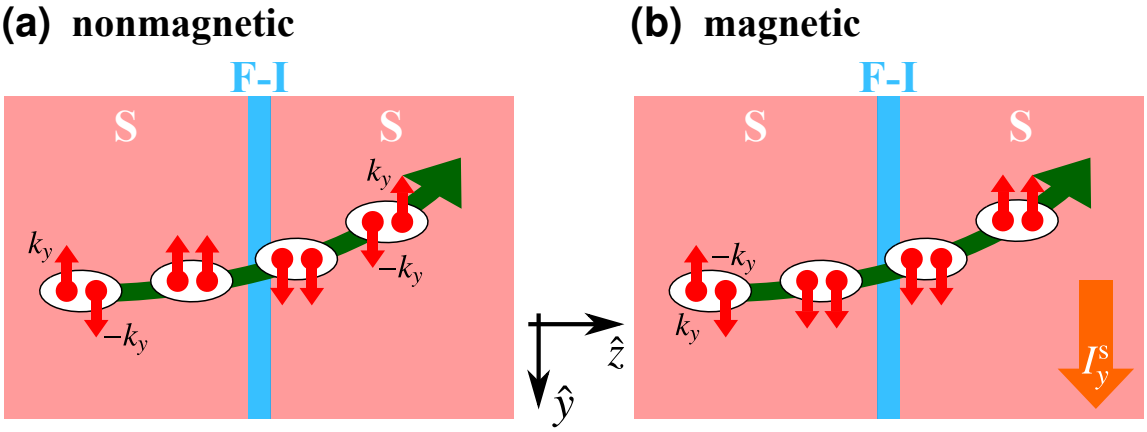


Fig. 9.7: (a) Schematical illustration of the Cooper pair skew tunneling from the left into the right superconductor (S). Each Cooper pair initially consists of one spin-up electron with transverse momentum $k_y > 0$ and one spin-down electron with $-k_y$, assuming, for simplicity, $k_x = 0$. When tunneling through the ferromagnetic-insulator (F-I) interface, at which the present SOC gives rise to nonzero *spin-flip probabilities*, some Cooper pair electrons flip their spins, converting spin-unpolarized singlet into spin-polarized triplet pairs. In the absence of magnetic tunnelings (meaning that $\lambda_{\mathrm{MA}} = 0$), interfacial spin flips generate *on average* the same amounts of polarized $|\uparrow\uparrow\rangle$- and $|\downarrow\downarrow\rangle$-Cooper pairs (per transverse channel), and the overall transverse spin current vanishes. **(b)** If magnetic tunneling is present ($\lambda_{\mathrm{MA}} \neq 0$), interfacial spin flips cause an excess of either $|\uparrow\uparrow\rangle$- or $|\downarrow\downarrow\rangle$-pairs in the $(-\hat{y})$-skew tunneling channel and vice versa in the channel along $\hat{y}$. The result is a finite transverse spin supercurrent, denoted by I_y^s and highlighted by the orange arrow.

spin filter" and generates nonzero transverse spin supercurrent flows, combining the advantages of the conventional spin Hall effect [429, 430] with the dissipationless character of supercurrents.

Anyhow, earlier studies [449] concluded that superconducting junctions' fundamental electron-hole (time-reversal) symmetry suppresses the spin Hall effect. The recent prediction of sizable TSHE spin currents in N/N junctions [440], essentially triggered by interfacial skew tunnelings analogously to our study, boosted new hopes to efficiently integrate the spin Hall effect into superconducting tunnel junction geometries. Nonetheless, we demonstrated in Sec. 8.5 that replacing one of the junctions' normal-conducting electrodes by a superconductor dramatically impacts the underlying physics. The resulting strong competition between skew specular and skew Andreev reflections (being another consequence of the electron-hole symmetry) must again heavily suppress the superconducting systems' TSHE spin currents.

Before evaluating the transverse spin current components that flow through the considered S/F-I/S Josephson junction, we therefore need to understand their intimate relation to triplet pair skew tunnelings in order to make precise predictions concerning the required parameter regimes that might support sizable spin currents. Both superconductors act as reservoirs for spin-singlet Cooper pairs, each consisting of two electrons with opposite spins and antiparallel transverse wave vectors (recall that $\mathbf{k}_\parallel = [k_x, k_y, 0]^\top$). To be more specific, the allowed spin and transverse wave vector configurations of the Cooper pairs are $(\mathbf{k}_\parallel, \uparrow; -\mathbf{k}_\parallel, \downarrow)$, $(-\mathbf{k}_\parallel, \downarrow; \mathbf{k}_\parallel, \uparrow)$, $(\mathbf{k}_\parallel, \downarrow; -\mathbf{k}_\parallel, \uparrow)$, and $(-\mathbf{k}_\parallel, \uparrow; \mathbf{k}_\parallel, \downarrow)$; the two parts always indicate the transverse wave vector and spin of the first and second electron forming one singlet pair.[4] Approaching the barrier, the Cooper pairs are exposed to the aforementioned skew tunnelings, which spatially separate

[4] As the electrons forming one Cooper pair are indistinguishable, the first and second (as well as the third and fourth) of the given Cooper pair configurations are identical. However, we mention all four configurations since each is essentially related to one of the four Andreev reflection processes whose reflection coefficients finally enter the formula to evaluate the transverse spin current components [see, e.g., Eq. (9.11)].

them along the transverse $\hat{\eta} \in \{\hat{x}; \hat{y}\}$-directions. If the $(\mathbf{k}_\parallel, \uparrow; -\mathbf{k}_\parallel, \downarrow)$- and $(-\mathbf{k}_\parallel, \downarrow; \mathbf{k}_\parallel, \uparrow)$-pairs are, e.g., predominantly transmitted at $\eta < 0$, the remaining pairs preferentially tunnel at positive η.

As long as the barrier is *nonmagnetic*, the numbers of Cooper pairs involved in the skew tunneling processes at $\eta < 0$ and $\eta > 0$ are equal. Thus, the transverse $\hat{\eta}$- and $(-\hat{\eta})$-channels always generate equal AJHE charge current contributions that flow along reversed directions and explain the nonmagnetic junction's overall vanishing AJHE currents. Close to the barrier, the interfacial SOC gives additionally rise to nonzero *spin-flip probabilities*, mostly determined by the respective spin-flip potential V_{flip}. In the nonmagnetic junction (and assuming $\beta = 0$, as well as $k_x = 0$, to further simplify our considerations), we deduce $V_{\text{flip}} \propto \alpha k_y \sigma$, where k_y and σ denote one Cooper pair electron's $\hat{y}$-component of $\mathbf{k}_\parallel$ and its spin [note the close analogy with Eq. (9.6)]. In our case, this means that a Cooper pair's spin-up electron with $k_y > 0$ flips its spin with the same probability as the pair's spin-down electron with $-k_y$. Each transverse skew tunneling channel (along $\pm\hat{y}$) contains then *on average* the same amounts of $|\uparrow\uparrow\rangle$- and $|\downarrow\downarrow\rangle$-triplet pairs, and no transverse spin currents occur [see Fig. 9.7(a) for illustration]. To get the full picture, one would also need to include the electron Cooper pairs tunneling oppositely, i.e., from right to left (or hole pairs tunneling from left to right), just as when unraveling the AJHE currents' ϕ_{S}-dependence in Fig. 9.4. But since similar arguments apply to hole Cooper pairs, this would still not lead to finite transverse spin currents.

The physics becomes more intriguing if the barrier gets (at least weakly) *magnetic*. The Cooper pair electrons' spin-flip probabilities are then governed by the spin-flip potential $V_{\text{flip}} \propto \lambda_{\text{MA}} \sin(\Phi)\sigma + \alpha k_y \sigma$ and become asymmetric with respect to the electrons' spins. A k_y-electron with spin up flips its spin now with a different probability than a spin-down electron with opposite momentum $-k_y$. Therefore, each skew tunneling channel along $-\hat{y}$ comprises an excess of either $|\uparrow\uparrow\rangle$- or $|\downarrow\downarrow\rangle$-pairs and the channels along $\hat{y}$ either more $|\downarrow\downarrow\rangle$- or $|\uparrow\uparrow\rangle$-pairs. The result is a nonzero transverse spin current; see Fig. 9.7(b). Note that, aside from the configuration involving magnetic barriers, one could achieve similar effects, e.g., by replacing one of the superconducting electrodes by a noncentrosymmetric superconductor inducing strong bulk Rashba SOC [470]. Furthermore, our qualitative explanations suggest that a reversal of λ_{MA}'s sign must be sufficient to reverse the direction (sign) of the spin current since this concurrently reverses the sign of the spin-dependent magnetization part of the spin-flip determining V_{flip}.

9.5.1 Generalized Furusaki-Tsukada spin supercurrent formula

To quantify the transverse $\hat{\sigma}_z$-*particle*[5] spin currents in our junction, we can either extend the Furusaki-Tsukada technique (see, e.g., Ref. [451] for similar generalizations) or the bound state-based approach. The $\hat{\sigma}_x$- and $\hat{\sigma}_y$-spin currents vanish owing to the specific structure of the scattering states inside the superconductors (see Appendix F). *Close to the interface*, the generalized Furusaki-Tsukada description yields

$$I^{\text{s}}_{\eta,\hat{z}} \approx -\frac{k_{\text{B}}T}{4}|\Delta_{\text{S}}(T)|\frac{\mathcal{A}_\eta}{(2\pi)^2}\int \text{d}^2\mathbf{k}_\parallel \sum_{\omega_n} \frac{k_\eta}{\sqrt{k_{\text{F}}^2 - \mathbf{k}_\parallel^2}}\left[\frac{-C^{(1)}(\text{i}\omega_n) + \mathcal{D}^{(2)}(\text{i}\omega_n) + \mathcal{A}^{(3)}(\text{i}\omega_n) - \mathcal{B}^{(4)}(\text{i}\omega_n)}{\sqrt{\omega_n^2 + |\Delta_{\text{S}}(T)|^2}}\right]$$

$$= \frac{k_{\text{B}}T}{4}|\Delta_{\text{S}}(T)|\frac{\mathcal{A}_\eta}{(2\pi)^2}\int \text{d}^2\mathbf{k}_\parallel \sum_{\omega_n} \frac{k_\eta}{\sqrt{k_{\text{F}}^2 - \mathbf{k}_\parallel^2}}\left[\frac{C^{(1)}(\text{i}\omega_n) - \mathcal{D}^{(2)}(\text{i}\omega_n) - \mathcal{A}^{(3)}(\text{i}\omega_n) + \mathcal{B}^{(4)}(\text{i}\omega_n)}{\sqrt{\omega_n^2 + |\Delta_{\text{S}}(T)|^2}}\right]. \quad (9.11)$$

Equation (9.11) basically follows from the related AJHE charge current formula [recall Eq. (9.7)] replacing the electron charge $-e$ by $\hbar/(2e)$ and weighting the involved Andreev reflections' contributions

[5] We compute again *particle* spin currents that only distinguish between spins, but do not take care of electrons' and holes' opposite charges – in contrast to the AJHE charge currents.

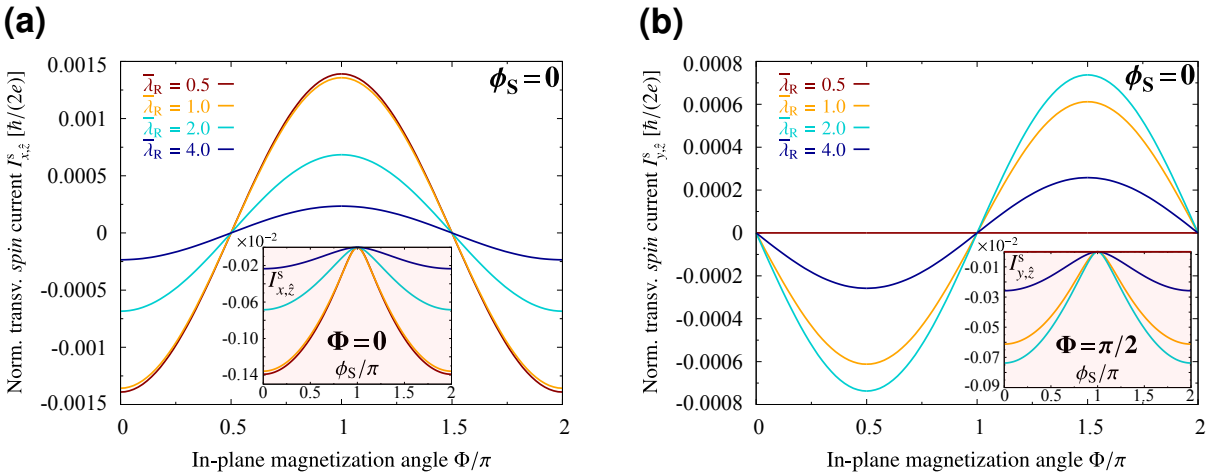


Fig. 9.8: Calculated dependence of the *zero-phase difference* $\hat{\sigma}_z$-spin currents **(a)** $I^s_{x,\hat{z}}$ and **(b)** $I^s_{y,\hat{z}}$ [given in units of $\hbar/(2e)$ and normalized according to $[I^s_{x\,(y),\hat{z}} e R_S]/[|\Delta_S(0)|\pi]$, where $R_S = (2\pi h)/(\mathcal{A}e^2 k_F^2)$ corresponds to Sharvin's resistance of a perfectly transparent (three-dimensional) metallic point contact] on the ferromagnetic insulator's in-plane magnetization angle Φ and for the same parameters considered in Fig. 9.3. The insets show the *maximal* spin currents (i.e., $I^s_{x,\hat{z}}$ at $\Phi = 0$ and $I^s_{y,\hat{z}}$ at $\Phi = \pi/2$) as functions of the superconducting phase difference ϕ_S.

according to the reflected electrons' (holes') spins. To give one particular example, we focus on the part scaling with $C^{(1)}$ that characterizes an incident spin-up electronlike quasiparticle propagating along the transverse $\hat{\eta}$-directions and getting Andreev reflected as a spin-up holelike quasiparticle. Although the retroreflected hole still possesses the *same spin*, it moves along the *opposite transverse directions* when compared to the initial electron and its contribution to the overall particle spin currents must be counted *negatively*. Given the sign of the $C^{(1)}$-term, those of all other Andreev reflections can be consistently chosen, finally ending up with the expression stated in Eq. (9.11).

Alternatively, we can extract the spin currents from the junction's bound state spectrum, analogously to the procedure we applied to attain the AJHE charge currents. Substituting $-e \longmapsto \hbar/(2e)$ in the bound state AJHE current formula [see Eq. (9.8)], and recognizing that the electronlike parts of spin-up [$\propto |e(\mathbf{k}_\parallel; E_B)|^2$] and spin-down [$\propto |f(\mathbf{k}_\parallel; E_B)|^2$] bound states enter with opposite signs – and vice versa for the holelike parts [$\propto |g(\mathbf{k}_\parallel; E_B)|^2$ and $\propto |h(\mathbf{k}_\parallel; E_B)|^2$] which move per se along reversed transverse directions –, we obtain

$$I^s_{\eta,\hat{z}} = \frac{\hbar}{2} \sum_{E_B} \frac{|\Delta_S(T)|}{2E_B} \frac{\mathcal{A}_\eta}{(2\pi)^2} \int \mathrm{d}^2\mathbf{k}_\parallel \frac{\hbar k_\eta}{m} \Big[\big|e(\mathbf{k}_\parallel; E_B)\big|^2 - \big|f(\mathbf{k}_\parallel; E_B)\big|^2 - \big|g(\mathbf{k}_\parallel; E_B)\big|^2 + \big|h(\mathbf{k}_\parallel; E_B)\big|^2 \Big] \tanh\left(\frac{E_B}{2k_B T}\right). \quad (9.12)$$

9.5.2 Discussion of results

Figure 9.8 illustrates the dependence of the transverse spin current components $I^s_{x,\hat{z}}$ and $I^s_{y,\hat{z}}$ on the ferromagnetic insulator's in-plane magnetization angle Φ – computed from the Furusaki-Tsukada spin current formula in Eq. (9.11) setting $\mathcal{A}_x = \mathcal{A}_y = \mathcal{A}$ – for the same set of parameters considered when elaborating on the AJHE charge currents (see Fig. 9.3). As we deduced from the preceding qualitative skew tunneling arguments, the transverse spin currents immediately vanish once the barrier becomes nonmagnetic (i.e., if we set $\lambda_{MA} = 0$). Already the weak magnetic tunneling strength $\bar{\lambda}_{MA} = (2m\lambda_{MA})/(\hbar^2 k_F) = 0.005$,

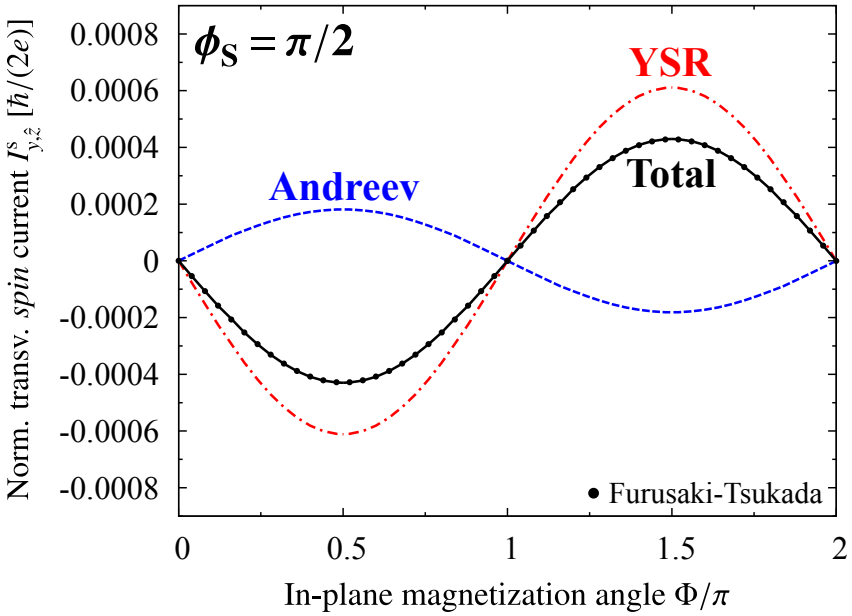


Fig. 9.9: Calculated (*from the bound state spectrum*) dependence of the $\hat{\sigma}_z$-spin current $I^s_{y,\hat{z}}$ [given in units of $\hbar/(2e)$ and normalized as in Fig. 9.8] on the ferromagnetic insulator's in-plane magnetization angle Φ and for the Rashba SOC strength $\bar{\lambda}_R = 1$. Apart from the superconducting phase difference $\phi_S = \pi/2$, all parameters are the same as in Fig. 9.3. The individual contributions of Andreev bound states and YSR states are separately resolved, while the black dots represent the respective spin current obtained from the Furusaki-Tsukada approach as a crosscheck.

however, triggers sizable transverse spin current responses, whose directions (signs) can moreover be reversed by changing $\bar{\lambda}_{MA}$'s sign, just as predicted when inspecting the generic form of the spin-flip potential that creates the spin current-carrying triplet pairs. Regarding the spin currents' Φ-dependencies, we observe an experimentally promising trend. While the AJHE charge currents scale as $I_x \propto \sin(\Phi)$ and $I_y \propto \cos(\Phi)$, the spin currents obey $I^s_{x,\hat{z}} \propto \cos(\Phi)$ and $I^s_{y,\hat{z}} \propto \sin(\Phi)$. The reason for that behavior must be traced back to the characteristic spin-flip potentials V_{flip} that modulate with Φ in the same ways as the spin currents; recall, e.g., our previous comments on V_{flip} responsible for the spin current along $\hat{y}$. The spin-flip potentials facilitate interfacial spin flips, which convert spin-unpolarized singlet into spin-polarized triplet pairs and therefore drive the transverse spin currents, justifying the intimate coincidence between the spin-flip potentials' and the emergent spin currents' Φ-dependencies. The AJHE charge and transverse spin currents' well-distinguished Φ-variations serve not only as a fundamental fingerprint to separate both phenomena, but additionally allow for maximal spin currents precisely at those magnetization orientations at which their AJHE charge current counterparts (along one fixed transverse direction) vanish. Tuning the magnetization angle provides consequently an efficient control knob to switch between pure AJHE charge and transverse spin current regimes – in sharp contrast to F/S junctions, in which this control is missing and finite transverse spin currents inevitably come along with nonzero TAHE charge currents. The strong suppression of TSHEs probably counts to F/S junctions' greatest deficit in the framework of future spintronics applications. Our predictions to implement distinct charge and spin current regimes into one single S/F-I/S Josephson junction, utilizing their unique magnetization direction variations, might make such systems much more attractive to researchers. Owing to the occurring (pure) spin currents' close analogy with the conventional spin Hall effect, we term the phenomenon *anomalous Josephson spin Hall effect*; *anomalous* emphasizes that the junction needs to be (at least weakly) magnetic which is not essential for the conventional spin Hall effect.

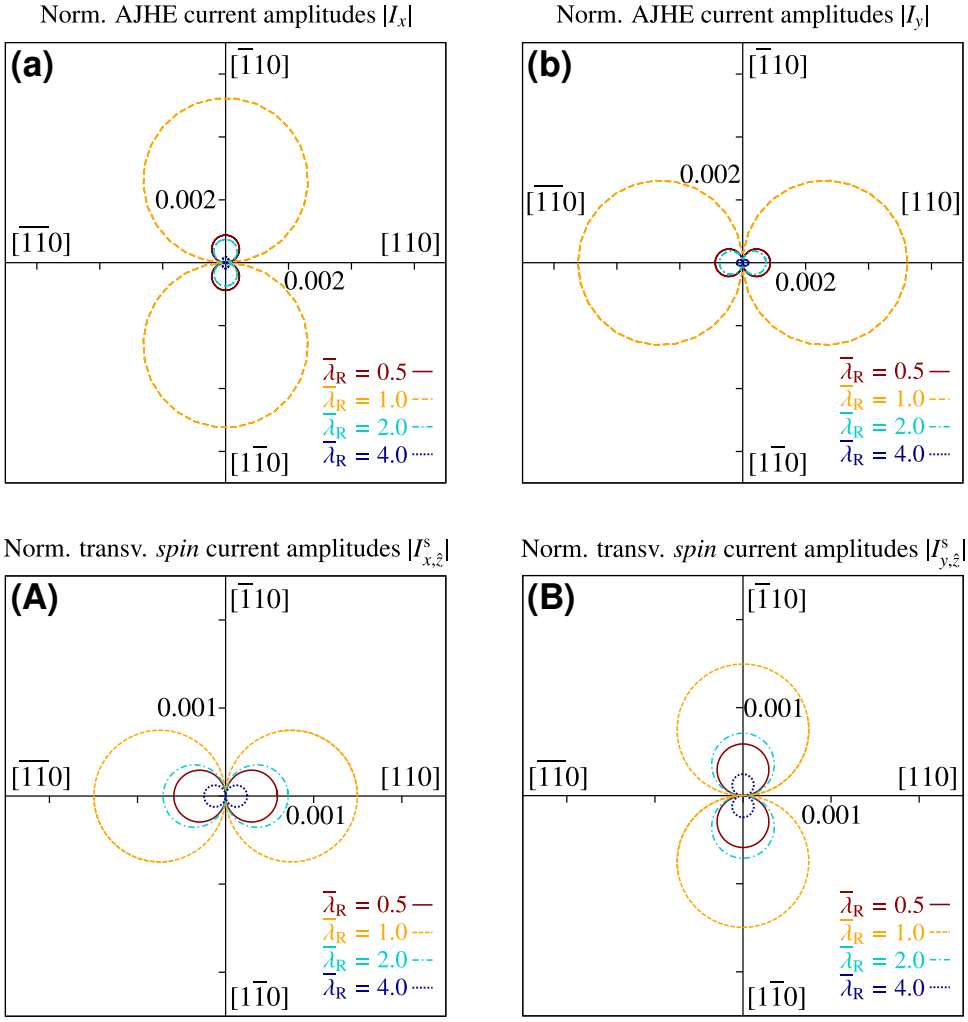


Fig. 9.10: (a) [**(b)**] Calculated *angular* dependence of the *zero-phase difference* AJHE charge current *amplitudes* $|I_x|$ ($|I_y|$) on the ferromagnetic insulator's in-plane magnetization angle Φ. All parameters and the normalization are the same as in Fig. 9.3 except that Dresselhaus SOC is now absent ($\bar{\lambda}_D = 0$). **(A)** [**(B)**] Similar calculations as in **(a)** [**(b)**], but for the transverse $\hat{\sigma}_z$-spin current *amplitudes* $|I^s_{x,\hat{z}}|$ ($|I^s_{y,\hat{z}}|$), given in units of $\hbar/(2e)$ and normalized as in Fig. 9.8.

Keeping in mind that the spin currents' features are dominated by the respective spin-flip potentials, we can also understand the superconducting phase difference's role. The spin-flip potentials do not explicitly depend on ϕ_S. Varying ϕ_S does hence not qualitatively alter the spin current flows, i.e., not change the currents' directions (signs), but simply introduces the previously mentioned "bias" between forward and backward tunnelings. The larger ϕ_S (restricting ourselves to $0 \leq \phi_S \leq \pi$), the less Cooper pairs skew tunnel through the interface and contribute to the spin currents (after being converted into triplet pairs). The spin current amplitudes must therefore monotonically decay with increasing ϕ_S (as long as $0 \leq \phi_S \leq \pi$), as the numerical calculations shown in Fig. 9.8's insets reveal. As mentioned before, equal Rashba and Dresselhaus SOCs completely suppress the skew tunneling mechanism along $\hat{y}$, leading not only to vanishing AJHE charge current ($I_y = 0$), but simultaneously also to zero spin current ($I^s_{y,\hat{z}} = 0$) along that direction; see the dark red curves in Figs. 9.3(b) and 9.8(b).

Similarly to our AJHE charge current analyses, we additionally evaluate the transverse spin currents starting from the junction's bound state spectrum [by means of Eq. (9.12)]. We exemplarily present $I^s_{y,\hat{z}}$, together with its individual Andreev bound state and YSR state spin current parts, for the

Rashba SOC strength $\overline{\lambda}_{\mathrm{R}} = (2m\beta)/\hbar^2 = 1$ and the superconducting phase difference $\phi_{\mathrm{S}} = \pi/2$ in Fig. 9.9; all remain junction parameters are the same as before. Analogously to the AJHE charge currents, the transverse spin currents' amplitudes are likewise mostly determined by the YSR states, which contribute again with an opposite sign to the overall spin currents when compared to the Andreev bound states. The negative (positive) sign of the YSR states' (Andreev bound states') spin currents at magnetization angles $0 < \Phi < \pi$ indicates that spin-down (spin-up) Cooper pair electrons with transverse wave vectors $\mathbf{k}_{\parallel} = [k_x > 0,\, k_y > 0,\, 0]^{\top}$ are predominantly transferred through the ferromagnetic-insulator interface via the available YSR states (Andreev bound states). This observation's physical origin must be attributed to the states' peculiar spin characteristics we encountered in Sec. 7.2. For the given parameters, the YSR states at fixed $\mathbf{k}_{\parallel} = [k_x > 0,\, k_y > 0,\, 0]^{\top}$ correspond to spin-down states through which indeed only the spin-down electrons tunnel and the Andreev bound states refer to the spin-up states enabling spin-up electrons to overcome the barrier. An excess of spin-down electrons at $\mathbf{k}_{\parallel} = [k_x > 0,\, k_y > 0,\, 0]^{\top}$ eventually raises a negative spin current (as it is the case for the YSR states) and an excess of spin-up electrons a positive spin current (becoming evident in the Andreev bound states' contribution). The prefect agreement between the total spin currents obtained from the bound states and the moreover depicted spin currents extracted from the Furusaki-Tsukada formula [see Eq. (9.11)] persuades that both approaches yield reliable results and that the underlying bound state wave function asymmetries must indeed act as the universal microscopic driving force of AJHE charge and transverse spin currents in S/F-I/S Josephson junctions.

To demonstrate that the discovered physics does not necessarily require coexisting Rashba and Dresselhaus SOCs, we furthermore calculate all AJHE charge and transverse spin current components' magnetization angle dependencies assuming that just Rashba SOC (with different strengths) is present and Dresselhaus SOC is absent ($\overline{\lambda}_{\mathrm{D}} \propto \beta = 0$); the other parameters are not altered. This situation might often mimic the more common one in experiments since tunneling barriers inevitably introduce interfacial Rashba SOC due to the broken space-inversion symmetry, whereas only those additionally lacking bulk-inversion symmetry give rise to Dresselhaus SOC. The outcomes of our simulations are summarized in Fig. 9.10. Contrary to the (tunneling) Josephson current, whose magnetoanisotropic properties disappear if only either Rashba or Dresselhaus SOC is there (not explicitly shown; recall, e.g., the vanishing in-plane MAJCs we mentioned in Sec. 6.2), the AJHE charge and transverse spin currents' unique Φ-magnetoanisotropies remain clearly visible. The $\hat{x}$- and $\hat{y}$-AJHE currents' *maximal amplitudes* are given by $|I_x| \propto \alpha + \beta$ and $|I_y| \propto \alpha - \beta$ (similar relations hold for the transverse spin currents), and become therefore equal in the absence of Dresselhaus SOC. Appropriately chosen Rashba SOC strengths support even stronger AJHE charge and transverse spin current signals than interfering Rashba and Dresselhaus SOCs. Recording the currents' magnetization angle scaling and fitting the experimental data to our modeling might thus provide valuable insight into Josephson junctions' interfacial SOC.

9.6 Spin-charge-current cross ratios

In *weakly magnetic junctions*, both the AJHE charge and transverse spin currents increase in the same manner *linearly* with the magnetic tunneling parameter $\overline{\lambda}_{\mathrm{MA}} = (2m\lambda_{\mathrm{MA}})/(\hbar^2 k_{\mathrm{F}})$. The *spin-charge-current cross ratios*[6]

$$r_1 := \left| \frac{I^{\mathrm{s}}_{x,\hat{z}}}{I_y} \right| \qquad \text{and} \qquad r_2 := \left| \frac{I^{\mathrm{s}}_{y,\hat{z}}}{I_x} \right|, \tag{9.13}$$

[6] An alternative, and probably more intuitive, definition of spin-charge-current ratios might read as $r_1 := |I^{\mathrm{s}}_{x,\hat{z}}/I_x|$ and $r_2 := |I^{\mathrm{s}}_{y,\hat{z}}/I_y|$. However, owing to the distinct Φ-dependencies of $I^{\mathrm{s}}_{x,\hat{z}}$ and I_x ($I^{\mathrm{s}}_{y,\hat{z}}$ and I_y), these ratios would *not* become completely magnetization independent, i.e., only the $\overline{\lambda}_{\mathrm{MA}}$-dependence would drop out, but the Φ-dependence would remain.

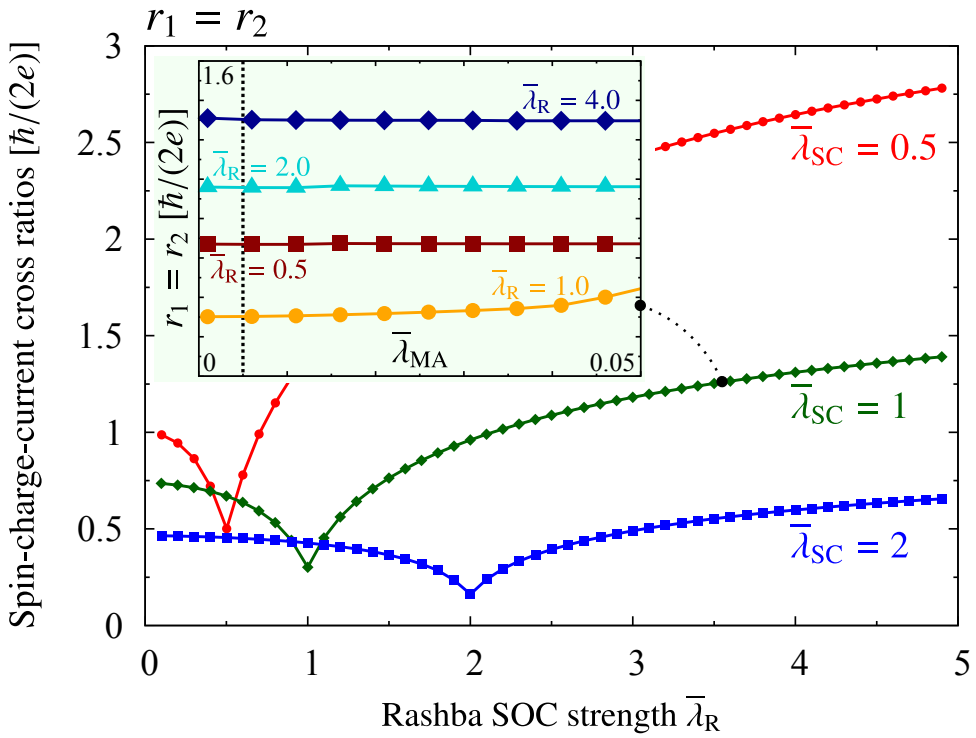


Fig. 9.11: Calculated dependence of the universal spin-charge-current cross ratios r_1 and r_2 [given in units of $\hbar/(2e)$] on the Rashba SOC strength $\overline{\lambda}_R$. Since Dresselhaus SOC is absent ($\overline{\lambda}_D = 0$), $r_1 = r_2$. All remaining parameters are the same as in Fig. 9.3 (i.e., also $\phi_S = 0$) except that the scalar tunneling strength gets gradually increased from $\overline{\lambda}_{SC} = 0.5$ (red) to $\overline{\lambda}_{SC} = 1$ (green) and finally to $\overline{\lambda}_{SC} = 2$ (blue). The inset shows r_1 (= r_2) as a function of the magnetic tunneling parameter $\overline{\lambda}_{MA}$ and for various indicated Rashba SOC strengths $\overline{\lambda}_R$ (again setting $\overline{\lambda}_D = 0$ for the Dresselhaus SOC), while $\overline{\lambda}_{SC} = 1$ is kept constant. The dotted vertical line indicates $\overline{\lambda}_{MA} = 0.005$ (assumed for all AJHE charge and spin current calculations), for which the spin-charge-current cross ratios become indeed universal (magnetization independent).

define then universal, *magnetization-independent*, measures that are uniquely determined by the SOCs' strengths [keeping the scalar tunneling measure $\overline{\lambda}_{SC} = (2m\lambda_{SC})/(\hbar^2 k_F)$ and the superconducting phase difference ϕ_S constant, and restricting ourselves to parameters for which all currents are nonzero] and might offer another possibility to classify Josephson junctions' interfacial SOC. Both ratios become, for instance, equal (i.e., $r_1 = r_2$) if only Rashba SOC is present, whereas the constructive (destructive) interferences of finite Rashba and Dresselhaus SOCs generally impact the $\hat{x}$- and $\hat{y}$-currents in a different manner so that generally $r_1 \neq r_2$ (as r_1 and r_2 both relate $\hat{x}$- and $\hat{y}$-currents at the same time). In Fig. 9.11, we illustrate the spin-charge-current cross ratios' scaling with respect to the Rashba SOC parameter $\overline{\lambda}_R = (2m\alpha)/\hbar^2$ in the absence of Dresselhaus SOC ($\overline{\lambda}_D \propto \beta = 0$). Extracting r_1 and r_2 from experimental transport measurements might provide an alternative way to identify the SOC parameters of the junction's ferromagnetic-insulator interface, without having exact knowledge of $\overline{\lambda}_{MA}$ or the magnetization orientation.

Once $\overline{\lambda}_{MA}$ overcomes some critical value, the AJHE charge and transverse spin current parts are additionally governed by *nonlinear* $\overline{\lambda}_{MA}$-terms and the r-ratios are no longer universal quantities of the system. To estimate the relevance of these nonlinearities, the inset of Fig. 9.11 shows r_1 ($r_1 = r_2$ since Dresselhaus SOC is not present) as a function of $\overline{\lambda}_{MA}$ and for various Rashba SOC strengths. Apparently, the spin-charge-current cross ratios remain indeed universal (magnetization independent) for the small magnetic tunneling strengths considered in all previously discussed current calculations (i.e.,

for $\overline{\lambda}_{\mathrm{MA}} = 0.005$). Nonlinear $\overline{\lambda}_{\mathrm{MA}}$-terms do not affect the AJHE charge and transverse spin currents unless $\overline{\lambda}_{\mathrm{MA}}$ gets further enhanced by at least one order of magnitude.

Another peculiar feature becomes visible once the Rashba SOC parameter approaches the scalar tunneling strength, i.e., at $\overline{\lambda}_{\mathrm{R}} \approx \overline{\lambda}_{\mathrm{SC}}$, as the spin-charge-current cross ratios' amplitudes always drop into a sharp dip there. To strengthen the generality of this finding, we distinguish between three different $\overline{\lambda}_{\mathrm{SC}}$-values in Fig. 9.11, which essentially all cause the same behavior. Recalling our qualitative picture formulated in Sec. 9.2, the AJHE charge currents are caused by skew Andreev reflections of incident spin-up and spin-down electrons at the ferromagnetic-insulator barrier's effective scattering potential $V_{\mathrm{eff}}^{\sigma}$. The latter is stated in Eq. (9.6) for the limiting case of restricting ourselves to the current along $\hat{y}$, I_y (similar arguments hold also for the I_x-current). Inspecting Eq. (9.6), we deduce that incoming spin-down (spin-up) electrons are exposed to the lowest (largest) possible interfacial scattering potential exactly when the Rashba SOC and the scalar tunneling measures are equal (neglecting the small magnetic tunneling strength). As a result, the spin-down channel carries its maximal amount of AJHE current, while the (oppositely oriented) contribution of the spin-up channel becomes minimal. The overall AJHE current I_y reaches its maximum and even significantly overcomes the related spin currents. Our numerical calculations discussed in Fig. 9.10 confirm these predictions. Since the AJHE charge currents enter the spin-charge-current cross ratios' denominators, maximal I_y (I_x) eventually comes along with strongly suppressed r-ratios, manifested by the r-$\overline{\lambda}_{\mathrm{R}}$ relations' sharp dips at $\overline{\lambda}_{\mathrm{R}} \approx \overline{\lambda}_{\mathrm{SC}}$. At moderate scalar tunnelings (e.g., at $\overline{\lambda}_{\mathrm{SC}} = 0.5$), strong Rashba SOC raises sizable spin currents when compared to their AJHE charge current counterparts (as a great fraction of singlet Cooper pairs is then converted into spin-polarized triplet pairs), leading to rather large current cross ratios. Nevertheless, further increasing $\overline{\lambda}_{\mathrm{SC}}$ remarkably damps the current cross ratios at $\overline{\lambda}_{\mathrm{R}} > \overline{\lambda}_{\mathrm{SC}}$, as strong interfacial scalar tunnelings usually act against *spin-flip* skew tunnelings and thereby suppress the generation of spin currents (triplet Cooper pairs) much faster than their AJHE charge current counterparts.

9.7 Short summary

In summary, we investigated AJHE charge and transverse spin currents arising from the intriguing interplay of interfacial SOC and magnetic exchange inside S/F-I/S Josephson junctions' ferromagnetic-insulator barrier. Starting from simplified qualitative arguments, we related the spontaneously emerging AJHE supercurrents to Cooper pair skew tunnelings through the ferromagnetic-insulator interface. Numerically evaluating the AJHE current amplitudes by means of a generalized Furusaki-Tsukada method for a variety of realistic junction parameters demonstrated the AJHE responses' wide tunability. The strength of the interfacial Rashba SOC, which is mostly determined by the junctions' material compositions, and the magnetically adjustable phase difference between the superconducting electrodes offer particularly auspicious and experimentally feasible ways to vary the AJHE current magnitudes over several orders of magnitude. Even extremely weak magnetic ferromagnetic-insulator layers, which are rather advantageous in experiments since they do not heavily suppress the junctions' superconducting characteristics, cause maximal AJHE currents that can reach more than ten percent of the (tunneling) Josephson current and thereby significantly exceed normal-state TAHE conductances (usually remaining far below one percent of the respective tunneling conductances [440]).

To gain more physical insight into the microscopic mechanism behind AJHEs, we established an alternative bound state-based approach, which eventually allowed us to connect sizable AJHE signals with marked SOC-induced asymmetries in the junctions' Andreev bound state and YSR state energies. Resolving the distinct states' individual AJHE current contributions convinced ourselves that the cur-

rent responses are predominantly raised by the peculiar YSR states, whose appearance counts for sure to magnetic Josephson junctions' most striking features.

Finally, we outlined that SOC simultaneously triggers interfacial spin flips of Cooper pair electrons, converting initially spin-unpolarized singlet into spin-polarized triplet pairs. Since the latter are also subject to the aforementioned skew tunnelings when approaching the ferromagnetic-insulator barrier, we proposed that the AJHE charge currents inevitably come along with their transverse spin current counterparts. We qualitative unraveled the spin currents' general properties and computed their amplitudes once from an extended Furusaki-Tsukada spin current formula and once exploiting the discovered bound state asymmetries, again revealing great tunabilities with the Rashba SOC parameter or the superconducting phase difference. We illustrated the spin currents' well-distinct magnetization direction modulations when compared to the AJHE charge currents, which offer efficient experimental control knobs to switch between pure AJHE charge and transverse spin current regimes. Such a control – basically lacking in the previously studied F/S junctions (recall Chap. 8) – belongs to one of the most essential ingredients for tailoring future spintronics applications and opens novel perspectives for S/F-I/S Josephson junction technologies. As another experimental tool to probe the systems' interfacial SOC, we introduced the universal, magnetization-independent, spin-charge-current cross ratios and briefly elaborated on their generic parameter dependencies.

Part V

Conclusions and Outlook

Chapter 10
Conclusions and Outlook

This thesis was dedicated to investigating charge and spin transport through superconducting tunnel junctions and demonstrating these systems' unprecedented physical characteristics that arise from the subtle competition between superconductivity, ferromagnetism, and SOC effects. At the end, we wish to briefly conclude the most notable findings of our work and draw the reader's attention towards some essential open questions that undoubtedly require further analyses.

After motivating our studies and summarizing the fundamentals associated with superconductivity, ferromagnetism, and SOC (see Chaps. 1 and 2), Chaps. 3 and 4 focused on superconducting junctions' distinct tunneling conductance features. Starting from the well-established BTK model [164], we characterized F/F-S contacts' tunneling conductance-bias voltage relations. Ferromagnetic superconductors (F-S) have only been sporadically considered so far and might still hide unexpected physics. We showed that the additional exchange splitting in the ferromagnetic superconductor remarkably alters the junctions' conductance-voltage characteristics and splits F/S contacts' gap-edge FBCP into two spin-resolved peaks below and above the superconducting energy gap. The splitting's amplitude is determined by the ferromagnetic superconductor's exchange gap, and might therefore be experimentally exploited to quantify the latter analogously to F/S junctions' FBCP heights from which ferromagnets' spin polarization can be deduced.

Fully understanding the (quasiparticle) conductance features of S/metal/S Josephson junctions turned out to become slightly more challenging, mostly due to the possibility that electrons (holes) that approach the metal/superconductor interfaces may undergo Andreev reflections multiple times. We argued that such multiple Andreev reflections can eventually result in greatly enhanced probabilities for electrons to tunnel from one into the second superconductor and hence in a disproportionate increase of the tunneling current. This happens whenever the electron energies become comparable to integer submultiples of the doubled superconducting gap, causing local conductance maxima there and finally founding Josephson junctions' unique subharmonic conductance gap structure. We elaborated on the self-consistent OTBK approach [216–218] that extends the initial BTK formulation by additionally accounting for multiple reflections, and applied the theoretical framework to simple S/F/S junctions. Apart from the characteristic subharmonic conductance oscillations, which we could one-to-one reproduce, we commented on the likewise from multiple Andreev reflections originating nonzero excess currents and quantified them even in the ferromagnetic case. Our results enrich previous OTBK-based studies and might become relevant to future experiments.

Afterwards, we were concerned with Al/Ni/Ga junctions and aimed at comparing the theoretically expected tunneling conductance features against experimentally recorded data. These systems are particularly appealing since proximity effects turn the intrinsically weakly ferromagnetic nickel interlayer superconducting and allow for a practically well-controllable realization of the aforementioned ferromagnetic superconductors [219, 220]. We observed that the OTBK modeling faces serious issues once the outer gallium electrode's thickness can no longer be treated as "infinite" when compared to the nickel re-

gion and marked finite-size effects raise. To capture the latter, we computed the junctions' tunneling DOS within the Python transport package KWANT [221] and mapped the appearing DOS anomalies to the experimentally detected conductance modulations. Increasing the fabricated samples' nickel-gallium thickness ratios lets an additional series of conductance oscillations arise that have not yet been reported in earlier studies. We qualitatively captured these oscillations assuming triplet superconducting pairings close to the Ni/Ga interface and proposed that their appearance might provide strong indications of triplet superconducting correlations. From that viewpoint, Ni/Ga bilayer junctions might gain enormous attention to efficiently generate and control spin-polarized triplet supercurrents. Nevertheless, the unambiguous experimental evidence that the conductance anomalies are a real precursor of triplet pairings is still missing and further work is indispensable. We will suggest various possibilities for a more thorough experimental characterization later.

Throughout Chaps. 5–7, we explored the DC Josephson effect in different magnetic junctions. We began with a short generic overview about Josephson effects in simple S/I/S prototype junctions before coming back to more puzzling S/F/S geometries, in which the broken space-inversion symmetry at the interfaces invariably introduces strong SOC and notably impacts electrical transport. Owing to their complexity, SOC phenomena have only been rarely discussed in previous Josephson junction studies and our analyses might offer valuable contributions to close gaps in the literature. To mention only our most significant findings, we demonstrated that the junctions' current-reversing 0-π transitions can either be controlled electrically by tuning the SOC strengths or fully magnetically exploiting the Josephson current's SOC-induced magnetoanisotropies. These MAJCs – basically the Josephson counterparts of the TAMR in normal-state magnetic tunnel junctions – reach extremely huge magnitudes close to 0-π transition points and serve yet as another experimental tool to detect such transitions. Moreover, we generalized the employed Furusaki-Tsukada Green's function formalism [266] to more intricate S/F/I/F/S Josephson spin valves and unraveled another magnetic control knob to vary the Josephson currents. Switching the spin-valve magnetizations from their parallel to their antiparallel alignments increases (decreases) the critical current not only by more than one order of magnitude (depending on whether the current is mostly carried by singlet or triplet pairs), but can even trigger 0-π transitions.

These results found reliable ways to experimentally verify the aforementioned triplet pairings in Ni/Ga bilayers. Growing Ni/Ga on top of another Ga/Ni bilayer (probably separated by a thin insulating spacer like EuS) mimics the theoretically considered S/F/I/F/S configuration and the measured critical Josephson current must therefore resemble the characteristics we deduced, i.e., singlet currents must become maximal for antiparallel and triplet currents for parallel magnetized spin valves. The latter would provide the unambiguous proof that Ni/Ga bilayers indeed facilitate the formation of triplet Cooper pairs. Alternatively, one could look deeper into Ga/Ni/Ga Josephson junctions and align nickel's magnetization by means of an external magnetic field, giving direct access to the (in-plane) MAJCs. Detecting nonzero MAJCs indicates the presence of interfacial Rashba [149, 150] and Dresselhaus [152] SOCs, and is thus taken as an indirect evidence that triplet pairs are created at the interface. Fitting the taken data to our modeling, we could extract the Ni/Ga interfaces' specific SOC parameters, study their dependence on nickel's thickness, and compare the outcomes to first-principles calculations.

On the microscopic level, we attributed nonzero Josephson current flows to Cooper pair electrons tunneling through the nonsuperconducting part via bound states. The most interesting physics occurs again in magnetic junctions, in which the bound state spectrum splits into distinct Andreev bound states [179, 227] on the one and YSR states [361–363] on the other hand. We comprehensively classified these bound states in simplified S/F-I/S Josephson junctions and put special emphasis on zero-energy YSR states and their intriguing spin properties, which eventually signaled the ground-state phase transitions between the usual 0- and the π-state junction regimes. This unique connection between zero-energy YSR states and 0-π transitions is thus universal that it persists also in the presence of strong SOC and likewise

in more complex diffusive S/F/S junctions [401], and might become particularly relevant to upcoming experiments.

Interfacial SOC causes not only the marked Josephson current magnetoanisotropies we thoroughly investigated, but stand in fact behind a great wealth of unprecedented physical phenomena that uniquely arise in magnetic tunnel junctions. As another experimentally auspicious perspective, we studied F/S contacts' TAHEs, together with their Josephson junction AJHE analogs, in Chaps. 8 and 9. We convinced ourselves that spin- and transverse momentum-dependent skew reflections at the considered junctions' spin-active interfaces generate transverse electron imbalances and give thereby rise to net Hall current flows. While the resulting TAHE conductances are typically tiny and barely measurable in normal-conducting F/N junctions, we deduced that the simultaneously present skew specular and skew Andreev reflections at F/S interfaces act together and significantly amplify the TAHE signals, drawing upcoming experiments' attention more towards superconducting junctions. We classified the TAHE conductances' magnetization and bias voltage dependencies within a generalized BTK model – providing distinct fingerprints to experimentally separate the skew reflection-related TAHE from "usual" anomalous Hall effect contributions –, and argued that the normal-state Hall currents inside the ferromagnet come along with their transverse supercurrent counterparts building up in the superconducting electrode.

We eventually extended our qualitative skew reflection picture to cover the tunneling of Cooper pairs through S/F-I/S Josephson junctions' ferromagnetic-insulator barriers and identified Cooper pair skew tunnelings as the sizable AJHE currents' physical origin. We mapped the AJHE current amplitudes that we computed from an adapted Furusaki-Tsukada approach to the systems' spectral characteristics, suggesting that SOC-controlled asymmetries in the forming bound states – mostly apparent in the subtle YSR state branches – microscopically drive AJHEs. Besides the AJHE charge current responses, we identified their transverse spin current counterparts that are essentially generated by interfacial spin flips, converting initially unpolarized singlet into spin-polarized triplet Cooper pairs. We showed that tuning the ferromagnetic insulators' magnetization orientations offers an efficient control knob to switch between pure AJHE charge and transverse spin current regimes, and related both defining the universal, magnetization-independent, spin-charge-current cross ratios. The latter give direct experimental access to real junctions' interfacial Rashba and Dresselhaus SOC strengths, which might then be compared to first-principles calculations and offer the necessary input to design systems with tailored physical properties.

Since superconducting junctions inherently combine various experimental possibilities to generate spin-polarized triplet supercurrents with dissipationless transport, quantum coherence, and even strongly enhanced quasiparticle spin lifetimes [45], these systems undoubtedly offer great advantages when it comes to designing novel spintronics functionalities [49–51] or quantum computing circuits [57–60, 62–64]. In this work, we focused on junctions in which interfacial SOC gives rise to spin flips of Cooper pair electrons and thereby converts unpolarized singlet into spin-polarized triplet pairs (currents). Paving the way towards commercial applicability of such triplet supercurrents needs, nevertheless, still a much deeper understanding of their underlying physical characteristics. Shortly before we started to explore SOC effects in Josephson junctions, Jacobsen and coworkers [79] predicted that separating lateral S/F/S junctions' superconducting electrodes and the ferromagnetic link by means of thin heavy normal-metal films, like platinum, remarkably enhances SOC and allows for an efficient generation of triplet supercurrents when rotating the ferromagnet's magnetization. However, several experimental attempts by Satchell *et al.* [471, 472] could not detect clear signatures of triplet currents in these geometries, demonstrating that the reliable generation and manipulation of triplet supercurrents is rather challenging in practice. More thorough theoretical descriptions [473, 474] have indicated in the meantime that the triplet supercurrents occur solely for certain magnetization orientations and were therefore not measurable

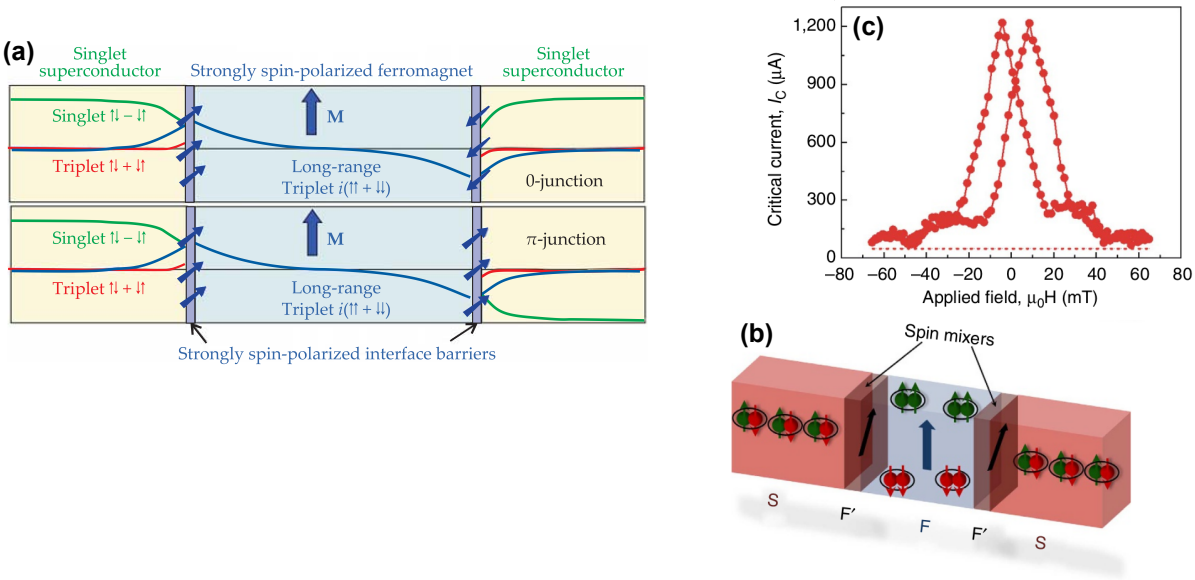


Fig. 10.1: (a) Schematical illustration of a Josephson junction that consists of two singlet (s-wave) superconductors coupled by means of a strongly spin-polarized ferromagnet. The likewise strongly spin-polarized ferromagnetic interface barriers' magnetizations are tilted with respect to the massive ferromagnet's magnetization direction (the magnetization orientations are indicated by black and dark blue arrows), which eventually leads to interfacial "spin mixing" and generates triplet supercurrents. Switching the barriers' magnetizations between their antiparallel (top) and parallel (bottom) alignments is moreover expected to induce transitions from 0- to π-states. Taken from Ref. [50]. **(b)** and **(c)** Experimental implementation of the predicted π-state regime in Nb/Py/Co/Py/Nb junctions. The spin mixers' magnetizations are aligned through an external magnetic field that points along the massive ferromagnetic link's magnetization orientation. At weak external fields, the magnetization misalignment facilitates sizable triplet (critical) supercurrents. Increasing the field strength aligns the interfaces' magnetizations parallel to the link's and only strongly suppressed singlet supercurrents are detectable. Taken from Ref. [73]. The interplay between noncollinear magnetizations and interfacial SOC – arising from the broken space-inversion symmetry – might offer further ways to optimize the triplet-singlet supercurrent ratio and certainly deserves more thorough studies.

in Satchell's experiments. A comprehensive understanding of the intimate connections between SOC and the emergence of triplet supercurrents requires thus profound experimental and theoretical studies. We are optimistic that the results presented in this thesis will stimulate further efforts into that direction.

Apart from SOC-related phenomena, triplet supercurrents are also expected to arise when thin ferromagnetic spacers, whose magnetization directions are tilted with respect to the massive ferromagnet's magnetization, separate S/F/S junctions' ferromagnetic and superconducting regions. Cooper pairs that penetrate the magnetic link acquire nonzero center-of-mass momenta (to compensate the spin-dependent potential), inducing a unique superposition of oscillating short-range singlet and triplet superconducting pairing potentials there – the famous FFLO phase [53, 54]. We explained earlier that these oscillations cause many striking features like the unprecedented 0-π transitions. Before entering the junctions' ferromagnetic link, the Cooper pair electrons must travel through the thin (likewise ferromagnetic) interfaces. Owing to these spacers' tilted magnetization orientations (when compared to the central interlayer), the electrons are then exposed to a rotation of the spin quantization axis and the different triplet states' spins "mix". Such a "spin mixing" converts the initially short-ranged singlet into long-range triplet correlations and allows even for an alternative, and perhaps more feasible, control of 0-π transitions [50], as illustrated in Fig. 10.1(a). While early theoretical concepts mostly relied on Josephson junctions in

which the noncollinear magnetizations originate from ferromagnetic spacers whose magnetizations get rotated in an intricate spiral-like manner [65–67, 69], subsequent works suggested that atomically thin interfaces with homogeneously tilted magnetizations are better controllable and likewise sufficient to cause long-range triplet supercurrents [50, 68, 70–72]. After Keizer *et al.* [74] had indeed measured sizable (triplet) currents in Josephson junctions containing strongly spin-polarized CrO_2 links, many other groups intensified their activities and deduced strong indications of such supercurrents in a vast of magnetic multilayer geometries (see, e.g., Refs. [288], [475], and [476]), until Banerjee and coworkers [73] recently succeeded to reliably switch between the singlet and triplet current regimes by means of external magnetic fields [see Figs. 10.1(b)–(c)]. Practical ways to routinely generate and manipulate triplet supercurrents, exploiting noncollinearly magnetized arrays, are hence already within reach.

Anyhow, including thin ferromagnetic spacers into Josephson junctions simultaneously breaks the systems' space-inversion symmetry and induces strong interfacial SOC, which will for sure alter the triplet supercurrents' features and tunability. Owing to the geometries' complexity, the competition between noncollinear magnetizations and SOC has not been investigated so far, but will be crucial to engineer applications that benefit from both ingredients. The methodologies that we worked out within this thesis provide a solid basis for the theoretical analyses of such intricate multilayer junction configurations and might eventually give insight into yet unforeseen physics. The interplay of noncollinearly magnetized regions and (interfacial) SOC will not only have a remarkable impact on the tunneling and Josephson currents themselves, but moreover significantly alter the TAHE and AJHE currents' properties. After understanding all resulting modifications, one of the next goals will be the integration of normal-state magnetic spin valves into Josephson junctions. The pioneering experimental work of Gingrich *et al.* [87] elucidated that flipping the relative magnetizations of F/N/F spin-valve Josephson junctions' adjacent ferromagnetic layers from their antiparallel to their parallel alignments triggers Josephson current-reversing 0-π transitions and might bring new dynamics into Josephson junction-based quantum computing circuits [57–64]. The main disadvantages of the investigated systems are their rather small normal-state TMR ratios. In recent years, Vávra and his colleagues [88] successfully implemented S/F/I/F/S stackings, replacing the initial normal-metal buffer layer by a thin insulating region. Such junctions support not only sizable Josephson currents, but at the same time also marked normal-state TMRs, and might attract enormous attention for applications that utilize both effects in one single set-up. Most of the recorded transport data has remained puzzling up to now and certainly deserves further investigations, employing, e.g., the formalisms that were applied in this thesis.

The spell to tailor devices that take advantage of triplet supercurrents' fascinating physical characteristics seems to be broken and the interest in the related superconducting spintronics research area [49–51] is overwhelming. With a bit of luck and enthusiastic scientists around the world developing seminal concepts, the first (high-T_C) superconductor-based information devices might become available within the next decade(s) and revolutionize our everyday life, just as their normal-state TMR counterparts once did when unimaginably improving the storage capacities on modern computers' hard disks [12].

Appendix

Appendix A

Step-by-step OTBK modeling of Al/Ni/Ga Josephson junctions

In Sec. 4.3, we employ two different approaches to calculate the tunneling currents that are expected to flow through biased Al/Ni/Ga Josephson junctions and compare our theoretical predictions to experimental data taken in the group of Jagadeesh Moodera at MIT. The first description relies on the OTBK model, which we initially recovered in all details considering a much simpler S/F/S junction in Sec. 4.2, whereas the second method is based on a fully numerical implementation within the Python transport code KWANT. The latter can be straightforwardly reproduced starting from the discretized Bogoljubov-de Gennes Hamiltonian stated in Eq. (4.22). The OTBK modeling, however, requires additional analytical input that we wish to provide in this chapter. We follow the same strategy as outlined in Sec. 4.2, idealizing the experimentally investigated stacking in terms of a *one-dimensional* Al/N/Ni/NiGa/Ga junction along $\hat{z}$ [see Fig. 4.10(b)]. The thin normal-state region (N) is separated from its neighboring aluminum and nickel layers by means of two ultrathin (deltalike) tunneling barriers, and essentially mimics the oxide tunneling barriers present in the experimental samples. The overall tunneling current flow inside the normal link is then quantified by Eq. (4.14). Before evaluating Eq. (4.14), we need to unravel the self-consistent distribution functions describing left- and right-moving electrons. The distribution of right-movers can be extracted from Eq. (4.13) once the reflection and transmission probabilities at the N/Al and N/. . . /Ga interfaces are known.

Let us first focus on the left half-junction involving scattering of incident electrons at the N/Al interface; see left part of Fig. A.1. A spin-σ electron ($\sigma = 1$ for spin up and $\sigma = -1$ for spin down) traveling towards the interface from the normal region can either be reflected back or transmitted into the aluminum electrode. The corresponding probabilities can be deduced analogously to the F/F-S junctions we studied in Chap. 3. The Nambu-space Bogoljubov-de Gennes Hamiltonian [139] of the N/Al half-junction,

$$\hat{\mathcal{H}}_{\mathrm{BdG}} = \begin{bmatrix} \hat{\mathcal{H}}_{\mathrm{e}} & \hat{\Delta}_{\mathrm{S}}(z) \\ \hat{\Delta}_{\mathrm{S}}^{\dagger}(z) & \hat{\mathcal{H}}_{\mathrm{h}} \end{bmatrix}, \tag{A.1}$$

includes the single-electron Hamiltonian

$$\hat{\mathcal{H}}_{\mathrm{e}} = \left(-\frac{\hbar^2}{2m} \frac{\mathrm{d}^2}{\mathrm{d}z^2} - \mu \right) \hat{\sigma}_0 + \tilde{V}_{\mathrm{I}} \tilde{d}_{\mathrm{I}} \hat{\sigma}_0 \delta(z), \tag{A.2}$$

its hole-like counterpart

$$\hat{\mathcal{H}}_{\mathrm{h}} = -\hat{\sigma}_y \hat{\mathcal{H}}_{\mathrm{e}}^{*} \hat{\sigma}_y, \tag{A.3}$$

and the (idealized) s-wave superconducting pairing potential

$$\hat{\Delta}_{\mathrm{S}}(z) = |\Delta_{\mathrm{S,Al}}| \hat{\sigma}_0 \Theta(z) \tag{A.4}$$

inside the superconducting aluminum electrode. We use the same notation as in the rest of this thesis, i.e., m (μ) indicate the equal quasiparticle masses (chemical potentials) in all parts of the junction,

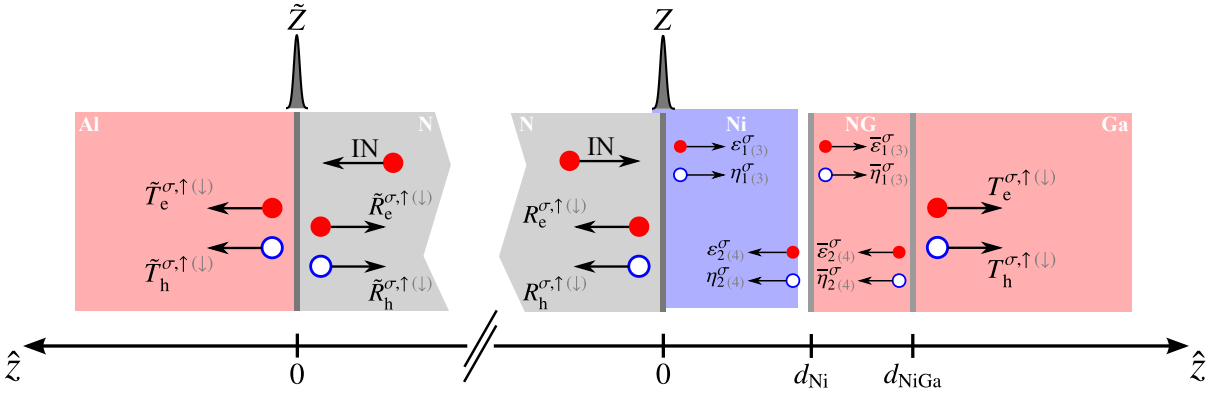


Fig. A.1: Schematical illustration of the possible scattering processes an incoming electron (IN) from the normal-conducting region (light gray) can undergo at the left and right half-junctions' tunneling barriers (dark gray), parameterized by the barrier measures $\tilde{Z}$ and Z. Electrons are colored red and holes blue; black arrows point along the electrons' and holes' propagation directions. The depicted scattering processes include specular reflections [with probabilities $\tilde{R}_e^{\sigma,\uparrow(\downarrow)}$ and $R_e^{\sigma,\uparrow(\downarrow)}$], Andreev reflections [with probabilities $\tilde{R}_h^{\sigma,\uparrow(\downarrow)}$ and $R_h^{\sigma,\uparrow(\downarrow)}$], electronlike transmissions [with probabilities $\tilde{T}_e^{\sigma,\uparrow(\downarrow)}$ and $T_e^{\sigma,\uparrow(\downarrow)}$], and holelike transmissions [with probabilities $\tilde{T}_h^{\sigma,\uparrow(\downarrow)}$ and $T_h^{\sigma,\uparrow(\downarrow)}$]. The remaining coefficients entering the scattering states are indicated by Greek symbols.

$\tilde{V}_I$ ($\tilde{d}_I$) the tunneling barrier's height (width), and $|\Delta_{S,Al}|$ represents aluminum's superconducting energy gap (see Tab. 4.1 for its zero-temperature value).

Solving the junction's stationary Bogoljubov-de Gennes equation $\hat{\mathcal{H}}_{BdG}\psi^\sigma(z) = E\psi^\sigma(z)$, the scattering state in the normal layer ($z < 0$) reads as

$$\psi^\sigma(z<0) = \frac{1}{\sqrt{2}}\begin{bmatrix}\sigma\sqrt{1+\sigma}\\ \sqrt{1-\sigma}\\ 0\\ 0\end{bmatrix} e^{ik_e z} + \tilde{r}_e^{\sigma,\uparrow}\begin{bmatrix}1\\0\\0\\0\end{bmatrix} e^{-ik_e z} + \tilde{r}_e^{\sigma,\downarrow}\begin{bmatrix}0\\1\\0\\0\end{bmatrix} e^{-ik_e z} + \tilde{r}_h^{\sigma,\downarrow}\begin{bmatrix}0\\0\\1\\0\end{bmatrix} e^{ik_h z} + \tilde{r}_h^{\sigma,\uparrow}\begin{bmatrix}0\\0\\0\\1\end{bmatrix} e^{ik_h z}, \quad \text{(A.5)}$$

where the scattering coefficients $\tilde{r}_e^{\sigma,\uparrow(\downarrow)}$ refer to the situation that the incident spin-σ electron gets specularly reflected as a spin-up (spin-down) electron, and $\tilde{r}_h^{\sigma,\uparrow(\downarrow)}$ indicates Andreev reflections as a spin-up (spin-down) hole, respectively. The $\hat{z}$-projected wave vectors of electrons and holes with energy E are given by

$$k_e = k_e(E) = \sqrt{\frac{2m}{\hbar^2}(\mu + E)} \qquad \text{and} \qquad k_h = k_h(E) = \sqrt{\frac{2m}{\hbar^2}(\mu - E)}; \quad \text{(A.6)}$$

to avoid unnecessary indices when regarding the right half-junction later on, we omit the spatial z-index in the wave vectors used in all other chapters of this thesis.

In the same spirit, we obtain in the superconducting aluminum electrode ($z > 0$)

$$\psi^\sigma(z>0) = \tilde{t}_e^{\sigma,\uparrow}\begin{bmatrix}u_{Al}\\0\\v_{Al}\\0\end{bmatrix} e^{iq_{e,Al}z} + \tilde{t}_e^{\sigma,\downarrow}\begin{bmatrix}0\\u_{Al}\\0\\v_{Al}\end{bmatrix} e^{iq_{e,Al}z} + \tilde{t}_h^{\sigma,\uparrow}\begin{bmatrix}v_{Al}\\0\\u_{Al}\\0\end{bmatrix} e^{-iq_{h,Al}z} + \tilde{t}_h^{\sigma,\downarrow}\begin{bmatrix}0\\v_{Al}\\0\\u_{Al}\end{bmatrix} e^{-iq_{h,Al}z}, \quad \text{(A.7)}$$

with the BCS coherence factors

$$u_{\mathrm{Al}} = u_{\mathrm{Al}}(E) = \sqrt{\frac{1}{2}\left(1 + \sqrt{1 - \frac{|\Delta_{\mathrm{S,Al}}|^2}{E^2}}\right)} \qquad \text{and} \qquad v_{\mathrm{Al}} = v_{\mathrm{Al}}(E) = \sqrt{1 - [u_{\mathrm{Al}}(E)]^2}. \tag{A.8}$$

The $\hat{z}$-projections of electronlike and holelike quasiparticles' wave vectors are

$$q_{\mathrm{e,Al}} = q_{\mathrm{e,Al}}(E) = \sqrt{\frac{2m}{\hbar^2}\left(\mu + \sqrt{E^2 - |\Delta_{\mathrm{S,Al}}|^2}\right)} \quad \text{and} \quad q_{\mathrm{h,Al}} = q_{\mathrm{h,Al}}(E) = \sqrt{\frac{2m}{\hbar^2}\left(\mu - \sqrt{E^2 - |\Delta_{\mathrm{S,Al}}|^2}\right)}, \tag{A.9}$$

while the coefficients $\tilde{t}_{\mathrm{e}}^{\sigma,\uparrow(\downarrow)}$ and $\tilde{t}_{\mathrm{h}}^{\sigma,\uparrow(\downarrow)}$ capture electronlike and holelike transmissions into aluminum. To attain the unknown reflection and transmission coefficients, we apply the interfacial ($z = 0$) boundary conditions

$$\psi^{\sigma}(z)\big|_{z=0_-} = \psi^{\sigma}(z)\big|_{z=0_+} \tag{A.10}$$

and

$$\left(\frac{\hbar^2}{2m}\frac{\mathrm{d}}{\mathrm{d}z} + \tilde{V}_{\mathrm{I}}\tilde{d}_{\mathrm{I}}\right)\hat{\eta}\psi^{\sigma}(z)\big|_{z=0_-} = \frac{\hbar^2}{2m}\frac{\mathrm{d}}{\mathrm{d}z}\hat{\eta}\psi^{\sigma}(z)\big|_{z=0_+}, \tag{A.11}$$

with $\hat{\eta} = \mathrm{diag}[\hat{\sigma}_0, -\hat{\sigma}_0]$, to the scattering states and numerically solve the resulting system of equations.

After we identified the scattering coefficients, the related scattering *probabilities* can be extracted considering the underlying probability current densities as clarified in Chap. 3, eventually yielding

$$\tilde{R}_{\mathrm{e}}^{\sigma,\uparrow} = \tilde{R}_{\mathrm{e}}^{\sigma,\uparrow}(E) = \left|\tilde{r}_{\mathrm{e}}^{\sigma,\uparrow}\right|^2, \tag{A.12}$$

$$\tilde{R}_{\mathrm{e}}^{\sigma,\downarrow} = \tilde{R}_{\mathrm{e}}^{\sigma,\downarrow}(E) = \left|\tilde{r}_{\mathrm{e}}^{\sigma,\downarrow}\right|^2, \tag{A.13}$$

$$\tilde{R}_{\mathrm{h}}^{\sigma,\uparrow} = \tilde{R}_{\mathrm{h}}^{\sigma,\uparrow}(E) = \mathrm{Re}\left(\frac{k_{\mathrm{h}}}{k_{\mathrm{e}}}\right)\left|\tilde{r}_{\mathrm{h}}^{\sigma,\uparrow}\right|^2, \tag{A.14}$$

$$\tilde{R}_{\mathrm{h}}^{\sigma,\downarrow} = \tilde{R}_{\mathrm{h}}^{\sigma,\downarrow}(E) = \mathrm{Re}\left(\frac{k_{\mathrm{h}}}{k_{\mathrm{e}}}\right)\left|\tilde{r}_{\mathrm{h}}^{\sigma,\downarrow}\right|^2, \tag{A.15}$$

$$\tilde{T}_{\mathrm{e}}^{\sigma,\uparrow} = \tilde{T}_{\mathrm{e}}^{\sigma,\uparrow}(E) = \mathrm{Re}\left(\frac{q_{\mathrm{e,Al}}}{k_{\mathrm{e}}}\right)\left|\tilde{t}_{\mathrm{e}}^{\sigma,\uparrow}\right|^2\left[\,|u_{\mathrm{Al}}|^2 - |v_{\mathrm{Al}}|^2\,\right]\Theta\Big(E - |\Delta_{\mathrm{S,Al}}|\Big), \tag{A.16}$$

$$\tilde{T}_{\mathrm{e}}^{\sigma,\downarrow} = \tilde{T}_{\mathrm{e}}^{\sigma,\downarrow}(E) = \mathrm{Re}\left(\frac{q_{\mathrm{e,Al}}}{k_{\mathrm{e}}}\right)\left|\tilde{t}_{\mathrm{e}}^{\sigma,\downarrow}\right|^2\left[\,|u_{\mathrm{Al}}|^2 - |v_{\mathrm{Al}}|^2\,\right]\Theta\Big(E - |\Delta_{\mathrm{S,Al}}|\Big), \tag{A.17}$$

$$\tilde{T}_{\mathrm{h}}^{\sigma,\uparrow} = \tilde{T}_{\mathrm{h}}^{\sigma,\uparrow}(E) = \mathrm{Re}\left(\frac{q_{\mathrm{h,Al}}}{k_{\mathrm{e}}}\right)\left|\tilde{t}_{\mathrm{h}}^{\sigma,\uparrow}\right|^2\left[\,|u_{\mathrm{Al}}|^2 - |v_{\mathrm{Al}}|^2\,\right]\Theta\Big(E - |\Delta_{\mathrm{S,Al}}|\Big), \tag{A.18}$$

as well as

$$\tilde{T}_{\mathrm{h}}^{\sigma,\downarrow} = \tilde{T}_{\mathrm{h}}^{\sigma,\downarrow}(E) = \mathrm{Re}\left(\frac{q_{\mathrm{h,Al}}}{k_{\mathrm{e}}}\right)\left|\tilde{t}_{\mathrm{h}}^{\sigma,\downarrow}\right|^2\left[\,|u_{\mathrm{Al}}|^2 - |v_{\mathrm{Al}}|^2\,\right]\Theta\Big(E - |\Delta_{\mathrm{S,Al}}|\Big). \tag{A.19}$$

To shorten the upcoming equations, we combine the reflection probabilities belonging to the spin-up and spin-down subbranches, and likewise all transmission probabilities, to end up with

$$\tilde{R}_{\mathrm{e}}^{\sigma}(E) := \tilde{R}_{\mathrm{e}}^{\sigma,\uparrow}(E) + \tilde{R}_{\mathrm{e}}^{\sigma,\downarrow}(E), \tag{A.20}$$

$$\tilde{R}_{\mathrm{h}}^{\sigma}(E) := \tilde{R}_{\mathrm{h}}^{\sigma,\uparrow}(E) + \tilde{R}_{\mathrm{h}}^{\sigma,\downarrow}(E), \tag{A.21}$$

and

$$\tilde{T}^{\sigma}(E) := \tilde{T}_{\mathrm{e}}^{\sigma}(E) + \tilde{T}_{\mathrm{h}}^{\sigma}(E) = \tilde{T}_{\mathrm{e}}^{\sigma,\uparrow}(E) + \tilde{T}_{\mathrm{e}}^{\sigma,\downarrow}(E) + \tilde{T}_{\mathrm{h}}^{\sigma,\uparrow}(E) + \tilde{T}_{\mathrm{h}}^{\sigma,\downarrow}(E). \tag{A.22}$$

Second, we proceed in the same way to find the scattering probabilities in the right half-junction, illustrated in the right part of Fig. A.1. The Bogoljubov-de Gennes Hamiltonian's single-electron Hamiltonian takes then the form

$$\hat{\mathcal{H}}_{\mathrm{e}} = \left(-\frac{\hbar^2}{2m}\frac{\mathrm{d}^2}{\mathrm{d}z^2} - \mu\right)\hat{\sigma}_0 - \frac{\Delta_{\mathrm{XC,Ni}}}{2}\hat{\sigma}_z\Theta(z)\Theta(d_{\mathrm{Ni}} - z) + V_{\mathrm{I}}d_{\mathrm{I}}\hat{\sigma}_0\delta(z), \tag{A.23}$$

accounting for the ferromagnetic exchange gap $\Delta_{\mathrm{XC,Ni}}$ in the nickel layer and for the tunneling barrier height (width) V_{I} (d_{I}), which might differ from the left barrier's measures. The (idealized) s-wave superconducting pairing potential

$$\hat{\Delta}_{\mathrm{S}}(z) = |\Delta_{\mathrm{S,Ni}}|\hat{\sigma}_0\Theta(z)\Theta(d_{\mathrm{Ni}} - z) + |\Delta_{\mathrm{S,NiGa}}|\hat{\sigma}_0\Theta(z - d_{\mathrm{Ni}})\Theta(d_{\mathrm{NiGa}} - z) + |\Delta_{\mathrm{S,Ga}}|\hat{\sigma}_0\Theta(z - d_{\mathrm{NiGa}}) \tag{A.24}$$

captures the differing superconducting gaps of nickel ($|\Delta_{\mathrm{S,Ni}}|$), the interfacial alloy ($|\Delta_{\mathrm{S,NiGa}}|$), and gallium ($|\Delta_{\mathrm{S,Ga}}|$); their zero-temperature values are listed in Tab. 4.1. Since we are solely concerned with scattering inside the right half-junction, we can shift the N/Ni interface to $z = 0$ without losing generality. The scattering states in the normal region ($z < 0$),

$$\begin{aligned}\psi^{\sigma}(z<0) = \frac{1}{\sqrt{2}}\begin{bmatrix}\sigma\sqrt{1+\sigma}\\ \sqrt{1-\sigma}\\ 0\\ 0\end{bmatrix}\mathrm{e}^{\mathrm{i}k_{\mathrm{e}}z} + r_{\mathrm{e}}^{\sigma,\uparrow}\begin{bmatrix}1\\0\\0\\0\end{bmatrix}\mathrm{e}^{-\mathrm{i}k_{\mathrm{e}}z} + r_{\mathrm{e}}^{\sigma,\downarrow}\begin{bmatrix}0\\1\\0\\0\end{bmatrix}\mathrm{e}^{-\mathrm{i}k_{\mathrm{e}}z}\\ + r_{\mathrm{h}}^{\sigma,\downarrow}\begin{bmatrix}0\\0\\1\\0\end{bmatrix}\mathrm{e}^{\mathrm{i}k_{\mathrm{h}}z} + r_{\mathrm{h}}^{\sigma,\uparrow}\begin{bmatrix}0\\0\\0\\1\end{bmatrix}\mathrm{e}^{\mathrm{i}k_{\mathrm{h}}z},\end{aligned} \tag{A.25}$$

in the nickel layer ($0 < z < d_{\mathrm{Ni}}$),

$$\begin{aligned}\psi^{\sigma}(0<z<d_{\mathrm{Ni}}) = \left(\varepsilon_1^{\sigma}\mathrm{e}^{\mathrm{i}q_{\mathrm{e,Ni}}^{\uparrow}z} + \varepsilon_2^{\sigma}\mathrm{e}^{-\mathrm{i}q_{\mathrm{e,Ni}}^{\uparrow}z}\right)\begin{bmatrix}u_{\mathrm{Ni}}^{\uparrow}\\0\\v_{\mathrm{Ni}}^{\uparrow}\\0\end{bmatrix} + \left(\varepsilon_3^{\sigma}\mathrm{e}^{\mathrm{i}q_{\mathrm{e,Ni}}^{\downarrow}z} + \varepsilon_4^{\sigma}\mathrm{e}^{-\mathrm{i}q_{\mathrm{e,Ni}}^{\downarrow}z}\right)\begin{bmatrix}0\\u_{\mathrm{Ni}}^{\downarrow}\\0\\v_{\mathrm{Ni}}^{\downarrow}\end{bmatrix}\\ + \left(\eta_1^{\sigma}\mathrm{e}^{-\mathrm{i}q_{\mathrm{h,Ni}}^{\uparrow}z} + \eta_2^{\sigma}\mathrm{e}^{\mathrm{i}q_{\mathrm{h,Ni}}^{\uparrow}z}\right)\begin{bmatrix}v_{\mathrm{Ni}}^{\uparrow}\\0\\u_{\mathrm{Ni}}^{\uparrow}\\0\end{bmatrix} + \left(\eta_3^{\sigma}\mathrm{e}^{-\mathrm{i}q_{\mathrm{h,Ni}}^{\downarrow}z} + \eta_4^{\sigma}\mathrm{e}^{\mathrm{i}q_{\mathrm{h,Ni}}^{\downarrow}z}\right)\begin{bmatrix}0\\v_{\mathrm{Ni}}^{\downarrow}\\0\\u_{\mathrm{Ni}}^{\downarrow}\end{bmatrix},\end{aligned} \tag{A.26}$$

in the interfacial NiGa alloy ($d_{\mathrm{Ni}} < z < d_{\mathrm{NiGa}}$),

$$\begin{aligned}\psi^{\sigma}(d_{\mathrm{Ni}}<z<d_{\mathrm{NiGa}}) = \left(\overline{\varepsilon}_1^{\sigma}\mathrm{e}^{\mathrm{i}q_{\mathrm{e,NiGa}}z} + \overline{\varepsilon}_2^{\sigma}\mathrm{e}^{-\mathrm{i}q_{\mathrm{e,NiGa}}z}\right)\begin{bmatrix}u_{\mathrm{NiGa}}\\0\\v_{\mathrm{NiGa}}\\0\end{bmatrix} + \left(\overline{\varepsilon}_3^{\sigma}\mathrm{e}^{\mathrm{i}q_{\mathrm{e,NiGa}}z} + \overline{\varepsilon}_4^{\sigma}\mathrm{e}^{-\mathrm{i}q_{\mathrm{e,NiGa}}z}\right)\begin{bmatrix}0\\u_{\mathrm{NiGa}}\\0\\v_{\mathrm{NiGa}}\end{bmatrix}\\ + \left(\overline{\eta}_1^{\sigma}\mathrm{e}^{-\mathrm{i}q_{\mathrm{h,NiGa}}z} + \overline{\eta}_2^{\sigma}\mathrm{e}^{\mathrm{i}q_{\mathrm{h,NiGa}}z}\right)\begin{bmatrix}v_{\mathrm{NiGa}}\\0\\u_{\mathrm{NiGa}}\\0\end{bmatrix} + \left(\overline{\eta}_3^{\sigma}\mathrm{e}^{-\mathrm{i}q_{\mathrm{h,NiGa}}z} + \overline{\eta}_4^{\sigma}\mathrm{e}^{\mathrm{i}q_{\mathrm{h,NiGa}}z}\right)\begin{bmatrix}0\\v_{\mathrm{NiGa}}\\0\\u_{\mathrm{NiGa}}\end{bmatrix},\end{aligned} \tag{A.27}$$

and in the gallium electrode ($z > d_{\mathrm{NiGa}}$),

$$\psi^{\sigma}(z > d_{\mathrm{NiGa}}) = t_{\mathrm{e}}^{\sigma,\uparrow}\begin{bmatrix} u_{\mathrm{Ga}} \\ 0 \\ v_{\mathrm{Ga}} \\ 0 \end{bmatrix} \mathrm{e}^{\mathrm{i}q_{\mathrm{e,Ga}}z} + t_{\mathrm{e}}^{\sigma,\downarrow}\begin{bmatrix} 0 \\ u_{\mathrm{Ga}} \\ 0 \\ v_{\mathrm{Ga}} \end{bmatrix} \mathrm{e}^{\mathrm{i}q_{\mathrm{e,Ga}}z} + t_{\mathrm{h}}^{\sigma,\uparrow}\begin{bmatrix} v_{\mathrm{Ga}} \\ 0 \\ u_{\mathrm{Ga}} \\ 0 \end{bmatrix} \mathrm{e}^{-\mathrm{i}q_{\mathrm{h,Ga}}z} + t_{\mathrm{h}}^{\sigma,\downarrow}\begin{bmatrix} 0 \\ v_{\mathrm{Ga}} \\ 0 \\ u_{\mathrm{Ga}} \end{bmatrix} \mathrm{e}^{-\mathrm{i}q_{\mathrm{h,Ga}}z}, \quad \text{(A.28)}$$

come again as solutions from the stationary Bogoljubov-de Gennes equation. The reflection and transmission coefficients are denoted in the same manner as in the left half-junction except that we omit the tilde to clarify the distinct tunneling barrier heights (widths). The coherence factors fulfill

$$u_{\mathrm{Ni}}^{\uparrow(\downarrow)} = u_{\mathrm{Ni}}^{\uparrow(\downarrow)}(E) = \sqrt{\frac{1}{2}\left\{1 + \sqrt{1 - \frac{|\Delta_{\mathrm{S,Ni}}|^2}{\left[E + (-)\Delta_{\mathrm{XC,Ni}}/2\right]^2}}\right\}} \quad \text{(A.29)}$$

and

$$v_{\mathrm{Ni}}^{\uparrow(\downarrow)} = v_{\mathrm{Ni}}^{\uparrow(\downarrow)}(E) = \sqrt{1 - \left[u_{\mathrm{Ni}}^{\uparrow(\downarrow)}(E)\right]^2} \quad \text{(A.30)}$$

in nickel, as well as

$$u_{\mathrm{X}} = u_{\mathrm{X}}(E) = \sqrt{\frac{1}{2}\left(1 + \sqrt{1 - \frac{|\Delta_{\mathrm{S,X}}|^2}{E^2}}\right)} \qquad \text{and} \qquad v_{\mathrm{X}} = v_{\mathrm{X}}(E) = \sqrt{1 - [u_{\mathrm{X}}(E)]^2} \quad \text{(A.31)}$$

in the alloy and gallium electrode (setting $\mathrm{X} \in \{\mathrm{NiGa}; \mathrm{Ga}\}$). The electronlike and holelike wave vectors are analogously

$$q_{\mathrm{e,Ni}}^{\uparrow(\downarrow)} = q_{\mathrm{e,Ni}}^{\uparrow(\downarrow)}(E) = \sqrt{\frac{2m}{\hbar^2}\left\{\mu + \sqrt{\left[E + (-)\frac{\Delta_{\mathrm{XC,Ni}}}{2}\right]^2 - |\Delta_{\mathrm{S,Ni}}|^2}\right\}} \quad \text{(A.32)}$$

and

$$q_{\mathrm{h,Ni}}^{\uparrow(\downarrow)} = q_{\mathrm{h,Ni}}^{\uparrow(\downarrow)}(E) = \sqrt{\frac{2m}{\hbar^2}\left\{\mu - \sqrt{\left[E + (-)\frac{\Delta_{\mathrm{XC,Ni}}}{2}\right]^2 - |\Delta_{\mathrm{S,Ni}}|^2}\right\}}, \quad \text{(A.33)}$$

as well as

$$q_{\mathrm{e,X}} = q_{\mathrm{e,X}}(E) = \sqrt{\frac{2m}{\hbar^2}\left(\mu + \sqrt{E^2 - |\Delta_{\mathrm{S,X}}|^2}\right)} \quad \text{and} \quad q_{\mathrm{h,X}} = q_{\mathrm{h,X}}(E) = \sqrt{\frac{2m}{\hbar^2}\left(\mu - \sqrt{E^2 - |\Delta_{\mathrm{S,X}}|^2}\right)}; \quad \text{(A.34)}$$

the wave vectors in the normal-state region are essentially the same as encountered in the left half-junction and do not need to be repeated another time. Requiring the scattering states to obey the interfacial ($z = 0$, $z = d_{\mathrm{Ni}}$, and $z = d_{\mathrm{NiGa}}$) boundary conditions

$$\psi^{\sigma}(z)\big|_{z=0_-} = \psi^{\sigma}(z)\big|_{z=0_+}, \qquad \psi^{\sigma}(z)\big|_{z=d_{\mathrm{Ni}_-}} = \psi^{\sigma}(z)\big|_{z=d_{\mathrm{Ni}_+}}, \quad \text{(A.35)}$$

$$\psi^{\sigma}(z)\big|_{z=d_{\mathrm{NiGa}_-}} = \psi^{\sigma}(z)\big|_{z=d_{\mathrm{NiGa}_+}}, \qquad \left(\frac{\hbar^2}{2m}\frac{\mathrm{d}}{\mathrm{d}z} + V_{\mathrm{I}}d_{\mathrm{I}}\right)\hat{\eta}\psi^{\sigma}(z)\big|_{z=0_-} = \frac{\hbar^2}{2m}\frac{\mathrm{d}}{\mathrm{d}z}\hat{\eta}\psi^{\sigma}(z)\big|_{z=0_+}, \quad \text{(A.36)}$$

$$\frac{\mathrm{d}}{\mathrm{d}z}\psi^{\sigma}(z)\big|_{z=d_{\mathrm{Ni}_-}} = \frac{\mathrm{d}}{\mathrm{d}z}\psi^{\sigma}(z)\big|_{z=d_{\mathrm{Ni}_+}}, \quad \text{and} \qquad \frac{\mathrm{d}}{\mathrm{d}z}\psi^{\sigma}(z)\big|_{z=d_{\mathrm{NiGa}_-}} = \frac{\mathrm{d}}{\mathrm{d}z}\psi^{\sigma}(z)\big|_{z=d_{\mathrm{NiGa}_+}}, \quad \text{(A.37)}$$

and numerically solving the resulting system of equations, we initially arrive at the scattering coefficients and afterwards at the related scattering *probabilities*

$$R_{\mathrm{e}}^{\sigma,\uparrow} = R_{\mathrm{e}}^{\sigma,\uparrow}(E) = \left| r_{\mathrm{e}}^{\sigma,\uparrow} \right|^2, \tag{A.38}$$

$$R_{\mathrm{e}}^{\sigma,\downarrow} = R_{\mathrm{e}}^{\sigma,\downarrow}(E) = \left| r_{\mathrm{e}}^{\sigma,\downarrow} \right|^2, \tag{A.39}$$

$$R_{\mathrm{h}}^{\sigma,\uparrow} = R_{\mathrm{h}}^{\sigma,\uparrow}(E) = \mathrm{Re}\left(\frac{k_{\mathrm{h}}}{k_{\mathrm{e}}}\right) \left| r_{\mathrm{h}}^{\sigma,\uparrow} \right|^2, \tag{A.40}$$

$$R_{\mathrm{h}}^{\sigma,\downarrow} = R_{\mathrm{h}}^{\sigma,\downarrow}(E) = \mathrm{Re}\left(\frac{k_{\mathrm{h}}}{k_{\mathrm{e}}}\right) \left| r_{\mathrm{h}}^{\sigma,\downarrow} \right|^2, \tag{A.41}$$

$$T_{\mathrm{e}}^{\sigma,\uparrow} = T_{\mathrm{e}}^{\sigma,\uparrow}(E) = \mathrm{Re}\left(\frac{q_{\mathrm{e,Ga}}}{k_{\mathrm{e}}}\right) \left| t_{\mathrm{e}}^{\sigma,\uparrow} \right|^2 \left[|u_{\mathrm{Ga}}|^2 - |v_{\mathrm{Ga}}|^2 \right] \Theta\Big(E - |\Delta_{\mathrm{S,Ga}}|\Big), \tag{A.42}$$

$$T_{\mathrm{e}}^{\sigma,\downarrow} = T_{\mathrm{e}}^{\sigma,\downarrow}(E) = \mathrm{Re}\left(\frac{q_{\mathrm{e,Ga}}}{k_{\mathrm{e}}}\right) \left| t_{\mathrm{e}}^{\sigma,\downarrow} \right|^2 \left[|u_{\mathrm{Ga}}|^2 - |v_{\mathrm{Ga}}|^2 \right] \Theta\Big(E - |\Delta_{\mathrm{S,Ga}}|\Big), \tag{A.43}$$

$$T_{\mathrm{h}}^{\sigma,\uparrow} = T_{\mathrm{h}}^{\sigma,\uparrow}(E) = \mathrm{Re}\left(\frac{q_{\mathrm{h,Ga}}}{k_{\mathrm{e}}}\right) \left| t_{\mathrm{h}}^{\sigma,\uparrow} \right|^2 \left[|u_{\mathrm{Ga}}|^2 - |v_{\mathrm{Ga}}|^2 \right] \Theta\Big(E - |\Delta_{\mathrm{S,Ga}}|\Big), \tag{A.44}$$

as well as

$$T_{\mathrm{h}}^{\sigma,\downarrow} = T_{\mathrm{h}}^{\sigma,\downarrow}(E) = \mathrm{Re}\left(\frac{q_{\mathrm{h,Ga}}}{k_{\mathrm{e}}}\right) \left| t_{\mathrm{h}}^{\sigma,\downarrow} \right|^2 \left[|u_{\mathrm{Ga}}|^2 - |v_{\mathrm{Ga}}|^2 \right] \Theta\Big(E - |\Delta_{\mathrm{S,Ga}}|\Big). \tag{A.45}$$

For short, we write the scattering probabilities as

$$R_{\mathrm{e}}^{\sigma}(E) := R_{\mathrm{e}}^{\sigma,\uparrow}(E) + R_{\mathrm{e}}^{\sigma,\downarrow}(E), \tag{A.46}$$

$$R_{\mathrm{h}}^{\sigma}(E) := R_{\mathrm{h}}^{\sigma,\uparrow}(E) + R_{\mathrm{h}}^{\sigma,\downarrow}(E), \tag{A.47}$$

and

$$T^{\sigma}(E) := T_{\mathrm{e}}^{\sigma}(E) + T_{\mathrm{h}}^{\sigma}(E) = T_{\mathrm{e}}^{\sigma,\uparrow}(E) + T_{\mathrm{e}}^{\sigma,\downarrow}(E) + T_{\mathrm{h}}^{\sigma,\uparrow}(E) + T_{\mathrm{h}}^{\sigma,\downarrow}(E). \tag{A.48}$$

Resubstituting the obtained scattering probability expressions of both half-junctions into Eq. (4.13), we are fully equipped to compute the distribution of right-movers and subsequently also the one of left-movers making use of Eq. (4.12). The outcomes enter finally Eq. (4.14) and give direct access to the tunneling current flow and tunneling conductance we wish to compute. Numerical results extracted from this OTBK modeling are analyzed in Sec. 4.3 (see particularly Fig. 4.13). When evaluating the current at finite temperature, all superconducting energy gaps are approximated by their BCS-like temperature scaling $|\Delta_{\mathrm{S,X}}(T \neq 0)| = |\Delta_{\mathrm{S,X}}(0)| \tanh(1.74\sqrt{T_{\mathrm{C,X}}/T - 1})$ with $\mathrm{X} \in \{\mathrm{Al}; \mathrm{Ni}; \mathrm{NiGa}; \mathrm{Ga}\}$; the respective values of $|\Delta_{\mathrm{S,X}}(0)|$ and $T_{\mathrm{C,X}}$ are listed in Tab. 4.1.

Appendix B

Matsubara Green's function of S/F/S Josephson junctions

Derivation of the electrical current density in terms of the Matsubara Green's function

The electrical current's *stationary* continuity equation

$$\frac{\partial}{\partial z}\left[j_z^q(z) + \int_0^z \mathrm{d}z'\, s(z')\right] = 0, \tag{B.1}$$

with the electrical current density $j_z^q(z)$ and the source term $s(z)$, is our starting point for deriving the Josephson current in Sec. 6.2. The source term accounts for the additional supercurrent contributions that are not already captured by the electrical current density. To extract the total (conserved) Josephson current flow from Eq. (B.1), we need to determine explicit analytical expressions for its two separate parts.

We initially evaluate the bare contribution of $j_z^q(z)$, following Ref. [140] and adapting the notation to the one used in this thesis. Since we wish to compute the current at finite temperature, the net current contribution coming from $j_z^q(z)$ is quantum mechanically given by the *thermally averaged* expectation value $\langle \ldots \rangle_{\text{thermal}}$ of the related current density *operator* $\hat{j}_z^q$ within our Bogoljubov-de Gennes scattering picture,

$$\left\langle j_z^q(z)\big|_{\mathbf{k}_\parallel=\text{const.}}\right\rangle_{\text{thermal}} = \sum_{E\lesseqgtr 0}\left\langle u(E)\middle|\hat{j}_z^q\middle|u(E)\right\rangle f^0(E) + \sum_{E\lesseqgtr 0}\left\langle v(E)\middle|\left(\hat{j}_z^q\right)^*\middle|v(E)\right\rangle\left[1-f^0(E)\right]. \tag{B.2}$$

At the moment, we treat the transverse wave vector $\mathbf{k}_\parallel$ as a constant. We furthermore used that the Bogoljubov-de Gennes scattering state inside the left superconductor, $\psi^{(i)}(z<0)$, is fully determined knowing its electronlike part u and its holelike part v; i refers again to the four quasiparticle injection processes we need to take care of [see our detailed discussions in Sec. 6.2]. Although the notation is similar, it will turn our later on that u and v do *not* simply refer to the BCS coherence factors. Instead, we additionally accumulated the scattering states' plane-wave factors in u and v. The current's expectation value can then be computed separately for the electronlike [first summand in Eq. (B.2)] and holelike [second summand in Eq. (B.2)] parts of the Bogoljubov-de Gennes states. Since we need to perform thermal averaging, the individual electronlike (holelike) expectation values get multiplied by the probability that the states are occupied (unoccupied), generically described by the Fermi-Dirac distribution function $f^0(E)$.

Due to the characteristic *electron-hole symmetry* within our approach, each positive-energy state ($E>0$) is accompanied by a second one with negative energy ($E<0$), which is obtained replacing the BCS coherence factors according to $u(E>0)\longmapsto -v^*(E<0)$ and $v(E>0)\longmapsto u^*(E<0)$. To bring Eq. (B.2)

into a compact form, we split the sum over E into positive- and negative-energy contributions,

$$\begin{aligned}\left\langle j_z^q(z)\big|_{\mathbf{k}_\parallel=\text{const.}}\right\rangle_{\text{thermal}} &= \sum_{E>0}\left\langle u(E>0)\middle|\hat{j}_z^q\middle|u(E>0)\right\rangle f^0(E>0)\\ &+\sum_{E>0}\left\langle v(E>0)\middle|\left(\hat{j}_z^q\right)^*\middle|v(E>0)\right\rangle\left[1-f^0(E>0)\right]\\ &+\sum_{E<0}\left\langle u(E<0)\middle|\hat{j}_z^q\middle|u(E<0)\right\rangle f^0(E<0)\\ &+\sum_{E<0}\left\langle v(E<0)\middle|\left(\hat{j}_z^q\right)^*\middle|v(E<0)\right\rangle\left[1-f^0(E<0)\right],\end{aligned}\tag{B.3}$$

and transform the red contribution into a sum over *negative* energies, and analogously the blue contribution into a sum over *positive* energies, exploiting the stated electron-hole symmetry and $1-f^0(-E)=f^0(E)$. This yields

$$\begin{aligned}\left\langle j_z^q(z)\big|_{\mathbf{k}_\parallel=\text{const.}}\right\rangle_{\text{thermal}} &= \sum_{E>0}\left\langle u(E>0)\middle|\hat{j}_z^q\middle|u(E>0)\right\rangle f^0(E>0)\\ &+\sum_{E<0}\left\langle u(E<0)\middle|\hat{j}_z^q\middle|u(E<0)\right\rangle f^0(E<0)\\ &+\sum_{E<0}\left\langle u(E<0)\middle|\hat{j}_z^q\middle|u(E<0)\right\rangle f^0(E<0)\\ &+\sum_{E>0}\left\langle u(E>0)\middle|\hat{j}_z^q\middle|u(E>0)\right\rangle f^0(E>0),\end{aligned}\tag{B.4}$$

which can be contracted to

$$\left\langle j_z^q(z)\big|_{\mathbf{k}_\parallel=\text{const.}}\right\rangle_{\text{thermal}} = 2\sum_{E\lesseqgtr 0}\left\langle u(E)\middle|\hat{j}_z^q\middle|u(E)\right\rangle f^0(E).\tag{B.5}$$

To further evaluate Eq. (B.5), we substitute the explicit form of the ($\hat{z}$-component of the) electrical current density operator to obtain

$$\left\langle j_z^q(z)\big|_{\mathbf{k}_\parallel=\text{const.}}\right\rangle_{\text{thermal}} = -\frac{e\hbar}{\mathrm{i}m}\sum_{E\lesseqgtr 0}\left[u^*(E;z)\frac{\partial}{\partial z}u(E;z)-u(E;z)\frac{\partial}{\partial z}u^*(E;z)\right]f^0(E);\tag{B.6}$$

e is the positive elementary charge. Recall that the Bogoljubov-de Gennes scattering states [see Eqs. (6.32)–(6.34)] propagate along $\hat{z}$. The respective plane-wave factors got now indeed additionally accumulated in the BCS coherence factors, highlighted by stating their spatial dependence $u(E;z)$ and $v(E;z)$. Rewriting Eq. (B.6) as

$$\left\langle j_z^q(z)\big|_{\mathbf{k}_\parallel=\text{const.}}\right\rangle_{\text{thermal}} = -\frac{e\hbar}{\mathrm{i}m}\lim_{z'\to z}\sum_{E\lesseqgtr 0}\left[\left(\frac{\partial}{\partial z}-\frac{\partial}{\partial z'}\right)u(E;z)u^*(E;z')\right]f^0(E),\tag{B.7}$$

and replacing the Fermi-Dirac function $f^0(E)$ by its Matsubara series representation

$$f^0(E)=\sum_{\omega_n}\frac{k_\mathrm{B}T}{\mathrm{i}\omega_n-E},\tag{B.8}$$

where k_B denotes Boltzmann's constant and ω_n are the fermionic Matsubara frequencies [see Eq. (6.56) for their definition], leads to

$$\left\langle j_z^q(z)\big|_{\mathbf{k}_\parallel=\text{const.}}\right\rangle_\text{thermal} = -\frac{e\hbar}{\mathrm{i}m}\lim_{z'\to z}\sum_{E\lesseqgtr 0}\sum_{\omega_n}\left[\left(\frac{\partial}{\partial z}-\frac{\partial}{\partial z'}\right)u(E;z)u^*(E;z')\right]\frac{k_\mathrm{B}T}{\mathrm{i}\omega_n - E}. \tag{B.9}$$

We finally identify

$$\mathrm{Tr}\left\{\check{\mathcal{G}}(z,z';\mathrm{i}\omega_n)^{(i)}\right\} \equiv \sum_{E\lesseqgtr 0}\frac{u(E;z)u^*(E;z')}{\mathrm{i}\omega_n - E} \tag{B.10}$$

as the trace taken over the series representation of the ith scattering state's Matsubara Green's function $\check{\mathcal{G}}(z,z';\mathrm{i}\omega_n)^{(i)}$ and reduce Eq. (B.9) to

$$\left\langle j_z^q(z)\big|_{\mathbf{k}_\parallel=\text{const.}}\right\rangle_\text{thermal} = -\frac{e\hbar}{\mathrm{i}m}k_\mathrm{B}T\lim_{z'\to z}\left(\frac{\partial}{\partial z}-\frac{\partial}{\partial z'}\right)\sum_{\omega_n}\mathrm{Tr}\left\{\check{\mathcal{G}}(z,z';\mathrm{i}\omega_n)^{(i)}\right\}. \tag{B.11}$$

When solving for the Bogoljubov-de Gennes scattering states in our three-dimensional junction, we assumed translational invariance parallel to the interfaces, i.e., $\mathbf{k}_\parallel$ is conserved and is simply an effective measure that counts the number of transverse channels in our system. So far, we considered $\mathbf{k}_\parallel$ to be constant. The current contributions originating from all transverse channels are extracted from our description evaluating Eq. (B.11) for *each* $\mathbf{k}_\parallel$ and summing up all contributions. Moreover, computing the total Josephson current requires us to include all four possible quasiparticle injection processes. Each of them can be uniquely identified by one scattering state and its corresponding Matsubara Green's function. Since all four processes are *equally probable*, we average the total Josephson current considering the full Matsubara Green's function $\check{\mathcal{G}}(z,z';\mathrm{i}\omega_n)$, which is basically the sum of the four processes' individual Matsubara Green's functions, and dividing the result by a factor of four. The final expression for the Josephson current reads then

$$\begin{aligned}\left\langle j_z^q(z)\right\rangle_\text{thermal} &= -\frac{e\hbar}{4\mathrm{i}m}k_\mathrm{B}T\lim_{z'\to z}\left(\frac{\partial}{\partial z}-\frac{\partial}{\partial z'}\right)\sum_{\mathbf{k}_\parallel}\sum_{\omega_n}\mathrm{Tr}\left\{\check{\mathcal{G}}(z,z';\mathrm{i}\omega_n)\right\}\\ &= \frac{e\hbar}{4\mathrm{i}m}k_\mathrm{B}T\lim_{z'\to z}\left(\frac{\partial}{\partial z'}-\frac{\partial}{\partial z}\right)\sum_{\mathbf{k}_\parallel}\sum_{\omega_n}\mathrm{Tr}\left\{\check{\mathcal{G}}(z,z';\mathrm{i}\omega_n)\right\},\end{aligned} \tag{B.12}$$

which we stated as Eq. (6.55) in the main part. Equation (B.12) is general and can be applied to any Josephson geometry. All junction-specific information is hidden in the Matsubara Green's function, which we will figure out in the following. Afterwards, we evaluate Eq. (B.12), extract the corresponding source term contribution from the current's continuity equation, and put both together to access the total Josephson current. The details are worked out in Sec. 6.2.

Matsubara Green's function for S/F/S Josephson junctions

To benefit from Eq. (B.12), we need to find the Matsubara Green's function $\check{\mathcal{G}}(z,z';\mathrm{i}\omega_n)$ of our ballistic S/F/S Josephson junction. Since we compute the Josephson current in the asymptotic region of the left superconductor, it is also sufficient to identify $\check{\mathcal{G}}(z,z';\mathrm{i}\omega_n)$ there. According to McMillan's approach [477], which was initially developed to extract superconductor/metal junctions' single-particle quantities (e.g., their DOS), the *retarded* Green's function for particles with energy E, $\check{G}_\mathrm{R}(z,z'<z;E)$, is proportional to the direct product of their incoming (at position z') and scattered (at position z) waves. An incident spin-up electronlike quasiparticle is, for instance, described by the incoming wave $\psi^{(1)}_\text{incoming}(z'<0)$ [see Eq. (6.35)], while the respective scattered state at $z>z'$ is given

by $\psi^{(1)}(z<0)$ [see Eq. (6.32)]. In the same way, we take care of the remaining processes, covering incoming spin-down electronlike quasiparticles, as well as spin-up and spin-down holelike quasiparticles. All required incident and scattered states are known from our considerations in Sec. 6.2.

Putting everything together, we can formulate the ansatz

$$\begin{aligned}\check{G}_{\mathrm{R}}(z,z'<z;E) = {} & a\,\psi^{(1)}(z<0)\,\left[\psi^{(1)}_{\text{incoming}}(z'<z)\right]^{\dagger}\\ & + b\,\psi^{(2)}(z<0)\,\left[\psi^{(2)}_{\text{incoming}}(z'<z)\right]^{\dagger}\\ & + c\,\psi^{(3)}(z<0)\,\left[\psi^{(3)}_{\text{incoming}}(z'<z)\right]^{\dagger}\\ & + d\,\psi^{(4)}(z<0)\,\left[\psi^{(4)}_{\text{incoming}}(z'<z)\right]^{\dagger}\end{aligned} \tag{B.13}$$

for the retarded Green's function $\check{G}_{\mathrm{R}}(z,z'<z;E)$; the one in the case $z'>z$ is constructed analogously. The normalization coefficients a, b, c, and d need to be chosen such that $\check{G}_{\mathrm{R}}(z,z';E)$ fulfills the interfacial ($z=0$) boundary conditions

$$\check{G}_{\mathrm{R}}(z,z';E)\big|_{z'=z-0_+} = \check{G}_{\mathrm{R}}(z,z';E)\big|_{z'=z+0_+} \tag{B.14}$$

and

$$\frac{\mathrm{d}}{\mathrm{d}z}\check{G}_{\mathrm{R}}(z,z';E)\big|_{z=z'+0_+} - \frac{\mathrm{d}}{\mathrm{d}z}\check{G}_{\mathrm{R}}(z,z';E)\big|_{z=z'-0_+} = \frac{2m}{\hbar^2}\begin{bmatrix}\hat{\sigma}_0 & \hat{0}\\ \hat{0} & -\hat{\sigma}_0\end{bmatrix}; \tag{B.15}$$

$\hat{0}$ is the two-by-two zero matrix. Once we obtained an analytical expression for $\check{G}_{\mathrm{R}}(z,z';E)$, we recover the related Matsubara Green's function $\check{\mathcal{G}}(z,z';\mathrm{i}\omega_n)$ through analytically continuing the excitation energies E to the complex plane, $E\longmapsto \mathrm{i}\omega_n$; ω_n are again the fermionic Matsubara frequencies [see Eq. (6.56)]. To be specific, the analytic continuation needs to be done in the BCS coherence factors, in the quasiparticles' wave vectors, and in all scattering coefficients (stressed in the following by explicitly stating their ω_n-dependence). After a long and rather technical calculation, we end up with the Matsubara Green's function of the considered S/F/S Josephson junction,

$$\check{\mathcal{G}}(z,z';\mathrm{i}\omega_n) = \check{\mathcal{G}}^{(1)}(z,z';\mathrm{i}\omega_n) + \check{\mathcal{G}}^{(2)}(z,z';\mathrm{i}\omega_n) + \check{\mathcal{G}}^{(3)}(z,z';\mathrm{i}\omega_n) + \check{\mathcal{G}}^{(4)}(z,z';\mathrm{i}\omega_n), \tag{B.16}$$

where the four individual constituents are given within the next pages. Substituting Eq. (B.16) into Eq. (B.12) and continuing with the procedure explained in Sec. 6.2, we eventually recover Eq. (6.59) for the S/F/S junction's total Josephson current.

The individual components entering Eq. (B.16) have the form

$$
\begin{aligned}
\check{\mathcal{G}}^{(1)}(z,z';\mathrm{i}\omega_n) = -\frac{\mathrm{i}m}{\hbar^2 q_{z,\mathrm{e}}(\mathrm{i}\omega_n)\left[|u(\mathrm{i}\omega_n)|^2-|v(\mathrm{i}\omega_n)|^2\right]}
&\left(\mathrm{e}^{\mathrm{i}q_{z,\mathrm{e}}(\mathrm{i}\omega_n)|z-z'|}
\begin{bmatrix}
|u(\mathrm{i}\omega_n)|^2 & 0 & u(\mathrm{i}\omega_n)v^*(\mathrm{i}\omega_n) & 0\\
0 & 0 & 0 & 0\\
v(\mathrm{i}\omega_n)u^*(\mathrm{i}\omega_n) & 0 & |v(\mathrm{i}\omega_n)|^2 & 0\\
0 & 0 & 0 & 0
\end{bmatrix}\right.\\
&+\mathcal{A}^{(1)}(\mathrm{i}\omega_n)\,\mathrm{e}^{-\mathrm{i}q_{z,\mathrm{e}}(\mathrm{i}\omega_n)(z+z')}
\begin{bmatrix}
|u(\mathrm{i}\omega_n)|^2 & 0 & u(\mathrm{i}\omega_n)v^*(\mathrm{i}\omega_n) & 0\\
0 & 0 & 0 & 0\\
v(\mathrm{i}\omega_n)u^*(\mathrm{i}\omega_n) & 0 & |v(\mathrm{i}\omega_n)|^2 & 0\\
0 & 0 & 0 & 0
\end{bmatrix}\\
&+\mathcal{B}^{(1)}(\mathrm{i}\omega_n)\,\mathrm{e}^{-\mathrm{i}q_{z,\mathrm{e}}(\mathrm{i}\omega_n)(z+z')}
\begin{bmatrix}
0 & 0 & 0 & 0\\
|u(\mathrm{i}\omega_n)|^2 & 0 & u(\mathrm{i}\omega_n)v^*(\mathrm{i}\omega_n) & 0\\
0 & 0 & 0 & 0\\
v(\mathrm{i}\omega_n)u^*(\mathrm{i}\omega_n) & 0 & |v(\mathrm{i}\omega_n)|^2 & 0
\end{bmatrix}\\
&+C^{(1)}(\mathrm{i}\omega_n)\,\mathrm{e}^{\mathrm{i}\left[q_{z,\mathrm{h}}(\mathrm{i}\omega_n)z-q_{z,\mathrm{e}}(\mathrm{i}\omega_n)z'\right]}
\begin{bmatrix}
v(\mathrm{i}\omega_n)u^*(\mathrm{i}\omega_n) & 0 & |v(\mathrm{i}\omega_n)|^2 & 0\\
0 & 0 & 0 & 0\\
|u(\mathrm{i}\omega_n)|^2 & 0 & u(\mathrm{i}\omega_n)v^*(\mathrm{i}\omega_n) & 0\\
0 & 0 & 0 & 0
\end{bmatrix}\\
&\left.+\mathcal{D}^{(1)}(\mathrm{i}\omega_n)\,\mathrm{e}^{\mathrm{i}\left[q_{z,\mathrm{h}}(\mathrm{i}\omega_n)z-q_{z,\mathrm{e}}(\mathrm{i}\omega_n)z'\right]}
\begin{bmatrix}
0 & 0 & 0 & 0\\
v(\mathrm{i}\omega_n)u^*(\mathrm{i}\omega_n) & 0 & |v(\mathrm{i}\omega_n)|^2 & 0\\
0 & 0 & 0 & 0\\
|u(\mathrm{i}\omega_n)|^2 & 0 & u(\mathrm{i}\omega_n)v^*(\mathrm{i}\omega_n) & 0
\end{bmatrix}\right),
\end{aligned}
\tag{B.17}
$$

$$\check{\mathcal{G}}^{(2)}(z,z';\mathrm{i}\omega_n) = -\frac{\mathrm{i}m}{\hbar^2 q_{z,\mathrm{e}}(\mathrm{i}\omega_n)\left[\left|u(\mathrm{i}\omega_n)\right|^2 - \left|v(\mathrm{i}\omega_n)\right|^2\right]} \Bigg\{ \mathrm{e}^{\mathrm{i}q_{z,\mathrm{e}}(\mathrm{i}\omega_n)|z-z'|} \begin{bmatrix} 0 & 0 & 0 & 0 \\ 0 & \left|u(\mathrm{i}\omega_n)\right|^2 & 0 & u(\mathrm{i}\omega_n)v^*(\mathrm{i}\omega_n) \\ 0 & 0 & 0 & 0 \\ 0 & v(\mathrm{i}\omega_n)u^*(\mathrm{i}\omega_n) & 0 & \left|v(\mathrm{i}\omega_n)\right|^2 \end{bmatrix}$$

$$+ \mathcal{A}^{(2)}(\mathrm{i}\omega_n)\, \mathrm{e}^{-\mathrm{i}q_{z,\mathrm{e}}(\mathrm{i}\omega_n)(z+z')} \begin{bmatrix} 0 & \left|u(\mathrm{i}\omega_n)\right|^2 & 0 & u(\mathrm{i}\omega_n)v^*(\mathrm{i}\omega_n) \\ 0 & 0 & 0 & 0 \\ 0 & v(\mathrm{i}\omega_n)u^*(\mathrm{i}\omega_n) & 0 & \left|v(\mathrm{i}\omega_n)\right|^2 \\ 0 & 0 & 0 & 0 \end{bmatrix}$$

$$+ \mathcal{B}^{(2)}(\mathrm{i}\omega_n)\, \mathrm{e}^{-\mathrm{i}q_{z,\mathrm{e}}(\mathrm{i}\omega_n)(z+z')} \begin{bmatrix} 0 & 0 & 0 & 0 \\ 0 & \left|u(\mathrm{i}\omega_n)\right|^2 & 0 & u(\mathrm{i}\omega_n)v^*(\mathrm{i}\omega_n) \\ 0 & 0 & 0 & 0 \\ 0 & v(\mathrm{i}\omega_n)u^*(\mathrm{i}\omega_n) & 0 & \left|v(\mathrm{i}\omega_n)\right|^2 \end{bmatrix}$$

$$+ C^{(2)}(\mathrm{i}\omega_n)\, \mathrm{e}^{\mathrm{i}\left[q_{z,\mathrm{h}}(\mathrm{i}\omega_n)z - q_{z,\mathrm{e}}(\mathrm{i}\omega_n)z'\right]} \begin{bmatrix} 0 & v(\mathrm{i}\omega_n)u^*(\mathrm{i}\omega_n) & 0 & \left|v(\mathrm{i}\omega_n)\right|^2 \\ 0 & 0 & 0 & 0 \\ 0 & \left|u(\mathrm{i}\omega_n)\right|^2 & 0 & u(\mathrm{i}\omega_n)v^*(\mathrm{i}\omega_n) \\ 0 & 0 & 0 & 0 \end{bmatrix}$$

$$+ \mathcal{D}^{(2)}(\mathrm{i}\omega_n)\, \mathrm{e}^{\mathrm{i}\left[q_{z,\mathrm{h}}(\mathrm{i}\omega_n)z - q_{z,\mathrm{e}}(\mathrm{i}\omega_n)z'\right]} \begin{bmatrix} 0 & 0 & 0 & 0 \\ 0 & v(\mathrm{i}\omega_n)u^*(\mathrm{i}\omega_n) & 0 & \left|v(\mathrm{i}\omega_n)\right|^2 \\ 0 & 0 & 0 & 0 \\ 0 & \left|u(\mathrm{i}\omega_n)\right|^2 & 0 & u(\mathrm{i}\omega_n)v^*(\mathrm{i}\omega_n) \end{bmatrix} \Bigg\}, \tag{B.18}$$

$$\check{\mathcal{G}}^{(3)}(z,z';\mathrm{i}\omega_n) = -\frac{\mathrm{i}m}{\hbar^2 q_{z,\mathrm{h}}(\mathrm{i}\omega_n)\left[|u(\mathrm{i}\omega_n)|^2 - |v(\mathrm{i}\omega_n)|^2\right]} \left\{ \mathrm{e}^{-\mathrm{i}q_{z,\mathrm{h}}(\mathrm{i}\omega_n)|z-z'|} \begin{bmatrix} |v(\mathrm{i}\omega_n)|^2 & 0 & v(\mathrm{i}\omega_n)u^*(\mathrm{i}\omega_n) & 0 \\ 0 & 0 & 0 & 0 \\ u(\mathrm{i}\omega_n)v^*(\mathrm{i}\omega_n) & 0 & |u(\mathrm{i}\omega_n)|^2 & 0 \\ 0 & 0 & 0 & 0 \end{bmatrix} \right.$$

$$+ \mathcal{A}^{(3)}(\mathrm{i}\omega_n)\,\mathrm{e}^{-\mathrm{i}\left[q_{z,\mathrm{e}}(\mathrm{i}\omega_n)z - q_{z,\mathrm{h}}(\mathrm{i}\omega_n)z'\right]} \begin{bmatrix} u(\mathrm{i}\omega_n)v^*(\mathrm{i}\omega_n) & 0 & |u(\mathrm{i}\omega_n)|^2 & 0 \\ 0 & 0 & 0 & 0 \\ |v(\mathrm{i}\omega_n)|^2 & 0 & v(\mathrm{i}\omega_n)u^*(\mathrm{i}\omega_n) & 0 \\ 0 & 0 & 0 & 0 \end{bmatrix}$$

$$+ \mathcal{B}^{(3)}(\mathrm{i}\omega_n)\,\mathrm{e}^{-\mathrm{i}\left[q_{z,\mathrm{e}}(\mathrm{i}\omega_n)z - q_{z,\mathrm{h}}(\mathrm{i}\omega_n)z'\right]} \begin{bmatrix} 0 & 0 & 0 & 0 \\ u(\mathrm{i}\omega_n)v^*(\mathrm{i}\omega_n) & 0 & |u(\mathrm{i}\omega_n)|^2 & 0 \\ 0 & 0 & 0 & 0 \\ |v(\mathrm{i}\omega_n)|^2 & 0 & v(\mathrm{i}\omega_n)u^*(\mathrm{i}\omega_n) & 0 \end{bmatrix}$$

$$+ \mathcal{C}^{(3)}(\mathrm{i}\omega_n)\,\mathrm{e}^{\mathrm{i}q_{z,\mathrm{h}}(\mathrm{i}\omega_n)(z+z')} \begin{bmatrix} |v(\mathrm{i}\omega_n)|^2 & 0 & v(\mathrm{i}\omega_n)u^*(\mathrm{i}\omega_n) & 0 \\ 0 & 0 & 0 & 0 \\ u(\mathrm{i}\omega_n)v^*(\mathrm{i}\omega_n) & 0 & |u(\mathrm{i}\omega_n)|^2 & 0 \\ 0 & 0 & 0 & 0 \end{bmatrix}$$

$$\left. + \mathcal{D}^{(3)}(\mathrm{i}\omega_n)\,\mathrm{e}^{\mathrm{i}q_{z,\mathrm{h}}(\mathrm{i}\omega_n)(z+z')} \begin{bmatrix} 0 & 0 & 0 & 0 \\ |v(\mathrm{i}\omega_n)|^2 & 0 & v(\mathrm{i}\omega_n)u^*(\mathrm{i}\omega_n) & 0 \\ 0 & 0 & 0 & 0 \\ u(\mathrm{i}\omega_n)v^*(\mathrm{i}\omega_n) & 0 & |u(\mathrm{i}\omega_n)|^2 & 0 \end{bmatrix} \right\}, \tag{B.19}$$

and

$$\check{\mathcal{G}}^{(4)}(z,z';\mathrm{i}\omega_n) = -\frac{\mathrm{i}m}{\hbar^2 q_{z,\mathrm{h}}(\mathrm{i}\omega_n)\left[\left|u(\mathrm{i}\omega_n)\right|^2 - \left|v(\mathrm{i}\omega_n)\right|^2\right]} \left\{ \mathrm{e}^{-\mathrm{i}q_{z,\mathrm{h}}(\mathrm{i}\omega_n)|z-z'|} \begin{bmatrix} 0 & 0 & 0 & 0 \\ 0 & \left|v(\mathrm{i}\omega_n)\right|^2 & 0 & v(\mathrm{i}\omega_n)u^*(\mathrm{i}\omega_n) \\ 0 & 0 & 0 & 0 \\ 0 & u(\mathrm{i}\omega_n)v^*(\mathrm{i}\omega_n) & 0 & \left|u(\mathrm{i}\omega_n)\right|^2 \end{bmatrix} \right.$$

$$+ \mathcal{A}^{(4)}(\mathrm{i}\omega_n)\,\mathrm{e}^{-\mathrm{i}\left[q_{z,\mathrm{e}}(\mathrm{i}\omega_n)z - q_{z,\mathrm{h}}(\mathrm{i}\omega_n)z'\right]} \begin{bmatrix} 0 & u(\mathrm{i}\omega_n)v^*(\mathrm{i}\omega_n) & 0 & \left|u(\mathrm{i}\omega_n)\right|^2 \\ 0 & 0 & 0 & 0 \\ 0 & \left|v(\mathrm{i}\omega_n)\right|^2 & 0 & v(\mathrm{i}\omega_n)u^*(\mathrm{i}\omega_n) \\ 0 & 0 & 0 & 0 \end{bmatrix}$$

$$+ \mathcal{B}^{(4)}(\mathrm{i}\omega_n)\,\mathrm{e}^{-\mathrm{i}\left[q_{z,\mathrm{e}}(\mathrm{i}\omega_n)z - q_{z,\mathrm{h}}(\mathrm{i}\omega_n)z'\right]} \begin{bmatrix} 0 & 0 & 0 & 0 \\ 0 & u(\mathrm{i}\omega_n)v^*(\mathrm{i}\omega_n) & 0 & \left|u(\mathrm{i}\omega_n)\right|^2 \\ 0 & 0 & 0 & 0 \\ 0 & \left|v(\mathrm{i}\omega_n)\right|^2 & 0 & v(\mathrm{i}\omega_n)u^*(\mathrm{i}\omega_n) \end{bmatrix}$$

$$+ C^{(4)}(\mathrm{i}\omega_n)\,\mathrm{e}^{\mathrm{i}q_{z,\mathrm{h}}(\mathrm{i}\omega_n)(z+z')} \begin{bmatrix} 0 & \left|v(\mathrm{i}\omega_n)\right|^2 & 0 & v(\mathrm{i}\omega_n)u^*(\mathrm{i}\omega_n) \\ 0 & 0 & 0 & 0 \\ 0 & u(\mathrm{i}\omega_n)v^*(\mathrm{i}\omega_n) & 0 & \left|u(\mathrm{i}\omega_n)\right|^2 \\ 0 & 0 & 0 & 0 \end{bmatrix}$$

$$\left. + \mathcal{D}^{(4)}(\mathrm{i}\omega_n)\,\mathrm{e}^{\mathrm{i}q_{z,\mathrm{h}}(\mathrm{i}\omega_n)(z+z')} \begin{bmatrix} 0 & 0 & 0 & 0 \\ 0 & \left|v(\mathrm{i}\omega_n)\right|^2 & 0 & v(\mathrm{i}\omega_n)u^*(\mathrm{i}\omega_n) \\ 0 & 0 & 0 & 0 \\ 0 & u(\mathrm{i}\omega_n)v^*(\mathrm{i}\omega_n) & 0 & \left|u(\mathrm{i}\omega_n)\right|^2 \end{bmatrix} \right\}. \tag{B.20}$$

Appendix C

BTK-like conductance formula for N/buffer region/N junctions

In Chap. 6, we compare the qualitative and quantitative characteristics of the JTMR effect in superconducting S/F/I/F/S junctions to its normal-state TMR counterpart in the respective N/F/I/F/N junctions. For the latter, we need to compute the tunneling conductance once for parallel and once for antiparallel magnetized F/I/F spin valves. Several works [300–303] extended the BTK model [164], which we applied to simple two-electrode tunnel junctions in Chap. 3, to the more intricate case of N/buffer region/N [or, more generally, ferromagnet/buffer region/ferromagnet (F/buffer region/F)] junctions. In the following, we will briefly recapitulate the main steps necessary for such a generalization and adopt the formulas to the notation used in this thesis.

Similarly to our considerations in Chap. 3, we initially assume an (energy E) electron (with spin up or spin down) incident on the left metal/buffer region interface. The buffer region could, in principle, consist of a complicated superconducting or normal-conducting multilayer structure. In our case, we are simply concerned with the F/I/F geometry, but we will keep the model thus general that the final result can also be applied to junctions with superconducting interlayers (only the scattering probabilities would change in that case). Therefore, we account for *all* scattering processes the incoming electron may undergo at the interface. To be specific, we include specular and Andreev reflections, as well as transmissions into the right metallic region [see Fig. C.1 for illustration]. The associated tunneling current in the left normal-metal electrode[1] is then extracted from

$$\begin{aligned}(J_z)^{\mathrm{LEFT}} = -\frac{e}{h}\sum_{\mathbf{k}_\parallel}\int_{-\infty}^{\infty}\mathrm{d}E\,\Bigg[&f^0\left(E-\frac{eV}{2}\right)\\ &-R_\mathrm{e}(E)f^0\left(E-\frac{eV}{2}\right)-R_\mathrm{h}(E)f^0\left(E+\frac{eV}{2}\right)\\ &-T_\mathrm{e}(E)f^0\left(E+\frac{eV}{2}\right)-T_\mathrm{h}(E)f^0\left(E-\frac{eV}{2}\right)\Bigg]; \quad \text{(C.1)}\end{aligned}$$

one could compare the generic form of Eq. (C.1) to the one we obtained for F/F-S junctions [see Eq. (3.25)]. We need to pay special attention to properly accounting for the voltage drop across the buffer region (V), which generates a finite electrical potential and shifts the electrons' and holes' energy bands in the normal-metal electrodes. Using the common convention that the electrical potential vanishes exactly in the center of the junction, electrons with excitation energy E generically occupy states with energy $E - eV/2$ in the left and states with energy $E + eV/2$ in the right metal (vice versa

[1] Note that the procedure we follow here strongly differs from (and is, in fact, much simpler than) the one used for Josephson junctions in Chap. 4. Since we evaluate the tunneling current in the left metallic electrode, it is sufficient to consider only the incident and reflected (transmitted) electrons (holes). In Josephson junctions, however, the (quasiparticle) current is computed in the central metal layer (to get rid of the Cooper pair current in the superconductors). In the central layer, we then need to account for the possibility of *multiple* Andreev reflection cycles, which requires the self-consistent calculations presented in Chap. 4.

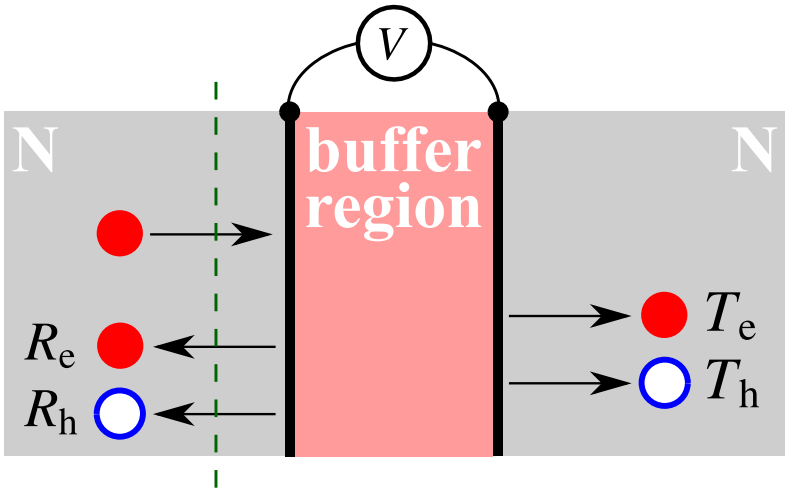


Fig. C.1: Schematical illustration of the considered biased (voltage V) N/buffer region/N junction (the buffer region could consist of a superconducting or normal-conducting multilayer structure). An electron incident from the left electrode may undergo specular reflection (with probability R_e), Andreev reflection (with probability R_h), electronlike transmission (with probability T_e), or holelike transmission (with probability T_h); electrons are colored red, holes blue, and black arrows represent the electrons' (holes') propagation directions. The total tunneling current is conserved. We evaluate it in a vertical plane inside the left metal, highlighted by the green dashed line.

for holes). Consequently, the Fermi-Dirac distribution function $f^0(E - eV/2)$ [first term in Eq. (C.1)] indeed models the incoming electron. Since the electron propagates *to the right*, its contribution to the tunneling current is counted *negatively*.[2] The second and third terms in Eq. (C.1) correspond to specular and Andreev reflections. Since the reflected electron and hole move both to the left, their respective contributions are counted *positively* in the overall tunneling current formula. Nevertheless, one would actually expect that the electron and hole parts should eventually enter with different signs, accounting for the fact that holes are time-reversed electrons and possess opposite charge ($+e$). In fact, we included that already into the Fermi-Dirac distribution functions (note the opposite signs there; we used the same convention when deriving the tunneling conductance formula for F/F-S junctions in Chap. 3) and do therefore not need to put an additional negative sign in front of the Andreev reflection term. To shorten the notation, we denote the total specular reflection (Andreev reflection) probability, considering spin-conserving *and* spin-flip specular reflections (Andreev reflections) of incoming spin-up *and* spin-down electrons, by R_e (R_h); summing over spin is thus no longer explicitly written in Eq. (C.1). We simultaneously need to take care of the "reversed" process, in which the incoming electron stems from the right metallic electrode. Such an electron may be transmitted as an electron (hole) into the left metal with probabilities T_e and T_h. Owing to the junction's symmetry, these probabilities are exactly the same as the ones for transmission of electrons (holes) from the left into the right metal. The transmitted electron (hole) moves towards the left (inside the left electrode) and thus enters the current formula with an overall positive sign – just as it was the case for specular and Andreev reflections of the initially incident right-moving electron. The two remaining summands in Eq. (C.1) precisely model that situation. When compared to Eq. (3.25), it must be noted that we already replaced the sum over the $\hat{z}$-projected wave vectors by the E-integral, which explains the prefactor's additional $1/h$. Using the conservation of scattering probabilities,

$$R_e(E) + R_h(E) + T_e(E) + T_h(E) = 1, \tag{C.2}$$

[2] The positive velocity of the electron must be multiplied by its charge $-e$ to obtain the related (negative) current flow.

we rewrite Eq. (C.1) in the compact form

$$(J_z)^{\mathrm{LEFT}} = -\frac{e}{h}\sum_{\mathbf{k}_\parallel}\int_{-\infty}^{\infty}\mathrm{d}E\,\left[R_\mathrm{h}(E)+T_\mathrm{e}(E)\right]\left[f^0\left(E-\frac{eV}{2}\right)-f^0\left(E+\frac{eV}{2}\right)\right]. \tag{C.3}$$

Within the original BTK model, Eq. (C.3) would fully determine the tunneling current (mind that BTK did *not* treat junctions with *two* normal-metal electrodes). Nevertheless, the more extensive analysis provided in Ref. [303] convinces that Eq. (C.3) is not yet sufficient to properly describe N/buffer region/N junctions (with superconducting buffer regions) since it would allow for *different* currents in the left and right electrodes, in contradiction to the fundamental current conservation law. The creation and annihilation of Cooper pairs inside the superconducting buffer region can lead to complicated physical effects (like accumulated phases, ...) that impact the tunneling current and are not captured by the simple BTK formula. Following Ref. [303], this issue can be solved additionally regarding an incident hole from the right electrode that can also undergo specular reflection, Andreev reflection, or transmissions. Treating the incoming hole in an analog way yields quite a surprising result. Incoming holes carry the same net tunneling current as the initially considered electrons, but flowing along the opposite direction, i.e.,

$$(J_z)^{\mathrm{RIGHT}} = -\,(J_z)^{\mathrm{LEFT}}\,. \tag{C.4}$$

Combining the electron and hole channels therefore effectively doubles the tunneling current,

$$J_z = (J_z)^{\mathrm{LEFT}} - (J_z)^{\mathrm{RIGHT}} = 2\,(J_z)^{\mathrm{LEFT}}\,. \tag{C.5}$$

Naively speaking, one can justify this result decomposing the N/buffer region/N junction into two BTK-like half-junctions, each contributing once the amount of tunneling current given by the usual BTK formula.

Substituting Eq. (C.3) into Eq. (C.5), the junction's *zero-temperature tunneling conductance* has the form

$$G_{z,z} = -\frac{\mathrm{d}J_z}{\mathrm{d}V} \approx \frac{G_0\mathcal{A}}{(2\pi)^2}\int \mathrm{d}^2\mathbf{k}_\parallel\left[R_\mathrm{h}(eV)+T_\mathrm{e}(eV)\right], \tag{C.6}$$

where $G_0 = (2e^2)/h$ denotes the usual conductance quantum and $\mathcal{A}$ indicates the interfacial cross-section area. Similarly to our considerations in Chap. 3, we approximated $\mathrm{d}f^0(E)/\mathrm{d}E \approx -\delta(E)$. The only remaining task is to elaborate on the Bogoljubov-de Gennes scattering description for the considered system, which incorporates all necessary junction-specific information (about the buffer region, interfaces, ...). Specifically for the N/F/I/F/N geometry we are predominantly interested in, the complete Bogoljubov-de Gennes framework is formulated in Sec. 6.3. Anticipating the scattering states stated there [see Eqs. (6.69)–(6.73)], we identify the scattering probabilities required for calculating the tunneling conductance by means of Eq. (C.6) as

$$R_\mathrm{h}(eV) = \mathcal{C}^{(1)}(eV)+\mathcal{D}^{(1)}(eV)+\mathcal{C}^{(2)}(eV)+\mathcal{D}^{(2)}(eV) \tag{C.7}$$

and

$$T_\mathrm{e}(eV) = \mathcal{E}^{(1)}(eV)+\mathcal{F}^{(1)}(eV)+\mathcal{E}^{(2)}(eV)+\mathcal{F}^{(2)}(eV); \tag{C.8}$$

the calligraphically written coefficients are numerically obtained applying the indicated boundary conditions to the scattering states and solving the resulting systems of equations in the limit $u(E)\to 1$, $v(E)\to 0$, and $|\Delta_\mathrm{S}|\to 0$ (referring to the normal-state N/F/I/F/N scenario). Finally, putting Eqs. (C.6), (C.7), and (C.8) together yields the junction's tunneling conductance [the zero-bias extrapolation is given as Eq. (6.82) in the main part], which we evaluate once for parallel and once for antiparallel magnetized F/I/F spin valves to eventually access the TMR ratio.

Appendix **D**

Bound state wave functions for S/F-I/S Josephson junctions

Bound state wave functions for the generic case

To evaluate Eq. (7.22) and obtain the Josephson current from S/F-I/S junctions' bound state spectra analyzed in Chap. 7, we need to extract explicit analytical expressions for the coefficients entering the bound state wave function ansatz in Eqs. (7.7)–(7.8). All these coefficients must be chosen such that the bound state wave functions are properly normalized. Using the fact that $\mathrm{Im}[q_{x,\mathrm{e}}^{\Uparrow\,(\Downarrow)}(E_\mathrm{B})] = -\mathrm{Im}[q_{x,\mathrm{h}}^{\Uparrow\,(\Downarrow)}(E_\mathrm{B})]$, which is fulfilled for each bound state energy $0 \leq |E_\mathrm{B}| \leq \Delta_\mathrm{S}^{\Uparrow\,(\Downarrow)}$ [see, e.g., Eqs. (7.9), (7.10), (7.12), and (7.13); $\mathrm{Im}(\ldots)$ indicates the imaginary part], the normalization condition can be translated into

$$\frac{\left|u^{\Uparrow}(E_\mathrm{B})\right|^2 + \left|v^{\Uparrow}(E_\mathrm{B})\right|^2}{\mathrm{Im}\left[q_{x,\mathrm{e}}^{\Uparrow}(E_\mathrm{B})\right]}\left[\left|a(E_\mathrm{B})\right|^2 + \left|b(E_\mathrm{B})\right|^2 + \left|e(E_\mathrm{B})\right|^2 + \left|f(E_\mathrm{B})\right|^2\right] + \frac{\left|u^{\Downarrow}(E_\mathrm{B})\right|^2 + \left|v^{\Downarrow}(E_\mathrm{B})\right|^2}{\mathrm{Im}\left[q_{x,\mathrm{e}}^{\Downarrow}(E_\mathrm{B})\right]}\left[\left|c(E_\mathrm{B})\right|^2 + \left|d(E_\mathrm{B})\right|^2 + \left|g(E_\mathrm{B})\right|^2 + \left|h(E_\mathrm{B})\right|^2\right] = 1. \quad \text{(D.1)}$$

Moreover, the bound state wave functions and their first derivatives must satisfy the interfacial boundary conditions stated in Eqs. (7.16)–(7.17). Applying them to the wave functions yields a set of eight coupled equations, which allow us to eliminate one coefficient after the other from Eq. (D.1) and recast the normalization condition in terms of just one remaining coefficient. More concretely, we initially apply the boundary condition in Eq. (7.16), ensuring that the wave functions are continuous right at the ferromagnetic-insulator interface, to Eqs. (7.7)–(7.8) and combine the resulting four equations such that we arrive at

$$a(E_\mathrm{B}) = \varphi_1(E_\mathrm{B})\, f(E_\mathrm{B}) + \gamma_1(E_\mathrm{B})\, g(E_\mathrm{B}), \quad \text{(D.2)}$$

$$b(E_\mathrm{B}) = \varepsilon_1(E_\mathrm{B})\, e(E_\mathrm{B}) + \eta_1(E_\mathrm{B})\, h(E_\mathrm{B}), \quad \text{(D.3)}$$

$$c(E_\mathrm{B}) = \varepsilon_2(E_\mathrm{B})\, e(E_\mathrm{B}) + \eta_2(E_\mathrm{B})\, h(E_\mathrm{B}), \quad \text{(D.4)}$$

and lastly

$$d(E_\mathrm{B}) = \varphi_2(E_\mathrm{B})\, f(E_\mathrm{B}) + \gamma_2(E_\mathrm{B})\, g(E_\mathrm{B}). \quad \text{(D.5)}$$

For the sake of compactness, we introduced the abbreviations

$$\varepsilon_1(E_\mathrm{B}) = \frac{u^{\Uparrow}(E_\mathrm{B})\, v^{\Downarrow}(E_\mathrm{B})\, \mathrm{e}^{\mathrm{i}\phi_\mathrm{S}} + \gamma\, u^{\Downarrow}(E_\mathrm{B})\, v^{\Uparrow}(E_\mathrm{B})}{v^{\Uparrow}(E_\mathrm{B})\, v^{\Downarrow}(E_\mathrm{B}) + \gamma\, u^{\Uparrow}(E_\mathrm{B})\, u^{\Downarrow}(E_\mathrm{B})}, \qquad \varepsilon_2(E_\mathrm{B}) = \frac{\left[u^{\Uparrow}(E_\mathrm{B})\right]^2 \mathrm{e}^{\mathrm{i}\phi_\mathrm{S}} - \left[v^{\Uparrow}(E_\mathrm{B})\right]^2}{u^{\Uparrow}(E_\mathrm{B})\, u^{\Downarrow}(E_\mathrm{B}) + \gamma\, v^{\Uparrow}(E_\mathrm{B})\, v^{\Downarrow}(E_\mathrm{B})}, \tag{D.6}$$

$$\varphi_1(E_\mathrm{B}) = \frac{u^{\Downarrow}(E_\mathrm{B})\, v^{\Uparrow}(E_\mathrm{B})\, \mathrm{e}^{\mathrm{i}\phi_\mathrm{S}} + \gamma\, u^{\Uparrow}(E_\mathrm{B})\, v^{\Downarrow}(E_\mathrm{B})}{u^{\Uparrow}(E_\mathrm{B})\, u^{\Downarrow}(E_\mathrm{B}) + \gamma\, v^{\Uparrow}(E_\mathrm{B})\, v^{\Downarrow}(E_\mathrm{B})}, \qquad \varphi_2(E_\mathrm{B}) = \frac{\left[v^{\Uparrow}(E_\mathrm{B})\right]^2 \mathrm{e}^{\mathrm{i}\phi_\mathrm{S}} - \left[u^{\Uparrow}(E_\mathrm{B})\right]^2}{v^{\Uparrow}(E_\mathrm{B})\, v^{\Downarrow}(E_\mathrm{B}) + \gamma\, u^{\Uparrow}(E_\mathrm{B})\, u^{\Downarrow}(E_\mathrm{B})}, \tag{D.7}$$

$$\gamma_1(E_\mathrm{B}) = \frac{\left[u^{\Downarrow}(E_\mathrm{B})\right]^2 \mathrm{e}^{\mathrm{i}\phi_\mathrm{S}} - \left[v^{\Downarrow}(E_\mathrm{B})\right]^2}{u^{\Uparrow}(E_\mathrm{B})\, u^{\Downarrow}(E_\mathrm{B}) + \gamma\, v^{\Uparrow}(E_\mathrm{B})\, v^{\Downarrow}(E_\mathrm{B})}, \qquad \gamma_2(E_\mathrm{B}) = \frac{u^{\Downarrow}(E_\mathrm{B})\, v^{\Uparrow}(E_\mathrm{B})\, \mathrm{e}^{\mathrm{i}\phi_\mathrm{S}} + \gamma\, u^{\Uparrow}(E_\mathrm{B})\, v^{\Downarrow}(E_\mathrm{B})}{v^{\Uparrow}(E_\mathrm{B})\, v^{\Downarrow}(E_\mathrm{B}) + \gamma\, u^{\Uparrow}(E_\mathrm{B})\, u^{\Downarrow}(E_\mathrm{B})}, \tag{D.8}$$

$$\eta_1(E_\mathrm{B}) = \frac{\left[v^{\Downarrow}(E_\mathrm{B})\right]^2 \mathrm{e}^{\mathrm{i}\phi_\mathrm{S}} - \left[u^{\Downarrow}(E_\mathrm{B})\right]^2}{v^{\Uparrow}(E_\mathrm{B})\, v^{\Downarrow}(E_\mathrm{B}) + \gamma\, u^{\Uparrow}(E_\mathrm{B})\, u^{\Downarrow}(E_\mathrm{B})}, \quad \text{and} \quad \eta_2(E_\mathrm{B}) = \frac{u^{\Uparrow}(E_\mathrm{B})\, v^{\Downarrow}(E_\mathrm{B})\, \mathrm{e}^{\mathrm{i}\phi_\mathrm{S}} + \gamma\, u^{\Downarrow}(E_\mathrm{B})\, v^{\Uparrow}(E_\mathrm{B})}{u^{\Uparrow}(E_\mathrm{B})\, u^{\Downarrow}(E_\mathrm{B}) + \gamma\, v^{\Uparrow}(E_\mathrm{B})\, v^{\Downarrow}(E_\mathrm{B})}. \tag{D.9}$$

The definition of the coherence factors $u^{\Uparrow\,(\Downarrow)}(E_\mathrm{B})$ and $v^{\Uparrow\,(\Downarrow)}(E_\mathrm{B})$ can be looked up in Eq. (7.14), while $\gamma = \mathrm{sgn}\left(|\Delta_\mathrm{S}^s| - |\Delta_\mathrm{S}^p|\right)$.

In the same spirit, imposing the boundary condition in Eq. (7.17), which accounts for the jumplike discontinuity in the wave functions' first derivative owing to the deltalike interfacial scalar and magnetic tunneling potentials, on Eqs. (7.7)–(7.8) results in another set of four equations. After substituting Eqs. (D.2)–(D.5), these equations depend just on the coefficients $e(E_\mathrm{B})$, $f(E_\mathrm{B})$, $g(E_\mathrm{B})$, and $h(E_\mathrm{B})$, originating from the wave function ansatz in the right superconductor. We can therefore utilize the four equations (for four unknown coefficients) to subsequently write three coefficients in terms of the fourth one, e.g., we can express $f(E_\mathrm{B})$, $g(E_\mathrm{B})$, and $h(E_\mathrm{B})$ solely via $e(E_\mathrm{B})$ according to

$$f(E_\mathrm{B}) = \Sigma_1(E_\mathrm{B})\, e(E_\mathrm{B}), \tag{D.10}$$

$$g(E_\mathrm{B}) = \Sigma_2(E_\mathrm{B})\, e(E_\mathrm{B}), \tag{D.11}$$

and

$$h(E_\mathrm{B}) = \Sigma_3(E_\mathrm{B})\, e(E_\mathrm{B}); \tag{D.12}$$

the prefactors are found to read

$$\begin{aligned}\Sigma_1(E_\mathrm{B}) = -\Big\{ &\Big[\overline{\varepsilon}_1(E_\mathrm{B})\,\overline{\gamma}_2(E_\mathrm{B}) - \overline{\varepsilon}_2(E_\mathrm{B})\,\overline{\gamma}_1(E_\mathrm{B})\Big]\Big[\overline{\eta}_3(E_\mathrm{B})\,\overline{\gamma}_4(E_\mathrm{B}) - \overline{\eta}_4(E_\mathrm{B})\,\overline{\gamma}_3(E_\mathrm{B})\Big] \\ &- \Big[\overline{\varepsilon}_3(E_\mathrm{B})\,\overline{\gamma}_4(E_\mathrm{B}) - \overline{\varepsilon}_4(E_\mathrm{B})\,\overline{\gamma}_3(E_\mathrm{B})\Big]\Big[\overline{\eta}_1(E_\mathrm{B})\,\overline{\gamma}_2(E_\mathrm{B}) - \overline{\eta}_2(E_\mathrm{B})\,\overline{\gamma}_1(E_\mathrm{B})\Big]\Big\} \Big/ \\ &\Big\{\Big[\overline{\varphi}_1(E_\mathrm{B})\,\overline{\gamma}_2(E_\mathrm{B}) - \overline{\varphi}_2(E_\mathrm{B})\,\overline{\gamma}_1(E_\mathrm{B})\Big]\Big[\overline{\eta}_3(E_\mathrm{B})\,\overline{\gamma}_4(E_\mathrm{B}) - \overline{\eta}_4(E_\mathrm{B})\,\overline{\gamma}_3(E_\mathrm{B})\Big] \\ &- \Big[\overline{\varphi}_3(E_\mathrm{B})\,\overline{\gamma}_4(E_\mathrm{B}) - \overline{\varphi}_4(E_\mathrm{B})\,\overline{\gamma}_3(E_\mathrm{B})\Big]\Big[\overline{\eta}_1(E_\mathrm{B})\,\overline{\gamma}_2(E_\mathrm{B}) - \overline{\eta}_2(E_\mathrm{B})\,\overline{\gamma}_1(E_\mathrm{B})\Big]\Big\},\end{aligned} \tag{D.13}$$

$$\begin{aligned}\Sigma_2(E_\mathrm{B}) = -\Big\{ &\Big[\overline{\varepsilon}_1(E_\mathrm{B})\,\overline{\eta}_2(E_\mathrm{B}) - \overline{\varepsilon}_2(E_\mathrm{B})\,\overline{\eta}_1(E_\mathrm{B})\Big]\Big[\overline{\varphi}_3(E_\mathrm{B})\,\overline{\eta}_4(E_\mathrm{B}) - \overline{\varphi}_4(E_\mathrm{B})\,\overline{\eta}_3(E_\mathrm{B})\Big] \\ &- \Big[\overline{\varepsilon}_3(E_\mathrm{B})\,\overline{\eta}_4(E_\mathrm{B}) - \overline{\varepsilon}_4(E_\mathrm{B})\,\overline{\eta}_3(E_\mathrm{B})\Big]\Big[\overline{\varphi}_1(E_\mathrm{B})\,\overline{\eta}_2(E_\mathrm{B}) - \overline{\varphi}_2(E_\mathrm{B})\,\overline{\eta}_1(E_\mathrm{B})\Big]\Big\} \Big/ \\ &\Big\{\Big[\overline{\gamma}_1(E_\mathrm{B})\,\overline{\eta}_2(E_\mathrm{B}) - \overline{\gamma}_2(E_\mathrm{B})\,\overline{\eta}_1(E_\mathrm{B})\Big]\Big[\overline{\varphi}_3(E_\mathrm{B})\,\overline{\eta}_4(E_\mathrm{B}) - \overline{\varphi}_4(E_\mathrm{B})\,\overline{\eta}_3(E_\mathrm{B})\Big] \\ &- \Big[\overline{\gamma}_3(E_\mathrm{B})\,\overline{\eta}_4(E_\mathrm{B}) - \overline{\gamma}_4(E_\mathrm{B})\,\overline{\eta}_3(E_\mathrm{B})\Big]\Big[\overline{\varphi}_1(E_\mathrm{B})\,\overline{\eta}_2(E_\mathrm{B}) - \overline{\varphi}_2(E_\mathrm{B})\,\overline{\eta}_1(E_\mathrm{B})\Big]\Big\},\end{aligned} \tag{D.14}$$

as well as

$$\begin{aligned}\Sigma_3(E_\mathrm{B}) = -\Big\{&\Big[\overline{\varepsilon}_1(E_\mathrm{B})\,\overline{\gamma}_2(E_\mathrm{B}) - \overline{\varepsilon}_2(E_\mathrm{B})\,\overline{\gamma}_1(E_\mathrm{B})\Big]\Big[\overline{\varphi}_3(E_\mathrm{B})\,\overline{\gamma}_4(E_\mathrm{B}) - \overline{\varphi}_4(E_\mathrm{B})\,\overline{\gamma}_3(E_\mathrm{B})\Big]\\ &- \Big[\overline{\varepsilon}_3(E_\mathrm{B})\,\overline{\gamma}_4(E_\mathrm{B}) - \overline{\varepsilon}_4(E_\mathrm{B})\,\overline{\gamma}_3(E_\mathrm{B})\Big]\Big[\overline{\varphi}_1(E_\mathrm{B})\,\overline{\gamma}_2(E_\mathrm{B}) - \overline{\varphi}_2(E_\mathrm{B})\,\overline{\gamma}_1(E_\mathrm{B})\Big]\Big\}\Big/\\ &\Big\{\Big[\overline{\eta}_1(E_\mathrm{B})\,\overline{\gamma}_2(E_\mathrm{B}) - \overline{\eta}_2(E_\mathrm{B})\,\overline{\gamma}_1(E_\mathrm{B})\Big]\Big[\overline{\varphi}_3(E_\mathrm{B})\,\overline{\gamma}_4(E_\mathrm{B}) - \overline{\varphi}_4(E_\mathrm{B})\,\overline{\gamma}_3(E_\mathrm{B})\Big]\\ &- \Big[\overline{\eta}_3(E_\mathrm{B})\,\overline{\gamma}_4(E_\mathrm{B}) - \overline{\eta}_4(E_\mathrm{B})\,\overline{\gamma}_3(E_\mathrm{B})\Big]\Big[\overline{\varphi}_1(E_\mathrm{B})\,\overline{\gamma}_2(E_\mathrm{B}) - \overline{\varphi}_2(E_\mathrm{B})\,\overline{\gamma}_1(E_\mathrm{B})\Big]\Big\},\end{aligned} \tag{D.15}$$

where the "overline" factors are defined as

$$\begin{aligned}\overline{\varepsilon}_1(E_\mathrm{B}) = \frac{q^{\Uparrow}_{x,\mathrm{e}}(E_\mathrm{B})}{k_\mathrm{F}}\,u^{\Uparrow}(E_\mathrm{B})\,\mathrm{e}^{\mathrm{i}\phi_\mathrm{S}} + \left[-\frac{q^{\Uparrow}_{x,\mathrm{h}}(E_\mathrm{B})}{k_\mathrm{F}} + \mathrm{i}\left(\overline{\lambda}_\mathrm{SC} + \overline{\lambda}_\mathrm{MA}\right)\right] v^{\Uparrow}(E_\mathrm{B})\,\varepsilon_1(E_\mathrm{B})\\ + \left[\frac{q^{\Downarrow}_{x,\mathrm{e}}(E_\mathrm{B})}{k_\mathrm{F}} + \mathrm{i}\left(\overline{\lambda}_\mathrm{SC} + \overline{\lambda}_\mathrm{MA}\right)\right] u^{\Downarrow}(E_\mathrm{B})\,\varepsilon_2(E_\mathrm{B}),\end{aligned} \tag{D.16}$$

$$\begin{aligned}\overline{\varphi}_1(E_\mathrm{B}) = \frac{q^{\Uparrow}_{x,\mathrm{h}}(E_\mathrm{B})}{k_\mathrm{F}}\,v^{\Uparrow}(E_\mathrm{B})\,\mathrm{e}^{\mathrm{i}\phi_\mathrm{S}} + \left[-\frac{q^{\Uparrow}_{x,\mathrm{e}}(E_\mathrm{B})}{k_\mathrm{F}} - \mathrm{i}\left(\overline{\lambda}_\mathrm{SC} + \overline{\lambda}_\mathrm{MA}\right)\right] u^{\Uparrow}(E_\mathrm{B})\,\varphi_1(E_\mathrm{B})\\ + \left[\frac{q^{\Downarrow}_{x,\mathrm{h}}(E_\mathrm{B})}{k_\mathrm{F}} - \mathrm{i}\left(\overline{\lambda}_\mathrm{SC} + \overline{\lambda}_\mathrm{MA}\right)\right] v^{\Downarrow}(E_\mathrm{B})\,\varphi_2(E_\mathrm{B}),\end{aligned} \tag{D.17}$$

$$\begin{aligned}\overline{\gamma}_1(E_\mathrm{B}) = -\frac{q^{\Downarrow}_{x,\mathrm{e}}(E_\mathrm{B})}{k_\mathrm{F}}\,u^{\Downarrow}(E_\mathrm{B})\,\mathrm{e}^{\mathrm{i}\phi_\mathrm{S}} + \left[-\frac{q^{\Uparrow}_{x,\mathrm{e}}(E_\mathrm{B})}{k_\mathrm{F}} - \mathrm{i}\left(\overline{\lambda}_\mathrm{SC} + \overline{\lambda}_\mathrm{MA}\right)\right] u^{\Uparrow}(E_\mathrm{B})\,\gamma_1(E_\mathrm{B})\\ + \left[\frac{q^{\Downarrow}_{x,\mathrm{h}}(E_\mathrm{B})}{k_\mathrm{F}} - \mathrm{i}\left(\overline{\lambda}_\mathrm{SC} + \overline{\lambda}_\mathrm{MA}\right)\right] v^{\Downarrow}(E_\mathrm{B})\,\gamma_2(E_\mathrm{B}),\end{aligned} \tag{D.18}$$

$$\begin{aligned}\overline{\eta}_1(E_\mathrm{B}) = -\frac{q^{\Downarrow}_{x,\mathrm{h}}(E_\mathrm{B})}{k_\mathrm{F}}\,v^{\Downarrow}(E_\mathrm{B})\,\mathrm{e}^{\mathrm{i}\phi_\mathrm{S}} + \left[-\frac{q^{\Uparrow}_{x,\mathrm{h}}(E_\mathrm{B})}{k_\mathrm{F}} + \mathrm{i}\left(\overline{\lambda}_\mathrm{SC} + \overline{\lambda}_\mathrm{MA}\right)\right] v^{\Uparrow}(E_\mathrm{B})\,\eta_1(E_\mathrm{B})\\ + \left[\frac{q^{\Downarrow}_{x,\mathrm{e}}(E_\mathrm{B})}{k_\mathrm{F}} + \mathrm{i}\left(\overline{\lambda}_\mathrm{SC} + \overline{\lambda}_\mathrm{MA}\right)\right] u^{\Downarrow}(E_\mathrm{B})\,\eta_2(E_\mathrm{B}),\end{aligned} \tag{D.19}$$

$$\begin{aligned}\overline{\varepsilon}_2(E_\mathrm{B}) = \frac{q^{\Uparrow}_{x,\mathrm{e}}(E_\mathrm{B})}{k_\mathrm{F}}\,u^{\Uparrow}(E_\mathrm{B})\,\mathrm{e}^{\mathrm{i}\phi_\mathrm{S}} + \left[-\frac{q^{\Uparrow}_{x,\mathrm{h}}(E_\mathrm{B})}{k_\mathrm{F}} + \mathrm{i}\left(\overline{\lambda}_\mathrm{SC} - \overline{\lambda}_\mathrm{MA}\right)\right] v^{\Uparrow}(E_\mathrm{B})\,\varepsilon_1(E_\mathrm{B})\\ + \left[\frac{q^{\Downarrow}_{x,\mathrm{e}}(E_\mathrm{B})}{k_\mathrm{F}} + \mathrm{i}\left(\overline{\lambda}_\mathrm{SC} - \overline{\lambda}_\mathrm{MA}\right)\right] u^{\Downarrow}(E_\mathrm{B})\,\varepsilon_2(E_\mathrm{B}),\end{aligned} \tag{D.20}$$

$$\overline{\varphi}_2(E_\mathrm{B}) = -\frac{q^{\Uparrow}_{x,\mathrm{h}}(E_\mathrm{B})}{k_\mathrm{F}}\, v^{\Uparrow}(E_\mathrm{B})\, \mathrm{e}^{\mathrm{i}\phi_\mathrm{S}} + \left[\frac{q^{\Uparrow}_{x,\mathrm{e}}(E_\mathrm{B})}{k_\mathrm{F}} + \mathrm{i}\left(\overline{\lambda}_\mathrm{SC} - \overline{\lambda}_\mathrm{MA}\right)\right] u^{\Uparrow}(E_\mathrm{B})\, \varphi_1(E_\mathrm{B}) + \left[-\frac{q^{\Downarrow}_{x,\mathrm{h}}(E_\mathrm{B})}{k_\mathrm{F}} + \mathrm{i}\left(\overline{\lambda}_\mathrm{SC} - \overline{\lambda}_\mathrm{MA}\right)\right] v^{\Downarrow}(E_\mathrm{B})\, \varphi_2(E_\mathrm{B}), \tag{D.21}$$

$$\overline{\gamma}_2(E_\mathrm{B}) = \frac{q^{\Downarrow}_{x,\mathrm{e}}(E_\mathrm{B})}{k_\mathrm{F}}\, u^{\Downarrow}(E_\mathrm{B})\, \mathrm{e}^{\mathrm{i}\phi_\mathrm{S}} + \left[\frac{q^{\Uparrow}_{x,\mathrm{e}}(E_\mathrm{B})}{k_\mathrm{F}} + \mathrm{i}\left(\overline{\lambda}_\mathrm{SC} - \overline{\lambda}_\mathrm{MA}\right)\right] u^{\Uparrow}(E_\mathrm{B})\, \gamma_1(E_\mathrm{B}) + \left[-\frac{q^{\Downarrow}_{x,\mathrm{h}}(E_\mathrm{B})}{k_\mathrm{F}} + \mathrm{i}\left(\overline{\lambda}_\mathrm{SC} - \overline{\lambda}_\mathrm{MA}\right)\right] v^{\Downarrow}(E_\mathrm{B})\, \gamma_2(E_\mathrm{B}), \tag{D.22}$$

$$\overline{\eta}_2(E_\mathrm{B}) = -\frac{q^{\Downarrow}_{x,\mathrm{h}}(E_\mathrm{B})}{k_\mathrm{F}}\, v^{\Downarrow}(E_\mathrm{B})\, \mathrm{e}^{\mathrm{i}\phi_\mathrm{S}} + \left[-\frac{q^{\Uparrow}_{x,\mathrm{h}}(E_\mathrm{B})}{k_\mathrm{F}} + \mathrm{i}\left(\overline{\lambda}_\mathrm{SC} - \overline{\lambda}_\mathrm{MA}\right)\right] v^{\Uparrow}(E_\mathrm{B})\, \eta_1(E_\mathrm{B}) + \left[\frac{q^{\Downarrow}_{x,\mathrm{e}}(E_\mathrm{B})}{k_\mathrm{F}} + \mathrm{i}\left(\overline{\lambda}_\mathrm{SC} - \overline{\lambda}_\mathrm{MA}\right)\right] u^{\Downarrow}(E_\mathrm{B})\, \eta_2(E_\mathrm{B}), \tag{D.23}$$

$$\overline{\varepsilon}_3(E_\mathrm{B}) = -\frac{q^{\Uparrow}_{x,\mathrm{e}}(E_\mathrm{B})}{k_\mathrm{F}}\, v^{\Uparrow}(E_\mathrm{B}) + \left[\frac{q^{\Uparrow}_{x,\mathrm{h}}(E_\mathrm{B})}{k_\mathrm{F}} - \mathrm{i}\left(\overline{\lambda}_\mathrm{SC} - \overline{\lambda}_\mathrm{MA}\right)\right] u^{\Uparrow}(E_\mathrm{B})\, \varepsilon_1(E_\mathrm{B}) + \left[\frac{q^{\Downarrow}_{x,\mathrm{e}}(E_\mathrm{B})}{k_\mathrm{F}} + \mathrm{i}\left(\overline{\lambda}_\mathrm{SC} - \overline{\lambda}_\mathrm{MA}\right)\right] \gamma\, v^{\Downarrow}(E_\mathrm{B})\, \varepsilon_2(E_\mathrm{B}), \tag{D.24}$$

$$\overline{\varphi}_3(E_\mathrm{B}) = -\frac{q^{\Uparrow}_{x,\mathrm{h}}(E_\mathrm{B})}{k_\mathrm{F}}\, u^{\Uparrow}(E_\mathrm{B}) + \left[\frac{q^{\Uparrow}_{x,\mathrm{e}}(E_\mathrm{B})}{k_\mathrm{F}} + \mathrm{i}\left(\overline{\lambda}_\mathrm{SC} - \overline{\lambda}_\mathrm{MA}\right)\right] v^{\Uparrow}(E_\mathrm{B})\, \varphi_1(E_\mathrm{B}) + \left[\frac{q^{\Downarrow}_{x,\mathrm{h}}(E_\mathrm{B})}{k_\mathrm{F}} - \mathrm{i}\left(\overline{\lambda}_\mathrm{SC} - \overline{\lambda}_\mathrm{MA}\right)\right] \gamma\, u^{\Downarrow}(E_\mathrm{B})\, \varphi_2(E_\mathrm{B}), \tag{D.25}$$

$$\overline{\gamma}_3(E_\mathrm{B}) = -\frac{q^{\Downarrow}_{x,\mathrm{e}}(E_\mathrm{B})}{k_\mathrm{F}}\, \gamma\, v^{\Downarrow}(E_\mathrm{B}) + \left[\frac{q^{\Uparrow}_{x,\mathrm{e}}(E_\mathrm{B})}{k_\mathrm{F}} + \mathrm{i}\left(\overline{\lambda}_\mathrm{SC} - \overline{\lambda}_\mathrm{MA}\right)\right] v^{\Uparrow}(E_\mathrm{B})\, \gamma_1(E_\mathrm{B}) + \left[\frac{q^{\Downarrow}_{x,\mathrm{h}}(E_\mathrm{B})}{k_\mathrm{F}} - \mathrm{i}\left(\overline{\lambda}_\mathrm{SC} - \overline{\lambda}_\mathrm{MA}\right)\right] \gamma\, u^{\Downarrow}(E_\mathrm{B})\, \gamma_2(E_\mathrm{B}), \tag{D.26}$$

$$\overline{\eta}_3(E_\mathrm{B}) = -\frac{q^{\Downarrow}_{x,\mathrm{h}}(E_\mathrm{B})}{k_\mathrm{F}}\, \gamma\, u^{\Downarrow}(E_\mathrm{B}) + \left[\frac{q^{\Uparrow}_{x,\mathrm{h}}(E_\mathrm{B})}{k_\mathrm{F}} - \mathrm{i}\left(\overline{\lambda}_\mathrm{SC} - \overline{\lambda}_\mathrm{MA}\right)\right] u^{\Uparrow}(E_\mathrm{B})\, \eta_1(E_\mathrm{B}) + \left[\frac{q^{\Downarrow}_{x,\mathrm{e}}(E_\mathrm{B})}{k_\mathrm{F}} + \mathrm{i}\left(\overline{\lambda}_\mathrm{SC} - \overline{\lambda}_\mathrm{MA}\right)\right] \gamma\, v^{\Downarrow}(E_\mathrm{B})\, \eta_2(E_\mathrm{B}), \tag{D.27}$$

and finally,

$$\overline{\varepsilon}_4(E_\mathrm{B}) = -\frac{q^{\Uparrow}_{x,\mathrm{e}}(E_\mathrm{B})}{k_\mathrm{F}}\, v^{\Uparrow}(E_\mathrm{B}) + \left[\frac{q^{\Uparrow}_{x,\mathrm{h}}(E_\mathrm{B})}{k_\mathrm{F}} - \mathrm{i}\left(\overline{\lambda}_\mathrm{SC} + \overline{\lambda}_\mathrm{MA}\right)\right] u^{\Uparrow}(E_\mathrm{B})\, \varepsilon_1(E_\mathrm{B}) + \left[\frac{q^{\Downarrow}_{x,\mathrm{e}}(E_\mathrm{B})}{k_\mathrm{F}} + \mathrm{i}\left(\overline{\lambda}_\mathrm{SC} + \overline{\lambda}_\mathrm{MA}\right)\right] \gamma\, v^{\Downarrow}(E_\mathrm{B})\, \varepsilon_2(E_\mathrm{B}), \tag{D.28}$$

$$\overline{\varphi}_4(E_\mathrm{B}) = \frac{q^{\Uparrow}_{x,\mathrm{h}}(E_\mathrm{B})}{k_\mathrm{F}}\, u^{\Uparrow}(E_\mathrm{B}) + \left[-\frac{q^{\Uparrow}_{x,\mathrm{e}}(E_\mathrm{B})}{k_\mathrm{F}} - \mathrm{i}\left(\overline{\lambda}_\mathrm{SC} + \overline{\lambda}_\mathrm{MA}\right)\right] v^{\Uparrow}(E_\mathrm{B})\, \varphi_1(E_\mathrm{B}) + \left[-\frac{q^{\Downarrow}_{x,\mathrm{h}}(E_\mathrm{B})}{k_\mathrm{F}} + \mathrm{i}\left(\overline{\lambda}_\mathrm{SC} + \overline{\lambda}_\mathrm{MA}\right)\right] \gamma\, u^{\Downarrow}(E_\mathrm{B})\, \varphi_2(E_\mathrm{B}), \tag{D.29}$$

$$\overline{\gamma}_4(E_\mathrm{B}) = \frac{q^{\Downarrow}_{x,\mathrm{e}}(E_\mathrm{B})}{k_\mathrm{F}}\, \gamma\, v^{\Downarrow}(E_\mathrm{B}) + \left[-\frac{q^{\Uparrow}_{x,\mathrm{e}}(E_\mathrm{B})}{k_\mathrm{F}} - \mathrm{i}\left(\overline{\lambda}_\mathrm{SC} + \overline{\lambda}_\mathrm{MA}\right)\right] v^{\Uparrow}(E_\mathrm{B})\, \gamma_1(E_\mathrm{B}) + \left[-\frac{q^{\Downarrow}_{x,\mathrm{h}}(E_\mathrm{B})}{k_\mathrm{F}} + \mathrm{i}\left(\overline{\lambda}_\mathrm{SC} + \overline{\lambda}_\mathrm{MA}\right)\right] \gamma\, u^{\Downarrow}(E_\mathrm{B})\, \gamma_2(E_\mathrm{B}), \tag{D.30}$$

as well as

$$\overline{\eta}_4(E_\mathrm{B}) = -\frac{q^{\Downarrow}_{x,\mathrm{h}}(E_\mathrm{B})}{k_\mathrm{F}}\, \gamma\, u^{\Downarrow}(E_\mathrm{B}) + \left[\frac{q^{\Uparrow}_{x,\mathrm{h}}(E_\mathrm{B})}{k_\mathrm{F}} - \mathrm{i}\left(\overline{\lambda}_\mathrm{SC} + \overline{\lambda}_\mathrm{MA}\right)\right] u^{\Uparrow}(E_\mathrm{B})\, \eta_1(E_\mathrm{B}) + \left[\frac{q^{\Downarrow}_{x,\mathrm{e}}(E_\mathrm{B})}{k_\mathrm{F}} + \mathrm{i}\left(\overline{\lambda}_\mathrm{SC} + \overline{\lambda}_\mathrm{MA}\right)\right] \gamma\, v^{\Downarrow}(E_\mathrm{B})\, \eta_2(E_\mathrm{B}). \tag{D.31}$$

In all preceding equations, $\overline{\lambda}_\mathrm{SC} = (2m\lambda_\mathrm{SC})/(\hbar^2 k_\mathrm{F})$ and $\overline{\lambda}_\mathrm{MA} = (2m\lambda_\mathrm{MA})/(\hbar^2 k_\mathrm{F})$ represent the scalar and magnetic tunneling strengths; $k_\mathrm{F} = \sqrt{2m\mu}/\hbar$ still refers to the Fermi wave vector.

Rewriting the normalization condition [recall Eq. (D.1)] by means of Eqs. (D.2)–(D.5) and (D.10)–(D.12), we end up with

$$\begin{aligned}\Bigg\{ &\frac{\left|u^{\Uparrow}(E_\mathrm{B})\right|^2 + \left|v^{\Uparrow}(E_\mathrm{B})\right|^2}{\mathrm{Im}\left[q^{\Uparrow}_{x,\mathrm{e}}(E_\mathrm{B})\right]} \Big[\left|\varphi_1(E_\mathrm{B})\,\Sigma_1(E_\mathrm{B}) + \gamma_1(E_\mathrm{B})\,\Sigma_2(E_\mathrm{B})\right|^2 + \left|\varepsilon_1(E_\mathrm{B}) + \eta_1(E_\mathrm{B})\,\Sigma_3(E_\mathrm{B})\right|^2 \\ &\qquad + 1 + \left|\Sigma_1(E_\mathrm{B})\right|^2\Big] \\ &+ \frac{\left|u^{\Downarrow}(E_\mathrm{B})\right|^2 + \left|v^{\Downarrow}(E_\mathrm{B})\right|^2}{\mathrm{Im}\left[q^{\Downarrow}_{x,\mathrm{e}}(E_\mathrm{B})\right]} \Big[\left|\varepsilon_2(E_\mathrm{B}) + \eta_2(E_\mathrm{B})\,\Sigma_3(E_\mathrm{B})\right|^2 + \left|\varphi_2(E_\mathrm{B})\,\Sigma_1(E_\mathrm{B}) + \gamma_2(E_\mathrm{B})\,\Sigma_2(E_\mathrm{B})\right|^2 \\ &\qquad + \left|\Sigma_2(E_\mathrm{B})\right|^2 + \left|\Sigma_3(E_\mathrm{B})\right|^2\Big]\Bigg\} \left|e(E_\mathrm{B})\right|^2 = 1. \end{aligned} \tag{D.32}$$

Since all appearing prefactors were already identified above, Eq. (D.32) can be immediately inverted to identify $\left|e(E_\mathrm{B})\right|^2$. Afterwards, the absolute squares of the remaining bound state wave function coefficients are uniquely determined going back with the set of given equations. Once all bound state wave function coefficients are specified, they can be substituted into Eq. (7.22) to compute the Josephson current flowing through the considered S/F-I/S junction.

Bound state wave functions for singlet pairing and absent SOC

Although the above constructed bound state wave functions are general and apply to any (one-dimensional) S/F-I/S Josephson junction with s- or p_x-wave superconducting pairing symmetry, we put special emphasis on the s-wave case in the main part. This is not only the most relevant situation in experimental studies,

but also reveals the universal connection between the junction's bound state characteristics and the Josephson current-reversing 0-π transitions most clearly. The superconducting pairing potential [see Eq. (7.5)] contains then just the singlet (s-wave) part

$$\hat{\Delta}_{\mathrm{S}}(x) = |\Delta_{\mathrm{S}}^{s}|\hat{\sigma}_0 \left[\Theta(-x) + \mathrm{e}^{\mathrm{i}\phi_{\mathrm{S}}}\Theta(x)\right]. \tag{D.33}$$

To shorten our analytical treatment, we additionally suppose that the bulk Rashba [149, 150] SOC inside the superconductors is absent, i.e., $\lambda_{\mathrm{R}} = 0$. Since the interfacial scalar and magnetic tunneling terms, entering the Bogoljubov-de Gennes equation's single-particle Hamiltonians [see, e.g., Eq. (7.4)] are diagonal in spin space, it is common to introduce a reduced *spin-resolved* Nambu basis, labeled by $\sigma = \uparrow = 1$ (for spin up, with respect to $\hat{\sigma}_z$) and $\sigma = \downarrow = -1$ (for spin down).[1] The spin-σ bound state wave functions in the new basis can be recast as

$$\begin{aligned}\psi^{\sigma}(x<0;E) &= \psi_{\mathrm{e}}^{\sigma}(x<0;E) + \psi_{\mathrm{h}}^{\sigma}(x<0;E) \\ &= A^{\sigma}(E)\begin{bmatrix}u(E)\\ v(E)\end{bmatrix}\mathrm{e}^{-\mathrm{i}q_{x,\mathrm{e}}(E)x} + B^{\sigma}(E)\begin{bmatrix}v(E)\\ u(E)\end{bmatrix}\mathrm{e}^{\mathrm{i}q_{x,\mathrm{h}}(E)x}\end{aligned} \tag{D.34}$$

inside the left superconductor ($x < 0$) and

$$\begin{aligned}\psi^{\sigma}(x>0;E) &= \psi_{\mathrm{e}}^{\sigma}(x>0;E) + \psi_{\mathrm{h}}^{\sigma}(x>0;E) \\ &= C^{\sigma}(E)\begin{bmatrix}u(E)\mathrm{e}^{\mathrm{i}\phi_{\mathrm{S}}}\\ v(E)\end{bmatrix}\mathrm{e}^{\mathrm{i}q_{x,\mathrm{e}}(E)x} + D^{\sigma}(E)\begin{bmatrix}v(E)\mathrm{e}^{\mathrm{i}\phi_{\mathrm{S}}}\\ u(E)\end{bmatrix}\mathrm{e}^{-\mathrm{i}q_{x,\mathrm{h}}(E)x}\end{aligned} \tag{D.35}$$

inside the right superconductor ($x > 0$); the spin-dependent wave function coefficients are denoted by $A^{\sigma}(E)$, $B^{\sigma}(E)$, $C^{\sigma}(E)$, and $D^{\sigma}(E)$ [for their physical meaning, see our explanations in Sec. 7.1]. For reasons that will become clear later on, we separated the wave functions' electronlike, $\psi_{\mathrm{e}}^{\sigma}(x;E)$, and holelike, $\psi_{\mathrm{h}}^{\sigma}(x;E)$, components. Due to the absence of SOC and triplet (p_x-wave) pairing, the coherence factors merge into the usual BCS coherence factors

$$u(E) = \sqrt{\frac{1}{2}\left(1 + \sqrt{1 - \frac{|\Delta_{\mathrm{S}}^{s}|^2}{E^2}}\right)} \qquad \text{and} \qquad v(E) = \sqrt{1 - [u(E)]^2}, \tag{D.36}$$

while the electronlike and holelike quasiparticles' wave vectors simultaneously simplify to

$$q_{x,\mathrm{e}}(E) = \sqrt{\frac{2m}{\hbar^2}\left(\mu + \sqrt{E^2 - |\Delta_{\mathrm{S}}^{s}|^2}\right)} \quad \text{and likewise} \quad q_{x,\mathrm{h}}(E) = \sqrt{\frac{2m}{\hbar^2}\left(\mu - \sqrt{E^2 - |\Delta_{\mathrm{S}}^{s}|^2}\right)}. \tag{D.37}$$

Similarly to Eqs. (7.16)–(7.17), the interfacial ($x = 0$) boundary conditions in the reduced Nambu space read as

$$\psi^{\sigma}(x;E)\big|_{x=0_-} = \psi^{\sigma}(x;E)\big|_{x=0_+} \tag{D.38}$$

and

$$\left\{\left(\frac{\hbar^2}{2m}\frac{\mathrm{d}}{\mathrm{d}x} + \lambda_{\mathrm{SC}}\right)\begin{bmatrix}1 & 0\\ 0 & -1\end{bmatrix} + \lambda_{\mathrm{MA}}\begin{bmatrix}\sigma & 0\\ 0 & \sigma\end{bmatrix}\right\}\psi^{\sigma}(x;E)\big|_{x=0_-} = \frac{\hbar^2}{2m}\frac{\mathrm{d}}{\mathrm{d}x}\begin{bmatrix}1 & 0\\ 0 & -1\end{bmatrix}\psi^{\sigma}(x;E)\big|_{x=0_+}. \tag{D.39}$$

[1] Decomposing the bound state wave function ansatz into its two spin-resolved blocks brings along the great advantage that we can attribute each state's spin by simply checking whether the related bound state energy comes as a solution from the up- or down-spin block. This saves us from explicitly calculating spin expectation values to determine the bound states' spins (at least as long as SOC remains absent).

To access the unknown wave function coefficients, describing a generic bound state with energy $0 \leq E_\mathrm{B} \leq |\Delta_\mathrm{S}^s|$, we follow the same strategy as in the previous section. Proper normalization of the wave functions requires

$$\frac{\left|u(E_\mathrm{B})\right|^2 + \left|v(E_\mathrm{B})\right|^2}{2\mathrm{Im}[q_{x,\mathrm{e}}(E_\mathrm{B})]} \left[\left|A^\sigma(E_\mathrm{B})\right|^2 + \left|B^\sigma(E_\mathrm{B})\right|^2 + \left|C^\sigma(E_\mathrm{B})\right|^2 + \left|D^\sigma(E_\mathrm{B})\right|^2\right] = 1, \tag{D.40}$$

using $\mathrm{Im}[q_{x,\mathrm{e}}(E_\mathrm{B})] = -\mathrm{Im}[q_{x,\mathrm{h}}(E_\mathrm{B})]$; see Eq. (D.37). Continuity of the bound state wave functions at the ferromagnetic-insulator interface, imposed by Eq. (D.38), relates the coefficients $C^\sigma(E_\mathrm{B})$ and $D^\sigma(E_\mathrm{B})$ to $A^\sigma(E_\mathrm{B})$ and $B^\sigma(E_\mathrm{B})$, particularly

$$C^\sigma(E_\mathrm{B}) = \alpha_1(E_\mathrm{B})\, A^\sigma(E_\mathrm{B}) + \beta_1(E_\mathrm{B})\, B^\sigma(E_\mathrm{B}), \tag{D.41}$$

as well as

$$D^\sigma(E_\mathrm{B}) = \alpha_2(E_\mathrm{B})\, A^\sigma(E_\mathrm{B}) + \beta_2(E_\mathrm{B})\, B^\sigma(E_\mathrm{B}), \tag{D.42}$$

with

$$\alpha_1(E_\mathrm{B}) = \frac{[u(E_\mathrm{B})]^2\, \mathrm{e}^{-\mathrm{i}\phi_\mathrm{S}} - [v(E_\mathrm{B})]^2}{[u(E_\mathrm{B})]^2 - [v(E_\mathrm{B})]^2}, \qquad \alpha_2(E_\mathrm{B}) = \frac{u(E_\mathrm{B})\, v(E_\mathrm{B}) \left(1 - \mathrm{e}^{-\mathrm{i}\phi_\mathrm{S}}\right)}{[u(E_\mathrm{B})]^2 - [v(E_\mathrm{B})]^2}, \tag{D.43}$$

$$\beta_1(E_\mathrm{B}) = \frac{u(E_\mathrm{B})\, v(E_\mathrm{B}) \left(\mathrm{e}^{-\mathrm{i}\phi_\mathrm{S}} - 1\right)}{[u(E_\mathrm{B})]^2 - [v(E_\mathrm{B})]^2}, \qquad \text{and} \qquad \beta_2(E_\mathrm{B}) = \frac{[u(E_\mathrm{B})]^2 - [v(E_\mathrm{B})]^2\, \mathrm{e}^{-\mathrm{i}\phi_\mathrm{S}}}{[u(E_\mathrm{B})]^2 - [v(E_\mathrm{B})]^2}. \tag{D.44}$$

Applying the second boundary condition, defined by Eq. (D.39), to the wave function ansatz in Eqs. (D.34) and (D.35), we can express $B^\sigma(E_\mathrm{B})$ in terms of $A^\sigma(E_\mathrm{B})$,

$$B^\sigma(E_\mathrm{B}) = \gamma^\sigma(E_\mathrm{B})\, A^\sigma(E_\mathrm{B}), \tag{D.45}$$

where the *spin-dependent* prefactor $\gamma^\sigma(E_\mathrm{B})$ has the form

$$\gamma^\sigma(E_\mathrm{B}) = \frac{\left\{\frac{q_{x,\mathrm{e}}(E_\mathrm{B})}{k_\mathrm{F}} \left[1 + \alpha_1(E_\mathrm{B})\, \mathrm{e}^{\mathrm{i}\phi_\mathrm{S}}\right] + \mathrm{i}\left(\overline{\lambda}_\mathrm{SC} + \sigma\overline{\lambda}_\mathrm{MA}\right)\right\} u(E_\mathrm{B}) - \frac{q_{x,\mathrm{h}}(E_\mathrm{B})}{k_\mathrm{F}}\, \alpha_2(E_\mathrm{B})\, \mathrm{e}^{\mathrm{i}\phi_\mathrm{S}}\, v(E_\mathrm{B})}{\left\{\frac{q_{x,\mathrm{h}}(E_\mathrm{B})}{k_\mathrm{F}} \left[1 + \beta_2(E_\mathrm{B})\, \mathrm{e}^{\mathrm{i}\phi_\mathrm{S}}\right] - \mathrm{i}\left(\overline{\lambda}_\mathrm{SC} + \sigma\overline{\lambda}_\mathrm{MA}\right)\right\} v(E_\mathrm{B}) - \frac{q_{x,\mathrm{e}}(E_\mathrm{B})}{k_\mathrm{F}}\, \beta_1(E_\mathrm{B})\, \mathrm{e}^{\mathrm{i}\phi_\mathrm{S}}\, u(E_\mathrm{B})}. \tag{D.46}$$

Eliminating $B^\sigma(E_\mathrm{B})$, $C^\sigma(E_\mathrm{B})$, and $D^\sigma(E_\mathrm{B})$ from the normalization condition [see Eq. (D.40)] – by substituting Eqs. (D.41), (D.42), and (D.45) –, and inverting the resulting equation, we finally arrive at

$$\left|A^\sigma(E_\mathrm{B})\right|^2 = \frac{2\mathrm{Im}[q_{x,\mathrm{e}}(E_\mathrm{B})] \Big/ \left[\left|u(E_\mathrm{B})\right|^2 + \left|v(E_\mathrm{B})\right|^2\right]}{\left[1 + \left|\gamma^\sigma(E_\mathrm{B})\right|^2 + \left|\alpha_1(E_\mathrm{B}) + \beta_1(E_\mathrm{B})\, \gamma^\sigma(E_\mathrm{B})\right|^2 + \left|\alpha_2(E_\mathrm{B}) + \beta_2(E_\mathrm{B})\, \gamma^\sigma(E_\mathrm{B})\right|^2\right]}. \tag{D.47}$$

Going back with all stated equations, we consecutively obtain $\left|B^\sigma(E_\mathrm{B})\right|^2$, $\left|C^\sigma(E_\mathrm{B})\right|^2$, and $\left|D^\sigma(E_\mathrm{B})\right|^2$.

Once we determined the absolute squares of all wave function coefficients, the electronlike and holelike bound state wave function probability densities (absolute squares) can be evaluated by means of

$$\left|\psi_\mathrm{e}^\sigma(x < 0; E_\mathrm{B})\right|^2 = \left[\left|u(E_\mathrm{B})\right|^2 + \left|v(E_\mathrm{B})\right|^2\right] \left|A^\sigma(E_\mathrm{B})\right|^2 \mathrm{e}^{2\mathrm{Im}[q_{x,\mathrm{e}}(E_\mathrm{B})]x} \tag{D.48}$$

and

$$\left|\psi_\mathrm{h}^\sigma(x < 0; E_\mathrm{B})\right|^2 = \left[\left|u(E_\mathrm{B})\right|^2 + \left|v(E_\mathrm{B})\right|^2\right] \left|B^\sigma(E_\mathrm{B})\right|^2 \mathrm{e}^{2\mathrm{Im}[q_{x,\mathrm{e}}(E_\mathrm{B})]x} \tag{D.49}$$

in the left superconductor ($x < 0$), as well as

$$\left|\psi_{\mathrm{e}}^{\sigma}(x>0;E_{\mathrm{B}})\right|^2 = \left[\left|u(E_{\mathrm{B}})\right|^2 + \left|v(E_{\mathrm{B}})\right|^2\right]\left|C^{\sigma}(E_{\mathrm{B}})\right|^2 \mathrm{e}^{-2\mathrm{Im}[q_{x,\mathrm{e}}(E_{\mathrm{B}})]x} \tag{D.50}$$

and

$$\left|\psi_{\mathrm{h}}^{\sigma}(x>0;E_{\mathrm{B}})\right|^2 = \left[\left|u(E_{\mathrm{B}})\right|^2 + \left|v(E_{\mathrm{B}})\right|^2\right]\left|D^{\sigma}(E_{\mathrm{B}})\right|^2 \mathrm{e}^{-2\mathrm{Im}[q_{x,\mathrm{e}}(E_{\mathrm{B}})]x} \tag{D.51}$$

in the right superconductor ($x > 0$).

As mentioned in the main part, each wave function $\psi^{\sigma}(x;E_{\mathrm{B}})$, corresponding to a bound state with energy $E_{\mathrm{B}} > 0$, comes along with a second one, $\tilde{\psi}^{\sigma}(x;-E_{\mathrm{B}})$, indicating another bound state of energy $-E_{\mathrm{B}}$. Formally, an ansatz for $\tilde{\psi}^{\sigma}(x;-E_{\mathrm{B}})$ can be extracted from Eqs. (D.34)–(D.35) interchanging the coherence factors according to $u(E_{\mathrm{B}}) \longmapsto -[v(-E_{\mathrm{B}})]^*$ and $v(E_{\mathrm{B}}) \longmapsto [u(-E_{\mathrm{B}})]^*$, and replacing the initially unknown coefficients by $\tilde{A}^{\sigma}(-E_{\mathrm{B}})$, $\tilde{B}^{\sigma}(-E_{\mathrm{B}})$, $\tilde{C}^{\sigma}(-E_{\mathrm{B}})$, and $\tilde{D}^{\sigma}(-E_{\mathrm{B}})$. To get explicit analytical expressions for the latter, we can proceed in the same way as with $\psi^{\sigma}(x;E_{\mathrm{B}})$, eventually yielding

$$\left|\tilde{A}^{\sigma}(-E_{\mathrm{B}})\right|^2 = \left|A^{-\sigma}(E_{\mathrm{B}})\right|^2, \tag{D.52}$$

$$\left|\tilde{B}^{\sigma}(-E_{\mathrm{B}})\right|^2 = \left|B^{-\sigma}(E_{\mathrm{B}})\right|^2, \tag{D.53}$$

$$\left|\tilde{C}^{\sigma}(-E_{\mathrm{B}})\right|^2 = \left|C^{-\sigma}(E_{\mathrm{B}})\right|^2, \tag{D.54}$$

and

$$\left|\tilde{D}^{\sigma}(-E_{\mathrm{B}})\right|^2 = \left|D^{-\sigma}(E_{\mathrm{B}})\right|^2. \tag{D.55}$$

One of the most important features of negative-energy bound states is therefore their opposite spin when compared to the related positive-energy bound states [note the σ on the left and the $-\sigma$ on the right-hand side of Eqs. (D.52)–(D.55)].

To illustrate our reasoning in the main part, drawing unique connections between the formation of zero-energy YSR states in the junction's bound state spectrum and the emerging 0-π transitions in the Josephson current, we evaluate the (spatial dependence of the) wave function probability densities in Eqs. (D.48)–(D.51) for one particular realistic junction. The results are presented in Fig. D.1. We also checked several other parameter regimes and essentially observed the same qualitative features. While the interfacial scalar tunneling strength got fixed to a moderate value of $\overline{\lambda}_{\mathrm{SC}} = 2$, the values of the magnetic tunneling strength measure $\overline{\lambda}_{\mathrm{MA}}$ are once chosen slightly below and once slightly above the junction's 0-π transition point, which is numerically estimated to lie between $\overline{\lambda}_{\mathrm{MA}} = 2.53619$ and $\overline{\lambda}_{\mathrm{MA}} = 2.53620$ (at zero temperature). The Andreev bound states are spatially less localized around the ferromagnetic-insulator barrier than their YSR counterparts. This becomes plausible when regarding the wave function probability densities' decay length $\kappa = 1/\{2\mathrm{Im}[q_{x,\mathrm{e}}(E_{\mathrm{B}})]\}$, which typically increases with increasing bound state energy E_{B}. Since the YSR states' energies $E_1^{\pm}$ are usually much lower (and hence much closer to the gap center) than the Andreev bound state energies $E_2^{\pm}$, the wave functions belonging to Andreev bound states decay much slower (in space) than their YSR state counterparts (meaning that they are less localized around the interface).

More remarkably, the spatial electron-hole contents of the bound state wave function probability densities are altered during the 0-π transition. While both the Andreev bound states and the YSR states initially (in the 0-state regime) possess a dominant electronlike character left and a dominant holelike character right of the interface, the YSR states' spin flips at the transition point reverse the electron-hole content of their

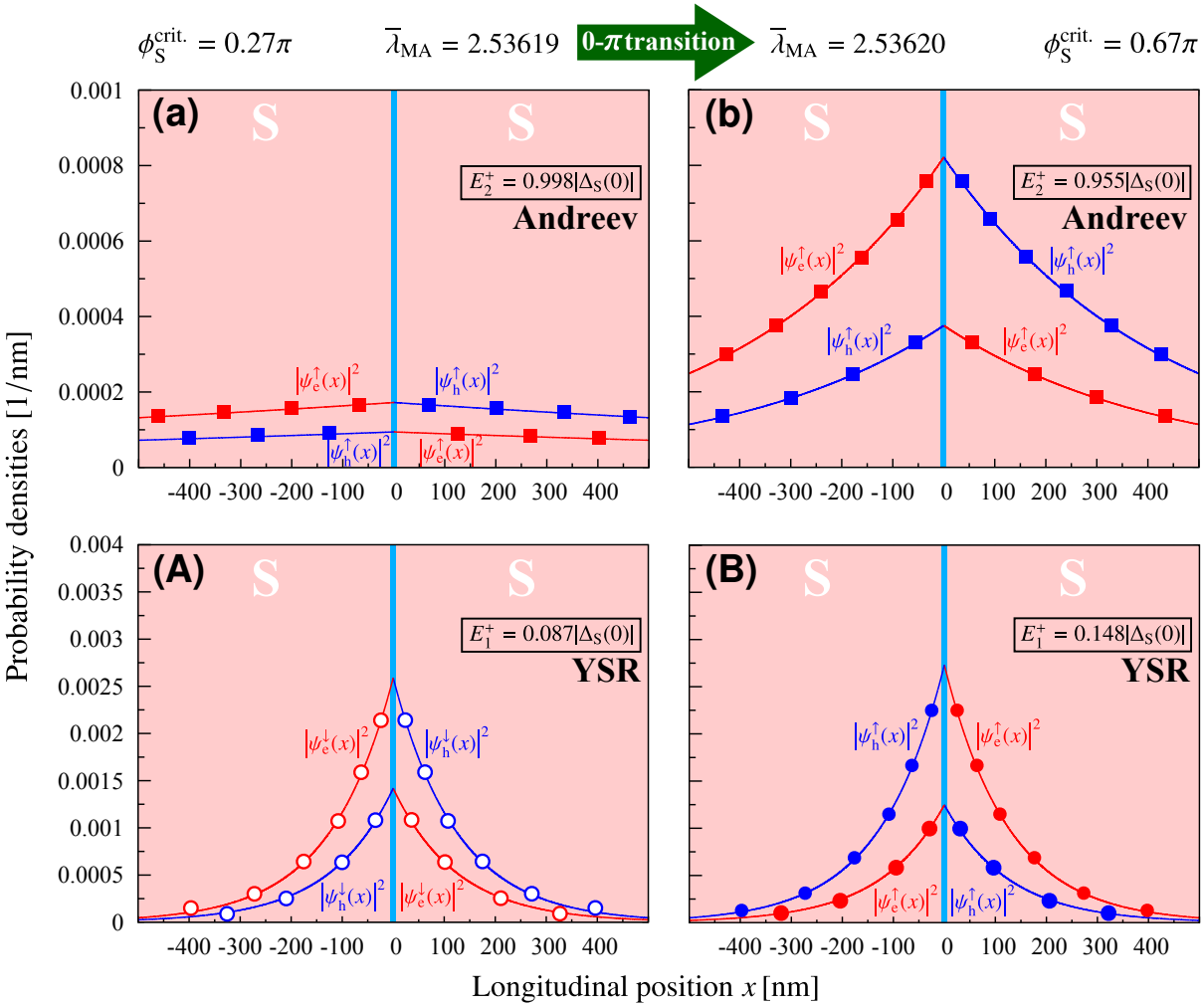


Fig. D.1: Calculated [by means of Eqs. (D.48)–(D.51)] spatial profiles of the *spin-resolved* (↑ for spin up and ↓ for spin down) and *electron-hole* (electron parts are colored red and hole parts blue) *separated* bound state wave function probability densities for positive-energy Andreev bound states [see panels **(a)** and **(b)**] and YSR states [see panels **(A)** and **(B)**]; the superconducting phase difference is always set to the given critical one, $\phi_S^{crit.}$, so that the stated bound state energies [note that we replaced $|\Delta_S^s|$ by the (zero-temperature) amplitude of the superconducting energy gap $|\Delta_S(0)|$] are directly related to the *oriented* critical Josephson current (positive for 0- and negative for π-junctions). The scalar tunneling strength is set to a moderate value of $\overline{\lambda}_{SC} = 2$, while Rashba SOC is absent. Panels **(a)** and **(A)** correspond to the 0-state junction regime ($\overline{\lambda}_{MA} = 2.53619$), whereas panels **(b)** and **(B)** reveal the π-state scenario ($\overline{\lambda}_{MA} = 2.53620$). Filled (empty) boxes indicate spin-up (spin-down) Andreev bound states and filled (empty) circles spin-up (spin-down) YSR states. The *change of the spin ordering* and the *reversal of the electron-hole content* in the YSR states' wave function behavior are clear indications of the accompanying 0-π transition.

wave functions;[2] the Andreev bound state wave functions (probability densities) are qualitatively not affected by the 0-π transition. In Sec. 7.2 of this thesis, we analyze in detail how such modifications of the electron-hole content of bound states' wave functions impact the tunneling of electron Cooper pairs from one superconductor into the other one (and thus directly the resulting Josephson current). We deduce there that it is indeed this intriguing change of the YSR states' wave function characteristics that eventually favors a transfer of electron Cooper pairs along the opposite direction [when compared to the initial (0-state) situation] and manifests itself in the measurable reversal of the Josephson current flow in the π-state regime. Instead of explicitly considering the wave function probability densities' resolved electron and hole parts, it is actually much simpler to just focus on their relative difference $\left|\psi_{\mathrm{e}}^{\sigma}(x;E_{\mathrm{B}})\right|^2-\left|\psi_{\mathrm{h}}^{\sigma}(x;E_{\mathrm{B}})\right|^2$; positive differences highlight then electronlike excess and negative differences holelike excess. We come back to that when pictorially illustrating the Cooper pair tunnelings between the S/F-I/S junction's superconducting electrodes in Fig. 7.7.

[2] The YSR states flip their spin as soon as they cross zero energy. Instead of plotting the wave function probability densities, one can simply inspect the σ-dependence in Eq. (D.46), stemming from the spin-selective magnetic tunneling, and go through the remaining steps to eventually arrive at the wave function probability densities. In the end, already the analytical equations lead to the conclusion that bound states' spin flips must necessarily reverse the electron-hole content of their underlying wave functions (probability densities).

Appendix E

Transverse BTK conductance and Furusaki-Tsukada supercurrent formulas for F/S junctions

Bogoljubov-de Gennes scattering states

In Chap. 8, we consider a *three-dimensional* F/S junction composed of semi-infinite ferromagnetic (F) and superconducting (S) regions that span the $z < 0$ and $z > 0$ half-spaces, respectively. Both electrodes are separated by an ultrathin semiconductor, breaking space-inversion symmetry and inducing interfacial Rashba [149, 150] and Dresselhaus [152] SOCs. We include that layer into our model in terms of a deltalike potential and SOC barrier, and start our description from the junction's stationary Nambu-space Bogoljubov-de Gennes equation [139]

$$\begin{bmatrix} \hat{\mathcal{H}}_\mathrm{e} & \hat{\Delta}_\mathrm{S}(z) \\ \hat{\Delta}_\mathrm{S}^\dagger(z) & \hat{\mathcal{H}}_\mathrm{h} \end{bmatrix} \Psi^\sigma(\mathbf{r}) = E\Psi^\sigma(\mathbf{r}), \tag{E.1}$$

with

$$\hat{\mathcal{H}}_\mathrm{e} = \left(-\frac{\hbar^2}{2m}\boldsymbol{\nabla}^2 - \mu\right)\hat{\sigma}_0 - \frac{\Delta_\mathrm{XC}}{2}(\hat{\mathbf{m}}\cdot\hat{\boldsymbol{\sigma}})\Theta(-z) + \Big[V_\mathrm{SMC}d_\mathrm{SMC}\hat{\sigma}_0 + \alpha(k_y\hat{\sigma}_x - k_x\hat{\sigma}_y) - \beta(k_y\hat{\sigma}_x + k_x\hat{\sigma}_y)\Big]\delta(z), \tag{E.2}$$

$$\hat{\mathcal{H}}_\mathrm{h} = -\hat{\sigma}_y\hat{\mathcal{H}}_\mathrm{e}^*\hat{\sigma}_y, \tag{E.3}$$

and

$$\hat{\Delta}_\mathrm{S}(z) = |\Delta_\mathrm{S}|\hat{\sigma}_0\Theta(z). \tag{E.4}$$

The individual components' physical meaning is explained in Sec. 8.1. Since the transverse wave vector $\mathbf{k}_\parallel = [k_x,\, k_y,\, 0]^\top$ (parallel to the semiconducting barrier) is conserved, we can substitute the ansatz

$$\Psi^\sigma(\mathbf{r}) = \psi^\sigma(z)\,\mathrm{e}^{\mathrm{i}(\mathbf{k}_\parallel\cdot\mathbf{r}_\parallel)}, \tag{E.5}$$

with $\mathbf{r}_\parallel = [x,\, y,\, 0]^\top$, into Eq. (E.1) to effectively reduce our problem to finding the *one-dimensional* scattering states $\psi^\sigma(z)$ for a given spin σ [$\sigma = +(-)1$ for spin up (spin down), meaning a spin parallel (antiparallel) to the ferromagnet's magnetization direction $\hat{\mathbf{m}}$].

Considering an incoming spin-σ electron from the ferromagnetic region, the scattering state inside the ferromagnet ($z < 0$) is found to be

$$\psi^\sigma(z<0) = \frac{1}{\sqrt{2}}\begin{bmatrix}1\\ \sigma\,\mathrm{e}^{\mathrm{i}\Phi}\\ 0\\ 0\end{bmatrix}\mathrm{e}^{\mathrm{i}k^\sigma_{z,\mathrm{e}}z} + r_\mathrm{e}^{\sigma,\sigma}\,\frac{1}{\sqrt{2}}\begin{bmatrix}1\\ \sigma\,\mathrm{e}^{\mathrm{i}\Phi}\\ 0\\ 0\end{bmatrix}\mathrm{e}^{-\mathrm{i}k^\sigma_{z,\mathrm{e}}z} + r_\mathrm{e}^{\sigma,-\sigma}\,\frac{1}{\sqrt{2}}\begin{bmatrix}1\\ -\sigma\,\mathrm{e}^{\mathrm{i}\Phi}\\ 0\\ 0\end{bmatrix}\mathrm{e}^{-\mathrm{i}k^{-\sigma}_{z,\mathrm{e}}z}$$
$$+ r_\mathrm{h}^{\sigma,-\sigma}\,\frac{1}{\sqrt{2}}\begin{bmatrix}0\\ 0\\ 1\\ \sigma\,\mathrm{e}^{\mathrm{i}\Phi}\end{bmatrix}\mathrm{e}^{\mathrm{i}k^{-\sigma}_{z,\mathrm{h}}z} + r_\mathrm{h}^{\sigma,\sigma}\,\frac{1}{\sqrt{2}}\begin{bmatrix}0\\ 0\\ 1\\ -\sigma\,\mathrm{e}^{\mathrm{i}\Phi}\end{bmatrix}\mathrm{e}^{\mathrm{i}k^{\sigma}_{z,\mathrm{h}}z}, \quad \text{(E.6)}$$

where $r_\mathrm{e}^{\sigma,\sigma}$ ($r_\mathrm{e}^{\sigma,-\sigma}$) denotes the spin-conserving (spin-flip) specular reflection coefficient and likewise $r_\mathrm{h}^{\sigma,-\sigma}$ ($r_\mathrm{h}^{\sigma,\sigma}$) the spin-conserving (spin-flip) Andreev reflection coefficient; similarly to Chap. 3, the first σ refers to the incident electron's spin and the second one to the spin of the reflected electron (hole). Note again that spin-conserving Andreev reflection indicates that the electron gets reflected as a hole with opposite spin. Analogously, $\psi^\sigma(z)$ inside the superconductor ($z > 0$) can be written as

$$\psi^\sigma(z>0) = t_\mathrm{e}^{\sigma,\sigma}\begin{bmatrix}u\\0\\v\\0\end{bmatrix}\mathrm{e}^{\mathrm{i}q_{z,\mathrm{e}}z} + t_\mathrm{e}^{\sigma,-\sigma}\begin{bmatrix}0\\u\\0\\v\end{bmatrix}\mathrm{e}^{\mathrm{i}q_{z,\mathrm{e}}z} + t_\mathrm{h}^{\sigma,\sigma}\begin{bmatrix}v\\0\\u\\0\end{bmatrix}\mathrm{e}^{-\mathrm{i}q_{z,\mathrm{h}}z} + t_\mathrm{h}^{\sigma,-\sigma}\begin{bmatrix}0\\v\\0\\u\end{bmatrix}\mathrm{e}^{-\mathrm{i}q_{z,\mathrm{h}}z}, \quad \text{(E.7)}$$

accounting for electronlike (coefficients $t_\mathrm{e}^{\sigma,\pm\sigma}$) and holelike (coefficients $t_\mathrm{h}^{\sigma,\pm\sigma}$) quasiparticle transmissions.

The $\hat{z}$-components of electrons' and holes' wave vectors in the ferromagnet are given by

$$k^\sigma_{z,\mathrm{e}} = k^\sigma_{z,\mathrm{e}}(E) = \sqrt{\frac{2m}{\hbar^2}\left[\mu + E + \sigma\frac{\Delta_\mathrm{XC}}{2}\right] - \mathbf{k}_\parallel^2} \quad \text{(E.8)}$$

and

$$k^\sigma_{z,\mathrm{h}} = k^\sigma_{z,\mathrm{h}}(E) = \sqrt{\frac{2m}{\hbar^2}\left[\mu - E + \sigma\frac{\Delta_\mathrm{XC}}{2}\right] - \mathbf{k}_\parallel^2}, \quad \text{(E.9)}$$

while those in the superconductor are

$$q_{z,\mathrm{e}} = q_{z,\mathrm{e}}(E) = \sqrt{\frac{2m}{\hbar^2}\left[\mu + \sqrt{E^2 - |\Delta_\mathrm{S}|^2}\right] - \mathbf{k}_\parallel^2} \quad \text{(E.10)}$$

and

$$q_{z,\mathrm{h}} = q_{z,\mathrm{h}}(E) = \sqrt{\frac{2m}{\hbar^2}\left[\mu - \sqrt{E^2 - |\Delta_\mathrm{S}|^2}\right] - \mathbf{k}_\parallel^2}, \quad \text{(E.11)}$$

respectively. The (quasi)particle excitation energies E and the superconducting energy gap $|\Delta_\mathrm{S}|$ are typically small compared to the chemical potential μ, and we can approximate the wave vectors by

$$k^\sigma_{z,\mathrm{e}} \approx k^\sigma_{z,\mathrm{h}} \approx k^\sigma_z = \sqrt{k_\mathrm{F}^2(1+\sigma P) - \mathbf{k}_\parallel^2}, \quad \text{(E.12)}$$

where $P = (\Delta_{\mathrm{XC}}/2)/\mu$ effectively measures the ferromagnet's spin polarization, and accordingly

$$q_{z,\mathrm{e}} \approx q_{z,\mathrm{h}} \approx q_z = \sqrt{k_{\mathrm{F}}^2 - \mathbf{k}_{\parallel}^2}; \tag{E.13}$$

as before, $k_{\mathrm{F}} = \sqrt{2m\mu}/\hbar$ represents the Fermi wave vector. The factors $u = u(E)$ and $v = v(E)$ appearing in the superconductor's scattering state are the usual BCS coherence factors that satisfy

$$u(E) = \sqrt{\frac{1}{2}\left(1 + \sqrt{1 - \frac{|\Delta_{\mathrm{S}}|^2}{E^2}}\right)} = \sqrt{1 - [v(E)]^2}. \tag{E.14}$$

To obtain the still unknown scattering coefficients, generally depending on the excitation energy E via the coherence factors and on the transverse momenta $\mathbf{k}_{\parallel}$ via the wave vectors, the scattering states in Eqs. (E.6) and (E.7) need to fulfill the interfacial ($z = 0$) boundary conditions

$$\psi^{\sigma}(z)\big|_{z=0_-} = \psi^{\sigma}(z)\big|_{z=0_+} \tag{E.15}$$

and

$$\left(\frac{\hbar^2}{2m}\frac{\mathrm{d}}{\mathrm{d}z} + V_{\mathrm{SMC}} d_{\mathrm{SMC}}\right)\hat{\eta}\psi^{\sigma}(z)\big|_{z=0_-} + \begin{bmatrix} \boldsymbol{\Omega}\cdot\hat{\boldsymbol{\sigma}} & \hat{0} \\ \hat{0} & -(\boldsymbol{\Omega}\cdot\hat{\boldsymbol{\sigma}}) \end{bmatrix}\psi^{\sigma}(z)\big|_{z=0_-} = \frac{\hbar^2}{2m}\frac{\mathrm{d}}{\mathrm{d}z}\hat{\eta}\psi^{\sigma}(z)\big|_{z=0_+}, \tag{E.16}$$

where $\hat{\eta} = \mathrm{diag}[\hat{\sigma}_0, -\hat{\sigma}_0]$ and $\boldsymbol{\Omega} = \big[(\alpha-\beta)k_y, -(\alpha+\beta)k_x, 0\big]$ contains the Rashba and Dresselhaus SOC terms; $\hat{0}$ is the two-by-two zero matrix. The resulting eight-dimensional system of equations (per spin) can be numerically solved for generic electron energies E to find all involved scattering coefficients.

Particularly relevant to evaluate the TAHE currents later on will be the case of *zero* electron energies ($E = 0$) since that corresponds to the zero-bias junction regime (substituting $E = eV = 0$; e is still the positive elementary charge). The BCS coherence factors simplify then to $u(E=0) = 1/\sqrt{2}$ and $v(E=0) = -\mathrm{i}/\sqrt{2}$, and we can extract fully analytical expressions for the *zero-energy reflection coefficients* that read as

$$\begin{aligned} r_{\mathrm{e}}^{\sigma,\sigma}(E=0) = \Big\{ &-\overline{\Omega}^2 \mathrm{e}^{4\mathrm{i}\Phi}\left(\tilde{k}_z^{-\sigma} - \tilde{k}_z^{\sigma}\right)\left(\tilde{k}_z^{-\sigma} + \tilde{k}_z^{\sigma}\right) + 4\mathrm{i}\sigma\tilde{k}_z^{-\sigma}\overline{\Omega}\mathrm{e}^{3\mathrm{i}\Phi}\left[\tilde{q}_z^2 + \left(\tilde{k}_z^{\sigma} - \mathrm{i}Z\right)^2 + |\overline{\Omega}|^2\right] \\ &+ 4\mathrm{i}\sigma\tilde{k}_z^{-\sigma}\overline{\Omega}^*\mathrm{e}^{\mathrm{i}\Phi}\left[\tilde{q}_z^2 + \left(\tilde{k}_z^{\sigma} - \mathrm{i}Z\right)^2 + |\overline{\Omega}|^2\right] + \left(\overline{\Omega}^*\right)^2\left[\left(\tilde{k}_z^{\sigma}\right)^2 - \left(\tilde{k}_z^{-\sigma}\right)^2\right] - 2\mathrm{e}^{2\mathrm{i}\Phi}\Big\{2\Big[\left(\tilde{k}_z^{-\sigma}\right)^2\left(\tilde{k}_z^{\sigma} - \mathrm{i}Z\right)^2 \\ &- \left(\tilde{q}_z^2 + \mathrm{i}\tilde{k}_z^{\sigma}Z + Z^2\right)^2\Big] - 2|\overline{\Omega}|^4 + \overline{\Omega}\,\overline{\Omega}^*\left[\left(\tilde{k}_z^{-\sigma}\right)^2 - 4\tilde{q}_z^2 - \left(\tilde{k}_z^{\sigma} - 2\mathrm{i}Z\right)^2\right]\Big\}\Big\} \Big/ \Gamma(E=0)\,, \end{aligned} \tag{E.17}$$

$$\begin{aligned} r_{\mathrm{e}}^{\sigma,-\sigma}(E=0) = \Big\{ &2\tilde{k}_z^{\sigma}\overline{\Omega}^2\Big\{\mathrm{e}^{4\mathrm{i}\Phi}\left(\tilde{k}_z^{\sigma} - \tilde{k}_z^{-\sigma}\right) + 2\mathrm{i}\sigma\overline{\Omega}\mathrm{e}^{3\mathrm{i}\Phi}\left[\tilde{q}_z^2 + \left(\tilde{k}_z^{-\sigma} - \mathrm{i}Z\right)\left(\tilde{k}_z^{\sigma} - \mathrm{i}Z\right) + |\overline{\Omega}|^2\right] \\ &- 2\mathrm{i}\sigma\overline{\Omega}^*\mathrm{e}^{\mathrm{i}\Phi}\left[\tilde{q}_z^2 + \left(\tilde{k}_z^{-\sigma} - \mathrm{i}Z\right)\left(\tilde{k}_z^{\sigma} - \mathrm{i}Z\right) + |\overline{\Omega}|^2\right] + \left(\overline{\Omega}^*\right)^2\left(\tilde{k}_z^{-\sigma} - \tilde{k}_z^{\sigma}\right)\Big\}\Big\} \Big/ \Gamma(E=0)\,, \end{aligned} \tag{E.18}$$

$$\begin{aligned} r_{\mathrm{h}}^{\sigma,-\sigma}(E=0) = \Big\{ &4\sigma\tilde{k}_z^{\sigma}\tilde{q}_z\mathrm{e}^{\mathrm{i}\Phi}\Big\{\overline{\Omega}\mathrm{e}^{2\mathrm{i}\Phi}\left(\tilde{k}_z^{\sigma} - \tilde{k}_z^{-\sigma} - 2\mathrm{i}Z\right) + 2\mathrm{i}\sigma\mathrm{e}^{\mathrm{i}\Phi}\left[\tilde{q}_z^2 + \left(\tilde{k}_z^{\sigma} - \mathrm{i}Z\right)\left(\tilde{k}_z^{-\sigma} + \mathrm{i}Z\right) + |\overline{\Omega}|^2\right] \\ &+ \overline{\Omega}^*\left(\tilde{k}_z^{\sigma} - \tilde{k}_z^{-\sigma} - 2\mathrm{i}Z\right)\Big\}\Big\} \Big/ \Gamma(E=0)\,, \end{aligned} \tag{E.19}$$

$$r_{\mathrm{h}}^{\sigma,\sigma}(E=0) = \Big\{ -8\mathrm{i}\sigma\tilde{k}_z^{\sigma}\tilde{q}_z Z\mathrm{e}^{\mathrm{i}\Phi}\left(\overline{\Omega}\mathrm{e}^{2\mathrm{i}\Phi} - \overline{\Omega}^*\right)\Big\} \Big/ \Gamma(E=0)\,, \tag{E.20}$$

with the common denominator

$$\begin{aligned}\Gamma(E=0) = \overline{\Omega}^2 \mathrm{e}^{4\mathrm{i}\Phi}\left(\tilde{k}_z^{-\sigma}-\tilde{k}_z^{\sigma}\right)^2 - 4\mathrm{i}\sigma\overline{\Omega}\mathrm{e}^{3\mathrm{i}\Phi}\left(\tilde{k}_z^{-\sigma}-\tilde{k}_z^{\sigma}\right)\left(\tilde{k}_z^{\sigma}\tilde{k}_z^{-\sigma}+\tilde{q}_z^2-Z^2+\left|\overline{\Omega}\right|^2\right)\\ - 4\mathrm{i}\sigma\overline{\Omega}^*\mathrm{e}^{\mathrm{i}\Phi}\left(\tilde{k}_z^{-\sigma}-\tilde{k}_z^{\sigma}\right)\left(\tilde{k}_z^{-\sigma}\tilde{k}_z^{\sigma}+\tilde{q}_z^2-Z^2+\left|\overline{\Omega}\right|^2\right)+\left(\overline{\Omega}^*\right)^2\left(\tilde{k}_z^{-\sigma}-\tilde{k}_z^{\sigma}\right)^2\\ - 2\mathrm{e}^{2\mathrm{i}\Phi}\Bigg\{2\left[\left(\tilde{k}_z^{-\sigma}\tilde{k}_z^{\sigma}+\tilde{q}_z^2\right)^2+\left[\left(\tilde{k}_z^{-\sigma}\right)^2+\left(\tilde{k}_z^{\sigma}\right)^2+2\tilde{q}_z^2\right]Z^2+Z^4\right]+2\left|\overline{\Omega}\right|^4\\ -\overline{\Omega}\,\overline{\Omega}^*\left[\left(\tilde{k}_z^{-\sigma}\right)^2-6\tilde{k}_z^{-\sigma}\tilde{k}_z^{\sigma}+\left(\tilde{k}_z^{\sigma}\right)^2-4\tilde{q}_z^2+4Z^2\right]\Bigg\}. \end{aligned} \tag{E.21}$$

The dimensionless "tilde wave vectors" are thereby obtained dividing the above ones [see Eqs. (E.12) and (E.13)] by the Fermi wave vector k_F. The usual spin-independent tunneling barrier's impact is determined by the BTK-like parameter $Z = (2mV_\mathrm{SMC}d_\mathrm{SMC})/(\hbar^2 k_\mathrm{F})$, while the effective dimensionless Rashba and Dresselhaus SOC strengths $\overline{\lambda}_\mathrm{R} = (2m\alpha)/\hbar^2$ and $\overline{\lambda}_\mathrm{D} = (2m\beta)/\hbar^2$ enter the SOC matrix element

$$\overline{\Omega} = \left(\overline{\lambda}_\mathrm{R}-\overline{\lambda}_\mathrm{D}\right)k_y/k_\mathrm{F} + \mathrm{i}\left(\overline{\lambda}_\mathrm{R}+\overline{\lambda}_\mathrm{D}\right)k_x/k_\mathrm{F}. \tag{E.22}$$

It is straightforward to check that the *spin-flip* reflection coefficients vanish in the absence of SOC, i.e., if $\overline{\Omega} = 0$.

In the same way, we can analytically compute the reflection coefficients for the related *normal-state* F/N junction. The scattering state in the superconductor reduces to the well-known one for a normal-conducting electrode when substituting $u(E=0) = 1$ and $v(E=0) = 0$. Solving the system of equations following from the boundary conditions in that scenario yields

$$\begin{aligned} r_\mathrm{e}^{\sigma,\sigma}(E=0) = \Big\{&\overline{\Omega}\mathrm{e}^{2\mathrm{i}\Phi}\left(\tilde{k}_z^{\sigma}+\tilde{k}_z^{-\sigma}\right)+\overline{\Omega}^*\left(\tilde{k}_z^{\sigma}+\tilde{k}_z^{-\sigma}\right)+2\mathrm{i}\sigma\mathrm{e}^{\mathrm{i}\Phi}\left[\left(\tilde{k}_z^{\sigma}-\tilde{q}_z-\mathrm{i}Z\right)\left(\tilde{k}_z^{-\sigma}+\tilde{q}_z+\mathrm{i}Z\right)\right.\\ &\left.-\overline{\Omega}\,\overline{\Omega}^*\right]\Big\}\Big/\gamma(E=0)\,, \end{aligned} \tag{E.23}$$

$$r_\mathrm{e}^{\sigma,-\sigma}(E=0) = \left\{2\tilde{k}_z^{\sigma}\left(\overline{\Omega}\mathrm{e}^{2\mathrm{i}\Phi}-\overline{\Omega}^*\right)\right\}\Big/\gamma(E=0)\,, \tag{E.24}$$

$$r_\mathrm{h}^{\sigma,-\sigma}(E=0) = 0, \tag{E.25}$$

$$r_\mathrm{h}^{\sigma,\sigma}(E=0) = 0, \tag{E.26}$$

with the common denominator

$$\gamma(E=0) = -\overline{\Omega}\mathrm{e}^{2\mathrm{i}\Phi}\left(\tilde{k}_z^{-\sigma}-\tilde{k}_z^{\sigma}\right)+2\mathrm{i}\sigma\mathrm{e}^{\mathrm{i}\Phi}\left[\left(\tilde{k}_z^{-\sigma}+\tilde{q}_z+\mathrm{i}Z\right)\left(\tilde{k}_z^{\sigma}+\tilde{q}_z+\mathrm{i}Z\right)+\left|\overline{\Omega}\right|^2\right]+\overline{\Omega}^*\left(\tilde{k}_z^{\sigma}-\tilde{k}_z^{-\sigma}\right). \tag{E.27}$$

The Andreev reflection coefficients must vanish in the normal-state system. Moreover, also the *spin-flip* specular reflection coefficient becomes zero if SOC is no longer present ($\overline{\Omega} = 0$).

Generalized BTK model for transverse TAHE conductances

After identifying the specular and Andreev reflection coefficients, we can proceed and evaluate the TAHE conductances when the bias voltage V gets applied across the junction. In Chap. 3, we derived the

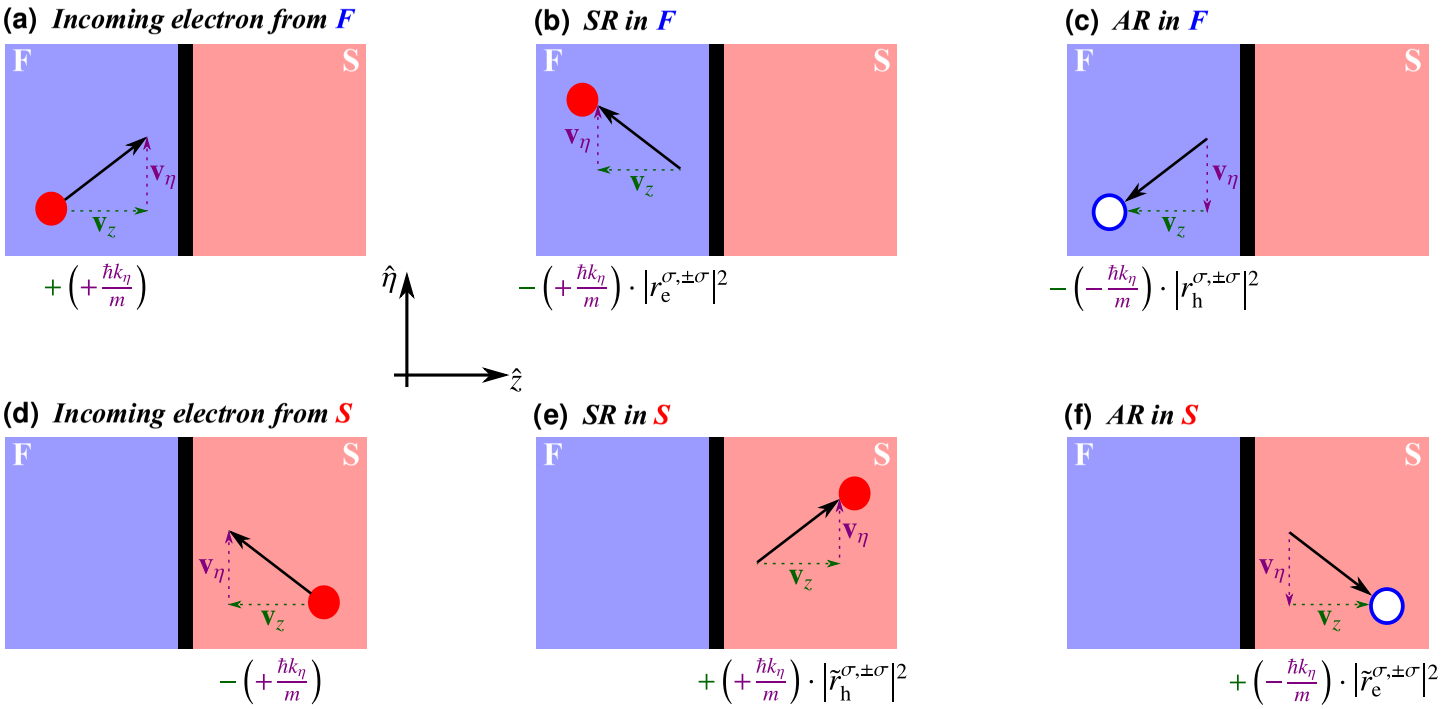


Fig. E.1: Schematical illustration of different scattering processes' contributions to the *transverse* TAHE current flows computed by means of Eq. (E.29). Panels **(a)**–**(f)** display the contributions in the same order as they enter Eq. (E.29). Electrons are colored red, holes blue, and the black arrows point along their propagation directions. Panel **(a)** shows an incident spin-σ electron from the ferromagnet, whose transverse velocity along the $\hat{\eta}$-direction is $|\mathbf{v}_\eta| = (+\hbar k_\eta)/m$ (violet). Since this electron propagates towards the barrier, we count its net contribution to the TAHE currents *positively* (green positive sign). Panels **(b)** and **(c)** indicate the two possible reflection processes the incoming electron can undergo: specular and Andreev reflection. The reflected electron's transverse velocity does not change in the first case, while the reflected hole in the second scenario has opposite transverse velocity. Contrary to the incoming electron, the reflected electron (hole) propagates away from the barrier. To get well-balanced current flows close to the barrier, we therefore have to subtract the reflected currents from the incident one (green negative signs). Reflection processes occur only with certain probabilities, which we account for multiplying their current contributions by the related reflection coefficients' absolute squares. Panels **(d)**–**(f)** show analogous considerations for an incoming electronlike quasiparticle from the superconductor. We mentioned in the text that it is more convenient to suppose instead a spin-σ *hole* in the ferromagnet that approaches the barrier and yields the same current contributions as incident electronlike quasiparticles in the superconductor. We followed that approach in Eq. (E.29), meaning that the processes depicted in panels **(e)** and **(f)** gain additional negative signs in Eq. (E.29) (as the shown processes' scattering coefficients must be translated from the electron into the hole picture). Incoming holes may generally be specularly and Andreev reflected with different probabilities than incident electrons, emphasized by introducing "tilde reflection coefficients" for holes. Finally, all contributions need to be properly weighted by Fermi-Dirac distribution functions in Eq. (E.29) to ensure that the involved electron (hole) states are occupied (unoccupied).

extended *zero-temperature* BTK [164] tunneling conductance formula (adapted to the present notation)

$$G_{z,z} \approx \frac{G_0 \mathcal{A}}{2(2\pi)^2} \sum_{\sigma=\pm 1} \int \mathrm{d}^2\mathbf{k}_\parallel \left\{ 1 - \left[\left| r_\mathrm{e}^{\sigma,\sigma}(eV) \right|^2 + \frac{k_z^{-\sigma}}{k_z^{\sigma}} \left| r_\mathrm{e}^{\sigma,-\sigma}(eV) \right|^2 \right] + \left[\frac{k_z^{-\sigma}}{k_z^{\sigma}} \left| r_\mathrm{h}^{\sigma,-\sigma}(-eV) \right|^2 + \left| r_\mathrm{h}^{\sigma,\sigma}(-eV) \right|^2 \right] \right\}, \quad \text{(E.28)}$$

which relates the tunneling conductance to *all* appearing reflection coefficients and applies therefore also to systems in which SOC causes spin-flip reflections, not being treated in the initial work by BTK [164]. Recall that $\mathcal{A}$ denotes the interfacial cross-section area and $G_0 = (2e^2)/h$ defines the conductance quantum; e indicates the positive elementary charge. The detailed derivation of Eq. (E.28) can be looked up in Chap. 3.

To access the considered junction's *transverse* TAHE conductances, we follow essentially a similar procedure and summarize thus only the main points. The most crucial point is to replace the longitudinal electron (hole) velocities (along $\hat{z}$) by their respective velocities $v_\eta = (\hbar k_\eta)/m$ along the transverse $\hat{\eta}$-directions (where $\hat{\eta} \in \{\hat{x}; \hat{y}\}$) and counting all contributions with proper signs. Again accounting for the currents carried by spin-σ electrons and holes incident from the ferromagnet – the latter model incoming electronlike quasiparticles from the superconducting electrode and cannot be neglected –, yields the *total interfacial* transverse TAHE currents

$$\begin{aligned} J_\eta = -e \sum_{\sigma=\pm 1} \sum_{\mathbf{k}_\parallel} \sum_{k_z^\sigma} \Bigg\{ & \left[\frac{\hbar k_\eta}{m} - \frac{\hbar k_\eta}{m} \left| r_\mathrm{e}^{\sigma,\sigma}(E) \right|^2 - \frac{\hbar k_\eta}{m} \left| r_\mathrm{e}^{\sigma,-\sigma}(E) \right|^2 \right] f^0(E - eV) \left[1 - f^0(E) \right] \\ & + \left[\frac{\hbar k_\eta}{m} \left| r_\mathrm{h}^{\sigma,-\sigma}(E) \right|^2 + \frac{\hbar k_\eta}{m} \left| r_\mathrm{h}^{\sigma,\sigma}(E) \right|^2 \right] \left[1 - f^0(-E - eV) \right] f^0(-E) \\ & + \left[-\frac{\hbar k_\eta}{m} - \frac{\hbar k_\eta}{m} \left| \tilde{r}_\mathrm{h}^{\sigma,\sigma}(E) \right|^2 - \frac{\hbar k_\eta}{m} \left| \tilde{r}_\mathrm{h}^{\sigma,-\sigma}(E) \right|^2 \right] \left[1 - f^0(E - eV) \right] f^0(E) \\ & + \left[\frac{\hbar k_\eta}{m} \left| \tilde{r}_\mathrm{e}^{\sigma,-\sigma}(E) \right|^2 + \frac{\hbar k_\eta}{m} \left| \tilde{r}_\mathrm{e}^{\sigma,\sigma}(E) \right|^2 \right] f^0(-E - eV) \left[1 - f^0(-E) \right] \Bigg\}. \end{aligned} \quad \text{(E.29)}$$

Contrary to Chap. 3, where we initially split the contributions of incident electrons and holes, Eq. (E.29) includes already both at the same time. The physical meaning of the different terms and the choice of signs are illustrated in Fig. E.1, and thoroughly explained in its caption.

Analogously to our treatment in Chap. 3, we can express the specular and Andreev reflection coefficients in case of incoming holes through the known ones for incident electrons (calculated above), namely

$$\sum_{\mathbf{k}_\parallel} \left[k_\eta \left| r_\mathrm{e}^{\sigma,\sigma}(E) \right|^2 + k_\eta \left| r_\mathrm{e}^{\sigma,-\sigma}(E) \right|^2 \right] = - \sum_{\mathbf{k}_\parallel} \left[k_\eta \left| \tilde{r}_\mathrm{h}^{\sigma,\sigma}(E) \right|^2 + k_\eta \left| \tilde{r}_\mathrm{h}^{\sigma,-\sigma}(E) \right|^2 \right] \quad \text{(E.30)}$$

and

$$\sum_{\mathbf{k}_\parallel} \left[k_\eta \left| r_\mathrm{h}^{\sigma,-\sigma}(E) \right|^2 + k_\eta \left| r_\mathrm{h}^{\sigma,\sigma}(E) \right|^2 \right] = - \sum_{\mathbf{k}_\parallel} \left[k_\eta \left| \tilde{r}_\mathrm{e}^{\sigma,-\sigma}(E) \right|^2 + k_\eta \left| \tilde{r}_\mathrm{e}^{\sigma,\sigma}(E) \right|^2 \right]. \quad \text{(E.31)}$$

The expression for the TAHE currents flowing through the Hall contact areas $\mathcal{A}_\eta$ simplifies then to

$$\begin{aligned} J_\eta = -e \sum_{\sigma=\pm 1} & \frac{\mathcal{A}_\eta}{(2\pi)^3} \int \mathrm{d}^2\mathbf{k}_\parallel \int_{-\infty}^{\infty} \mathrm{d}E \left(\frac{\partial k_z^\sigma}{\partial E} \right) \\ & \times \Bigg\{ \left[\frac{\hbar k_\eta}{m} - \frac{\hbar k_\eta}{m} \left| r_\mathrm{e}^{\sigma,\sigma}(E) \right|^2 - \frac{\hbar k_\eta}{m} \left| r_\mathrm{e}^{\sigma,-\sigma}(E) \right|^2 \right] \left[f^0(E - eV) - f^0(E) \right] \\ & + \left[\frac{\hbar k_\eta}{m} \left| r_\mathrm{h}^{\sigma,-\sigma}(E) \right|^2 + \frac{\hbar k_\eta}{m} \left| r_\mathrm{h}^{\sigma,\sigma}(E) \right|^2 \right] \left[f^0(E + eV) - f^0(E) \right] \Bigg\}, \end{aligned} \quad \text{(E.32)}$$

from which we deduce the *zero-temperature* TAHE conductances

$$
\begin{aligned}
G_{\eta,z} &= -\frac{\mathrm{d}J_\eta}{\mathrm{d}V} \\
&\approx \frac{G_0\mathcal{A}_\eta}{2(2\pi)^2}\sum_{\sigma=\pm1}\int \mathrm{d}^2\mathbf{k}_\parallel \frac{k_\eta}{k_z^\sigma}\left\{1-\left[\left|r_\mathrm{e}^{\sigma,\sigma}(eV)\right|^2+\left|r_\mathrm{e}^{\sigma,-\sigma}(eV)\right|^2\right]-\left[\left|r_\mathrm{h}^{\sigma,-\sigma}(-eV)\right|^2+\left|r_\mathrm{h}^{\sigma,\sigma}(-eV)\right|^2\right]\right\} \\
&= -\frac{G_0\mathcal{A}_\eta}{2(2\pi)^2}\sum_{\sigma=\pm1}\int \mathrm{d}^2\mathbf{k}_\parallel \frac{k_\eta}{k_z^\sigma}\left\{\left[\left|r_\mathrm{e}^{\sigma,\sigma}(eV)\right|^2+\left|r_\mathrm{e}^{\sigma,-\sigma}(eV)\right|^2\right]+\left[\left|r_\mathrm{h}^{\sigma,-\sigma}(-eV)\right|^2+\left|r_\mathrm{h}^{\sigma,\sigma}(-eV)\right|^2\right]\right\}. \quad \text{(E.33)}
\end{aligned}
$$

In the last step, we exploited that $\int \mathrm{d}^2\mathbf{k}_\parallel\, k_\eta/k_z^\sigma = 0$ due to the integrand's *odd* parity in k_η (which does not necessarily hold for the remaining terms since the reflection coefficients are also nontrivial functions of k_η). As deduced from our qualitative skew reflection picture in Sec. 8.2, specular and Andreev reflections remarkably enter the TAHE conductance formula with the same sign, contrary to what has been established in the BTK tunneling conductance formula [recall Eq. (E.28)]. This observation can be physically justified since – in contrast to electrons' (holes') longitudinal velocity vectors that are aligned along the same direction –, the specularly reflected electrons' and the Andreev-reflected holes' transverse velocity vectors point along opposite directions (see Fig. E.1). The accumulated relative sign between both contributions is then compensated by the fact that electrons and holes are simultaneously oppositely charged so that the specular and Andreev reflection parts must finally appear with the same signs in the TAHE conductance expression, formally confirming our claim that skew specular and skew Andreev reflections can constructively amplify the TAHE and noticeably enhance the associated conductances when compared to the normal-state junction counterpart.

To obtain the *zero-bias* TAHE conductances discussed in Sec. 8.3, we evaluate Eq. (E.33) substituting the analytical reflection coefficients [see Eqs. (E.17)–(E.20) in the superconducting and Eqs. (E.23)–(E.26) in the normal-state regime] and numerically performing the integration over $\mathbf{k}_\parallel$ by means of a Gaussian quadrature algorithm [181]. The upper limit in the $|\mathbf{k}_\parallel|$-integration, $|\mathbf{k}_\parallel|_{\mathrm{max}}^\sigma = \min[k_\mathrm{F}\sqrt{1+\sigma P}; k_\mathrm{F}]$, ensures that only propagating incident electrons (holes) contribute to the TAHE conductances. At *finite bias voltages*, we additionally unravel the reflection coefficients from the generic methodology described in the previous section using a numerical (generalized) LU Decomposition algorithm [181] to solve the system of equations (that results from matching the scattering states at the interface) before continuing with Eq. (E.33) and Eq. (E.28) when computing the tunneling conductance.

Generalized Furusaki-Tsukada approach for transverse supercurrent responses

In Sec. 8.4, we argue that Andreev reflections essentially transfer Cooper pairs across the barrier and the electrons forming these pairs are thereby also exposed to the spin- and transverse momentum-dependent skew tunneling mechanism,[1] eventually leading to *transverse supercurrent responses* in the superconductor. To compute these supercurrents' amplitudes, we generalize the Furusaki-Tsukada approach [266] – introduced in Sec. 6.2 to extract usual tunneling (Josephson) supercurrents – to cover currents that flow along the junction's transverse directions. For simplicity, we limit ourselves to the *zero-bias* scenario.

Similarly to our treatment in Sec. 6.2, we relate the currents to the scattering coefficients describing Andreev reflections of quasiparticles that approach the semiconducting barrier from the superconducting side. The Bogoljubov-de Gennes scattering states [corresponding to the Hamiltonian given in Eq. (E.1)]

[1] Since we are now interested in the electrons that Andreev reflections transfer into the superconductor and that form Cooper pairs there, we rather use the term *skew tunneling* instead of skew reflection.

in the superconductor ($z > 0$) read then as

$$\psi^{(i)}(z>0) = \psi^{(i)}_{\text{incoming}}(z>0) + \mathcal{A}^{(i)} \begin{bmatrix} u \\ 0 \\ v \\ 0 \end{bmatrix} \mathrm{e}^{\mathrm{i}q_z z} + \mathcal{B}^{(i)} \begin{bmatrix} 0 \\ u \\ 0 \\ v \end{bmatrix} \mathrm{e}^{\mathrm{i}q_z z} + \mathcal{C}^{(i)} \begin{bmatrix} v \\ 0 \\ u \\ 0 \end{bmatrix} \mathrm{e}^{-\mathrm{i}q_z z} + \mathcal{D}^{(i)} \begin{bmatrix} 0 \\ v \\ 0 \\ u \end{bmatrix} \mathrm{e}^{-\mathrm{i}q_z z}, \quad \text{(E.34)}$$

distinguishing between an incoming spin-up electronlike ($i = 1$), an incoming spin-down electronlike ($i = 2$), an incoming spin-up holelike ($i = 3$), and an incoming spin-down holelike ($i = 4$) quasiparticle (holelike quasiparticles mimic electrons approaching the interface from the ferromagnetic side) with the incoming waves

$$\psi^{(1)}_{\text{incoming}}(z>0) = [u,\, 0,\, v,\, 0]^{\top} \mathrm{e}^{-\mathrm{i}q_z z}, \quad \text{(E.35)}$$

$$\psi^{(2)}_{\text{incoming}}(z>0) = [0,\, u,\, 0,\, v]^{\top} \mathrm{e}^{-\mathrm{i}q_z z}, \quad \text{(E.36)}$$

$$\psi^{(3)}_{\text{incoming}}(z>0) = [v,\, 0,\, u,\, 0]^{\top} \mathrm{e}^{\mathrm{i}q_z z}, \quad \text{(E.37)}$$

and

$$\psi^{(4)}_{\text{incoming}}(z>0) = [0,\, v,\, 0,\, u]^{\top} \mathrm{e}^{\mathrm{i}q_z z}, \quad \text{(E.38)}$$

respectively, while the scattering states inside the ferromagnet ($z < 0$) can be written as

$$\psi^{(i)}(z<0) = \mathcal{E}^{(i)} \frac{1}{\sqrt{2}} \begin{bmatrix} 1 \\ \mathrm{e}^{\mathrm{i}\Phi} \\ 0 \\ 0 \end{bmatrix} \mathrm{e}^{-\mathrm{i}k_z^{\sigma=1} z} + \mathcal{F}^{(i)} \frac{1}{\sqrt{2}} \begin{bmatrix} 1 \\ -\mathrm{e}^{\mathrm{i}\Phi} \\ 0 \\ 0 \end{bmatrix} \mathrm{e}^{-\mathrm{i}k_z^{\sigma=-1} z} + \mathcal{G}^{(i)} \frac{1}{\sqrt{2}} \begin{bmatrix} 0 \\ 0 \\ 1 \\ -\mathrm{e}^{\mathrm{i}\Phi} \end{bmatrix} \mathrm{e}^{\mathrm{i}k_z^{\sigma=1} z} + \mathcal{H}^{(i)} \frac{1}{\sqrt{2}} \begin{bmatrix} 0 \\ 0 \\ 1 \\ \mathrm{e}^{\mathrm{i}\Phi} \end{bmatrix} \mathrm{e}^{\mathrm{i}k_z^{\sigma=-1} z}. \quad \text{(E.39)}$$

The (quasi)particle wave vectors and BCS coherence factors can be looked up above [see, i.e., Eqs. (E.12), (E.13), and (E.14)]. The calligraphic scattering coefficients are again determined applying interfacial ($z = 0$) boundary conditions similarly to those formulated in Eqs. (E.15) and (E.16) to these states, and numerically solving the resulting systems of equations. When setting up these boundary conditions, it is essential to note that quasiparticles approaching the superconductor/ferromagnet interface are essentially subject to the *oppositely oriented* Rashba and Dresselhaus spin-orbit fields when compared to the above conductance calculations for which we assumed that electrons (holes) are incident on the ferromagnet/superconductor interface (recall our similar argumentation for S/F/S Josephson junctions in Sec. 6.2).

Of particular interest are the *spin-conserving* Andreev reflection coefficients $\mathcal{C}^{(1)}$, $\mathcal{D}^{(2)}$, $\mathcal{A}^{(3)}$, and $\mathcal{B}^{(4)}$, which we can link with the transverse supercurrent responses analogously to the Furusaki-Tsukada approach presented in Sec. 6.2. To evaluate Eq. (6.55), we need to replace the derivatives along the longitudinal direction (indicated by $\hat{z}'$ and $\hat{z}$) – which were necessary to capture the longitudinal (tunneling) current flow – by their transverse counterparts ($\hat{\eta}'$ and $\hat{\eta}$, where $\hat{\eta} \in \{\hat{x}; \hat{y}\}$), and construct the

F/S junction's *full* Matsubara Green's function $\check{\mathcal{G}}(\mathbf{r},\mathbf{r}';\mathrm{i}\omega_n)$ that accounts for the *full* scattering states, i.e., also for their plane-wave parts along the transverse $\hat{\eta}$-directions. The latter can be accomplished in a similar manner as sketched in Appendix B. Afterwards, we follow the same methodology as in Sec. 6.2 to access the *interfacial* TAHE supercurrent responses, ending up with

$$I_\eta \approx \frac{e k_\mathrm{B} T}{2\hbar}\,|\Delta_\mathrm{S}(T)|\,\frac{\mathcal{A}_\eta}{(2\pi)^2}\int \mathrm{d}^2\mathbf{k}_\parallel \sum_{\omega_n}\frac{k_\eta}{\sqrt{k_\mathrm{F}^2-\mathbf{k}_\parallel^2}}\left[\frac{C^{(1)}(\mathrm{i}\omega_n)+\mathcal{D}^{(2)}(\mathrm{i}\omega_n)+\mathcal{A}^{(3)}(\mathrm{i}\omega_n)+\mathcal{B}^{(4)}(\mathrm{i}\omega_n)}{\sqrt{\omega_n^2+|\Delta_\mathrm{S}(T)|^2}}\right]; \quad \text{(E.40)}$$

k_B stands for Boltzmann's constant and $\omega_n = (2n+1)\pi k_\mathrm{B}T$, with integer n, denotes the fermionic Matsubara frequencies (at temperature T). The Andreev reflection coefficients are obtained through analytically continuing the excitation energies according to $E \longmapsto \mathrm{i}\omega_n$ in the respective coefficients we extracted from the above scattering description.

To compare the supercurrent responses with the TAHE conductance calculations performed inside the ferromagnet, we numerically evaluate Eq. (E.40) at *zero temperature* ($T = 0$) and analyze the outcomes in Sec. 8.4. One might guess that considering the zero-temperature limit could cause some trouble in Eq. (E.40) since the thermal energy $k_\mathrm{B}T$ appears in its numerator and taking $T \to 0_+$ might simply yield zero current. Nevertheless, we must be aware that also the Andreev reflection coefficients and Matsubara frequencies depend on temperature in a nontrivial way, which essentially compensates the $(k_\mathrm{B}T)$-prefactor and gives reasonable currents even at zero temperature. In all cases, we substitute the zero-temperature superconducting gap $|\Delta_\mathrm{S}(0)| \approx 1.6\,\mathrm{meV}$ of niobium [197].

Appendix F

Transverse Furusaki-Tsukada and bound state supercurrent formulas for S/F-I/S Josephson junctions

Bogoljubov-de Gennes scattering states

In Chap. 9, we consider a *three-dimensional* S/F-I/S Josephson junction, consisting of two semi-infinite superconducting electrodes (S) that span the $z < 0$ and $z > 0$ half-spaces and a separating ultrathin ferromagnetic-insulator (F-I) barrier. The latter introduces not only scalar and magnetic tunnelings, but simultaneously breaks space-inversion symmetry letting interfacial Rashba [149, 150] and Dresselhaus [152] SOCs emerge. We model the ferromagnetic-insulator layer in terms of an effective deltalike potential- and SOC-dependent barrier. The Josephson junction's stationary Bogoljubov-de Gennes equation [139] in Nambu representation reads as

$$\begin{bmatrix} \hat{\mathcal{H}}_\mathrm{e} & \hat{\Delta}_\mathrm{S}(z) \\ \hat{\Delta}_\mathrm{S}^\dagger(z) & \hat{\mathcal{H}}_\mathrm{h} \end{bmatrix} \Psi(\mathbf{r}) = E\Psi(\mathbf{r}), \tag{F.1}$$

with

$$\hat{\mathcal{H}}_\mathrm{e} = \left(-\frac{\hbar^2}{2m}\boldsymbol{\nabla}^2 - \mu\right)\hat{\sigma}_0 + \Big[\lambda_\mathrm{SC}\,\hat{\sigma}_0 + \lambda_\mathrm{MA}\,(\hat{\mathbf{m}}\cdot\hat{\boldsymbol{\sigma}}) + \alpha\,(k_y\,\hat{\sigma}_x - k_x\,\hat{\sigma}_y) - \beta\,(k_y\,\hat{\sigma}_x + k_x\,\hat{\sigma}_y)\Big]\,\delta(z), \tag{F.2}$$

$$\hat{\mathcal{H}}_\mathrm{h} = -\hat{\sigma}_y\hat{\mathcal{H}}_\mathrm{e}^*\hat{\sigma}_y, \tag{F.3}$$

and

$$\hat{\Delta}_\mathrm{S}(z) = |\Delta_\mathrm{S}|\hat{\sigma}_0\Big[\Theta(-z) + \mathrm{e}^{\mathrm{i}\phi_\mathrm{S}}\Theta(z)\Big]. \tag{F.4}$$

The individual terms' physical meaning is explained in Sec. 9.1.

Since the transverse wave vector $\mathbf{k}_\parallel = [k_x,\, k_y,\, 0]^\top$ (parallel to the ferromagnetic-insulator interface) is conserved, we can substitute the ansatz

$$\Psi(\mathbf{r}) = \psi(z)\,\mathrm{e}^{\mathrm{i}(\mathbf{k}_\parallel\cdot\mathbf{r}_\parallel)}, \tag{F.5}$$

with $\mathbf{r}_\parallel = [x,\, y,\, 0]^\top$, into Eq. (F.1) to reduce our problem to finding the *one-dimensional* scattering states $\psi(z)$ once in the left and once in the right superconductor. Generally speaking, we need to distinguish between *four* possible scenarios of incident quasiparticles that approach the ferromagnetic-insulator barrier from the left superconductor: (1) an incoming spin-up electronlike, (2) an incoming spin-down electronlike, (3) an incoming spin-up holelike, and (4) an incoming spin-down holelike quasiparticle. The latter two processes account for incident electronlike quasiparticles that originate from the

right electrode. The Bogoljubov-de Gennes scattering states in the left superconductor ($z < 0$) can then be written as

$$\psi^{(i)}(z<0) = \psi^{(i)}_{\text{incoming}}(z<0) + \mathcal{A}^{(i)} \begin{bmatrix} u \\ 0 \\ v \\ 0 \end{bmatrix} \mathrm{e}^{-\mathrm{i}q_{z,\mathrm{e}}z} + \mathcal{B}^{(i)} \begin{bmatrix} 0 \\ u \\ 0 \\ v \end{bmatrix} \mathrm{e}^{-\mathrm{i}q_{z,\mathrm{e}}z} + C^{(i)} \begin{bmatrix} v \\ 0 \\ u \\ 0 \end{bmatrix} \mathrm{e}^{\mathrm{i}q_{z,\mathrm{h}}z} + \mathcal{D}^{(i)} \begin{bmatrix} 0 \\ v \\ 0 \\ u \end{bmatrix} \mathrm{e}^{\mathrm{i}q_{z,\mathrm{h}}z} \tag{F.6}$$

and those in the right superconductor ($z > 0$) as

$$\psi^{(i)}(z>0) = \mathcal{E}^{(i)} \begin{bmatrix} u\mathrm{e}^{\mathrm{i}\phi_\mathrm{S}} \\ 0 \\ v \\ 0 \end{bmatrix} \mathrm{e}^{\mathrm{i}q_{z,\mathrm{e}}z} + \mathcal{F}^{(i)} \begin{bmatrix} 0 \\ u\mathrm{e}^{\mathrm{i}\phi_\mathrm{S}} \\ 0 \\ v \end{bmatrix} \mathrm{e}^{\mathrm{i}q_{z,\mathrm{e}}z} + \mathcal{G}^{(i)} \begin{bmatrix} v\mathrm{e}^{\mathrm{i}\phi_\mathrm{S}} \\ 0 \\ u \\ 0 \end{bmatrix} \mathrm{e}^{-\mathrm{i}q_{z,\mathrm{h}}z} + \mathcal{H}^{(i)} \begin{bmatrix} 0 \\ v\mathrm{e}^{\mathrm{i}\phi_\mathrm{S}} \\ 0 \\ u \end{bmatrix} \mathrm{e}^{-\mathrm{i}q_{z,\mathrm{h}}z}. \tag{F.7}$$

The superscript i, with $i \in \{1;2;3;4\}$, refers to the four possible quasiparticle injection scenarios ordered in the same way as stated above, and the related incoming waves are given by

$$\psi^{(1)}_{\text{incoming}}(z<0) = [u,\, 0,\, v,\, 0]^\top \mathrm{e}^{\mathrm{i}q_{z,\mathrm{e}}z}, \tag{F.8}$$

$$\psi^{(2)}_{\text{incoming}}(z<0) = [0,\, u,\, 0,\, v]^\top \mathrm{e}^{\mathrm{i}q_{z,\mathrm{e}}z}, \tag{F.9}$$

$$\psi^{(3)}_{\text{incoming}}(z<0) = [v,\, 0,\, u,\, 0]^\top \mathrm{e}^{-\mathrm{i}q_{z,\mathrm{h}}z}, \tag{F.10}$$

as well as

$$\psi^{(4)}_{\text{incoming}}(z<0) = [0,\, v,\, 0,\, u]^\top \mathrm{e}^{-\mathrm{i}q_{z,\mathrm{h}}z}. \tag{F.11}$$

The factors $u = u(E)$ and $v = v(E)$ are the usual BCS coherence factors that fulfill

$$u(E) = \sqrt{\frac{1}{2}\left(1 + \sqrt{1 - \frac{|\Delta_\mathrm{S}|^2}{E^2}}\right)} = \sqrt{1 - [v(E)]^2}, \tag{F.12}$$

while the $\hat{z}$-projections of the electronlike and holelike quasiparticles' wave vectors are

$$q_{z,\mathrm{e}} = q_{z,\mathrm{e}}(E) = \sqrt{\frac{2m}{\hbar^2}\left[\mu + \sqrt{E^2 - |\Delta_\mathrm{S}|^2}\right] - \mathbf{k}_\parallel^2} \tag{F.13}$$

and

$$q_{z,\mathrm{h}} = q_{z,\mathrm{h}}(E) = \sqrt{\frac{2m}{\hbar^2}\left[\mu - \sqrt{E^2 - |\Delta_\mathrm{S}|^2}\right] - \mathbf{k}_\parallel^2}. \tag{F.14}$$

Since the (quasi)particle excitation energies E and the superconducting energy gap $|\Delta_\mathrm{S}|$ are usually small compared to the chemical potential μ, we can approximate the wave vectors by

$$q_{z,\mathrm{e}} \approx q_{z,\mathrm{h}} \approx q_z = \sqrt{k_\mathrm{F}^2 - \mathbf{k}_\parallel^2}, \tag{F.15}$$

where $k_\mathrm{F} = \sqrt{2m\mu}/\hbar$ indicates the Fermi wave vector.

The scattering states' calligraphically written coefficients – again resembling spin-conserving (spin-flip) specular and Andreev reflections, as well as quasiparticle transmissions – are determined requiring the states to satisfy the interfacial ($z = 0$) boundary conditions

$$\psi(z)\big|_{z=0_-} = \psi(z)\big|_{z=0_+} \tag{F.16}$$

and

$$\left\{\left(\frac{\hbar^2}{2m}\frac{\mathrm{d}}{\mathrm{d}z} + \lambda_{\mathrm{SC}}\right)\hat{\eta} + \lambda_{\mathrm{MA}}\hat{\omega}\right\}\psi(z)\big|_{z=0_-} + \begin{bmatrix}\boldsymbol{\Omega}\cdot\hat{\boldsymbol{\sigma}} & \hat{0}\\ \hat{0} & -(\boldsymbol{\Omega}\cdot\hat{\boldsymbol{\sigma}})\end{bmatrix}\psi(z)\big|_{z=0_-} = \frac{\hbar^2}{2m}\frac{\mathrm{d}}{\mathrm{d}z}\hat{\eta}\psi(z)\big|_{z=0_+}, \tag{F.17}$$

where

$$\hat{\eta} = \begin{bmatrix}1 & 0 & 0 & 0\\ 0 & 1 & 0 & 0\\ 0 & 0 & -1 & 0\\ 0 & 0 & 0 & -1\end{bmatrix} \qquad \text{and} \qquad \hat{\omega} = \begin{bmatrix}0 & \mathrm{e}^{-\mathrm{i}\Phi} & 0 & 0\\ \mathrm{e}^{\mathrm{i}\Phi} & 0 & 0 & 0\\ 0 & 0 & 0 & \mathrm{e}^{-\mathrm{i}\Phi}\\ 0 & 0 & \mathrm{e}^{\mathrm{i}\Phi} & 0\end{bmatrix}; \tag{F.18}$$

$\boldsymbol{\Omega} = \big[(\alpha-\beta)k_y, -(\alpha+\beta)k_x, 0\big]$ comprises the Rashba and Dresselhaus SOCs, and $\hat{0}$ is the two-by-two zero matrix. For each of the four quasiparticle injection processes, Eqs. (F.16)–(F.17) represent a system of eight linear equations for eight unknown scattering coefficients. Due to the equations' complexity, we do not give analytical expressions for the coefficients, but rather solve for them numerically starting from a generalized LU Decomposition algorithm [181].

Generalized Furusaki-Tsukada approach for transverse AJHE currents

To access the AJHE current components I_η – flowing along the $\hat{\eta} \in \{\hat{x};\hat{y}\}$-directions –, we basically follow the same methodology as for computing the transverse supercurrent responses in F/S junctions (see Appendix E for details) and generalize the Furusaki-Tsukada approach [266]. The individual steps are the same as explained in Appendix E and therefore not explicitly addressed here. After some calculations, the AJHE currents *close to the ferromagnetic-insulator barrier* can be extracted from

$$I_\eta \approx \frac{ek_{\mathrm{B}}T}{2\hbar}|\Delta_{\mathrm{S}}(T)|\frac{\mathcal{A}_\eta}{(2\pi)^2}\int \mathrm{d}^2\mathbf{k}_\parallel \sum_{\omega_n}\frac{k_\eta}{\sqrt{k_{\mathrm{F}}^2-\mathbf{k}_\parallel^2}}\left[\frac{\mathcal{C}^{(1)}(\mathrm{i}\omega_n)+\mathcal{D}^{(2)}(\mathrm{i}\omega_n)+\mathcal{A}^{(3)}(\mathrm{i}\omega_n)+\mathcal{B}^{(4)}(\mathrm{i}\omega_n)}{\sqrt{\omega_n^2+|\Delta_{\mathrm{S}}(T)|^2}}\right], \tag{F.19}$$

where e is the positive elementary charge, k_{B} corresponds to Boltzmann's constant, $\mathcal{A}_\eta$ quantifies the Hall contact areas, and $\omega_n = (2n+1)\pi k_{\mathrm{B}}T$, with integer n, denotes the fermionic Matsubara frequencies (at temperature T). The scattering coefficients $\mathcal{C}^{(1)}$, $\mathcal{D}^{(2)}$, $\mathcal{A}^{(3)}$, and $\mathcal{B}^{(4)}$ – belonging to *spin-conserving* Andreev reflections – are obtained solving the previous scattering problem and analytically continuing the excitation energies according to $E \longmapsto \mathrm{i}\omega_n$.

Numerically evaluating Eq. (F.19) for the given junction parameters yields the AJHE currents thoroughly analyzed in Sec. 9.3. The integration over $\mathbf{k}_\parallel$ is again performed by means of a Gaussian quadrature algorithm [181]. At finite temperature, we additionally need to account for the superconducting energy gap's BCS-like temperature dependence $|\Delta_{\mathrm{S}}(T \neq 0)| = |\Delta_{\mathrm{S}}(0)|\tanh(1.74\sqrt{T_{\mathrm{C}}/T-1})$. Regarding the (two similar) superconductors' material parameters, we use realistic values of $|\Delta_{\mathrm{S}}(0)| \approx 2.5\,\mathrm{meV}$ for their zero-temperature gap and $T_{\mathrm{C}} \approx 16\,\mathrm{K}$ for their critical temperature. For all calculations presented in Chap. 9, we consider a temperature of $T = 0.1T_{\mathrm{C}}$.

Bound state technique

The formation of subgap Andreev bound states [179, 227] and YSR states [361–363] counts for sure to the most intriguing spectroscopic fingerprints of S/F-I/S Josephson junctions (recall particularly our comprehensive study of one-dimensional S/F-I/S contacts in Chap. 7). In Sec. 9.4, we formulate an alternative approach that allows us to directly evaluate the AJHE current components from the junctions' bound state spectra. These calculations serve not only as an important crosscheck to verify the results obtained from the Furusaki-Tsukada formulas, but simultaneously allow us to gain more physical insight and draw unique connections between the bound state characteristics on the one and the AJHE on the other hand. Before introducing the bound state-based current formula, we need to unravel the bound states' energies and their underlying wave functions – both provide inevitable input for the final current formula.

Bound state energies

To extract the considered S/F-I/S junction's bound state spectrum from its Bogoljubov-de Gennes equation stated in Eq. (F.1), we basically follow the same strategy as in Sec. 7.1 and initially construct the general ansatz for the bound state wave function components $\psi(z)$ *without considering incoming waves*. For *positive* energies ($E > 0$), $\psi(z)$ reads as

$$\begin{aligned}\psi(z<0;\mathbf{k}_\parallel;E) = a(\mathbf{k}_\parallel;E)\begin{bmatrix}u(E)\\0\\v(E)\\0\end{bmatrix}\mathrm{e}^{-\mathrm{i}q_{z,\mathrm{e}}(\mathbf{k}_\parallel;E)z} + b(\mathbf{k}_\parallel;E)\begin{bmatrix}0\\u(E)\\0\\v(E)\end{bmatrix}\mathrm{e}^{-\mathrm{i}q_{z,\mathrm{e}}(\mathbf{k}_\parallel;E)z}\\ + c(\mathbf{k}_\parallel;E)\begin{bmatrix}v(E)\\0\\u(E)\\0\end{bmatrix}\mathrm{e}^{\mathrm{i}q_{z,\mathrm{h}}(\mathbf{k}_\parallel;E)z} + d(\mathbf{k}_\parallel;E)\begin{bmatrix}0\\v(E)\\0\\u(E)\end{bmatrix}\mathrm{e}^{\mathrm{i}q_{z,\mathrm{h}}(\mathbf{k}_\parallel;E)z}\end{aligned} \tag{F.20}$$

in the left superconductor ($z < 0$) and

$$\begin{aligned}\psi(z>0;\mathbf{k}_\parallel;E) = e(\mathbf{k}_\parallel;E)\begin{bmatrix}u(E)\mathrm{e}^{\mathrm{i}\phi_\mathrm{S}}\\0\\v(E)\\0\end{bmatrix}\mathrm{e}^{\mathrm{i}q_{z,\mathrm{e}}(\mathbf{k}_\parallel;E)z} + f(\mathbf{k}_\parallel;E)\begin{bmatrix}0\\u(E)\mathrm{e}^{\mathrm{i}\phi_\mathrm{S}}\\0\\v(E)\end{bmatrix}\mathrm{e}^{\mathrm{i}q_{z,\mathrm{e}}(\mathbf{k}_\parallel;E)z}\\ + g(\mathbf{k}_\parallel;E)\begin{bmatrix}v(E)\mathrm{e}^{\mathrm{i}\phi_\mathrm{S}}\\0\\u(E)\\0\end{bmatrix}\mathrm{e}^{-\mathrm{i}q_{z,\mathrm{h}}(\mathbf{k}_\parallel;E)z} + h(\mathbf{k}_\parallel;E)\begin{bmatrix}0\\v(E)\mathrm{e}^{\mathrm{i}\phi_\mathrm{S}}\\0\\u(E)\end{bmatrix}\mathrm{e}^{-\mathrm{i}q_{z,\mathrm{h}}(\mathbf{k}_\parallel;E)z}\end{aligned} \tag{F.21}$$

in the right superconductor ($z > 0$), respectively. The BCS coherence factors and wave vectors are still given by Eqs. (F.12)–(F.14). Since we are now concerned with a *three-dimensional junction*, in which the transverse wave vector $\mathbf{k}_\parallel = [k_x,\, k_y,\, 0]^\top$ plays a crucial role when studying transverse transport (i.e., along $\hat{x}$ and $\hat{y}$) contrary to our description in Chap. 7, we additionally stress the wave vectors' and wave functions' explicit $\mathbf{k}_\parallel$-dependencies from now on. The full bound state wave functions are then

$$\Psi(x,y,z;\mathbf{k}_\parallel;E) = \psi(z;\mathbf{k}_\parallel;E)\,\mathrm{e}^{\mathrm{i}(\mathbf{k}_\parallel\cdot\mathbf{r}_\parallel)}. \tag{F.22}$$

Although we are now primarily interested in the bound state spectrum and not in solving the real scattering problem, the wave functions' formal structure is to some extent comparable to the actual

scattering states so that one might still identify the coefficients $a(\mathbf{k}_\parallel; E)$ $[b(\mathbf{k}_\parallel; E)]$, $c(\mathbf{k}_\parallel; E)$ $[d(\mathbf{k}_\parallel; E)]$, $e(\mathbf{k}_\parallel; E)$ $[f(\mathbf{k}_\parallel; E)]$, and $g(\mathbf{k}_\parallel; E)$ $[h(\mathbf{k}_\parallel; E)]$ as the spin-conserving (spin-flip) specular reflection, Andreev reflection, electronlike transmission, and holelike transmission coefficients encountered in the real scattering problem. All these coefficients depend on $\mathbf{k}_\parallel$ and E. To access the bound state energies, we apply the boundary conditions in Eqs. (F.16) and (F.17) to the bound state wave functions and end up with an eight-dimensional system of equations. Fixing $\mathbf{k}_\parallel$, nontrivial solutions for E (indicating the formation of a bound state at precisely that energy) require that the system's coefficient matrix determinant vanishes. Imposing that condition yields a secular equation, which we numerically solve for these nontrivial solutions E that finally correspond to the bound state energies $E_\mathrm{B} = E$. Due to the system's fundamental electron-hole symmetry, each bound state at positive energy $E_\mathrm{B} > 0$ always comes along with another bound state at energy $-E_\mathrm{B}$, setting up the whole bound state spectrum.

Even without explicitly calculating the bound state energies, we can deduce their most puzzling property. The system of equations that results from requiring the bound state wave functions to satisfy the interfacial boundary conditions comprises the components of the transverse wave vector $\mathbf{k}_\parallel = [k_x,\, k_y,\, 0]^\top$ once through substituting the quasiparticle wave vectors [see Eqs. (F.13) and (F.14)] and once via the spin-orbit field $\mathbf{\Omega} = [(\alpha-\beta)k_y,\, -(\alpha+\beta)k_x,\, 0]$ occurring in the second boundary condition. We do not need to take care of the first since $\mathbf{k}_\parallel$ enters the wave vectors *quadratically* so that reversing $\mathbf{k}_\parallel$'s sign leaves the wave vectors unaffected. Contrary, the spin-orbit field $\mathbf{\Omega}$ contains terms that scale *linearly* with $\mathbf{k}_\parallel$'s components (i.e., with k_x and k_y). Reversals of $\mathbf{k}_\parallel$ modify therefore the resulting equations' SOC-dependent parts and simultaneously the allowed energies at which bound states can form. In other words, SOC raises unique $\mathbf{k}_\parallel$-asymmetries in the junction's bound state spectrum. This observation has a remarkable impact on the junction's transport features. Recall that electrical currents are actually carried by electrons that tunnel through the Josephson junction's barrier via the available bound states. However, if interfacial SOC is present, tunneling electrons with the transverse wave vector $\mathbf{k}_\parallel = [k_x > 0,\, k_y > 0,\, 0]^\top$ (transversely propagating along the $\hat{x}$- and $\hat{y}$-directions) and their $(-\mathbf{k}_\parallel)$-counterparts (transversely propagating along $-\hat{x}$ and $-\hat{y}$) need to tunnel via distinct bound states with *differing* energies. But tunnelings via different bound states happen usually not with the same probabilities. As a consequence, either the electrons that move along $\hat{x}$ (and/or $\hat{y}$) or those traveling along $-\hat{x}$ (and/or $-\hat{y}$) are preferentially transmitted through the barrier and form Cooper pairs. The resulting transverse electron imbalance supports the flow of transverse AJHE currents and is another clear evidence for the proposed skew tunneling mechanism (see, e.g., Sec. 9.2). The SOC-induced $\mathbf{k}_\parallel$-asymmetries in the bound state energies found hence the AJHE's *microscopic* physical origin, as we outline more thoroughly in Sec. 9.4.

Bound state wave functions

After determining *all* bound state energies, we need to find the related bound state wave function coefficients. As we mentioned above, these coefficients are not only functions of the bound state energies E_B, but also of the transverse wave vectors $\mathbf{k}_\parallel$ (explicitly and implicitly since the bound state energies themselves also depend on $\mathbf{k}_\parallel$). To attain analytical expressions for the coefficients, we exploit the interfacial boundary conditions [see Eqs. (F.16) and (F.17)] for another time. Applying Eq. (F.16) to the bound state wave functions – essentially ensuring their continuity at the interface –, we can rewrite the wave function coefficients in the region left of the ferromagnetic-insulator interface, $a(\mathbf{k}_\parallel; E_\mathrm{B})$, $b(\mathbf{k}_\parallel; E_\mathrm{B})$, $c(\mathbf{k}_\parallel; E_\mathrm{B})$, and $d(\mathbf{k}_\parallel; E_\mathrm{B})$, in terms of the remaining four coefficients, which initially appeared in the right half-junction's wave functions. To become more concrete, we get

$$a(\mathbf{k}_\parallel; E_\mathrm{B}) = \varepsilon_1(E_\mathrm{B})\, e(\mathbf{k}_\parallel; E_\mathrm{B}) + \gamma_1(E_\mathrm{B})\, g(\mathbf{k}_\parallel; E_\mathrm{B}), \tag{F.23}$$

$$b(\mathbf{k}_\parallel; E_\mathrm{B}) = \varphi_1(E_\mathrm{B})\, f(\mathbf{k}_\parallel; E_\mathrm{B}) + \eta_1(E_\mathrm{B})\, h(\mathbf{k}_\parallel; E_\mathrm{B}), \tag{F.24}$$

$$c(\mathbf{k}_\parallel; E_\mathrm{B}) = \varepsilon_2(E_\mathrm{B})\, e(\mathbf{k}_\parallel; E_\mathrm{B}) + \gamma_2(E_\mathrm{B})\, g(\mathbf{k}_\parallel; E_\mathrm{B}), \tag{F.25}$$

and lastly

$$d(\mathbf{k}_\parallel; E_\mathrm{B}) = \varphi_2(E_\mathrm{B})\, f(\mathbf{k}_\parallel; E_\mathrm{B}) + \eta_2(E_\mathrm{B})\, h(\mathbf{k}_\parallel; E_\mathrm{B}), \tag{F.26}$$

where we introduced the abbreviations

$$\varepsilon_1(E_\mathrm{B}) = \frac{\mathrm{e}^{\mathrm{i}\phi_\mathrm{S}} - [v(E_\mathrm{B})]^2/[u(E_\mathrm{B})]^2}{1 - [v(E_\mathrm{B})]^2/[u(E_\mathrm{B})]^2}, \qquad \varepsilon_2(E_\mathrm{B}) = \frac{\left(1 - \mathrm{e}^{\mathrm{i}\phi_\mathrm{S}}\right) v(E_\mathrm{B})/u(E_\mathrm{B})}{1 - [v(E_\mathrm{B})]^2/[u(E_\mathrm{B})]^2}, \tag{F.27}$$

$$\varphi_1(E_\mathrm{B}) = \varepsilon_1(E_\mathrm{B}), \qquad \varphi_2(E_\mathrm{B}) = \varepsilon_2(E_\mathrm{B}), \tag{F.28}$$

$$\gamma_1(E_\mathrm{B}) = \frac{\left(\mathrm{e}^{\mathrm{i}\phi_\mathrm{S}} - 1\right) v(E_\mathrm{B})/u(E_\mathrm{B})}{1 - [v(E_\mathrm{B})]^2/[u(E_\mathrm{B})]^2}, \qquad \gamma_2(E_\mathrm{B}) = \frac{1 - \mathrm{e}^{\mathrm{i}\phi_\mathrm{S}}[v(E_\mathrm{B})]^2/[u(E_\mathrm{B})]^2}{1 - [v(E_\mathrm{B})]^2/[u(E_\mathrm{B})]^2}, \tag{F.29}$$

$$\eta_1(E_\mathrm{B}) = \gamma_1(E_\mathrm{B}), \qquad \text{and} \qquad \eta_2(E_\mathrm{B}) = \gamma_2(E_\mathrm{B}). \tag{F.30}$$

All bound state wave function coefficients need to be chosen such that the wave functions are properly normalized. Using $\mathrm{Im}\big[q_{z,\mathrm{e}}(\mathbf{k}_\parallel; E_\mathrm{B})\big] = -\mathrm{Im}\big[q_{z,\mathrm{h}}(\mathbf{k}_\parallel; E_\mathrm{B})\big]$, which holds for all bound state energies $0 \leq |E_\mathrm{B}| \leq |\Delta_\mathrm{S}|$ [see Eqs. (F.13) and (F.14); Im(...) indicates the imaginary part], the normalization condition can be recast as

$$\frac{\big|u(E_\mathrm{B})\big|^2 + \big|v(E_\mathrm{B})\big|^2}{2\mathrm{Im}\big[q_{z,\mathrm{e}}(\mathbf{k}_\parallel; E_\mathrm{B})\big]} \Big[\big|a(\mathbf{k}_\parallel; E_\mathrm{B})\big|^2 + \big|b(\mathbf{k}_\parallel; E_\mathrm{B})\big|^2 + \big|c(\mathbf{k}_\parallel; E_\mathrm{B})\big|^2 + \big|d(\mathbf{k}_\parallel; E_\mathrm{B})\big|^2 + \big|e(\mathbf{k}_\parallel; E_\mathrm{B})\big|^2 + \big|f(\mathbf{k}_\parallel; E_\mathrm{B})\big|^2 + \big|g(\mathbf{k}_\parallel; E_\mathrm{B})\big|^2 + \big|h(\mathbf{k}_\parallel; E_\mathrm{B})\big|^2\Big] = 1. \tag{F.31}$$

Substituting Eqs. (F.23)–(F.26), we can bring this normalization condition into a form in which only the wave function coefficients in the right half-junction enter. To reduce the problem further, we take advantage of the remaining boundary condition in Eq. (F.17) that accounts for the jumplike discontinuities of the bound state wave functions' first derivatives. Requiring the wave functions to fulfill this boundary condition and resubstituting Eqs. (F.23)–(F.26) yields four equations for four unknown coefficients. Therefore, we can successively eliminate two different coefficients from the equations and consecutively express $f(\mathbf{k}_\parallel; E_\mathrm{B})$, $g(\mathbf{k}_\parallel; E_\mathrm{B})$, and $h(\mathbf{k}_\parallel; E_\mathrm{B})$ solely by $e(\mathbf{k}_\parallel; E_\mathrm{B})$. In particular, we extract the relations

$$f(\mathbf{k}_\parallel; E_\mathrm{B}) = \Sigma_1(\mathbf{k}_\parallel; E_\mathrm{B})\, e(\mathbf{k}_\parallel; E_\mathrm{B}), \tag{F.32}$$

$$g(\mathbf{k}_\parallel; E_\mathrm{B}) = \Sigma_2(\mathbf{k}_\parallel; E_\mathrm{B})\, e(\mathbf{k}_\parallel; E_\mathrm{B}), \tag{F.33}$$

as well as

$$h(\mathbf{k}_\parallel; E_\mathrm{B}) = \Sigma_3(\mathbf{k}_\parallel; E_\mathrm{B})\, e(\mathbf{k}_\parallel; E_\mathrm{B}), \tag{F.34}$$

with the prefactors

$$\begin{aligned}\Sigma_1(\mathbf{k}_\parallel; E_\mathrm{B}) = \Big[&\overline{\varepsilon}_3(\mathbf{k}_\parallel; E_\mathrm{B})\,\overline{\eta}_2(\mathbf{k}_\parallel; E_\mathrm{B})\,\overline{\gamma}_1(\mathbf{k}_\parallel; E_\mathrm{B}) - \overline{\varepsilon}_2(\mathbf{k}_\parallel; E_\mathrm{B})\,\overline{\eta}_3(\mathbf{k}_\parallel; E_\mathrm{B})\,\overline{\gamma}_1(\mathbf{k}_\parallel; E_\mathrm{B}) \\ &- \overline{\varepsilon}_3(\mathbf{k}_\parallel; E_\mathrm{B})\,\overline{\eta}_1(\mathbf{k}_\parallel; E_\mathrm{B})\,\overline{\gamma}_2(\mathbf{k}_\parallel; E_\mathrm{B}) + \overline{\varepsilon}_1(\mathbf{k}_\parallel; E_\mathrm{B})\,\overline{\eta}_3(\mathbf{k}_\parallel; E_\mathrm{B})\,\overline{\gamma}_2(\mathbf{k}_\parallel; E_\mathrm{B}) \\ &+ \overline{\varepsilon}_2(\mathbf{k}_\parallel; E_\mathrm{B})\,\overline{\eta}_1(\mathbf{k}_\parallel; E_\mathrm{B})\,\overline{\gamma}_3(\mathbf{k}_\parallel; E_\mathrm{B}) - \overline{\varepsilon}_1(\mathbf{k}_\parallel; E_\mathrm{B})\,\overline{\eta}_2(\mathbf{k}_\parallel; E_\mathrm{B})\,\overline{\gamma}_3(\mathbf{k}_\parallel; E_\mathrm{B})\Big] \Big/ \Lambda(\mathbf{k}_\parallel; E_\mathrm{B}),\end{aligned} \tag{F.35}$$

$$\begin{aligned}\Sigma_2(\mathbf{k}_\parallel; E_\mathrm{B}) = \Big[&- \overline{\varepsilon}_3(\mathbf{k}_\parallel; E_\mathrm{B})\,\overline{\eta}_2(\mathbf{k}_\parallel; E_\mathrm{B})\,\overline{\varphi}_1(\mathbf{k}_\parallel; E_\mathrm{B}) + \overline{\varepsilon}_2(\mathbf{k}_\parallel; E_\mathrm{B})\,\overline{\eta}_3(\mathbf{k}_\parallel; E_\mathrm{B})\,\overline{\varphi}_1(\mathbf{k}_\parallel; E_\mathrm{B}) \\ &+ \overline{\varepsilon}_3(\mathbf{k}_\parallel; E_\mathrm{B})\,\overline{\eta}_1(\mathbf{k}_\parallel; E_\mathrm{B})\,\overline{\varphi}_2(\mathbf{k}_\parallel; E_\mathrm{B}) - \overline{\varepsilon}_1(\mathbf{k}_\parallel; E_\mathrm{B})\,\overline{\eta}_3(\mathbf{k}_\parallel; E_\mathrm{B})\,\overline{\varphi}_2(\mathbf{k}_\parallel; E_\mathrm{B}) \\ &- \overline{\varepsilon}_2(\mathbf{k}_\parallel; E_\mathrm{B})\,\overline{\eta}_1(\mathbf{k}_\parallel; E_\mathrm{B})\,\overline{\varphi}_3(\mathbf{k}_\parallel; E_\mathrm{B}) + \overline{\varepsilon}_1(\mathbf{k}_\parallel; E_\mathrm{B})\,\overline{\eta}_2(\mathbf{k}_\parallel; E_\mathrm{B})\,\overline{\varphi}_3(\mathbf{k}_\parallel; E_\mathrm{B})\Big] \Big/ \Lambda(\mathbf{k}_\parallel; E_\mathrm{B}),\end{aligned} \tag{F.36}$$

and

$$\Sigma_3(\mathbf{k}_\parallel;E_\mathrm{B}) = \Big[\overline{\varepsilon}_3(\mathbf{k}_\parallel;E_\mathrm{B})\,\overline{\gamma}_2(\mathbf{k}_\parallel;E_\mathrm{B})\,\overline{\varphi}_1(\mathbf{k}_\parallel;E_\mathrm{B}) - \overline{\varepsilon}_2(\mathbf{k}_\parallel;E_\mathrm{B})\,\overline{\gamma}_3(\mathbf{k}_\parallel;E_\mathrm{B})\,\overline{\varphi}_1(\mathbf{k}_\parallel;E_\mathrm{B}) - \overline{\varepsilon}_3(\mathbf{k}_\parallel;E_\mathrm{B})\,\overline{\gamma}_1(\mathbf{k}_\parallel;E_\mathrm{B})\,\overline{\varphi}_2(\mathbf{k}_\parallel;E_\mathrm{B}) + \overline{\varepsilon}_1(\mathbf{k}_\parallel;E_\mathrm{B})\,\overline{\gamma}_3(\mathbf{k}_\parallel;E_\mathrm{B})\,\overline{\varphi}_2(\mathbf{k}_\parallel;E_\mathrm{B}) + \overline{\varepsilon}_2(\mathbf{k}_\parallel;E_\mathrm{B})\,\overline{\gamma}_1(\mathbf{k}_\parallel;E_\mathrm{B})\,\overline{\varphi}_3(\mathbf{k}_\parallel;E_\mathrm{B}) - \overline{\varepsilon}_1(\mathbf{k}_\parallel;E_\mathrm{B})\,\overline{\gamma}_2(\mathbf{k}_\parallel;E_\mathrm{B})\,\overline{\varphi}_3(\mathbf{k}_\parallel;E_\mathrm{B})\Big] \Big/ \Lambda(\mathbf{k}_\parallel;E_\mathrm{B}). \quad \text{(F.37)}$$

The “overline” coefficients are found to be

$$\overline{\varepsilon}_1(\mathbf{k}_\parallel;E_\mathrm{B}) = -\frac{q_{z,\mathrm{e}}(\mathbf{k}_\parallel;E_\mathrm{B})}{k_\mathrm{F}}\,u(E_\mathrm{B})\,\mathrm{e}^{\mathrm{i}\phi_\mathrm{S}} - \left[\frac{q_{z,\mathrm{e}}(\mathbf{k}_\parallel;E_\mathrm{B})}{k_\mathrm{F}} + \mathrm{i}\overline{\lambda}_\mathrm{SC}\right] u(E_\mathrm{B})\,\varepsilon_1(E_\mathrm{B}) - \left[-\frac{q_{z,\mathrm{h}}(\mathbf{k}_\parallel;E_\mathrm{B})}{k_\mathrm{F}} + \mathrm{i}\overline{\lambda}_\mathrm{SC}\right] v(E_\mathrm{B})\,\varepsilon_2(E_\mathrm{B}), \quad \text{(F.38)}$$

$$\overline{\varphi}_1(\mathbf{k}_\parallel;E_\mathrm{B}) = -\mathrm{i}\left[\overline{\lambda}_\mathrm{MA}\mathrm{e}^{-\mathrm{i}\Phi} + \overline{\Omega}(\mathbf{k}_\parallel)\right] u(E_\mathrm{B})\,\varepsilon_1(E_\mathrm{B}) - \mathrm{i}\left[\overline{\lambda}_\mathrm{MA}\mathrm{e}^{-\mathrm{i}\Phi} + \overline{\Omega}(\mathbf{k}_\parallel)\right] v(E_\mathrm{B})\,\varepsilon_2(E_\mathrm{B}), \quad \text{(F.39)}$$

$$\overline{\gamma}_1(\mathbf{k}_\parallel;E_\mathrm{B}) = \frac{q_{z,\mathrm{h}}(\mathbf{k}_\parallel;E_\mathrm{B})}{k_\mathrm{F}}\,v(E_\mathrm{B})\,\mathrm{e}^{\mathrm{i}\phi_\mathrm{S}} - \left[\frac{q_{z,\mathrm{e}}(\mathbf{k}_\parallel;E_\mathrm{B})}{k_\mathrm{F}} + \mathrm{i}\overline{\lambda}_\mathrm{SC}\right] u(E_\mathrm{B})\,\gamma_1(E_\mathrm{B}) - \left[-\frac{q_{z,\mathrm{h}}(\mathbf{k}_\parallel;E_\mathrm{B})}{k_\mathrm{F}} + \mathrm{i}\overline{\lambda}_\mathrm{SC}\right] v(E_\mathrm{B})\,\gamma_2(E_\mathrm{B}), \quad \text{(F.40)}$$

$$\overline{\eta}_1(\mathbf{k}_\parallel;E_\mathrm{B}) = -\mathrm{i}\left[\overline{\lambda}_\mathrm{MA}\mathrm{e}^{-\mathrm{i}\Phi} + \overline{\Omega}(\mathbf{k}_\parallel)\right] u(E_\mathrm{B})\,\gamma_1(E_\mathrm{B}) - \mathrm{i}\left[\overline{\lambda}_\mathrm{MA}\mathrm{e}^{-\mathrm{i}\Phi} + \overline{\Omega}(\mathbf{k}_\parallel)\right] v(E_\mathrm{B})\,\gamma_2(E_\mathrm{B}), \quad \text{(F.41)}$$

$$\overline{\varepsilon}_2(\mathbf{k}_\parallel;E_\mathrm{B}) = -\mathrm{i}\left[\overline{\lambda}_\mathrm{MA}\mathrm{e}^{\mathrm{i}\Phi} + \overline{\Omega}^*(\mathbf{k}_\parallel)\right] u(E_\mathrm{B})\,\varepsilon_1(E_\mathrm{B}) - \mathrm{i}\left[\overline{\lambda}_\mathrm{MA}\mathrm{e}^{\mathrm{i}\Phi} + \overline{\Omega}^*(\mathbf{k}_\parallel)\right] v(E_\mathrm{B})\,\varepsilon_2(E_\mathrm{B}), \quad \text{(F.42)}$$

$$\overline{\varphi}_2(\mathbf{k}_\parallel;E_\mathrm{B}) = -\frac{q_{z,\mathrm{e}}(\mathbf{k}_\parallel;E_\mathrm{B})}{k_\mathrm{F}}\,u(E_\mathrm{B})\,\mathrm{e}^{\mathrm{i}\phi_\mathrm{S}} - \left[\frac{q_{z,\mathrm{e}}(\mathbf{k}_\parallel;E_\mathrm{B})}{k_\mathrm{F}} + \mathrm{i}\overline{\lambda}_\mathrm{SC}\right] u(E_\mathrm{B})\,\varepsilon_1(E_\mathrm{B}) - \left[-\frac{q_{z,\mathrm{h}}(\mathbf{k}_\parallel;E_\mathrm{B})}{k_\mathrm{F}} + \mathrm{i}\overline{\lambda}_\mathrm{SC}\right] v(E_\mathrm{B})\,\varepsilon_2(E_\mathrm{B}), \quad \text{(F.43)}$$

$$\overline{\gamma}_2(\mathbf{k}_\parallel;E_\mathrm{B}) = -\mathrm{i}\left[\overline{\lambda}_\mathrm{MA}\mathrm{e}^{\mathrm{i}\Phi} + \overline{\Omega}^*(\mathbf{k}_\parallel)\right] u(E_\mathrm{B})\,\gamma_1(E_\mathrm{B}) - \mathrm{i}\left[\overline{\lambda}_\mathrm{MA}\mathrm{e}^{\mathrm{i}\Phi} + \overline{\Omega}^*(\mathbf{k}_\parallel)\right] v(E_\mathrm{B})\,\gamma_2(E_\mathrm{B}), \quad \text{(F.44)}$$

$$\overline{\eta}_2(\mathbf{k}_\parallel;E_\mathrm{B}) = \frac{q_{z,\mathrm{h}}(\mathbf{k}_\parallel;E_\mathrm{B})}{k_\mathrm{F}}\,v(E_\mathrm{B})\,\mathrm{e}^{\mathrm{i}\phi_\mathrm{S}} - \left[\frac{q_{z,\mathrm{e}}(\mathbf{k}_\parallel;E_\mathrm{B})}{k_\mathrm{F}} + \mathrm{i}\overline{\lambda}_\mathrm{SC}\right] u(E_\mathrm{B})\,\gamma_1(E_\mathrm{B}) - \left[-\frac{q_{z,\mathrm{h}}(\mathbf{k}_\parallel;E_\mathrm{B})}{k_\mathrm{F}} + \mathrm{i}\overline{\lambda}_\mathrm{SC}\right] v(E_\mathrm{B})\,\gamma_2(E_\mathrm{B}), \quad \text{(F.45)}$$

$$\overline{\varepsilon}_3(\mathbf{k}_\parallel;E_\mathrm{B}) = \frac{q_{z,\mathrm{e}}(\mathbf{k}_\parallel;E_\mathrm{B})}{k_\mathrm{F}}\,v(E_\mathrm{B}) + \left[\frac{q_{z,\mathrm{e}}(\mathbf{k}_\parallel;E_\mathrm{B})}{k_\mathrm{F}} + \mathrm{i}\overline{\lambda}_\mathrm{SC}\right] v(E_\mathrm{B})\,\varepsilon_1(E_\mathrm{B}) + \left[-\frac{q_{z,\mathrm{h}}(\mathbf{k}_\parallel;E_\mathrm{B})}{k_\mathrm{F}} + \mathrm{i}\overline{\lambda}_\mathrm{SC}\right] u(E_\mathrm{B})\,\varepsilon_2(E_\mathrm{B}), \quad \text{(F.46)}$$

$$\overline{\varphi}_3(\mathbf{k}_\parallel;E_\mathrm{B}) = \mathrm{i}\left[-\overline{\lambda}_\mathrm{MA}\mathrm{e}^{-\mathrm{i}\Phi} + \overline{\Omega}(\mathbf{k}_\parallel)\right] v(E_\mathrm{B})\,\varepsilon_1(E_\mathrm{B}) + \mathrm{i}\left[-\overline{\lambda}_\mathrm{MA}\mathrm{e}^{-\mathrm{i}\Phi} + \overline{\Omega}(\mathbf{k}_\parallel)\right] u(E_\mathrm{B})\,\varepsilon_2(E_\mathrm{B}), \quad \text{(F.47)}$$

$$\overline{\gamma}_3(\mathbf{k}_\parallel;E_\mathrm{B}) = -\frac{q_{z,\mathrm{h}}(\mathbf{k}_\parallel;E_\mathrm{B})}{k_\mathrm{F}}\,u(E_\mathrm{B}) + \left[\frac{q_{z,\mathrm{e}}(\mathbf{k}_\parallel;E_\mathrm{B})}{k_\mathrm{F}} + \mathrm{i}\overline{\lambda}_\mathrm{SC}\right] v(E_\mathrm{B})\,\gamma_1(E_\mathrm{B}) + \left[-\frac{q_{z,\mathrm{h}}(\mathbf{k}_\parallel;E_\mathrm{B})}{k_\mathrm{F}} + \mathrm{i}\overline{\lambda}_\mathrm{SC}\right] u(E_\mathrm{B})\,\gamma_2(E_\mathrm{B}), \quad \text{(F.48)}$$

$$\overline{\eta}_3(\mathbf{k}_\parallel;E_\mathrm{B}) = \mathrm{i}\left[-\overline{\lambda}_\mathrm{MA}\mathrm{e}^{-\mathrm{i}\Phi} + \overline{\Omega}(\mathbf{k}_\parallel)\right] v(E_\mathrm{B})\,\gamma_1(E_\mathrm{B}) + \mathrm{i}\left[-\overline{\lambda}_\mathrm{MA}\mathrm{e}^{-\mathrm{i}\Phi} + \overline{\Omega}(\mathbf{k}_\parallel)\right] u(E_\mathrm{B})\,\gamma_2(E_\mathrm{B}), \quad \text{(F.49)}$$

and finally

$$\overline{\varepsilon}_4(\mathbf{k}_\parallel;E_\mathrm{B}) = \mathrm{i}\left[-\overline{\lambda}_\mathrm{MA}\mathrm{e}^{\mathrm{i}\Phi} + \overline{\Omega}^*(\mathbf{k}_\parallel)\right] v(E_\mathrm{B})\,\varepsilon_1(E_\mathrm{B}) + \mathrm{i}\left[-\overline{\lambda}_\mathrm{MA}\mathrm{e}^{\mathrm{i}\Phi} + \overline{\Omega}^*(\mathbf{k}_\parallel)\right] u(E_\mathrm{B})\,\varepsilon_2(E_\mathrm{B}), \quad \text{(F.50)}$$

$$\overline{\varphi}_4(\mathbf{k}_\parallel;E_\mathrm{B}) = \frac{q_{z,\mathrm{e}}(\mathbf{k}_\parallel;E_\mathrm{B})}{k_\mathrm{F}}\,v(E_\mathrm{B}) + \left[\frac{q_{z,\mathrm{e}}(\mathbf{k}_\parallel;E_\mathrm{B})}{k_\mathrm{F}} + \mathrm{i}\overline{\lambda}_\mathrm{SC}\right] v(E_\mathrm{B})\,\varepsilon_1(E_\mathrm{B}) + \left[-\frac{q_{z,\mathrm{h}}(\mathbf{k}_\parallel;E_\mathrm{B})}{k_\mathrm{F}} + \mathrm{i}\overline{\lambda}_\mathrm{SC}\right] u(E_\mathrm{B})\,\varepsilon_2(E_\mathrm{B}), \quad \text{(F.51)}$$

$$\overline{\gamma}_4(\mathbf{k}_\parallel;E_\mathrm{B}) = \mathrm{i}\left[-\overline{\lambda}_\mathrm{MA}\mathrm{e}^{\mathrm{i}\Phi} + \overline{\Omega}^*(\mathbf{k}_\parallel)\right] v(E_\mathrm{B})\,\gamma_1(E_\mathrm{B}) + \mathrm{i}\left[-\overline{\lambda}_\mathrm{MA}\mathrm{e}^{\mathrm{i}\Phi} + \overline{\Omega}^*(\mathbf{k}_\parallel)\right] u(E_\mathrm{B})\,\gamma_2(E_\mathrm{B}), \quad \text{(F.52)}$$

as well as

$$\overline{\eta}_4(\mathbf{k}_\parallel;E_\mathrm{B}) = -\frac{q_{z,\mathrm{h}}(\mathbf{k}_\parallel;E_\mathrm{B})}{k_\mathrm{F}}\,u(E_\mathrm{B}) + \left[\frac{q_{z,\mathrm{e}}(\mathbf{k}_\parallel;E_\mathrm{B})}{k_\mathrm{F}} + \mathrm{i}\overline{\lambda}_\mathrm{SC}\right] v(E_\mathrm{B})\,\gamma_1(E_\mathrm{B}) + \left[-\frac{q_{z,\mathrm{h}}(\mathbf{k}_\parallel;E_\mathrm{B})}{k_\mathrm{F}} + \mathrm{i}\overline{\lambda}_\mathrm{SC}\right] u(E_\mathrm{B})\,\gamma_2(E_\mathrm{B}), \quad \text{(F.53)}$$

while the common denominator in Eqs. (F.35)–(F.37) can be written as

$$\begin{aligned}\Lambda(\mathbf{k}_\parallel;E_\mathrm{B}) = {}& -\overline{\eta}_3(\mathbf{k}_\parallel;E_\mathrm{B})\,\overline{\gamma}_2(\mathbf{k}_\parallel;E_\mathrm{B})\,\overline{\varphi}_1(\mathbf{k}_\parallel;E_\mathrm{B}) + \overline{\eta}_2(\mathbf{k}_\parallel;E_\mathrm{B})\,\overline{\gamma}_3(\mathbf{k}_\parallel;E_\mathrm{B})\,\overline{\varphi}_1(\mathbf{k}_\parallel;E_\mathrm{B}) \\ & + \overline{\eta}_3(\mathbf{k}_\parallel;E_\mathrm{B})\,\overline{\gamma}_1(\mathbf{k}_\parallel;E_\mathrm{B})\,\overline{\varphi}_2(\mathbf{k}_\parallel;E_\mathrm{B}) - \overline{\eta}_1(\mathbf{k}_\parallel;E_\mathrm{B})\,\overline{\gamma}_3(\mathbf{k}_\parallel;E_\mathrm{B})\,\overline{\varphi}_2(\mathbf{k}_\parallel;E_\mathrm{B}) \\ & - \overline{\eta}_2(\mathbf{k}_\parallel;E_\mathrm{B})\,\overline{\gamma}_1(\mathbf{k}_\parallel;E_\mathrm{B})\,\overline{\varphi}_3(\mathbf{k}_\parallel;E_\mathrm{B}) + \overline{\eta}_1(\mathbf{k}_\parallel;E_\mathrm{B})\,\overline{\gamma}_2(\mathbf{k}_\parallel;E_\mathrm{B})\,\overline{\varphi}_3(\mathbf{k}_\parallel;E_\mathrm{B}). \quad \text{(F.54)}\end{aligned}$$

In all preceding equations, we used the dimensionless parameters $\overline{\lambda}_\mathrm{SC} = (2m\lambda_\mathrm{SC})/(\hbar^2 k_\mathrm{F})$ and $\overline{\lambda}_\mathrm{MA} = (2m\lambda_\mathrm{MA})/(\hbar^2 k_\mathrm{F})$ representing the scalar and magnetic tunneling strengths; $k_\mathrm{F} = \sqrt{2m\mu}/\hbar$ still abbreviates the Fermi wave vector. The influence of SOC is captured by the dimensionless SOC matrix element

$$\overline{\Omega}(\mathbf{k}_\parallel) = \left(\overline{\lambda}_\mathrm{R} - \overline{\lambda}_\mathrm{D}\right) k_y/k_\mathrm{F} + \mathrm{i}\left(\overline{\lambda}_\mathrm{R} + \overline{\lambda}_\mathrm{D}\right) k_x/k_\mathrm{F}, \quad \text{(F.55)}$$

where the effective dimensionless Rashba and Dresselhaus SOC parameters are $\overline{\lambda}_\mathrm{R} = (2m\alpha)/\hbar^2$ and $\overline{\lambda}_\mathrm{D} = (2m\beta)/\hbar^2$.

Putting Eqs. (F.23)–(F.26) and Eqs. (F.32)–(F.34) all together into the normalization condition in Eq. (F.31) yields

$$\frac{\left|u(E_\mathrm{B})\right|^2+\left|v(E_\mathrm{B})\right|^2}{2\mathrm{Im}\left[q_{z,\mathrm{e}}(\mathbf{k}_\parallel;E_\mathrm{B})\right]}\Big[\left|\varepsilon_1(E_\mathrm{B})+\gamma_1(E_\mathrm{B})\,\Sigma_2(\mathbf{k}_\parallel;E_\mathrm{B})\right|^2+\left|\varepsilon_1(E_\mathrm{B})\,\Sigma_1(\mathbf{k}_\parallel;E_\mathrm{B})+\gamma_1(E_\mathrm{B})\,\Sigma_3(\mathbf{k}_\parallel;E_\mathrm{B})\right|^2$$
$$+\left|\varepsilon_2(E_\mathrm{B})+\gamma_2(E_\mathrm{B})\,\Sigma_2(\mathbf{k}_\parallel;E_\mathrm{B})\right|^2+\left|\varepsilon_2(E_\mathrm{B})\,\Sigma_1(\mathbf{k}_\parallel;E_\mathrm{B})+\gamma_2(E_\mathrm{B})\,\Sigma_3(\mathbf{k}_\parallel;E_\mathrm{B})\right|^2$$
$$+1+\left|\Sigma_1(\mathbf{k}_\parallel;E_\mathrm{B})\right|^2+\left|\Sigma_2(\mathbf{k}_\parallel;E_\mathrm{B})\right|^2+\left|\Sigma_3(\mathbf{k}_\parallel;E_\mathrm{B})\right|^2\Big]\left|e(\mathbf{k}_\parallel;E_\mathrm{B})\right|^2=1, \quad \text{(F.56)}$$

which can be inverted to initially identify $\left|e(\mathbf{k}_\parallel;E_\mathrm{B})\right|^2$ (note that we already specified all individual prefactors above). All remaining (absolute squares of the) bound state wave function coefficients are afterwards uniquely determined going back with the previously given equations.

Once all coefficients are known, the bound state wave function squares (i.e., their probability densities) can be expressed as

$$\left|\Psi(x,y,z<0;\mathbf{k}_\parallel;E_\mathrm{B})\right|=2\,u(E_\mathrm{B})\,v(E_\mathrm{B})\,\mathrm{e}^{2\mathrm{Im}[q_{z,\mathrm{e}}(\mathbf{k}_\parallel;E_\mathrm{B})]z}\Big[\left|a(\mathbf{k}_\parallel;E_\mathrm{B})\right|^2+\left|b(\mathbf{k}_\parallel;E_\mathrm{B})\right|^2$$
$$+\left|c(\mathbf{k}_\parallel;E_\mathrm{B})\right|^2+\left|d(\mathbf{k}_\parallel;E_\mathrm{B})\right|^2\Big] \quad \text{(F.57)}$$

in the left superconductor ($z<0$) and

$$\left|\Psi(x,y,z>0;\mathbf{k}_\parallel;E_\mathrm{B})\right|=2\,u(E_\mathrm{B})\,v(E_\mathrm{B})\,\mathrm{e}^{-2\mathrm{Im}[q_{z,\mathrm{e}}(\mathbf{k}_\parallel;E_\mathrm{B})]z}\Big[\left|e(\mathbf{k}_\parallel;E_\mathrm{B})\right|^2+\left|f(\mathbf{k}_\parallel;E_\mathrm{B})\right|^2$$
$$+\left|g(\mathbf{k}_\parallel;E_\mathrm{B})\right|^2+\left|h(\mathbf{k}_\parallel;E_\mathrm{B})\right|^2\Big] \quad \text{(F.58)}$$

in the right superconductor ($z>0$), respectively. The plane-wave propagation parallel to the ferromagnetic-insulator interface (i.e., along the transverse $\hat{x}$- and $\hat{y}$-directions) does not contribute to the *bound state wave function squares*. The results presented in Fig. 9.6(a) are then obtained from numerically solving for the Andreev bound state and YSR state energies E_B, extracting the bound state wave function coefficient squares – both according to the above discussed methodology –, and eventually evaluating Eqs. (F.57) and (F.58). The inset of Fig. 9.6(a) depicts the spatial dependence of the bound state wave functions' absolute square *differences*

$$\Delta\text{ W. f. s.}=\left|\Psi(x,y,z;k_x>0,k_y>0;E_\mathrm{B})\right|^2-\left|\Psi(x,y,z;-k_x,-k_y;E_\mathrm{B})\right|^2 \quad \text{(F.59)}$$

for the transverse momentum $k_y=0.99k_\mathrm{F}$ (and $k_x=0$), essentially measuring the strength of the bound states' SOC-controlled $\mathbf{k}_\parallel$-asymmetries.[1] To provide a more comprehensive characterization, motivating the choice of these parameters, the color plots in Fig. F.1 illustrate the spatial dependence of Δ W. f. s. for all possible values of $|k_y|\in[0;k_\mathrm{F}]$ (assuming $k_x=0$ and the same parameters as in Fig. 9.6), once for the Andreev bound states and once for the YSR states. The data shown in Fig. 9.6(a)'s inset basically represents a cut through the color plots along $|k_y|=0.99k_\mathrm{F}$. Deducing the bound state-based AJHE current formula in the next part will demonstrate that the bound states' individual AJHE current contributions increase proportionally with Δ W. f. s. and the overall AJHE current amplitudes are therefore mostly determined by states for which Δ W. f. s. becomes maximal. This is precisely the case whenever $|\mathbf{k}_\parallel|\to k_\mathrm{F}$ and gives reasoning for focusing on $|k_y|=0.99k_\mathrm{F}$ in Fig. 9.6(a)

[1] As long as the interfacial SOC remains completely absent, the energies of the bound states occupied by an electron propagating along $\hat{x}$ (and/or $\hat{y}$) and by the respective counterpropagating electron are identical. Therefore, the bound state wave function squares are the same for both and Δ W. f. s., basically quantifying wave function *differences*, vanishes. Finite (Δ W. f. s.)-values serve hence as a clear signature of present bound state SOC asymmetries and are crucially related to the AJHE current amplitudes, as we will learn in the next part.

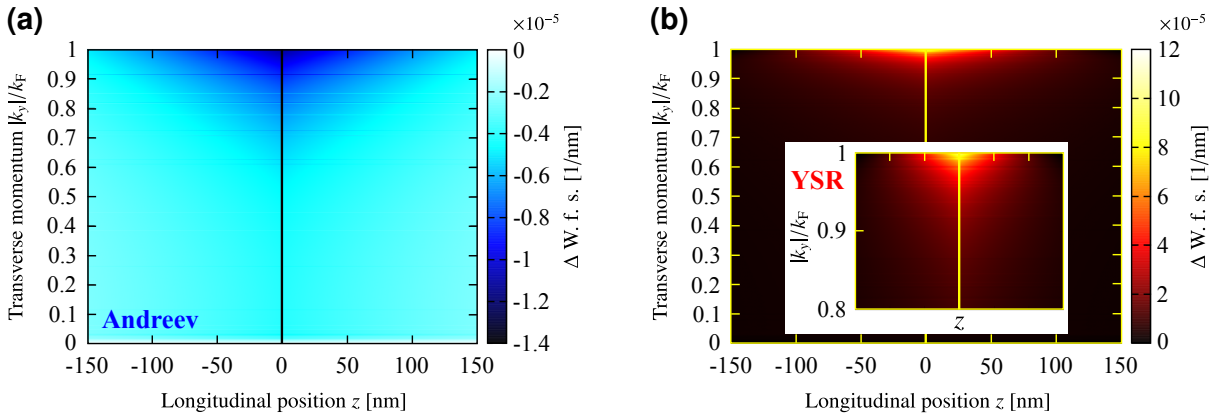


Fig. F.1: (a) Calculated spatial dependence of the Andreev bound state wave functions' absolute square *differences* Δ W. f. s. for all allowed transverse momenta $0 \leq |k_y| \leq k_F$ (assuming $k_x = 0$). Positive Δ W. f. s. indicates that the bound state wave functions at $k_y > 0$ exceed those at the respective $-k_y$ and vice versa. All other parameters are the same as in Fig. 9.6. **(b)** Same calculation as in **(a)**, but for the bound state spectrum's YSR part. The inset shows a zoom at $0.8k_F \leq |k_y| \leq k_F$.

to observe clear trends. The YSR states' (Δ W. f. s.)-amplitudes can remarkably overcome their Andreev bound state counterparts and explain the YSR states' dominant role when investigating AJHEs. The reason for that observation lies in the states' distinct typical energy ranges. The YSR states are always located more inside the superconducting gap than their Andreev bound state counterparts (see our analysis in Chap. 7) and thus much more sensitive to changing any system parameter, i.e., also to reversals of $\mathbf{k}_\parallel$. Furthermore, both states' respective (Δ W. f. s.)-values differ in sign, suggesting that their individual AJHE currents must flow along opposite directions. A more detailed analysis of the coincidence between the bound state features and the AJHE is provided in Sec. 9.4. The bound state wave functions (and likewise their squares) decay exponentially with increasing distance from the ferromagnetic-insulator interface and over the characteristic decay length $\kappa = 1/\{2\mathrm{Im}[q_{z,\mathrm{e}}(\mathbf{k}_\parallel; E_\mathrm{B})]\}$, where $q_{z,\mathrm{e}}(\mathbf{k}_\parallel; E_\mathrm{B})$ refers to the aforementioned electronlike wave vector at the bound state energy E_B. Inspecting Fig. F.1, this exponential damping becomes most clearly evident at larger $|k_y|$. At rather small $|k_y|$-values, Δ W. f. s. becomes so small that we cannot properly resolve its exponential decay on the color plots' common scale, though still being there.

Bound state-based formula for transverse AJHE currents

Given the full bound state wave functions, *including all their coefficients*, we can proceed and compute the considered S/F-I/S Josephson junction's AJHE current flows in a similar manner as its (tunneling) Josephson current in Sec. 7.1. We evaluate the currents inside the ferromagnetic-insulator region, which saves us from explicitly dealing with Cooper pairs. Electrons that initially formed Cooper pairs in one of the superconducting electrodes tunnel through the ferromagnetic-insulator barrier via the available bound states and pair again in the second superconductor. Provided that more Cooper pairs enter one superconductor than simultaneously leave, such effective Cooper pair exchanges establish nonzero (tunneling) Josephson currents. While being transferred through the ferromagnetic-insulator interface, the Cooper pairs are additionally exposed to the striking interfacial skew tunneling mechanism, which gives eventually rise to the peculiar AJHE, as we thoroughly address in Sec. 9.2. The great advantage of the bound state-based picture is that all electrical current inside the ferromagnetic insulator is solely carried by single electrons that occupy bound states. The latter, and thereby also the current flows, are uniquely characterized within the above introduced methodology.

To quantify the AJHE currents associated with *one single occupied bound state* at energy E_B, we apply the corresponding electrical current density operators $\hat{j}_\eta$ – where $\hat{\eta} \in \{\hat{x}; \hat{y}\}$ labels the junction's transverse $\hat{x}$- and $\hat{y}$-directions parallel to the ferromagnetic-insulator interface – to its underlying bound state wave function $\Psi(x, y, z; \mathbf{k}_\parallel; E_\mathrm{B})$. Since the ferromagnetic insulator is supposed to be ultrathin and the bound state wave function must be continuous at the interface, we can either make use of $\Psi(x, y, z < 0; \mathbf{k}_\parallel; E_\mathrm{B})$ valid in the left half-junction or $\Psi(x, y, z > 0; \mathbf{k}_\parallel; E_\mathrm{B})$ obtained in the right half-junction, and finally take the limiting case $z \to 0_+$. Keeping the transverse wave vector $\mathbf{k}_\parallel$ fixed, the *average* contributions of the *occupied* bound state $\Psi(x, y, z > 0; \mathbf{k}_\parallel; E_\mathrm{B})$ to the *interfacial* AJHE current densities $j_\eta(\mathbf{k}_\parallel; E_\mathrm{B})$ are determined by

$$j_\eta(\mathbf{k}_\parallel; E_\mathrm{B}) = \lim_{z \to 0_+} \left\{ \left\langle \Psi(x, y, z > 0; \mathbf{k}_\parallel; E_\mathrm{B}) \middle| \hat{j}_\eta \middle| \Psi(x, y, z > 0; \mathbf{k}_\parallel; E_\mathrm{B}) \right\rangle \tanh\left(\frac{E_\mathrm{B}}{2k_\mathrm{B}T} \right) \right\}, \tag{F.60}$$

where

$$\hat{j}_\eta = -e \begin{bmatrix} \left. \frac{\partial \hat{\mathcal{H}}_\mathrm{e}}{\hbar \partial k_\eta} \right|_{k_\eta \longmapsto -\mathrm{i}(\partial/\partial\eta)} & \hat{0} \\ \hat{0} & -\hat{\sigma}_\mathrm{y} \left[\left. \frac{\partial \hat{\mathcal{H}}_\mathrm{e}}{\hbar \partial k_\eta} \right|_{k_\eta \longmapsto -\mathrm{i}(\partial/\partial\eta)} \right]^* \hat{\sigma}_\mathrm{y} \end{bmatrix} = -e \begin{bmatrix} -\frac{\mathrm{i}\hbar}{m}\frac{\partial}{\partial\eta} & 0 & 0 & 0 \\ 0 & -\frac{\mathrm{i}\hbar}{m}\frac{\partial}{\partial\eta} & 0 & 0 \\ 0 & 0 & -\frac{\mathrm{i}\hbar}{m}\frac{\partial}{\partial\eta} & 0 \\ 0 & 0 & 0 & -\frac{\mathrm{i}\hbar}{m}\frac{\partial}{\partial\eta} \end{bmatrix} \tag{F.61}$$

resembles the AJHE current density operators, whose general structure is similar to what we encountered when computing the usual (tunneling) Josephson currents in Sec. 7.1. Since we are now concerned with currents along the transverse directions, we simply need to replace the single-particle velocity operators by the ones acting along the $\hat{\eta}$-directions, i.e., by $\hat{v}_\eta = (-\mathrm{i}\hbar)/m(\partial/\partial\eta)$. Nevertheless, one must be aware that that formally calculating $\hat{j}_\eta$ yields additional off-diagonal terms that originate from the ferromagnetic insulator's k_η-dependent SOC Hamiltonian and would therefore couple the bound state wave functions' up- and down-spin components. In our case, however, SOC is only present right at the interface and not inside the bulk superconducting electrodes. The bound state wave functions contain consequently only pure up- or down-spin parts and no spin mixtures, suggesting that the off-diagonal $\hat{j}_\eta$-terms vanish anyway after applying the operators to the bound state wave functions. We decided thus to neglect them from the beginning on. Analogously to Sec. 7.1, the thermal occupation factor $\tanh[E_\mathrm{B}/(2k_\mathrm{B}T)]$ in Eq. (F.60) ensures that only occupied states are included into the calculation.

Substituting Eq. (F.61) and the related bound state wave function stated in Eq. (F.21) into Eq. (F.60), and averaging over all transverse $\mathbf{k}_\parallel$-channels, leads to the AJHE currents *per* occupied bound state,

$$\begin{aligned} I_\eta(E_\mathrm{B}) &= \frac{\mathcal{A}_\eta}{(2\pi)^2} \int \mathrm{d}^2\mathbf{k}_\parallel \, j_\eta(\mathbf{k}_\parallel; E_\mathrm{B}) \\ &= -2e\, u(E_\mathrm{B})\, v(E_\mathrm{B}) \frac{\mathcal{A}_\eta}{(2\pi)^2} \int \mathrm{d}^2\mathbf{k}_\parallel \, \frac{\hbar k_\eta}{m} \Big[\big|e(\mathbf{k}_\parallel; E_\mathrm{B})\big|^2 + \big|f(\mathbf{k}_\parallel; E_\mathrm{B})\big|^2 \\ &\qquad + \big|g(\mathbf{k}_\parallel; E_\mathrm{B})\big|^2 + \big|h(\mathbf{k}_\parallel; E_\mathrm{B})\big|^2 \Big] \tanh\left(\frac{E_\mathrm{B}}{2k_\mathrm{B}T} \right) \\ &= -e \frac{|\Delta_\mathrm{S}(T)|}{E_\mathrm{B}} \frac{\mathcal{A}_\eta}{(2\pi)^2} \int \mathrm{d}^2\mathbf{k}_\parallel \, \frac{\hbar k_\eta}{m} \Big[\big|e(\mathbf{k}_\parallel; E_\mathrm{B})\big|^2 + \big|f(\mathbf{k}_\parallel; E_\mathrm{B})\big|^2 \\ &\qquad + \big|g(\mathbf{k}_\parallel; E_\mathrm{B})\big|^2 + \big|h(\mathbf{k}_\parallel; E_\mathrm{B})\big|^2 \Big] \tanh\left(\frac{E_\mathrm{B}}{2k_\mathrm{B}T} \right). \end{aligned} \tag{F.62}$$

In the last step, we noted that $u(E_\mathrm{B})\, v(E_\mathrm{B}) = |\Delta_\mathrm{S}(T)|/(2E_\mathrm{B})$ for all bound state energies $0 \leq |E_\mathrm{B}| \leq |\Delta_\mathrm{S}(T)|$. The AJHE currents are basically extracted regarding all electrons that move along the $\hat{\eta}$-directions and multiplying their transverse velocities $v_\eta = (\hbar k_\eta)/m$ by the electron charge $-e$ and an

additional wave function-dependent "weighting factor", which basically plays the role of the electron density arising in usual quantum-mechanical current formulas.

The final expression for the AJHE currents that accounts for all allowed bound states, i.e., for the Andreev bound state and the YSR state branches, reads then as

$$I_\eta = -e \sum_{E_\mathrm{B}} \frac{|\Delta_\mathrm{S}(T)|}{2E_\mathrm{B}} \frac{\mathcal{A}_\eta}{(2\pi)^2} \int \mathrm{d}^2\mathbf{k}_\parallel \, \frac{\hbar k_\eta}{m} \Big[\big|e(\mathbf{k}_\parallel; E_\mathrm{B})\big|^2 + \big|f(\mathbf{k}_\parallel; E_\mathrm{B})\big|^2 + \big|g(\mathbf{k}_\parallel; E_\mathrm{B})\big|^2 + \big|h(\mathbf{k}_\parallel; E_\mathrm{B})\big|^2 \Big] \tanh\left(\frac{E_\mathrm{B}}{2k_\mathrm{B}T}\right). \quad \text{(F.63)}$$

Recalling the definition of the bound state wave functions' absolute square *differences*

$$\Delta \text{ W. f. s.} = \big|\Psi(x, y, z; k_x > 0, k_y > 0; E_\mathrm{B})\big|^2 - \big|\Psi(x, y, z; -k_x, -k_y; E_\mathrm{B})\big|^2 \quad \text{(F.64)}$$

and looking up its ingredients [see, e.g., Eq. (F.58)], we deduce

$$I_\eta \propto -|k_\eta| \sum_{E_\mathrm{B}} \int_{k_x>0} \mathrm{d}k_x \int_{k_y>0} \mathrm{d}k_y \; (\Delta \text{ W. f. s.})\Big|_{z\to 0_+} \tanh\left(\frac{E_\mathrm{B}}{2k_\mathrm{B}T}\right). \quad \text{(F.65)}$$

As predicted in the previous part and analyzed more comprehensively in Sec. 9.4, the AJHE currents are therefore indeed caused by the SOC-induced $\mathbf{k}_\parallel$-asymmetries (that raise nonzero Δ W. f. s.). Moreover, Eq. (F.65) reveals that stronger bound state asymmetries simultaneously enhance the AJHE currents. Experimentally detecting sizable AJHE responses provides hence unambiguous signatures of distinct SOC-controlled bound state asymmetries (mostly present in the YSR part of the spectrum as mentioned above).

Although the presented bound state-based approach initially seems to be somewhat cumbersome, it allows us to gain valuable physical insight, attributing the different AJHE current contributions to the individual bound states. The (tunneling) Josephson current might be calculated either in a similar way (see Sec. 7.1) or by relying on the thermodynamic relation

$$I_\mathrm{J} = -\frac{2e}{\hbar} \sum_{E_\mathrm{B}} \frac{1}{2} \frac{\partial E_\mathrm{B}(\phi_\mathrm{S})}{\partial \phi_\mathrm{S}} \tanh\left(\frac{E_\mathrm{B}}{2k_\mathrm{B}T}\right). \quad \text{(F.66)}$$

To get the complete picture, we rather recommend to follow again the first strategy as the second is, for instance, not able to capture transverse AJHE currents.

The AJHE current data plotted in Fig. 9.6(b) is then obtained from (1) numerically solving for the regarded S/F-I/S junction's bound state spectrum, (2) setting up the full bound state wave functions – steps (1) and (2) are performed according to the strategy presented in earlier parts of this chapter –, and (3) inserting the results into Eq. (F.63). We furthermore resolve the AJHE currents coming from the Andreev bound states and the YSR states to unravel their individual impact.

Back matter

References

[1] *NIST database: Fundamental Physical Constants*, https://physics.nist.gov/constants.

[2] G. E. Moore, *Cramming more components onto integrated circucits*, Electronics **38** (1965).

[3] *Fun Facts: Exactly how small (and cool) is 22 Nanometers?*, Intel Corp., Available at https://www.intel.com/content/dam/www/public/us/en/documents/corporate-information/history-moores-law-fun-facts-factsheet.pdf (2012).

[4] J. R. Powell, *The Quantum Limit to Moore's Law*, Proc. IEEE **96**, 1247 (2008).

[5] I. Žutić, J. Fabian, and S. Das Sarma, *Spintronics: Fundamentals and applications*, Rev. Mod. Phys. **76**, 323 (2004).

[6] A. Fert, *The present and the future of spintronics*, Thin Solid Films **517**, 2 (2008).

[7] V. K. Joshi, *Spintronics: A contemporary review of emerging electronics devices*, Eng. Sci. Technol. **19**, 1503 (2016).

[8] A. Hirohata, K. Yamada, Y. Nakatani, I.-L. Prejbeanu, B. Diény, P. Pirro, and B. Hillebrands, *Review on spintronics: Principles and device applications*, J. Magn. Magn. Mater. **509**, 166711 (2020).

[9] M. Jullière, *Tunneling between ferromagnetic films*, Phys. Lett. A **54**, 225 (1975).

[10] M. N. Baibich, J. M. Broto, A. Fert, F. N. Van Dau, F. Petroff, P. Eitenne, G. Creuzet, A. Friederich, and J. Chazelas, *Giant Magnetoresistance of (001)Fe/(001)Cr Magnetic Superlattices*, Phys. Rev. Lett. **61**, 2472 (1988).

[11] G. Binasch, P. Grünberg, F. Saurenbach, and W. Zinn, *Enhanced magnetoresistance in layered magnetic structures with antiferromagnetic interlayer exchange*, Phys. Rev. B **39**, 4828(R) (1989).

[12] M. Kölling, *Revolution auf der Festplatte*, Technology Review, Available (in German) at https://www.heise.de/tr/artikel/Revolution-auf-der-Festplatte-279355.html (2007).

[13] E. Hirota, H. Sakakima, and K. Inomata, *Giant Magneto-Resistance Devices*, Vol. 40, Springer Series in Surface Sciences (Springer-Verlag, Berlin, Heidelberg, 2002).

[14] S. S. P. Parkin, "Applications of magnetic nanostructures", in *Spin Dependent Transport in Magnetic Nanostructures*, edited by S. Maekawa and T. Shinjo (Taylor and Francis, New York, 2002), pp. 237–271.

[15] J. M. Slaughter, M. DeHerrera, and H. Dürr, "Magnetoresistive RAM", in *Nanoelectronics and Information Technology*, edited by R. Waser (Wiley-VCH and Co. KGaA, Weinheim, 2003), pp. 591–606.

[16] S. Bhatti, R. Sbiaa, A. Hirohata, H. Ohno, S. Fukami, and S. Piramanayagam, *Spintronics based random access memory: a review*, Mater. Today **20**, 530 (2017).

[17] *Moore's Law and Murphy's Law*, Silicon Palms (Internet blog), Available at http://www.siliconpalms.com/moores-law-and-murphys-law/ (2019).

[18] L. Esaki, P. J. Stiles, and S. von Molnar, *Magnetointernal Field Emission in Junctions of Magnetic Insulators*, Phys. Rev. Lett. **19**, 852 (1967).

[19] T. Kasuya and A. Yanase, *Anomalous Transport Phenomena in Eu-Chalcogenide Alloys*, Rev. Mod. Phys. **40**, 684 (1968).

[20] E. L. Nagaev, *Physics of Magnetic Semiconductors* (Mir Publishers, Moscow, 1983).

[21] J. S. Moodera, X. Hao, G. A. Gibson, and R. Meservey, *Electron-Spin Polarization in Tunnel Junctions in Zero Applied Field with Ferromagnetic EuS Barriers*, Phys. Rev. Lett. **61**, 637 (1988).

[22] X. Hao, J. S. Moodera, and R. Meservey, *Spin-filter effect of ferromagnetic europium sulfide tunnel barriers*, Phys. Rev. B **42**, 8235 (1990).

[23] P. M. Tedrow and R. Meservey, *Spin-Dependent Tunneling into Ferromagnetic Nickel*, Phys. Rev. Lett. **26**, 192 (1971).

[24] P. M. Tedrow and R. Meservey, *Spin Polarization of Electrons Tunneling from Films of Fe, Co, Ni, and Gd*, Phys. Rev. B **7**, 318 (1973).

[25] R. Meservey and P. M. Tedrow, *Spin-polarized electron tunneling*, Phys. Rep. **238**, 173 (1994).

[26] D. D. Awschalom and M. E. Flatté, *Challenges for semiconductor spintronics*, Nat. Phys. **3**, 153 (2007).

[27] J. Fabian, A. Matos-Abiague, C. Ertler, P. Stano, and I. Žutić, *Semiconductor Spintronics*, Acta Phys. Slovaca **57**, 565 (2007).

[28] T. Schäpers, *Semiconductor Spintronics* (De Gruyter, Berlin, Boston, Jan. 2016), pp. 305–306.

[29] S. Datta and B. Das, *Electronic analog of the electro-optic modulator*, Appl. Phys. Lett. **56**, 665 (1990).

[30] A. G. Aronov, *Spin injection in metals and polarization of nuclei*, Pis'ma Zh. Eksp. Teor. Fiz. **24**, 37 (1976).
English translation: JETP Lett. **24**, 32 (1976).

[31] W. G. Clark and G. Feher, *Nuclear Polarization in InSb by a dc Current*, Phys. Rev. Lett. **10**, 134 (1963).
Erratum: Phys. Rev. Lett. **12**, 717(E) (1964).

[32] M. Johnson and R. H. Silsbee, *Interfacial charge-spin coupling: Injection and detection of spin magnetization in metals*, Phys. Rev. Lett. **55**, 1790 (1985).

[33] M. Johnson and R. H. Silsbee, *Spin-injection experiment*, Phys. Rev. B **37**, 5326 (1988).

[34] R. R. Parsons, *Band-To-Band Optical Pumping in Solids and Polarized Photoluminescence*, Phys. Rev. Lett. **23**, 1152 (1969).

[35] A. I. Ekimov and V. I. Safarov, *Optical orientation of carriers in interband transitions in semiconductors*, Pis'ma Zh. Eksp. Teor. Fiz. **12**, 293 (1970).
English translation: JETP Lett. **12**, 198 (1970).

[36] A. I. Ekimov and V. I. Safarov, *Observation of optical orientation of equilibrium electrons in n-type semiconductors*, Pis'ma Zh. Eksp. Teor. Fiz. **13**, 251 (1971).
English translation: JETP Lett. **13**, 177 (1971).

[37] B. I. Zakharchenya, V. G. Fleisher, R. I. Dzhioev, Y. P. Veshchunov, and I. B. Rusanov, *Effect of optical orientation of electron spins in a GaAs crystal*, Pis'ma Zh. Eksp. Teor. Fiz. **13**, 195 (1971).
English translation: JETP Lett. **13**, 137 (1971).

[38] M. Oestreich, J. Hübner, D. Hägele, M. Bender, N. Gerhardt, M. Hofmann, W. W. Rühle, H. Kalt, T. Hartmann, P. Klar, W. Heimbrodt, and W. Stolz, "Spintronics: Spin Electronics and Optoelectronics in Semiconductors", in *Advances in Solid State Physics*, edited by B. Kramer (Springer-Verlag, 2001), pp. 173–186.

[39] R. J. Elliott, *Theory of the Effect of Spin-Orbit Coupling on Magnetic Resonance in Some Semiconductors*, Phys. Rev. **96**, 266 (1954).

[40] Y. Yafet, "g factors and spin-lattice relaxation of conduction electrons", in *Solid State Physics*, Vol. 14, edited by F. Seitz and D. Turnbull (Academic, New York, 1963), p. 2.

[41] M. I. Dyakonov and V. I. Perel, *Current-induced spin orientation of electrons in semiconductors*, Phys. Lett. A **35**, 459 (1971).

[42] M. Johnson and R. H. Silsbee, *Coupling of electronic charge and spin at a ferromagnetic-paramagnetic metal interface*, Phys. Rev. B **37**, 5312 (1988).

[43] J. Slonczewski, *Current-driven excitation of magnetic multilayers*, J. Magn. Magn. Mater. **159**, L1 (1996).

[44] L. Berger, *Emission of spin waves by a magnetic multilayer traversed by a current*, Phys. Rev. B **54**, 9353 (1996).

[45] H. Yang, S.-H. Yang, S. Takahashi, S. Maekawa, and S. S. P. Parkin, *Extremely long quasiparticle spin lifetimes in superconducting aluminium using MgO tunnel spin injectors*, Nat. Mater. **9**, 586 (2010).

[46] B. Li, N. Roschewsky, B. A. Assaf, M. Eich, M. Epstein-Martin, D. Heiman, M. Münzenberg, and J. S. Moodera, *Superconducting Spin Switch with Infinite Magnetoresistance Induced by an Internal Exchange Field*, Phys. Rev. Lett. **110**, 097001 (2013).

[47] J. Bardeen, L. N. Cooper, and J. R. Schrieffer, *Microscopic Theory of Superconductivity*, Phys. Rev. **106**, 162 (1957).

[48] J. Bardeen, L. N. Cooper, and J. R. Schrieffer, *Theory of Superconductivity*, Phys. Rev. **108**, 1175 (1957).

[49] J. Linder and J. W. A. Robinson, *Superconducting spintronics*, Nature Phys. **11**, 307 (2015).

[50] M. Eschrig, *Spin-polarized supercurrents for spintronics*, Phys. Today **64**, 43 (2011).

[51] K. Ohnishi, S. Komori, G. Yang, K.-R. Jeon, L. A. B. Olde Olthof, X. Montiel, M. G. Blamire, and J. W. A. Robinson, *Spin-transport in superconductors*, Appl. Phys. Lett. **116**, 130501 (2020).

[52] M. B. Maple, *Superconductivity seen in ferromagnet*, Phys. World **10**, 27 (1997).

[53] P. Fulde and R. A. Ferrell, *Superconductivity in a Strong Spin-Exchange Field*, Phys. Rev. **135**, A550 (1964).

[54] I. Larkin and Y. N. Ovchinnikov, *Nonuniform State of Superconductors*, Zh. Eksp. Teor. Fiz. **47**, 1136 (1964).

[55] L. N. Bulaevskii, V. V. Kuzii, and A. A. Sobyanin, *Superconducting system with weak coupling to the current in the ground state*, Pis'ma Zh. Eksp. Teor. Fiz. **25**, 314 (1977).
English translation: JETP Lett. **25**, 290 (1977).

[56] V. V. Ryazanov, V. A. Oboznov, A. Y. Rusanov, A. V. Veretennikov, A. A. Golubov, and J. Aarts, *Coupling of Two Superconductors through a Ferromagnet: Evidence for a π Junction*, Phys. Rev. Lett. **86**, 2427 (2001).

[57] L. B. Ioffe, V. B. Geshkenbein, M. V. Feigel'man, A. L. Fauchère, and G. Blatter, *Environmentally decoupled sds-wave Josephson junctions for quantum computing*, Nature **398**, 679 (1999).

[58] J. E. Mooij, T. P. Orlando, L. Levitov, L. Tian, C. H. van der Wal, and S. Lloyd, *Josephson Persistent-Current Qubit*, Science **285**, 1036 (1999).

[59] G. Blatter, V. B. Geshkenbein, and L. B. Ioffe, *Design aspects of superconducting-phase quantum bits*, Phys. Rev. B **63**, 174511 (2001).

[60] A. V. Ustinov and V. K. Kaplunenko, *Rapid single-flux quantum logic using π-shifters*, J. Appl. Phys. **94**, 5405 (2003).

[61] T. Yamashita, K. Tanikawa, S. Takahashi, and S. Maekawa, *Superconducting π Qubit with a Ferromagnetic Josephson Junction*, Phys. Rev. Lett. **95**, 097001 (2005).

[62] A. K. Feofanov, V. A. Oboznov, V. V. Bol'ginov, J. Lisenfeld, S. Poletto, V. V. Ryazanov, A. N. Rossolenko, M. Khabipov, D. Balashov, A. B. Zorin, P. N. Dmitriev, V. P. Koshelets, and A. V. Ustinov, *Implementation of superconductor/ferromagnet/ superconductor π-shifters in superconducting digital and quantum circuits*, Nat. Phys. **6**, 593 (2010).

[63] M. I. Khabipov, D. V. Balashov, F. Maibaum, A. B. Zorin, V. A. Oboznov, V. V. Bolginov, A. N. Rossolenko, and V. V. Ryazanov, *A single flux quantum circuit with a ferromagnet-based Josephson π-junction*, Supercond. Sci. Technol. **23**, 045032 (2010).

[64] M. H. Devoret and R. J. Schoelkopf, *Superconducting Circuits for Quantum Information: An Outlook*, Science **339**, 1169 (2013).

[65] F. S. Bergeret, A. F. Volkov, and K. B. Efetov, *Long-Range Proximity Effects in Superconductor-Ferromagnet Structures*, Phys. Rev. Lett. **86**, 4096 (2001).

[66] A. Kadigrobov, R. I. Shekhter, and M. Jonson, *Quantum spin fluctuations as a source of long-range proximity effects in diffusive ferromagnet-super conductor structures*, Europhys. Lett. **54**, 394 (2001).

[67] F. S. Bergeret, A. F. Volkov, and K. B. Efetov, *Josephson current in superconductor-ferromagnet structures with a nonhomogeneous magnetization*, Phys. Rev. B **64**, 134506 (2001).

[68] M. Eschrig, J. Kopu, J. C. Cuevas, and G. Schön, *Theory of Half-Metal/Superconductor Heterostructures*, Phys. Rev. Lett. **90**, 137003 (2003).

[69] F. S. Bergeret, A. F. Volkov, and K. B. Efetov, *Odd triplet superconductivity and related phenomena in superconductor-ferromagnet structures*, Rev. Mod. Phys. **77**, 1321 (2005).

[70] M. Houzet and A. I. Buzdin, *Long range triplet Josephson effect through a ferromagnetic trilayer*, Phys. Rev. B **76**, 060504(R) (2007).

[71] M. Eschrig and T. Löfwander, *Triplet supercurrents in clean and disordered half-metallic ferromagnets*, Nat. Phys. **4**, 138 (2008).

[72] R. Grein, M. Eschrig, G. Metalidis, and G. Schön, *Spin-Dependent Cooper Pair Phase and Pure Spin Supercurrents in Strongly Polarized Ferromagnets*, Phys. Rev. Lett. **102**, 227005 (2009).

[73] N. Banerjee, J. W. A. Robinson, and M. G. Blamire, *Reversible control of spin-polarized supercurrents in ferromagnetic Josephson junctions*, Nat. Commun. **5**, 1 (2014).

[74] R. S. Keizer, S. T. B. Goennenwein, T. M. Klapwijk, G. Miao, G. Xiao, and A. Gupta, *A spin triplet supercurrent through the half-metallic ferromagnet CrO_2*, Nature **439**, 825 (2006).

[75] Z. M. Zheng and D. Y. Xing, *Josephson supercurrent with spin-equal pairing through a half-metallic link*, J. Phys.: Condens. Matter **21**, 385703 (2009).

[76] M. Duckheim and P. W. Brouwer, *Andreev reflection from noncentrosymmetric superconductors and Majorana bound-state generation in half-metallic ferromagnets*, Phys. Rev. B **83**, 054513 (2011).

[77] F. S. Bergeret and I. V. Tokatly, *Singlet-Triplet Conversion and the Long-Range Proximity Effect in Superconductor-Ferromagnet Structures with Generic Spin Dependent Fields*, Phys. Rev. Lett. **110**, 117003 (2013).

[78] F. S. Bergeret and I. V. Tokatly, *Spin-orbit coupling as a source of long-range triplet proximity effect in superconductor-ferromagnet hybrid structures*, Phys. Rev. B **89**, 134517 (2014).

[79] S. H. Jacobsen and J. Linder, *Giant triplet proximity effect in π-biased Josephson junctions with spin-orbit coupling*, Phys. Rev. B **92**, 024501 (2015).

[80] X. Waintal and P. W. Brouwer, *Magnetic exchange interaction induced by a Josephson current*, Phys. Rev. B **65**, 054407 (2002).

[81] E. Zhao and J. A. Sauls, *Theory of nonequilibrium spin transport and spin-transfer torque in superconducting-ferromagnetic nanostructures*, Phys. Rev. B **78**, 174511 (2008).

[82] F. Konschelle and A. Buzdin, *Magnetic Moment Manipulation by a Josephson Current*, Phys. Rev. Lett. **102**, 017001 (2009).
Erratum: Phys. Rev. Lett. **123**, 169901(E) (2019).

[83] J. Linder and T. Yokoyama, *Supercurrent-induced magnetization dynamics in a Josephson junction with two misaligned ferromagnetic layers*, Phys. Rev. B **83**, 012501 (2011).

[84] I. Kulagina and J. Linder, *Spin supercurrent, magnetization dynamics, and φ-state in spin-textured Josephson junctions*, Phys. Rev. B **90**, 054504 (2014).

[85] P. G. De Gennes, *Coupling between ferromagnets through a superconducting layer*, Phys. Lett. **23**, 10 (1966).

[86] J. J. Hauser, *Coupling Between Ferrimagnetic Insulators Through a Superconducting Layer*, Phys. Rev. Lett. **23**, 374 (1969).

[87] E. C. Gingrich, B. M. Niedzielski, J. A. Glick, Y. Wang, D. L. Miller, R. Loloee, W. P. Pratt Jr., and N. O. Birge, *Controllable 0-π Josephson junctions containing a ferromagnetic spin valve*, Nat. Phys. **12**, 564 (2016).

[88] O. Vávra, R. Soni, A. Petraru, N. Himmel, I. Vávra, J. Fabian, H. Kohlstedt, and C. Strunk, *Coexistence of tunneling magnetoresistance and Josephson effects in SFIFS junctions*, AIP Adv. **7**, 025008 (2017).

[89] E. Rutherford, *LXXIX. The Scattering of α and β Particles by Matter and the Structure of the Atom*, Philos. Mag. **21**, 669 (1911).

[90] H. K. Onnes, *Further experiments with liquid helium. C. On the change of electric resistance of pure metals at very low temperatures etc. IV. The resistance of pure mercury at helium temperatures*, Comm. Phys. Lab. Univ. Leiden **120b**, 1274 (1911).

[91] H. K. Onnes, *Further Experiments with Liquid Helium. D. On the Change of the Electrical Resistance of Pure Metals at very low Temperatures, etc. V. The Disappearance of the resistance of mercury*, Comm. Phys. Lab. Univ. Leiden **122b**, 113 (1911).

[92] H. K. Onnes, *Further experiments with Liquid Helium. G. On the Electrical Resistance of Pure Metals, etc. VI. On the Sudden Change in the Rate at which the Resistance of Mercury Disappears.* Comm. Phys. Lab. Univ. Leiden **124c**, 818 (1911).

[93] B. D. Josephson, *Possible new effects in superconductive tunnelling*, Phys. Lett. **1**, 251 (1962).

[94] R. C. Jaklevic, J. Lambe, A. H. Silver, and J. E. Mercereau, *Quantum Interference Effects in Josephson Tunneling*, Phys. Rev. Lett. **12**, 159 (1964).

[95] S. K. Range, *Gravity Probe B. Examining Einstein's Universe with Gyroscopes*, Available at `https://einstein.stanford.edu/content/education/GP-B_T-Guide4-2008.pdf` (National Aeronautics and Space Administration, 2004).

[96] D. D. Laukien and W. H. Tschopp, *Superconducting NMR Magnet Design*, Concepts Magn. Reson. **6**, 255 (1994).

[97] L. R. Evans, *LHC accelerator physics and technology challenges*, Proc. 1999 Part. Accel. Conf. (1999).

[98] *Facts and figures about the LHC*, CERN, Available at `https://home.cern/resources/faqs/facts-and-figures-about-lhc`.

[99] R. de Bruyn Ouboter, *Heike Kamerlingh Onnes's Discovery of Superconductivity*, Sci. Am. **276**, 98 (1997).

[100] D. van Delft and P. Kes, *The discovery of superconductivity*, Phys. Today **63**, 38 (2010).

[101] J. Wisniak, *William Ramsay*, Educ. Química **19**, 303 (2011).

[102] H. K. Onnes, *Investigations into the Properties of Substances at Low Temperatures, which Have Led, amongst Other Things, to the Preparation of Liquid Helium*, Available at `https://www.nobelprize.org/prizes/physics/1913/onnes/lecture/`, Nobel Lecture (1913).

[103] K. Fossheim and A. Sudbø, *Superconductivity: Physics and Applications* (John Wiley & Sons, Ltd., 2004).

[104] N. W. Ashcroft and N. D. Mermin, *Festkörperphysik* (Oldenbourg Verlag, 2012).

[105] W. Meissner and R. Ochsenfeld, *Ein neuer Effekt bei Eintritt der Supraleitfähigkeit*, Naturwissenschaften **21**, 787 (1933).

[106] V. L. Ginzburg, *Ferromagnetic Superconductors*, Zh. Eksp. Teor. Fiz. **31**, 202 (1957).
English translation: Sov. Phys. JETP **4**, 153 (1957).

[107] R. Wördenweber, *Engineering of superconductors and superconducting devices using artificial pinning sites*, Phys. Sci. Rev. **2**, 1 (2017).

[108] F. London and H. London, *The Electromagnetic Equations of the Supraconductor*, Proc. Roy. Soc. A **149**, 71 (1935).

[109] J. C. Maxwell, *III. On Physical Lines of Force*, Philos. Mag. **90**, 11 (1861).

[110] W. Meissner and H. Franz, *Messungen mit Hilfe von flüssigem Helium. VIII. Supraleitfähigkeit von Niobium*, Zeitschrift für Physik **63**, 558 (1930).

[111] C. W. Chu, P. H. Hor, R. L. Meng, L. Gao, Z. J. Huang, and Y. Q. Wang, *Evidence for superconductivity above 40 K in the La-Ba-Cu-O compound system*, Phys. Rev. Lett. **58**, 405 (1987).

[112] R. J. Cava, A. W. Hewat, E. A. Hewat, B. Batlogg, M. Marezio, K. M. Rabe, J. J. Krajewski, W. F. Peck Jr., and L. W. Rupp Jr., *Structural anomalies, oxygen ordering and superconductivity in oxygen deficient $Ba_2YCu_3O_x$*, Physica C **165**, 419 (1990).

[113] C. W. Chu, L. Gao, F. Chen, Z. J. Huang, R. L. Meng, and Y. Y. Xue, *Superconductivity above 150 K in $HgBa_2Ca_2Cu_3O_{8+\delta}$ at high pressures*, Nature **365**, 323 (1993).

[114] J. Akimitsu, *Symposium on Transition Metal Oxides* (Sendai, Japan, 2001).

[115] J. Nagamatsu, N. Nakagawa, T. Muranaka, Y. Zenitani, and J. Akimitsu, *Superconductivity at 39 K in magnesium diboride*, Nature **410**, 63 (2001).

[116] H. Y. Zhai, H. M. Christen, L. Zhang, C. Cantoni, M. Paranthaman, B. C. Sales, D. K. Christen, and D. H. Lowndes, *Superconducting magnesium diboride films on Si with $T_{c0} \sim 24$ K grown via vacuum annealing from stoichiometric precursors*, Appl. Phys. Lett. **79**, 2603 (2001).

[117] A. P. Drozdov, M. I. Eremets, I. A. Troyan, V. Ksenofontov, and S. I. Shylin, *Conventional superconductivity at 203 kelvin at high pressures in the sulfur hydride system*, Nature **525**, 73 (2015).

[118] E. Cartlidge, *Superconductor high spurs wave of physics*, Nature **524**, 277 (2015).

[119] Y. Cao, V. Fatemi, A. Demir, S. Fang, S. L. Tomarken, J. Y. Luo, J. D. Sanchez-Yamagishi, K. Watanabe, T. Taniguchi, E. Kaxiras, R. C. Ashoori, and P. Jarillo-Herrero, *Correlated insulator behaviour at half-filling in magic-angle graphene superlattices*, Nature **556**, 80 (2018).

[120] Y. Cao, V. Fatemi, S. Fang, K. Watanabe, T. Taniguchi, E. Kaxiras, and P. Jarillo-Herrero, *Unconventional superconductivity in magic-angle graphene superlattices*, Nature **556**, 43 (2018).

[121] E. Snider, N. Dasenbrock-Gammon, R. McBride, M. Debessai, H. Vindana, K. Vencatasamy, K. V. Lawler, A. Salamat, and R. P. Dias, *Room-temperature superconductivity in a carbonaceous sulfur hydride*, Nature **586**, 373 (2020).

[122] A. Mourachkine, *Room-Temperature Superconductivity* (Cambridge International Science Publishing, 2004).

[123] J. F. Schooley, W. R. Hosler, and M. L. Cohen, *Superconductivity in Semiconducting $SrTiO_3$*, Phys. Rev. Lett. **12**, 474 (1964).

[124] M. Tinkham, *Introduction to Superconductivity* (McGraw-Hill, Inc., 1996).

[125] L. D. Landau, *On the theory of phase transitions*, Zh. Eksp. Teor. Fiz. **7**, 19 (1937).
German translation: Phys. Z. Sowjet. **11**, 26 (1937).
English translation in: *Collected papers of L. D. Landau*, edited by D. Ter-Haar (Pergamon Press Ltd., Oxford, 1965), pp. 193–216.

[126] V. L. Ginzburg and L. D. Landau, *To the Theory of Superconductivity*, Zh. Eksp. Teor. Fiz. **20**, 1064 (1950).
English translation in: *Collected papers of L. D. Landau*, edited by D. Ter-Haar (Pergamon Press Ltd., Oxford, 1965), pp. 546–568.

[127] B. D. Josephson, *Coupled Superconductors*, Rev. Mod. Phys. **36**, 216 (1964).

[128] R. Holm and W. Meissner, *Messungen mit Hilfe von flüssigem Helium. XIII. Kontaktwiderstand zwischen Supraleitern und Nichtsupraleitern.* Zeitschrift für Physik **74**, 715 (1932).

[129] L. P. Gor'kov, *Microscopic Derivation of the Ginzburg-Landau Equations in the Theory of Superconductivity*, Zh. Eksp. Teor. Fiz. **36**, 1918 (1959).
English translation: Sov. Phys. JETP **9**, 1364 (1959).

[130] T. Saint-James and G. Sarma, *Type-II Superconductivity* (Pergamon Press Ltd., Oxford, 1969).

[131] R. Hübener, *Magnetic Flux Structures in Superconductors*, edited by P. Fulde (Springer-Verlag, 1992).

[132] C. Kittel, *Introduction to Solid State Physics* (John Wiley & Sons, Ltd., 1996).

[133] J. Bardeen, *Semiconductor Research Leading to the Point Contact Transistor*, Available at `https://www.nobelprize.org/prizes/physics/1956/bardeen/lecture/`, Nobel Lecture (1956).

[134] L. N. Cooper, *Bound Electron Pairs in a Degenerate Fermi Gas*, Phys. Rev. **104**, 1189 (1956).

[135] S. Ran, C. Eckberg, Q.-P. Ding, Y. Furukawa, T. Metz, S. R. Saha, I.-L. Liu, M. Zic, H. Kim, J. Paglione, and N. P. Butch, *Nearly ferromagnetic spin-triplet superconductivity*, Science **365**, 684 (2019).

[136] C. Timm, *Theory of Superconductivity*, Lecture Notes (TU Dresden, 2011/2012).

[137] N. N. Bogoljubov, *On a New Method in the Theory of Superconductivity*, Il Nuovo Cimento **7**, 794 (1958).

[138] I. Giaever, *Energy Gap in Superconductors Measured by Electron Tunneling*, Phys. Rev. Lett. **5**, 147 (1960).

[139] P. G. De Gennes, *Superconductivity of Metals and Alloys* (Addison Wesley, Redwood City, 1989).

[140] S. Datta, P. F. Bagwell, and M. P. Anantram, *Scattering Theory of Transport for Mesoscopic Superconductors*, ECE Tech. Reports **107** (1996).

[141] K. Halterman and O. T. Valls, *Proximity effects at ferromagnet-superconductor interfaces*, Phys. Rev. B **65**, 014509 (2001).

[142] E. Beaurepaire, J.-C. Merle, A. Daunois, and J.-Y. Bigot, *Ultrafast Spin Dynamics in Ferromagnetic Nickel*, Phys. Rev. Lett. **76**, 4250 (1996).

[143] E. C. Stoner, *Collective electron ferromagnetism in metals and alloys*, J. Phys. Radium **12**, 372 (1951).

[144] S. Hunklinger, *Festkörperphysik* (Oldenbourg Wissenschaftsverlag, 2011).

[145] M. Bowen, A. Barthélémy, M. Bibes, E. Jacquet, J. P. Contour, A. Fert, D. Wortmann, and S. Blügel, *Half-metallicity proven using fully spin-polarized tunnelling*, J. Phys.: Condens. Matter **17**, L407 (2005).

[146] J. Hübner, S. Döhrmann, D. Hägele, and M. Oestreich, *Temperature-dependent electron Landé g factor and the interband matrix element of GaAs*, Phys. Rev. B **79**, 193307 (2009).

[147] R. Winkler, *Spin-Orbit Coupling Effects in Two-Dimensional Electron and Hole systems* (Springer-Verlag, 2003).

[148] H. A. Kramers, *Théorie générale de la rotation paramagnétique daws lew cristaux*, Proceedings Koninklijke Akademie van Wetenschappen **33**, 959 (1930).

[149] Y. A. Bychkov and E. I. Rashba, *Oscillatory effects and the magnetic susceptibility of carriers in inversion layers*, J. Phys. C **17**, 6039 (1984).

[150] Y. A. Bychkov and E. I. Rashba, *Properties of a 2D electron gas with lifted spectral degeneracy*, Pis'ma Zh. Eksp. Teor. Fiz. **39**, 66 (1984).
English translation: JETP Lett. **39**, 78 (1984).

[151] E. O. Kane, *Band structure of indium antimonide*, J. Phys. Chem. Solids **1**, 249 (1957).

[152] G. Dresselhaus, *Spin-Orbit Coupling Effects in Zinc Blende Structures*, Phys. Rev. **100**, 580 (1955).

[153] M. Razavy, *Quantum Theory of Tunneling* (World Scientific, 2003).

[154] L. Esaki, Y. Kurose, and T. Suzuki, *Ge p–n Junction – Internal Field Emission*, Meeting Abstracts of the Physical Society of Japan **12**, 85 (1957).

[155] L. Esaki, *New Phenomenon in Narrow Germanium p – n Junctions*, Phys. Rev. **109**, 603 (1958).

[156] G. Binnig and H. Rohrer, *Scanning Tunneling Microscopy*, Surf. Sci. **126**, 236 (1983).

[157] S. K. Upadhyay, A. Palanisami, R. N. Louie, and R. A. Buhrman, *Probing Ferromagnets with Andreev Reflection*, Phys. Rev. Lett. **81**, 3247 (1998).

[158] R. J. Soulen Jr., M. S. Osofsky, B. Nadgorny, T. Ambrose, P. Broussard, S. F. Cheng, J. Byers, C. T. Tanaka, J. Nowack, J. S. Moodera, G. Laprade, A. Barry, and M. D. Coey, *Andreev reflection: A new means to determine the spin polarization of ferromagnetic materials*, J. Appl. Phys. **85**, 4589 (1999).

[159] J. Aumentado and V. Chandrasekhar, *Mesoscopic ferromagnet-superconductor junctions and the proximity effect*, Phys. Rev. B **64**, 054505 (2001).

[160] J. Gramich, P. Brenner, C. Sürgers, H. v. Löhneysen, and G. Goll, *Experimental verification of contact-size estimates in point-contact spectroscopy on superconductor/ferromagnet heterocontacts*, Phys. Rev. B **86**, 155402 (2012).

[161] C. Morrison, D. Wang, G. J. Bowden, R. C. C. Ward, and P. A. J. de Groot, *Determination of the spin polarization of RFe_2 (R = Dy, Er, Y) by point contact Andreev reflection*, J. Appl. Phys. **111**, 063917 (2012).

[162] V. N. Krivoruchko, A. I. D'yachenko, and V. Y. Tarenkov, *Point-contact Andreev-reflection spectroscopy of doped manganites: Charge carrier spin-polarization and proximity effects (Review Article)*, Low Temp. Phys. **39**, 211 (2013).

[163] F. Giubileo, F. Romeo, R. Citro, A. Di Bartolomeo, C. Attanasio, C. Cirillo, A. Polcari, and P. Romano, *Point contact Andreev reflection spectroscopy on ferromagnet/superconductor bilayers*, Physica C **503**, 158 (2014).

[164] G. E. Blonder, M. Tinkham, and T. M. Klapwijk, *Transition from metallic to tunneling regimes in superconducting microconstrictions: Excess current, charge imbalance, and supercurrent conversion*, Phys. Rev. B **25**, 4515 (1982).

[165] M. J. M. de Jong and C. W. J. Beenakker, *Andreev Reflection in Ferromagnet-Superconductor Junctions*, Phys. Rev. Lett. **74**, 1657 (1995).

[166] I. Žutić and O. T. Valls, *Spin-polarized tunneling in ferromagnet/unconventional superconductor junctions*, Phys. Rev. B **60**, 6320 (1999).

[167] I. Žutić and O. T. Valls, *Tunneling spectroscopy for ferromagnet/superconductor junctions*, Phys. Rev. B **61**, 1555 (2000).
Erratum: Phys. Rev. B **61**, 14845(E) (2000).

[168] J. Linder and A. Sudbø, *Tunneling conductance in s- and d-wave superconductor-graphene junctions: Extended Blonder-Tinkham-Klapwijk formalism*, Phys. Rev. B **77**, 064507 (2008).

[169] R. Mélin, *Spin-resolved Andreev reflection in ferromagnet-superconductor junctions with Zeeman splitting*, Europhys. Lett. **51**, 202 (2000).

[170] T. Yokoyama and Y. Tanaka, *Theory of the tunneling spectroscopy of ferromagnetic superconductors*, Phys. Rev. B **75**, 132503 (2007).

[171] F. Giazotto and F. Taddei, *Superconductors as spin sources for spintronics*, Phys. Rev. B **77**, 132501 (2008).

[172] H. Emamipour, *Spin-polarized current in Zeeman-split d-wave superconductor/quantum wire junctions*, Solid State Commun. **236**, 17 (2016).

[173] T. Hashimoto, A. A. Golubov, Y. Tanaka, and J. Linder, *Tunability of Andreev levels via spin-orbit coupling in Zeeman-split Josephson junctions*, Phys. Rev. B **96**, 134508 (2017).

[174] H. Nam, H. Chen, T. Liu, J. Kim, C. Zhang, J. Yong, T. R. Lemberger, P. A. Kratz, J. R. Kirtley, K. Moler, P. W. Adams, A. H. MacDonald, and C.-K. Shih, *Ultrathin two-dimensional superconductivity with strong spin–orbit coupling*, Proc. Natl. Acad. Sci. **113**, 10513 (2016).

[175] J. Flouquet and A. Buzdin, *Ferromagnetic superconductors*, Phys. World **15**, 41 (2002).

[176] P. Högl, A. Matos-Abiague, I. Žutić, and J. Fabian, *Magnetoanisotropic Andreev Reflection in Ferromagnet-Superconductor Junctions*, Phys. Rev. Lett. **115**, 116601 (2015).
ERRATUM: Phys. Rev. Lett. **115**, 159902(E) (2015).

[177] K. K. Likharev, *Superconducting weak links*, Rev. Mod. Phys. **51**, 101 (1979).

[178] C. W. J. Beenakker, *Random-matrix theory of quantum transport*, Rev. Mod. Phys. **69**, 731 (1997).

[179] A. F. Andreev, *The Thermal Conductivity of the Intermediate State in Superconductors*, Zh. Eksp. Teor. Fiz. **46**, 1823 (1964).
ENGLISH TRANSLATION: J. Exp. Theor. Phys. **19**, 1228 (1964).

[180] T. M. Klapwijk, *Proximity Effect From an Andreev Perspective*, J. Supercond. **17**, 593 (2004).

[181] W. H. Press, S. A. Teukolsky, W. T. Vetterling, and B. P. Flannery, *Numerical Recipes. The Art of Scientific Computing*, 3rd ed. (Cambridge University Press, Cambridge, 2007).

[182] I. Martínez, P. Högl, C. González-Ruano, J. P. Cascales, C. Tiusan, Y. Lu, M. Hehn, A. Matos-Abiague, J. Fabian, I. Žutić, and F. G. Aliev, *Interfacial Spin-Orbit Coupling: A Platform for Superconducting Spintronics*, Phys. Rev. Appl. **13**, 014030 (2020).

[183] S. De Franceschi, F. Giazotto, F. Beltram, L. Sorba, M. Lazzarino, and A. Franciosi, *Andreev reflection in Si-engineered Al/InGaAs hybrid junctions*, Appl. Phys. Lett. **73**, 3890 (1998).

[184] V. A. Vas'ko, K. R. Nikolaev, V. A. Larkin, P. A. Kraus, and A. M. Goldman, *Differential conductance of the ferromagnet/superconductor interface of* $DyBa_2Cu_3O_7/La_{2/3}Ba_{1/3}MnO_3$ *heterostructures*, Appl. Phys. Lett. **73**, 844 (1998).

[185] Z. Wan, A. Kazakov, M. J. Manfra, L. N. Pfeiffer, K. W. West, and L. P. Rokhinson, *Induced superconductivity in high-mobility two-dimensional electron gas in gallium arsenide heterostructures*, Nat. Commun. **6**, 7426 (2015).

[186] B. S. Chandrasekhar, *A note on the maximum critical field of high-field superconductors*, Appl. Phys. Lett. **1**, 7 (1962).

[187] A. M. Clogston, *Upper Limit for the Critical Field in Hard Superconductors*, Phys. Rev. Lett. **9**, 266 (1962).

[188] C. Pfleiderer, M. Uhlarz, S. M. Hayden, R. Vollmer, H. v. Löhneysen, N. R. Bernhoeft, and G. G. Lonzarich, *Coexistence of superconductivity and ferromagnetism in the d-band metal* $ZrZn_2$, Nature **412**, 58 (2001).
ERRATUM: Nature **412**, 660 (2001).

[189] D. Aoki, A. Huxley, E. Ressouche, D. Braithwaite, J. Flouquet, J.-P. Brison, E. Lhotel, and C. Paulsen, *Coexistence of superconductivity and ferromagnetism in URhGe*, Nature **413**, 613 (2001).

[190] S. S. Saxena, P. Agarwal, K. Ahilan, F. M. Grosche, R. K. W. Haselwimmer, M. J. Steiner, E. Pugh, I. R. Walker, S. R. Julian, P. Monthoux, G. G. Lonzarich, A. Huxley, I. Sheikin, D. Braithwaite, and J. Flouquet, *Superconductivity on the border of itinerant-electron ferromagnetism in* UGe_2, Nature **406**, 587 (2000).

[191] B. Wu, G. Bastien, M. Taupin, C. Paulsen, L. Howald, D. Aoki, and J.-P. Brison, *Pairing mechanism in the ferromagnetic superconductor UCoGe*, Nat. Commun. **8**, 14480 (2017).

[192] S. Redner, *Citation Statistics From More Than a Century of Physical Review*, arXiv: 0407137v1.

[193] B. N. Taylor and E. Burstein, *Excess Currents in Electron Tunneling Between Superconductors*, Phys. Rev. Lett. **10**, 14 (1963).

[194] C. J. Adkins, *Two-Particle Tunnelling between Superconductors*, Philos. Mag. **8**, 1051 (1963).

[195] C. J. Adkins, *Multi-Particle Tunneling between Superconductors*, Rev. Mod. Phys. **36**, 211 (1964).

[196] W. M. van Huffelen, T. M. Klapwijk, D. R. Heslinga, M. J. de Boer, and N. van der Post, *Carrier transport in mesoscopic silicon-coupled superconducting junctions*, Phys. Rev. B **47**, 5170 (1993).

[197] J. P. Carbotte, *Properties of boson-exchange superconductors*, Rev. Mod. Phys. **62**, 1027 (1990).

[198] U. Zimmermann, S. Abens, D. Dikin, K. Keck, and V. M. Dmitriev, *Multiple Andreev-reflection in asymmetric superconducting weak-links*, Z. Phys. B **97**, 59 (1995).

[199] M. Kuhlmann, U. Zimmermann, D. Dikin, S. Abens, K. Keck, and V. M. Dmitriev, *Andreev-reflection in semiconductor-coupled superconducting weak-links*, Z. Phys. B **96**, 13 (1994).

[200] J. M. Rowell, *Tunneling between Superconductors*, Rev. Mod. Phys. **36**, 199 (1964).

[201] J. M. Rowell and W. L. Feldmann, *Excess Currents in Superconducting Tunnel Junctions*, Phys. Rev. **172**, 393 (1968).

[202] P. E. Gregers-Hansen, E. Hendricks, M. T. Levinsen, and G. R. Pickett, *Subharmonic Energy-Gap Structure and a Josephson-Radiation-Enhanced Gap in Dayem Bridges*, Phys. Rev. Lett. **31**, 524 (1973).

[203] O. Hoffmann Soerensen, B. Kofoed, N. F. Pedersen, and S. Shapiro, *Effect of rf on subharmonic gap structure in superconducting junctions*, Rev. Phys. Appl. **9**, 153 (1974).

[204] D. G. McDonald, E. G. Johnson, and R. E. Harris, *Modeling Josephson junctions*, Phys. Rev. B **13**, 1028 (1976).

[205] M. Octavio, W. Skocpol, and M. Tinkham, *Improved performance of tin variable-thickness superconducting microbridges*, IEEE Transactions on Magnetics **13**, 739 (1977).

[206] M. Octavio, W. J. Skocpol, and M. Tinkham, *Nonequilibrium-enhanced supercurrents in short superconducting weak links*, Phys. Rev. B **17**, 159 (1978).

[207] Y. Y. Divin and F. Y. Nad', *Dependence of the excess current in superconducting point contacts on temperature and voltage*, Pis'ma Zh. Eksp. Teor. Fiz. **29**, 567 (1979).
English translation: JETP Lett. **29**, 516 (1979).

[208] J. R. Schrieffer and J. W. Wilkins, *Two-Particle Tunneling Processes Between Superconductors*, Phys. Rev. Lett. **10**, 17 (1963).

[209] G. B. Arnold, *Superconducting tunneling without the tunneling Hamiltonian*, J. Low Temp. Phys. **59**, 143 (1985).

[210] G. B. Arnold, *Superconducting tunneling without the tunneling Hamiltonian. II. Subgap harmonic structure*, J. Low Temp. Phys. **68**, 1 (1987).

[211] N. R. Werthamer, *Nonlinear Self-Coupling of Josephson Radiation in Superconducting Tunnel Junctions*, Phys. Rev. **147**, 255 (1966).

[212] S. N. Artemenko, A. F. Volkov, and A. V. Zaitsev, *Theory of the nonstationary Josephson effect in short superconducting contacts*, Zh. Eksp. Teor. Fiz. **76**, 1816 (1979).
English translation: J. Exp. Theor. Phys. **49**, 924 (1979).

[213] A. V. Zaitsev, *Theory of pure short S-c-S and S-c-N microjunctions*, Zh. Eksp. Teor. Fiz. **78**, 221 (1980).
English translation: J. Exp. Theor. Phys. **51**, 111 (1980).

[214] A. V. Zaitsev, Erratum: *Theory of pure short S-c-S and S-c-N microjunctions*, Zh. Eksp. Teor. Fiz. **79**, 2016 (1980).
English translation: J. Exp. Theor. Phys. **52**, 1018 (1980).

[215] T. M. Klapwijk, G. E. Blonder, and M. Tinkham, *Explanation of subharmonic energy gap structure in superconducting contacts*, Physica **109 & 110B**, 1657 (1982).

[216] M. Octavio, M. Tinkham, G. E. Blonder, and T. M. Klapwijk, *Subharmonic energy-gap structure in superconducting constrictions*, Phys. Rev. B **27**, 6739 (1983).

[217] K. Flensberg, J. Bindslev Hansen, and M. Octavio, *Subharmonic energy-gap structure in superconducting weak links*, Phys. Rev. B **38**, 8707 (1988).

[218] K. Flensberg and J. Bindslev Hansen, *Subharmonic energy-gap structure and heating effects in superconducting niobium point contacts*, Phys. Rev. B **40**, 8693 (1989).

[219] J. S. Moodera and R. Meservey, *Superconducting phases of Bi and Ga induced by deposition on a Ni sublayer*, Phys. Rev. B **42**, 179 (1990).

[220] P. LeClair, J. S. Moodera, J. Philip, and D. Heiman, *Coexistence of Ferromagnetism and Superconductivity in Ni/Bi Bilayers*, Phys. Rev. Lett. **94**, 037006 (2005).

[221] C. W. Groth, M. Wimmer, A. R. Akhmerov, and X. Waintal, *Kwant: a software package for quantum transport*, New J. Phys. **16**, 063065 (2014).

[222] Y. M. Blanter and F. W. J. Hekking, *Supercurrent in long SFFS junctions with antiparallel domain configuration*, Phys. Rev. B **69**, 024525 (2004).

[223] H. Jeffreys and B. S. Jeffreys, *Methods of Mathematical Physics*, 3rd ed. (Cambridge University Press, Cambridge, 1988).

[224] M. Galassi, J. Davies, J. Theiler, B. Gough, G. Jungman, P. Alken, M. Booth, F. Rossi, and R. Ulerich, *GNU Scientific Library*, Release 2.6 (2019).

[225] P. M. Tedrow, J. E. Tkaczyk, and A. Kumar, *Spin-Polarized Electron Tunneling Study of an Artificially Layered Superconductor with Internal Magnetic Field: EuO-Al*, Phys. Rev. Lett. **56**, 1746 (1986).

[226] C. W. Groth, M. Wimmer, A. R. Akhmerov, and X. Waintal, *Kwant 1.4.0 documentation*, Available at `https://downloads.kwant-project.org/doc/latest.pdf` (2019).

[227] A. F. Andreev, *Electron Spectrum of the Intermediate State of Superconductors*, Zh. Eksp. Teor. Fiz. **49**, 655 (1966).
English translation: J. Exp. Theor. Phys. **22**, 455 (1966).

[228] D. G. McDonald, *The Nobel Laureate Versus the Graduate Student*, Phys. Today **54**, 46 (2001).

[229] H. Meissner, *Measurements on Superconducting Contacts*, Phys. Rev. **109**, 686 (1958).

[230] J. Bardeen, *Electron-Phonon Interactions and Superconductivity*, Available at `https://www.nobelprize.org/prizes/physics/1972/bardeen/lecture/`, Nobel Lecture (1972).

[231] L. N. Cooper, *Microscopic Quantum Interference Effects in the Theory of Superconductivity*, Available at `https://www.nobelprize.org/prizes/physics/1972/cooper/lecture/`, Nobel Lecture (1972).

[232] J. R. Schrieffer, *Macroscopic Quantum Phenomena From Pairing in Superconductors*, Available at `https://www.nobelprize.org/prizes/physics/1972/schrieffer/lecture/`, Nobel Lecture (1972).

[233] P. W. Anderson and J. M. Rowell, *Probable Observation of the Josephson Superconducting Tunneling Effect*, Phys. Rev. Lett. **10**, 230 (1963).

[234] J. M. Rowell, *Magnetic Field Dependence of the Josephson Tunnel Current*, Phys. Rev. Lett. **11**, 200 (1963).

[235] B. D. Josephson, *The Discovery of Tunnelling Supercurrents*, Available at `https://www.nobelprize.org/prizes/physics/1973/josephson/lecture/`, Nobel Lecture (1973).

[236] R. P. Feynman, R. B. Leighton, and M. L. Sands, *The Feynman Lectures on Physics*, Vol. III (Pearson/Addison-Wesley, 1963).

[237] S. M. Frolov, D. J. Van Harlingen, V. A. Oboznov, V. V. Bolginov, and V. V. Ryazanov, *Measurement of the current-phase relation of superconductor/ferromagnet/superconductor π Josephson junctions*, Phys. Rev. B **70**, 144505 (2004).

[238] C. C. Grimes and S. Shapiro, *Millimeter-Wave Mixing with Josephson Junctions*, Phys. Rev. **169**, 397 (1968).

[239] S. Shapiro, *Josephson Currents in Superconducting Tunneling: The Effect of Microwaves and Other Observations*, Phys. Rev. Lett. **11**, 80 (1963).

[240] P. G. De Gennes, *Boundary Effects in Superconductors*, Rev. Mod. Phys. **36**, 225 (1964).

[241] J. Clarke, *Supercurrents in lead—copper—lead sandwiches*, Proc. Roy. Soc. A **308**, 447 (1969).

[242] A. I. Buzdin, L. N. Bulaevskii, and S. V. Panyukov, *Critical-current oscillations as a function of the exchange field and thickness of the ferromagnetic metal (F) in an S-F-S Josephson junction*, Pis'ma Zh. Eksp. Teor. Fiz. **35**, 147 (1982).
English translation: JETP Lett. **35**, 178 (1982).

[243] E. A. Demler, G. B. Arnold, and M. R. Beasley, *Superconducting proximity effects in magnetic metals*, Phys. Rev. B **55**, 15174 (1997).

[244] A. A. Golubov, M. Y. Kupriyanov, and E. Il'ichev, *The current-phase relation in Josephson junctions*, Rev. Mod. Phys. **76**, 411 (2004).

[245] A. I. Buzdin, *Proximity effects in superconductor-ferromagnet heterostructures*, Rev. Mod. Phys. **77**, 935 (2005).

[246] L. Y. Yang, Z. M. Zheng, and D. Y. Xing, *Josephson current in superconductor/ferromagnet/superconductor junctions*, Eur. Phys. J. B **47**, 479 (2005).

[247] T. Kontos, M. Aprili, J. Lesueur, F. Genêt, B. Stephanidis, and R. Boursier, *Josephson Junction through a Thin Ferromagnetic Layer: Negative Coupling*, Phys. Rev. Lett. **89**, 137007 (2002).

[248] J. W. A. Robinson, S. Piano, G. Burnell, C. Bell, and M. G. Blamire, *Critical Current Oscillations in Strong Ferromagnetic π Junctions*, Phys. Rev. Lett. **97**, 177003 (2006).

[249] K. K. Likharev, *Superconductor digital electronics*, Physica C **482**, 6 (2012).

[250] A. Matos-Abiague and J. Fabian, *Anisotropic tunneling magnetoresistance and tunneling anisotropic magnetoresistance: Spin-orbit coupling in magnetic tunnel junctions*, Phys. Rev. B **79**, 155303 (2009).

[251] J. Moser, A. Matos-Abiague, D. Schuh, W. Wegscheider, J. Fabian, and D. Weiss, *Tunneling Anisotropic Magnetoresistance and Spin-Orbit Coupling in Fe/GaAs/Au Tunnel Junctions*, Phys. Rev. Lett. **99**, 056601 (2007).

[252] V. Mourik, K. Zuo, S. M. Frolov, S. R. Plissard, E. P. A. M. Bakkers, and L. P. Kouwenhoven, *Signatures of Majorana Fermions in Hybrid Superconductor-Semiconductor Nanowire Devices*, Science **336**, 1003 (2012).

[253] L. P. Rokhinson, X. Liu, and J. K. Furdyna, *The fractional a.c. Josephson effect in a semiconductor–superconductor nanowire as a signature of Majorana particles*, Nat. Phys. **8**, 795 (2012).

[254] E. J. H. Lee, X. Jiang, R. Aguado, G. Katsaros, C. M. Lieber, and S. De Franceschi, *Zero-Bias Anomaly in a Nanowire Quantum Dot Coupled to Superconductors*, Phys. Rev. Lett. **109**, 186802 (2012).

[255] S. Nadj-Perge, I. K. Drozdov, J. Li, H. Chen, S. Jeon, J. Seo, A. H. MacDonald, B. A. Bernevig, and A. Yazdani, *Observation of Majorana fermions in ferromagnetic atomic chains on a superconductor*, Science **346**, 602 (2014).

[256] E. Dumitrescu, B. Roberts, S. Tewari, J. D. Sau, and S. Das Sarma, *Majorana fermions in chiral topological ferromagnetic nanowires*, Phys. Rev. B **91**, 094505 (2015).

[257] R. Pawlak, M. Kisiel, J. Klinovaja, T. Meier, S. Kawai, T. Glatzel, D. Loss, and E. Meyer, *Probing atomic structure and Majorana wavefunctions in mono-atomic Fe chains on superconducting Pb surface*, npj Quantum Inf. **2**, 16035 (2016).

[258] M. Ruby, B. W. Heinrich, Y. Peng, F. von Oppen, and K. J. Franke, *Exploring a Proximity-Coupled Co Chain on Pb(110) as a Possible Majorana Platform*, Nano Lett. **17**, 4473 (2017).

[259] G. Livanas, M. Sigrist, and G. Varelogiannis, *Alternative paths to realize Majorana Fermions in Superconductor-Ferromagnet Heterostructures*, Sci. Rep. **9**, 6259 (2019).

[260] A. F. Morpurgo, B. J. van Wees, T. M. Klapwijk, and G. Borghs, *Energy Spectroscopy of Andreev Levels between Two Superconductors*, Phys. Rev. Lett. **79**, 4010 (1997).

[261] I. O. Kulik, *Macroscopic Quantization and the Proximity Effect in S-N-S Junctions*, Zh. Eksp. Teor. Fiz. **57**, 1745 (1969).
English translation: J. Exp. Theor. Phys. **30**, 944 (1970).

[262] C. Ishii, *Josephson Currents through Junctions with Normal Metal Barriers*, Prog. Theor. Phys. **44**, 1525 (1970).

[263] J. Bardeen and J. L. Johnson, *Josephson Current Flow in Pure Superconducting-Normal-Superconducting Junctions*, Phys. Rev. B **5**, 72 (1972).

[264] A. Costa, *Spin-orbit coupling in Josephson junctions*, Master's Thesis (University of Regensburg, 2016).

[265] J. Cayssol and G. Montambaux, *Incomplete Andreev reflection in a clean superconductor-ferromagnet-superconductor junction*, Phys. Rev. B **71**, 012507 (2005).

[266] A. Furusaki and M. Tsukada, *Dc Josephson effect and Andreev reflection*, Solid State Commun. **78**, 299 (1991).

[267] A. Costa, P. Högl, and J. Fabian, *Magnetoanisotropic Josephson effect due to interfacial spin-orbit fields in superconductor/ferromagnet/superconductor junctions*, Phys. Rev. B **95**, 024514 (2017).

[268] A. A. Abrikosov, L. P. Gor'kov, and I. E. Cjalošinskij, *Methods of Quantum Field Theory in Statistical Physics* (Dover Publications, New York, 1975).

[269] L.-F. Chang and P. F. Bagwell, *Ballistic Josephson-current flow through an asymmetric superconductor–normal-metal–superconductor junction*, Phys. Rev. B **49**, 15853 (1994).

[270] A. Brinkman and A. A. Golubov, *Coherence effects in double-barrier Josephson junctions*, Phys. Rev. B **61**, 11297 (2000).

[271] A. Buzdin and I. Baladié, *Theoretical description of ferromagnetic π junctions near the critical temperature*, Phys. Rev. B **67**, 184519 (2003).

[272] Z. Radović, N. Lazarides, and N. Flytzanis, *Josephson effect in double-barrier superconductor-ferromagnet junctions*, Phys. Rev. B **68**, 014501 (2003).

[273] T. Yokoyama, M. Eto, and Y. V. Nazarov, *Critical current in semiconductor nanowire Josephson junctions in the presence of magnetic field*, J. Phys.: Conf. Ser. **568**, 052035 (2014).

[274] T. Yokoyama and Y. V. Nazarov, *Magnetic anisotropy of critical current in nanowire Josephson junction with spin-orbit interaction*, Europhys. Lett. **108**, 47009 (2014).

[275] J. Nitta, T. Akazaki, H. Takayanagi, and T. Enoki, *Gate Control of Spin-Orbit Interaction in an Inverted $In_{0.53}Ga_{0.47}As/In_{0.52}Al_{0.48}As$ Heterostructure*, Phys. Rev. Lett. **78**, 1335 (1997).

[276] T. Koga, J. Nitta, T. Akazaki, and H. Takayanagi, *Rashba Spin-Orbit Coupling Probed by the Weak Antilocalization Analysis in $InAlAs/InGaAs/InAlAs$ Quantum Wells as a Function of Quantum Well Asymmetry*, Phys. Rev. Lett. **89**, 046801 (2002).

[277] L. Chen, M. Gmitra, M. Vogel, R. Islinger, M. Kronseder, D. Schuh, D. Bougeard, J. Fabian, D. Weiss, and C. H. Back, *Electric-field control of interfacial spin–orbit fields*, Nat. Electron. **1**, 350 (2018).

[278] J. Arjoranta and T. T. Heikkilä, *Intrinsic spin-orbit interaction in diffusive normal wire Josephson weak links: Supercurrent and density of states*, Phys. Rev. B **93**, 024522 (2016).

[279] S. H. Jacobsen, I. Kulagina, and J. Linder, *Controlling superconducting spin flow with spin-flip immunity using a single homogeneous ferromagnet*, Sci. Rep. **6**, 23926 (2016).

[280] A. N. Chantis, K. D. Belashchenko, E. Y. Tsymbal, and M. van Schilfgaarde, *Tunneling Anisotropic Magnetoresistance Driven by Resonant Surface States: First-Principles Calculations on an Fe(001) Surface*, Phys. Rev. Lett. **98**, 046601 (2007).

[281] C. Betthausen, T. Dollinger, H. Saarikoski, V. Kolkovsky, G. Karczewski, T. Wojtowicz, K. Richter, and D. Weiss, *Spin-Transistor Action via Tunable Landau-Zener Transitions*, Science **337**, 324 (2012).

[282] S. Maekawa and U. Gäfvert, *Electron tunneling between ferromagnetic films*, IEEE Transactions on Magnetics **18**, 707 (1982).

[283] T. Miyazaki and N. Tezuka, *Giant magnetic tunneling effect in $Fe/Al_2O_3/Fe$ junction*, J. Magn. Magn. Mater. **139**, L231 (1995).

[284] J. S. Moodera, L. R. Kinder, T. M. Wong, and R. Meservey, *Large Magnetoresistance at Room Temperature in Ferromagnetic Thin Film Tunnel Junctions*, Phys. Rev. Lett. **74**, 3273 (1995).

[285] R. Mattana, J.-M. George, H. Jaffrès, F. Nguyen Van Dau, A. Fert, B. Lépine, A. Guivarc'h, and G. Jézéquel, *Electrical Detection of Spin Accumulation in a p-Type GaAs Quantum Well*, Phys. Rev. Lett. **90**, 166601 (2003).

[286] D. Chiba, F. Matsukura, and H. Ohno, *Tunneling magnetoresistance in (Ga,Mn)As-based heterostructures with a GaAs barrier*, Physica E **21**, 966 (2004).

[287] M. Elsen, O. Boulle, J.-M. George, H. Jaffrès, R. Mattana, V. Cros, A. Fert, A. Lemaitre, R. Giraud, and G. Faini, *Spin transfer experiments on (Ga,Mn)As/(In,Ga)As/(Ga,Mn)As tunnel junctions*, Phys. Rev. B **73**, 035303 (2006).

[288] J. W. A. Robinson, G. B. Halász, A. I. Buzdin, and M. G. Blamire, *Enhanced Supercurrents in Josephson Junctions Containing Nonparallel Ferromagnetic Domains*, Phys. Rev. Lett. **104**, 207001 (2010).

[289] C. Klose, T. S. Khaire, Y. Wang, W. P. Pratt Jr., N. O. Birge, B. J. McMorran, T. P. Ginley, J. A. Borchers, B. J. Kirby, B. B. Maranville, and J. Unguris, *Optimization of Spin-Triplet Supercurrent in Ferromagnetic Josephson Junctions*, Phys. Rev. Lett. **108**, 127002 (2012).

[290] B. Baek, W. H. Rippard, S. P. Benz, S. E. Russek, and P. D. Dresselhaus, *Hybrid superconducting-magnetic memory device using competing order parameters*, Nat. Commun. **5**, 3888 (2014).

[291] M. Abd El Qader, R. K. Singh, S. N. Galvin, L. Yu, J. M. Rowell, and N. Newman, *Switching at small magnetic fields in Josephson junctions fabricated with ferromagnetic barrier layers*, Appl. Phys. Lett. **104**, 022602 (2014).
ERRATUM: Appl. Phys. Lett. **104**, 099903 (2014).

[292] M. Weides, M. Kemmler, E. Goldobin, D. Koelle, R. Kleiner, H. Kohlstedt, and A. Buzdin, *High quality ferromagnetic 0 and π Josephson tunnel junctions*, Appl. Phys. Lett. **89**, 122511 (2006).

[293] C. Bell, G. Burnell, C. W. Leung, E. J. Tarte, D.-J. Kang, and M. G. Blamire, *Controllable Josephson current through a pseudospin-valve structure*, Appl. Phys. Lett. **84**, 1153 (2004).

[294] I. P. Nevirkovets, O. Chernyashevskyy, G. V. Prokopenko, O. A. Mukhanov, and J. B. Ketterson, *Superconducting-Ferromagnetic Transistor*, IEEE Transactions on Applied Superconductivity **24**, 1 (2014).

[295] F. S. Bergeret, A. F. Volkov, and K. B. Efetov, *Enhancement of the Josephson Current by an Exchange Field in Superconductor-Ferromagnet Structures*, Phys. Rev. Lett. **86**, 3140 (2001).

[296] A. A. Golubov, M. Y. Kupriyanov, and Y. V. Fominov, *Critical current in SFIFS junctions*, J. Exp. Theor. Phys. Lett. **75**, 190 (2002).

[297] A. V. Zaitsev, *Peculiarities of the proximity effect in superconductor-multilayered ferromagnet structures with collinear magnetizations in ferromagnetic layers*, Pis'ma Zh. Eksp. Teor. Fiz. **90**, 521 (2009).
ENGLISH TRANSLATION: JETP Lett. **90**, 475 (2009).

[298] Y. C. Tao, *Josephson current in a ferromagnetic semiconductor/semiconductor/ferromagnetic semiconductor junction with superconducting contacts*, J. Appl. Phys. **100**, 063901 (2006).

[299] Y. C. Tao, *Josephson current through a ferromagnetic semiconductor/semiconductor/ ferromagnetic semiconductor structure*, Eur. Phys. J. B **56**, 83 (2007).

[300] C. J. Lambert, *Generalized Landauer formulae for quasi-particle transport in disordered superconductors*, J. Phys.: Condens. Matter **3**, 6579 (1991).

[301] M. Božović and Z. Radović, *Coherent effects in double-barrier ferromagnet/superconductor/ferromagnet junctions*, Phys. Rev. B **66**, 134524 (2002).
ERRATUM: Phys. Rev. B **71**, 229901(E) (2005).

[302] T. Yamashita, H. Imamura, S. Takahashi, and S. Maekawa, *Andreev reflection in ferromagnet/superconductor/ferromagnet double junction systems*, Phys. Rev. B **67**, 094515 (2003).

[303] Z. C. Dong, R. Shen, Z. M. Zheng, D. Y. Xing, and Z. D. Wang, *Coherent quantum transport in ferromagnet/superconductor/ferromagnet structures*, Phys. Rev. B **67**, 134515 (2003).

[304] Z. Pajović, M. Božović, Z. Radović, J. Cayssol, and A. Buzdin, *Josephson coupling through ferromagnetic heterojunctions with noncollinear magnetizations*, Phys. Rev. B **74**, 184509 (2006).

[305] Y. S. Barash, I. V. Bobkova, and T. Kopp, *Josephson current in S-FIF-S junctions: Nonmonotonic dependence on misorientation angle*, Phys. Rev. B **66**, 140503(R) (2002).

[306] B. Crouzy, S. Tollis, and D. A. Ivanov, *Josephson current in a superconductor-ferromagnet junction with two noncollinear magnetic domains*, Phys. Rev. B **75**, 054503 (2007).

[307] I. B. Sperstad, J. Linder, and A. Sudbø, *Josephson current in diffusive multilayer superconductor/ferromagnet/superconductor junctions*, Phys. Rev. B **78**, 104509 (2008).

[308] M. Alidoust and J. Linder, *Spin-triplet supercurrent through inhomogeneous ferromagnetic trilayers*, Phys. Rev. B **82**, 224504 (2010).

[309] M. Alidoust, J. Linder, G. Rashedi, T. Yokoyama, and A. Sudbø, *Spin-polarized Josephson current in superconductor/ferromagnet/superconductor junctions with inhomogeneous magnetization*, Phys. Rev. B **81**, 014512 (2010).

[310] J.-F. Liu and K. S. Chan, *Anomalous Josephson current through a ferromagnetic trilayer junction*, Phys. Rev. B **82**, 184533 (2010).

[311] K. Halterman, O. T. Valls, and C.-T. Wu, *Charge and spin currents in ferromagnetic Josephson junctions*, Phys. Rev. B **92**, 174516 (2015).

[312] T. E. Baker, A. Richie-Halford, and A. Bill, *Classification of magnetic inhomogeneities and 0-π transitions in superconducting-magnetic hybrid structures*, Phys. Rev. B **94**, 104518 (2016).

[313] H. Meng, J. Wu, X. Wu, M. Ren, and Y. Ren, *Long-range superharmonic Josephson current and spin-triplet pairing correlations in a junction with ferromagnetic bilayers*, Sci. Rep. **6**, 21308 (2016).

[314] J. Alicea, *Majorana fermions in a tunable semiconductor device*, Phys. Rev. B **81**, 125318 (2010).

[315] R. M. Lutchyn, J. D. Sau, and S. Das Sarma, *Majorana Fermions and a Topological Phase Transition in Semiconductor-Superconductor Heterostructures*, Phys. Rev. Lett. **105**, 077001 (2010).

[316] Y. Oreg, G. Refael, and F. von Oppen, *Helical Liquids and Majorana Bound States in Quantum Wires*, Phys. Rev. Lett. **105**, 177002 (2010).

[317] A. Das, Y. Ronen, Y. Most, Y. Oreg, M. Heiblum, and H. Shtrikman, *Zero-bias peaks and splitting in an Al–InAs nanowire topological superconductor as a signature of Majorana fermions*, Nat. Phys. **8**, 887 (2012).

[318] M. T. Deng, C. L. Yu, G. Y. Huang, M. Larsson, P. Caroff, and H. Q. Xu, *Anomalous Zero-Bias Conductance Peak in a Nb–InSb Nanowire–Nb Hybrid Device*, Nano Lett. **12**, 6414 (2012).

[319] A. D. K. Finck, D. J. Van Harlingen, P. K. Mohseni, K. Jung, and X. Li, *Anomalous Modulation of a Zero-Bias Peak in a Hybrid Nanowire-Superconductor Device*, Phys. Rev. Lett. **110**, 126406 (2013).

[320] H. O. H. Churchill, V. Fatemi, K. Grove-Rasmussen, M. T. Deng, P. Caroff, H. Q. Xu, and C. M. Marcus, *Superconductor-nanowire devices from tunneling to the multichannel regime: Zero-bias oscillations and magnetoconductance crossover*, Phys. Rev. B **87**, 241401(R) (2013).

[321] E. J. H. Lee, X. Jiang, M. Houzet, R. Aguado, C. M. Lieber, and S. De Franceschi, *Spin-resolved Andreev levels and parity crossings in hybrid superconductor–semiconductor nanostructures*, Nat. Nanotechnol. **9**, 79 (2014).

[322] R. Aguado, *Majorana quasiparticles in condensed matter*, Riv. Nuovo Cim. **40**, 523 (2017).

[323] M. Hell, M. Leijnse, and K. Flensberg, *Two-Dimensional Platform for Networks of Majorana Bound States*, Phys. Rev. Lett. **118**, 107701 (2017).

[324] F. Pientka, A. Keselman, E. Berg, A. Yacoby, A. Stern, and B. I. Halperin, *Topological Superconductivity in a Planar Josephson Junction*, Phys. Rev. X **7**, 021032 (2017).

[325] J. Liu, C. F. Chan, and M. Gong, *Majorana fermions in semiconducting nanowire and Fulde–Ferrell superconductor hybrid structures*, Front. Phys. **14**, 13609 (2019).

[326] B. Scharf, F. Pientka, H. Ren, A. Yacoby, and E. M. Hankiewicz, *Tuning topological superconductivity in phase-controlled Josephson junctions with Rashba and Dresselhaus spin-orbit coupling*, Phys. Rev. B **99**, 214503 (2019).

[327] H. Ren, F. Pientka, S. Hart, A. T. Pierce, M. Kosowsky, L. Lunczer, R. Schlereth, B. Scharf, E. M. Hankiewicz, L. W. Molenkamp, B. I. Halperin, and A. Yacoby, *Topological superconductivity in a phase-controlled Josephson junction*, Nature **569**, 93 (2019).

[328] R. Delagrange, D. J. Luitz, R. Weil, A. Kasumov, V. Meden, H. Bouchiat, and R. Deblock, *Manipulating the magnetic state of a carbon nanotube Josephson junction using the superconducting phase*, Phys. Rev. B **91**, 241401(R) (2015).

[329] S. Li, N. Kang, P. Caroff, and H. Q. Xu, *0–π phase transition in hybrid superconductor–InSb nanowire quantum dot devices*, Phys. Rev. B **95**, 014515 (2017).

[330] D. J. van Woerkom, A. Proutski, B. van Heck, D. Bouman, J. I. Väyrynen, L. I. Glazman, P. Krogstrup, J. Nygård, L. P. Kouwenhoven, and A. Geresdi, *Microwave spectroscopy of spinful Andreev bound states in ballistic semiconductor Josephson junctions*, Nat. Phys. **13**, 876 (2017).

[331] L. I. Glazman and K. A. Matveev, *Resonant Josephson current through Kondo impurities in a tunnel barrier*, Pis'ma Zh. Eksp. Teor. Fiz. **49**, 570 (1989).
English translation: JETP Lett. **49**, 659 (1989).

[332] A. A. Clerk and V. Ambegaokar, *Loss of π-junction behavior in an interacting impurity Josephson junction*, Phys. Rev. B **61**, 9109 (2000).

[333] E. Vecino, A. Martín-Rodero, and A. Levy Yeyati, *Josephson current through a correlated quantum level: Andreev states and π junction behavior*, Phys. Rev. B **68**, 035105 (2003).

[334] M.-S. Choi, M. Lee, K. Kang, and W. Belzig, *Kondo effect and Josephson current through a quantum dot between two superconductors*, Phys. Rev. B **70**, 020502(R) (2004).

[335] F. Siano and R. Egger, *Josephson Current through a Nanoscale Magnetic Quantum Dot*, Phys. Rev. Lett. **93**, 047002 (2004).
Erratum: Phys. Rev. Lett. **94**, 039902(E) (2005).

[336] J. Bauer, A. Oguri, and A. C. Hewson, *Spectral properties of locally correlated electrons in a Bardeen–Cooper–Schrieffer superconductor*, J. Phys.: Condens. Matter **19**, 486211 (2007).

[337] C. Karrasch, A. Oguri, and V. Meden, *Josephson current through a single Anderson impurity coupled to BCS leads*, Phys. Rev. B **77**, 024517 (2008).

[338] T. Meng, S. Florens, and P. Simon, *Self-consistent description of Andreev bound states in Josephson quantum dot devices*, Phys. Rev. B **79**, 224521 (2009).

[339] D. J. Luitz and F. F. Assaad, *Weak-coupling continuous-time quantum Monte Carlo study of the single impurity and periodic Anderson models with s-wave superconducting baths*, Phys. Rev. B **81**, 024509 (2010).

[340] A. Martín-Rodero and A. Levy Yeyati, *Josephson and Andreev transport through quantum dots*, Adv. Phys. **60**, 899 (2011).

[341] D. J. Luitz, F. F. Assaad, T. Novotný, C. Karrasch, and V. Meden, *Understanding the Josephson Current through a Kondo-Correlated Quantum Dot*, Phys. Rev. Lett. **108**, 227001 (2012).

[342] G. Kiršanskas, M. Goldstein, K. Flensberg, L. I. Glazman, and J. Paaske, *Yu-Shiba-Rusinov states in phase-biased superconductor–quantum dot–superconductor junctions*, Phys. Rev. B **92**, 235422 (2015).

[343] M. R. Buitelaar, T. Nussbaumer, and C. Schönenberger, *Quantum Dot in the Kondo Regime Coupled to Superconductors*, Phys. Rev. Lett. **89**, 256801 (2002).

[344] H. I. Jørgensen, T. Novotný, K. Grove-Rasmussen, K. Flensberg, and P. E. Lindelof, *Critical Current 0–π Transition in Designed Josephson Quantum Dot Junctions*, Nano Lett. **7**, 2441 (2007).

[345] A. Eichler, R. Deblock, M. Weiss, C. Karrasch, V. Meden, C. Schönenberger, and H. Bouchiat, *Tuning the Josephson current in carbon nanotubes with the Kondo effect*, Phys. Rev. B **79**, 161407(R) (2009).

[346] R. S. Deacon, Y. Tanaka, A. Oiwa, R. Sakano, K. Yoshida, K. Shibata, K. Hirakawa, and S. Tarucha, *Tunneling Spectroscopy of Andreev Energy Levels in a Quantum Dot Coupled to a Superconductor*, Phys. Rev. Lett. **104**, 076805 (2010).

[347] J.-D. Pillet, C. H. L. Quay, P. Morfin, C. Bena, A. Levy Yeyati, and P. Joyez, *Andreev bound states in supercurrent-carrying carbon nanotubes revealed*, Nat. Phys. **6**, 965 (2010).

[348] K. J. Franke, G. Schulze, and J. I. Pascual, *Competition of Superconducting Phenomena and Kondo Screening at the Nanoscale*, Science **332**, 940 (2011).

[349] R. Maurand, T. Meng, E. Bonet, S. Florens, L. Marty, and W. Wernsdorfer, *First-Order 0-π Quantum Phase Transition in the Kondo Regime of a Superconducting Carbon-Nanotube Quantum Dot*, Phys. Rev. X **2**, 011009 (2012).
Erratum: Phys. Rev. X **2**, 019901(E) (2012).

[350] W. Chang, V. E. Manucharyan, T. S. Jespersen, J. Nygård, and C. M. Marcus, *Tunneling Spectroscopy of Quasiparticle Bound States in a Spinful Josephson Junction*, Phys. Rev. Lett. **110**, 217005 (2013).

[351] B.-K. Kim, Y.-H. Ahn, J.-J. Kim, M.-S. Choi, M.-H. Bae, K. Kang, J. S. Lim, R. López, and N. Kim, *Transport Measurement of Andreev Bound States in a Kondo-Correlated Quantum Dot*, Phys. Rev. Lett. **110**, 076803 (2013).

[352] J.-D. Pillet, P. Joyez, R. Žitko, and M. F. Goffman, *Tunneling spectroscopy of a single quantum dot coupled to a superconductor: From Kondo ridge to Andreev bound states*, Phys. Rev. B **88**, 045101 (2013).

[353] A. Kumar, M. Gaim, D. Steininger, A. Levy Yeyati, A. Martín-Rodero, A. K. Hüttel, and C. Strunk, *Temperature dependence of Andreev spectra in a superconducting carbon nanotube quantum dot*, Phys. Rev. B **89**, 075428 (2014).

[354] A. Assouline, C. Feuillet-Palma, A. Zimmers, H. Aubin, M. Aprili, and J.-C. Harmand, *Shiba Bound States across the Mobility Edge in Doped InAs Nanowires*, Phys. Rev. Lett. **119**, 097701 (2017).

[355] Z. Su, A. B. Tacla, M. Hocevar, D. Car, S. R. Plissard, E. P. A. M. Bakkers, A. J. Daley, D. Pekker, and S. M. Frolov, *Andreev molecules in semiconductor nanowire double quantum dots*, Nat. Commun. **8**, 585 (2017).

[356] L. Fu and C. L. Kane, *Superconducting Proximity Effect and Majorana Fermions at the Surface of a Topological Insulator*, Phys. Rev. Lett. **100**, 096407 (2008).

[357] L. Fu and C. L. Kane, *Josephson current and noise at a superconductor/quantum-spin-Hall-insulator/superconductor junction*, Phys. Rev. B **79**, 161408(R) (2009).

[358] A. A. Abrikosov and L. P. Gor'kov, *Contribution to the theory of superconducting alloys with paramagnetic impurities*, Zh. Eksp. Teo. Fiz. **39**, 1781 (1960).
English translation: Sov. Phys. JETP **12**, 1243 (1961).

[359] T. Soda, T. Matsuura, and Y. Nagaoka, *s-d Exchange Interaction in a Superconductor*, Prog. Theor. Phys. **38**, 551 (1967).

[360] M. Fowler and K. Maki, *Conditions for Bound States in a Superconductor with a Magnetic Impurity*, Phys. Rev. **164**, 484 (1967).

[361] L. Yu, *Bound state in superconductors with paramagnetic impurities*, Acta Phys. Sin. **21**, 75 (1965).

[362] H. Shiba, *Classical Spins in Superconductors*, Prog. Theor. Phys. **40**, 435 (1968).

[363] A. I. Rusinov, *Superconductivity near a Paramagnetic Impurity*, Zh. Eksp. Teor. Fiz. Pisma Red. **9**, 146 (1968).
English translation: JETP Lett. **9**, 85 (1969).

[364] K. Satori, H. Shiba, O. Sakai, and Y. Shimizu, *Numerical Renormalization Group Study of Magnetic Impurities in Superconductors*, J. Phys. Soc. Jpn. **61**, 3239 (1992).

[365] J. Simonin and R. Allub, *Rare-Earth Impurity in a Superconductive Matrix*, Phys. Rev. Lett. **74**, 466 (1995).

[366] M. I. Salkola, A. V. Balatsky, and J. R. Schrieffer, *Spectral properties of quasiparticle excitations induced by magnetic moments in superconductors*, Phys. Rev. B **55**, 12648 (1997).

[367] A. V. Balatsky, I. Vekhter, and J.-X. Zhu, *Impurity-induced states in conventional and unconventional superconductors*, Rev. Mod. Phys. **78**, 373 (2006).

[368] W.-F. Tsai, Y.-Y. Zhang, C. Fang, and J. Hu, *Impurity-induced bound states in iron-based superconductors with s-wave cos $k_x \cdot$ cos k_y pairing symmetry*, Phys. Rev. B **80**, 064513 (2009).

[369] M. Ruby, Y. Peng, F. von Oppen, B. W. Heinrich, and K. J. Franke, *Orbital Picture of Yu-Shiba-Rusinov Multiplets*, Phys. Rev. Lett. **117**, 186801 (2016).

[370] V. Kaladzhyan, S. Hoffman, and M. Trif, *Dynamical Shiba states from precessing magnetic moments in an s-wave superconductor*, Phys. Rev. B **95**, 195403 (2017).

[371] S. Körber, B. Trauzettel, and O. Kashuba, *Collective Yu-Shiba-Rusinov states in magnetic clusters at superconducting surfaces*, Phys. Rev. B **97**, 184503 (2018).

[372] R. Žitko, J. S. Lim, R. López, and R. Aguado, *Shiba states and zero-bias anomalies in the hybrid normal-superconductor Anderson model*, Phys. Rev. B **91**, 045441 (2015).

[373] A. Jellinggaard, K. Grove-Rasmussen, M. H. Madsen, and J. Nygård, *Tuning Yu-Shiba-Rusinov states in a quantum dot*, Phys. Rev. B **94**, 064520 (2016).

[374] N. Read and D. Green, *Paired states of fermions in two dimensions with breaking of parity and time-reversal symmetries and the fractional quantum Hall effect*, Phys. Rev. B **61**, 10267 (2000).

[375] A. Y. Kitaev, *Unpaired Majorana fermions in quantum wires*, Phys.-Usp. **44**, 131 (2001).

[376] A. A. Abrikosov, *Superconductivity in a quasi-one-dimensional metal with impurities*, J. Low Temp. Phys. **53**, 359 (1983).

[377] A. G. Lebed, *Revival of superconductivity in high magnetic fields and a possible p-wave pairing in $(TMTSF)_2PF_6$*, Phys. Rev. B **59**, R721(R) (1999).

[378] A. G. Lebed, K. Machida, and M. Ozaki, *Triplet electron pairing and anisotropic spin susceptibility in organic superconductors $(TMTSF)_2X$*, Phys. Rev. B **62**, R795(R) (2000).

[379] Y. Maeno, M. Sigrist, and T. M. Rice, *The Intriguing Superconductivity of Strontium Ruthenate*, Phys. Today **54**, 42 (2001).
Erratum: Phys. Today **54**, 104 (2001).

[380] A. P. Mackenzie and Y. Maeno, *The superconductivity of Sr_2RuO_4 and the physics of spin-triplet pairing*, Rev. Mod. Phys. **75**, 657 (2003).

[381] A. Fornieri, A. M. Whiticar, F. Setiawan, E. Portolés, A. C. C. Drachmann, A. Keselman, S. Gronin, C. Thomas, T. Wang, R. Kallaher, G. C. Gardner, E. Berg, M. J. Manfra, A. Stern, C. M. Marcus, and F. Nichele, *Evidence of topological superconductivity in planar Josephson junctions*, Nature **569**, 89 (2019).

[382] S. Kawabata, Y. Tanaka, A. A. Golubov, A. S. Vasenko, and Y. Asano, *Spectrum of Andreev bound states in Josephson junctions with a ferromagnetic insulator*, J. Magn. Magn. Mater. **324**, 3467 (2012).

[383] J. D. Sau and E. Demler, *Bound states at impurities as a probe of topological superconductivity in nanowires*, Phys. Rev. B **88**, 205402 (2013).

[384] F. Pientka, Y. Peng, L. Glazman, and F. von Oppen, *Topological superconducting phase and Majorana bound states in Shiba chains*, Phys. Scr. **2015**, 014008 (2015).

[385] N. Hatter, B. W. Heinrich, M. Ruby, J. I. Pascual, and K. J. Franke, *Magnetic anisotropy in Shiba bound states across a quantum phase transition*, Nat. Commun. **6**, 8988 (2015).

[386] A. Sakurai, *Comments on Superconductors with Magnetic Impurities*, Prog. Theor. Phys. **44**, 1472 (1970).

[387] B. M. Andersen, I. V. Bobkova, P. J. Hirschfeld, and Y. S. Barash, $0 - \pi$ *Transitions in Josephson Junctions with Antiferromagnetic Interlayers*, Phys. Rev. Lett. **96**, 117005 (2006).

[388] S. Kawabata, Y. Asano, Y. Tanaka, A. A. Golubov, and S. Kashiwaya, *Josephson π State in a Ferromagnetic Insulator*, Phys. Rev. Lett. **104**, 117002 (2010).

[389] S. Yip, *Noncentrosymmetric Superconductors*, Annu. Rev. Condens. Matter Phys. **5**, 15 (2014).

[390] H.-J. Kwon, K. Sengupta, and V. M. Yakovenko, *Fractional ac Josephson effect in p- and d-wave superconductors*, Eur. Phys. J. B **37**, 349 (2004).

[391] Y. Tanaka, T. Yokoyama, A. V. Balatsky, and N. Nagaosa, *Theory of topological spin current in noncentrosymmetric superconductors*, Phys. Rev. B **79**, 060505(R) (2009).

[392] A. Furusaki, *Josephson current carried by Andreev levels in superconducting quantum point contacts*, Superlattices Microstruct. **25**, 809 (1999).

[393] S. R. Elliott and M. Franz, *Colloquium: Majorana fermions in nuclear, particle, and solid-state physics*, Rev. Mod. Phys. **87**, 137 (2015).

[394] A. Costa, J. Fabian, and D. Kochan, *Connection between zero-energy Yu-Shiba-Rusinov states and 0-π transitions in magnetic Josephson junctions*, Phys. Rev. B **98**, 134511 (2018).

[395] T. Ideue, K. Hamamoto, S. Koshikawa, M. Ezawa, S. Shimizu, Y. Kaneko, Y. Tokura, N. Nagaosa, and Y. Iwasa, *Bulk rectification effect in a polar semiconductor*, Nat. Phys. **13**, 578 (2017).

[396] J. Wiedenmann, E. Bocquillon, R. S. Deacon, S. Hartinger, O. Herrmann, T. M. Klapwijk, L. Maier, C. Ames, C. Brüne, C. Gould, A. Oiwa, K. Ishibashi, S. Tarucha, H. Buhmann, and L. W. Molenkamp, *4π-periodic Josephson supercurrent in HgTe-based topological Josephson junctions*, Nat. Commun. **7**, 10303 (2016).

[397] D. Laroche, D. Bouman, D. J. van Woerkom, A. Proutski, C. Murthy, D. I. Pikulin, C. Nayak, R. J. J. van Gulik, J. Nygård, P. Krogstrup, L. P. Kouwenhoven, and A. Geresdi, *Observation of the 4π-periodic Josephson effect in indium arsenide nanowires*, Nat. Commun. **10**, 245 (2019).

[398] D. I. Pikulin and Y. V. Nazarov, *Phenomenology and dynamics of a Majorana Josephson junction*, Phys. Rev. B **86**, 140504(R) (2012).

[399] G. Tkachov and E. M. Hankiewicz, *Helical Andreev bound states and superconducting Klein tunneling in topological insulator Josephson junctions*, Phys. Rev. B **88**, 075401 (2013).

[400] Q. Cheng, K. Zhang, D. Yu, C. Chen, Y. Zhang, and B. Jin, *Tunable ground states in helical p-wave Josephson junctions*, Supercond. Sci. Technol. **29**, 075010 (2016).

[401] M. Rouco, I. V. Tokatly, and F. S. Bergeret, *Spectral properties and quantum phase transitions in superconducting junctions with a ferromagnetic link*, Phys. Rev. B **99**, 094514 (2019).

[402] D. Kochan, M. Barth, A. Costa, K. Richter, and J. Fabian, *Spin Relaxation in s-Wave Superconductors in the Presence of Resonant Spin-Flip Scatterers*, Phys. Rev. Lett. **125**, 087001 (2020).

[403] P. W. Bridgman, *Bibliographical Memoir of Edwin Herbert Hall*, Available at `http://www.nasonline.org/publications/biographical-memoirs/memoir-pdfs/hall-edwin.pdf` (National Academy of Sciences, 1939).

[404] J. C. Maxwell, *VIII. On Faraday's Lines of Force*, Transactions of the Cambridge Philosophical Society **x** (1855).

[405] J. C. Maxwell, *VIII. A dynamical theory of the electromagnetic field*, Philos. Trans. R. Soc. **155**, 459 (1865).

[406] E. H. Hall, *On a New Action of the Magnet on Electric Currents*, Am. J. Math. **2**, 287 (1879).

[407] E. H. Hall, *XXXVIII. On the new Action of Magnetism on a permanent Electric Current*, Philos. Mag. **10**, 301 (1880).

[408] N. Nagaosa, J. Sinova, S. Onoda, A. H. MacDonald, and N. P. Ong, *Anomalous Hall effect*, Rev. Mod. Phys. **82**, 1539 (2010).

[409] J. J. Thomson, *XL. Cathode Rays*, Philos. Mag. **44**, 293 (1897).

[410] H. A. Lorentz, *Versuch einer Theorie der elektrischen und optischen Erscheinungen in bewegten Körpern* (1895).

[411] E. Ramsden, *Hall-Effect Sensors*, 2nd ed. (Elsevier, 2006).

[412] B. K. Cho and J. S. Rhyee, *Hall effect and charge carrier density in $Eu_{1-x}Ca_xB_6$ (x = 0.2, 0.4, 0.6, and 0.9)*, J. Magn. Magn. Mater. **272-276**, E7 (2004).

[413] E. H. Hall, *XVIII. On the "Rotational Coefficient" in nickel and cobalt*, Philos. Mag. **12**, 157 (1881).

[414] R. Karplus and J. M. Luttinger, *Hall Effect in Ferromagnetics*, Phys. Rev. **95**, 1154 (1954).

[415] J. M. Luttinger, *Theory of the Hall Effect in Ferromagnetic Substances*, Phys. Rev. **112**, 739 (1958).

[416] M.-C. Chang and Q. Niu, *Berry Phase, Hyperorbits, and the Hofstadter Spectrum*, Phys. Rev. Lett. **75**, 1348 (1995).

[417] G. Sundaram and Q. Niu, *Wave-packet dynamics in slowly perturbed crystals: Gradient corrections and Berry-phase effects*, Phys. Rev. B **59**, 14915 (1999).

[418] M. Onoda and N. Nagaosa, *Topological Nature of Anomalous Hall Effect in Ferromagnets*, J. Phys. Soc. Jpn. **71**, 19 (2002).

[419] T. Jungwirth, Q. Niu, and A. H. MacDonald, *Anomalous Hall Effect in Ferromagnetic Semiconductors*, Phys. Rev. Lett. **88**, 207208 (2002).

[420] Z. Fang, N. Nagaosa, K. S. Takahashi, A. Asamitsu, R. Mathieu, T. Ogasawara, H. Yamada, M. Kawasaki, Y. Tokura, and K. Terakura, *The Anomalous Hall Effect and Magnetic Monopoles in Momentum Space*, Science **302**, 92 (2003).

[421] Y. Yao, L. Kleinman, A. H. MacDonald, J. Sinova, T. Jungwirth, D.-s. Wang, E. Wang, and Q. Niu, *First Principles Calculation of Anomalous Hall Conductivity in Ferromagnetic bcc Fe*, Phys. Rev. Lett. **92**, 037204 (2004).

[422] M. V. Berry, *Quantal phase factors accompanying adiabatic changes*, Proc. Roy. Soc. A **392**, 45 (1984).

[423] J. Sinova, T. Jungwirth, and J. Černe, *Magneto-transport and magneto-optical properties of ferromagnetic (III,Mn)V semiconductors: a review*, Int. J. Mod. Phys. B **18**, 1083 (2004).

[424] N. Nagaosa, *Anomalous Hall Effect –A New Perspective–*, J. Phys. Soc. Jpn. **75**, 042001 (2006).

[425] L. Berger, *Side-Jump Mechanism for the Hall Effect of Ferromagnets*, Phys. Rev. B **2**, 4559 (1970).

[426] L. Berger, *Application of the Side-Jump Model to the Hall Effect and Nernst Effect in Ferromagnets*, Phys. Rev. B **5**, 1862 (1972).

[427] J. Smit, *The spontaneous hall effect in ferromagnetics I*, Physica **21**, 877 (1955).

[428] J. Smit, *The spontaneous hall effect in ferromagnetics II*, Physica **24**, 39 (1958).

[429] M. I. Dyakonov and V. I. Perel, *Possibility of Orienting Electron Spins with Current*, Zh. Eksp. Teor. Fiz. Pisma Red. **13**, 657 (1971).
English translation: JETP Lett. **13**, 467 (1971).

[430] M. I. Dyakonov and V. I. Perel, *Current-induced spin orientation of electrons in semiconductors*, Phys. Lett. A **35**, 459 (1971).

[431] Y. K. Kato, R. C. Myers, A. C. Gossard, and D. D. Awschalom, *Observation of the Spin Hall Effect in Semiconductors*, Science **306**, 1910 (2004).

[432] J. Wunderlich, B. Kaestner, J. Sinova, and T. Jungwirth, *Experimental Observation of the Spin-Hall Effect in a Two-Dimensional Spin-Orbit Coupled Semiconductor System*, Phys. Rev. Lett. **94**, 047204 (2005).

[433] S. Murakami, N. Nagaosa, and S.-C. Zhang, *Dissipationless Quantum Spin Current at Room Temperature*, Science **301**, 1348 (2003).

[434] K. v. Klitzing, G. Dorda, and M. Pepper, *New Method for High-Accuracy Determination of the Fine-Structure Constant Based on Quantized Hall Resistance*, Phys. Rev. Lett. **45**, 494 (1980).

[435] F. D. M. Haldane, *Model for a Quantum Hall Effect without Landau Levels: Condensed-Matter Realization of the "Parity Anomaly"*, Phys. Rev. Lett. **61**, 2015 (1988).

[436] C. L. Kane and E. J. Mele, *Quantum Spin Hall Effect in Graphene*, Phys. Rev. Lett. **95**, 226801 (2005).

[437] M. König, S. Wiedmann, C. Brüne, A. Roth, H. Buhmann, L. W. Molenkamp, X.-L. Qi, and S.-C. Zhang, *Quantum Spin Hall Insulator State in HgTe Quantum Wells*, Science **318**, 766 (2007).

[438] A. Vedyayev, N. Ryzhanova, N. Strelkov, and B. Dieny, *Spontaneous Anomalous and Spin Hall Effects Due to Spin-Orbit Scattering of Evanescent Wave Functions in Magnetic Tunnel Junctions*, Phys. Rev. Lett. **110**, 247204 (2013).

[439] A. V. Vedyayev, M. S. Titova, N. V. Ryzhanova, M. Y. Zhuravlev, and E. Y. Tsymbal, *Anomalous and spin Hall effects in a magnetic tunnel junction with Rashba spin-orbit coupling*, Appl. Phys. Lett. **103**, 032406 (2013).

[440] A. Matos-Abiague and J. Fabian, *Tunneling Anomalous and Spin Hall Effects*, Phys. Rev. Lett. **115**, 056602 (2015).

[441] T. H. Dang, H. Jaffrès, T. L. Hoai Nguyen, and H.-J. Drouhin, *Giant forward-scattering asymmetry and anomalous tunnel Hall effect at spin-orbit-split and exchange-split interfaces*, Phys. Rev. B **92**, 060403(R) (2015).

[442] T. H. Dang, D. Quang To, E. Erina, T. L. Hoai Nguyen, V. I. Safarov, H. Jaffrès, and H.-J. Drouhin, *Theory of the anomalous tunnel hall effect at ferromagnet-semiconductor junctions*, J. Magn. Magn. Mater. **459**, 37 (2018).

[443] V. V. Rylkov, S. N. Nikolaev, K. Y. Chernoglazov, V. A. Demin, A. V. Sitnikov, M. Y. Presnyakov, A. L. Vasiliev, N. S. Perov, A. S. Vedeneev, Y. E. Kalinin, V. V. Tugushev, and A. B. Granovsky, *Tunneling anomalous Hall effect in nanogranular CoFe-B-Al-O films near the metal-insulator transition*, Phys. Rev. B **95**, 144202 (2017).

[444] M. Y. Zhuravlev, A. Alexandrov, L. L. Tao, and E. Y. Tsymbal, *Tunneling anomalous Hall effect in a ferroelectric tunnel junction*, Appl. Phys. Lett. **113**, 172405 (2018).

[445] S. Mironov and A. Buzdin, *Spontaneous Currents in Superconducting Systems with Strong Spin-Orbit Coupling*, Phys. Rev. Lett. **118**, 077001 (2017).

[446] A. Costa, A. Matos-Abiague, and J. Fabian, *Skew Andreev reflection in ferromagnet/superconductor junctions*, Phys. Rev. B **100**, 060507(R) (2019).

[447] V. M. Edelstein, *Magnetoelectric Effect in Polar Superconductors*, Phys. Rev. Lett. **75**, 2004 (1995).

[448] V. M. Edelstein, *Triplet superconductivity and magnetoelectric effect near the s-wave-superconductor–normal-metal interface caused by local breaking of mirror symmetry*, Phys. Rev. B **67**, 020505(R) (2003).

[449] A. G. Mal'shukov and C. S. Chu, *Spin Hall effect in a Josephson contact*, Phys. Rev. B **78**, 104503 (2008).

[450] A. G. Mal'shukov and C. S. Chu, *Spin-Hall current and spin polarization in an electrically biased SNS Josephson junction*, Phys. Rev. B **84**, 054520 (2011).

[451] Y. Asano, *Spin current in p-wave superconducting rings*, Phys. Rev. B **72**, 092508 (2005).

[452] Y. Asano, *Josephson spin current in triplet superconductor junctions*, Phys. Rev. B **74**, 220501(R) (2006).

[453] C.-K. Lu and S. Yip, *Spin current and spin accumulation near a Josephson junction between a singlet and triplet superconductor*, Phys. Rev. B **80**, 024504 (2009).

[454] A. G. Mal'shukov, S. Sadjina, and A. Brataas, *Inverse spin Hall effect in superconductor/normal-metal/superconductor Josephson junctions*, Phys. Rev. B **81**, 060502(R) (2010).

[455] P. M. R. Brydon, Y. Asano, and C. Timm, *Spin Josephson effect with a single superconductor*, Phys. Rev. B **83**, 180504(R) (2011).
Erratum: Phys. Rev. B **85**, 139901(E) (2012).

[456] J. Wang, Z. H. Yang, Y. H. Yang, and K. S. Chan, *Spin and charge transport in hybrid triplet Josephson junctions*, Supercond. Sci. Technol. **24**, 125002 (2011).

[457] J. Wang, L. Hao, Y. H. Yang, and K. S. Chan, *Josephson Hall current in a noncentrosymmetric superconductor/ferromagnet/superconductor junction*, J. Appl. Phys. **110**, 113717 (2011).

[458] B. Bujnowski, C. Timm, and P. M. R. Brydon, *The Josephson effect between triplet superconductors through a finite ferromagnetic barrier*, J. Phys.: Condens. Matter **24**, 045701 (2012).

[459] C.-D. Ren and J. Wang, *Spin Josephson current in a ferromagnet/noncentrosymmetric superconductor junction*, Eur. Phys. J. B **86**, 190 (2013).

[460] M. Alidoust and K. Halterman, *Spontaneous edge accumulation of spin currents in finite-size two-dimensional diffusive spin–orbit coupled SFS heterostructures*, New J. Phys. **17**, 033001 (2015).

[461] T. Wakamura, H. Akaike, Y. Omori, Y. Niimi, S. Takahashi, A. Fujimaki, S. Maekawa, and Y. Otani, *Quasiparticle-mediated spin Hall effect in a superconductor*, Nat. Mater. **14**, 675 (2015).

[462] T. Yokoyama, *Anomalous Josephson Hall effect in magnet/triplet superconductor junctions*, Phys. Rev. B **92**, 174513 (2015).

[463] F. S. Bergeret and I. V. Tokatly, *Manifestation of extrinsic spin Hall effect in superconducting structures: Nondissipative magnetoelectric effects*, Phys. Rev. B **94**, 180502(R) (2016).

[464] J. Linder, M. Amundsen, and V. Risinggård, *Intrinsic superspin Hall current*, Phys. Rev. B **96**, 094512 (2017).

[465] V. Risinggård and J. Linder, *Direct and inverse superspin Hall effect in two-dimensional systems: Electrical detection of spin supercurrents*, Phys. Rev. B **99**, 174505 (2019).

[466] T. Yokoyama, *Transverse Josephson effect due to spin-orbit coupling: Generation of transverse current without time-reversal symmetry breaking*, arXiv: 1107.4202.

[467] J. A. Ouassou, S. H. Jacobsen, and J. Linder, *Conservation of spin supercurrents in superconductors*, Phys. Rev. B **96**, 094505 (2017).

[468] T. Hupfauer, A. Matos-Abiague, M. Gmitra, F. Schiller, J. Loher, D. Bougeard, C. H. Back, J. Fabian, and D. Weiss, *Emergence of spin–orbit fields in magnetotransport of quasi-two-dimensional iron on gallium arsenide*, Nat. Commun. **6**, 7374 (2015).

[469] P. Wachter, in *Handbook on the Physics and Chemistry of Rare Earths*, edited by K. A. Gschneidner Jr. and L. Eyring (North Holland, Amsterdam, 1979).

[470] Y. Zhi-Hong, Y. Yong-Hong, and W. Jun, *Interfacial spin Hall current in a Josephson junction with Rashba spin—orbit coupling*, Chin. Phys. B **21**, 057402 (2012).

[471] N. Satchell and N. O. Birge, *Supercurrent in ferromagnetic Josephson junctions with heavy metal interlayers*, Phys. Rev. B **97**, 214509 (2018).

[472] N. Satchell, R. Loloee, and N. O. Birge, *Supercurrent in ferromagnetic Josephson junctions with heavy-metal interlayers. II. Canted magnetization*, Phys. Rev. B **99**, 174519 (2019).

[473] J. R. Eskilt, M. Amundsen, N. Banerjee, and J. Linder, *Long-ranged triplet supercurrent in a single in-plane ferromagnet with spin-orbit coupled contacts to superconductors*, Phys. Rev. B **100**, 224519 (2019).

[474] B. Bujnowski, R. Biele, and F. S. Bergeret, *Switchable Josephson current in junctions with spin-orbit coupling*, Phys. Rev. B **100**, 224518 (2019).

[475] T. S. Khaire, M. A. Khasawneh, W. P. Pratt Jr., and N. O. Birge, *Observation of Spin-Triplet Superconductivity in Co-Based Josephson Junctions*, Phys. Rev. Lett. **104**, 137002 (2010).

[476] J. W. A. Robinson, J. D. S. Witt, and M. G. Blamire, *Controlled Injection of Spin-Triplet Supercurrents into a Strong Ferromagnet*, Science **329**, 59 (2010).

[477] W. L. McMillan, *Theory of Superconductor–Normal-Metal Interfaces*, Phys. Rev. **175**, 559 (1968).

Curriculum Vitae

Personal data

Name	**Andreas Costa**
Date of birth	November 15th, 1992
Place of birth	Viechtach
Nationality	German

Positions

2016 – present	University of Regensburg **Research and Teaching Assistant**

Education

2016 – 2020	**Postgraduate studies in Physics**
07/2016	**Master of Science in Physics** *Thesis title:* Spin-orbit coupling in Josephson junctions *Thesis advisor:* Prof. Dr. Jaroslav Fabian
07/2014	**Bachelor of Science in Physics** *Thesis title:* Andreev reflection in N/S and F/S junctions *Thesis advisor:* Prof. Dr. Jaroslav Fabian
2011 – 2020	University of Regensburg
07/2011	**Abitur**
2003 – 2011	Benedikt-Stattler-Gymnasium Bad Kötzting
1999 – 2003	Grundschule Bad Kötzting

List of Publications

2020

D. Kochan, M. Barth, A. Costa, K. Richter, and J. Fabian, *Spin Relaxation in s-Wave Superconductors in the Presence of Resonant Spin-Flip Scatterers*, Phys. Rev. Lett. **125**, 087001 (2020).

A. Costa and J. Fabian, *Anomalous Josephson Hall effect charge and transverse spin currents in superconductor/ferromagnetic-insulator/superconductor junctions*, Phys. Rev. B **101**, 104508 (2020).

2019

A. Costa, A. Matos-Abiague, and J. Fabian, *Skew Andreev reflection in ferromagnet/superconductor junctions*, Phys. Rev. B **100**, 060507(R) (2019).

2018

A. Costa, J. Fabian, and D. Kochan, *Connection between zero-energy Yu-Shiba-Rusinov states and* 0-π *transitions in magnetic Josephson junctions*, Phys. Rev. B **98**, 134511 (2018).

2017

A. Costa, P. Högl, and J. Fabian, *Magnetoanisotropic Josephson effect due to interfacial spin-orbit fields in superconductor/ferromagnet/superconductor junctions*, Phys. Rev. B **95**, 024514 (2017).

Acknowledgments

This thesis would not have been possible without all the people supporting me during my time as a PhD student. First and foremost, I want to thank Prof. Dr. Jaroslav Fabian for giving me the possibility to work on interesting projects in his research group, for his continuous scientific support and advice throughout the past years, and for the numerous opportunities to attend international schools and conferences.

Second, I would like to thank the theory colleagues in Regensburg and abroad with whom I collaborated on one or more projects, particularly Dr. Denis Kochan and Dr. Alex Matos-Abiague (Wayne State University Detroit), for many interesting discussions and their feedback on results and manuscript drafts. Moreover, I am grateful to Prof. Dr. Jagadeesh Moodera (MIT) for extending my theoretical viewpoint to practical difficulties arising in experiments, our productive ongoing experiment-theory collaboration on Josephson junctions' peculiar conductance features, and for his kind invitation to visit his institute and the guided tour through his labs.

I also want to mention the inspiring meetings with the Richter group's superconducting transport team consisting of Michael Barth and Jacob Fuchs. I really enjoyed the insight into your exciting projects and benefited a lot from your KWANT expertise.

I acknowledge financial support from the Elite Network of Bavaria through the International Doctorate Program *Topological Insulators*, from the European Union's Horizon 2020 research and innovation programme *Graphene Flagship*, and from Deutsche Forschungsgemeinschaft (DFG; German Research Foundation) through SFB Grants 689 and 1277.

Finally, I want to thank all others who contributed to this thesis with their mental support, especially my friends and loved ones.